POLARIZATION PATTERNS IN NATURE

Imaging Polarimetry with Atmospheric Optical and Biological Applications

D.Sc. Thesis

Doctor of the Hungarian Academy of Sciences

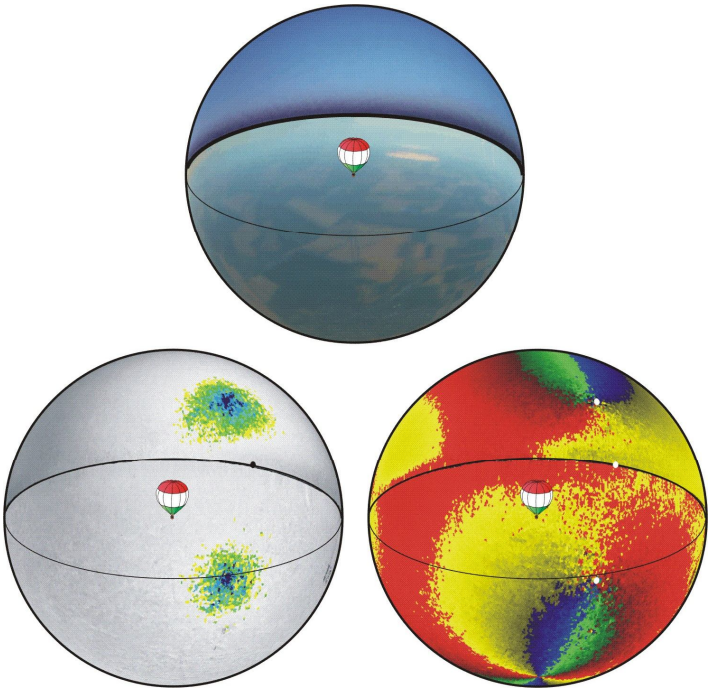

Dr. habil. Gábor Horváth

Loránd Eötvös University
Faculty of Natural Sciences
Department of Biological Physics
Biooptics Laboratory

Budapest, Hungary

7 September 2003

Caption for the Cover Picture

Patterns of the radiance I (top), degree of linear polarization p (bottom, left) and angle of polarization α (bottom, right) of skylight and earthlight displayed on the surface of a sphere and measured by 180^{o} field-of-view imaging polarimetry in the blue (450 nm) part of the spectrum from a hot air balloon at an altitude of 4000 m. In the p- and α-patterns the dots from the top toward the bottom show the positions of the Arago neutral point, the antisolar point and the fourth neutral point, respectively. The colour codes of p and α are given in Fig. 7.4.7. More details can be found in Chapter 7.4.

PREFACE

This treatise summarizes my results achieved in the fields of imaging polarimetry and insect polarization sensitivity. Its subject is twofold: it gathers typical polarization patterns occurring in the nature and surveys some polarization-sensitive insects and their polarization-guided behaviour. My research attempts to build a bridge between these two physical and biological fields. The majority of this treatise is part of my monograph entitled *Polarized Light in Animal Vision – Polarization Patterns in Nature* written together with my friend and mentor, Professor Dezső Varjú (from the University of Tübingen, Germany), and published recently by the Springer-Verlag.

Imaging polarimetry helps to understand and reveal the message hidden in polarization patterns of the optical environment not directly accessible to the human visual system, but measurable by polarimetry and perceived by many animal species. This technique can be efficiently used e.g. in atmospheric optics, remote sensing and biology. Earlier, the polarizational characteristics of natural optical environments could be presented only in form of graphs or pairs of photographs taken through linear polarizers with two orthogonal directions of their transmission axes. Due to the imaging polarimetric methods developed by me, the polarization patterns can be visualized as high resolution colour-coded maps of the degree and angle of linear polarization of light.

In the first half of the treatise (Chapters 1–15), after giving a brief history of the discovery of phenomena concerning light polarization, I deal with typical polarization patterns of the natural optical environment. Sunrise/sunset, clear skies, cloudy skies, moonshine and total solar eclipses all mean quite different illumination conditions, which affect the spatial distribution and strength of celestial polarization. I present the polarization patterns of the sky and its unpolarized (neutral) points under sunlit, moonlit, clear, cloudy and eclipsed conditions as a function of the solar elevation. The polarization pattern of a rainbow is also shown. That part of the spectrum is derived in which perception of skylight polarization is optimal under partly cloudy skies. The reader becomes acquainted with the polarization of the solar corona and can follow how the polarization pattern of the sky changed during a total solar eclipse. I also treat the polarizational characteristics of water surfaces, mirages and certain aspects of the underwater polarized light field. It is explained why water insects are not attracted by mirages.

The second half of the treatise (Chapters 16–24) is devoted to the description of some typical behavioural mechanisms indicating how insects use certain natural polarization patterns. I present several case studies of known behavioural patterns in insects determined or influenced by polarization sensitivity. The role of the reflection-polarization patterns of water surfaces in the water detection by insects is discussed. I illustrate how reflection-polarization patterns of anthropogeneous origin can deceive water-seeking polarotactic insects. The natural environment is more or less affected by the human civilization and is overwhelmed by man-made objects, such as crude or waste oil surfaces, asphalt roads, glass surfaces, or plastic sheets used in the agriculture, for instance. I explain why these surfaces are more attractive to water-seeking polarotactic insects than the water surface itself. I reveal why do mayflies or dragonflies lay their eggs *en masse* on dry asphalt roads or car-bodies. I show how dangerous

can open-air oil reservoirs be for polarotactic insects and why do oil surfaces function as efficient insect traps. Some other biological functions of polarization sensitivity, such as contrast enhancement and camouflage breaking, for instance, are also discussed. I also present my experimental results on the polarization-sensitive optomotor reaction in two water insect species. Due to the interference of polarization and colour sensitivity, polarization-induced false colours could be perceived by polarization- and colour-sensitive visual systems. I calculate and visualize these false colours by means of a computer model of butterfly retinae, and investigate their chromatic diversity. On the basis of my polarimetric measurements in the field I explain why is it worth flying at dusk for polarotactic water-seeking acquatic insects. Finally, some misinterpretations, misleading nomenclatures, misbelieves and errors concerning polarized light and polarization sensitivity are discussed and corrected.

In addition to reliance on my own contributions to the field, I have quoted from the numerous publications of many other investigators with appropriate reference given in each case. While the bibliography at the end of this treatise is not complete, it is fairly representative of the field.

Gábor Horváth Göd (Hungary), 7 September 2003

ACKNOWLEDGMENTS

To write this work I received an essential financial support from the German Alexander von Humboldt Fundation, providing me with a Humboldt research fellowship for spending 14 months at the Department of Cognitive Neuroscience of the Eberhard Karls University in Tübingen under the supervision of Professor Dezső Varjú. I am very much indebted. Many thanks also to Professor Hanspeter Mallot, head of the Department of Cognitive Neuroscience. He provided me with equipments and materials I needed. The secretarial and informatical assistance of Mrs. Annemarie Kehrer and Dr. Heinz Bendele, furthermore the valuable discussions with Dr. Hansjürgen Dahmen at the Department of Cognitive Neuroscience are kindly appreciated. My three-year István Széchenyi scholarship from the Hungarian Ministry of Education is also very much acknowledged.

I am very grateful to the following scientist for providing me with important literature and professional advice: K.P. Able, S. Akesson, E.J.H. Bechara, H.I. Browman, M.A.J.M. Coemans, T. Cronin, M. Dacke, R.B. Forward, M. Freake, W. Haupt, C.W. Hawryshyn, F.I. Hárosi, U. Homberg, G.W. Kattawar, A. Kelber, K. Kirschfeld, G.P. Können, T. Labhart, M.F. Land, R.L. Lee Jr., D.K. Lynch, E.P. Meyer, V.B. Meyer-Rochow, F.R. Moore, U. Munro, D.E. Nilsson, I. Novales-Flamarique, J.F.W. Nuboer, S. Rossel, R. Schwind, N. Shashar, A. Ugolini, K.J. Voss, J.A. Waldvogel, T.H. Waterman, R. Wehner, H. Wildermuth, W. Wiltschko, J. Zeil.

The financial support of the Hungarian Science Foundation (grant numbers: OTKA F014923, T020931, F025826) is acknowledged.

I am also grateful to the following students and colleagues for their continuous help during the polarimetric measurements in the field and the evaluation and visualization of the polarization patterns: András Barta, Balázs Bernáth, Ferenc Mizera, Gergely Molnár, Bence Suhai, Gábor Szedenics, Drs. Sándor Anrikovics, József Gál, Ottó Haiman, György Kriska and István Pomozi.

The polarimetric measurements in Finland, in the Tunisian desert and in Switzerland were possible due to fruitful cooperations with Professors Viktor Benno Meyer-Rochow, Rüdiger Wehner and Hansruedi Wildermuth, respectively. Many thanks are for their financial support, valuable help and encouragement.

My parents, Mária Fischer and János Horváth rendered me indispensable help and support during the field experiments in the Hungarian Great Plain (Kiskunhalas, Kecel and Kunfehértó).

Finally, I am very much indebted to my wife, Zsuzsanna Horváth-Tatár, who ensured the ideal and quiet familiar atmosphere, which was the most important prerequisite of this work.

TABLE OF CONTENTS

1 Brief History of the Discovery of Phenomena Concerning Light Polarization

In this preliminary chapter the main landmarks in the evolution of ideas and the discovery of phenomena concerning the light polarization are summarized. The survey consists of data taken from Shurcliff (1962), Gehrels (1974), Können (1985), Coulson (1988) and Born and Wolf (1999). Many further important steps and discoveries in connection with polarization, not listed here, are mentioned and discussed in the appropriate chapters of this work. Generally, historical notes and references are given at the start of many of these chapters. It is a widespread belief that the history of light polarization began with the Vikings, who are supposed to have used certain enigmatic birefringent crystals to analyse the skylight polarization for navigational purposes. Since the alleged Viking navigation by skylight polarization has no any culture historical or archeological evidence, we start the history of polarization with 1669 when Bartholinus discovered the birefringence of the calc-spar.

- The history of light polarization began with the Danish physicist, physician and mathematician, Erasmus Bartholinus (1625-1698), who in **1669** discovered the phenomenon of double refraction of calc-spar (or Iceland spar, a variety of calcite), although he was not yet aware of the phenomenon of polarization.
- Christian Huygens (1629-1695) Dutch physicist and astronomer interpreted the double refraction by assuming that in the crystal there is, in addition to a primary spherical wave, a secondary ellipsoidal wave. It was in the course of this investigation that Huygens made the fundamental discovery of polarization in **1690**: each of the two rays arising from refraction by calcit may be extinguished by passing it through a second crystal of the same material if the latter crystal is rotated about the direction of the ray.[1] Isaac Newton (1642-1727) English physicist, astronomer and mathematician explained these phenomena by assuming that rays have "sides". Due to this "transversality" rejected Newton the wave theory of light – proposed by Robert Hooke (1635-1703) English physicist and chemist, and improved and extended later by Huygens –, since at that time scientists were familiar only with longitudinal waves from the propagation of sound.

[1] Huygens C (1690) Traité de la lumiére. Leyden (completed in 1678, published in 1690)

- Étienne Louis Malus (1775-1812) French engineer discovered the polarization of light by reflection[2]: One evening in **1808** he observed the reflection of direct sunlight from a window pane through a calcit crystal, and found that the two images obtained by double refraction varied in relative intensities as the crystal was rotated about the line of sight. However, Malus did not attempt to interpret this phenomenon. He formulated the Malus law, that is, the proportionality of the intensity of light transmitted by a polarizer to the square of the cosine of the angle of direction of the transmission axis for linearly polarized incident light. In fact, Malus applied as first the term "polarization" to light. He hypothesized that the light corpuscles were aligned after reflection in a manner similar to the way magnetic bodies are aligned by the poles of a magnet.
- In **1809** Dominique Francois Jean Arago (1786-1853) French physicist and astronomer discovered the polarization of light from the clear blue sky.[3] Later he established that the skylight polarization is maximal at 90^{o} from the sun and found the first neutral point of the firmament, later named after him.
- In **1811** Arago observed the optical activity of quartz, and Jean Baptiste Biot (1774-1862) French physicist discovered the high polarization of the rainbow.
- In **1812** Arago constructed a filter from a pile of glass sheets.
- In **1815** Biot established the optical activity of certain liquids (e.g. turpentine) and discovered the strong dichroism of tourmaline crystals. In the same year, David Brewster (1781-1868) Scottish physicist discovered the law giving the relationship between the refractive index of a medium and the angle of incidence at which reflected light is totally linearly polarized. However, in 1810 Malus was the first, who recognized the existence of such an angle in the reflection of light from the water surface.
- Together with Arago, Augustin Jean Fresnel (1788-1827) French physicist and engineer investigated the interference of polarized rays of light and found in **1816** that two rays polarized at right angles to each other never interfere.[4] This fact could not be reconciled with the assumption of longitudinal waves of light, which had hitherto been taken for granted. Thomas Young (1773-1829) English physicist and physician, who had heard of this discovery from Arago, found in **1817** the key to the solution when he assumed that the vibrations were transverse.
- In **1818** Biot observed the optical activity of gaseous turpentine, and Brewster discovered the coloured brush in pleochroic crystals, later named after him.
- In **1819** Arago discovered the polarization of light from comet tails.

---

[2] Malus ÉL (1809) Sur une propriété de la lumiére réfléctie par les corps diaphanes. Nouveau Bull d Sci, par la Soc Philomatique (Paris) 1:266-269; Mém de la Soc d'Arcueil 2

[3] Barral MJA (1858) Oeuvres de Francois Arago I-V., Gide - Paris, Weigel - Leipzig

[4] Fresnel AJ (1866-1870) Oeuvres Complétes d'Augustin Fresnel (Paris) 1:767

- In **1824** Arago observed the polarization of light emitted by incandescent metals.[5] He discovered also the polarization of moonlight and found higher polarization on the maria than on the highlands.
- In **1825** Arago established the polarization of 22° haloes.
- In **1828** William Nicol (1768-1851) Scottish physicist invented a prism, which was the first easily usable polarizing filter.
- Dynamical models of the mechanism of aether[6] vibrations led Fresnel (**1832**, 1866-1870) to deduce the laws which now bear his name, governing the intensity and polarization of reflected and refracted light.
- In **1840** Jacques Babinet (1794-1872) French physicist and meteorologist discovered the second neutral point of the celestial hemisphere, bearing his name nowadays.[7] According to Coulson (1988, p. 5), the lateness of the discovery of the Babinet point is surprising in view of the previous interest in skylight polarization and the fact that this neutral point is not difficult to see with the Savart polariscope which was in use at that time.
- In **1842** Brewster discovered the third neutral point of skylight polarization, later named after him.[8]
- In **1844** Wilhelm Karl von Haidinger (1795-1871) Austrian physicist, geologist and mineralogist discovered that the human eye is able to perceive the linear polarization of light due to an entoptic phenomenon (Haidinger brushes).[9] Later he also discovered circular dichroism in crystals of amethyst and quartz.
- In **1845** Michael Faraday (1791-1867) English physicist and chemist discovered the rotation of the plane of linear polarization of light in magnetic fields.
- In **1848** Louis Pasteur (1822-1895) French physician and chemist described optically active hemihedral crystals.
- In **1852** W. B. Herapath English physician constructed a synthetic crystal (a drug combination of iodine and quinine) with very high dichroism and optical properties similar to those of tourmaline. This later became the basis of the manufacture of simple sheet polarizers. In the same year, George Gabriel

[5] Arago DFJ (1824) Ann Chem Phys (2) 27:89 [reference from Sandus O (1965) A review of emission polarization. Appl Opt 4:1634-1642]

[6] René Descartes (1596-1650) French scientist considered light to be essentially a pressure transmitted through a perfectly elastic solid medium, the aether filling all space. In that time scientists tried to explain all natural phenomena by mechanical laws: light was considered as the rapid vibration of aetherial particles. In spite of many difficulties, the theory of aether persisted for a long time and most of the great physicists of the 19th century contributed to it.

[7] Babinet J (1840) Sur un nouveau point neutre dans l'atmosphere. Compt Rend 11:618-620

[8] Brewster D (1842) On the existence of a new neutral point and two secondary neutral points. Rept British Assoc Adv Sci 2:13

[9] Haidinger W (1844) Über das direkte Erkennen des polarisierten Lichts und der Lage der Polarisationsebene. Annal Phys (Leipzig) 63:29-39

Stokes (1819-1903) Irish physicist described the four Stokes parameters of polarized light.[10]

- In **1858** Emmanuel Liais (1826-1900) French astronomer discovered the linear polarization of the solar corona.
- In **1860** Gustav Robert Kirchhoff (1824-1887) German physicist found that incandescent tourmaline emits polarized light due to dichroism.[11]
- In **1869** John Tyndall (1820-1893) Irish physicist established the fact that the polarization of light scattered by particles changes strongly with the dimensions of the particles, explaining earlier observations on smoke particles.
- In **1871** John William Strutt, alias Lord Rayleigh (1842-1919) English physicist explained theoretically the polarization of scattered skylight.[12]
- In **1872** William Parsons, alias Lord Rosse (1800-1867) Irish astronomer found that the light from the Venus is slightly polarized.
- In **1873**, according to theoretical considerations, James Clerk Maxwell (1831-1879) Scottish theoretical physicist has conjectured that light is an electromagnetic wave.[13]
- In **1874** A. W. Wright American astronomer discovered the polarization of zodiacal light.[14]
- In **1875** John Kerr (1824-1907) Scottish physicist discovered the birefringence of electrified media (Kerr effect). Later he also established changes in metallic reflection of polarized light in the presence of magnetic fields (Kerr magneto-optic effect).
- In **1884** J. Kiessling German physicist discovered the polarization of the glory.[15]
- In **1888** Heinrich Hertz (1857-1894) German physicist verified by direct experiments that light is an electromagnetic wave.[16]

---

[10] Stokes GG (1852) On the composition and resolution of streams of polarized light from different sources. Trans Cambr Phil Soc 9:233-258

[11] Kirchhoff GR (1860) Pogg Ann 109:299 [reference from Pflüger A (1902) Prüfung des Kirchhoff'schen gesetzes an der Emission und Absorption glühenden Turmalins. Ann Phys 7:806-817]

[12] Strutt JW (Lord Rayleigh) (1871) On the light from the sky, its polarisation and colour. Phil Magaz 41:107-120, 274-279

[13] Maxwell JC (1873) A treatise on electricity and magnetism. Oxford, 2 vols

[14] Wright AW (1874) On the polarization of the zodiacal light. Am J Sci Arts (3rd ser) 7:451-459 [reference from Weinberg JL (1974) Polarization of the zodiacal light. In: Gehrels T (1974) pp 781-793]

[15] Kiessling J (1884) Abh Naturw Ver Hamburg-Altona III, abt 1; Kiessling J (1885) Zur Erklärung der ringförmigen Gegen-Dämmerung. Meteorol Z 2:70-72 [references from Meyer R (1942-1961) Optik der Tropfen I., Abschnitt 2: Kränze, Glorien und verwandte Erscheinungen, Handbuch der Geophysik, Kapitel 14, Band 8, Physik der Atmosphäre I., Linke F, Möller F (eds), Gebrüders Bornträger, Berlin, pp 898-942]

[16] Hertz H (1888) Wiedem Ann 34:551 (English translation in his Electric Waves, 1893, Macmillan, London, p. 107)

- In **1889** Marie Alfred Cornu (1841-1902) French physicist observed that artificial haloes in sodium nitrate crystals are highly polarized because of the double refraction of the crystals.
- In **1896** Pieter Zeeman (1865-1943) Dutch physicist found that spectral lines can be broadened when the radiating atoms are in the presence of an intense magnetic field. He observed later the splitting of spectral lines by magnetic fields and their associated polarization (Zeeman effect).
- In **1905** N. A. Umow (1846-1915) Russian physicist described the relationship between the degree of linear polarization of light reflected from rough surfaces and the albedo of the surface.[17]
- In **1908** George Ellery Hale (1868-1938) American astronomer showed the existence of strong magnetic fields in sunspots by means of polarization measurements of the Zeeman effect. In the same year, Gustav Mie (1868-1957) German physicist and Pieter Debye (1884-1966) Dutch-American physicochemist independently developed the theory of light scattering by spherical particles of arbitrary size.
- In **1911** Albert Abraham Michelson (1852-1931) American astronomer discovered the circular polarization of light reflected from the carapace of certain beetles.[18]
- In **1928** Edwin Herbert Land (1909-1991) American physicist constructed his first successful sheet-type dichroic linear polarizer (as an undergraduate student at the Harvard University).[19]
- In **1929** Bernard Lyot (1897-1952) French astronomer published his discoveries on the linear polarization of light from planets and terrestrial objects.
- In **1935** Richard Beth discovered that circularly polarized light exerts a slight mechanical torque on materials and thus proved directly the rotating character of the electric field vector of such light.
- In **1939** Y. LeGrand French and K. Kalle German physicists reported independently of each other that underwater scattered light is linearly polarized.[20]
- In **1940** J. Bricard French meteorologist observed that supernumerary fog-bows shift when one looks at them through a rotating linear polarizer.[21]
- In **1942** Yngve Öhman found polarized light emitted by the galaxy M31.
- In **1947** H. C. van de Hulst Dutch physicist gave a feasible explanation of the glory and explained its directions of polarization.

---

[17] Umow N (1905) Chromatische Depolarisation durch Lichtzerstreuung. Phys Z 6:674-676

[18] Michelson AA (1911) On the metallic colour of birds and insects. Phil Magaz 21:554

[19] Land EH (1951) Some aspects of the development of sheet polarizers. J Opt Soc Am 41:957-963

[20] LeGrand Y (1939) Ann Inst Océanolog Monaco 19:393; Kalle K (1939) Die Farbe des Meeres. Rapports et procès-verbaux des Reunions. Conseil permanent international pour exploration de la mer 109(3):98-105 [references from Waterman TH (1954) Polarization patterns in submarine illumination. Science 120:927-932]

[21] Bricard J (1940) Contribution a l'étude des brouillards naturels. Ann Phys 14:148-236

- In **1948** Hans Mueller German physicist developed a phenomenological calculus to problems involving wide-band partially polarized light, using 4×4 matrices (Mueller matrix and Mueller calculus).[22]
- In **1949** Karl von Frisch (1886-1982) Austrian zoologist discovered the polarization sensitivity of honeybees.[23] In the same year, J. S. Hall and W. A. Hiltner found that the light from stars is polarized.
- In **1950** Subrahmanyan Chandrasekhar (1910-1995) Indian-American physicist and astronomer gave a solution of radiative transfer in a sunlit plane-parallel planetary atmosphere with Rayleigh scattering.[24] In **1960** the solutions were tabulated in convenient form by Kinsell L. Coulson, J. V. Dave and Zdenek Sekera.[25]
- In **1954** V. A. Dombrovskij Russian astronomer discovered the strong polarization of the Crab Nebula predicted with synchrotron radiation by the Russian astronomer I. S. Shklovskij. In the same year, Talbot H. Waterman American biologist rediscovered the underwater polarization.[26]
- In **1955** William A. Shurcliff discovered that the human eye is also capable of perceiving circularly polarized light (Shurcliff brushes).[27]
- In **1956** Lionel Jaffe American biologist discovered that, when certain algae cells are illuminated by linearly polarized light, they tend to develop in the direction of vibration.[28]
- In **1959** R. A. Duncan Australian meteorologist reported on the polarization of the aurora.[29] However, in later correspondence between Duncan and Günther P. Können (personal communication) this claim was disputed. Thus, the claim of Duncan is probably untrue, so the auroral light may be unpolarized.
- In **1960** Georg Witt Swedish meteorologist established the polarization of noctilucent clouds.[30]
- In **1974** the first comprehensive monograph, edited by T. Gehrels American astronomer, was published about planets, stars and nebulae studied with photopolarimetry.[31]

---

[22] Mueller H (1948) The foundation of optics. (abstr, Proc Wint Meet OSA, New York, 4-6 March 1948) J Opt Soc Am 38:661

[23] Frisch K von (1949) Die Polarisation des Himmelslichtes als orientierender Faktor bei den Tänzen der Bienen. Experientia 5:142-148

[24] Chandrasekhar S (1950) Radiative transfer. Clarendon Press, Oxford

[25] Coulson KL, Dave JV, Sekera Z (1960) Tables related to radiation emerging from a planetary atmosphere with Rayleigh scattering. Univ California Press, Berkeley Los Angeles

[26] Waterman TH (1954) Polarization patterns in submarine illumination. Science 120:927-932

[27] Shurcliff WA (1955) Haidinger's brushes and circularly polarized light. J Opt Soc Am 45:399

[28] Jaffe L (1956) Effect of polarized light on polarity of Fucus. Science 123:1081-1082

[29] Duncan RA (1959) Polarization of the red oxygen auroral line. Planet Space Sci 1:112-120

[30] Witt G (1960) Polarization of noctilucent clouds. J Geophys Res 65:925-933 (1960)

- In **1977** Günther P. Können Dutch meteorologist discovered the strong polarization of the inner-edges of refraction halos.[32]
- In **1985** G. P. Können published his famous book about polarized light in nature.[33] In the same year appeared the monograph of the American physicist Walter G. Egan about photometry and polarization in remote sensing.[34]
- In **1988** appeared the comprehensive monograph of the American meteorologist, Kinsell L. Coulson on polarization and intensity of light in the atmosphere.[35]
- In **1989** R. M A. Azzam and N. M. Bashara American physicists published their book dealing with ellipsometry and polarized light.[36]
- In **1990** the comprehensive book edited by Jin Au Kong was published about polarimetric remote sensing.[37]
- In **1993** was published the book of the American physicist Edward Collett on the fundamentals and applications of polarized light.[38]
- In **1999** Gábor Horváth, István Pomozi and József Gál Hungarian physicists discovered several neutral points of skylight polarization during the totality of a solar eclipse.[39]
- In **2001** G. Horváth and his students (András Barta, Balázs Bernáth and Bence Suhai) observed as first the fourth (the last) neutral point of atmospheric polarization from a hot air balloon.[40]
- In **2003** G. Horváth and Dezső Varjú published their monograph about polarized light in animal vision and polarization patterns in nature.[41]

---

[31] Gehrels T (ed) (1974) Planets, stars and nebulae studied with photopolarimetry. Univ Arizona Press, Tucson, Arizona

[32] Können GP (1977) Polarisation of haloes and double refraction. Weather 32:467-468

[33] Können GP (1985) Polarized light in nature. Cambridge Univ Press, Cambridge

[34] Egan WG (1985) Photometry and polarization in remote sensing. Elsevier, Amsterdam New York

[35] Coulson KL (1988) Polarization and intensity of light in the atmosphere. A Deepak Publishing, Hampton, Virginia, USA

[36] Azzam RMA, Bashara NM (1989) Ellipsometry and polarized light. North-Holland, Amsterdam, New York

[37] Kong JA (ed) (1990) Polarimetric remote sensing. Progress in Electromagnetics Research, Elsevier, Amsterdam London New York

[38] Collett E (1993) Polarized light: fundamentals and applications. Marcel Dekker Inc, New York

[39] Horváth G, Pomozi I, Gál J (2003) Neutral points of skylight polarization observed during the total eclipse on 11 August 1999. Appl Opt 42:465-475

[40] Horváth G, Bernáth B, Suhai B, Barta A, Wehner R (2002) First observation of the fourth neutral polarization point in the atmosphere. J Opt Soc Am A 19:2085-2099

[41] Horváth G, Varjú D (2003) Polarized light in animal vision – polarization patterns in nature. Springer, Berlin Heidelberg New York

2 Polarimetry: From Point-Source to Imaging Polarimeters

Biologists dealing with polarization sensitivity of animals, or engineers designing robots using polarization-sensitive imaging detectors to enhance the contrast of objects, for example, need a technique to measure the spatial distribution of polarization in the optical environment. In the 1980's, 1990's and early 2000's, different kinds of imaging polarimetry have been developed to measure the polarization patterns of objects and natural scenes in a wide field of view. The conventional non-imaging point-source polarimeters average polarization over an area of a few degrees only. The conception of "polarization imagery" or "imaging polarimetry" was introduced by Walraven (1977, 1981), capitalizing on the commercial availability of relatively low-cost products and processes to obtain high-resolution information about the polarized components of the skylight radiance. There are two different approaches to build imaging polarimeters:

1. either using a point-source polarimeter with a scanning unit (e.g. Dreher et al. 1992),
2. or substituting the routinely used point-source photodetector by a camera (e.g. Pezzaniti and Chipman 1995).

As a further development of the latter technique, the addition of depth to two-dimensional pictures displaying the spatial distribution of polarization was realized by Mizera et al. (2001), who designed one kind of stereo video polarimetry to measure and visualize in three dimensions the polarization patterns in nature and to mimic the ability of animal eyes to receive visual information from a binocular field of view. Table 2.1 summarizes the most important properties of imaging polarimeters built by different researchers and used for various purposes. In Chapters 2-6 these imaging polarimeters are briefly described after a short introduction into the basic elements of polarimetry and its evolution.

Imaging polarimetry can be efficiently used in all fields of basic research, technology and industry, where the state of polarization of light is an important information. Below some possible applications of polarization are listed, where also imaging polarimetry is routinely used or could be applied in the future:

- stereo cinematography
- studying animal polarization sensitivity
- astronomy (e.g. Gehrels 1974), solar physics (e.g. Beckers and Wagner 1970), spectroscopy (e.g. Kliger et al. 1990), radar polarimetry (e.g. Boerner et al. 1992)
- aerial reconnaissance and automatic target recognition, camouflage breaking (e.g. detections of camouflaged tanks or mines) (e.g. Cariou et al. 1990)
- remote sensing of oil on sea waters (Kondratyev et al. 1974): The detection of regions of the sea surface polluted by an oil film can be improved by airborne polarimetric measurements performed in different spectral ranges, at different directions of view relative to the sun and at various viewing angles from the horizontal, since there is a polarization contrast between the clean and polluted water surface.
- estimation of soil moisture (Curran 1978, 1979), discrimination between vegetation and soil, classification of different vegetation and soil types, determination of plant/canopy form and orientation (Curran 1982; Buschmann 1993), growth stage estimation of grain crops (Fitch et al. 1984), measurement of the reflection-polarizational characteristics of plant leaves as a function of the leaf surface features (Shul'gin and Moldau 1964; Vanderbilt and Grant 1985a,b; Vanderbilt et al. 1985a,b; Grant et al. 1987a,b; Sarto et al. 1989)
- quality inspection and control of materials during manufacturing, material classification: from the way materials alter the state of polarization of light passing through them, information can be obtained about their crystalline structure or weaknesses (mechanical tensions) in them can be detected.
- discrimination between dielectric and metal materials by illuminating them with light of known polarizational characteristics and measuring the polarization of reflected light (Wolff 1990)
- image segmentation (e.g. quantitative separation of specular and diffuse reflection components), identification of occluding contours, detection of orientation of objects and surfaces (Wolff and Boult 1991)
- polarization-based determination of shape (Koshikawa and Shirai 1987; Jones and Fairney 1989)
- ophthalmology: measurement of the birefringent, dichroic and polarizational characteristics of the ocular media (cornea, lens, vitreous, retina) of the human eye
- polarization-based contrast enhancement (Kalayjian et al. 1996)
- autonomous navigation (Lambrinos et al. 1997)
- robot vision: Consider the problem of an autonomous land vehicle viewing a scene, part of which is reflected by a flat lake or river. How does the vehicle know which are the real elements of the scene? How does a mobile robot know when it is running into a glass door, or if navigating according to edge cues, which are geometric edge cues opposed to specular ones? These non-trivial problems can be solved by using the measured polarization patterns of the scene, because the real objects and their mirror images can be distinguished on

the basis of the differences between their polarizational characteristics (Wolff 1993).
- remote sensing of polarized light in atmospheric physics and meteorology (e.g. Fraser 1968, 1981; Egan and Sidran 1994)

2.1 Different Ways of Qualitative Demonstration of Polarization in the Optical Environment

The presence of linearly or circularly polarized light in the optical environment can be qualitatively demonstrated by the use of a linearly or circularly polarizing filter. Looking through such a filter and rotating it in front of our eyes, the change of intensity of light coming from certain directions may be observed. This intensity change is an unambiguous sign of the polarization of light. If we take colour photographs from a scene through linear polarizers with differently oriented transmission axes and compare them, striking intensity and colour differences may occur in those regions, from which highly polarized light originates, furthermore the brightness and colour contrasts may change drastically between different parts of the scene (Figs. 2.1 and 2.2). This simple way of demonstration of the occurrence of polarized light in nature, that is, translating polarization into brightness and colour shade differences for the human eye, is frequently used in the scientific as well as popular literature (e.g. Wehner 1976, 1982, 1997; Harkness and Wehner 1977; Lythgoe 1979; Schwind 1985b; Können 1985, 1986, 1992; Coulson et al. 1986; Curran 1978, 1979; Land 1993).

Können (1985, 1986, 1992), for instance, published numerous pairs of colour photographs of natural scenes taken through a common linearly polarizing filter directed in such a way that in the first and second picture the polarizer maximally transmitted and extinguished the light from a selected region of the scene, respectively, with the transmission axes perpendicular to each other. In the first picture, where the filter was maximally transmissive, the appearance of the selected region did not differ very much from that viewed with the naked eye, while in the second picture, where the filter was in a direction of maximal extinction, the most striking differences between the scenes viewed with and without a polarizer occurred.

During four Space Shuttle missions Coulson et al. (1986) took photographs about the earth surface with a pair of cameras, both of which contained a linearly polarizing filter with different orientation of the transmission axis. Some qualitative data could have been deduced from the comparison of the obtained picture pairs.

Since for a complete imaging polarimetry at least three "polarizational pictures" are needed if the circular polarization is negligible (see Chapters 2.2, 2.4 and 2.5), these methods are, of course, inappropriate for quantitative measurement of the radiance as well as the degree and angle of linear polarization. The mentioned pairs of polarizational pictures can be considered as the forerunners of imaging polarimetry. If the cited authors had have also taken a third photograph of the

investigated scene with a third orientation of the transmission axis of the polarizer (similarly as in Figs. 2.1 and 2.2), the resulting triplet could have been the basis of an imaging polarimetric evaluation procedure.

Using triangles cut from a sheet of linearly polarizing filter, Karl von Frisch (1953, 1965, 1967) has constructed a simple device, the so-called "Sternfolie" ("star foil"), with which the gross distribution of linear polarization of skylight could be demonstrated (Fig. 2.3). This pioneering instrument was used by Frisch to investigate qualitatively the degree and angle of linear polarization of skylight, which was important to interpret the results of his behavioural experiments with honeybees. Wehner (1976, 1982, 1997), Harkness and Wehner (1977) as well as Lythgoe (1979), for example, took photographs of the full sky by using a 180^{o} field-of-view fisheye lens equipped with a linear polarizer to portray qualitatively the celestial polarization pattern for different solar elevations, as did Können (1985) in his book on polarized light in nature.

A linear polarizer with constant direction of its transmission axis must be rotated in front of the eye in order to perceive the change of intensity of transmitted light if the incident light is polarized. Then the angle of polarization of light coming from a given direction of view can be estimated by finding that orientation of the known transmission axis, at which the transmitted light is the brightest. There is, however, a simpler way to find the E-vector direction. Using a so-called "radial linearly polarizing filter" (the transmission axis of which runs along concentric circles rather than along parallel straight lines), the intensity of transmitted light along each circular transmission axis changes sinusoidally for every 180^{o} turn, if the state of partial linear polarization of the incident light beam is the same across the filter. A characteristic cross-shaped brightness pattern is visible looking through such a radial polarizer (see Fig. 2.4A). The centre of the cross coincides with that of the filter, and the darkest and brightest axes of the cross are the directions where the E-vector of linearly polarized incident light is perpendicular and parallel to the circular transmission axes of the filter, respectively. Due to this feature, radial polarization filters are termed often as "axis finders", since the darkest axis of the seen brightness cross tells the orientation of the transmission axis of another common (non-radial) linearly polarizing filter held in front of the radial one. From the cross pattern produced by a radial filter also the degree of linear polarization can be qualitatively estimated: the greater the contrast between the darkest and brightest axes of the cross, the higher the degree of polarization. If the incident light is unpolarized, a homogeneous brightness pattern is seen across a radial filter.

Figure 2.4A shows a photograph of the entire celestial hemisphere taken by Wehner (1994b, 1997, 1998) with the use of a set of 41 axis-finders, which were mounted on a transparent Plexiglas dome (Fig. 2.4B). Wolff (1993) suggested to build a low-cost "one-big-pixel polarization camera", using such an axis-finder to automate the computation of the state of partial linear polarization of light. A radial filter makes it possible to simultaneously measure the angle of polarization as well as the maximum and minimum of transmitted intensity, from which the degree of linear polarization can be derived.

Some of the above examples demonstrate also the need of quantitative information about the distribution of polarization over the whole sky, for instance. Until only such qualitative techniques and point-source scanning polarimeters existed, the polarization pattern of the whole sky under a given meteorological situation could not have been measured. Thus, earlier the distribution of polarization over the full sky could be represented only by maps obtained either by numerical simulations (Fig. 2.5), or by gathering and averaging data from the sky during an extended period restricted to certain advantageous meteorological conditions (e.g. clear skies). The polarization pattern of the entire sky at a given, often quickly changing atmospheric situation can be measured only by simultaneous full-sky imaging polarimetry, the most novel technique of recent development (Horváth et al. 2002a).

What could have been demonstrated only qualitatively by Frisch (1953, 1965, 1967) with his "Sternfolie", or by Wehner (1976, 1982, 1994b, 1997, 1998), Harkness and Wehner (1977), Lythgoe (1979) and Können (1985) by their fisheye photographs, nowadays can already be measured quantitatively by different kinds of full-sky imaging polarimeters developed by North and Duggin (1997), Voss and Liu (1997), Liu and Voss (1997), Gál et al. (2001a,b,c), Pomozi et al. (2001a,b), Horváth et al. (2002a,b, 2003) as well as Barta et al. (2003). Figures 7.4.4 and 7.4.7 show two examples for the visualization of the polarization pattern of the whole sky measured by full-sky imaging polarimetry. Figures 2.3-2.5, 7.4.4 and 7.4.7 demonstrate well the advance of polarimetry happened in the last 50 years.

2.2 Elements of the Stokes and Mueller Formalism of Polarization

Polarized light can be decomposed into two components vibrating coherently (that is, with a constant phase difference) and perpendicularly to each other. The state of polarization of transversal electromagnetic waves (e.g. light) is usually described by a four-element vector known as Stokes vector $\underline{S}$, first introduced by Stokes (1852) with the following components:

$$\begin{aligned} \underline{S} &= (I, Q, U, V), \\ I &= I_r + I_p = I_{45} + I_{135} = I_{rc} + I_{lc}, \\ Q &= I_r - I_p = I \cdot p \cdot \cos(2\varepsilon) \cdot \cos(2\alpha), \\ U &= I_{45} - I_{135} = I \cdot p \cdot \cos(2\varepsilon) \cdot \sin(2\alpha), \\ V &= I_{rc} - I_{lc} = I \cdot p \cdot \sin(2\varepsilon), \end{aligned} \tag{2.1}$$

where I is the total intensity of light, I_r and I_p are the intensities of the light components polarized totally linearly in a reference plane and perpendicularly to it, I_{45} and I_{135} are the intensities of the components polarized totally linearly in

planes 45° and 135° to the reference plane, I_{rc} and I_{lc} are the intensities of the components polarized circularly right- and left-handed, p is the degree of linear polarization, ε is the ellipticity of polarization, and α is the angle of polarization, which is the angle of the direction of oscillation from a given plane. Q quantifies the fraction of linear polarization parallel to the reference plane, U gives the proportion of linear polarization at 45° with respect to the reference plane, and V quantifies the fraction of right-handed circular polarization. The degree of polarization P, the degree of linear polarization p, the angle of polarization α and the ellipticity ε can be expressed by the components of the Stokes vector as follows (Shurcliff 1962):

$$\begin{aligned} P &= (Q^2 + U^2 + V^2)^{1/2}/I, \quad 0 \le P \le 1, \\ p &= (Q^2 + U^2)^{1/2}/I, \quad 0 \le p \le 1, \\ \alpha &= 0.5 \cdot \arctan(U/Q), \\ \varepsilon &= 0.5 \cdot \arcsin[V/(Q^2+U^2+V^2)^{1/2}]. \end{aligned} \tag{2.2}$$

For partially polarized light the Stokes vector $\underline{S}$ can be decomposed into two vectors, a completely unpolarized vector $\underline{S}_u$ and an elliptically polarized one $\underline{S}_e$:

$$\underline{S} = \underline{S}_u + \underline{S}_e; \quad \underline{S}_u = [I-(Q^2+U^2+V^2)^{1/2}, 0, 0, 0]; \quad \underline{S}_e = [(Q^2+U^2+V^2)^{1/2}, Q, U, V]. \tag{2.3}$$

A change in the state of polarization of light produced by an optical system, that is, a transformation of the Stokes vector $\underline{S}_0 = (I_0, Q_0, U_0, V_0)$ of the incident light into a new Stokes vector $\underline{S} = (I, Q, U, V)$ by an optical process (e.g. reflection, refraction, scattering, diffraction, birefringence, optical activity) can be expressed as a linear transformation in a four-dimensional space:

$$\underline{S} = \mathbf{M} \cdot \underline{S}_0, \tag{2.4}$$

where $\boldsymbol{M}$ is a four-by-four matrix called "Mueller matrix" with real elements M_{ij} (i,j=0,1,2,3) containing information on all polarization properties of light. In general, the matrix element M_{00} represents the intensity of the emergent light when unpolarized ($P = p = 0$) light is entering the system. Elements M_{01}, M_{02}, M_{03} describe the diattenuation or dichroism, and M_{10}, M_{20}, M_{30} characterize the polarizance. The lower 3×3 submatrix with elements M_{kl} (k,l=1,2,3) contains the retardation. The 16 elements of the Mueller matrix of a given optical system can be obtained by 16 measurements with independent combinations of states of polarization (degrees and angles of linear and circular polarization) of the incident light. The degree of polarization P in the Mueller formalism is (Azzam and Bashara 1992):

$$P = [(\Sigma - M_{00}^2)/3]^{1/2}/M_{00}, \qquad \text{where } \Sigma = \sum_{i,j=0}^{3} M_{ij}^2. \tag{2.5}$$

If the incident light is unpolarized, the degree of polarization of transmitted light, called polarizance or polarizing power *PO* is (Collett 1994):

$$PO = [(M_{10}^2+M_{20}^2+M_{30}^2)/M_{00}^2]^{1/2}, \quad 0 \le PO \le 1,$$

$$\underline{PO} = (PO_1, PO_2, PO_3), \quad PO_i = M_{i0}/M_{00}, \quad i = 1, 2, 3, \tag{2.6}$$

where $\underline{PO}$ is the polarizance vector.

2.3 Principle of Polarimetry with Polarization-Insensitive Detectors

Consider an optical instrument with elements such as imaging lenses, spectral filters, polarizers, quarter-wave plates and/or birefringent crystals, for instance. In general, this instrument may cause absorption, scattering, reflection, refraction, diffraction, birefringence, and so on. These actions are represented by the system Mueller matrix $\boldsymbol{M}$, and the change of the Stokes vector $\underline{S_0}(I_0,Q_0,U_0,V_0)$ of incident light to $\underline{S}(I,Q,U,V)$ of transmitted light is described by Eqn. (2.4). If a polarization-insensitive detector, e.g. a photoemulsion or a charge-coupled device (CCD) with the light at approximately normal incidence, is placed behind the optical system, then only the intensity $I = M_{00}\cdot I_0 + M_{01}\cdot Q_0 + M_{02}\cdot U_0 + M_{03}\cdot V_0$ of light exiting the system can be measured. If the elements M_{00}, M_{01}, M_{02} and M_{03} in the first row of the system Mueller matrix are known and variable, the Stokes vector $\underline{S_0}$ of the incoming light can be determined in four measurements, in which the intensities I_1, I_2, I_3 and I_4 are registered for four independent and known combinations of polarizational states of the incident light. The states of polarization of incoming light can be changed by varying the orientation of the polarizer's transmission axis, for instance. Then the system of equations

$$\begin{aligned}
I_1 &= M_{00}^{(1)}\cdot I_0 + M_{01}^{(1)}\cdot Q_0 + M_{02}^{(1)}\cdot U_0 + M_{03}^{(1)}\cdot V_0,\\
I_2 &= M_{00}^{(2)}\cdot I_0 + M_{01}^{(2)}\cdot Q_0 + M_{02}^{(2)}\cdot U_0 + M_{03}^{(2)}\cdot V_0,\\
I_3 &= M_{00}^{(3)}\cdot I_0 + M_{01}^{(3)}\cdot Q_0 + M_{02}^{(3)}\cdot U_0 + M_{03}^{(3)}\cdot V_0,\\
I_4 &= M_{00}^{(4)}\cdot I_0 + M_{01}^{(4)}\cdot Q_0 + M_{02}^{(4)}\cdot U_0 + M_{03}^{(4)}\cdot V_0
\end{aligned} \tag{2.7}$$

has to be solved for I_0, Q_0, U_0 and V_0. These equations form the basis of the analyser-type polarimeters using intensity detectors, called radiometers. What must be determined through the calibration process are the elements $M_{00}^{(i)}$, $M_{01}^{(i)}$, $M_{02}^{(i)}$, $M_{03}^{(i)}$ (i=1,2,3,4) in the first row of the Mueller matrix with each orientation

of the transmission axis of the polarizer. For example, if a linearly polarizing filter is used as polarizer, its Mueller matrix is (Voss and Liu 1997):

$$\begin{aligned}
&M_{00} = t+\tau, \quad M_{01} = (t-\tau)\cos 2\beta, \quad M_{02} = (t-\tau)\sin 2\beta, \quad M_{10} = (t-\tau)\cos 2\beta,\\
&M_{11} = (t+\tau)\cos^2 2\beta + 2(t\tau)^{1/2}\sin^2 2\beta, \quad M_{12} = [t+\tau-2(t\tau)^{1/2}]\cos 2\beta \sin 2\beta,\\
&M_{20} = (t-\tau)\sin 2\beta, \quad M_{21} = [t+\tau-2(t\tau)^{1/2}]\cos 2\beta \sin 2\beta,\\
&M_{22} = (t+\tau)\sin^2 2\beta + 2(t\tau)^{1/2}\cos^2 2\beta, \quad M_{33} = 2(t\tau)^{1/2}\\
&M_{03} = M_{13} = M_{23} = M_{30} = M_{31} = M_{32} = 0,
\end{aligned} \tag{2.8}$$

where t and τ are the transmittances of the polarizer along the transmission axis and perpendicularly to it, and β is the angle of the transmission axis relative to a reference plane. If a sequence of perfect ($t = 1$, $\tau = 0$) linear polarizers with say $\beta = 0^o$, 45^o, 90^o are used as analysers for the Stokes vector $\underline{S_0} = (I_0, Q_0, U_0, V_0)$ of incoming light, then using Eqns. (2.7) and (2.8), the intensities measured by a detector after the polarizers are

$$I_1(\beta=0^o) = I_0 + Q_0, \qquad I_2(\beta=45^o) = I_0 + U_0, \qquad I_3(\beta=90^o) = I_0 - Q_0. \tag{2.9}$$

From this system of equations the elements I_0, Q_0 and U_0 of the Stokes vector of incoming light can be determined. If the Stokes parameter V_0, characterizing the fraction of circular polarization, is also required, then a fourth measurement, using a circular polarizer as an analyser, is needed.

2.4 Polarimetry of Circularly Unpolarized Light by Means of Intensity Detectors

Light in the natural optical environment is usually not circularly polarized. The few known exceptions are listed and discussed in the book of Horváth and Varjú (2003). Skylight polarization, for instance, is predominantly linear and the component of circular polarization of skylight can be neglected (Hannemann and Raschke 1974). Thus the contribution of the Stokes parameter V characterizing circular polarization to the total intensity is negligible in comparison with that of the linearly polarized component. In other words, the minimal degree of circular polarization V/I of light in nature can be generally ignored. The remaining Stokes vector components I, Q and U, components of the so-called "partial Stokes vector", can be determined from three intensity measurements, using a rotating linear polarizer in front of a radiometer, for instance. If these three measurements happen with angles of orientation $\beta = 0^o$, 60^o and 120^o of the transmission axis of a perfect polarizer, for example, and the state of polarization of light is not changed by other components of the polarimeter, then the transmitted intensities I are the following (Prosch et al. 1983):

$$I(\beta=0^o) \equiv I_0 = I_i\cdot[1 + p\cdot\cos(2\alpha)]/2,$$
$$I(\beta=60^o) \equiv I_{60} = I_i\cdot[1 - 0.5\cdot p\cdot\cos(2\alpha) + 0.5\cdot p\cdot 3^{1/2}\cdot\sin(2\alpha)]/2,$$
$$I(\beta=120^o) \equiv I_{120} = I_i\cdot[1 - 0.5\cdot p\cdot\cos(2\alpha) - 0.5\cdot p\cdot 3^{1/2}\cdot\sin(2\alpha)]/2, \quad (2.10)$$

where I_i is the intensity of incident light. The components Q_i and U_i of the incident Stokes vector are:

$$Q_i = 2(2I_0 - I_{60} - I_{120})/3,$$
$$U_i = -2(I_{120} - I_{60})\cdot 3^{-1/2}. \quad (2.11)$$

Finally, the intensity I_i, degree of linear polarization p and angle of polarization α of incident light can be calculated as follows:

$$I_i = 2(I_0 + I_{60} + I_{120})/3, \qquad p = (Q_i^2+U_i^2)^{1/2}/I_i, \qquad \alpha = 0.5\cdot\text{arc tan}(U_i/Q_i). \quad (2.12)$$

2.5 Point-Source, Scanning and Imaging Polarimetry

The major aim of polarimetry is to measure the four components I, Q, U and V of the Stokes vector $\underline{S}$, from which further quantities of the incident light can be derived, according to Eqn (2.2). These measurements can be done either by a point-source polarimeter or by an imaging one. The only principal difference between them is that the former performs measurements in a given direction representing a very narrow field of view within which the optical variables I, Q, U and V are averaged, while the latter measures the polarization simultaneously in many directions in a wide field of view.

There is an intermediate technique, the scanning point-source polarimetry between these two extrema. Such a polarimeter scans a given area of the optical environment and measures sequentially the polarization in many directions (Fig. 2.6). If there is no temporal change of polarization, a polarization pattern obtained by imaging polarimetry can also be measured equivalently by scanning point-source polarimetry. However, scanning a greater area of the optical environment with a point-source polarimeter is a troublesome and time-consuming task, which generally can be performed only in the laboratory using complicated, computer-controlled procedures. It is, therefore, not surprising that this technique has been used only sporadically (e.g. Shaw 1975; Brines and Gould 1982).

Using imaging polarimetry, the spatial distribution of polarization can be easily and quickly determined. The need to receive polarized optical information pixel-by-pixel from a wide field of view has resulted in the rapid development of imaging polarimetry in the 1980's, 1990's and early 2000's. This technique has

been used for different purposes in computer vision (e.g. Wolff 1993), in atmospheric remote sensing (e.g. Walraven 1981; Prosch et al. 1983; Egan 1986; Deschamps et al. 1994; North and Duggin 1997; Voss and Liu 1997; Horváth et al. 1998b, 2002a,b, 2003; Horváth and Wehner 1999; Gál et al. 2001a,c; Pomozi et al. 2001a,b; Barta et al. 2003), and in biology (e.g. Shashar et al. 1995a,b; Horváth and Zeil 1996; Horváth and Varjú 1997; Horváth et al. 1997, 1998a, 2002c; Kriska et al. 1998; Bernáth et al. 2001b, 2002, 2003).

2.6 Sequential and Simultaneous Polarimetry

If the (at least necessary) 3 intensity measurements with different orientations of the transmission axis of the polarizer are performed one after the other, we speak about "sequential polarimetry". When all these measurements happen at the same time, it is called "simultaneous polarimetry". For the latter at least 3 separate polarimeters are needed. The advantage of simultaneous polarimetry is, that also temporally changing radiation fields (e.g. light from cloudy skies with rapidly moving clouds, or skylight after sunset or prior to sunrise, or measurements from a moving platform) can be measured with it, if the time of measurement is not longer than the characteristic period during which considerable changes occur in the radiation field. Its disadvantage is that at least 3 polarimeters have to be handled simultaneously, which is not a simple task, furthermore such a group of polarimeters is heavy, voluminous, its setting up, dismounting and transferring is difficult and time-consuming. These disadvantages make frequently impossible the use of simultaneous polarimetry in the field.

The disadvantage of sequential polarimetry is that temporally changing radiation fields cannot be measured with it. Its advantage is, that only one polarimeter has to be handled, the setting up, dismounting and transferring of which is much easier and quicker. In the field, the polarization of certain optical phenomena – like rainbows (Barta et al. 2003), for example, the occurrence of which is accidental – can practically be measured only with a simple and portable sequential polarimeter, which can be set up quickly anywhere and at any time. The advantage of a sequential polarimeter against a heavy simultaneous polarimeter composed of several separate parts has been experienced, for instance during the first observation of the fourth neutral polarization point in the atmosphere (Horváth et al. 2002b), when the polarization of the upwelling earthlight has been measured by a simple sequential polarimeter in the gondola of a hot air balloon. This measurement could not have been performed by a heavy, voluminous simultaneous polarimeter.

2.7 Colour Coding and Visualization of Polarization Patterns

On the basis of the functional similarity between polarization vision and colour vision, Bernard and Wehner (1977) suggested a hue-saturation-brightness visualization method for partially linearly polarized light. This "composite visualization" scheme was used by Wolff and collaborators (e.g. Wolff 1993; Cronin et al. 1994; Shashar et al. 1995a), for example, who coded the measured angle of polarization α, degree of linear polarization p and intensity I of partially linearly polarized light by the hue, saturation and brightness, respectively. In their polarization maps, unpolarized light appears achromatic, strongly polarized regions show up chromatically saturated, and the intensity of light is the brightness regardless of colour. The advantage of this visualization lies in its compactness: it displays the distribution of all three optical parameters (I, p, α) in a single, false-coloured picture. The disadvantage of this coding is, that it is difficult to decompose, since in a complex false-coloured picture it is not easy to separate and decode the values of I, p and α from each other. Changes in hue (coding α) appear to the human visual system more strikingly than changes in saturation (coding p), furthermore the perception of the hue-saturation-brightness scale is very non-linear (Shashar et al. 1995a).

The latter problem does not occur if the distributions of I, p and α are displayed in three separate patterns with arbitrary unambiguous colour coding. This "separate visualization" of the I-, p- and α-patterns is preferred by Horváth and collaborators, for instance (e.g. Horváth and Varjú 1997; Horváth and Wehner 1999; Gál et al., 2001c; Pomozi et al. 2001b; Barta et al. 2003; Bernáth et al. 2002), for instance.

Other authors (e.g. Dürst 1982; Sivaraman et al. 1984; Liu and Voss 1997; Gabryl et al. 1998) display the I-, p- or α-patterns measured by imaging polarimetry in the form of the conventional contour plots used frequently in the cartography, for example. Although this "contour plot visualization" is the most traditional, it can hardly reproduce the image feature of the spatial distribution of polarization, which is the most important characteristic of data gained by imaging polarimetry.

2.8 Field of View of Imaging Polarimetry

The field of view of an imaging polarimeter is limited by that of the imaging optics used. In the case of common photographic and video cameras, the field of view of the lens system is about 30^o-50^o (horizontal) $\times$ 20^o-40^o (vertical) depending on the focal length and the aperture. This common field of view can be extended e.g. by decreasing the focal length. A fisheye lens with 8 mm focal length mounted onto a normal photographic camera is an extremum, ensuring a

conical field of view with an aperture angle of 180°, by which the whole hemisphere of the optical environment can be imaged.

As an alternative, a 180° field-of-view fisheye lens can be replaced by a spherical mirror with a 180° field of view, and the camera can be suspended by a holder above the mirror. A similar construction is used in the TS-990 Total Sky Imager (Fig. 2.7) produced by the Yankee Environmental Systems Inc. (YES 2001) and used to detect radiometrically the clouds (see Chapter 7.7), or in the full-sky imaging polarimeter (Fig. 5.1) designed by North and Duggin (1997). 180° field-of-view imaging polarimetry is ideal to study the polarization patterns of the full sky or the reflection-polarization patterns of water surfaces (Fig. 2.8), for instance.

2.9 Narrow Field-of-View Imaging Polarimetry with Photographic Technique

Walraven (1977) has as first demonstrated by simple photographic technique that the state of polarization is a valuable parameter for identifying different ground targets, aerosol and dust layers as well as the water phase of clouds.

2.9.1 A Forerunner of Imaging Polarimetry Using Savart Filter

One of the forerunners of the development of imaging polarimetry was Gerharz (1976), who measured the polarization of the circumsolar scatter field in a field of view of 12°×15° during the total solar eclipse on 7 March 1970. He photographed the scene by a 30 cm focal length camera through external objective filters consisting of a modified Savart polariscope and an interference filter (535 nm). On the negatives dark interference bands with low contrast have been produced, which extended through almost the entire field of view. These bands originate from the scattered polarized skylight that had been intercepted by the filters before entering the camera. The contrast of the bands is a measure of the degree of linear polarization p: the greater the contrast, the higher is p. The exposed plates were analysed by a microdensitometer and indicated a maximum p of 2.5% in the immediate solar vicinity. The mechanism of the formation of interference bands by a Savart filter and the evaluation of the contrast of these bands are described in detail by Gerharz (1975).

2.9.2 Simultaneous Photographic Polarimeter

Fitch et al. (1984) designed a simultaneous imaging photopolarimeter, which makes four photographs of a scene through linear polarizers with four different directions (0°, 45°, 90° and 135°) of the transmission axis relative to a reference

direction. With this polarimeter the polarization of light reflected from grain crops was studied during the heading growth stage.

2.9.3 Sequential Photographic Polarimeters

Solar physicists and astronomers have also developed different imaging polarimetric techniques for the ground-based measurement of the polarization pattern of the solar corona during total solar eclipses (see Chapter 9.3). One of the first astronomers using imaging polarimetric technique for this purpose was Dürst (1982), who took sequential photographs about the corona during the solar eclipse of 16 February 1980. He used a camera with 370 mm focal length equipped with six neutral density filters, one colour (600 nm) filter and one linearly polarizing filter mounted between glass plates in front of the objective with four orientations of the transmission axis 45^o apart. After digitisation by an automatic microdensitometer and evaluation of the four polarizational pictures taken sequentially from the corona, two-dimensional maps of the degree p and angle α of linear polarization of the corona light were obtained. There are two possibilities for analysing these data:

1. The first uses all four exposures together leading to p and α.
2. The second assumes that the polarization of the so-called K-corona is produced by Thomson scattering of light on free electrons and therefore the E-vector of the corona light is perpendicular to the radial scattering plane. In this case only two exposures with 90^o difference in the orientation of the transmission axes of the polarizers are combined to obtain p.

Sivaraman et al. (1984) measured the polarization pattern of the solar corona during the total eclipse on 16 February 1980 with the use of a four-lens camera (focal length = 1 m) equipped with linearly polarizing sheets with four different orientations of their transmission axes 45^o apart. The polarizational photographs were digitised by a microdensitometer. Later, similar photopolarimetric methods were routinely used in the investigation of the polarization of the solar corona during eclipses (e.g. Gabryl et al. 1998).

Lee (1998a) designed a rotating-analyzer sequential photographic polarimeter and estimated with it the approximate values of the degree p of linear polarization of light from the clear sky near sunset at inland and coastal sites. He also observed the Arago and Babinet neutral points in the resulting approximative p-maps. His method used only two digitised pictures of colour slides taken from a scene through a linearly polarizing filter with two orthogonal directions of the transmission axis. These two directions were the directions that gave the brightest and darkest image as measured by the camera's light meter. He also demonstrated that more reliable results are obtained if four photographs are taken through a linearly polarizing filter with four different (0^o, 45^o, 90^o, 135^o) directions of the transmission axis.

Table

Table 1.1. The most important properties of some imaging polarimeters designed by different authors and used for various purposes. Since all instruments contain linearly polarizing filter(s) of different types, the polarizers are not mentioned and specified in the column "imaging optics" (IO). *1D*: one-dimensional (linear). *B*: binned. *CAMO*: camera optics. *CCD*: charge-coupled device. *CF*: colour filter. *CIR*: circular. *D*: digital. *DET*: detector. *DPLSM*: differential polarization laser scanning microscopy. *FEL*: fisheye lens. *FIP*: forerunner of imaging polarimetry. *FOV*: field of view. *IR*: infrared ($\lambda > 750$ nm). *IT*: imaging tube. *MMI*: Mueller matrix imaging polarimeter. *NF*: neutral density filter. *PCC*: polarization camera chip. *PE*: photoemulsion. *PEM*: piezoelastic modulator. *PHO*: photopolarimeter. *POR*: portable. *PP*: photographic plate. *PPBS*: polarizing plate beam-splitter. *PSC*: polarization-sensitive chip. *RES*: spatial resolution (pixel × pixel). *SEQ*: sequential. *SIM*: simultaneous. *SR*: spectral region (nm). *STE*: stereo. *STO*: imaging Stokes polarimeter. *SUB*: submersible. *TNLC*: twisted-nematic liquid crystal. *UV*: ultraviolet. *V*: video. *VID*: video polarimeter. *VIS*: visible (400–750 nm). *WL*: white light.

Author(s)	Type	IO	DET	FOV	RES	SR	Application
Gerharz (1976)	FIP	CAMO + Savart filter + CF	PP	12×15°	–	535	Polarization distribution of the circumsolar scatter field during a total solar eclipse
Dürst (1982)	SEQ PHO	CAMO + 6 NF + 1 CF	PE	8×10°	50×50	600	Polarization pattern of the solar corona during a total solar eclipse
Prosch *et al.* (1983)	SIM VID	3 lens systems	IT	25×25°	36×36	VIS	Ground- and air-borne remote sensing of landscape features
Sivaraman *et al.* (1984)	SIM PHO	four-lens CAMO	PE	3×3°	32×32	WL	*p*-pattern of the solar corona during a total solar eclipse
Fitch *et al.* (1984)	POR SEQ PHO	CAMO	PE	30×40°	512×512	VIS	Polarization pattern of light reflected from grain crops during the heading growth stage
POLDER (1994-1997) Deschamps *et al.* (1994)	SEQ VID	wide field-of-view optics + filter wheel	CCD	114× 114°	242×274	443, 670, 865	Space-borne measurement of the polarizational characteristics of earthlight
Wolff (1993), Cronin *et al.* (1994), Shashar *et al.* (1995a, 1996)	SEQ VID SUB	CAMO + 2 TNLC	CCD	30×40°	165×192 (D) 240×320 (V)	VIS	Polarization patterns of objects and biotopes
Wolff (1994), Wolff & Andreou (1995)	SEQ VID	2 CAMO + PPBS + TNLC	CCD	20×20°	165×192	VIS	Polarization patterns of objects for robot vision
Wolff & Andreou (1995)	1D SIM PCC	lens system	PSC	-	3×128	VIS	Prototype of future 2D polarization camera chips
Povel (1995)	SIM STO	telescope + PEMs	CCD	0.42'× 0.83'	288×385	VIS	Observation of solar magnetic fields
Pezzaniti & Chipman (1995)	MMI SEQ	lens system + retarders + laser	CCD	42×42°	512×512	VIS+ IR	Polarizational properties of static optical systems and samples
North & Duggin (1997)	SIM PHO	four-lens CAMO + spherical mirror	PE	180° CIR	300×300	VIS	Ground-borne measurement of skylight polarization
Voss & Liu (1997)	SEQ VID	FEL	CCD	178° CIR	528×528 (B)	VIS	Ground-borne measurement of skylight polarization
Horváth & Varjú (1997)	POR SEQ VID	CAMO	CCD	50×40°	736×560	VIS	Polarization patterns of sky, objects and biotopes
Lee (1998)	POR SEQ PHO	CAMO	PE	36×24°	550×370	VIS	Polarization patterns of clear skies
Horváth & Wehner (1999)	POR SEQ VID	CAMO	UV IT	20×15°	736×560	UV+ VIS	Polarization patterns of sky, objects and biotopes
Bueno & Artal (1999), Bueno (2000)	SEQ MMI	CAMO + 2 TNL + 2 quarter-wave plate + laser	CCD	1×1°	60×60	630	Polarizational properties of static optical systems and samples (e.g. human eye)
Hanlon *et al.* (1999)	SIM VID	3-tube CAMO + prismatic beam-splitter	IT	20×30°	512×384	VIS	Polarization patterns of moving animals

Author(s)	Type	IO	DET	FOV	RES	SR	Application
Mizera *et al.* (2001)	POR SEQ STE VID	CAMO	CCD	50×40°	736×560	VIS	Polarization patterns of objects and biotopes
Gál *et al.* (2001c)	POR SEQ PHO	FEL + filter wheel	PE	180° CIR	670×670	VIS	Ground- and air-borne measurements of polarization patterns of the atmosphere, objects and biotopes
Shashar *et al.* (2001)	SEQ VID	microscope	CCD	5×5°	512×384	VIS	Polarization patterns of microscopic targets
Horváth *et al.* (2002a)	POR SIM PHO	3 FEL	PE	180° CIR	670×670	VIS	Ground-borne measurements of skylight polarization
Pomozi (2002), Pomozi *et al.* (2003), Garab *et al.* (2003)	DPL SM	laser scanning microscope	CCD	256× 256 μm	1024×1024	VIS	Study of the anisotropic architecture of microscopic samples and the interaction of the sample with polarized light

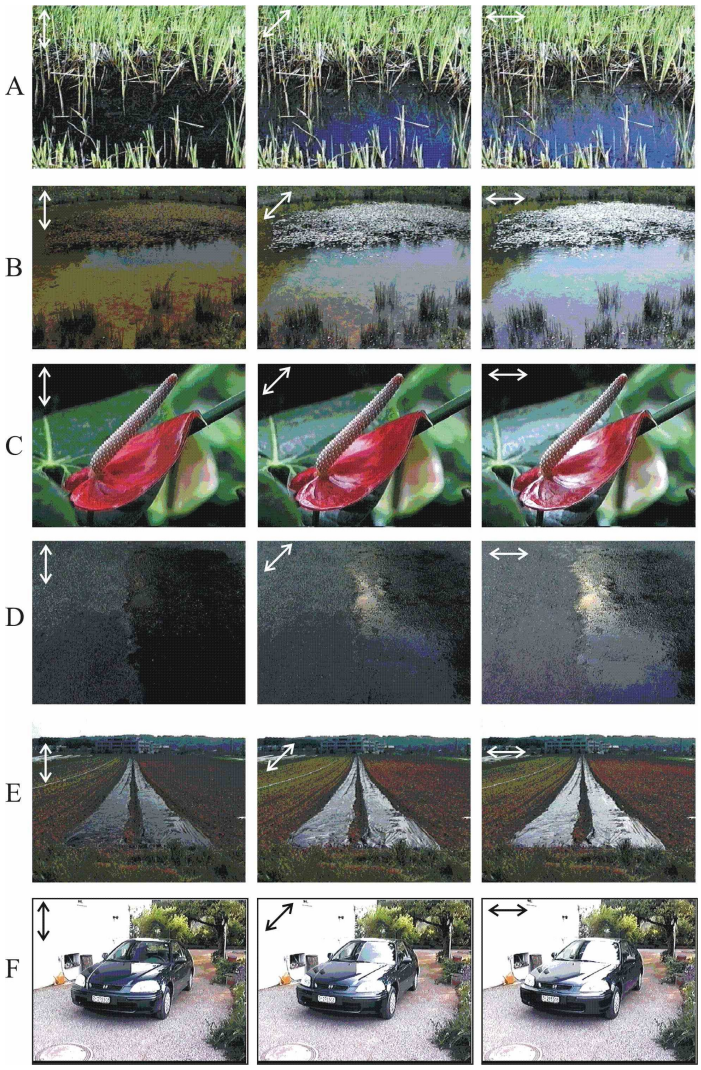

Fig. 2.1. Triplets of colour pictures of various scenes from which highly polarized light originates. The pictures are taken by a video camera through a sheet of linearly polarizing filter with three different orientations of the transmission axis shown by double-headed arrows. A: A dark brown bottomed pond, the surface of which reflects blue light from the clear sky. B: A bright yellow bottomed pond with some plants on its surface under a clear sky. C: The flower of *Epipremnum aureum* (Aracea) possessing a shiny petal-imitating red leaf called spathe. In the background there are shiny green leaves illuminated by light of a full clear sky from above through the glass panes of a greenhouse. D: Surface of a grey asphalt road under a clear sunset sky. The upper half of the road is rough and light grey, the lower half is smooth and dark grey, the left half is dry, the right half is wet. E: Stripes of shiny black plastic sheets used in the agriculture laid onto a plough-land under a clear sky. F: A car under a clear sky.

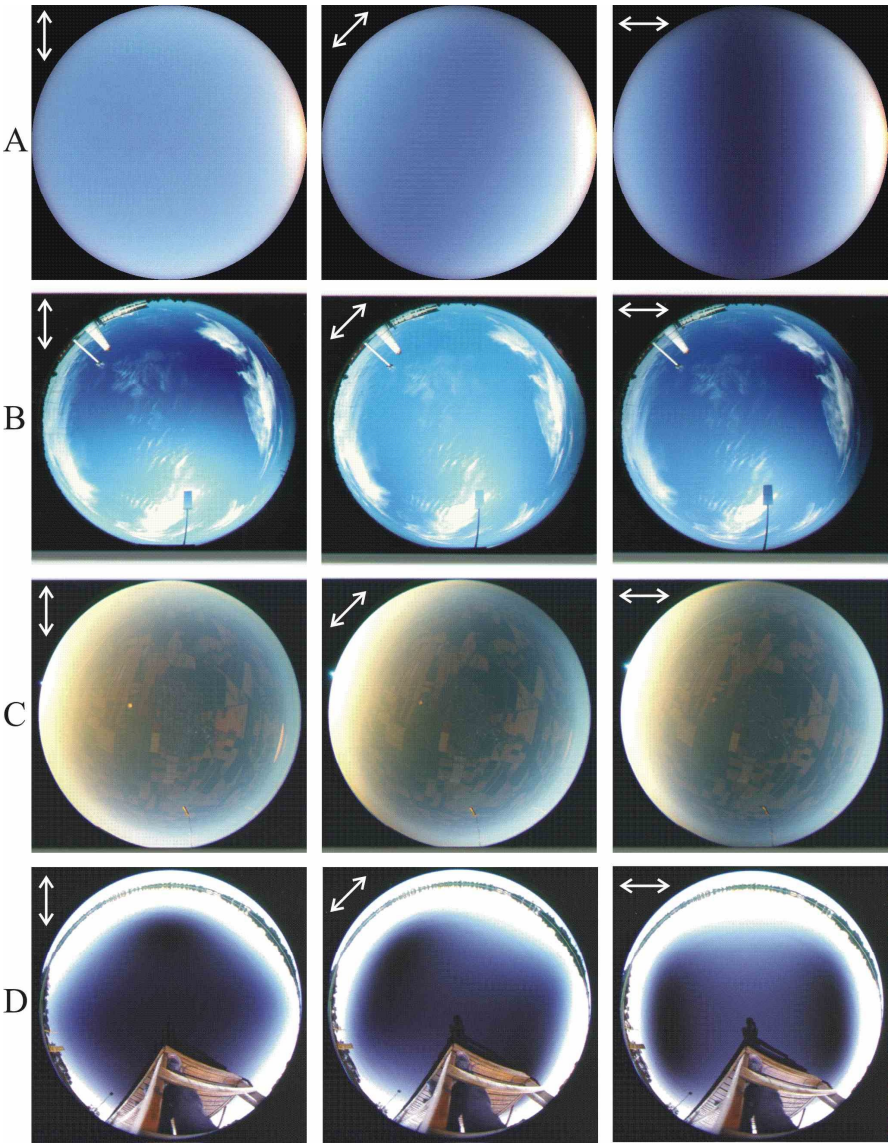

Fig. 2.2. Triplets of colour photographs of various scenes with highly polarized light taken by a 180° field-of-view fisheye lens through a linear polarizer with three different orientations of the transmission axis shown by double-headed arrows. The optical axis of the lens is vertical, the periphery of the circular pictures is the horizon, while the centre is the zenith (A, B) or nadir (C, D). A: A clear sky at sunrise. B: A partly cloudy sky with sun occluded by a metal sheet. C: Sunlight reflected from the ground and scattered in the atmosphere below a hot air balloon photographed at sunrise at an altitude of 4000 m. D: A dark lake with smooth surface photographed at sunset from a jetty.

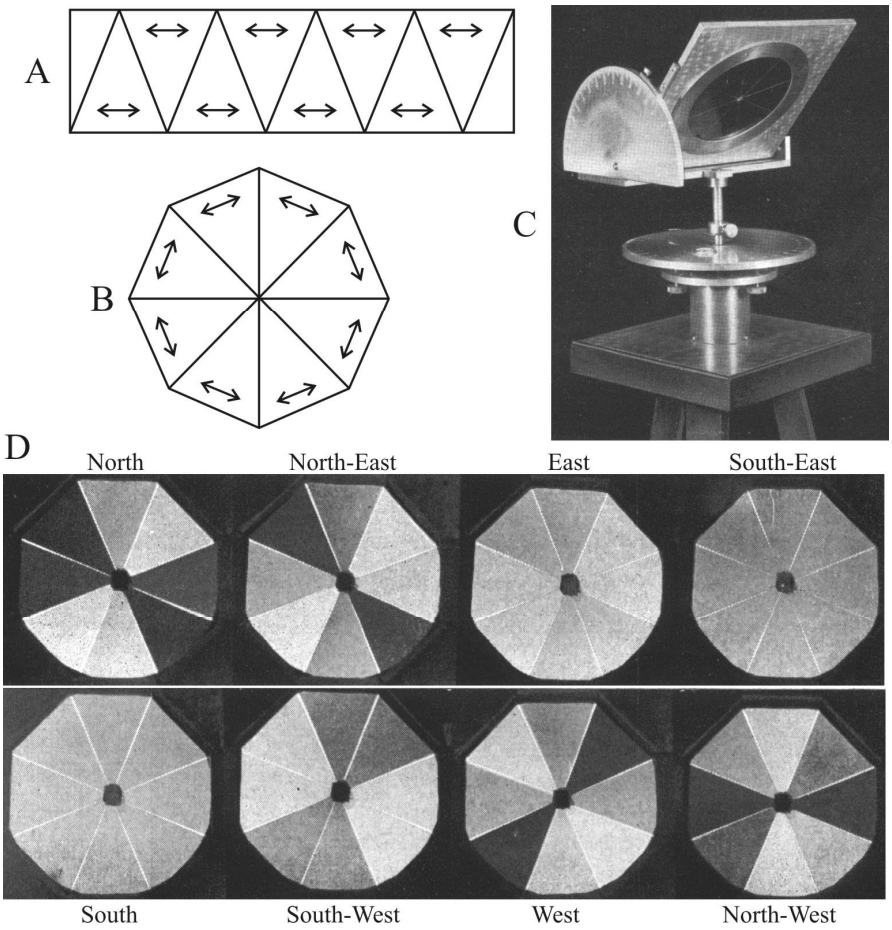

Fig. 2.3. A: Schematic drawing of a sheet of linearly polarizing filter with cut pattern to construct the "Sternfolie" ("star foil") used to demonstrate the gross distribution of linear polarization of skylight by Karl von Frisch (1953, 1965, 1967). The orientation of the transmission axis is shown by double-headed arrows. B: The geometry of the "Sternfolie". C: Simple instrument – a "Sternfolie" mounted onto a metal holder in such a way that both the elevation and azimuth of the viewing direction through the foil can be changed –, with which Frisch (1953, 1965, 1967) investigated qualitatively the polarization of skylight. D: View through the "Sternfolie" in eight different directions in the sky with an angle of elevation of 45^{o}. (After Fig. 59, p. 85; Fig. 69, p. 99, Fig. 70, p. 100 of Frisch 1953).

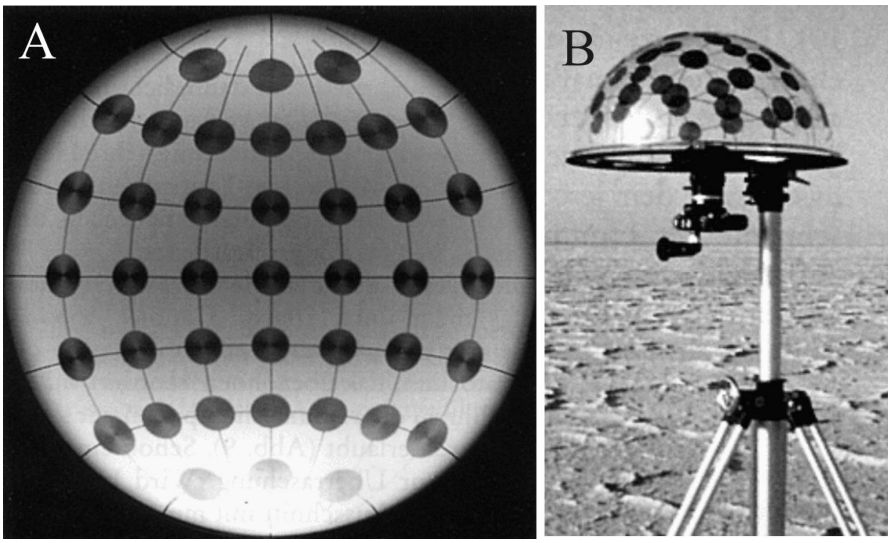

Fig. 2.4. Photograph of the entire sky (A) taken by a 180^{o} field-of-view fisheye lens with the use of a set of 41 circular axis-finders, which were mounted on a transparent Plexiglas dome (B). The dark axis of the cross-shaped brightness pattern seen in the axis-finders gives the E-vector orientation of skylight. (After Fig. 7, p. 15 of Wehner 1994b).

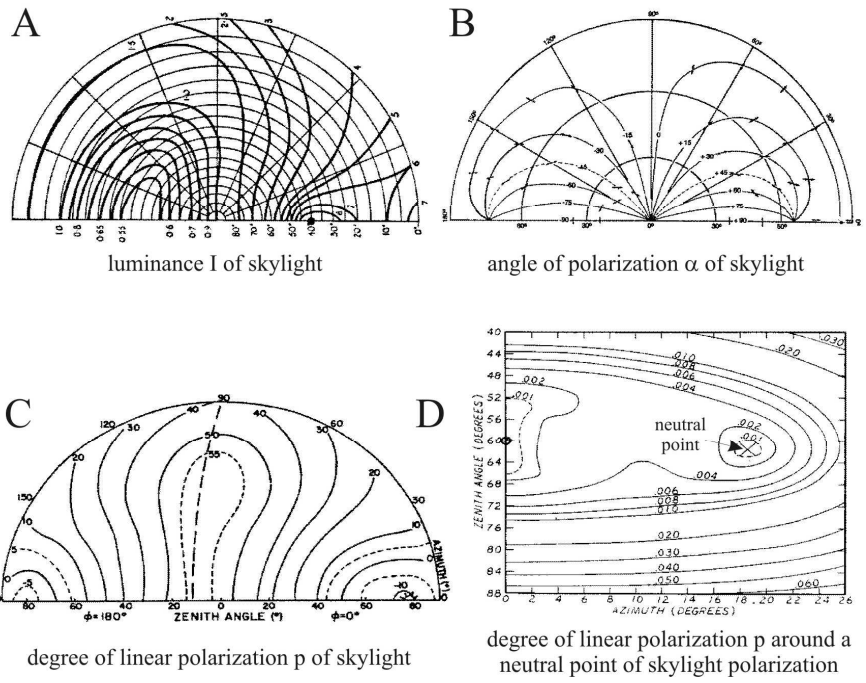

Fig. 2.5. Numerically calculated maps displaying the distribution of luminance I (A, wavelength λ = 312 nm, solar zenith angle θ_s = 50°), angle of polarization α (B, λ = 495 nm, θ_s = 85.4°) and degree of linear polarization p (C, λ = 312 nm, θ_s = 78.5°; D, λ = 550 nm, θ_s = 30°) of light from half of the clear sky. (After Fig. 6.1, p. 335; Fig. 4.36, p. 261; Fig. 4.12, p. 215; Fig. 7.7, p. 392 of Coulson 1988).

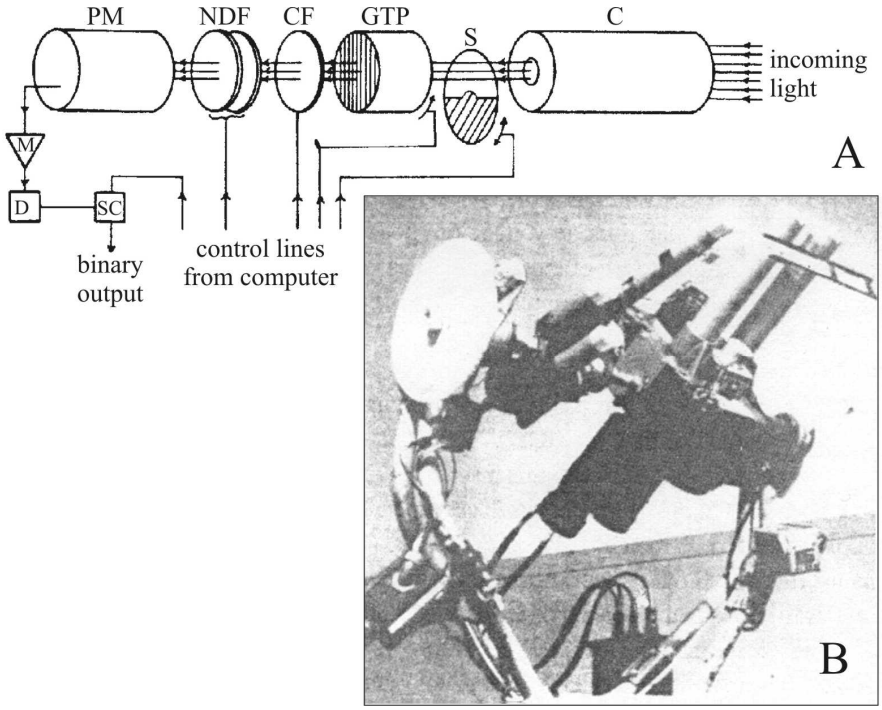

Fig. 2.6. Schematic diagram of a stepped analyser-type non-imaging point-source polarimeter (A). C: collimator tube, S: shutter, GTP: Glan-Thompson prism, CF: colour filter, NDF: neutral density filters, PM: photomultiplier tube, M: amplifier, D: discriminator, SC: scaler. (After Fig. 11.10, p. 556 of Coulson 1988). Photograph of a Seaman-Sekera dual-channel scanning point-source polarimeter (B). (After Fig. 11.11, p. 561 of Coulson 1988).

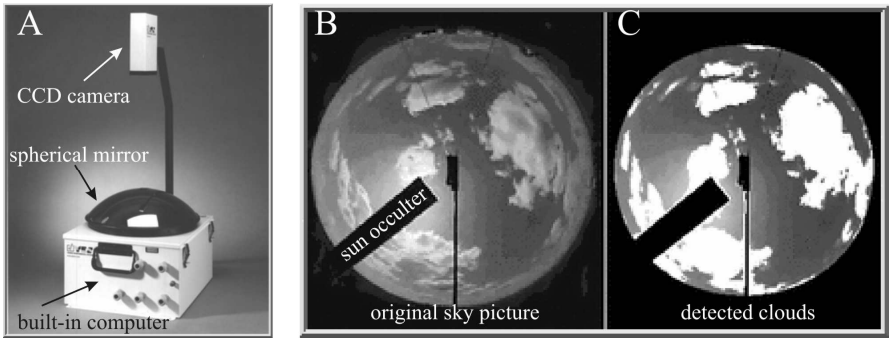

Fig. 2.7. A: The TSI-990 Total Sky Imager with a spherical mirror possessing 180^{o} field of view. B: Picture of a cloudy sky taken by the instrument. C: The clouds (white) and clear sky regions (grey) detected radiometrically by the instrument. (After YES 2001).

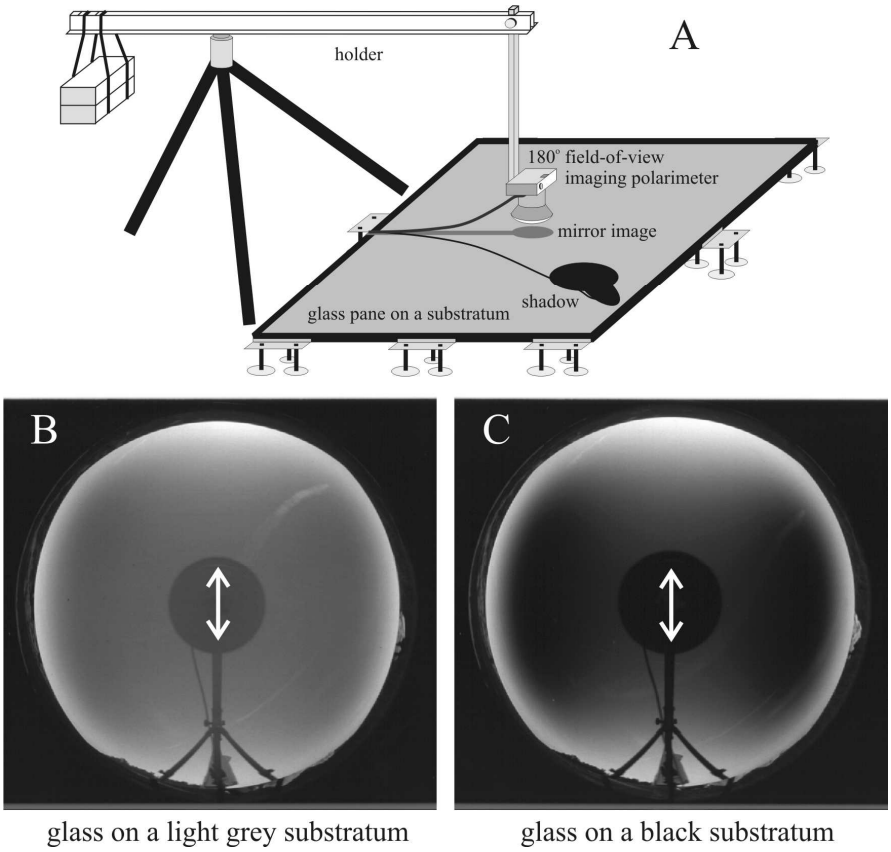

Fig. 2.8. A: The experimental setup used to measure the polarization patterns of skylight reflected from a glass pane by 180° field-of-view imaging polarimetry. B, C: Photographs taken by the 180° field-of-view fisheye lens of the polarimeter from glass on a light grey (B) and black (C) substratum through a linearly polarizing filter, the transmission axis of which is shown by double-headed arrows. (After Fig. 2A of Bernáth et al. 2003).

3 Video Polarimetry

3.1 Simultaneous Video Polarimeters

The technique of video polarimetry developed by Prosch et al. (1983) generated the polarizational images of a scene instantaneously allowing real-time identification and selection of light sources of defined degrees and/or angles of polarization. Selected targets were scanned optoelectronically, and the digitised image information was stored by electronic means or could be displayed on-line. This was a measuring technique offering the advantages of instantaneous quick-look analysis, high-resolution wide field-of-view polarization maps in real time enabling the study of dynamic processes (e.g. motions or rippling water surfaces).

The video polarimeter of Prosch et al. (1983) consisted of three synchronously scanning imaging tubes (Plumbicon XQ 1270) equipped with linearly polarizing filters, spectral filters and lens systems. These three camera systems were mounted side by side on an optical bench carrying adjustment plates to align the optical axes (Fig. 3.1). The video signals were amplified, sampled and digitised. To generate false colour images in real time, a standard phase alternating line (PAL) composite video signal was generated. A minicomputer supported the system on-line transferring data from the AD-converters to magnetic tape, or processing the instantaneous radiances. Computational results were displayed simultaneously with the false colour image on the same screen. A colour ladder was generated and could be monitored atop the screen showing specific colours corresponding to predefined polarizational properties. A second display mode – colour representation of the voltage differences between the three channels – allowed to make sources of unpolarized light invisible on the screen. Three scan modes were available:

- In the manually controlled sampling, a cursor was positioned within the screen, the related video signals were continuously digitised and processed, and the degree and angle of linear polarization as well as the components of the Stokes vector were displayed on the same screen.
- The repetitive one-dimensional horizontal scan was used in case of air-borne measurements, when the instrument was operating as a cross-track scanner.
- Using the two-dimensional scan of the complete field of view, stationary imaging was performed, where all sampled and digitised data were transferred

directly to magnetic tape. The final data evaluation was done off-line by a powerful computer.

In the calibration of their instrument, Prosch et al. (1983) took into account the measured incident-angle-dependent response of the imaging tubes across the field of view, and the analytically calculated incident-angle-dependent dichroic extinction properties of the polarizing filters. After calibration, the video polarimeter could measure the degree of linear polarization p by an error less than 3%. The error $\Delta\alpha$ in determination of the angle of polarization α depended strongly on p and on the radiometric precision r of the imaging tubes. The smaller the value of p and/or r, the larger was $\Delta\alpha$.

In this video polarimeter, three voltages were generated, which were proportional to the radiances. Coding a colour TV signal by these voltages, the resulting colour vector was determined for a standard PAL composite video signal. Using the resulting normalized colour vector in a standard two-dimensional colour table with p as parameter, the Stokes vector was projected in the colour table in such a way, that unpolarized light was white, and increasing p caused a deviation from these colourless loci. α defined the tint, whereas p was represented by the hue. Prosch et al. (1983) used 60^o spacing between the orientation of the transmission axes of the polarizers, because then the discernability of the colour-coded polarization status was improved in comparison with that for a 45^o spacing, which is commonly used in other polarimeters.

The pioneering video polarimeter of Prosch et al. (1983) has been flown in an aircraft over different terrain features and lakes. Over land, many features have been made much more clearly discernible than with unpolarized radiance measurements only. Prosch et al. (1983) suggested, that p is a useful source of information for remote earth resource observations.

Hanlon et al. (1999) designed a simultaneous video polarimeter based on a standard three-tube camera using a dichroic prism block for colour separation. This prism is replaced with a neutral prismatic beam-splitter such that each of the three videochannels receive one third of the broad-spectrum image input. Since this assembly lacks the colour-trimming filters cemented to the original dichroic prism, magnification errors due to pathlength differences are corrected with small quartz discs of appropriate thickness. A small disc of linear polarizer (HNP'B, Polaroid) is placed immediately in front of each camera tube to impart polarization sensitivity to the channels. The direction of the transmission axis of the polarizers is 0^o, 45^o and 90^o from the vertical. The camera electronics encodes the three polarizational images as if they were colour, making it possible to store all the data on a regular portable videocassette recorder and allowing for immediate viewing of a colour-coded polarization pattern on a colour monitor in such a way that unpolarized regions of the scene are colorless, whereas polarized areas appear false-coloured. The signal in all three channels is identical, and the output of the tubes is adjusted to give white for overexposure. Monochromatic images of a scene taken from the three channels separately can be transferred through a frame grabber into a computer and their degree and angle of linear polarization can be

calculated. This simultaneous video polarimeter was used for aerial recording of the polarization patterns of cephalopods moving in an aquarium.

3.2 Sequential Imaging Polarimeters Using Liquid Crystal Polarizers

Obtaining the polarizational pictures by rotating a polarizing filter in front of an intensity detector is a mechanically active process that may produce optical distortion if the plane of the filter is not exactly perpendicular to the optical axis of the camera and is difficult to fully automate. Using liquid crystals (LCs), errors caused by mechanical rotation (e.g. inertia with acceleration and brake times, misalignments of the signal on the detector) can be eliminated. The main disadvantage is that the retardation introduced by a LC is dependent on external factors, such as the temperature, for example.

Twisted nematic LCs have a helical molecular structure, which gradually rotates from one side of the crystal to the other; the degree of rotation is preset during the manufacture (Priestly et al. 1975). The molecules can be stretched by applying an alternating voltage; when the voltage is zero, the molecules return to their twisted stage. The angle of polarization α of partially linearly polarized light transmitted through the LC is rotated by a preset value. When the molecules of the crystal are stretched, α of the transmitted light is not changed. These LCs do not distort the geometry of the incoming image, and transmit light across a broad band of the spectrum. However, time (several 10 ms) is required for stretching and relaxing the molecules.

Wolff (1993) designed an imaging polarimeter using a monochrome CCD camera with a fixed linearly polarizing filter and two twisted nematic LCs set between UV-absorbing glass plates in front of the lens system of the camera. The LCs can rotate electro-optically the totally polarized component of the incoming light by a given angle φ, while they do not affect the unpolarized component. Wolff (1993) used $\varphi = 0^o$, 45^o and 90^o to take three polarizational pictures from a given scene. Hence, in this case not the linearly polarizing filter rotates mechanically at a fixed α of the incident light, but the filter is fixed and α is rotated electro-optically prior to the transmission through the filter. The results are the same as if the filter was rotated. A driver for the LCs modulates a high frequency alternating voltage so as to produce the mentioned three rotational (or twist) states of the two LCs. The driver also provides synchronization, which ensures that an image from the camera is digitised when the LC is in a fully relaxed state, and ensures that the twist state of both LCs is known with respect to each digitised image.

After computer evaluation of the three polarizational images, a false-coloured picture is obtained, which displays the distribution of intensity, degree and angle of linear polarization in the composite (hue-saturation-brightness) visualization scheme. Using a colour video camera for recording polarizational images that are analysed at a later stage, Cronin et al. (1994) and Shashar et al. (1995a,b) built a

portable version of the sequential imaging polarimeter of Wolff (1993). The state of the LCs is independently recorded by placing small linearly polarizing stripes in the field of view of the camera. In the laboratory, an on-line version of the polarimeter is used based on a digital camera connected to a personal computer. The electronic card controlling the twist and relaxation of the LCs is synchronized with the video signal of the camera. Both polarimeters can be placed in waterproof protective submersible housings for underwater measurements. Cronin et al. (1994) and Shashar et al. (1995a,b) used their portable and submersible polarimeter to record polarization patterns occurring in a tropical rain forest and in submarine habitats (e.g. coral reefs, underwater objects and animals).

3.3 Mueller Matrix Sequential Imaging Polarimeter

Pezzaniti and Chipman (1995) has built the first Mueller matrix imaging polarimeter. Mueller matrix polarimeters are widely used to measure different polarizational properties in optical systems and samples. Most of these systems are point-source polarimeters.

Using a CCD camera as detector in the recording state and liquid crystals (LCs) adapted to an ophthalmoscopic double-pass apparatus, Bueno and Artal (1999) designed a Mueller matrix imaging polarimeter in order to calculate spatially resolved Mueller matrices of the human eye. The theoretical basis of this system is described by Bueno (2000a). The polarimeter uses a pair of LC variable retarders (LCVRs), both in the input and output optical paths. A LCVR is composed of a fixed linearly polarizing filter followed by a LC cell, which can rotate the E-vector of linearly polarized incident light, and thus can produce three independent polarizational states. The first LCVR acts as a polarizational state generator (PSG) and the second as a polarizational state analyser (PSA). In transmission mode, the sample is placed between the two LCVRs, between the PSG and PSA. For a fixed position of the generator-analyser system, only $3\times3=9$ elements of the Mueller matrix can be obtained, because 9 independent polarizational states can be generated by the two LCVRs. A removable quarter-wave plate (RQWP) can produce the fourth independent polarizational state. The effect of such a plate is to rotate counter-clockwise the incident Stokes vector at an angle of 90^o around its fast axis. Thus, the other 7 elements of the Mueller matrix are accessible when two RQWPs, one behind the PSG and other in front of the PSA, are introduced. In this way, $4\times4=16$ intensities are recorded, each corresponding to a different independent[1] combination of polarizational states of the PSG-PSA system. The calculation of the Mueller matrix (completely describing the polarizational properties of the sample) involves 16 independent images, that is, 16 independent linear equations of intensity measurements at every pixel. This system of

[1] In mathematical terms, 4 vectors with 4 components are independent, if the determinant of the 4×4 matrix composed by them is not zero. For Stokes vectors, the largest possible value of this determinant is 2, meaning total independence.

equations can be solved by a matrix inversion method, for example. This Mueller matrix imaging polarimeter allows to obtain the polarizational properties of static samples both in transmission and reflection mode. It can be used, for instance, in the study of polarizational characteristics of substrata and samples with anisotropic layers, scattering effects at rough surfaces and *in vitro* samples (e.g. Bueno 2000b, 2001; Bueno and Artal 1999, 2001; Bueno and Jaronski 2001).

3.4 Sequential Imaging Polarimeter Using Beamsplitter and Liquid Crystal Polarizer

To speed up the time of measurement, Wolff (1994) as well as Wolff and Andreou (1995) used a polarizing plate beamsplitter to direct light onto two CCD detectors and a twisted nematic liquid crystal in front of the beamsplitter to rotate the angle of polarization of the transmitted light. With this instrument two sequential recordings with two polarizational image pairs is needed instead of three. After evaluation, the intensity, degree and angle of linear polarization are obtained with pixel resolution and visualized in the hue-saturation-brightness scheme. This instrument is not portable and can function only in the laboratory at its present state of development.

3.5 Rotating-Analyzer Sequential Video Polarimeter

Horváth and Varjú (1997) used a rotating-analyser sequential video polarimeter to measure the polarization patterns of different terrestrial objects and habitats. Their aim was to obtain a database, a "digital atlas of polarization patterns". The four main steps of their technique, based on a video camera set up on a tripod are illustrated in Fig. 3.2. A given scene is recorded by a video camera through a neutral density rotatable linearly polarizing filter in front of the objective lens. Prior to recording, the focus, aperture, shutter speed and gain are manually selected. The initial alignment of the transmission axis of the polarizer is vertical. After a few seconds, it is turned manually twice by 45^{o} counter-clockwise. The actual direction of the transmission axis is spoken into the built-in microphone during recording.

The recorded scenes are digitised frame-by-frame using a frame grabber in the computer connected to a video recorder. The digitised response of the single pixels of the CCD detector is approximately a linear function of brightness when light intensities are not too high. In order to remain in this linear region, an appropriate set of values of the aperture, shutter speed and gain must always be selected, a procedure that requires a high level of experience. For all three orientations of the polarizer´s transmission axis 25 digitised frames can be averaged to filter the inevitable small noise of the video signal. After calibration of the camera/frame grabber combination for response versus intensity coding, from

these three averaged colour video pictures, the modulation of the intensity I is obtained as a function of φ. A sinusoid $I = A\ sin2(\varphi - \alpha + \pi/4) + B$ is fitted to this intensity modulation for each pixel of the picture in order to determine $I_{max} = B + A$, $I_{min} = B - A$ and the angle of polarization α, that is, the angular position of I_{max}. From these parameters the total intensity $I = (I_{max} + I_{min})/2 = B$ and the degree of linear polarization $p = (I_{max} - I_{min})/(I_{max} + I_{min}) = A/B$ are calculated for every point in the image.

Finally, two-dimensional colour- or grey-coded maps of I, p and α are produced with pixel resolution in the red (650 nm), green (550 nm) and blue (450 nm) spectral ranges, in which the three colour-sensitive CCDs of the camera have their maximal sensitivity. The outputs of this technique are 3×3 pictures of the scene recorded: the two-dimensional patterns of the intensity, degree and angle of linear polarization measured in the red, green and blue spectral ranges (Fig. 3.3).

3.6 Sequential Stereo Video Polarimetry: Visualizing Polarization Patterns in Three Dimensions

Mizera et al. (2001) realized stereo video polarimetry, by which polarization patterns can be visualized in three dimensions. This method is applicable to both scientific and educational purposes despite that there is no information that any animal visual system uses polarization as an input of binocular fusion, or stereopsis. The essence of stereo video polarimetry is the addition of depth to scenes imaging the distribution of polarization. Stereo video polarimetry is actually nothing more than the match-making of two different methods, namely, stereoscopic imagery (e.g. Brown 1994; Drouin 1995) and imaging polarimetry.

During a stereo video-polarimetric recording two video-polarimetric recordings of the investigated scene must be performed from two different, properly selected directions of view (Fig. 3.2A) to simulate the distance between the two eyes. Mizera et al. (2001) moved the camera by about 6 cm between the two images, which baseline corresponds with the average distance between the two human eyes but exceeds the ocular separation in several animals having polarization sensitivity.

In order to obtain a stereo effect of high quality one has to follow the general guidelines of stereo imagery (e.g. Waack 1985; Burder and Whitehouse 1992). The most common viewing method of stereo pairs is known as parallel, or free, or wall-eye viewing, and is reached most conveniently with the help of proper stereoscopic viewing lenses or prisms (Fig. 3.2E). Without such devices, one can use simply the palm of the hand or a sheet of paper (Burder and Whitehouse 1992). The palm of the hand or the sheet must be held vertically in front of the nose, parallel to the symmetry plane of the head. By selecting properly the distance of the eyes from the stereo pair, one can arrange that the left eye looks at, and only at, the left image, and the right eye looks at the right image (Fig. 3.2E), then in the mind a three-dimensional image is formed.

As an example, Fig. 3.4 shows the stereo pairs of the reflection-polarization patterns of a car with a shiny bodywork measured with stereo video polarimetry. We can see in rows 2 and 3 of Fig. 3.4 that in some regions of the scene, p and α change strongly from point to point, which results in a rather erratic false colour distribution in these regions. The consequence of this is that the false colours of a given pixel on the stereo pair can be frequently different. Thus, the three-dimensional image cannot be developed, or at least the stereo effect is considerably reduced, because the mind of the observer is not able to or can hardly discover the corresponding pixels in the stereo pair.

The human visual system extracts spatial information from the two, slightly different images perceived by the right and left eyes on the basis of retinal disparities. Our mind is not adapted to reconstruct three-dimensional (3D) images from false-coloured stereo pairs encoding the spatial distribution of polarization. This is the reason why the 3D image is so difficultly formed when viewing the fully false-coloured stereo pairs of p and α. Thus, our mind needs some help to produce the 3D image of a polarized scene. Such help can be the use of the false colour combination of the stereo pair of the colour picture and the polarization patterns of the investigated scene.

Rows 4 and 5 in Fig. 3.4 show the stereo combination of the intensity (I) distribution of the car with the p- and α-pattern, respectively. In these combined stereo pairs I is coded by the brightness and the polarization information is displayed by the colour. The function of the stereo pair of the I-pattern of the scene in a given spectral range (rows 4 and 5 of Fig. 3.4) is to construct a "visual skeleton", on the basis of which the 3D image can be formed. This skeleton is then filled with the polarization information, either p or α, which is coded by colour shades.

Until now there is no evidence of binocular polarization channels in any visual system, just as there is no combination of colour binocularly in animal or human vision (stereo vision is achromatic and polarization-blind). Thus for this reason stereo video polarimetry is nothing else as a useful technique to visualize for a human observer how polarization varies with distance in a scene.

3.7 Ultraviolet-Sensitive Rotating-Analyzer Sequential Video Polarimeter

Horváth and Wehner (1999) designed a portable, UV-sensitive rotating-analyser sequential video polarimeter, which is composed of a tube camera (Hamamatsu Beam Finder III) with spectral sensitivity ranging from 200 to 750 nm. In front of the objective lens system a rotating linearly polarizing filter (HNP'B, Polaroid) is mounted with good polarizational characteristics also in the UV-C range of the spectrum (300 nm $< \lambda <$ 400 nm). Onto this polarizer a colour filter can be screwed on. If this is an UV-transmissing filter, video-polarimetric measurements can be performed in the UV. Using colour filters with transmission maxima in the

visible spectral range, the polarization patterns can be measured in the visible part of the spectrum.

The camera set on a tripod is connected to a portable video recorder (Sony 8 mm video walkman GV-S50E) for data storage. All technical details are spoken into a microphone and recorded as an audio signal by this video walkman too. The recording, evaluation and visualization of the polarization patterns happen similarly as in the case of the normal video polarimetry described above. To obtain light intensity data that are proportional to the real radiant intensities in a given range of the spectrum, the spectral transmission characteristics of the polarization filter and the camera optics as well as the spectral sensitivity of the camera sensor are taken into account. With this UV-sensitive video polarimeter the polarization patterns of the sky (Horváth and Wehner 1999) and the reflection-polarizational characteristics of water surfaces (Bernáth et al. 2002) were studied both in the UV and visible parts of the spectrum.

3.8 Sequential Video Polarimeters using Microscopes

3.8.1 Polarization Video Microscopy

Shashar et al. (2001) equipped a Zeiss SVII dissecting microscope with a digital camera and a rotatable linearly polarizing filter (HN38S) installed in the outgoing light path. Taking three consecutive images through the polarizer at three different directions of its transmission axis under depolarized epi-illumination, the p- and α-patterns of the target in the microscope can be determined as in the case of other types of imaging polarimetry.

3.8.2 Differential Polarization Laser Scanning Microscopy

In differential polarization (DP) microscopy the images are constructed from data derived from measurements using two orthogonally polarized light beams in the excitation or emission and light scattering pathway. The resulting images are two-dimensional maps of the measured DP and carry information on the anisotropic structure of the microscopic sample and/or the interaction of the sample with polarized light. In contrast to the macroscopic DP (usually representing a mean value after averaging for the whole sample volume) microscopic DP directly relates to a well-defined and oriented microscopic volume of the sample. Thus microscopic DP maps local DP properties in the sample within the constrains of the resolution of light microscopy.

Polarized light microscopy (e.g. Módis 1991; Robinson and Bradbury 1992) usually provides qualitative information, and is limited to some relatively easily determinable quantities, such as linear birefringence and linear dichroism, for

example. It is also used to enhance the contrast of the microscopy images. The performance of classical polarization microscopy can be improved considerably by applying digital recording and image analysis (e.g. Kocsis et al. 1998). Passive polarizers have been utilized in laser scanning microscopy (LSM)[2] either in the transmitted or in the fluorescence beam (Verbelen and Kerstens 2000). This technique can reveal the presence of certain anisotropic structures in the sample.

In DP microscopy usually well-established techniques of DP spectroscopy are employed: (i) high frequency modulation produces two orthogonally polarized states of light for the excitation; or (ii) the emitted or scattered light is analyzed for its content of orthogonally polarized components. Data in each pixel are obtained after demodulation and calculation of the DP quantities. DP microscopy provides much better resolution and higher sensitivity than the conventional polarization microscopy.

For transmitted and scattered light, theory of DP imaging has been elaborated by Kim et al. (1987). 16 independent Mueller DP images can be obtained which all carry information on specific light-matter interactions. Some of these images, such as patterns of the linear dichroism (LD) or circular dichroism (CD) are of special importance, and have been measured by using an image dissector camera (Beach et al. 1987) and a scanning confocal-stage microscope (Finzi et al. 1989). In a polarization modulation laser scanning microscope (Gupta and Kornfield 1994) DP imaging has been used in the transmission regime of a laser scanning microscope to determine LD and linear birefringence of polymer films with high sensitivity and precision.

Recently, a differential polarization laser scanning microscope (DPLSM) has been constructed by Pomozi (2002), Garab et al. (2003) and Pomozi et al. (2003). This technique is based on a Zeiss LSM 410 and uses high frequency modulation techniques. It can measure the following quantities:

- Fluorescence emission anisotropy r, which reflects the linear polarization of the luminescence emission and provides information on the anisotropic distribution of the emission dipoles.
- Circularly polarized luminescence (*CPL*) content of the emission, providing information on the chiral structure of the sample.
- The degree of linear polarization (p) of the fluorescence emission upon an excitation of the sample with linearly polarized light, allowing conclusion e.g. on energy transfer between the dipoles, the microviscosity of the sample in the vicinity of the emitting chromophore, and its excitation lifetime.

[2] In LSM the objective lens focuses a laser beam to a well-defined volume of the object at the focal point. By raster scanning a rectangular field, the intensity distribution of reflected or emitted light originating from the illuminated points is determined and stored as a digital image of the scanned area. Positioning a pin-hole in front of the detector in the fluorescence beam, only the light from the irradiated volume passes through to the detector and the light originating from out of the focal plane is filtered. The confocality provides optical slicing of the sample and clearer pictures.

- Linear dichroism (*LD*), providing information on the anisotropic distribution of the absorbance dipoles.
- Circular dichroism (*CD*) signals, being given rise by chirally organized molecules and/or molecular assemblies.
- Fluorescence-detected linear and circular dichroisms (*FDLD* and *FDCD*), providing the same information as *LD* and *CD* but with the use of fluorescence detection and thus reducing the effect of scattering.

Linear and circular birefringence patterns are given rise in anisotropic and optically active materials. For all DP parameters which use fluorescence, i.e. *r*, *p*, *FDLD* and *FDCD*, the images can be recorded in confocal regime, which thus provides better spatial resoltuion and the possibility of optical slicing and three-dimensional reconstruction.

Figure 3.5 shows the DP patterns of a phloem of *Convallaria majalis* measured by differential polarization laser scanning microscopy. Figure 3.5A shows the pattern of the fluorescence intensity *I* upon unpolarized excitation. Figures 3.5B and 3.5C display the patterns of anisotropies r_0 (with respect to the horizontal) and r_{45} (relative to 45º from the horizontal). The fluorescence anisotropy *r* is the ratio of the difference between the intensities of the two orthogonally polarized components of emitted light upon the unpolarized excitation and the total intensity of emission. The bright and dark areas indicate positive and negative *r*-values, respectively. The white parts of the *r*-images represent very low intensities *I*, where the determination of *r* is ambigous. Figures 3.5B,C show that *r* depends significantly on the orientation of different parts of the cell wall. Figure 3.5D displays the change of *I*, r_0 and r_{45} along the black line in Figs 3.5A-C. It is clear from Fig. 3.5D that the variations in *r* are not correlated with those in *I*, but identify the orientation of fibers in the cell wall.

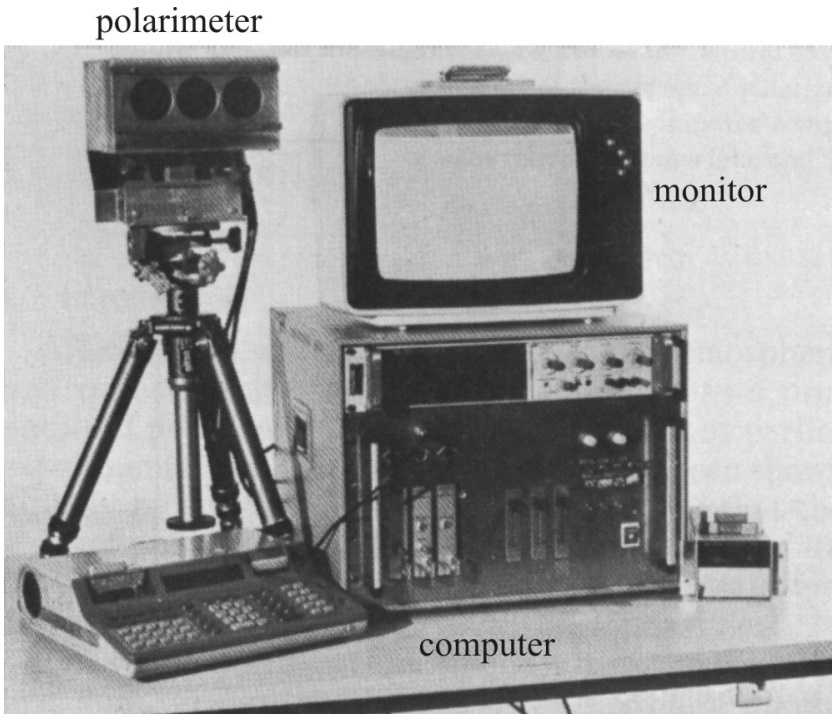

Fig. 3.1. The video polarimeter designed by Prosch et al. (1983, Fig. 4, p. 1362).

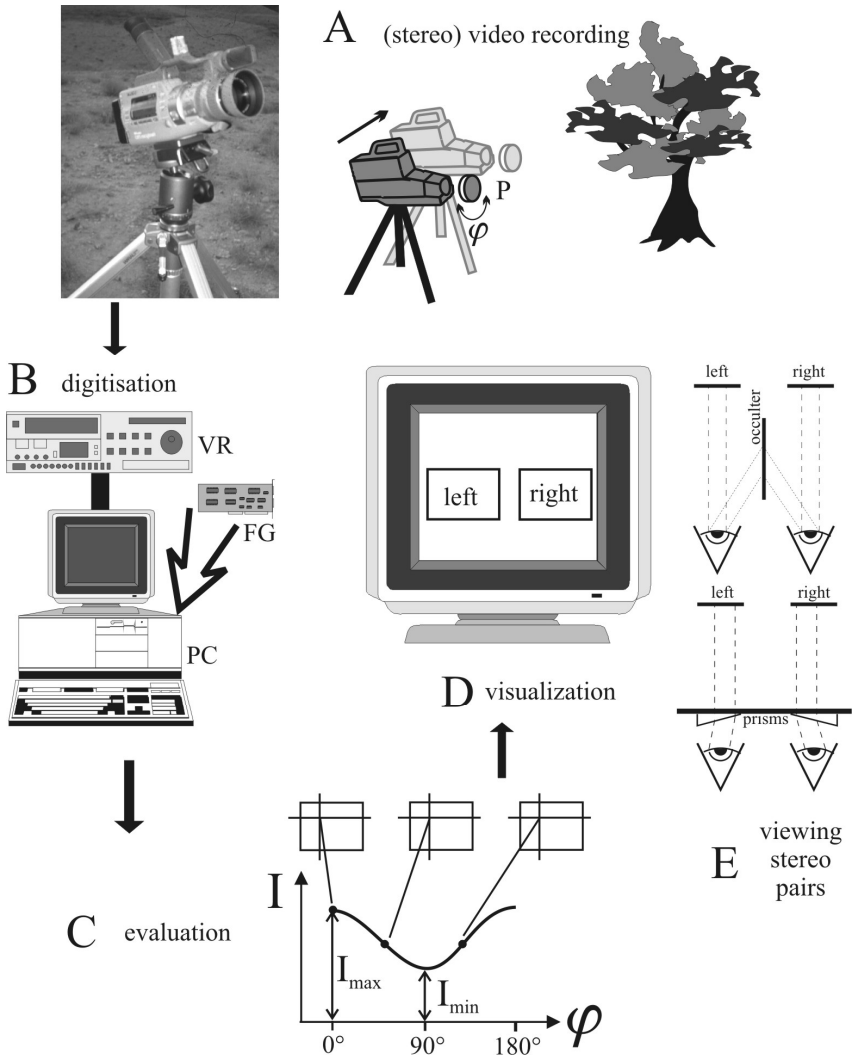

Fig. 3.2. Schematic representation of the technique of rotating-analyzer (stereo) video polarimetry. A: Recording with a video camera mounted with a rotating linearly polarizing filter (P) in front of the objective lens. At stereo video polarimetry two recordings are taken from two different directions of view. φ: angle of rotation of the transmission axis of the polarizer. B: Digitisation of the recorded pictures using a frame grabber (FG) in a personal computer (PC) connected directly to the video camera recorder or to a video recorder (VR). C: Evaluation of the light intensity I, the degree of linear polarization p and the angle of polarization α from pixel to pixel of the recorded scene. D: Visualization of the patterns of I, p and α on the computer screen (in the case of stereo video polarimetry in form of false coloured stereo image pairs). E: Two common possibilities of viewing stereo pairs with the use of an occulter or prisms. (After Fig. 1 of Mizera et al. 2001, p. 395).

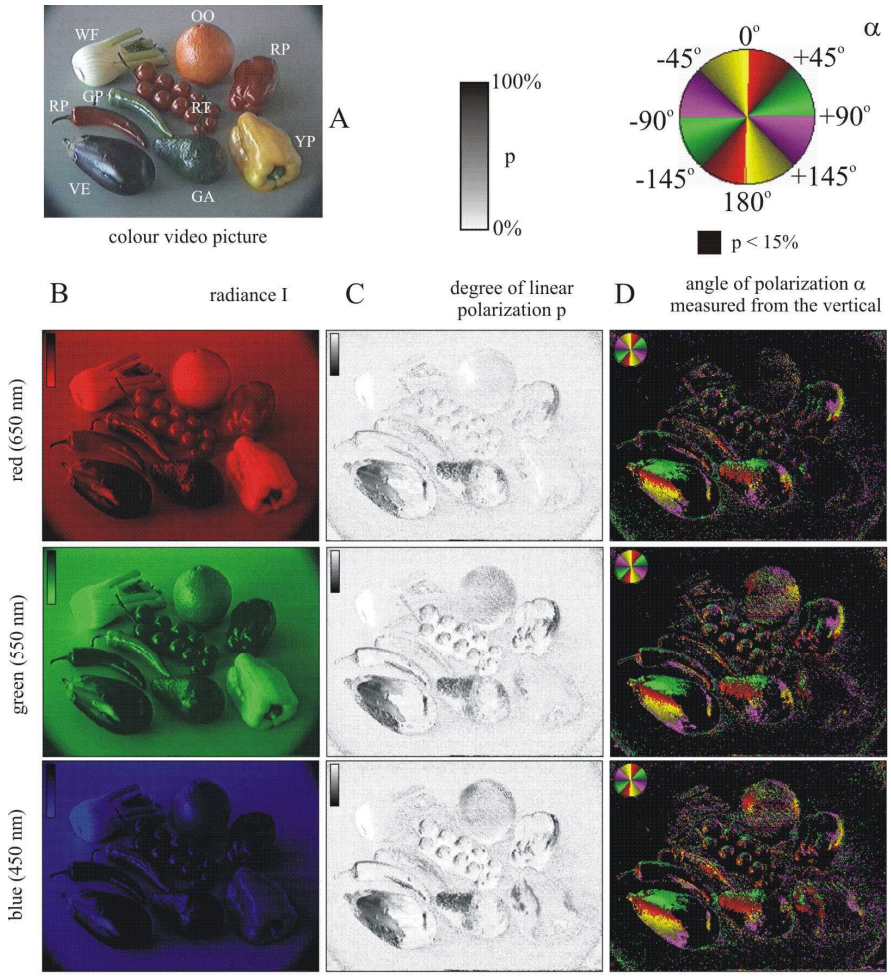

Fig. 3.3. A: Video picture of a collection of fruits and vegetables of different colours. B-D: The patterns of the intensity I, degree of linear polarization p and angle of polarization α of light reflected from the collection measured by video polarimetry in the red (650 nm), green (550 nm) and blue (450 nm) ranges of the spectrum. The different numerical values of I, p and α are coded by different colour and grey tones as shown in the insets. In the α-patterns black represents areas with $p < 15\%$. WF: white fennel root, OO: ochre orange, RT: red tomato, RP: red paprika and red pepper, YP: yellow paprika, GP: green pepper, GA: green avocado, VE: violet egg-fruit. (After Fig. 2 of Horváth and Varjú 1997, p. 1157).

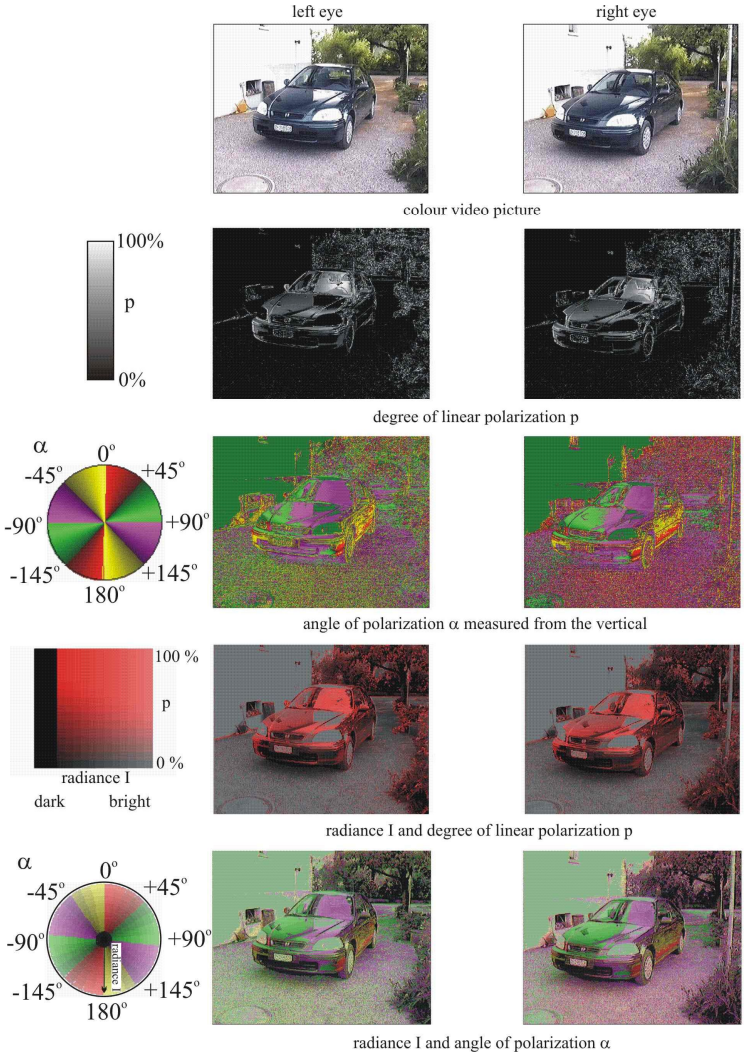

Fig. 3.4. The reflection-polarizational characteristics of a car with a shiny bodywork represented in parallel view stereo format and the corresponding colour and grey palettes encoding the numerical values of the degree of linear polarization p and angle of polarization α. First row: Stereo pair of the colour video picture of the car. Second row: Stereo pair of the p-pattern measured in the green (550 nm). Third row: Stereo pair of the α-pattern at 550 nm. Fourth row: Stereo pair of the combined patterns of p and radiance I. The higher the p-value, the deeper is the red hue. If $I < 20\ \% = I_{threshold}$, then p is not represented by red. We used $I_{threshold}$, else due to the inevitable small noise of p at low I-values erratic deep red patches or pixels would be occur in the picture. Fifth row: Stereo pair of the combined patterns of I and α. The higher the I-value, the brighter the colours coding α. The same $I_{threshold}$ is used again as in row 4 to remove the noise of α at low I-values.

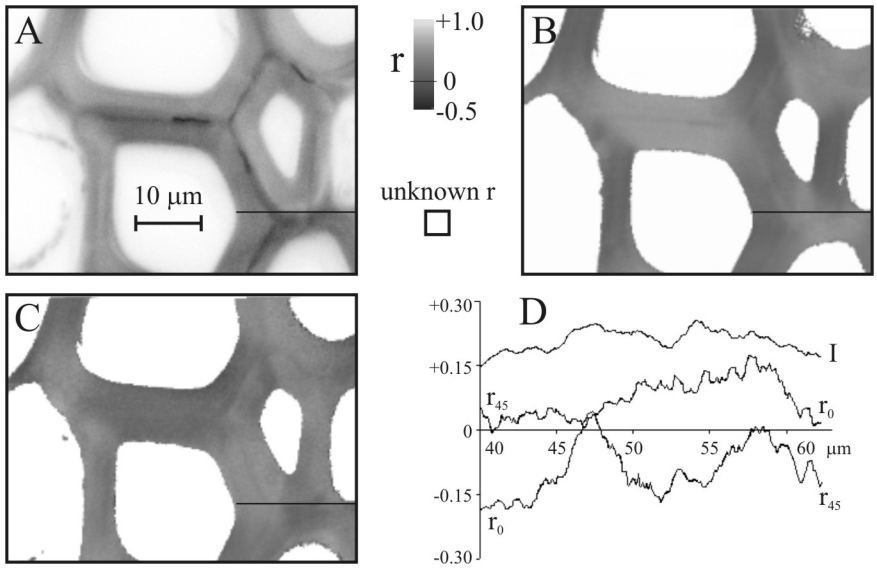

Fig. 3.5. Patterns of the fluorescence intensity *I* (A), anisotropy r_0 relative to the horizontal (B) and anisotropy r_{45} relative to 45º from the horizontal (C) measured by differential polarization laser scanning microscopy. D: Quantitative data of *I*, r_0 and r_{45} measured along the black line in A-C. *I* is displayed on an arbitrary scale in such a way that darker grey shades code higher *I*-values. (Courtesy of G. Garab and I. Pomozi, Biological Research Center, Hungarian Acadmey of Sciences, Szeged).

4 Space-Borne Measurement of the Polarizational Characteristics of Earthlight: The POLDER Instrument

The POLDER (**POL**arization and **D**irectionality of the **E**arth's **R**eflectance) space-borne sequential imaging polarimeter aboard the Japanese ADEOS (**AD**vanced **E**arth **O**bserving **S**atellite) over a three year period (1996-1998) was designed to measure the directionality and polarization of the earthlight, that is, the sunlight reflected from the earth´s surface and scattered by the atmosphere (Deschamps et al. 1994). The inclination of the optical axis and the altitude of the instrument were 98.6^o from the horizontal and 796 km from the sea level, respectively. The instrument was composed of a CCD detector (with pixel resolution = 242×274; from the ADEOS one pixel corresponds to an area of 6×7 km^2 on the earth´s surface at the nadir; spectral sensitivity = 400-1050 nm), a wide (114^o×114^o) field-of-view telecentric optics (focal length = 3.57 mm, f-number = 4.5) and a rotating filter wheel carrying the colour and linearly polarizing filters (Fig. 4.1A). It could observe a terrestrial target from different viewing angles during the same orbit. An air-borne simulator of the instrument has also been developed and experimental air-borne campaigns have been conducted too.

As opposed to single scattering, multiple scattering or reflection of light can induce elliptic polarization. Radiative transfer simulations showed that in the atmosphere of the earth the fourth component V of the Stokes vector (characterizing elliptical and circular polarization) of light is negligible compared to the other components. Thus, the polarization of earthlight is mostly linear for prevailing atmospheric conditions. Therefore the POLDER instrument sensed only the linearly polarized component of earthlight.

This was achieved by three subsequent measurements with the transmission axes of the linear polarizers turned by steps of 60^o at 443, 670 and 865 nm. A combination of the three measurements yielded the Stokes parameters I, Q, U, from which the total radiance $R = I$, the linearly polarized radiance (the product of the total radiance and the degree of linear polarization p) $R_p = pR = (Q^2+U^2)^{1/2}$, and the angle of polarization α were computed. The POLDER-team prefers to use R_p, which is nearly additive with respect to the contributions of molecules, aerosols and land surfaces, rather than p, in which the contributions of polarized and unpolarized light are mixed ambiguously. Thus, in the publications of the POLDER-team colour-coded maps of R and R_p have been used, like those in Figs. 4.1B-E and 4.2B,C.

The POLDER radiometric measurements yielded target reflectance and polarization properties as well as bi-directional reflectance and polarization distribution functions from one or several orbits. An alternative instrument to POLDER planned to measure polarized reflectance from space is the EOSP (**E**arth **O**bserving **S**canning **P**olarimeter), which was scheduled for launch in 2003. The POLDER observations are used in studies of the biogeochemical cycles as well as the global energy, water and mass budgets and took part in the World Climate Research Program and the International Geosphere Biosphere Program. The main scientific objectives of the POLDER mission were (Deschamps et al. 1994):

- mapping atmospheric aerosols, including their sources and transport, and studying their influence on the earth's radiation budget (e.g. Deuzé et al. 1993; Bréon et al. 1997; Herman et al. 1997; Leroy et al. 1997);
- assessing cloud properties, such as cloud top height, phase and type (e.g. Goloub et al. 1994; Descloitres et al. 1995);
- estimating total integrated water vapour amount (e.g. Leroy et al. 1997);
- improving earth radiation budget estimates (Deschamps et al. 1994);
- estimating ocean colour and its role in the carbon cycle (Deschamps et al. 1994);
- characterizing land surface properties and vegetation cover (e.g. Deuzé et al. 1993; Bréon et al. 1995; Herman et al. 1997; Leroy et al. 1997).

The POLDER system provides new opportunities for estimating atmospheric aerosol content over land surfaces. While radiances reflected from most land surfaces are only slightly polarized, radiances scattered by the molecules and aerosols in the atmosphere are highly polarized. Consequently, the polarization of earthlight measured from the space originates primarily from the atmosphere (Fig. 4.1C), and aerosol properties can be derived from polarized reflectance measurements. Computing theoretically the polarized reflectance expected for an aerosol-free atmosphere (Rayleigh scattering only), the difference between the computed and measured polarized radiances corresponds to polarized radiance scattered by the aerosols. Thus, the polarized reflectance measurements by POLDER at 443, 670 and 865 nm yield the aerosol spectral behaviour, which provides an indication of their type (i.e., size distribution and refractive index).

POLDER polarization measurements allow also an estimate of the cloud pressure level. The measured polarized radiance is related to the atmospheric molecular optical thickness above the cloud, assuming that the radiance originating from the cloud is negligibly polarized and spectrally neutral. This assumption is not true for particular directions, such as that of the rainbow, which are avoided. In other viewing directions the measured polarized reflectance is mainly generated by the atmosphere and is nearly proportional to the molecular optical thickness above the cloud. This relationship leads to estimate the pressure at the top of clouds. Since the polarization induced by molecular scattering is maximal at 90^{o} from the solar direction, this viewing direction is preferred. Although the aerosols above the cloud layer can also produce some perturbing polarized radiance, the bulk of atmospheric aerosols is contained in the boundary layer below the cloud layer. For this method polarization measurements at 443 nm

are used because the molecular scattering contribution to the polarized reflectance is maximal relative to other contributions.

Cloud type determination and thermodynamic studies of the atmosphere require recognition of the cloud phase, a parameter that POLDER polarization measurements can access. Radiative transfer simulations have shown that the polarization of cloud-reflected radiance in specific directions (e.g. that of the rainbow) is very sensitive to the cloud phase, which can be either ice or liquid water (Fig. 4.2). Liquid cloud droplets are evidenced by the characteristic strong polarization of the rainbow (Fig. 4.2C) exhibited by spherical particles for scattering angles near 140^{o} from the solar direction. The rainbow characteristic disappears as soon as the scattering particles depart from spherical geometry. The lack of this characteristic feature in cloud polarization signature, therefore, is indicative of the presence of ice crystals. The method utilizes the polarizational data measured at 865 nm, since this spectral channel is the least polluted by molecular scattering among the other channels. These informations are very useful also for polarimetric cloud detection.

Leaf cuticle and wax specularly reflect part of the incident solar radiation on the canopy. Because this radiance does not interact with chlorophyll pigments, and hence cannot participate in photosynthesis, it should not be considered when the aim is to remotely sense the vegetation. Since specularly reflected radiance is partially linearly polarized, polarization measurements over land surfaces can be applied to correct for the specular component of the reflectance. POLDER polarization observations help also to characterize the vegetation cover, because they are sensitive to the microscale structure of the canopy (Curran 1982). However, since the polarized reflectance measured from the space originates mostly from the atmosphere, accurate atmospheric corrections (subtracting the contribution of atmospheric scattering) are necessary before space-borne polarized reflectance measurements can be used for vegetation monitoring applications.

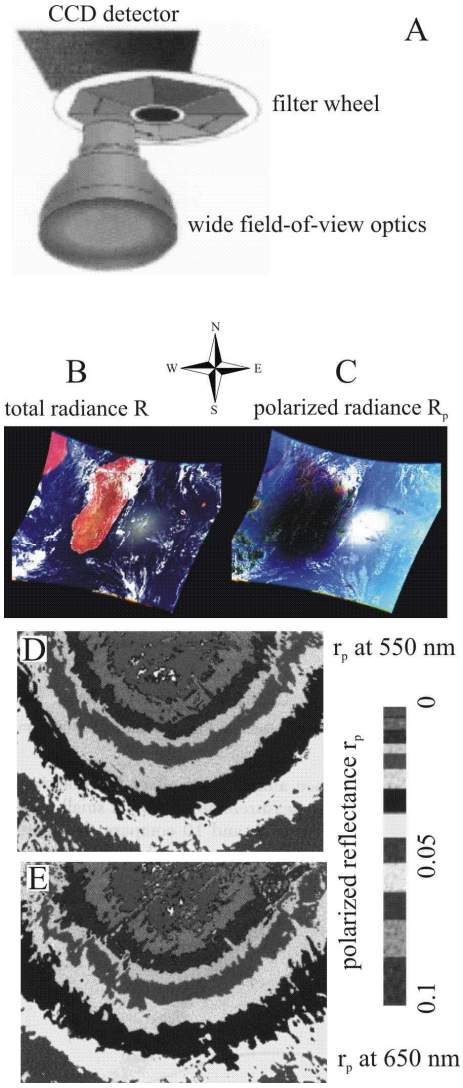

Fig. 4.1. A: Schematic picture of the POLDER sequential imaging polarimeter. (After Fig. 1 of Deschamps et al. 1994, p. 600). B, C: False-coloured patterns of the total radiance R and polarized radiance R_p of earthlight measured by the POLDER instrument above Madagascar. For both pictures red, green and blue codes the radiances measured at 865, 670 and 443 nm, respectively. The R_p-pattern is mainly blue because of the high linear polarization of molecular scattering at 443 nm. The ground surface has a very low contribution to the polarized signal, which depends mainly on the atmospheric light scattering. (After http://ceos.cnes.fr:8100/cdrom-00b2/ceos1/satellit/polder/index.html). D-F: Patterns of the dimensionless polarized reflectance r_p of earthlight measured by the airborn version of the POLDER instrument at 550 nm (D) and 650 nm (E). (After Fig. 6 of Deuzé et al. 1993, p. 145).

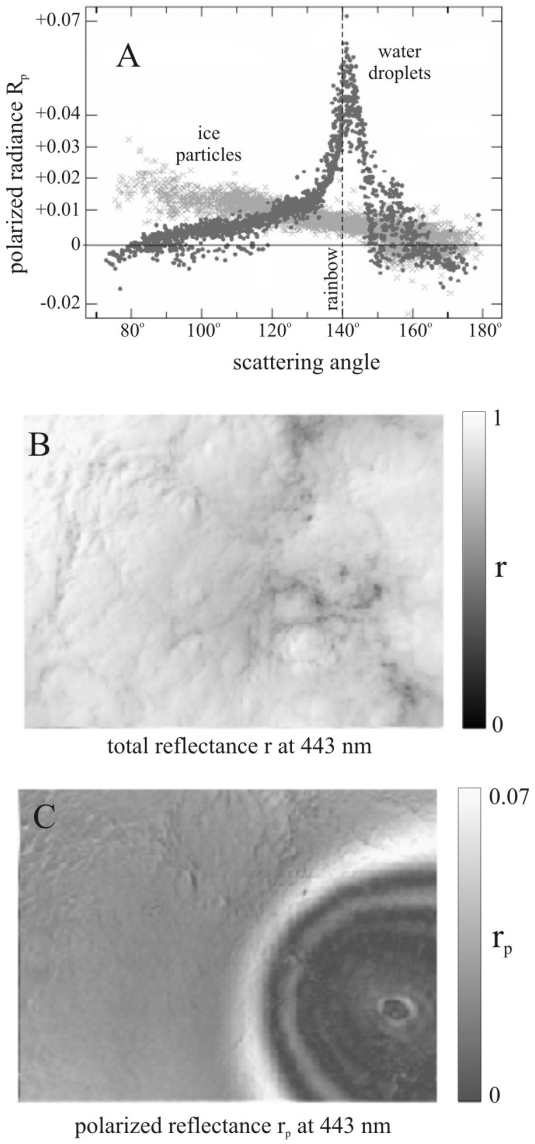

Fig. 4.2. A: The dimensionless polarized radiance R_p of clouds composed of either water droplets (dark grey dots) or ice particles (light grey ×) as a function of the scattering angle from the solar direction measured by the POLDER instrument at 865 nm. (After http://ceos.cnes.fr:8100/cdrom-00b2/ceos1/satellit/polder/index.html; similar graphs are seen in Figs. 4, 10, 11, 12 of Goloub et al. 1994, p. 81, 83, 84). B, C: Patterns of the total reflectance r and polarized reflectance r_p over stratocumulus clouds measured by the airborne version of the POLDER instrument at 443 nm. In the r_p-pattern the strongly polarized primary and higher order rainbows are clearly discernible. (After Figs. 2 and 3 of Goloub et al. 1994, p. 80 and 81).

5 180° Field-of-View Imaging Polarimetry

5.1 Simultaneous Full-Sky Imaging Polarimeter with a Spherical Convex Mirror

North and Duggin (1997) developed a practical method to obtain colour-coded maps of the partial Stokes vector (I,Q,U) of polarized light and its derivatives (p, α) across the whole sky. They used a four-lens camera (Nishika N8000, focal length = 30 mm) with negative colour roll films. The four apertures of the camera were covered by neutral density linearly polarizing filters (HN38, Polaroid), the transmission axes of which were oriented at 0°, 45°, 90° and 135° with respect to a given reference direction. Hence, all polarizational pictures of the sky were taken simultaneously, which is the main advantage of this simultaneous imaging polarimeter. The polarimeter was suspended 2.7 m over a spherical security convex mirror (46 cm diameter, back-surface aluminium coating on an acrylic matrix) by four thin rods. This height was required to mitigate the parallax effects created by the finite separation of the four lenses. Figure 5.1 illustrates the setup providing a circular image of the nearly complete skydome reflecting off the mirror and onto the focal planes of the four cameras. A 6 m air-driven shutter release was used to minimize obscuration by the photographer. Although the spherical mirror of this imaging polarimeter encompassed a field of view of almost 180°, the instrument could not record data of the entire skydome, since the camera above the mirror and the tetrapod screened out certain areas of the firmament.

After taking the polarizational photographs of the mirror-reflected skydome, the developed film was converted by a standard photo-CD process to digital images of the sky. Although the aluminium coating on the mirror might induce a small amount of circular polarization, the fourth component V of the Stokes vector was assumed to be zero. This simplifying assumption allowed to obtain images of the partial Stokes vector (I,Q,U) by using only linear polarizers. The digitised images were then evaluated by a commercial image-processing software. The resulting spatial distributions of the partial Stokes vector components were obtained over the full sky in the red, green and blue part of the spectrum, where the colour film had its sensitivity maxima.

Since the polarimeter of North and Duggin (1997) was not calibrated, the Stokes vector $\underline{S}_{sky}$ of the incident skylight could not have been measured. With this

system only the spatial distribution of the Stokes vector $\underline{S}_{image}$ of skylight reflected from the spherical mirror could be determined, which is the major disadvantage of this polarimeter. The underlying mathematics is described by Clarke and Grainger (1971). From the resulting partial Stokes vector $\underline{S}_{image}$ the radiance I_{image}, degree of linear polarization p_{image} and angle of polarization α_{image} were derived, which inform qualitatively about I, p and α of skylight. Thus, a controlled experiment remains to be executed to provide absolute polarimetric calibration, to obtain full polarimetric characterization of the optical system, and to invert $\underline{S}_{image}$ to derive $\underline{S}_{sky}$. This work has not been done until now. Furthermore, the equipment is voluminous and cumbersome (Fig. 5.1), which does not permit easy and rapid setting up, disassembly, transfer and transport. These may be the reasons why results on skylight polarization obtained with this mirror-based simultaneous imaging polarimeter have been never published. Nevertheless, an improved version of this polarimeter could be a next generation of the radiometric total sky imager (Fig. 2.7). Such a polarimetric total sky imager could monitor continuously the radiance, spectral and polarizational properties of the full sky.

5.2 Sequential Full-Sky Imaging Polarimeter with a Fisheye Lens and a CCD

To measure the polarized radiance distribution of skylight over the whole celestial hemisphere, Voss and Liu (1997) developed a sequential full-sky imaging polarimeter (Fig. 5.2). It is based on a 178° field-of-view fisheye camera lens, a cooled (–30 °C < T < –40 °C) CCD sensor controlled by a computer interface card and a remotely controlled filter changer. Typical integration times of the CCD are between 0.5 and 15 s. With the spectral filter changer, measurement in several spectral ranges can be performed. With linearly polarizing filters placed in one of the filter wheels the Mueller matrix of the instrument can be varied. The data process involves taking three polarizational images with different orientations of the transmission axes of the polarizers. The overall time period for one complete measurement is 1.5–2 minutes. After digitisation the images are stored in a hard drive of a personal computer. From these three images the components I, Q, U of the Stokes vector as well as the degree p and angle α of linear polarization of the incident light are computed, saved and displayed in image format. The accuracy of the polarization measurement is about 2%.

During the measurements a sun occulter blocks the direct solar radiation to avoid camera lens flaring and overexposure of the CCD. This occulter also blocks a rectangular portion of the sky, as a result, no data are available within a celestial area of about 20° around the sun ranging radially from the horizon almost up to the zenith. Due to the sun occulter this polarimeter cannot measure the part of the sky where the Babinet and Brewster neutral points occur. Calibrations of the system linearity, spectral and polarizational responses, camera system roll-off and absolute response of the instrument are described in detail by Voss and Liu (1997).

Using this polarimeter, Liu and Voss (1997) measured the polarized radiance distribution of skylight at different sites, under various atmospheric conditions, at different wavelengths, and studied the position of the Arago neutral point. Although the setting up of this polarimeter is much easier than that of the full-sky imaging polarimeter of North and Duggin (1997), this equipment is not portable either, because it needs a mains power supply and connection with a computer, furthermore its CCD has to be thermoelectrically cooled.

5.3 Portable 180° Field-of-View Sequential Rotating-Analyzer Imaging Photopolarimeter

Gál et al. (2001c) designed a portable, 180° field-of-view, sequential, rotating-analyzer imaging photopolarimeter, with which numerous successfull measurements have been performed in the field (e.g. Gál et al. 2001a,b,c; Pomozi et al. 2001a,b; Barta et al. 2003; Bernáth et al. 2003; Horváth et al. 2002b, 2003; Barta and Horváth 2003) due to the portability of the instrument and because it is easy to manage.

The setup of this polarimeter is shown in Fig. 5.3A-C. An angle of view of 180° is ensured by a Nikon-Nikkor fisheye lens (F-number = 2.8, focal length = 8 mm) including a built-in rotating filter wheel mounted with three neutral density linearly polarizing (HNP'B, Polaroid) filters with three different orientation (0°, 45° and 90° measured from the radius of the wheel) of their transmission axis, and the detector is a photoemulsion in a Nikon F801 photographic camera. Different types of colour reversal film is used; the maxima of their spectral sensitivity curves are usually at about 650 nm (red), 550 nm (green) and 450 nm (blue). In the calibration of the instrument the following are involved: the determination of the system Mueller matrix, which describes the influence of the fisheye objective on the optical parameters of the light passing through it, and the determination of the transfer function of the whole evaluation process, that is, the function between the real light intensity I fallen onto the photoemulsion and the digital value of the intensity taken from the digitisation process.

From a given sky three photographs are taken for the three different alignments of the transmission axis of the polarizers on the built-in filter wheel. In skylight measurements, the camera is set up on a tripod in such a way that its axis passing through the view-finder points northward (Fig. 5.3C) and the optical axis of the fisheye lens is vertical pointing towards the zenith (Figs. 5.3A,B). In order to eliminate distorting internal reflections of direct sunlight from the refracting surfaces of the fisheye lens, the sun is blocked by a sun occulter. Under normal illumination conditions of the sunlit sky, the overall time needed for one complete measurement is about 6-8 sec.

After chemical development of the colour reversal films, the framed colour dia slides are digitised with a scanner. The triplet of the digitised polarizational pictures of a given scene are then evaluated and the patterns of the intensity, degree and angle of linear polarization are visualized as high-resolution colour-

coded two-dimensional circular maps in the red, green and blue spectral ranges, in which the three colour-sensitive layers of the photoemulsion have the maximal sensitivity. The calculation of the intensity, degree and angle of linear polarization of skylight is the same as in the case of video polarimetry (Horváth and Varjú 1997). In the case of skylight measurements, the three-dimensional celestial hemisphere (Fig. 5.3D) is represented in two dimensions by a polar-coordinate system, where the zenith angle θ and the azimuth angle φ from the solar meridian are measured radially and tangentially, respectively (Fig. 5.3E). In these circular images the centre is the zenith, the horizon is the perimeter, and the zenith angle θ is directly proportional to the radius from the centre. Modifying appropriately the design, this 1-lens 1-camera 180° field-of-view imaging polarimeter can be adapted to underwater measurements too, like the submersible video polarimeter designed by Shashar et al. (1995b).

5.4 Portable 3-Lens 3-Camera Full-Sky Simultaneous Imaging Photopolarimeter

The major shortcoming of the 180° field-of-view polarimeters described in the preceding two sections is their slowness due to they record the three polarizational pictures of the full sky sequentially. One cycle of three exposures and, in between, exchanging the polarizer may well take several seconds or minutes depending on the time of exposure. Thus, these instruments cannot be used if the cycle duration is comparable with the time, during which the optical characteristics of the sky change considerably. Such situations occur in the following cases:

- The sky is cloudy and the clouds move fast.
- Moving aerial objects (e.g. birds or airplanes) occur in the firmament.
- Immediately after sunset or prior to sunrise when the radiance of skylight changes rapidly and moreover the time of exposure increases considerably due to the relatively low radiance of skylight.
- The platform of the polarimeter, being on the board of a ship, for example, is moving or rocking.

In order to eliminate the major shortcoming of the mentioned polarimeters, Horváth et al. (2002a) designed a 3-lens 3-camera full-sky imaging polarimeter, which takes the 3 polarizational pictures of the entire sky simultaneously rather than sequentially. Thus, celestial polarization patterns can be recorded with this instrument even if rapid temporal changes occur in the sky. The ability of this polarimeter to provide full-sky polarization patterns without motion artefacts has great potential for application in atmospheric optics and radiative transfer problems in the earth-ocean system, because data can be collected simultaneously, thus changes in the atmosphere during measurement can be neglected.

The setup of the polarimeter of Horváth et al. (2002a) is shown in Fig. 5.4. The polarimeter is composed of three Nikon F801 roll-film photographic cameras (Fig.

5.4A), each of them equipped with a Sigma fisheye lens (Figs. 5.4B,C). The F-number of the lenses is 4, their focal length is 8 mm, and their field of view is 180°. The cameras are fixed on a tripod parallel to each other onto a horizontal guide pointing always northward during the measurements (Fig. 5.4D) with the optical axes of the fisheye lenses vertical, pointing towards the zenith. On one of the outside cameras the vertical direction of looking through the view-finder is turned to horizontal by means of a 90° angle-finder. The simultaneous triggering of all three cameras is mechanically ensured by synchronous pressing the buttons of the remote exposure cords. The same values of aperture and exposure are set manually on all three cameras, which are focussed to infinity.

Each Sigma fisheye lens (Fig. 5.4B) is composed of two lens groups with a circular filter mount in between (Fig. 5.4C). Into the mounts neutral density linearly polarizing filters (HNP'B, Polaroid) are inserted in such a way that the angles β between their transmission axes and the horizontal guide pointing northward are 0°, 60° and 120° in the first, second and third camera, respectively (Fig. 5.4D). The type and sensitivity of film material used as detector depends on the type of recording.

To minimize ghost effects due to internal reflections of direct sunlight from the refracting surfaces within the fisheye lenses and the blooming effect caused by the direct solar radiation and the limited dynamic range of the photoemulsion, the direct sunlight is blocked. A sun occulter is fixed to a rod held by an assistant (Figs. 5.4E,F) and positioned at a distance as great as possible from the polarimeter to minimize the area of its shadow on the picture of the skydome to be photographed. The evaluation of the three polarizational pictures taken with this 3-lens 3-camera full-sky imaging polarimeter is the same as in the case of the 1-lens 1-camera full-sky imaging polarimeter of Gál et al. (2001c). The calibration of both polarimeters was also the same.

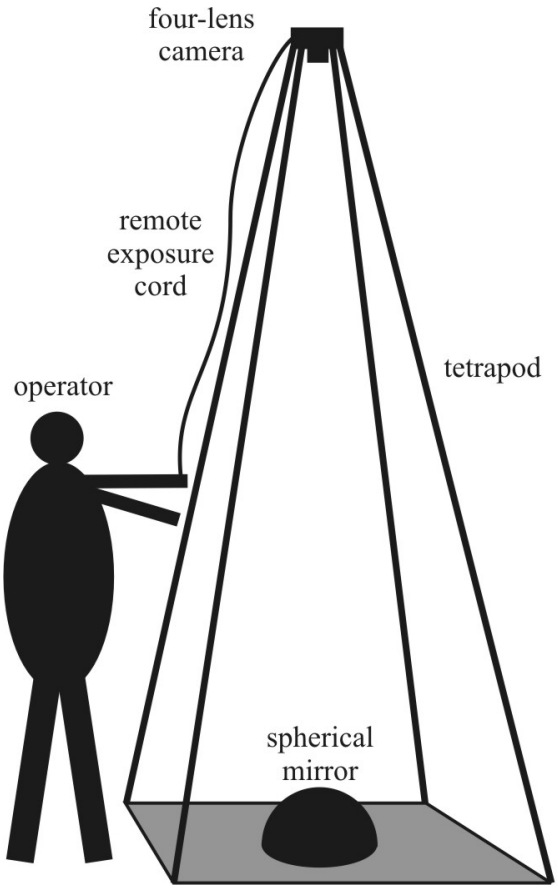

Fig. 5.1. Setup of the simultaneous full-sky imaging polarimeter of North and Duggin (1997, Fig. 2, p. 725).

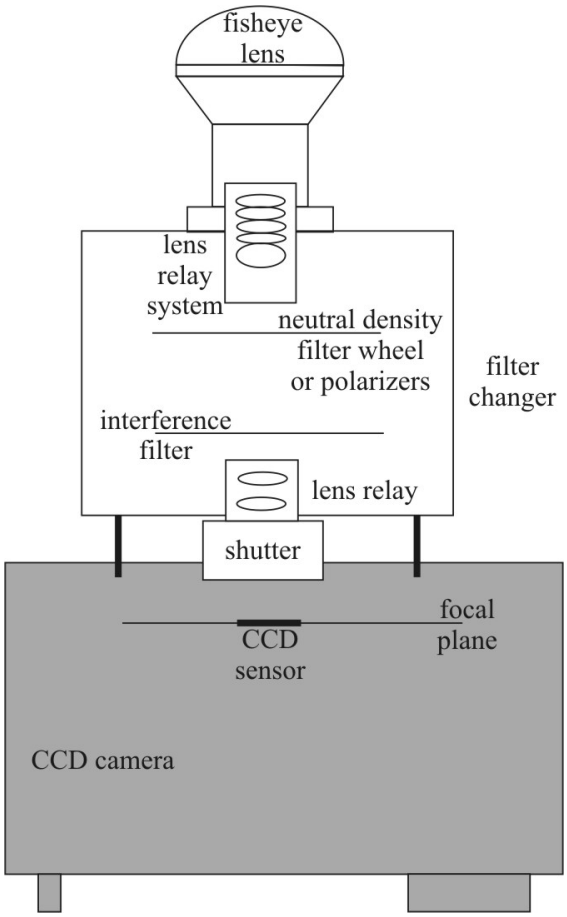

Fig. 5.2. Block diagram of the sequential full-sky imaging polarimeter of Voss and Liu (1997, Fig. 1, p. 6086).

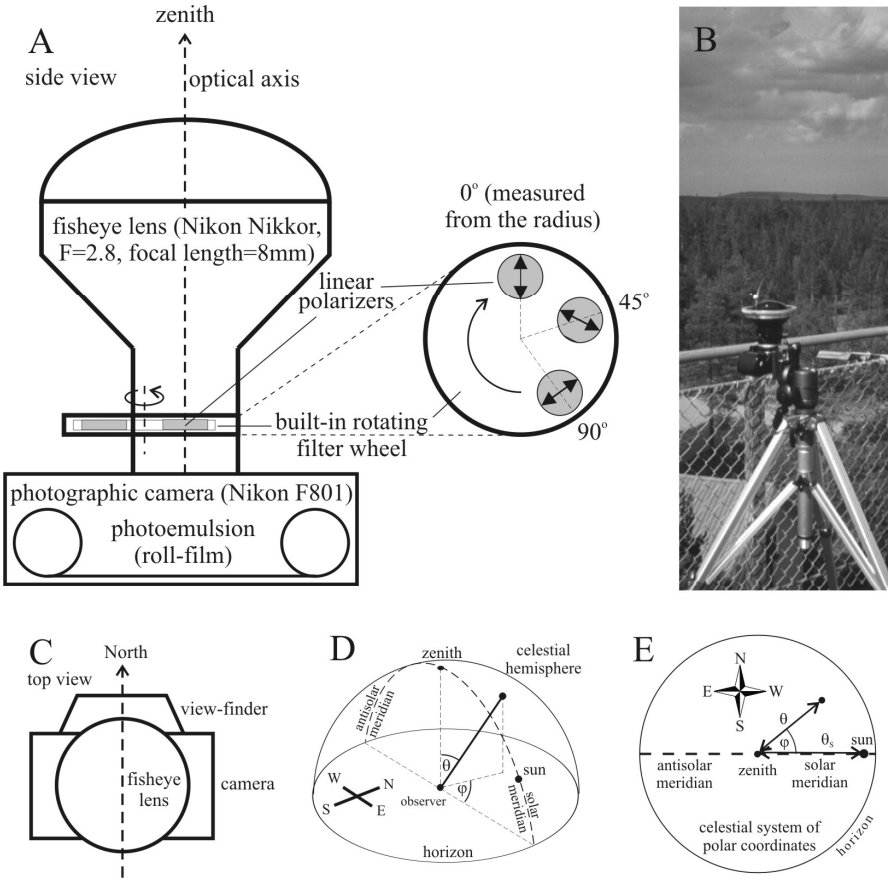

Fig. 5.3. A, C: Schematic representation of the portable, 180° field-of-view, sequential, rotating-analyzer imaging photopolarimeter of Gál et al. (2001c). The orientation of the transmission axis of the linearly polarizing filters is indicated by double-headed arrows. B: In-field setup of the polarimeter. D: Three-dimensional celestial polar coordinate system. E: Two-dimensional celestial system of polar coordinates used in the representation of the polarization patterns of the full sky measured by the instrument. East is on the left (rather than on the right) of the compass rose because we are looking up through the celestial dome rather than down onto a map. (After Fig. 1 of Gál et al. 2001c, p. 1388).

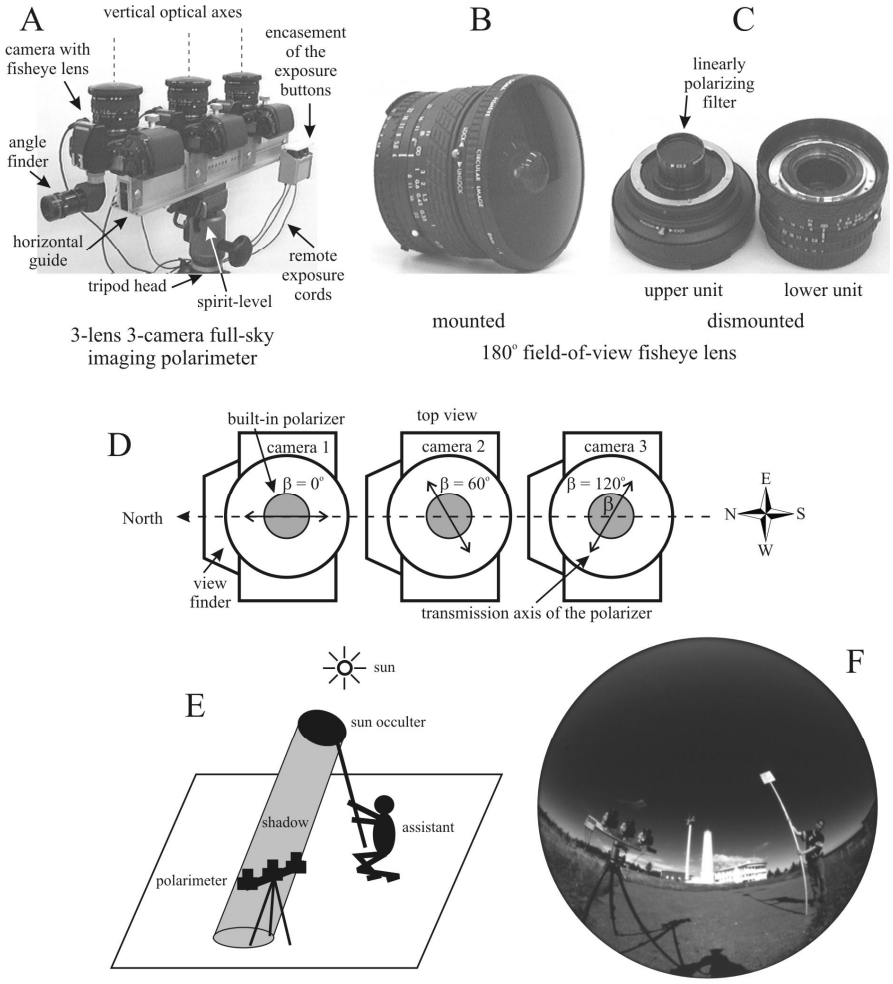

Fig. 5.4. The setup of the 3-lens 3-camera full-sky (180° field-of-view) imaging polarimeter of Horváth et al. (2002a). A: Photograph of the polarimeter. B, C: Photographs of the Sigma fisheye lens in mounted and dismounted state. D: Direction of the transmission axis of the built-in linearly polarizing filters indicated by double-headed arrows. E: Blocking the direct solar radiation by a sun occulter held by an assistant to eliminate multiple internal reflections at the refracting surfaces within the fisheye lenses. F: 180° field-of-view photograph showing the in-field setup of the polarimeter and an assistant with the sun occulter. (After Figs. 1-4 of Horváth et al. 2002a, p. 544, 545).

6 Future Polarizational Cameras

6.1 Polarization-Sensitive Chips

The polarimeters described in Chapters 2-5 utilize optical imaging systems that are external to the detectors. Compactness of design and speed of generating polarization images can be enhanced greatly by incorporating an array of microscopic polarization filtering optics directly onto a photosensitive chip. Wolff and Andreou (1995) started to develop a next generation of polarizational cameras. They designed a prototype of a polarization-sensitive chip with three photosensitive scanlines. Each scanlines consist of 128 pixels and are coated with one of 0^o, 45^o or 90^o orientations of linearly polarizing material deposited directly onto each column of sensing elements. Three horizontally adjacent pixels with, respectively, 0^o, 45^o and 90^o orientations produce one measurement of partial linear polarization. The controller of the chip is interfaced with a computer-guided scanning digitiser. The three columns of polarization component data are digitised, and are converted, using the composite (hue-saturation-brightness) visualization scheme, into a pixel column of false-coloured image. This one-dimensional polarization-sensitive chip is a precursor of two-dimensional polarizational camera chip arrays, which are currently under development.

6.2 Polarizational Cameras

A common design for colour cameras is to use a non-polarizing beam-splitter that directs equal amounts of incoming light onto three separate CCD sensors for the red, green and blue spectral ranges. If a linearly polarizing filter is placed over every CCD, each filter having a unique direction of its transmission axis, a so-called "polarizational camera" using a non-polarizing beam-splitter can be built that operates in white light or in a given part of the spectrum, if a colour filter is added in front of the lens system of the camera. This design was suggested by Wolff (1993) and first realized by Hanlon et al. (1999).

Wolff and collaborators are in the process of developing self-contained VLSI versions of polarizational cameras that sense complete states of partial linear polarization on-chip, compute state of linear polarization, and compute visualization or physical information related to sensed polarization. VLSI offers

very high computational throughput so that VLSI polarizational cameras enable operations at very high speeds.

Kalayjian et al. (1996) designed a one-dimensional polarization contrast retina that can be used as polarimetric scanning sensor for real-time, automated vision tasks. The retina employs two parallel linear arrays of 29 photodiodes as sensing elements. Polarizing material is placed directly over the photodiodes so that each diode array receives totally linearly polarized light. The transmission axis of the polarizer on the first row of diodes is perpendicular to that on the second row. An on-chip analog circuit computes the polarization contrast with comparing the output signals of the two diode rows. In order to enhance the spatial resolution and to extend the one-dimensional array to high-density two-dimensional polarization contrast sensors, the commercially fabricated macroscopical linear polarizer should be replaced by a two-dimensional array of microscopical, pixel-sized areas of linear polarizers with lithographic techniques used in CMOS circuit fabrication.

A polarizational camera is a generalization of the conventional intensity camera. If necessary, the former can function as the latter. Adding colour-sensing capability to a polarizational camera makes it possible to sense the complete set of electromagnetic parameters of light incident on the camera. Polarizational cameras have more general capabilities than standard intensity cameras, and can be applied for different purposes (see Chapter 2).

7 Polarizational Characteristics of the Sky

7.1 Skylight Polarization

7.1.1 The Importance of Skylight Polarization in Atmospheric Science

Solar radiation as a natural light source is unpolarized before entering the earth's atmosphere. The natural light field originating from the sky is partially linearly polarized through scattering interactions (Liou 1980; Hulst 1981) with the atmospheric constituents, such as the permanent gases (e.g. N_2, O_2), gases with variable concentration (e.g. O_3, SO_2) and various solid and liquid particles (aerosol particles, water droplets, ice crystals). The intensity and polarization of skylight have long been studied for many reasons. Early interest involved explaining natural phenomena such as the colour of the sky and rainbows (Young 1982; Coulson 1988). Since the discovery of skylight polarization by Arago in 1809, studies of the polarization of skylight and neutral points have been emphasized, as these can be used as indicators of atmospheric turbidity (Kimball 1913, Coulson 1980) and surface properties (Coulson 1974). The principal interest in measurements of skylight polarization is its sensitivity to dust, haze and pollution in the atmosphere (Sekera 1956; Bullrich 1964). The maximum degree of polarization, for example, is diminished by the effects of aerosol scattering, and at the same time the neutral points of skylight polarization are shifted from their normal positions.

The clear sky has a characteristic polarization pattern depending on the solar position, the distribution of various components of the atmosphere and the underlying surface properties (Coulson 1988). The polarization of skylight has been the subject of numerous theoretical and experimental investigations (e.g. Chandrasekhar 1950; Neuberger 1950; Hulst 1952; Sekera 1957a,b; Holzworth and Rao 1965; Bellver 1987; Coulson 1988; North and Duggin 1997; Voss and Liu 1997; Horváth et al. 1998b; Horváth and Wehner 1999). The principal features of the intensity and polarization of the sunlit sky can be explained in terms of Rayleigh scattering by molecules in the atmosphere (Coulson 1988). Modern radiative transfer theory in the investigation of polarization (Chandrasekhar 1950; Liou 1980; Hulst 1981) has been applied to studies on planetary atmospheres (e.g.

Coulson et al. 1960; Chamberlain 1978) as well as the earth-ocean system (e.g. Plass and Kattawar 1970; Kattawar et al. 1973; Kattawar and Adams 1989).

Understanding the intensity and polarization of light in the atmosphere is also important in atmospheric correction of remotely sensed data (e.g. Gordon 1978; Gordon and Wang 1992). Neglecting the polarization in radiance calculations in an atmosphere-ocean system can introduce errors as large as 30% (Adams and Kattawar 1993). Measurements of the total sky polarized radiance distribution can be used to test the validity of exact (vector) radiative transfer models. Through inversion techniques this distribution can also be used in the determination of physical and optical properties, such as the absorption and scattering phase function of aerosols (Wang and Gordon 1993), for instance.

7.1.2 Measuring Skylight Polarization

Early measurements of skylight polarization were made mainly by visual means. As the semiconductor technology advanced, new photodetectors in conjunction with computer technology made the automatic measurement of light and its polarization possible. A large number of optical systems have been developed for observations of skylight polarization. Coulson (1988) listed the various types of point-source polarimeters developed until 1988 for observations of the atmosphere and surface of the earth. Although photomultiplier tubes have been used as detectors for most of these systems, some devices use other detectors such as silicon cells or photographic films.

Most ground-based measurements of skylight polarization were performed by means of point-source polarimeters using narrow-band interference filters to determine the degree and angle of linear polarization for different wavelengths of light. As these polarimeters possess a very small aperture (ca. 1^o-5^o, in which the optical information are averaged), the polarizational characteristics of the sky can be analyzed by them only within very restricted fields of view. The spatial distribution of skylight polarization could be determined by scanning the firmament with such a point-source polarimeter, but this is a time-consuming task done rarely and only in special cases: Using a point-source polarimeter and making repeated scans along the solar-antisolar meridian and perpendicularly to the solar meridian, Shaw (1975) measured the skylight polarization at 400 nm during the total solar eclipse of 30 June 1973 in Kenya. Brines and Gould (1982) undertook similar measurements at several points of the firmament by means of a point-source scanning polarimeter. They could measure points at every 5^o of zenith angle and azimuth of a half hemisphere of the sky within 7-8 minutes, during which the sun moved about 2^o along its arc. Certain unavoidable errors were a consequence of their rapid measurement process, such as inaccuracies attendant upon setting the axes of the instrument. If one wished to enhance the spatial resolution of the samples by one or two orders to obtain a picture-like scan of the polarization of the entire sky, the measurements would require 70-80 or 700-800 minutes, a period during which the celestial polarization pattern would change considerably due to the rotation of the earth (it takes 80 minutes for the

sun to move by 20°). It is clear that the polarization pattern of the entire firmament cannot reliably be measured by such a time-consuming method.

The development of full-sky imaging polarimetry (North and Duggin 1997; Voss and Liu 1997; Gál et al. 2001a,b,c; Pomozi et al. 2001a,b; Horváth et al. 2002a,b, 2003) offered new methods for observing the distribution of skylight polarization over the whole celestial hemisphere in several ranges of the spectrum quickly and accurately. Although various aspects of the intensity and polarization in the sunlit atmosphere have been studied in the past (reviewed by Coulson 1988), rapid measurements of the polarization distribution over the entire sky were not possible before the development of these different types of full-sky imaging polarimetry. The ability of these imaging polarimeters to provide polarization distribution over the full sky has great potential for application in studies of atmospheric aerosols as well as radiative transfer problems in the earth-ocean system, because data can be collected in a short time; thus changes in the atmosphere during measurement can be avoided or minimized. With these polarimeters neutral points can also be easily detected (Liu and Voss 1997; Gál et al. 2001a,b,c; Pomozi et al. 2001a,b; Horváth et al. 2002a,b, 2003).

7.2 Celestial Polarization Measured by Video Polarimetry in the Tunisian Desert in the UV and Green Spectral Ranges

In his seminal paper on skylight navigation in insects, especially in ants, Santschi (1923) wondered why certain genera and species used the sun as a compass, while others relied predominantly on the sun-free parts of the sky. In his lifetime, it was not known yet that the decisive aspect of light perceived by insects in the sky was the distribution of E-vectors of linearly polarized light – later discovered in bees (Frisch 1949), and now extensively studied in desert ants of the genus *Cataglyphis* (Wehner 1994a). The differences, however, that Santschi had observed among different genera and species are still a riddle. Are they really due to differences among different taxonomic groups of ants, or are they caused by characteristics of the habitats occupied by the different species? As the habitats of the *Aphenogaster*, *Messor*, *Monomorium* and *Cataglyphis* species are rather varied and include desert regions in mountains, sand-dune areas, salt pans or coastal inundation plains, several parameters such as water content, haze, frequency of clouds and the turbidity of the atmosphere vary accordingly. All these factors have strong influences on various optical aspects of scattered skylight (Coulson 1988, p. 350, 423).

One can imagine, for example, that due to the lower level of aerosols and haze in totally arid, vegetation-free desert mountain areas, the degree of skylight polarization p is higher there than in coastal regions, where haze commonly occurs. The atmosphere above salt pans, even if covered by hard, dried-out soil, can contain large amounts of water vapour due to the evaporation of water from the moist underground. How much do these differences in the structure of the ants'

habitats affect p? This is an important question, because p largely influences the accuracy of navigation (Wehner 1982, Edrich and Helversen 1987). Furthermore, to what extent does p depend on the spectral composition of skylight? The *Cataglyphis* retina is equipped with UV and green photoreceptors, but only the former are used in E-vector navigation. Do the atmospheric factors mentioned above influence p of skylight more strongly in the UV than in the green, or *vice versa*?

In order to answer these questions, Horváth and Wehner (1999) measured the degree of linear polarization p and angle of polarization α of skylight in the UV and green by an UV-sensitive video polarimeter in three different North African habitats. The geometry of the celestial windows from which the measurements were taken is shown in Fig. 7.2.1. No recordings were taken of the celestial windows, in which the sun appeared at a particular time of day. Due to the low levels of radiance at sunrise and sunset and because of the low UV transmittance of the polarizers and UV filters, UV recordings could not be taken when the sun was at the horizon. Measurements were taken under clear-sky conditions in three Tunisian habitats occupied by different species of desert ants (genera *Cataglyphis, Messor, Aphenogaster, Monomorium*):

1. within the vast expanses of salt-pan area of the Chott el Djerid (site "Tozeur", east of El Mahassen; 33.9°N, 8.5°E)
2. in the extremely arid and vegetation-free highland area of the south-eastern parts of the North African Dorsale (close to the Tunisian/Algerian border; site "Metlaoui", halfway between Metlaoui and Moulares; 34.3°N, 8.2°E)
3. in the coastal inundation plains of the Tunisian Sahel zone (site "Maharés", 34.6°N, 10.5°E)

In Tables 7.2.1 and 7.2.2 p is given in the green (550 nm) and UV (360 nm) range of the spectrum for two different solar elevations (θ_s = 35° and θ_s = 70°) at the above three different types of habitat. None of the three study sites exhibited significantly higher or lower p-values than any of the other sites. Whenever two measurements have been performed at the same site on two subsequent days, p differed, sometimes remarkably, from one day to another. For example, at the *Maharés* site at 550 nm in celestial window AS-20 p exhibited values of 20.1% and 29.9% on August 8 and 10, 1996, respectively, even though the human observer could not detect any obvious differences in the appearance of the sky. The same statistically significant differences hold for all measurements made on two separate days in the same region of the sky; with the only exception of celestial window Z, at Maharés, for $\theta_s = 70^o$ (Table 7.2.2). In conclusion, the temporal (day-to-day) variations at one particular site always exceeded the variations that are due to the spatial (geographical) location of that site. In all celestial windows p was always higher in the green than in the UV. This is in accord with what one would expect to occur in the normal atmosphere (Coulson 1988). Even in the cloudless sky vaulting a subtropical desert landscape p within medium-sized (20°×15°) celestial windows never exceeded mean values of 60%, and 75% in individual celestial directions.

The starting point of the investigation of Horváth and Wehner (1999) was the question whether different types of habitat occupied by different insect navigators varied in one or another optical aspect of skylight polarization. Such conjectures are not unwarranted. Water vapour and aerosols, which cause absorption and multiple scattering events, might occur in the atmosphere more frequently above one type of habitat than above another. Furthermore, differential reflections from the ground are known to influence the optical properties of skylight patterns as well.

The general result emerging from the measurements of Horváth and Wehner (1999) is that the question posed above cannot be answered in the affirmative. p, which is much more affected by atmospheric disturbances and surface reflections than is α, does not vary systematically among the different types of desert habitat. The day-to-day fluctuations of p are much larger than the habitat-based variations. Hence, Santschi's (1923) early observation that for navigation some ant species inhabiting particular geographical regions relied more on scattered skylight than direct sunlight, cannot be explained on the basis of the distinctness of skylight cues available to the ants in these different habitats. Instead, the interspecific and intergeneric differences must be caused by peculiarities of the ants' species-specific navigational systems.

Tables

Table 7.2.1. Degree of linear polarization p of skylight measured by video polarimetry in the ultraviolet (UV, 360 nm) and green (G, 450 nm) spectral range (window size: $20^o \times 15^o$) at three different Tunisian study sites (Tozeur: salt pan, 04.08.1996; Metlaoui: mountains, 05.08.1996 and 06.08.1996; Maharés: coastal area, 08.08.1996 and 10.08.1996). Solar elevation: $\theta_s = 35^o$, local time 16:30 (= UTC+1). Mean values ± standard deviations. For conventions of direction of view see Fig. 7.2.1.

degree of linear polarization p (%) for solar elevation $\theta_s = 35^o$				
direction of view	**spectral range**	**Tozeur (salt pan)**	**Metlaoui (mountains)**	**Maharés (coast)**
AS-20	UV	8.2 ± 3.9	11.6 ± 4.3 10.3 ± 4.3	10.9 ± 3.2
AS-20	G	13.1 ± 5.9	16.1 ± 6.6 14.2 ± 6.0	14.9 ± 6.3
AS-55	UV	17.3 ± 5.1	14.4 ± 4.7 18.7 ± 5.2	20.3 ± 3.8
AS-55	G	30.4 ± 6.2	36.7 ± 5.7 32.7 ± 6.0	38.9 ± 7.1
Z	UV	11.4 ± 3.9	10.6 ± 4.2 12.3 ± 4.4	13.0 ± 3.3
Z	G	24.2 ± 6.9	26.2 ± 7.9 24.8 ± 7.6	29.8 ± 9.0
Z-OFF	UV	16.9 ± 3.9	17.8 ± 3.9 17.3 ± 3.5	19.9 ± 2.6
Z-OFF	G	27.9 ± 6.2	29.0 ± 6.9 27.9 ± 6.5	34.0 ± 7.2
S-55	UV	3.8 ± 2.1	5.1 ± 3.1	4.8 ± 2.4
S-55	G	6.0 ± 4.1	6.3 ± 3.5	7.5 ± 4.2

Table 7.2.2: As Table 7.2.1 for solar elevation θ_s = 70° at local summer time 14:00 (= UTC+1).

degree of linear polarization *p* (%) for solar elevation θ_s = 70°				
direction of view	**spectral range**	**Tozeur (salt pan)**	**Metlaoui (mountains)**	**Maharés (coast)**
AS-20	UV	20.4 ± 3.6	22.0 ± 4.1 22.4 ± 4.1	19.1 ± 3.2 23.8 ± 3.5
AS-20	G	26.2 ± 4.5	28.6 ± 3.4 25.1 ± 3.7	20.1 ± 5.1 29.9 ± 7.6
AS-55	UV	16.5 ± 3.6	16.5 ± 3.7 16.5 ± 4.2	17.5 ± 2.9 19.1 ± 3.2
AS-55	G	24.1 ± 4.6	25.4 ± 5.7 23.7 ± 5.3	23.5 ± 3.9 31.5 ± 6.8
Z	UV	4.9 ± 2.5	5.1 ± 2.9 5.1 ± 2.9	4.8 ± 2.1 4.8 ± 2.1
Z	G	8.1 ± 3.9	7.5 ± 3.9 7.7 ± 4.0	7.6 ± 3.7 9.5 ± 4.8
Z-OFF	UV	13.2 ± 3.7	14.2 ± 4.7 13.3 ± 4.4	14.9 ± 6.3 17.1 ± 3.2
Z-OFF	G	18.2 ± 6.5	16.0 ± 6.9 16.3 ± 6.6	24.3 ± 3.2 22.2 ± 8.8

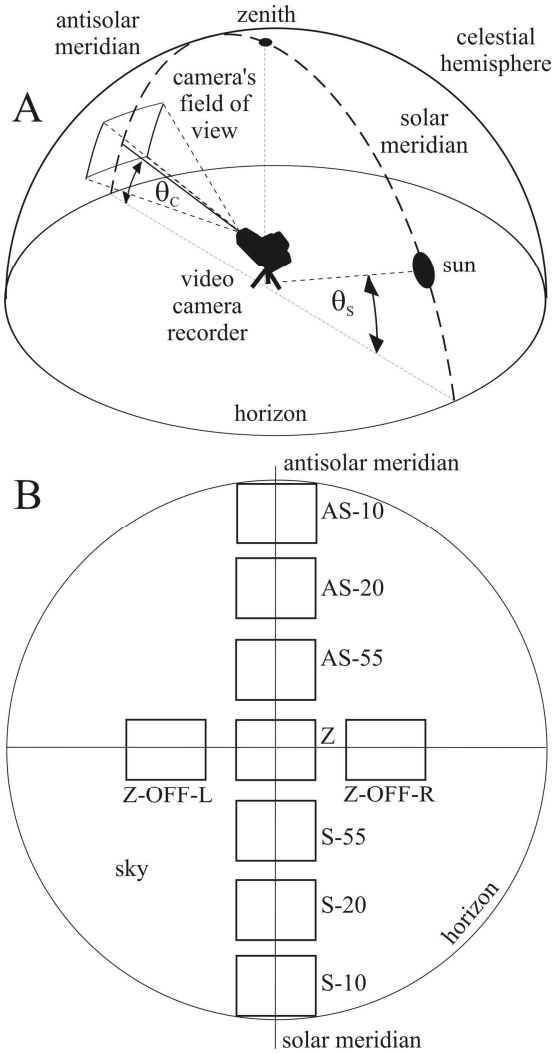

Fig. 7.2.1. A: Geometry of the video-polarimetric recording of skylight polarization taken by Horváth and Wehner (1999). The elevation of the video camera and the sun is θ_c and θ_s, respectively. B: The positions of the celestial windows within which video-polarimetric data were obtained. When the camera was oriented towards the antisolar and solar meridian, the rectangular window representing the field of view of the camera is designated by "AS-" and "S-", respectively. The numbers following these designations indicate the elevation θ_c of the camera in degrees. Window "Z" means that the camera recorded the region around the zenith. In case of window "Z-OFF" the camera was first rotated by 90^o from the solar meridian then elevated by 45^o in the plane perpendicular to the solar meridian (R: right, L: left). The field of view of the camera, i.e. the size of the celestial windows, is $20^o \times 15^o$ (horizontal and vertical extent, respectively). (After Fig. 1 of Horváth and Wehner 1999, p. 2).

7.3 Video Polarimetry of the Arago Neutral Point of Skylight Polarization

The most important optical characteristics of the clear sunlit sky are well described by the Rayleigh theory (Coulson 1988). The fine details of skylight polarization, however, differ from the ideal Rayleigh model. This failure, called the polarization defect, is caused by multiple scattering, molecular anisotropy, scattering by aerosol particles, size distribution and particle shapes of aerosol, and the light reflected from the ground. One of the most remarkable feature of this defect is the phenomenon of the neutral points where the degree of linear polarization is zero.

Under normal clear atmospheric conditions, the only neutral points of skylight polarization are the Arago, Babinet and Brewster points located along the solar and antisolar meridian (see Figs. 7.4.1A,B). Although in his pivotal paper on sky colour and polarization Strutt (1871), alias Lord Rayleigh, provided a succinct theoretical explanation for the maximum polarization of skylight at 90^o from the sun, he surprisingly did not mention the neutral points observed in 1810, 1840 and 1842 along the solar and antisolar meridian by Arago, Babinet and Brewster. These neutral points have been observed much more than any other characteristic of the skylight polarization. Hulst (1952) gave an approximate derivation for the angular position of these neutral points, which vary with the solar altitude, the wavelength and the haze aerosol composition. Neuberger (1950) suggested that the systematic observation of the Arago point would provide an appropriate index of atmospheric turbidity. Sekera (1957a), Holzworth and Rao (1965) and Bellver (1987) found a reasonably good correlation between positions of the neutral points and the intensity of air pollution. The positions of the neutral points are also strongly modified by clouds and debris from large volcanic eruptions, even for periods of several years (Coulson 1988).

Most ground-based observations of the neutral points were performed visually by means of the Savart polariscope (Coulson 1988). This simple device was widely used for more than a century. The neutral points can be detected and their position can accurately be determined by using the Savart polariscope. However, this polariscope is not well suited for determining the degree of linear polarization. Modern electronic point-source polarimeters use narrow band interference filters to determine the position of the neutral points for different wavelengths. Horváth et al. (1998b) measured the spatial distributions of the degree p and angle α of linear polarization within the areas of the neutral points by video polarimetry. They recorded the neutral points under clear sky conditions on 8 August 1996 in the vicinity of Metlaoui in the mountainous area of central Tunisia. This site and time was ideal for the measurements, because the atmosphere was very clear exhibiting a minimal amount of haze and aerosol. As

a consequence, p of skylight was high enough to allow video-polarimetric imaging of the neutral points.

Figure 7.3.1A shows a video picture of the sky in the region of the Arago point. It is obvious from Figs. 7.3.1A, 7.3.1B1, 7.3.1C1 and 7.3.1D1 that the positions of the neutral points are not correlated with the radiance of skylight. In contrast, the Arago point is clearly visible in the p-patterns (row 2 in Fig. 7.3.1) and the α-patterns (row 3 in Fig. 7.3.1). As it is clearly demonstrated in row 2 of Fig. 7.3.1, skylight is unpolarized (p = 0%) at the Arago neutral point, and p gradually increases with increasing angular distance from the neutral point.

The patterns of the E-vector alignment in row 3 of Fig. 7.3.1 show that the direction of polarization is more or less vertical, that is, the polarization is negative between the Arago point and the antisun, but above the Arago point the E-vectors are more or less horizontal indicating positive polarization. Furthermore as can be seen in the patterns of E-vector orientation, polarization switches from negative to positive as one passes the neutral point parallel to the antisolar meridian.

Rows 2 and 3 of Fig. 7.3.1 clearly show that the Arago point is farest away from the antisun in the blue. The measured angular distance β of the Arago point from the antisun is $\beta_{red} = 24.4^{o}$, $\beta_{green} = 22.4^{o}$, $\beta_{blue} = 29.3^{o}$ in the red, green and blue, respectively. Hence at the time of the video-polarimetric recordings by Horváth et al. (1998b) the Arago point was slightly closer to the antisun in the green than in the red. This exceptional situation was caused by the ground reflection of light.

Reflection from rough ground surfaces can introduce more or less vertically polarized light into the atmosphere. This effect enhances the region of negative polarization of the sky in those spectral ranges in which the reflectivity of the ground is high. At the site of the video-polarimetric measurements by Horváth et al. (1998b), in the vicinity of Metlaoui in central Tunisia the soil and the mountains had a typical reddish brown colour. Thus, the ground reflection (albedo) was high in the red. The consequence was that in the red a considerable amount of vertically polarized light was reflected from the ground, which enhanced the contribution of negative polarization in the atmosphere. Thus, the Arago point shifted slightly farer away from the antisun in the red.

Similar shift of the position of the Arago point due to reflection from snow or bright sand has also been reported by other authors (e.g. Können 1985; Coulson 1988). In such cases, however, the shift of the Arago point was observed in all ranges of the spectrum, because the ground reflection was high in all spectral ranges due to the whiteness of snow or sand. Reflection of light from huge water surfaces (lakes or sea) affects the position of the Arago point in the opposite direction. Light reflected from water surfaces introduces horizontally polarized light into the atmosphere in all spectral ranges, which enhances the region of positive polarization. This effect results in a shift of the Arago point towards the antisun in every part of the spectrum (Können 1985; Coulson 1988). Figure 7.3.1 shows the main characteristics of the Arago, Babinet and Brewster neutral points:

- their angular distances from the antisun and sun
- how their angular distances vary as a function of the wavelength of light
- how ground reflection affects their position
- what regions of positive and negative polarization occur around them
- there is no correlation between the positions of the neutral points and the radiance and colour distributions in the sky

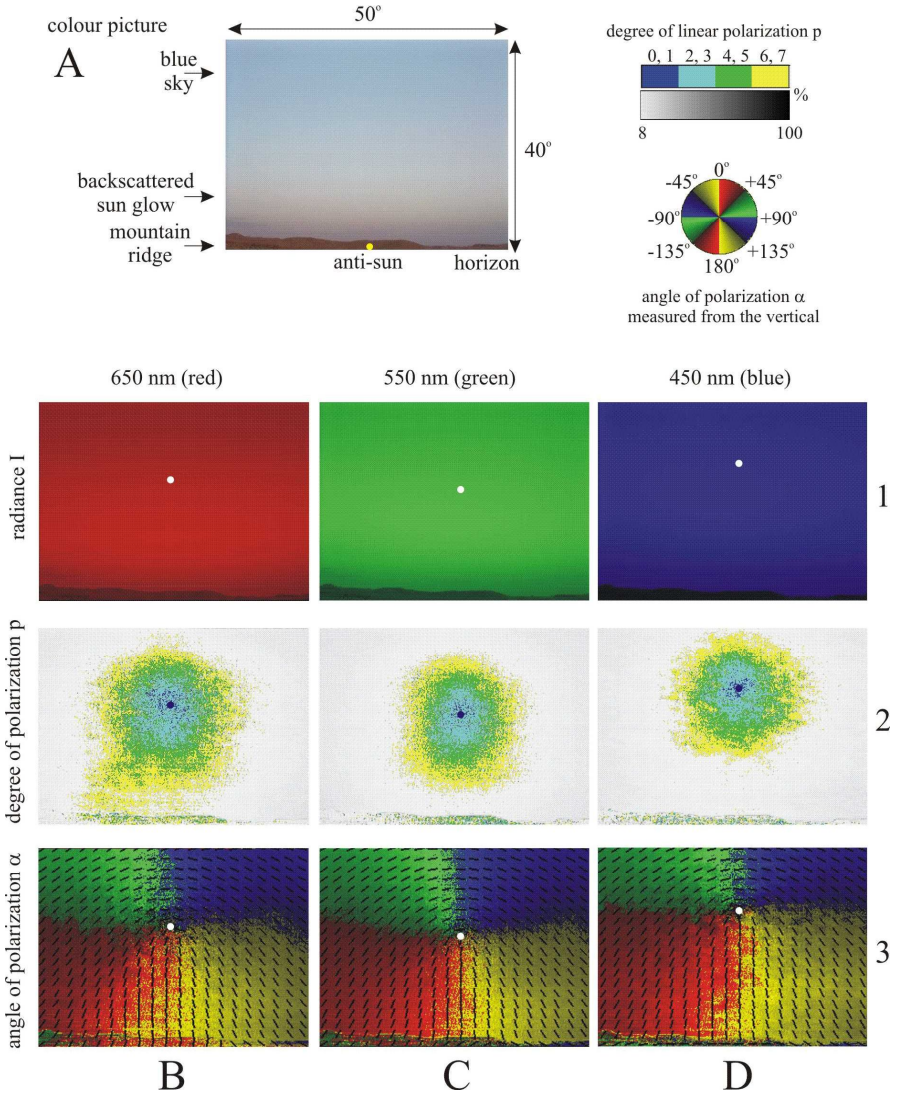

Fig. 7.3.1. Video-polarimetric imaging of the Arago neutral point of skylight polarization. A: Video picture of the sky around the Arago point. The position of the antisun is indicated by a dot. The horizon is demarcated by a mountain ridge. B-D: The patterns of radiance I, degree of linear polarization p and angle of polarization α of skylight measured by video polarimetry at 650, 550 and 450 nm. In the α–patterns any particular black bar represents the local orientation of the E-vector as averaged over a small rectangular region around the bar. The positions of the Arago point are indicated by dots. (After Fig. 2 of Horváth et al. 1998b, p. 336).

7.4 First Observation of the Fourth Neutral Polarization Point in the Atmosphere

7.4.1 The Last Neutral Point of Atmospheric Polarization

In the clear sunlit normal sky there exist only three loci, the Arago, Babinet and Brewster neutral points, where the skylight is unpolarized (Können 1985). The antecedents date back to 1809 when the French astronomer Dominique Francois Jean Arago discovered the partial linear polarization of skylight, and soon thereafter, above the antisun he observed a neutral point which nowadays bears his name (see Barral 1858). In 1840 the French meteorologist Jacques Babinet discovered a second neutral point situated above the sun (Babinet 1840). Since a neutral point existed above the sun, from considerations of symmetry, the Scottish physicist David Brewster predicted a third point of zero degree of polarization positioned at a similar angular distance below the sun along the solar meridian. This celestial point, called nowadays the Brewster neutral point, was found later at the theoretically predicted position (Brewster 1842). Only in 1846 could confirm Babinet the existence of the Brewster point (Brewster 1847).

Figures 7.4.1A and 7.4.1B show the relative positions of the Arago, Babinet and Brewster neutral points in the sky. Occasionally, some secondary neutral points have also been observed under special conditions associated with reflections from water surfaces (Brewster 1847; Soret 1888), turbid atmospheres after volcanic eruptions (Cornu 1884), or total solar eclipses (Pomozi et al. 2001a; Horváth et al. 2003).

With Brewster's discovery, the three principal neutral points, and the only ones now bearing the names of their discoverers, were known. They have been the subject of many ground-based investigations since their first observation, because their positions have been proven to be sensitive indicators of the amount and type of atmospheric turbidity (Coulson 1988). In the second half of the 20th century, however, the neutral points have lost their importance in applied meteorology and became a neglected tool in meteorological research (Neuberger 1950).

Theoretically, for reasons of symmetry, a fourth neutral point should exist below the antisun (Fig. 7.4.1). However, it cannot be observed from the ground, because the region below the antisolar point is either under the horizon after sunrise (Figs. 7.4.1A,B), or after sunset it is in the shadow of the earth (Fig. 7.4.1C) thus the sub-antisolar region is not illuminated by direct sunlight, which is the prerequisite of the occurrence of the fourth neutral point. The fourth neutral point can be observed only in the sunlit atmosphere and at appropriately high altitudes in the air (Fig. 7.4.1E) or space (Fig. 7.4.1F) somewhere below the antisun. The light field in the atmosphere can be divided into two components (Fig. 7.4.1):

1. The radiation scattered downward to the earth's surface (downwelling light field) from the sunlit sky is called "skylight".
2. The radiation directed to space (upwelling light field) and originating from scattering of sunlight in the atmosphere and reflection of light from the earth's surface is termed "earthlight" (Coulson 1988).

For a ground-based observer, the Arago, Babinet and Brewster points are the neutral points of polarized skylight scattered downward to the surface of the earth (Figs. 7.4.1A,B). For an air- or space-borne observer the Brewster point and the fourth neutral point result from the upward scattering of sunlight within the atmosphere and from the reflection of sunlight from the surface of the earth (Figs. 7.4.1E,F).

Before 2001, no observation of the fourth neutral point has been reported and so it has remained nameless. Apparently, the fourth neutral point has been overlooked in observational atmospheric optics, even though theoretical considerations (e.g. Rozenberg 1966) or model computations (Bréon et al. 1997) have predicted its existence. It has been mentioned only occasionally in the literature. Rozenberg (1966), for example, called it the "point observable from above", but it is not even mentioned in the most famous monographs on polarized light in nature (Gehrels 1974; Können 1985; Coulson 1988). Until 2001, this anonymous "fourth" neutral point has not been observed during air- or space-borne polarimetric experiments (e.g. Rao 1969; Coulson et al. 1986; Herman et al. 1986; Deuzé et al. 1989, 1993; Deschamps et al. 1994) and has been forgotten, despite that the neutral points were a basic tool in atmospheric research for a century (Neuberger 1950).

With this in mind, Horváth et al. (2002b) (Fig. 7.4.7D) performed two hot air balloon flights over Hungary immediately after sunrise. Using 180^{o} field-of-view imaging polarimetry, they measured the patterns of the degree p and angle α of linear polarization of earthlight in the red (650 nm), green (550 nm) and blue (450 nm) parts of the spectrum below the balloon's gondola as functions of the altitude and solar elevation. This technique has been proven to be an effective tool for the quantitative study of neutral points (Gál et al. 2001a,b,c; Pomozi et al. 2001a,b; Horváth et al. 2002a,b, 2003).

The aim of the first flight of Horváth et al. (2002b) was to test the measuring apparatus onboard and to check whether the 4000 m operational ceiling of the hot air balloon is enough to observe the fourth neutral point during and immediately after sunrise when the cloudless atmosphere is illuminated by approximately horizontally directed sunlight, which situation is ideal for this observation. The first flight was successful and Horváth et al. (2002b) were able as first to observe the fourth neutral point at different altitudes between 2000 and 3500 m. Then they performed a second flight to determine the lowest altitude, at which the fourth neutral point can be still observed.

7.4.2 Conditions of the Hot Air Balloon Flights to Observe the Fourth Neutral Point

Horváth et al. (2002b) conducted the two flights with a hot air balloon of the Hungarian Airlines Aero Club (MALÉV, Budapest). The operational ceiling of hot air balloons without oxygen-masks for the crew is 4000 m above the ground level. The flights and measurements were performed with the following crews:

- Gábor Horváth (group leader), Balázs Bernáth (Ph.D. student), Bence Suhai (undergraduate student) and Attila Bakos (pilot) on 28 June 2001 at local sunrise 04:52 (= local summer time = UTC+2);
- Gábor Horváth, Balázs Bernáth, András Barta (Ph.D. student) and Attila Bakos on 25 August 2001 at local sunrise 05:56.

In both cases the balloon launched prior to the local sunrise from the immediate vicinity of the Hungarian town Pákozd (47°13´N, 18°33´E). Horváth et al. (2002b) chose this time for launching, because at sunrise and sunset the contribution of light reflected from the ground is small to the earthlight which is dominated by atmospheric light scattering, especially for shorter (UV, blue) wavelengths. Furthermore, at sunrise and sunset the antisun has a minimal (zero) elevation resulting in a maximal distance between the aerial observer and the earth's surface in the predicted direction of the fourth neutral point (about 20°-35° below the antisun).

The first prerequisite of observation of the fourth neutral point is an appropriately thick air layer below the antisun in which the sunlight can be backscattered towards the aerial observer (Fig. 7.4.1E). The second prerequisite is that this backscattered light must not be suppressed by the ground-reflected light. Thus, the sunrise and sunset are ideal periods to observe the fourth neutral point. Depending on the meteorological conditions, a hot air balloon can climb to 4000 m within about 15-20 minutes, and to lose its height up to the ground needs about 20-25 minutes. Since hot air balloons must stay grounded from sunset until sunrise, and safe landing require good visibility, one could not measure the polarization pattern of earthlight at sunset at high altitude. This is the reason why Horváth et al. (2002b) measured at sunrise.

During the first flight the balloon drifted slowly toward south-east and landed in the immediate vicinity of the town Adony (47°06´N, 18°51´E), while during the second flight the balloon hovered approximately above Pákozd due to calm weather conditions at the relatively low (below 1400 m) altitudes of this flight. Figure 7.4.2A shows the trajectory of the balloon on the map of Hungary during the first flight. In Fig. 7.4.2B the altitude of the balloon is seen as a function of time after sunrise for both flights. The altitudes and the points of time at which polarimetric measurements were done are represented by small black-filled triangles in the two plots of Fig. 7.4.2B.

During the first flight, the minimum and maximum altitude at which the polarization pattern of earthlight was measured was 2000 and 3500 m. During the second flight measurements were performed when the balloon hovered between

800 and 1400 m. Figure 7.4.2C shows the solar elevation versus the time after sunrise derived for the ground from the latitude and longitude of the launching site at Pákozd and from the time of measurements. The dependence of the solar elevation on the change of the balloon´s longitude and latitude (during the first flight) as well as altitude (during both flights) was negligible.

During both flights the atmosphere was slightly hazy but cloudless, the rising sun was not occluded by distant clouds. At Pákozd (launching site) and between Pákozd and Adony (landing site), the ground surface was a mixture of areas which are typical for agricultural cultivation: green grass-land, fields, meadows, plough-land with a mosaic pattern of different albedos. Near Pákozd there is lake Velence partly occupied by areas of green reed and reed-grass. During the second flight in some places there was a thin (2-5 m) fog layer immediately above the ground surface.

7.4.3 Measurement of the Polarization Patterns of Earthlight by 180° Field-of-View Imaging Polarimetry

The objective was to measure the degree and angle of linear polarization of the upwelling earthlight in the whole terrestrial hemisphere. For this purpose a 180° field-of-view, rotating-analyzer imaging photopolarimeter was used (Gál et al. 2001c). The down-facing polarimeter was mounted onto a holder which hung on the outside of the gondola. The holder made it possible to slide up and down the polarimeter vertically. The verticality of the optical axis of the fisheye lens was checked by two orthogonal water levels on the camera and ensured by appropriate adjustments of the holder. Performing the measurements in the tiny gondola of the balloon required strict choreography. One measurement section happened in the following way:

1. Leaning out cautiously from the gondola, and after setting the time of exposure and the aperture of the camera, the first member of the crew (G. Horváth) let down the polarimeter below the bottom level of the gondola.
2. Squating in one of the corners of the gondola, the second member of the crew (B. Bernáth) reached out with one of its arms through an opening of the gondola to expose and turn away the filter wheel of the polarimeter three times, which lasted about 6 s.
3. Then the first person lifted the polarimeter, reset the time of exposure and the aperture, and let down again the polarimeter.
4. In the meantime, the third member of the crew (B. Suhai or A. Barta) took a note of the time of measurement, the aperture, the time of exposure and the altitude of the balloon. The fourth member of the crew was the pilot (A. Bakos) of the hot air balloon.

During the evaluation of the three polarizational pictures the following problem arose from the aerial manner of the measurements from the gondola: During the 6 s of one measurement the gondola drifted a little and turned away sometimes,

which resulted in more or less translations and rotations of the corresponding pixels of the three pictures relative to each other. The small spatial disparities (shifts) between the corresponding pixels induced by the drift caused small motion artefacts only in the polarization patterns of the ground surface, but did not affect those of the atmospheric light scattering. This is well seen in Figs. 7.4.3H,I,J, for example, where in the red spectral range small motion artefacts occur, which disappear in the blue part of the spectrum (Figs. 7.4.3B,C,D). However, the rotation of the corresponding pixels around the nadir due to the rotation of the gondola during the measurements must have been compensated in many cases. This was performed in such a way that at a given triplet of the digitized polarizational pictures, every picture was rotated around the nadir until some special selected common points of the pictures (small bright spots, road intersections, or the edges and angles of bright regions of the ground surface) coincided with a pixel accuracy.

7.4.4 Control Measurement of the Polarization Patterns of the Full Sky at Sunrise

The polarization patterns of the full sky was measured by the same 180^o field-of-view imaging polarimeter as those of the earthlight from the gondola of the hot air balloon. The skylight measurement was performed from the ground on 26 August 1999 at local sunrise (06:00 = local summer time = UTC+1, solar elevation = 0^o) in the Tunisian salt pan Chott el Djerid, 10 km from Kriz (33^o52'N, 8^o22'E) as described by Pomozi et al. (2001b). The desert ground was flat reddish/yellowish sand. The measured polarization patterns of skylight served as a control for comparison with the polarization distribution of earthlight and the Arago and Babinet neutral points of skylight polarization, which are not visible on the earthlight patterns.

7.4.5 Characteristics of the Fourth Neutral Point

Figure 7.4.3 shows the patterns of radiance I, degree p and angle α of linear polarization of earthlight measured by 180^o field-of-view imaging polarimetry at an altitude of 3500 m immediately after sunrise at a solar elevation of 2^o in the red (650 nm), green (550 nm) and blue (450 nm) spectral ranges during the first flight on 28 June 2001. In the p-patterns (Figs. 7.4.3C,F,I) two neutral points are clearly discernible in all three spectral ranges: the neutral point located along the solar meridian is the Brewster point, and the other along the antisolar meridian is the fourth neutral point. At both neutral points $p = 0$, and moving off them p gradually increases. In Figs. 7.4.3C,F,I low p-values are coded by blue, green and yellow colours, and the neutral points are positioned in the centre of two regions of very low p. These weakly polarized areas are the most compact in the blue, and are the most diffuse in the red.

The reason for this is that the longer the wavelength, the greater is the contribution of ground-reflected light to the earthlight. The neutral points are the result of higher order scattering of sunlight in the atmosphere, and due to the Rayleigh law these higher order scattering events dominate at shorter (UV and blue) wavelengths over ground reflection. At longer wavelengths the intensity of atmospheric scattering decreases and the relative influence of ground reflection increases as can be well seen in the *I*-patterns (Figs. 7.4.3B,E,H). This can also be seen in the *p*-patterns: in the blue *p* of earthlight changes smoothly and gradually as a function of the direction of view, while in the red *p* changes suddenly at the edges of neighbouring dark and bright regions of the ground.

In the α-patterns of Fig. 7.4.3 we see that both neutral points are positioned along the so-called "neutral lines", coinciding with the border line between the eight-shaped blue/green regions and the yellow/red areas, along which $\alpha = \pm 45^{\circ}$ or $\pm 135^{\circ}$ (Stokes parameter $Q = 0$). Generally, p is not equal to zero at neutral lines except as they intersect the solar and antisolar meridian at the neutral points, where $p = 0$. On the other hand, crossing the neutral points along the solar or antisolar meridian, α has a sudden change of 90°, because the polarization switches from "positive" (shaded with bright green and blue in the α-patterns, and meaning direction of polarization perpendicular to the scattering plane determined by the observer, the sun and the point observed) to "negative" (shaded with bright red and yellow, and meaning direction of polarization parallel to the scattering plane). Also in the α-patterns we can see the increasing disturbing effect of ground-reflected light as the wavelength increases.

The nadir angles of the Brewster and fourth neutral points determined on the basis of the *p*- and α-patterns of Fig. 7.4.3 are seen in Table 7.4.1. The general trend is that the shorter the wavelength, the closer are located the neutral points to the nadir, which phenomenon is explained below. Horváth et al. (2002b) evaluated also several other imaging polarimetric measurements done at different altitudes between 2000 and 3500 m during their first flight, and obtained similar results as shown in Fig. 7.4.3: in all of these *p*- and α-patterns the fourth neutral point as well as the Brewster point were visible in all three spectral ranges.

The aim of the second hot air balloon flight conducted on 25 August 2001 during and immediately after sunrise was to estimate the lowest altitude, at which the fourth neutral point can be still observed. At an altitude of 900 m and at a solar elevation of 3° the fourth neutral point could still be discerned in the polarization patterns measured in the blue and green. In the red the area of very low *p* around the theoretical position of the fourth neutral point was very diffuse, and only the Brewster point could be clearly observed in the *p*- and α-patterns. Due to the low altitude, in the red the disturbing effect of ground reflection was so great and the relative contribution of atmospheric scattering to the earthlight was so small that the fourth neutral point was not clearly seen yet. Nevertheless, in the red there was a local minimum of *p* at the predicted position of the fourth neutral point. Under the meteorological conditions during the second flight the lower limit of the altitude was about 900 m at which the fourth neutral point could be observed.

In order to compare the polarization patterns of earthlight measured at near zero solar elevations at sunrise with those of skylight when the sun is on the horizon, in Fig. 7.4.4 the polarization patterns of skylight, measured by 180° field-of-view imaging polarimetry from the ground at 650, 550 and 450 nm on 26 August 1999 at sunrise in the Tunisian salt pan Chott el Djerid, are presented. Comparing Fig. 7.4.3 with Fig. 7.4.4, a great similarity between the polarization patterns can be established. In all polarization patterns of Fig. 7.4.4 the Arago and Babinet points are clearly discernible, and these patterns possess similar qualitative features as those in Fig. 7.4.3. There are, of course, some quantitative differences between the polarization patterns of earthlight and skylight:

- At given angles from the solar meridian and the nadir/zenith, p of skylight is much higher than that of earthlight.
- The neutral points of skylight polarization are located at greater angular distances from the zenith than those of earthlight from the nadir (see Table 7.4.1).
- The change of polarization versus direction of view is smoother in the skylight patterns than it is in the earthlight patterns.

One reason for these differences is that the polarization of skylight observed from the ground is the result of scattering of sunlight within the whole atmosphere, while the air layer below the balloon comprises only part of the earth´s atmosphere. Another reason is that skylight has only one component (downwelling scattered light), while earthlight is the combination of light backscattered by the atmosphere and light reflected from the ground, the latter influencing strongly the upwelling radiation field.

Figures 7.4.5 and 7.4.6 show p and α of earthlight and skylight along the solar and antisolar meridian measured at 650, 550 and 450 nm as a function of the viewing angle θ from the nadir or zenith. These data for the earthlight and skylight originate from the polarization patterns in Figs. 7.4.3 and 7.4.4, respectively. In the plots of Fig. 7.4.5, the local minima $p = 0$ at the neutral points and the maxima of p at the nadir/zenith are clearly visible. The maximum of p of earthlight is about the half or third of that of skylight due to the depolarizing effect of light reflected from the ground and multiply scattered on aerosols. The slight haze in the atmosphere during the balloon-borne measurements enhanced multiple scattering of the first component of earthlight, the sunlight scattered by aerosols (Bohren 1987), which resulted in a reduction of p of earthlight (Figs. 7.4.5A,C,E) and an increase of the area of negative polarization (Figs. 7.4.6A,C,E). The latter effect decreased the nadir angle of the Brewster and fourth neutral points (Table 7.4.1). The second component of earthlight, the sunlight reflected diffusely from the rough terrain, suffered also depolarization, which also decreased p of earthlight, especially at longer (green and red) wavelengths. These effects explain why earthlight was less polarized than skylight above the arid Tunisian desert, and why the Arago and Babinet points of skylight polarization in Tunisia were nearer the horizon than the Brewster and fourth neutral points of earthlight polarization.

In Fig. 7.4.6 we can see that along the solar and antisolar meridian, α of both earthlight and skylight is always approximately 90^o (perpendicular to the scattering plane, which means positive polarization) between the (fourth and Brewster as well as Arago and Babinet) neutral points, and passing the neutral points, α switches to approximately 0^o and 180^o (parallel to the scattering plane, which means negative polarization). The noise of the measured α-values is maximal at and near the neutral points due to the very low degrees of polarization. In Figs. 7.4.5 and 7.4.6 the noise of both the p- and α-plots of earthlight gradually increases from the short (blue) wavelengths to the long (red) ones because of the increasing influence of ground-reflected light. Figures 7.4.7A-C, summarizing the essence of the balloon-borne measurements, show the three-dimensional distribution of polarization as well as the Arago and fourth neutral points observable around a hot air balloon in the blue (450 nm) spectral range at an altitude of 3500 m.

7.4.6. Origin and Characteristics of the Principal Neutral Points

In the clear atmosphere, a neutral point occurs if the radiance of the normally positively polarized sky- or earthlight is matched exactly by an equal quantity of negatively polarized light. Multiple scattering of light by dust, haze and other aerosol particles in the atmosphere introduce positive or negative polarization, depending on characteristics of the particles and the incident radiation. Under clear atmospheric conditions, multiple scattering causes more negative polarization than positive one, thus the net p of skylight is reduced. The stronger the multiple scattering, the more negative polarization is introduced in the atmosphere, and the more the neutral points are displaced from the sun or antisun. The amount of multiple scattering is strongly affected by atmospheric turbidity.

The different angular positions of the neutral points observed in the red, green and blue ranges of the spectrum (Figs. 7.3.1, 7.4.3, 7.4.4, Table 7.4.1) are the consequence of the dispersion of polarization, the influence of wavelength-dependent ground reflection and the spectral composition of direct sunlight. Under normal, clear atmospheric conditions and when the atmosphere is illuminated by sunlight (for higher solar elevations from the horizon) and the ground reflection is approximately independent of wavelength (for colourless grounds covered by snow or grey/white sand, black soil, for example), a general rule is that the shorter the wavelength of light, the lower the degree of skylight polarization (Coulson 1988). There is little spectral dependency at wavelengths $\lambda > 500$ nm, but strong dispersion for shorter wavelengths. The strong decrease of p towards shorter wavelengths is due mainly to multiple scattering, because p resulting from a single scattering event is independent of wavelength. At shorter wavelengths multiple scattering reduces p, increasing the magnitude of negative polarization and thus shifting the positions of the neutral points further away from the sun or antisun.

Thus, the region of negative polarization surrounding the sun and antisun is much more extended in the short-wavelength (UV and blue) than in the long-wavelength (green and red) range of the spectrum. This is the reason why under

these conditions the angular distances of the neutral points from the sun or antisun increase as the wavelength decreases. Then, the Arago, Babinet, Brewster and fourth neutral points are nearest the zenith or nadir in the blue; in the green they are positioned slightly further away from the zenith or nadir, and in the red their angular distance from the zenith or nadir is the greatest.

These features are more or less modified by wavelength-dependent reflection of light from the ground. If in a given spectral range the reflectivity of the ground is much higher than in other parts of the spectrum, in this spectral range the relatively greater amount of ground-reflected light alters strongly the skylight and earthlight polarization and the positions of the neutral points: If the ground-reflected light is horizontally (positively), vertically (negatively) polarized or unpolarized, it reduces, enhances or does not alter the area of negatively polarized region of the atmosphere around the sun and antisun, and therefore it decreases, increases or does not change the angular distance of the neutral points from the sun or antisun, respectively.

At sunset and sunrise, the spectral composition of direct sunlight changes considerably and the proportion of longer (yellow, orange, red) wavelengths increases. This phenomenon also changes the skylight and earthlight polarization as well as the neutral point positions. Similar effect occurs rarely after volcanic eruptions, when the wavelength-dependent absorption and scattering on the aerial particles of volcanic debris significantly modify the spectral composition of direct sunlight (Coulson 1988)

In the sky above the Tunisian desert, where the skylight polarization patterns in Figs. 7.3.1, 7.4.4 and plots of Figs. 7.4.5B,D,F and 7.4.6B,D,F were measured, the degree of skylight polarization was highest in the green rather than in the red. The reason for this anomaly is that the ground was reddish/yellowish sand, thus the amount of light reflected from the ground was largest in the red, which decreased the degree of skylight polarization in this part of the spectrum. This wavelength-dependent ground reflection and the reddish/orange direct sunlight at sunrise influenced also the positions of the Arago and Babinet points. The same phenomenon was observed by Horváth et al. (1998b) during the video-polarimetric study of the Arago point at sunset, at another place of the reddish Tunisian desert in 1996.

In the case of the air-borne observation of the Brewster and fourth neutral points, the characteristics and observability of both neutral points strongly depend on the altitude of the observer and the features of the underlying ground surface: Compared with the atmospheric contribution to polarized earthlight, the surface contribution is the smallest for the shorter (UV and blue) wavelengths and increases towards longer wavelengths. The higher the albedo of the surface in a given spectral range, the greater is the contribution of ground reflection to the polarized earthlight.

Under normal conditions, the four principal neutral points of atmospheric polarization are located in the solar vertical plane determined by the observer, the zenit/nadir and the sun. Depending on the meteorological conditions and the characteristics of the ground, at sunrise or sunset the Arago point and the fourth neutral point is positioned about 20^{o} to 30^{o} above and below the antisolar point,

respectively, while the Babinet and Brewster points are located 20^o to 30^o above and below the sun, but not necessarily mirror symmetrically. Under normal atmospheric conditions, from the ground only two of the four are visible at a given time, as the fourth neutral point is always below the horizon and the Arago point sets below the horizon at the same time the Brewster point appears above the horizon, and *vice versa*. The Babinet point is visible from before sunrise until after sunset. The Babinet and Brewster points as well as the Arago and fourth neutral points move closer to the sun and antisun, respectively, as the sun rises higher in the sky, merging into a single neutral point coincident with the sun and antisun when the sun reaches the zenith. The fourth neutral point can be observed only at higher altitudes (> about 900 m) from balloons, aircrafts or satellites, but not from higher mountains, because the shadow of mountains excludes direct sunlight from the region of the atmosphere below the antisun.

The Arago point has been observed more frequently than the Babinet or Brewster point, because its location in the portion of the sky with relatively small I and high p, opposite the sun makes it the easiest of the four to observe, and also since its position has been found to be more sensitive to the effects of atmospheric turbidity than the position of either the Babinet or Brewster point. While the Babinet point is also readily observed by visual means, the Brewster point is embedded in the brightest and least polarized region of the sky, and is therefore difficult to observe visually.

7.4.7 Why the Fourth Neutral Point has not been Observed in Previous Air- or Space-Borne Polarimetric Experiments?

In the past, several air-borne (balloon- or aircraft-borne) and space-borne polarimetric measurements have been performed, which could have been able to observe the fourth neutral point. Thus, it is rather surprising why has not been given any explicit, definite experimental evidence for the existence of this neutral point until the measurements of Horváth et al. (2002b). The reasons are manifold:

1. Earthlight contains a significant component due to scattering by the atmosphere, beside that due to surface reflection. For remotely sensed surface characterization and discrimination, however, such atmospheric contamination of the radiation field have generally been minimised or corrected for by use of radiative transfer models applicable to the conditions of observation. Since the polarization of sunlight due to atmospheric scattering is responsible for the origin of neutral points, the fourth neutral point had only little chance to be observed in air- or space-borne remote sensing measurements in which the atmospheric component of earthlight was minimised or corrected for to promote the observation of surface features.
2. The first attempt to measure the polarization of earthlight was done by Rao (1969): His balloon-borne measurements, performed over the White Sands area (New Mexico), exhibited depolarization of the Rayleigh scattering by a Lambertian ground, thus the fourth neutral point was not observable.

3. The first extensive measurements of earthlight polarization have been done during four Space Shuttle missions, and a preliminary presentation has been made by Coulson et al. (1986). Photographs were taken about the earth surface with a pair of cameras, each of which containing a linearly polarizating filter with different orientation of the transmission axis. Some qualitative data could have been deduced from the comparison of these polarizational picture pairs. Since for a complete imaging polarimetry three polarizational pictures are needed, the method used by Coulson et al. (1986) was inappropriate for the space-borne observation of the fourth neutral point.
4. Herman et al. (1986) performed a balloon-borne experiment to measure I and p of sunlight scattered by the stratospheric aerosol at near-infrared (850 and 1650 nm) wavelengths at an altitude of 20 km. Since only circular scans were done in a nearly ($\pm$ 0.1°) horizontal plane with a narrow (2°) field-of-view point-source polarimeter when the sun was just at the horizon, the fourth neutral point, located at sunrise or sunset about 20°-30° below the antisun, could not have been investigated with this polarimeter.
5. Using the polarimetric device of Herman et al. (1986), Deuzé et al. (1989) performed a balloon-borne experiment for directional observations of I and p of earthlight. This apparatus with a 2° field of view has been adapted to polarimetric measurements at near infrared (850 and 1650 nm) wavelengths scanning in a vertical plane. A sun pointer allowed the gondola of the balloon to be stabilized at a given azimuth, thus polarimetric measurements have been done in a vertical plane which departed from the sun's/antisun's vertical plane by about 8°. In vertical scans at altitudes 28-31 km there were two local minima of p of earthlight [Deuzé et al. 1989, page 98, plot $P(\theta)$ of sequence a) in Fig. 4]: one minimum in forward scattering (about 25° below the sun), and another minimum in backward scattering (about 25° below the antisun). The former and the latter minimum of p was observed near the Brewster point and the fourth neutral point, respectively. If the plane of the scan would have been exactly the sun's/antisun's vertical, Deuzé et al. (1989) could have observed as first the fourth neutral point.
6. The POLDER instrument (see Chapter 4), a space-borne imaging polarimeter, was designed to measure the directionality and polarization of the solar radiation scattered by the earth-atmosphere system (Deschamps et al. 1994). Three of the channels (443, 670, 865 nm) measured the linear polarization of the earthlight yielding the Stokes parameters I, Q, U, from which the total radiance $L = I$, the linearly polarized radiance $L_{pol} = p \cdot L = (Q^2+U^2)^{1/2}$, and the angle of polarization α were deduced. The POLDER-team prefers to use L_{pol} which is nearly additive with respect to the contributions of molecules, aerosols and land surfaces, rather than p in which polarized and unpolarized light are mixed ambiguously. Thus, in the publications of the POLDER-team colour-coded maps of L and L_{pol} have been used (see e.g. Fig. 6 of Deuzé et al. 1993, p. 145). Neutral points along the antisolar meridian, above and below the antisun never show up explicitly in the POLDER maps of L_{pol}. In these pictures, around the antisun there is usually an extended circular or elliptic dark grey or black spot (see Fig. 4.1C) representing zero and very low values of L_{pol} at all

three (443, 670, 865 nm) wavelengths. Farther away from the antisun, the picture gradually becomes more brighter and the colour more bluish because of the gradually increasing L_{pol} especially in the blue (443 nm) due to molecular (Rayleigh) scattering. At a given wavelength, L_{pol} is zero at the Brewster and fourth neutral point, the position of which depends on wavelength (Fig. 7.4.3, Table 7.4.1). These neutral points show up strikingly in the map of p measured at any wavelength, if very low p-values (0%, 1%, 2%, 3%, …) are coded and visualized by strongly contrasting colours. In the maps of L_{pol} used by the POLDER-team, three coloured dark (almost black) spots should be seen at the positions of the Brewster and fourth neutral point at the three (443, 670, 865 nm) wavelengths. These dark coloured spots are, however always merged into the great dark spot around the antisun, since the zero and the very low values of L_{pol} are coded practically by the same very dark grey shades. On the other hand, the information available in the angle of polarization α was practically not used by the POLDER-team; we do not know any published α-map measured by the POLDER instrument.

7. Using the Mie theory, Bréon et al. (1997) computed the polarized phase function $q(\gamma)$ for twelve different aerosol models as a function of the scattering angle γ. $q(\gamma)$ is the product of the phase function and p. In their model they used different size distributions and refractive indices of the aerosol particles. $q(\gamma)$ is negative when the direction of polarization is parallel to the plane of scattering and positive when it is perpendicular. Where the polarized phase function switches from negative to positive [$q(\gamma^*) = 0$] there is a neutral point. Depending on the model parameters, in the twelve $q(\gamma)$ plots computed by Bréon et al. (1997, p. 17188, Fig. 1b) $q(\gamma^*) = 0$ for different scattering angles γ_1^* and γ_2^* where $10^o < \gamma_1^* < 55^o$ and $120^o < \gamma_2^* < 170^o$. The neutral point at γ_1^* and γ_2^* corresponds with the Brewster and the fourth neutral point, respectively. Although from these numerical calculations a neutral point of earthlight polarization below the antisun can be deduced and predicted, in their numerous publications the POLDER-team never noted explicitly the existence of this neutral point and did not mention that it may correspond to the fourth principal neutral point. The most which was noted by Deuzé et al. (1993, pp. 144-145) is that around scattering angle "150^o the polarized reflectance equals the molecular one. It shows that the aerosols exhibit zero polarization for a 150^o scattering angle. For larger scattering angles, the aerosol polarization seems to increase again, with the polarization direction now parallel to the scattering plane ..."

According to their publications, the fourth as well as the Brewster neutral point have escaped the attention of the POLDER-team. Obviously, they used the polarization data collected by the POLDER instrument for practical, applied meteorological purposes. Nevertheless, the polarization data sensed remotely by the air-borne as well as space-borne versions of the POLDER instrument should latently contain the fourth neutral point of the normal clear sunlit atmosphere: It should have been calculated the p- and α-maps measured at the three (443, 670,

865 nm) wavelengths and visualized in a format similar to that presented in this chapter.

7.4.8 Concluding Remarks

One can conclude that the results of the two balloon-borne imaging polarimetric measurements of Horváth et al. (2002b) provided the first experimental/observational evidence for the existence of the fourth principal neutral point within the clear sunlit atmosphere. The fourth neutral point was observed from different altitudes between 900 m and 3500 m during and immediately after sunrise at the theoretically predicted position, at about 22^{o}-40^{o} below the antisun along the antisolar meridian, depending on the wavelength. The fourth neutral point has similar characteristics as the Arago, Babinet and Brewster points:

- It is located along the antisolar meridian at the edge of the areas of positive and negative polarization of earthlight.
- At sunrise, it is about at the same angular distance below the antisun as the Brewster point is below the sun.
- Its nadir angle decreases with decreasing wavelength.
- Its position and the polarizational characteristics of earthlight around it are influenced by ground reflection, the effect of which decreases as the altitude increases and/or the wavelength decreases.
- Its nadir angle is decreased by multiple scattering on atmospheric aerosols increasing the areas of negative polarization of earthlight.

The first balloon-borne observations by Horváth et al. (2002b) on the fourth neutral point are consistent with the earlier ground-based observations on the Arago, Babinet and Brewster points performed with video polarimetry (Horváth et al. 1998b; Horváth and Wehner 1999) or with full-sky imaging polarimetry (Gál et al. 2001a,b,c; Pomozi et al. 2001a,b; Horváth et al. 2002a, 2003). The fourth neutral point was not observed during earlier air- or space-borne polarimetric experiments and/or it escaped the attention of researchers, because

- some of these measurements were performed at longer (red or infrared) wavelengths in order to minimize the contribution of molecular scattering at shorter (UV and blue) wavelengths;
- the previous techniques were not adequate to measure neutral points;
- the routinely used non-imaging point-source scanning polarimeters were not pointed towards the fourth neutral point;
- unpolarized points did not show up explicitly in the polarization maps due to an inadequate, disadvantageous colour coding and displaying of the measured polarization data.

According to Coulson (1988, p. 242), more attention has been paid to the measurement of the positions of the Arago, Babinet and Brewster points than to any other feature of skylight polarization. This statement is now rounded off by the first observation, visualization and characterization of the fourth neutral point reported by Horváth et al. (2002b) 193 and 162 years after the discovery of the Arago point and the Babinet point, and 160 years following the first observation of the Brewster point.

Table

Table 7.4.1. The angular distance of the Arago, Babinet, Brewster and fourth neutral points from the nadir or the zenith as determined on the basis of the patterns of the degree and angle of linear polarization measured at 650, 550 and 450 nm at different altitudes *A*. (After Table 1 of Horváth et al. 2002b, p. 2092).

	skylight						**earthlight**					
neutral point	**Arago (from zenith)**			**Babinet (from zenith)**			**Brewster (from nadir)**			**fourth (from nadir)**		
spectral range	650 (nm)	550 (nm)	450 (nm)	650 (nm)	550 (nm)	450 (nm)	650 (nm)	550 (nm)	450 (nm)	650 (nm)	550 (nm)	450 (nm)
A = 3500 m	—	—	—	—	—	—	56.3°	51.1°	46.6°	65.3°	49.8°	49.2°
A = 1340 m	—	—	—	—	—	—	53.4°	50.2°	53.4°	55.6°	56.9°	54.0°
A = 900 m	—	—	—	—	—	—	62.4°	62.4°	62.4°	55° ±5°	55.3°	57.9°
A = 0 m	70.7°	64.4°	68.1°	59.0°	61.6°	65.5°	—	—	—	—	—	—

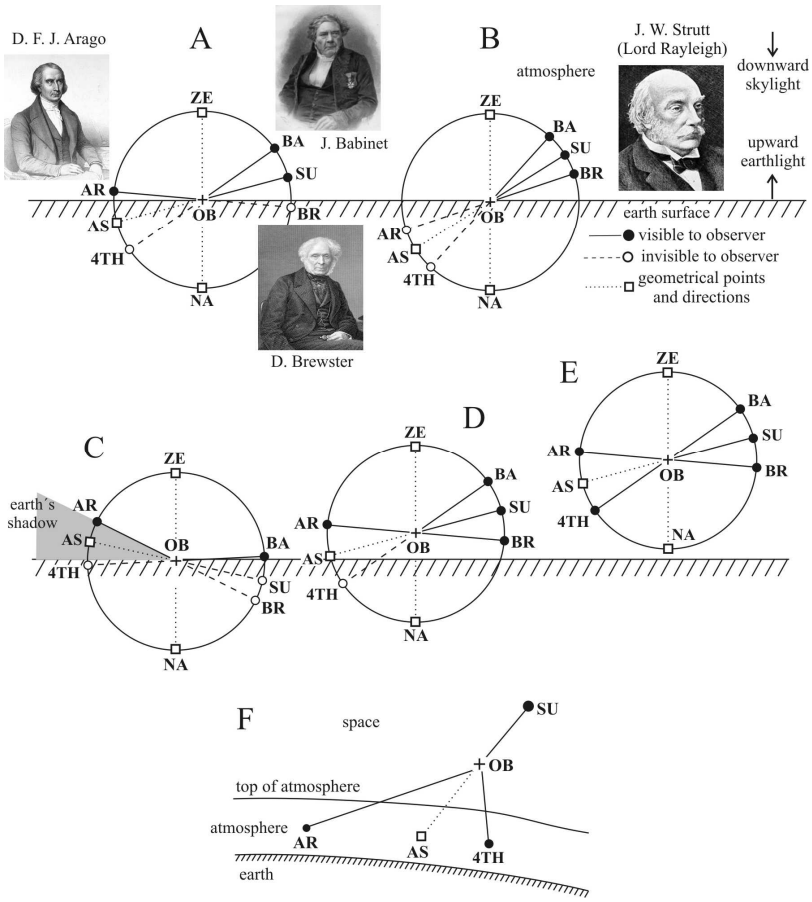

Fig. 7.4.1. A, B: Schematic diagram of the normal positions of the Arago (AR), Babinet (BA) and Brewster (BR) neutral points of skylight polarization in the vertical plane including the ground-based observer (OB), sun (SU), zenith (ZE), antisolar point (AS), and nadir (NA). From the ground, only two neutral points are visible simultaneously: either the Arago and Babinet points (A, for lower solar elevations), or the Babinet and Brewster points (B, for higher solar elevations). From the ground, the fourth neutral point (4TH) is not visible. The insets represent the portraits of Dominique Francois Jean Arago (1786-1853), Jacques Babinet (1794-1872) and David Brewster (1781-1868), the discoverer of the neutral points. The portrait of John William Strutt, alias Lord Rayleigh (1842-1919) who developed the first theory of skylight polarization, is also shown as an inset. C: The fourth neutral point cannot even be observed after sunset, because the atmosphere below the antisun is then in the shadow of the earth. D: Increasing the altitude of observation, above a certain height three neutral points can be observed simultaneously: the Arago, Babinet and Brewster points. E: At an appropriately high altitude, all four neutral points can be observed simultaneously. Then, the Arago and Babinet points are the neutral points of downwelling polarized skylight, while the Brewster and fourth neutral points are the neutral points of upwelling polarized earthlight. F: Geometry of the space-borne observation of the Arago and fourth neutral points. (After Fig. 1 of Horváth et al. 2002b, p. 2086).

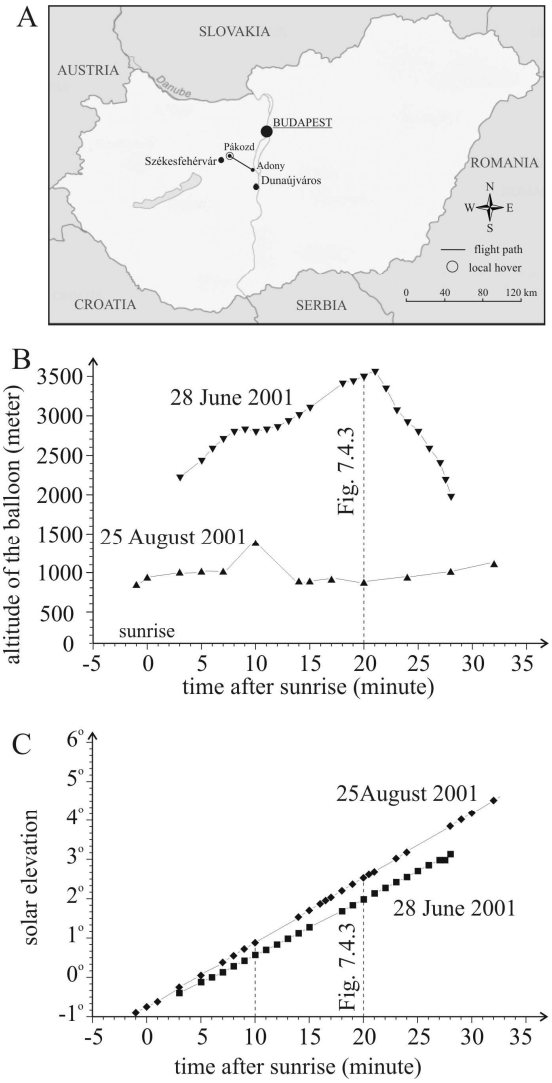

Fig. 7.4.2. Main parameters of the two hot air balloon flights of Horváth et al. (2002b) conducted on 28 June (local sunrise at 04:52 = local summer time = universal time code + 2 = UTC+2) and 25 August (sunrise at 05:56) 2001 to measure the polarization patterns of upwelling earthlight and the characteristics of the fourth neutral point of atmospheric polarization. A: The launching site (Pákozd, 47°13′N, 18°33′E), landing site (Adony, 47°06′N, 18°51′Et) and trajectory of the first flight (hovering above the launching site during the second flight) on the map of Hungary. B, C: Altitude of the balloon and solar elevation as a function of time after sunrise for both flights. In graph B the black-filled triangles represent the altitudes and points of time at which polarimetric measurements were done. In both plots a dashed vertical line marks the time of the measurement, the results of which are shown in Fig. 7.4.3. (After Fig. 2 of Horváth et al. 2002b, p. 2088).

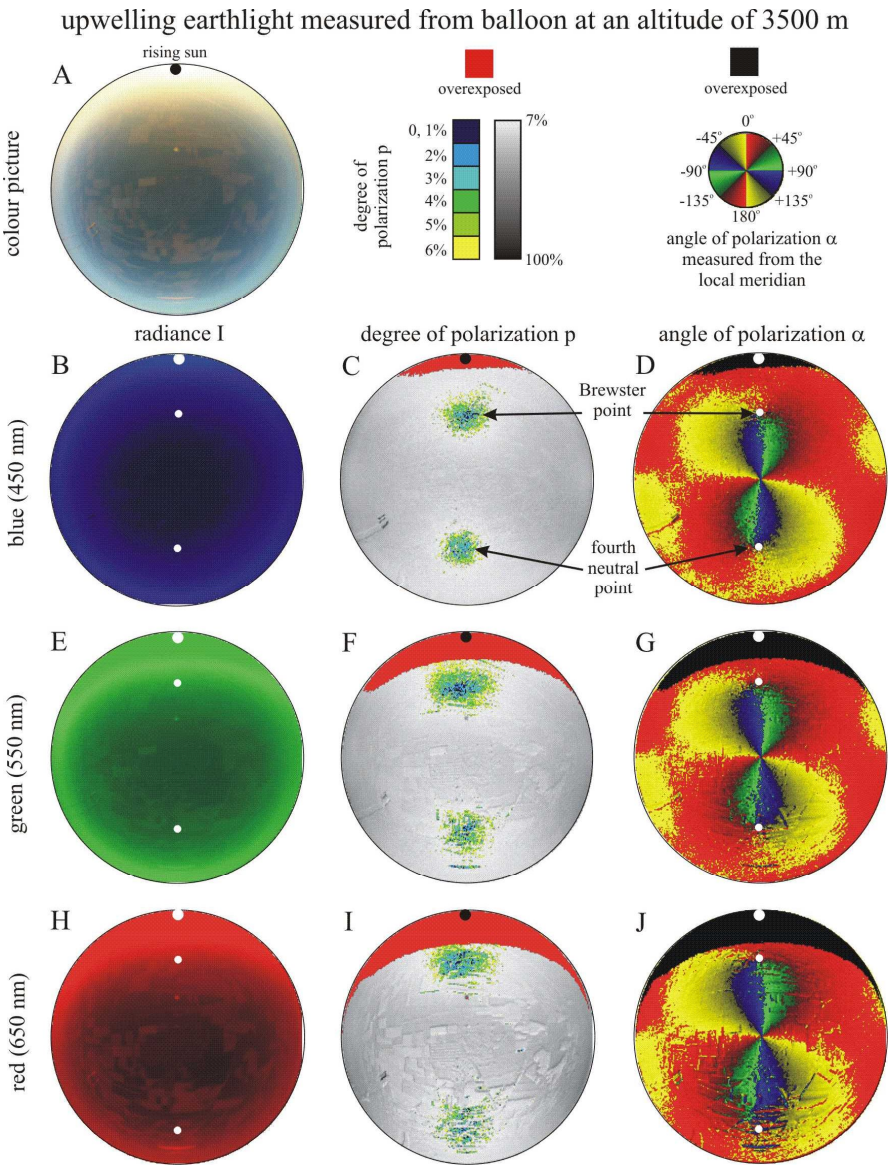

Fig. 7.4.3. 180° field-of-view photograph of the landscape below the gondola of the hot air balloon (A) and the patterns of radiance I (B, E, H), degree of linear polarization p (C, F, I) and angle of polarization α (D, G, J) of upwelling earthlight. Measurements were taken by using 180° field-of-view imaging polarimetry at an altitude of 3500 m and a solar elevation of 2° at 450, 550 and 650 nm immediately after local sunrise (05:12; local summer time = UTC+2; 28 June 2001). The position of the sun and the neutral points are indicated by dots. Time of exposure = 1/60 s, aperture = 2.8, colour reversal film: Fujichrome Sensia II, 100 ASA. (After Fig. 4 of Horváth et al. 2002b, p. 2090).

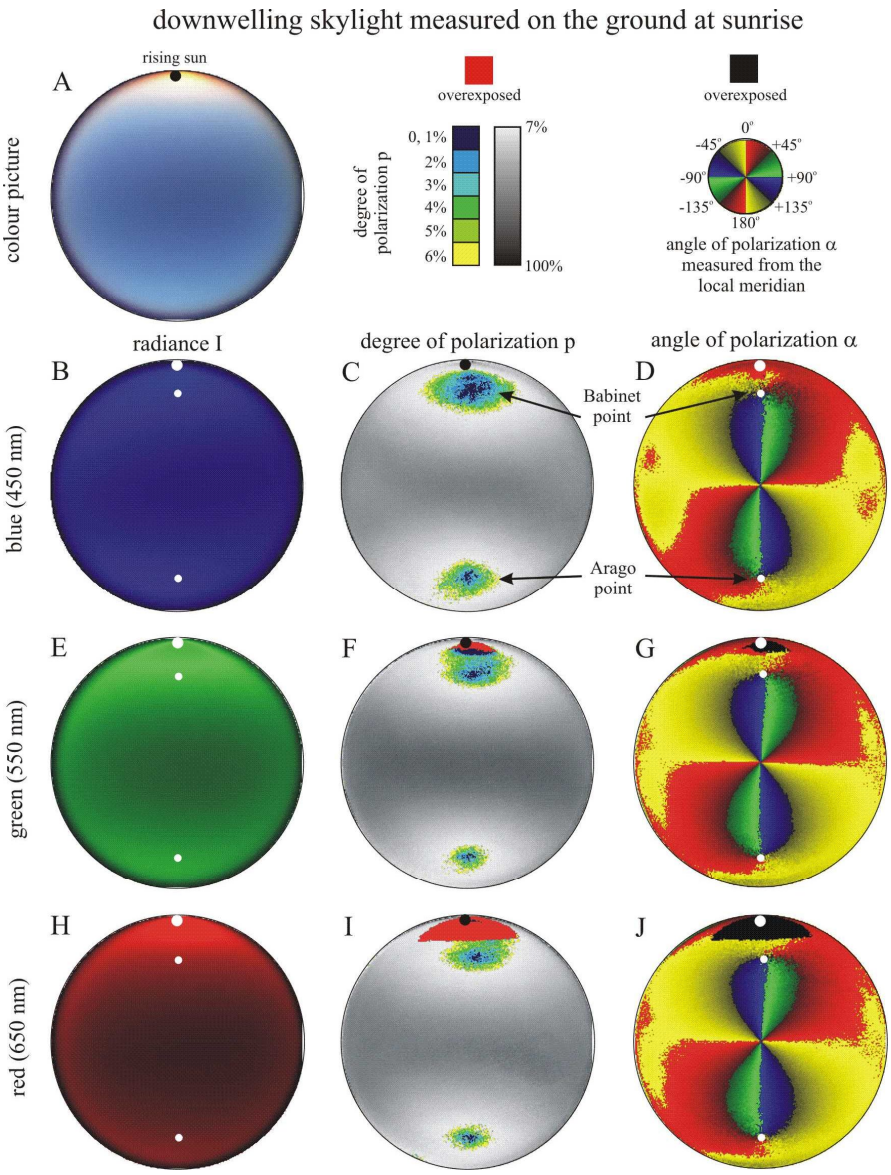

Fig. 7.4.4. As Fig. 7.4.3 for the full clear sky measured from the ground at local sunrise (26 August 1999, 06:00 = local summer time = UTC+1, solar elevation = 0°; salt pan Chott el Djerid, 10 km from Kriz, 33°52'N, 8°22'E, Tunisia). Note that on the compass rose East and West are transposed, because we are looking up towards the celestial dome rather than down towards the ground. Time of exposure = 1/60 s, aperture = 2.8, using Fujichrome Sensia II 100 ASA colour reversal film as detector. (After Fig. 5 of Horváth et al. 2002b, p. 2093).

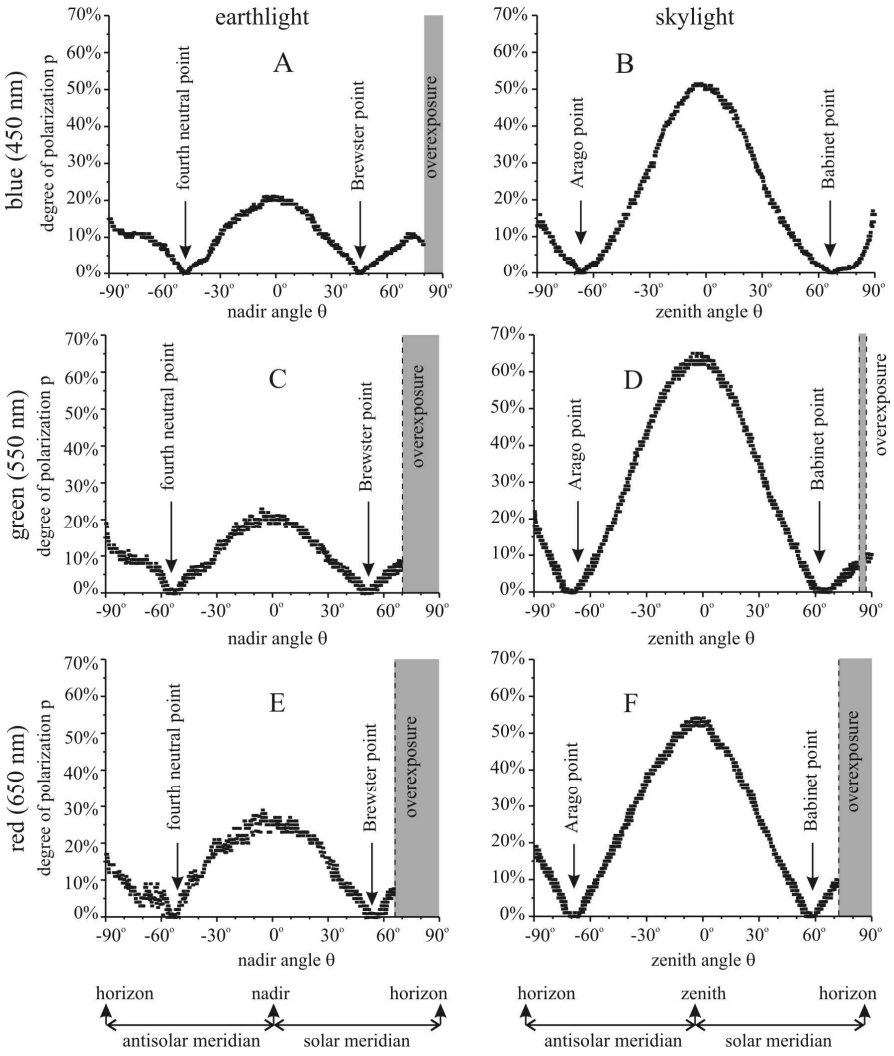

Fig. 7.4.5. Degree of linear polarization p of earthlight (A, C, E) and skylight (B, D, F) along the solar and antisolar meridian measured at 450, 550 and 650 nm as a function of the nadir/zenith angle θ. Data for earthlight and skylight originate from the polarization patterns in Figs. 7.4.3 and 7.4.4, respectively. Grey stripes show the overexposed areas. (After Fig. 6 of Horváth et al. 2002b, p. 2094).

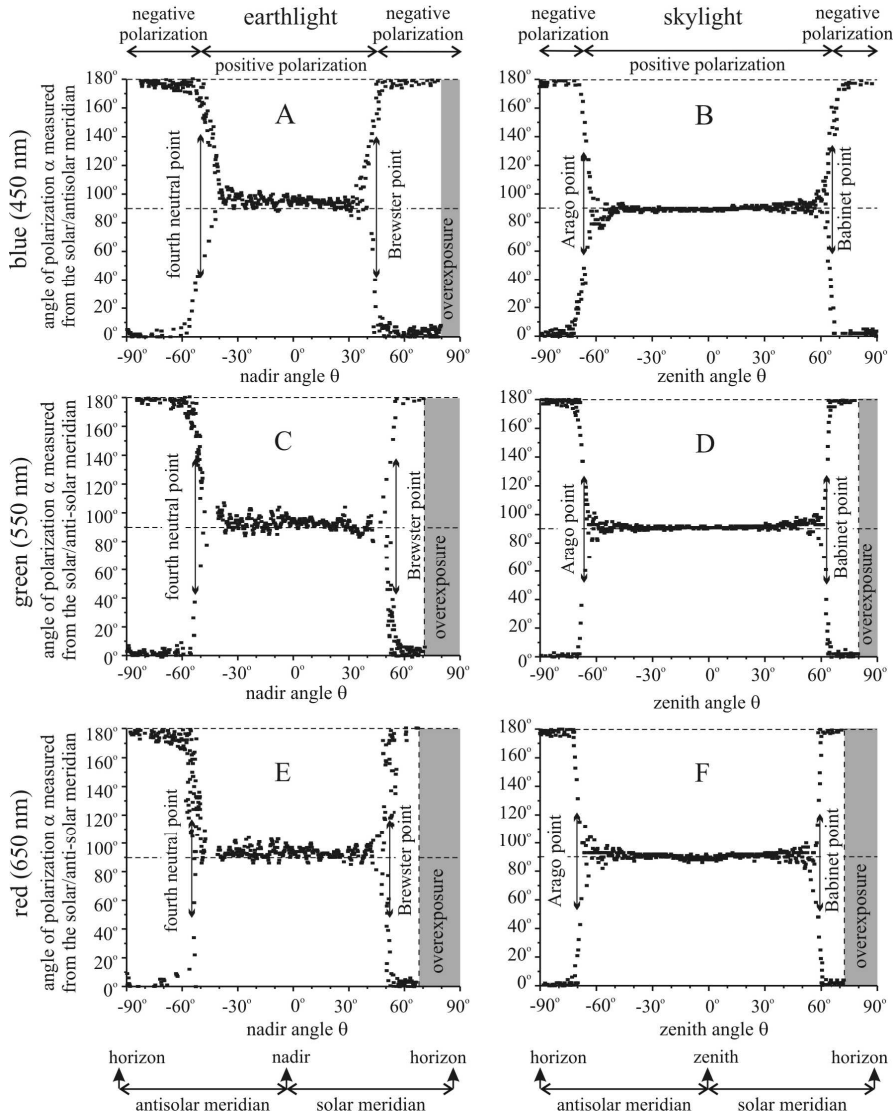

Fig. 7.4.6. As Fig. 7.4.5 for the angle of polarization α of earthlight and skylight measured from the solar/antisolar meridian. (After Fig. 7 of Horváth et al. 2002b, p. 2095).

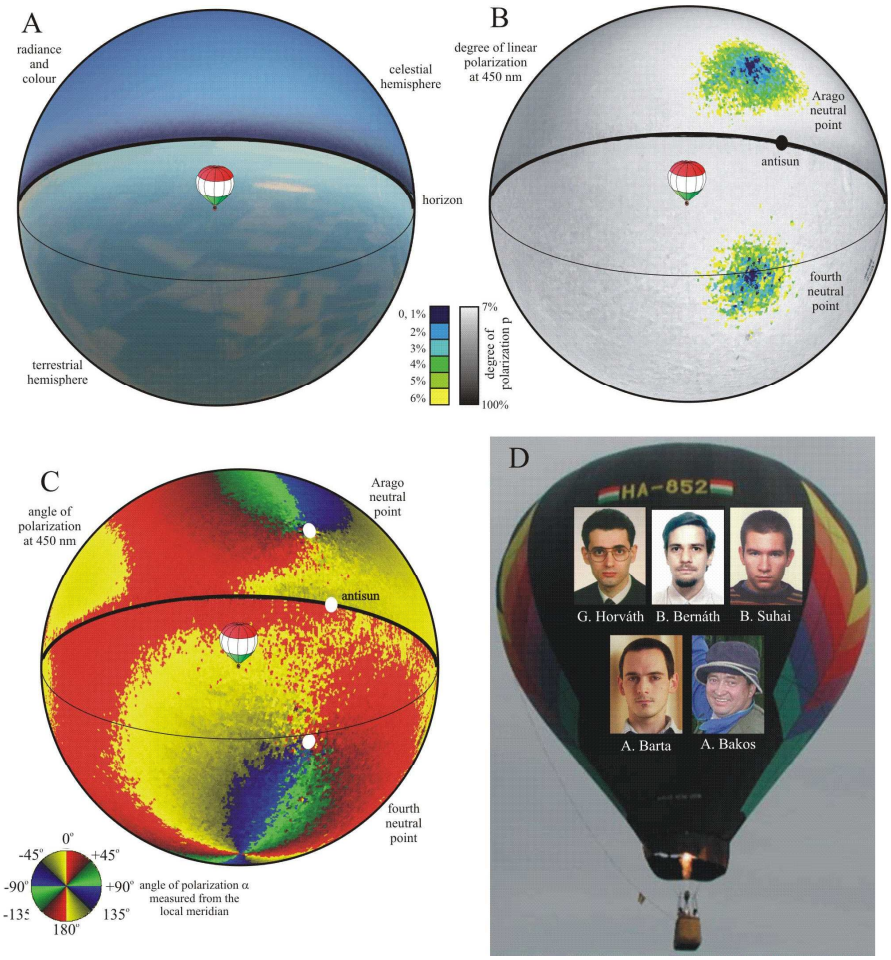

Fig. 7.4.7. Perspectivic representation of the three-dimensional spatial distribution of radiance and colour (A), degree (B) and angle (C) of linear polarization as well as the Arago and fourth neutral points on the surface of spheres. Similar patterns can be observed/measured around a hot air balloon in the blue (450 nm) spectral range at an altitude of 3500 m. Every sphere in the picture is the combination of the patterns in Figs. 7.4.3A,C,D and 7.4.4A,C,D. D: Portraits of Gábor Horváth, Balázs Bernáth, Bence Suhai and András Barta, who observed as first the fourth neutral point during two hot air balloon flights, the pilot of which was Attila Bakos. (After Fig. 8 of Horváth et al. 2002b, p. 2096).

7.5 24-Hour Change of the Polarization Pattern of the Summer Sky North of the Arctic Circle

Using full-sky imaging polarimetry, Gál et al. (2001c) measured the polarization pattern of the summer sky in Sodankylä (Finnish Lapland), north of the Arctic Circle. Since at the place and time of their measurements the sun did not set they could measure the 24-hour change of the celestial polarization pattern. This gave the opportunity to demonstrate how variable can be p of skylight and the position of the neutral points within 24 hours on a sunny, almost cloudless, visually clear day.

Figure 7.5.1A shows a series of the I-, p- and α-patterns of the sky as a function of the solar zenith angle θ_s measured at 450 nm. The p-pattern at 8 h demonstrates how p of skylight was reduced by the thin cirrus clouds near the horizon. Figures 7.5.1B,C show p and α of skylight measured at 450, 550 and 650 nm at 90° from the sun (where p is maximal for clear skies) along the antisolar meridian versus θ_s. During the 24-hour period investigated (from 2 h to 24+1 h) p was always the lowest in the red ($25\% \leq p_{red} \leq 57\%$ for $47.5^\circ \leq \theta_s \leq 83.1^\circ$). For certain θ_s p was higher in the blue than in the green, while for other θ_s the relation was the contrary. Although the temporal change of p was non-monotonous in all three spectral ranges, there was a general trend that p decreased with decreasing θ_s, especially in the red. There was a characteristic hysteresis in the temporal change of p: from 2 h to 13 h the change of p in all three spectral ranges was characterized by different graphs in comparison with the case between 14 h and 24+1(=25) h. Independently of the wavelength, α was always within the range of $80^\circ < \alpha < 100^\circ$ with an average of 90°, that is, the direction of polarization was always approximately perpendicular to the antisolar meridian as expected from the Rayleigh theory. There was no systematic temporal change of α.

Figure 7.5.2A represents the hourly positions of the Arago and Babinet neutral points evaluated from a 24-hour series of the celestial polarization patterns measured at 650, 550 and 450 nm. Figures 7.5.2B,C represent the change of the zenith angle of the Arago and Babinet points in the red, green and blue as a function of θ_s. The most important characteristics of the Arago and Babinet points read from Fig. 7.5.2 are the following:

- The smaller the solar zenith angle, the smaller or the larger is the zenith angle of the Babinet or Arago point, respectively.
- The longer the wavelength of skylight, the larger is the zenith angle of the Arago and Babinet points.

The latter property is explained in Chapter 7.4.5 and 7.4.6. During the 24 hours studied there was also a hysteresis in the temporal change of the zenith angle of the Arago and Babinet points: When the sun moved along the first half of its arc in

the sky, the change of the zenith angle of the neutral points in all three spectral ranges was characterized by different graphs in comparison with the case when the sun moved along the second half of its arc.

Figures 7.5.1B and 7.5.2 demonstrate that p of skylight and the zenith angle of the neutral points can considerably change within some hours even if the sky is visually relatively clear throughout 24 hours. The rather unsettled temporal variation of p of the clear sky and the hysteresis of this variation seen in Figs. 7.5.1B and 7.5.2B,C show that the p-pattern of the clear sky is temporally unstable (that is, for the same solar zenith angle at different times significantly different p-values can occur at a given point of the clear sky) in comparison with the relatively stable α-pattern (that is, the α-values at a given point of the clear sky are approximately the same at different times if the solar zenith angle is the same). Thus it is not surprising that polarization-sensitive animals which orient with the aid of celestial polarization use the α-pattern rather than the p-pattern (e.g. Wehner 1976, 1997).

The most anomalous feature in Fig. 7.5.1B is the relatively low p at 650 nm. This spectral dependence of p of skylight corresponds with that measured by Coulson (1988, pp. 308-312) under moderate haze, for instance. A decrease of p of skylight at the longer wavelengths is typical of hazy conditions, and the relatively high albedo of vegetated surfaces (pine forest in Sodankylä) in the longer wavelength range is an additional contributing factor. Generally, the turbidity (e.g. haze or dust) of the atmosphere strongly reduces the maximum of p, particularly at the longer wavelengths (Coulson 1988, p. 289).

Using a point-source polarimeter, Beaglehole and Carter (1992) measured the skylight polarization along the solar-antisolar meridian in a high-albedo environment in Antarctica during spring. They experienced that the skylight in Antarctica had a low maximum p of about 40%, essentially independent of wavelength across the visible spectrum due to multiple scattering in the atmosphere induced by the high snow albedo. Contrary to these findings, at Sodankylä Gál et al. (2001c) observed a greater spectral variation of p of skylight and higher maxima of p ranging from 25% to 72% (Fig. 7.5.1B). The zenith angle of the Arago and Babinet points depended also upon the wavelength (Fig. 7.5.2). These observations can be explained by the fact that these measurements were performed in summer in a pine forest and not in a snowy high-albedo environment. Thus, the spectral characteristics of the celestial polarization in Sodankylä were influenced less by the multiple scattering in the atmosphere induced by light reflected from the woody terrain.

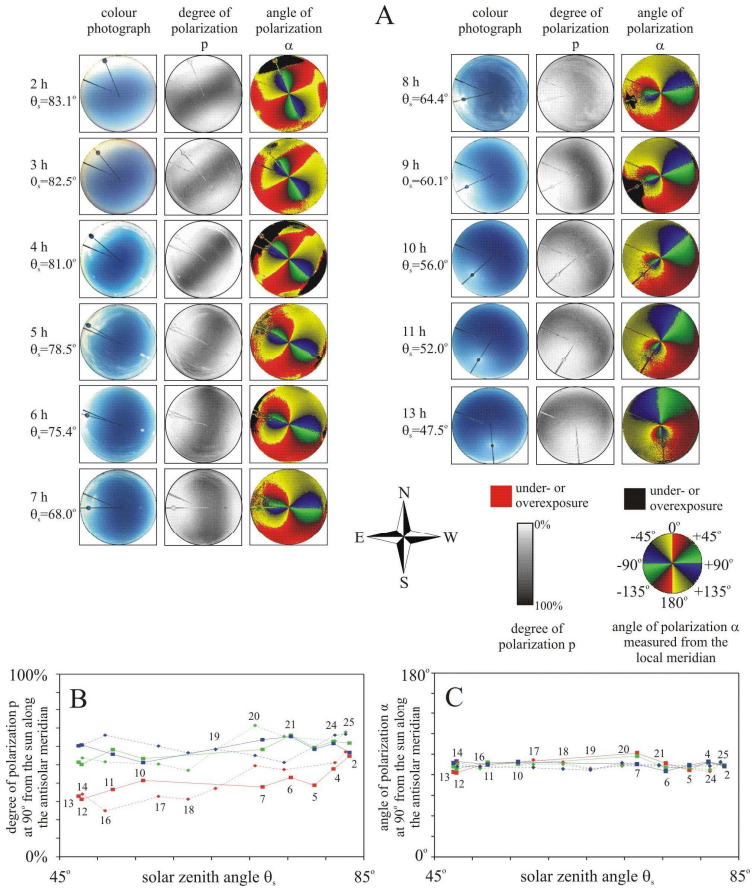

Fig. 7.5.1. A: The colour photograph and the patterns of the degree of linear polarization p and angle of polarization α of the entire sky versus the time and the solar zenith angle θ_S measured by full-sky imaging polarimetry at 450 nm from 2 h (local summer time = UTC+3) to 13 h on 25 June 1999 in Sodankylä (67°25'N, 26°30'E, Finnish Lapland). The two radial bars in the circular pictures come from a sun occulter and a pole (pointing approximately north-eastward and accommodating an anemometer) on the top of the meteorological tower where the measurement was performed. The position of the sun is indicated by the small disk of the occulter. B, C: Spectral dependence of p and α of skylight measured at 450 nm (blue), 550 nm (green) and 650 nm (red) at 90° from the sun (averaged on a small circular celestial region with a radius of 10 pixels; the radius of the entire sky was 334 pixels) along the antisolar meridian versus θ_S. The numbers around the graphs indicate the hours (UTC+3) of recording. In the first and second half of the course the neighbouring points of the graphs are connected with solid and dashed straight lines (linear interpolation), respectively. (After Fig. 2 of Gál et al. 2001c, pp. 1390-1391).

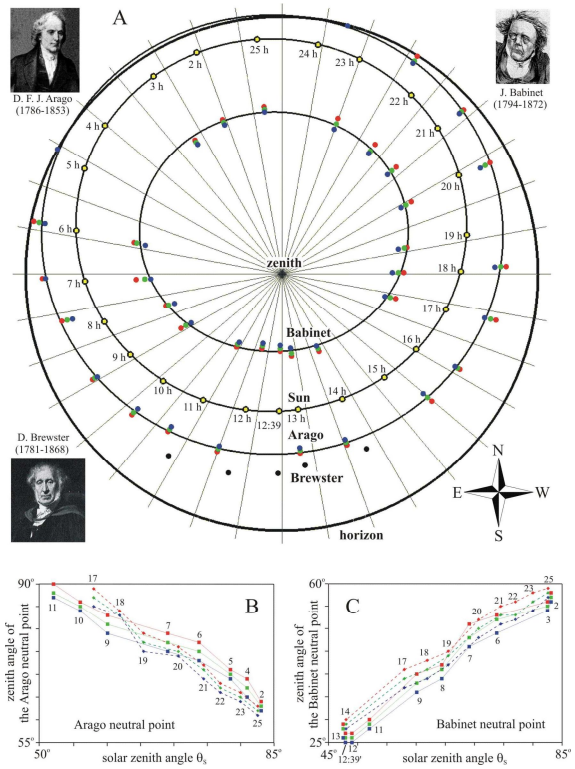

Fig. 7.5.2. A: Hourly positions of the sun and Arago, Babinet and Brewster neutral points of skylight polarization on the firmament evaluated from a 24-hour series of the celestial polarization patterns measured by full-sky imaging polarimetry on 25 June 1999 in Sodankylä. The positions of the sun are indicated by yellow dots, and next to them the times of recording are shown. The positions of the Arago and Babinet neutral points measured in the red (650 nm), green (550 nm) and blue (450 nm) spectral regions are indicated by red, green and blue dots, respectively. At a given solar position the Babinet point is placed on the solar meridian while the Arago point on the antisolar meridian. Black dots represent the predicted positions of the Brewster neutral point. For a few hours the positions of the Arago and Babinet points could not have been evaluated from the recordings. The ellipses represent the trajectories of the sun and the Arago and Babinet points fitted to their hourly measured positions by the method of least squares. The insets in the corners show the portraits of Arago, Babinet and Brewster. B, C: The change of the zenith angle of the Arago and Babinet points for the red, green and blue spectral ranges as a function of the solar zenith angle θ_S. The numbers around the graphs indicate the hours (local summer time, UTC+3) of recording. In the first and second half of the course the neighbouring points of the graphs are connected with solid and dashed straight lines (linear interpolation), respectively. (After Fig. 3 of Gál et al. 2001c, p. 1394).

7.6 How the Clear-Sky Angle of Polarization Pattern Continues Underneath Clouds: Full-Sky Measurements and Implications for Animal Orientation

One of the biologically most important parameters of a cloudy sky is the proportion q of the celestial polarization pattern that is available to the polarization compass of certain animals. This parameter of clear or cloudy skies has largely been ignored in measurements of skylight polarization. Exceptions are the studies of Brines and Gould (1982), who made point-source measurements, and of Labhart (1999), who used an opto-electronic model to draw qualitative conclusions on the important role of q in animal orientation. Using full-sky imaging polarimetry, Pomozi et al. (2001b) measured how q varies under different meteorological conditions.

It is a well-known phenomenon that distant objects near the horizon (e.g. forests or mountains) appear bluish because of Rayleigh scattering of light between the observer and these distant objects (Können 1985; Coulson 1988). The same phenomenon occurs in the air column underneath clouds. If part of this column is lit directly by the sun, the distribution of the angle of polarization α of scattered light originating from the sunlit part of the column is the same as that of the clear sky. It is less well known that the scattering of direct sunlight on the cloud particles results in the same E-vector pattern as that of the blue sky (Können 1985). As a result of these scattering phenomena, the α-pattern underneath certain clouds approximates that of the clear sky. Thus the celestial E-vector pattern continues underneath clouds under certain atmospheric conditions, such as when the air columns beneath clouds or parts of clouds are lit by direct sunlight

- obliquely from above for smaller solar zenith angles,
- from the side as with bright white cumuli, or
- from below as sometimes occurs at dawn and dusk.

Further on, we refer to these illumination conditions simply as "directly lit by the sun". Apart from heavy overcast skies with multiple cloud layers, such conditions occur frequently if the sky is partly cloudy.

Stockhammer (1959) hypothesized as first that the scattering of direct sunlight between clouds and the earth's surface may generate an E-vector pattern that continues the pattern present in the cloudless celestial regions. Brines and Gould (1982) as well as Pomozi et al. (2001b) and Horváth et al. (2002a) showed by measurements, that α is the most stable and predictable parameter of skylight even under a wide range of atmospheric conditions, whereas p, radiance and spectral composition are highly variable and hence less reliable as orientation cues for animals. Furthermore, α of skylight undergoes only minor changes with wavelength, while p is strongly dependent on wavelength, especially in the blue

and UV (Coulson 1988). Gerharz (1977) demonstrated that the polarization of light originating from the horizon of a cloudy sky is due to the scattered light reflected from extended surface features in the foreground.

The clear-sky polarimetric measurements of Pomozi et al. (2001b) were performed in the Tunisian Chott el Djerid when the sky was clear throughout the day. The polarization pattern of the entire clear sky was hourly measured after sunrise. The cloudy-sky polarimetric measurements were carried out at different places and times in Tunisia. From the cloudy-sky polarization patterns those were selected in which the solar zenith angles θ_s were approximately the same as those in the clear skies shown in Figs. 7.6.1A-C, 7.6.2A-C. Each circular map of skylight polarization in Figs. 7.6.1-7.6.3 contains approximately 543000 pixels, i.e. represents approximately 543000 measured numerical values in a given part of the spectrum. Clouds were recognized in the digitized pictures of the sky using the algorithm of Horváth et al. (2002a).

Figures 7.6.1B,C and 7.6.2B,C represent the p- and α-patterns of the clear skies shown in Figs. 7.6.1A and 7.6.2A, respectively, as measured at 450 nm from sunrise to sunset. For comparison, Figs. 7.6.1D,E and 7.6.2D,E depict the theoretical (single-scattering Rayleigh) patterns of p and α for the same solar positions as those in Figs. 7.6.1A-C and 7.6.2A-C. Comparison of the measured and theoretical patterns indicates that, apart from regions near the sun and antisun, the single-scattering Rayleigh theory describes the gross characteristics of the clear sky polarization patterns relatively well:

- p of skylight first increases with increasing angular distance from the sun, reaching its maximum at approximately 90^o from the sun, and then decreases towards the antisun, and
- the E-vector of skylight is approximately perpendicular to the scattering plane determined by the position of the observer, the sun and the point observed.

The most striking differences between the actual and the theoretical patterns are the consequences of the neutral points. However, since in the vicinity of these neutral points p is smaller than the perceptual threshold p_{min} = 5-10% in animals, the neutral points of skylight polarization are biologically irrelevant.

Figures 7.6.1G,H and 7.6.2G,H represent the p- and α-patterns of cloudy skies shown in Figs. 7.6.1F and 7.6.2F, respectively, measured again at 450 nm. We have chosen approximately the same solar zenith angles θ_s as those represented for clear skies in Figs. 7.6.1A-C and 7.6.2A-C. p is strongly reduced in those celestial regions in which clouds appear.

In many cases, the α-patterns suffer only minor distortions when clouds are present. Compare, for example, the E-vector distributions in Figs. 7.6.1C and 7.6.2C with those in Figs. 7.6.1H and 7.6.2H. Depending on the type, thickness and height of the clouds and on the visibility of the sun (whether it is visible or hidden by clouds), the α-pattern that is characteristic for a clear sky largely continues underneath the clouds (e.g. Fig. 7.6.1H rows 1-5 and Fig. 7.6.2H rows 2-7). In certain cases, especially if the sun is close to the zenith, the E-vector

pattern in cloudy sky regions is completely distorted (e.g. Fig. 7.6.1H rows 6, 7 and Fig. 7.6.2H row 1).

It is known from electrophysiological recordings from the polarization-sensitive interneurons in the cricket's (*Gryllus campestris*) medulla that these neurons respond reliably to E-vectors if $p > 5\%$ and that the standard deviation for the reliability of the E-vector measurements of these neurons is approximately $\pm 6.5^{\circ}$ for $5\% \leq p \leq 10\%$ and $\pm 4^{\circ}$ for $p > 10\%$ (Labhart 1988, 1996). If $p < p_{\text{threshold}} = 5\%$, crickets cannot perceive the skylight polarization. The polarization-sensitive visual system of crickets determines the direction of the sun from the distribution of α of the clear sky ($\alpha_{clear\ sky}$). If in a cloudy region of the sky the angle of polarization α_{cloud} differs considerably from $\alpha_{clear\ sky}$, the use of α_{cloud} will reduce the accuracy of the determination of the sun's direction if $p > p_{threshold}$. Crickets are not confronted with such a reduction in accuracy if the difference between $\alpha_{clear\ sky}$ and α_{cloud} is below a certain threshold $\Delta\alpha_{threshold}$, which is not smaller than the reliability (± 4-6.5°) of the E-vector measurements of their polarization-sensitive neurons. To summarise: regions of the sky that provide reliable compass information are characterized by $p > p_{threshold} = 5\%$ and/or $|\alpha_{clear\ sky} - \alpha_{cloud}| \leq \Delta\alpha_{threshold} = 4^{\circ}$–$6.5^{\circ}$.

The variable q gives the proportion of the skylight pattern that can be used by the insect for reliable E-vector orientation. Figure 7.6.3 presents two examples derived in the way described above from row 1 of Figs. 7.6.1A and 7.6.1F. They demonstrate that surprisingly large parts of a cloudy sky can be used by the insect for compass orientation. Increasing the value of $p_{threshold}$ and/or decreasing the value of $\Delta\alpha_{threshold}$ will decrease q. Since for Fig. 7.6.3 $\Delta\alpha_{threshold} = 6.5^{\circ}$ was used instead of 4°, the numerical values of q are slight overestimates, at least for the vision of the cricket.

Pomozi et al. (2001b) also investigated the wavelength-dependency of the E-vector compass under cloudy conditions. Measurements were made in the blue (450 nm), green (550 nm) and red (650 nm) for the clear and cloudy skies portrayed in Figs. 7.6.1A, 7.6.2A, and 7.6.1F, 7.6.2F, respectively. The following results were obtained:

1. Because of the spatial distribution of p, the value of q is smaller in the solar than in the antisolar half of the celestial hemisphere. The clear-skies data (Table 7.6.1, columns A-C in Figs. 7.6.1 and 7.6.2) largely confirm what has long been deduced from atmospheric optics.
2. The greater the amount of haze and/or aerosol concentration, the smaller is p, and hence the smaller is q.
3. In general, in clear skies, q is always very high (> 80%). It is influenced by the spectral content, the solar zenith angle and, of course, the meteorological conditions.
4. The lower the solar elevation, the larger is q.
5. In general, q increases with decreasing wavelength (see rows 5-7 of Fig. 7.6.1 and rows 1-4 of Fig. 7.6.2). This trend can no longer be observed for very small Δq values between the blue, green and red range of the spectrum.

Most importantly, as shown in Table 7.6.2 and in columns F-H in Figs. 7.6.1 and 7.6.2, conclusions 1-5 also hold for cloudy skies. Only if parts of the clouds and the air columns beneath them are not directly lit by sunlight, does q decrease. This can result from a low p (rows 2, 6 and 7 of Fig. 7.6.1 and row 1 of Fig. 7.6.2) and/or from situations in which the α-pattern does not extend into the air columns underneath clouds (row 6 of Fig. 7.6.1 and row 1 of Fig. 7.6.2). The closer the sun to the horizon, the larger the cloudy-sky values of q, because the low solar elevation increases the chance that the air volumes underneath clouds are directly illuminated by the sun. The shorter the wavelength, the larger the q-values underneath the clouds. These conclusions were drawn not only from the examples presented in this chapter but also from quantitative data obtained under a variety of other atmospheric conditions ranging from clear (cloudless) skies through cloudy to completely overcast skies and for solar zenith angles ranging from 15^o to 90^o.

The polarization of light originating from an area of the sky covered by cloud (termed "cloudlight") consists of two components (Fig. 8.6):

- The first originates from the cloud itself. White light illuminating the cloud remains white but becomes partially linearly polarized after scattering on the cloud particles (ice crystals or water droplets).
- The second component is caused by the scattering of light within the air column between the cloud and the observer. This column emits bluish and linearly polarized light.

Apart from very high clouds (higher than approximately 5 km), the intensity of the first component is much greater than that of the second. When the clouds and the atmosphere underneath them are directly lit by the sun (in a partly clouded sky, under thin clouds or in fog), α of cloudlight follows the same geometrical rule as in the case of blue sky. Because of the randomizing effect of multiple scattering within clouds, p of the first component is usually much lower than that of the clear sky. In general, the first component dominates (its intensity is much greater than that of the second component), so the net p of cloudlight is rather low and usually reaches maximal values of approximately 40% at 90^o from the sun (see pp. 40-41 in Können 1985). As there are many different types of clouds, and as p of cloudlight depends on a multitude of factors, p may differ from cloud to cloud: it is usually lower for denser clouds, because of the randomizing effect of diffuse scattering by the cloud particles.

In contrast to ice-clouds, water-clouds are strongly polarized not only at 90^o but also at approximately 145^o from the sun, where p can reach 60%, i.e. potentially higher values than in the background skylight (see pp. 42-43 in Können 1985). At 145^o from the sun, water-clouds are markedly brighter than at other regions in the sky.

If the clouds are not thin and/or parts of them are not directly illuminated by the sun, their polarizational characteristics differ from those discussed above. Under a heavily overcast sky, when the cloud layer is several km thick, the illumination comes more or less from all directions and, hence, p of the clouds is strongly

reduced (see pp. 42-43 in Können 1985). More light will come from the zenith, where the clouds look thinnest, than from the horizon, meaning that the cloudlight will be horizontally polarized. p of this cloudlight reaches maximal values of 10-20% just above the horizon and decreases rapidly towards the zenith, where it is 0%. A similar polarization pattern occurs in fog not illuminated by direct sunlight. When the clouds are very thick and the visibility is poor (e.g. during rain), the illumination is extremely diffuse, so that p of skylight is reduced to zero.

The full-sky imaging polarimetric measurements of Pomozi et al. (2001b) showed that, even though in cloudy skies p may differ markedly from that in a cloudless sky, α does not. Consider, for example, rows 2-7 in Fig. 7.6.2H: the majority of the sky was covered by thin strato-cumulus and stratus clouds, which considerably reduced p, but the α-pattern remained identical to that in the corresponding clear skies (rows 2-7 in Fig. 7.6.2C). In rows 1-5 of Fig. 7.6.1H thicker and lower clouds were present, which totally distorted the p-patterns, but left the α-patterns underneath clouds (Fig. 7.6.1C, rows 1-5) almost unaltered because parts of the clouds were illuminated directly by sunlight. In contrast, in rows 6 and 7 of Fig. 7.6.1H and row 1 of Fig. 7.6.2H the patterns of both p and α were quite different from those of clear skies (Figs. 7.6.1C, rows 6, 7 and Fig. 7.6.2C, row 1), because the sun was hidden by thicker clouds and the clouds were not directly lit by the sun.

On the basis of the physiological properties of polarization-sensitive interneurons recorded by Labhart (1996), one can compute the proportion of the celestial E-vector pattern, that even under cloudy skies, can be exploited for navigation (if compared with the full E-vector pattern under clear-sky conditions). Under all but the most extreme cloud-cover conditions, this proportion is rather large. Hence, clouds decrease the extent of skylight polarization useful for animal orientation much less than hitherto assumed.

It is a rather wide-spread belief that animals using celestial polarization compass can orient themselves solely by means of the polarization pattern of the clear, blue regions of the sky when the sun is not visible. The reason for this is the assumption that the clouds reduce the extent of sky polarization pattern useful for animal orientation by decrasing p and causing large disturbances in α. However, we have seen above that the celestial α-pattern continues below the clouds under certain atmospheric conditions. This phenomenon can apparently help animal orientation, because also the α-pattern underneath clouds enables polarization-sensitive animals to determine the position of the invisible sun, if p of the cloudlight is not lower than the perceptual threshold of the visual system. Hence, not only the α-pattern of clear, blue sky regions, but under certain atmospheric conditions also considerable parts of the α-pattern below clouds can be useful for animal orientation.

Tables

Table 7.6.1. Proportion q (in %) of the polarization pattern of the clear sky useful for cricket navigation at 650 nm (R), 550 nm (G) and 450 nm (B) evaluated from the clear-sky polarization patterns in Figs. 7.6.1A and 7.6.2A. The degree of linear polarization $p > 5\%$. Number of pixels for the entire sky = 543000. The union of overexposed regions of skies studied in the different spectral ranges was not included. (After Table 1 of Pomozi et al. 2001b, p. 2939).

	Fig. 7.6.1A			Fig. 7.6.2A		
row	R	G	B	R	G	B
1	98.2	98.9	98.5	84.2	91.1	93.0
2	99.9	99.9	99.8	87.8	94.5	96.6
3	97.8	98.9	97.7	91.1	97.4	98.6
4	98.5	98.9	98.7	90.2	97.1	97.8
5	90.7	94.3	94.6	98.6	99.6	99.2
6	87.5	92.9	93.1	99.6	99.6	99.6
7	83.6	90.7	92.9	98.7	99.5	98.9

Table 7.6.2. Proportion q (in %) of the polarization pattern of the clear-sky regions and the clouds useful for cricket navigation at 650 nm (R), 550 nm (G) and 450 nm (B) evaluated from the polarization patterns of cloudy skies in Figs. 7.6.1F and 7.6.2F. For clear-sky regions, the degree of linear polarization $p > 5\%$. For cloudy regions $p > 5\%$ and $|\alpha_{clear\ sky} - \alpha_{clouds}| \leq 6.5^{\circ}$, where α is the angle of polarization. Number of pixels for the entire sky = 543000. The union of overexposed regions of skies studied in the different spectral ranges was not included. (After Table 2 of Pomozi et al. 2001b, p. 2939).

	clear sky regions						clouds					
	Fig. 7.6.1F			Fig. 7.6.2F			Fig. 7.6.1F			Fig. 7.6.2F		
row	R	G	B	R	G	B	R	G	B	R	G	B
1	95.5	93.8	77.8	77.1	79.8	83.9	47.6	59.3	62.3	4.2	4.9	16.0
2	52.8	53.9	68.4	89.8	96.6	98.1	12.9	11.1	18.4	11.7	29.5	44.2
3	90.5	93.9	96.0	90.6	95.9	97.6	27.6	32.6	42.6	43.0	51.8	63.7
4	95.2	97.4	99.3	90.8	96.6	97.4	21.8	21.4	29.4	17.0	32.9	60.7
5	94.7	97.5	97.8	95.6	98.6	98.3	19.9	21.6	24.2	61.9	71.1	81.2
6	92.9	94.6	94.1	98.2	99.7	99.8	6.8	8.3	12.9	49.5	57.1	66.8
7	71.7	76.8	86.6	98.5	98.9	98.3	3.1	2.9	9.4	36.6	58.1	71.8

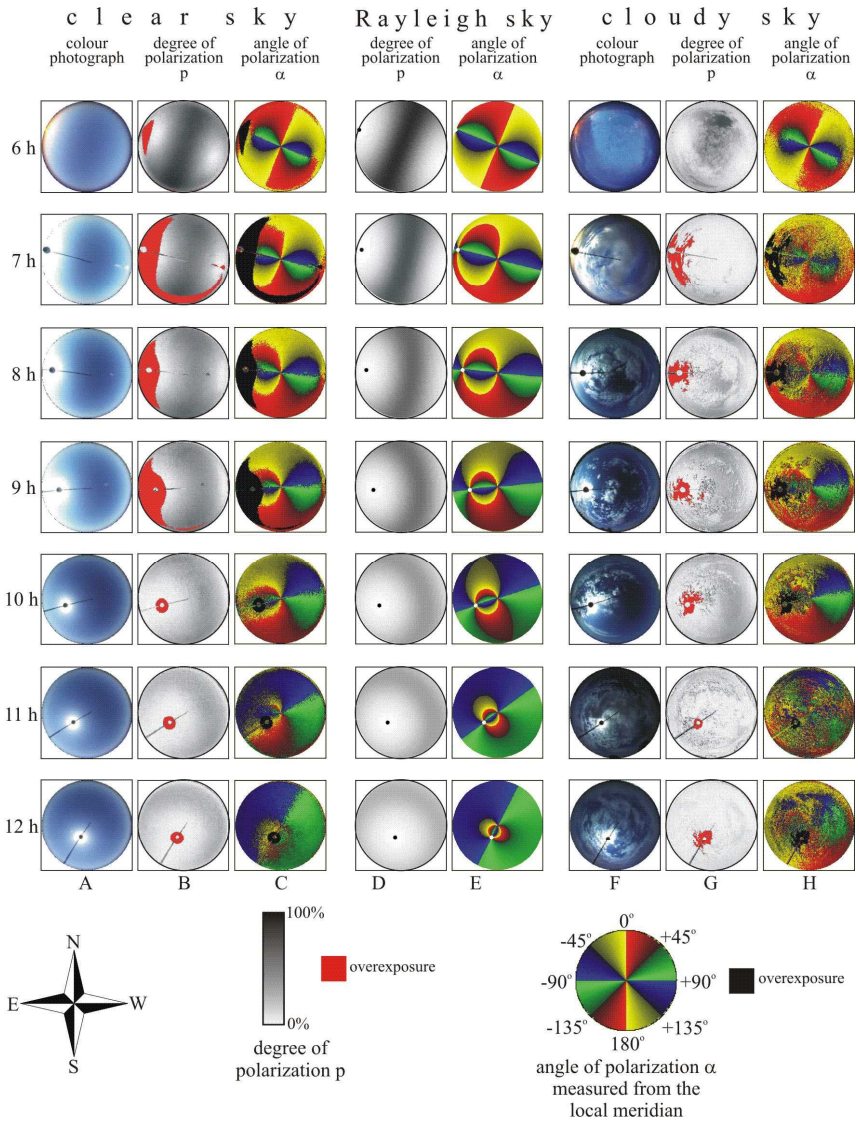

Fig. 7.6.1. A-C: Spatial distribution of radiance and colour, degree of linear polarization p and angle of polarization α (measured from the local meridian) over the entire clear sky measured by full-sky imaging polarimetry at 450 nm for different hourly positions of the sun – from sunrise (06:00 h = UTC+1) to noon (12:00 h) – on 26 August 1999 in the Tunisian Chott el Djerid. D, E: Patterns of p and α of skylight calculated using the single-scattering Rayleigh model for the same solar positions as those in A-C. F-H: Patterns for cloudy skies at different places in Tunisia between 27 August 1999 and 4 September 1999 measured at 450 nm for approximately the same solar zenith angles as those in A-C. The positions of the sun are indicated by dots. The radial bar in the pictures is the wire of the sun occulter. (After Fig. 1 of Pomozi et al. 2001b, p. 2936).

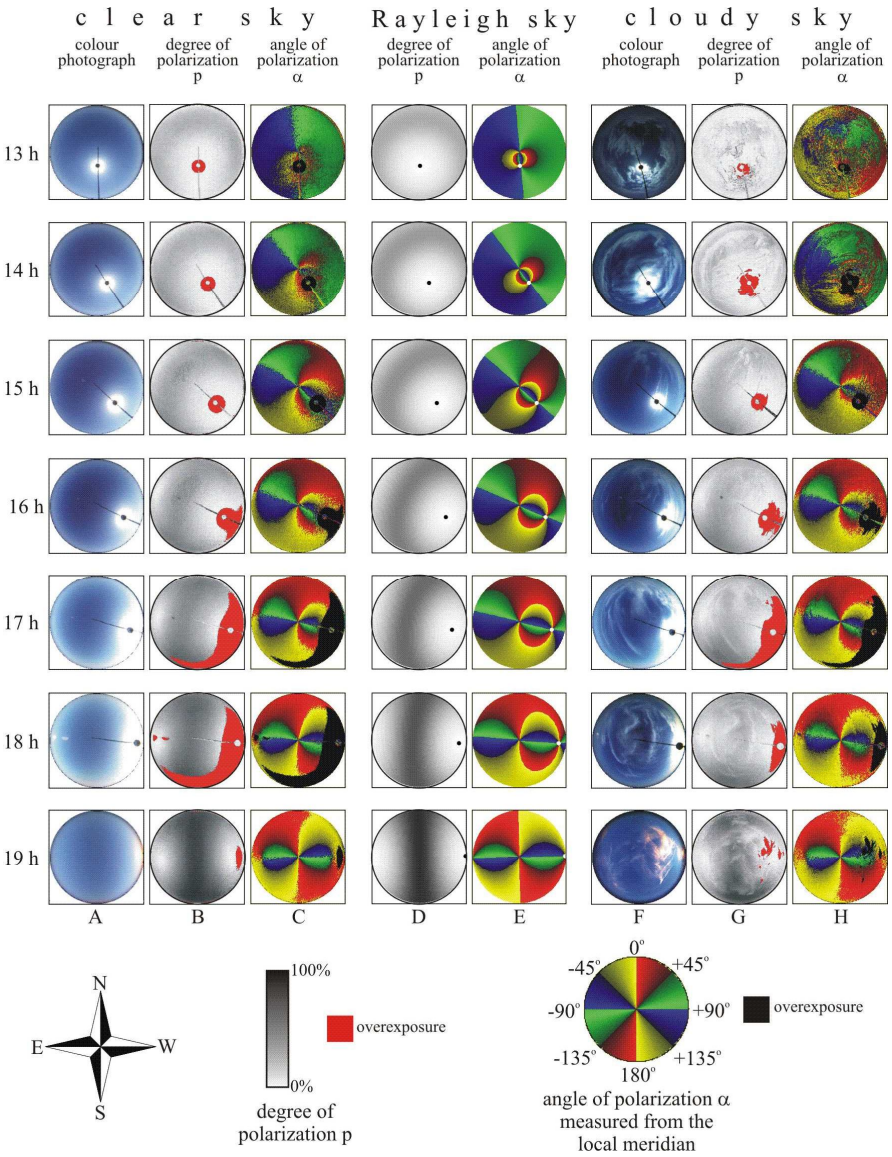

Fig. 7.6.2. As Fig. 7.6.1 from 13:00 h (= UTC+1) to 19:00 (sunset). (After Fig. 2 of Pomozi et al. 2001b, p. 2937).

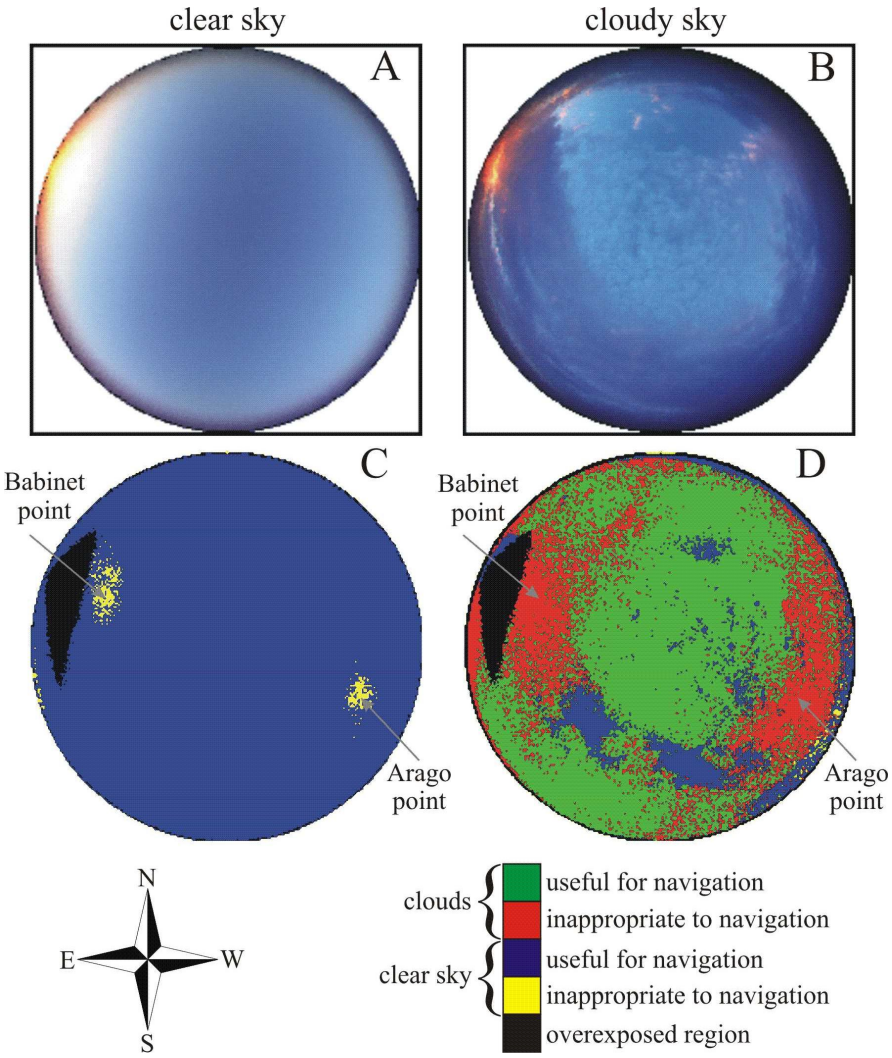

Fig. 7.6.3. The clear (A) and cloudy (B) sky shown in row 1 of Fig. 7.6.1A and in row 1 of Fig. 7.6.1F, respectively. C, D: Regions of the clear (C) and cloudy (D) sky with polarization patterns useful for or inappropriate to reliable cricket navigation calculated on the basis of the celestial polarization patterns measured by full-sky imaging polarimetry at 450 nm. *Blue* (useful for navigation): regions of the clear sky where the degree of linear polarization $p > 5\%$. *Yellow* (inappropriate to navigation): regions of the clear sky where $p \leq 5\%$. *Green* (useful for navigation): regions of the clouds where $p > 5\%$ and $|\alpha_{clear\ sky} - \alpha_{clouds}| \leq 6.5^{o}$, where α is the angle of polarization. *Red* (inappropriate to navigation): regions of the clouds where $p \leq 5\%$ and/or $|\alpha_{clear\ sky} - \alpha_{clouds}| > 6.5^{o}$. *Black*: region of the sky where the photoemulsion was overexposed. The numerical values of p, $\alpha_{clear\ sky}$ and α_{clouds} originate from quantitative full-sky measurements. (After Fig. 3 of Pomozi et al. 2001b, p. 2940).

7.7 Cloud Detection with the Use of Ground-Based Full-Sky Imaging Polarimetry

In many meteorological stations the accurate determination of sky conditions, especially the detection of clouds, is a desirable yet rarely attainable goal. Traditionally, sky conditions are reported by human observers with considerable discrepancies between individual and subjective reports. In practice, employing human observers is not always feasible due to budgetary constraints. Human observers can be replaced by automatic full-sky imager systems, like the Scripps-produced Whole Sky Imager, or the TSI-880 Total Sky Imager produced by the Yankee Environmental Systems, Inc. (YES 2001). These systems provide real-time processing and display of daytime sky conditions using common image processing algorithms, which detect the clouds radiometrically by filtering the colour picture of the sky so that the approximate value of the cloud cover fraction can be calculated.

Using the additional information obtained by evaluating both the degree and angle of polarization patterns of cloudy skies measured by full-sky imaging polarimetry in the red (650 nm), green (550 nm) and blue (450 nm) spectral ranges, the algorithms of radiometric cloud detection (e.g. Saunders 1986; Saunders and Kriebel 1988; Derrien et al. 1993; YES 2001) can be significantly improved. In this chapter we show an efficient combined radiometric and polarimetric algorithm developed by Horváth et al. (2002a), which performs the detection of clouds more efficiently and reliably than an exclusively radiometric cloud detection algorithm. In the future, this or similar improved polarimetric algorithms can accomplish cloud detection with ground-based automatic instruments, which could be a new generation of the presently existing ground-based automated total sky imagers using exclusively radiometric algorithms for cloud detection.

7.7.1 Algorithmic Cloud Detection

Using full-sky imaging polarimetry, one obtains the values of nine optical variables for every pixel of the sky image: I_r, I_g, I_b, p_r, p_g, p_b, α_r, α_g, α_b, that is, radiance I, degree of linear polarization p and angle of polarization α measured in the red (r), green (g) and blue (b) spectral ranges. The essence of the cloud detection algorithm of Horváth et al. (2002a) is that for every pixel of the sky picture seven decisions are made:

- (1) Analysing the values of I_r, I_g and I_b, the colour of the pixel is determined, and it is decided if the pixel may belong to a colourless cloud or to a blue sky region.
- (2)-(7) Using the values of p_r, p_g, p_b, α_r, α_g or α_b, it is again decided if the pixel may be part of a cloud or a clear sky region.

Every decision is the outcome of its specific subalgorithm, called "detector". Detector (1) is symbolized by *IRGB* since it uses the *I*-values measured in the red (*R*), green (*G*) and blue (*B*) spectral ranges. Detectors (2)-(7) are symbolized by *PR, PG, PB,* αR, αG and αB, because they use the measured values of p_r, p_g, p_b, α_r, α_g or α_b, respectively. If detector *IRGB* identifies a pixel as "cloud", the pixel qualification is weighted by 3, because the decision relies on the use of three input data. The total weight of a pixel qualification is *i*, if it is identified as "cloud" by *i* detectors among detectors *PR, PG, PB,* αR, αG, αB (these six detectors make their decisions using one input datum each). The partial weight is 0 in every case when the pixel is identified as "clear sky" by a given detector.

If the investigated pixel is under- or overexposed at least in one of the *R, G, B* spectral ranges, detector *IRGB* is inactive resulting in a 0 partial weight value. Similarly, any other detector is inactive, if the pixel is under- or overexposed in the corresponding spectral range. Let the number of active detectors be *m*. The partial weights are summed up, thus finally the investigated pixel has a total weight *n* ranging from 0 to 9. *n* tells how many times the pixel was identified as "cloud"; *n* is called the "number of cloud identification". At a given *m*-value, *n* is proportional to the likelihood of cloud: the higher is *n*, the greater the probability that the pixel belongs to a cloud in the picture. The authenticity (or reliability) of *n* is proportional to the number *m* of active detectors. The distributions of the *n*- and *m*-values in the sky can be represented by colour-coded maps (Fig. 7.7.5).

In the case of "radiometric cloud detection" only detector *IRGB* is used. "polarimetric cloud detection" uses only detectors *PR, PG, PB,* αR, αG and αB. We speak about "combined (radiometric and polarimetric) cloud detection" if all seven detectors are used. As we see below, the combined cloud detection algorithm has seven control parameters: c, $p_0(q)$, $\Delta\alpha(q)$, where $q = R, G, B$. Setting appropriately their values, certain types of clouds can be reliably detected.

The optimal values of these control parameters can be empirically determined in the following way: In the digitized colour picture of a given cloudy sky the clouds are visually identified by inspection with the nacked eye and each pixel is marked accordingly. The resulting cloud pattern serves as a "control pattern". Changing the value of the control parameter of a given detector, the visually detected control clouds are compared with the clouds recognized by the detector: The numbers of pixels are counted, where (i) there is cloud in the control pattern but the pixel is identified erroneously as clear sky; (ii) there is clear sky in the control pattern but the pixel is identified erroneously as cloud; (iii) the pixel is identified as cloud; (iv) the pixel is under- or overexposed. Dividing these numbers by the number of pixels of the entire sky picture, we obtain

- the proportion *PCDS* of clouds detected (erroneously) as (clear) sky,
- the proportion *PSDC* of (clear) sky detected (erroneously) as cloud,
- the proportion *PCC* of cloud cover,
- the proportion *PUO* of under- and/or overexposed pixels,
- the proportion $PED = PCDS + PSDC$ of erroneous detection.

That value of the control parameter of a given detector is considered as optimal $[c^*, p_0^*(q), \Delta\alpha^*(q)]$, ($q = R, G, B$) at which the *PED*-value is minimal (*PED**), that is, where the correlation between the pixels of the algorithmically and visually detected clouds and clear sky regions is maximal (Fig. 7.7.4).

7.7.2 Radiometric Detection of Colourless Clouds

Detector *IRGB* functions in the following way: Apart from the reddish orange clouds illuminated by the sunset or sunrise glow, or from the very high altitude bluish cirrus clouds, the clouds are generally colourless, ranging from dark grey to bright white, independently of their radiance and position in the sky (Können 1985; Coulson 1988). The pixels of such "grey" clouds on the sky picture possess approximately the same radiances in all three (*r, g, b*) spectral ranges. Thus, if the differences $\Delta I_{b-r} = |I_b - I_r|$ and $\Delta I_{b-g} = |I_b - I_g|$ are less than $\varepsilon = c \cdot I_b$, where c is a control parameter to be appropriately chosen as described above, then detector *IRGB* assumes that the given pixel belongs to a colourless cloud, else to the blue sky. ε is proportional to I_b due to the blueness of scattered skylight.

7.7.3 Radiometric Detection of Overexposed and Underexposed Parts of the Sky Image

Around the sun image disc the photoemulsion inevitably becomes overexposed. If in a given spectral range (*r, g, b*) the digitized brightness value I of a pixel reaches 254 (maximum is 255), the pixel is considered as overexposed in that part of the spectrum. At about 90^o from the sun, where the clear blue sky is the darkest, the photoemulsion may be underexposed, especially in the red, where the skylight intensity is the lowest. Landmarks and vegetation (usually near the horizon) may also show up in a sky picture, and they too, are generally underexposed on the photoemulsion, as are the sun occulter. These underexposed areas can be detected by the following algorithm: If the values I_r, I_g, I_b of a pixel are smaller than a given threshold t, it is assumed that the given pixel is underexposed. Setting appropriately the value of t, the underexposed regions of the sky as well as the underexposed landmarks and vegetation can be reliably identified.

7.7.4 Polarimetric Detection of Clouds on the Basis of the Degree and Angle of Linear Polarization

Detectors *PR, PG* and *PB* function as follows: Apart from 145° from the sun in the sky with water clouds (where rainbow scattering dominates with high p) independently of the wavelength, in a given celestial point p of cloud pixels is lower than that of clear sky pixels due to multiple scattering (Können 1985; Coulson 1988). As a first approximation the change of p of skylight versus the angular distance γ from the sun can be described by the single-scattering Rayleigh model, in which $p(\gamma) = p_{max} \cdot \sin^2\gamma/(1+\cos^2\gamma)$, $\cos\gamma = \sin\theta_s \sin\theta \cos\varphi + \cos\theta_s \cos\theta$, where θ_s is the solar zenith angle, θ and φ are the angular distances of the observed celestial point from the zenith and the solar meridian, respectively. Detector *Pq (q=R,G,B)* assumes that the given pixel positioned at angular distance γ from the sun belongs to a cloud if p is lower than the threshold $p_{threshold} = p_0(q) \cdot \sin^2\gamma/(1+\cos^2\gamma)$, where $p_0(q)$ is a control parameter to be appropriately chosen as described above.

Under certain meteorological conditions (if parts of the clouds and the air-space between the clouds and the surface of the earth are not directly lit by the sun) in a given celestial point the angle of polarization α of cloud pixels differs considerably from $\alpha_{clear\ sky}$ of clear sky pixels independently of the wavelength (Können 1985; Pomozi et al. 2001b). Detector αq *(q=R,G,B)* assumes that the given pixel belongs to a cloud if the difference $|\alpha - \alpha_{clear\ sky}|$ is larger than the threshold $\Delta\alpha(q)$, which is a control parameter to be appropriately chosen as described above. For these decisions the α-patterns of the clear sky (Fig. 7.7.2) measured in the *R, G, B* spectral ranges can be used as control with the same solar zenith angle as that of the investigated cloudy sky (Fig. 7.7.1). Prior to these decisions the α-patterns of both the corresponding clear and cloudy skies are smoothed by convolution with an appropriate two-dimensional rotation-symmetric Gaussian function to eliminate the inevitable small noise of higher spatial frequencies.

7.7.5 Detection of Clouds by Radiometric, Polarimetric and Combined Algorithms

Figure 7.7.1 shows the p-and α-patterns of a sky with fast moving cumuli measured by the three-lens three-camera full-sky imaging polarimeter of Horváth et al. (2002a) in the red (650 nm), green (550 nm) and blue (450 nm) spectral ranges. In Fig. 7.7.2 the corresponding patterns of a clear, cloudless sky are seen with the same solar position as in Fig. 7.7.1.

Figure 7.7.3A shows the photograph of the partially cloudy sky, the polarizational characteristics of which are represented in Fig. 7.7.1. To test the cloud detection performance of any algorithm control patterns would be needed with known, well-defined clouds. Unfortunately, such control cloud patterns are generally not available. Thus, the first step of cloud detection is to construct a

relatively good approximation of such control patterns: Placing trust in the excellent pattern recognition and good brightness and colour discrimination ability of the human visual system, one can detect and recognize visually the clouds in the colour picture of the sky (Fig. 7.7.3A), which is displayed on the screen of a computer, and those celestial regions can be shaded by a mouse-guided "paint brush" where clouds are seen. Figure 7.7.3B, serving as a control cloud pattern, shows the visually detected clouds in white and the clear sky regions in black. The percentage of cloud cover in this control pattern is $PCC = 56.1\%$.

Figure 7.7.3C represents the clouds detected radiometrically with the use of the algorithm (detector *IRGB*) described above. In Fig. 7.7.3C regions of the sky are checkered, if their pixels are under- or overexposed at least in one of the three (red, green, blue) spectral ranges in which measurements were performed. In these checkered regions detector *IRGB* is inactive. Figures 7.7.3D,E,F and 7.7.3G,H,I show the clouds detected polarimetrically at 650, 550 and 450 nm using the p-patterns in Fig. 7.7.1 and the α-patterns in Figs. 7.7.1 and 7.7.2, respectively.

The cloud detection performance of every detector is determined by a control parameter, the value of which is optimal if the proportion $PED = PCDS + PSDC$ of erroneous detection is minimal. Figure 7.7.4 shows the change of *PED* as a function of the corresponding control parameters c, or $p_0(q)$, or $\Delta\alpha(q)$ for detectors *IRGB, PR, PG, PB,* αR, αG and αB. We can see that the graphs $PED(c)$, $PED[p_0(q)]$, $PED[\Delta\alpha(q)]$ generally possess a definite minimum. The positions of these minima are chosen as the optimal values c^*, $p_0^*(q)$, $\Delta\alpha^*(q)$ of the control parameters.

A detector is inactive at those pixels of the picture of the sky where under- or overexposure occurs. This is the case in the checkered regions in Figs. 7.7.3C-I, where there is no information about the real sky conditions. The radiometric detector *IRGB* actually involves three detectors (*IR, IG* and *IB*), which can function only together. Since detector *IRGB* is inactive if under- or overexposure occurs in at least one of the three (red, green, blue) spectral ranges, the number m of active (neither underexposed nor overexposed) detectors can be 0, 2, 4 or 9, when the investigated celestial point is under- or overexposed in 3, 2, 1 or 0 spectral ranges, respectively. Thus, the number n of "cloud identification" can be 0,1,...,8,9. Figures 7.7.5A and 7.7.5B show the colour-coded celestial maps of n and m calculated for the partially cloudy sky in Fig. 7.7.3A, the optical characteristics of which are shown in Fig. 7.7.1. m is proportional to the authenticity (or reliability) of the (cloud or clear sky) detection. Figure 7.7.5C shows the map which combines maps A and B. At a given m-value, $n/n_{max}(m)$ is the likelihood of cloud, while $1-n/n_{max}(m)$ is the likelihood of clear sky.

Figure 7.7.5D shows the cloudy and clear sky regions detected by the combined (radiometric and polarimetric) algorithm such that the pixels with larger or smaller $n(m)$-values than $n(m)^*$ were considered to belong to clouds or clear sky regions, respectively. For $n(m)^*$ the proportion of erroneous detection $PED\ (= PCDS + PSDC)$ is minimal (PED^*). A similar procedure is applied in the case of the polarimetric cloud detection, when only the p- and α-patterns are used. Figure 7.7.5C shows the threshold values $n(m)^*$.

In Table 7.7.1 the lower and upper limits of the proportion of cloud cover determined by the radiometric, polarimetric and combined (radiometric and polarimetric) cloud detection algorithms are compared. PCC_{det} is the value of PCC determined by the radiometric (Fig. 7.7.3C), polarimetric (Figs. 7.7.3C-I) and combined (Fig. 7.7.5D) algorithms. The lower and upper limit of PCC is $PCC_{min} = PCC_{det} - PSDC$ and $PCC_{max} = PCC_{det} + PCDS + PUO$, respectively. The real value PCC_r of the proportion of cloud cover is somewhere between PCC_{min} and PCC_{max}. As an approximate value of PCC_r we obtained 56.1% by visual cloud detection (Fig. 7.7.3B). The reliability of a cloud detection algorithm is characterized by the difference $\Delta PCC = PCC_{max} - PCC_{min}$: the smaller is ΔPCC, the higher is the reliability. We can see in Table 7.7.1 that ΔPCC is largest (33.1%) for the radiometric, smaller (20.8%) for the polarimetric and smallest (14.7%) for the combined cloud detection. In the case of the combined cloud detection the interval, in which PCC_r can be, is about the half of that obtained for the radiometric cloud detection. This demonstrates well that the combined algorithm can detect clouds more reliably than the exclusively radiometric or the purely polarimetric algorithm alone. The power of the combined cloud detection algorithm in comparison with the radiometric one is ensured by the fact that the information contributed by the radiometric subalgorithm (subdetector *IRGB*) to the final decision (cloud or clear sky) is only one third by weight. The polarimetric algorithm is more reliable than the radiometric one, because the former is based on the use of twice as many detectors as the latter.

Table

Table 7.7.1. The results of cloud detection with the use of Figs. 7.7.1-7.7.5. *IRGB*: radiometric detector. *POL*: polarimetric detector involving detectors *PR, PG, PB, αR, αG* and *αB*. *COM*: combined detector combining the *IRGB* and *POL* detectors. *PUO* = *P*roportion of *U*nder- and/or *O*verexposure, *PED* = *P*roportion of *E*rroneous *D*etection, *PCDS* = *P*roportion of *C*louds *D*etected (erroneously) as (clear) *S*ky, *PSDC* = *P*roportion of (clear) *S*ky *D*etected (erroneously) as *C*loud, *PED* = *PCDS* + *PSDC*, *PCC* = *P*roportion of *C*loud *C*over, PCC_r = "real" value of *PCC* detected visually, PCC_{det} = value of *PCC* detected by a given algorithm, PCC_{min} = lower limit of *PCC*, PCC_{max} = upper limit of *PCC*. In the first row of the second (widest) column of the table the inequality $PCC_{min} \le PCC_r \le PCC_{max}$ is seen, where $PCC_{min} = PCC_{det} - PSDC$ and $PCC_{max} = PCC_{det} + PCDS + PUO$. The percentage values of these terms are given in the table for the different types of detector. Difference $\Delta PCC = PCC_{max} - PCC_{min}$ gives the uncertainty or error of PCC_r: the value of PCC_r is somewhere between PCC_{min} and PCC_{max}. The number of pixels of the entire sky is N = 346207, to which all percentage values are related. (After Table 3 of Horváth et al. 2002a, p. 555).

detection type	$PCC_{det} - PSDC =$		$PCC_{min} \le$	$PCC_r \le$	$PCC_{max} =$	$PCC_{det} + PCDS + PUO$			$\Delta PCC = PCC_{max} - PCC_{min}$
	(%)	*(%)*	*(%)*	*(%)*	*(%)*	*(%)*	*(%)*	*(%)*	*(%)*
PR	45,9	9,7	36,2	56,1	80,8	45,9	18,7	16,2	44,6
PG	38,2	6,4	31,8	56,1	62,9	38,2	22,3	2,4	31,1
PB	49,9	8,5	41,4	56,1	68,3	49,9	11,2	7,2	26,9
αR	59,7	13,8	45,9	56,1	84,8	59,7	8,9	16,2	38,9
αG	55,1	16,1	39,0	56,1	72,6	55,1	15,1	2,4	33,6
αB	51,6	16,0	35,6	56,1	75,8	51,6	17,0	7,2	40,2
IRGB	50,7	4,5	46,2	56,1	79,3	50,7	6,0	22,6	33,1
POL	59,4	12,1	47,3	56,1	68,1	59,4	7,9	0,8	20,8
COM	53,5	6,1	47,4	56,1	62,1	53,5	7,8	0,8	14,7

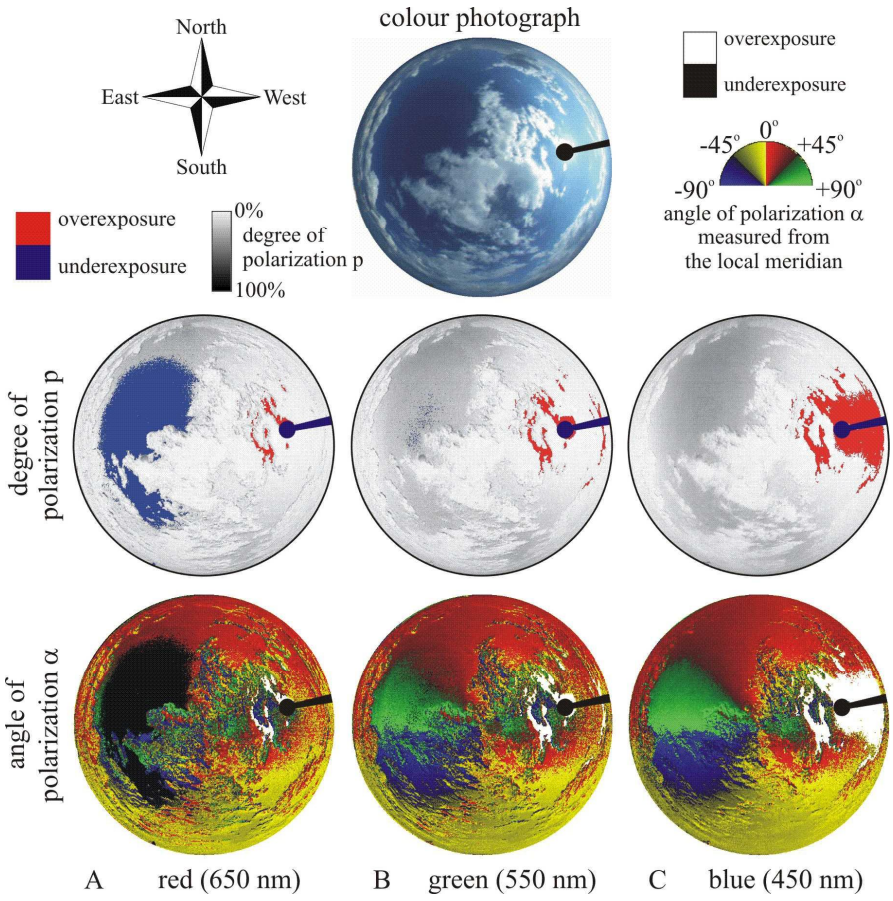

Fig. 7.7.1. Photograph and the patterns of the degree of linear polarization p and angle of polarization α of a sky with fast moving cumuli measured by the three-lens three-camera full-sky imaging polarimeter of Horváth et al. (2002a) in the red (650 nm), green (550 nm) and blue (450 nm) spectral ranges at Kunfehértó (46°23'N, 19°24'E, Hungary) on 15 August 2000 at 17:00 (local summer time = UTC+2). (After Fig. 7 of Horváth et al. 2002a, pp. 547-548).

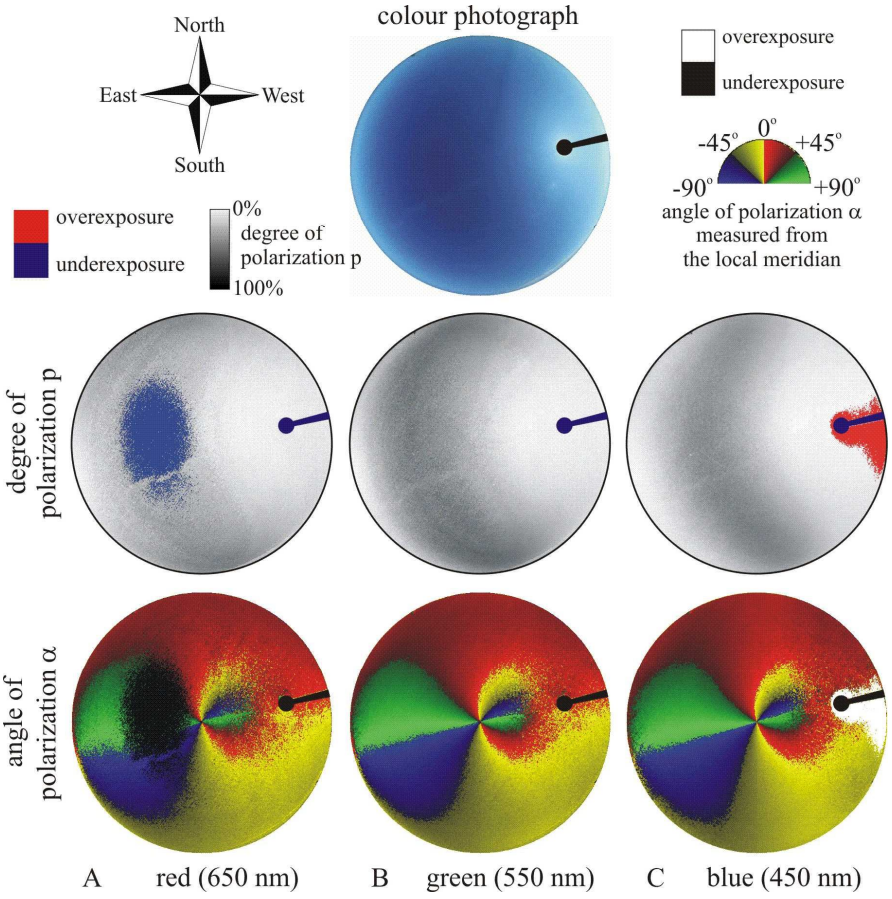

Fig. 7.7.2. As Fig. 7.7.1 for a clear, cloudless sky (with the same solar position) measured on 17 August 2000 at 17:00. (After Fig. 8 of Horváth et al. 2002a, pp. 548-549).

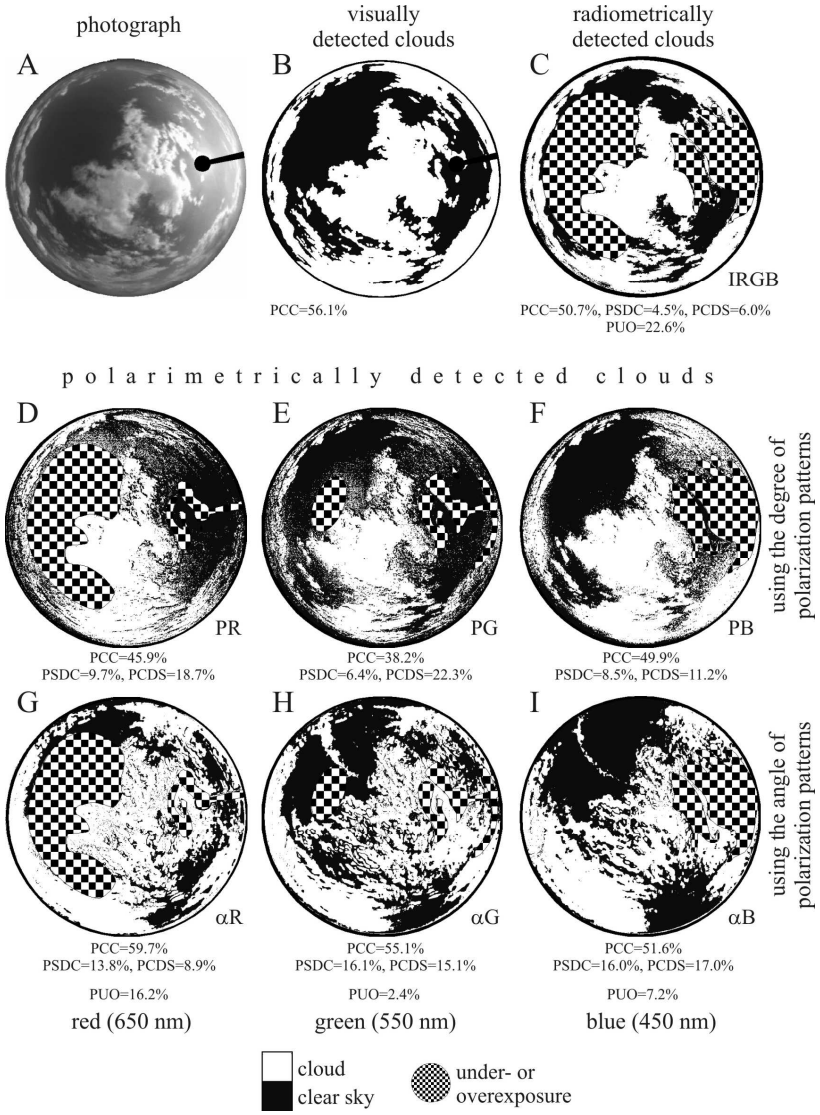

Fig. 7.7.3. A: Photograph (identical with that in the first row of Fig. 7.7.1) of the partially cloudy sky, the polarizational characteristics of which are shown in Fig. 7.7.1. B: Cloudy (white) and clear (black) sky regions detected visually by the nacked eye in picture A. C: Clouds detected radiometrically, where the under- or overexposed celestial areas are checkered. D-I: Clouds detected polarimetrically at 650, 550 and 450 nm using the *p*- or α-patterns in Figs. 7.7.1 and 7.7.2. *PCC* = *P*roportion of *C*loud *C*over determined by the different detectors *IRGB, PR, PG, PB, αR, αG* and *αB*. *PSDC* = *P*roportion of (clear) *S*ky *D*etected (erroneously) as *C*loud, *PCDS* = *P*roportion of *C*louds *D*etected (erroneously) as (clear) *S*ky, *PUO* = *P*roportion of *U*nder- and/or *O*verexposure. (After Figs. 9 and 10 of Horváth et al. 2002a, pp. 550-551).

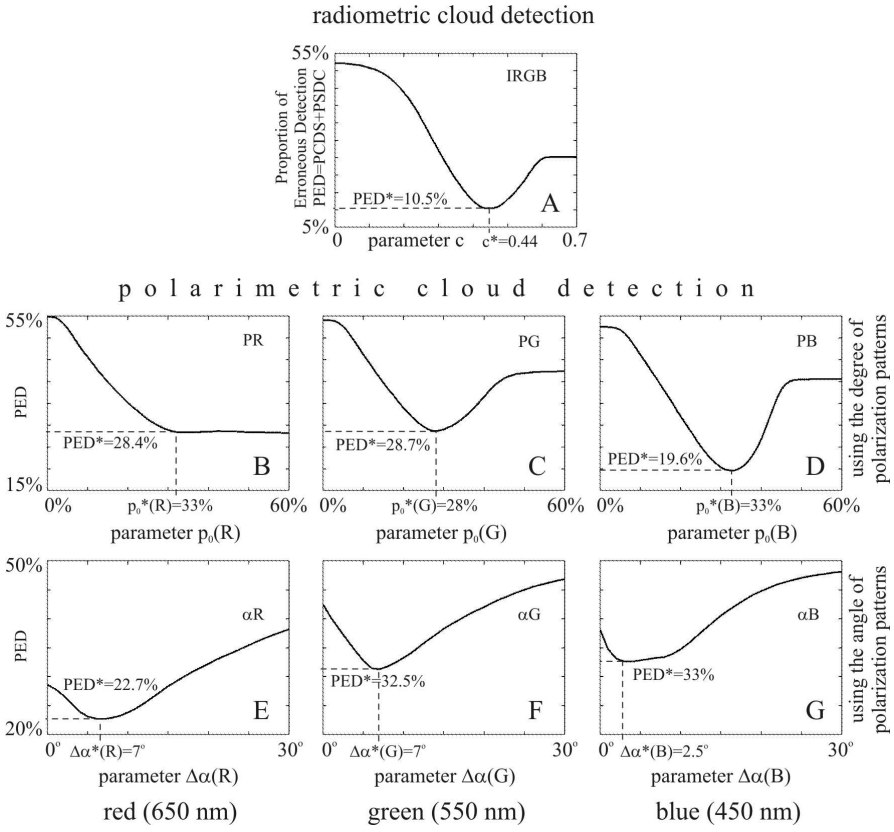

Fig. 7.7.4. Proportion *PED = PCDS + PSDC* of pixels of the sky detected erroneously by the different detectors *IRGB, PR, PG, PB, αR, αG* and *αB* as a function of parameters *z* [*z = c*, or $p_0(q=R,G,B)$, or $\Delta\alpha(q=R,G,B)$] in the red (650 nm), green (550 nm) and blue (450 nm) spectral ranges. The positions *z** of the minima *PED** of the graphs are marked with dashed straight lines. A: Radiometric cloud detection with control parameter *c*. B, C, D: Polarimetric cloud detection with control parameter $p_0(q=R,G,B)$ using the *p*-patterns in Fig. 7.7.1. E, F, G: Polarimetric cloud detection with control parameter $\Delta\alpha(q=R,G,B)$ using the α-patterns in Figs. 7.7.1 and 7.7.2.

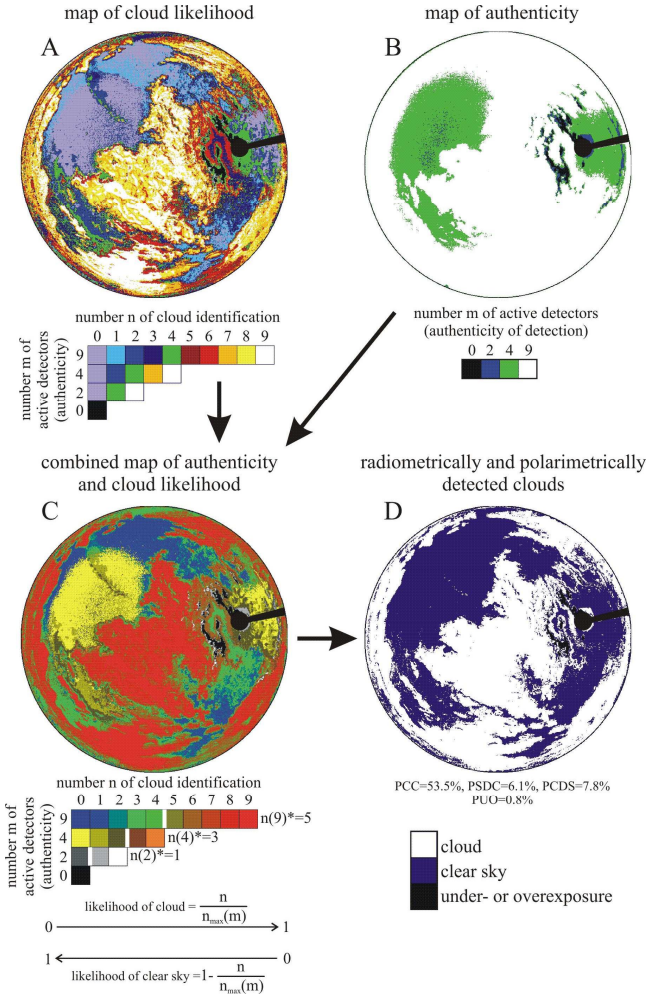

Fig. 7.7.5. A: Colour-coded map of the number *n* of cloud identification calculated for the partially cloudy sky in Fig. 7.7.3A, the optical characteristics of which are shown in Fig. 7.7.1. B: Colour-coded map of the number *m* of active (neither underexposed nor overexposed) detectors calculated for the partially cloudy sky in Fig. 7.7.3A. *m* is proportional to the authenticity of the (cloud or clear sky) detection. C: Map combining maps A and B. At a given *m*-value, $n/n_{max}(m)$ is the likelihood of cloud, while $1-n/n_{max}(m)$ is the likelihood of clear sky. D: Cloudy (white) and clear (blue) sky regions are detected by the combined (radiometric and polarimetric) algorithm such that pixels with larger or smaller $n(m)$ than $n(m)^*$ were considered to belong to clouds or clear sky regions, respectively. For $n(2)^* = 1$, $n(4)^* = 3$ and $n(9)^* = 5$ (the positions of which are indicated by white vertical bars in the colour palette) the proportion of erroneous detection $PED = PCDS + PSDC$ is minimal (PED^* in Fig. 7.7.4). The under- or overexposed sky regions ($m = 0$) in the maps are shaded with black. (After Figs. 11 and 12 of Horváth et al. 2002a, pp. 552-553).

7.8 Polarization Pattern of the Moonlit Clear Night Sky at Full Moon: Comparison of Moonlit and Sunlit Skies

The light of the night sky originates from the following main natural sources (in order of brightness): moonlight, stars and planets, the Milky Way, zodiacal light, airglow, and the light from these sources scattered by the earth's atmosphere. Unfortunately, light pollution from artificial city lighting also affects many sites' night skies. Most of these sources are weakly polarized, the airglow is unpolarized (Wolstencroft and Brandt 1974), and the skylight may be strongly polarized (Können 1985). In the polarimetry of the night sky the unpolarized airglow emission and the atmospheric scattering of light of bright sources (e.g. the moon) are unwanted, because the former causes a dilution of the degree of polarization, and the latter (the so-called "sky foreground") introduces a spurious polarization. The flux of these unwanted sources can be brighter than the source of interest, depending on direction and wavelength. At full moon, in extended regions of the sky around the moon and antimoon, the moonlight scattered and polarized in the atmosphere overwhelms all other sources of the night sky. This makes more difficult astronomical measurements, thus usually one must wait for moonless night to make delicate astronomical polarimetric measurements.

Although in the last decades several extensive polarimetric investigations of the night sky were carried out (e.g. Gehrels 1974), not much attention has been paid to the polarizational characteristics of the moonlit night sky. Therefore using full-sky imaging polarimetry, Gál et al. (2001a) checked experimentally the similarities between the polarization patterns of moonlit and sunlit skies.

Figures 7.8.1A-C show the spatial distribution of radiance I, degree p and angle α of linear polarization over the entire clear moonlit night sky measured in white light[1] for different positions of the moon. Figures 7.8.1D-F represent the same patterns of the clear sunlit day sky measured in simulated white light[2] for approximately the same positions of the sun as those of the moon in the night sky. Figure 7.8.2 shows the positions of the moon, sun, lunar/solar Arago and Babinet neutral points of the clear moonlit/sunlit night/day sky evaluated from the celestial polarization patterns in columns B,C/E,F of Fig. 7.8.1.

---

[1] In order to minimise the time of exposure, the polarizational characteristics of the moonlit sky must have been recorded by a highly sensitive photographic film. Gál et al. (2001a) used Kodak Tmax P3200 (pushed up to 6400 ASA) black and white photoemulsion. Thus the polarization of the moonlit night sky could be measured only in white light, that is, I, p and α were averaged by the photoemulsion over the full visible range of the spectrum.

[2] As detectors Gál et al. (2001a) used Fujichrome Sensia II 100 ASA colour reversal film for sunlight recordings. The colour pictures of the sunlit skies were transformed to averaged black and white pictures prior to polarimetric evaluation.

Comparing the measured polarization patterns of the moonlit night sky (Figs. 7.8.1B,C) with that of the sunlit day sky (Figs. 7.8.1E,F), it can be confirmed that the polarizational characteristics of a moonlit night sky are practically identical with those of a sunlit sky if the position of the moon in the firmament is the same as that of the sun. The small differences between the measured polarization patterns and positions of the neutral points (Fig. 7.8.2) of the moonlit clear night sky at full moon and those of the sunlit clear day sky can be attributed (in order of importance) to

1. the probably different meteorological conditions (e.g. aerosol concentration) during the nighttime and daytime measurements,
2. the different local ground albedo at the places of measurement with different type of area,
3. the small differences ($|\theta_{Moon} - \theta_{Sun}| \leq 2^o$) between the solar and lunar zenith angles,
4. the different types of the detector (white light for moonlight, simulated white light for sunlight),
5. the slightly different polarizational state of moonlight[3] and unpolarized sunlight,
6. the different spectral features of moonlight[4] compared with sunlight.

The Monte Carlo method used by Adams and Kattawar (1997), for example, is able to model these differences for any input state of polarization.

These results are not surprising, because they follow from the theory of light scattering: Considering the structure of the celestial polarization pattern, it is all the same if the moon or the sun is the light source. Nevertheless also this must be experimentally proven, and the importance of the investigation by Gál et al. (2001a) is the presentation of the first comprehensive experimental evidence for this theoretical prediction.

The results presented in this chapter may have functional significance for arthropod navigation. For example, Kerfoot (1967) reported that the foraging

[3] While the sunlight is always unpolarized, the moonlight is partially linearly polarized, and at full moon it is unpolarized (Dollfus 1961; Pellicori 1971). With the increase of the phase angle β, its polarization is negative, that is, its direction of polarization is parallel to the plane of sight. The degree p of negative polarization culminates at $\beta = 11^o$, then it decreases. At $\beta = 23.51^o$ the moonlight is unpolarized again. With the further increase of β the polarization of the moonlight becomes positive, that is, its direction of polarization becomes perpendicular to the plane of the direction of sight. In the positive range of polarization, the maximum $p = 8.7\%$ is reached on the first or second day following the fourth quarter. Then p decreases again until it becomes zero three days prior to and after the new moon. Following the new moon, p increases until its maximum of 6.6% one day prior to the first quarter. Following this stage, just the same way as after the full moon, p of the moonlight decreases to zero, then its angle of polarization turns over again.

[4] Moonlight is sunlight reflected from the lunar surface. It has nearly the same spectral composition as sunlight, but with a shift somewhat toward the red (Kopal 1969).

activities of nocturnal bees last as long as the moon stays above the horizon. Furthermore, several insect and crustacean species have been shown to use the moon as a navigational aid.

Desert ants of the genus *Cataglyphis* are exclusively diurnal foragers, but when experimentally tested at night, they take the full moon for the sun, and navigate according to what a time-compensated sun-compass would predict (Wehner 1982). However, what about nocturnal insects, i.e., species that usually forage at night? Even if they do not possess a moon-compass, they could use the moon and the nighttime α-pattern as a short-term compass which is calibrated anew each time the animals start a foraging journey (see e.g. Lambrinos et al. 1997). The relatively low radiance of the moonlit night sky may not be a serious limiting factor of the navigation by nocturnal insects, because field crickets (*Gryllus campestris*), for instance, can respond to polarization at intensities that are lower than that of the clear, moonless night sky (Herzmann and Labhart 1989). Crickets are active also at night and may orient on the basis of celestial polarization patterns during dawn and dusk, or even at night when the sky is lit by the moon. They perceive the skylight polarization in the blue with the dorsal rim area of their compound eyes.

Talitrid sandhoppers use sun- and moon-compass in their offshore-onshore orientation, that is, during their movements perpendicular to the shoreline (Papi 1960; Enright 1961, 1972; Papi and Pardi 1963; Craig 1971; Ugolini et al. 1999a,b), and it was suggested that they can use the celestial polarization pattern for this task if the sun is not visible (Ugolini et al. 1999a,b). The same could be true also at night during full moon, when the moon is occluded by clouds.

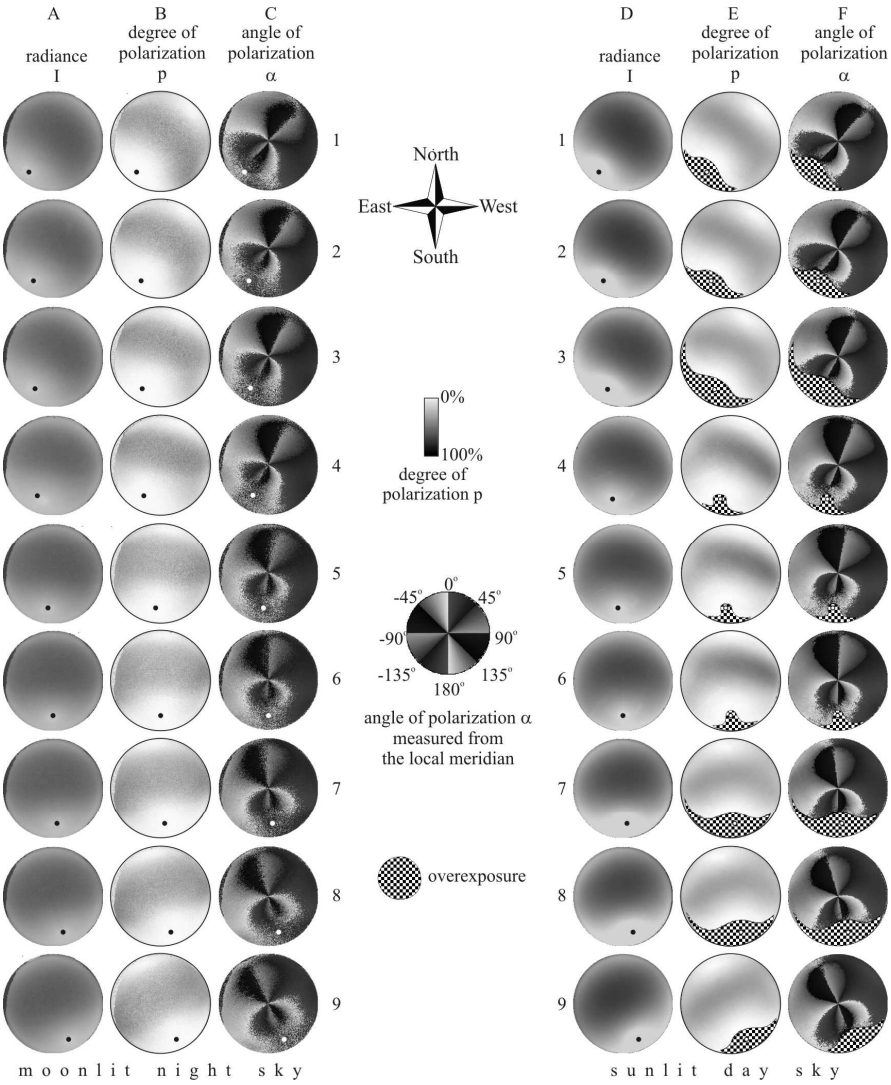

Fig. 7.8.1. A-C: Spatial distribution of radiance, degree and angle of linear polarization over the entire clear moonlit night celestial hemisphere approximately at full moon with a phase angle of $9^{o}4'$ measured in white light for different zenith angles of the moon. D-F: As columns A-C for the clear sunlit day sky measured in simulated white light for approximately the same zenith angles of the sun as those of the moon. The checkered regions are overexposed. The positions of the moon and sun are indicated by black or white dots. East is on the left of the compass rose because we are looking up through the celestial dome rather than down onto a map. (After Fig. 2 of Gál et al. 2001a, p. 22650).

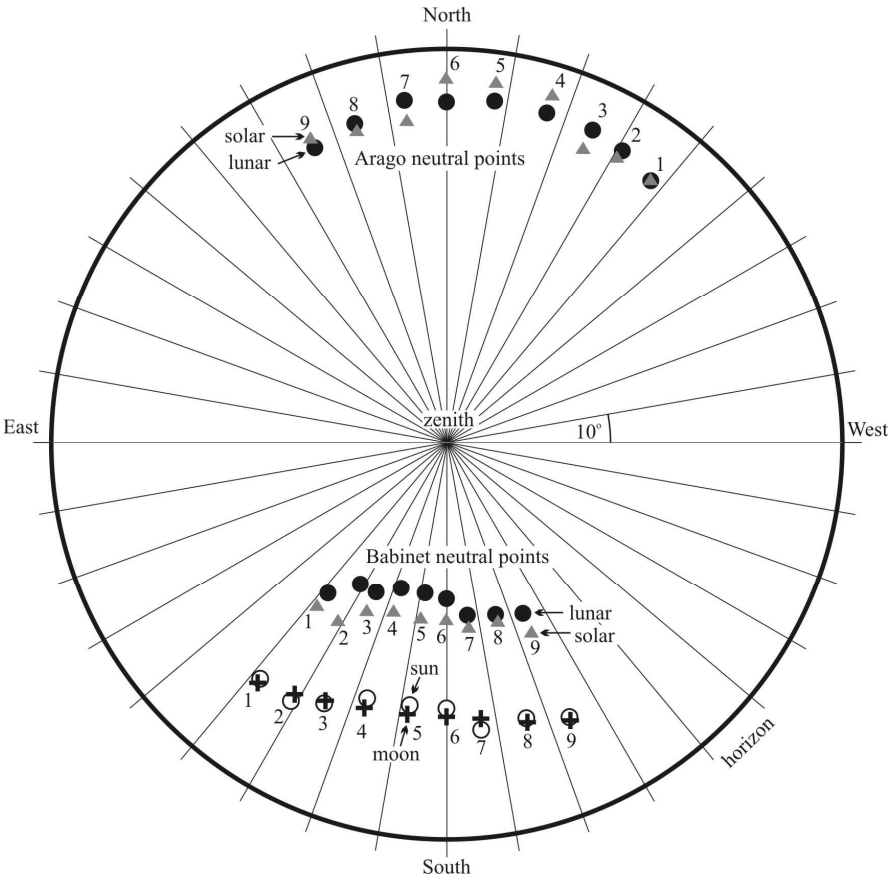

Fig. 7.8.2. Positions of the moon (crosses), sun (circles), lunar (black dots) and solar (grey triangles) Arago and Babinet neutral points of the clear moonlit/sunlit night/day sky evaluated from the measured celestial polarization patterns in Fig. 7.8.1B,C/E,F. The numbers next to the dots/triangles correspond with the row numbers in Fig. 7.8.1. (After Fig. 3 of Gál et al. 2001a, p. 22651).

7.9 Imaging Polarimetry of the Rainbow

The rainbow, a coloured circular band visible at about 42° from the antisolar point if sunlight falls onto water droplets underneath clouds, is one of the most spectacular phenomena in nature. It is not mere chance that many artists drew inspirations from rainbows (Lee and Fraser 2001). One of the peculiar characteristics of the rainbow is, that rainbow light is strongly polarized with the direction of polarization tangential to the bow, as discovered by the French physicist, Jean Baptiste Biot in 1811.

The light-scattering properties of large water spheres have been studied in great depth to explain the intensity and colouration of the rainbow light (Minnaert 1940; Tricker 1970; Greenler 1980; Coulson 1988). The polarizational characteristics of the rainbow have also been investigated theoretically. Assuming unpolarized incident light on water droplets of various sizes, Dave (1969) computed the intensity I and degree p of linear polarization of the scattered light. He concluded that there is a strong oscillation of p between the primary and secondary rainbows as well as in the areas of the supernumeraries of the primary rainbow. Khare and Nussenzveig (1974) proposed a theory of the rainbow and compared it with the exact Mie solution. Their improvement was particularly remarkable for electric polarization. Können and de Boer (1979) extended the Airy theory of the rainbow to polarized incident light with the direction of polarization perpendicular or parallel to the scattering plane, which is tangential or radial to the bow at any point along the rainbow. Nussenzveig (1979) developed a complex angular momentum theory of the rainbow including parallel and perpendicular polarization components. Mobbs (1979) gave a rainbow theory based on Huygens's principle and compared it with the complex angular momentum theory. He found a good agreement over a large range of scattering angles and size parameters for both the magnetic and electric polarizations. Using Mie theory for monodisperse water drops, Lynch and Schwartz (1991) calculated p of rainbow light without background contribution. They obtained that the maximum polarization p_{max} (occurring at the peak brightness of the bows) of both primary ($p_{max} < 90\%$) and secondary ($p_{max} < 50\%$) bows varies with drop size. Wang and van de Hulst (1991) compared the results of Mie computations with those of the Airy approximation. Lee (1998b) compared the differences in the perceptible colour and luminance as well as in the angular positions of luminance extrema between the Mie and Airy rainbow theories.

The rainbow is a relatively exceptional atmospheric phenomenon, the polarimetric study of which is made more difficult by the fact that its appearance cannot be predicted. It occurs by chance when generally there is no polarimeter at hand, and if there is a polarimeter, one may wait usually a long time for the possible occurrence of a rainbow. Due to the difficulties in observing rainbows, the experimental research of the rainbow's polarizational characteristics is scarce. Using a polar nephelometer employing a monochromatic linearly polarized laser

source, Sassen (1979) performed angular scattering measurements with vertically and horizontally polarized incident light to examine the rainbow generation of pendant water drops, a type of artificial near-spherical, vertically elongated particle, which models the distorted shape of larger (diameter > 0.3-1 mm) raindrops with circular cross section in the horizontal plane during fall. He measured linear polarization ratios as a function of scattering angle and compared the experimental data with theoretical predictions. Können (1986, 1992) published a pair of colour photographs taken by A. B. Fraser about a rainbow viewed through a linearly polarizing filter: on the left and right photograph the rainbow light was maximally transmitted and extinguished, respectively. In the 1991 "Light and colour in the open air" feature issue of Applied Optics (Lock 1991) also some rainbow photographs taken by A. B. Fraser through linear polarizers were presented. Lee (1991) used these photographs to isolate the rainbow's intrinsic colours exploiting the fact that rainbow light is highly linearly polarized compared with light from the background: The rainbow's perpendicular polarization component is defined as that seen through a linear polarizer when its transmission axis is perpendicular to the scattering plane determined by the sun, a raindrop contributing to the bow, and the observer. At this polarizer orientation, the rainbow is the brightest. If the polarizer is rotated by 90^o, the bow's much weaker parallel polarization component is practically invisible. Light from the backround (landscape and cloudy sky) is usually almost unpolarized. Thus an estimate of the rainbow's intrinsic colours (without background) can be obtained if the digitized image of a rainbow's perpendicularly polarized component is colourimetrically subtracted pixel by pixel from its parallelly polarized counterpart.

The spatially extended polarization patterns of rainbows existing only for short periods would be difficult to study by point-source scanning polarimeters; these patterns can be measured only with wide field-of-view imaging polarimetry. Barta et al. (2003) have performed the first imaging polarimetric investigation of the rainbow. Figure 7.9.1 shows the polarization patterns of a rainbow above the sea surface measured at 450, 550 and 650 nm. The primary rainbow was as usual red outside and blue inside and the innermost colours were paler than the red. At about 11^o outside the primary rainbow, a secondary rainbow with a reversed sequence of colours appeared, which was much fainter than the primary one and a few supernumerary rainbows were also visible below the primary one. These are unfortunately not recognisable in the prints. The plots in Fig. 7.9.2 represent the p- and α-values measured at 450, 550 and 650 nm as a function of the angle of elevation θ along the vertical arrows in Fig. 7.9.1 after subtracting the contribution of light from the sky background.

In the p-patterns, the rainbow shows up most strikingly at 650 nm (red), while at 450 nm (blue) it is hardly visible. In the red also the arc of the secondary bow is discernible. Crossing the primary rainbow upward, there is an abrupt decrease of p: at 650 nm, for example, p decreases from about 50% of the primary rainbow to about 5% of Alexander's dark band between the primary and secondary rainbows. The light in Alexander's dark band is unpolarized, because the background skylight is unpolarized. Lee (1991) and Gedzelman (1982) discussed the role of

the background skylight in observations of the rainbow. Moving off downward from the primary rainbow, p gradually decreases with some oscillations (Fig. 7.9.2. These oscillations are due to the supernumerary rainbows. At all three wavelengths, in the α-patterns (Fig. 7.9.1) and α-plots (Fig. 7.9.2) the rainbow does not show up, which demonstrates that there is no contrast in α between the rainbow and its celestial background.

According to Können and de Boer (1979) as well as Können (1985), the strong polarization of the rainbow is the consequence of the path that the beams of light generating the rainbow follow in the drops: In the primary or secondary rainbow, the beams suffer one or two reflections in the drop, respectively. Since these reflections happen at angles very near the Brewster angle, the reflected light is highly polarized, and the direction of polarization is always perpendicular to the scattering plane, that is, tangential to the arc of the bow. Since the light below the primary rainbow and above the secondary one rises in the same way as the light of the rainbow itself, its direction of polarization is also tangential to the bow. Though the scant light from the Alexander's band between the primary and secondary rainbow arises from reflections from the outside surface of the water droplets, background skylight plays a large role also. This light is also tangentially polarized with respect to the bows.

Hence, the direction of polarization of sunlight returned by the primary and secondary rainbows, as well as by the celestial regions below the primary rainbow, between the primary and secondary bows and above the secondary bow is always perpendicular to the scattering plane, that is, tangential to the bows. Thus, there is no contrast in α between the rainbows and their sunlit celestial surroundings, which usually is also characterized by E-vectors perpendicular to the scattering plane. This is why the rainbow does not show up in the α-patterns and α-plots.

The explanation of the observation, that in the p-patterns the investigated rainbow showed up best in the red, but was hardly visible in the blue, is that the background light was unpolarized or only very weakly polarized due to multiple scattering, and it was most intensive in the blue due to Rayleigh scattering, therefore it could most strongly desaturate and depolarize the coloured and polarized rainbow light in the blue. Furthermore, the partially polarized light scattered in the air column between the observer and the rainbow, and being most intense in the blue, partly overwhelms the rainbow light, especially in the blue. This is clearly seen in Fig. 7.9.2: p of blue light from the surrounding of the rainbow is much higher than p of green and red light.

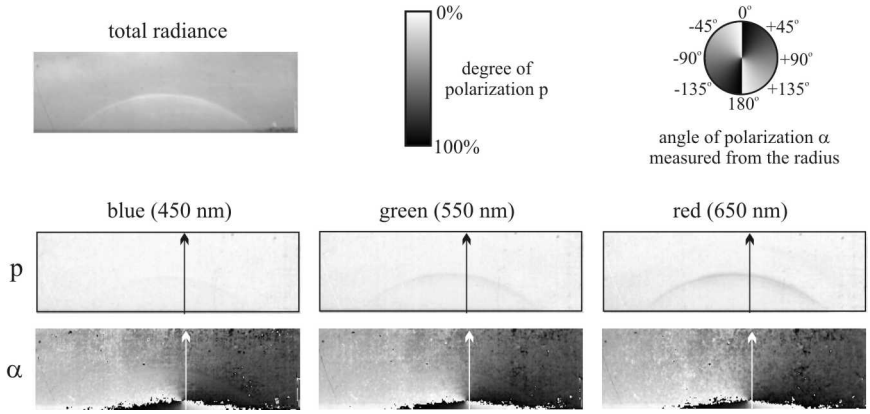

Fig. 7.9.1. Patterns of the total radiance, the degree of linear polarization p and the angle of polarization α of a rainbow above the sea surface at the shore of Oulu (65°0′N, 25°26′E, Finland) measured at 450, 550 and 650 nm by 180° field-of-view imaging polarimetry on 18 July 2001, at 17:42 (local summer time = UTC+3) when the solar elevation was 29°41′. Time of exposure = 1/250 s, aperture = 5.6, detector = Fujichrome Sensia II, 100 ASA colour reversal film. At a given point of the α-patterns, α is measured clockwise from the radius of the bow. (After Fig. 3 of Barta et al., 2003, p. 403).

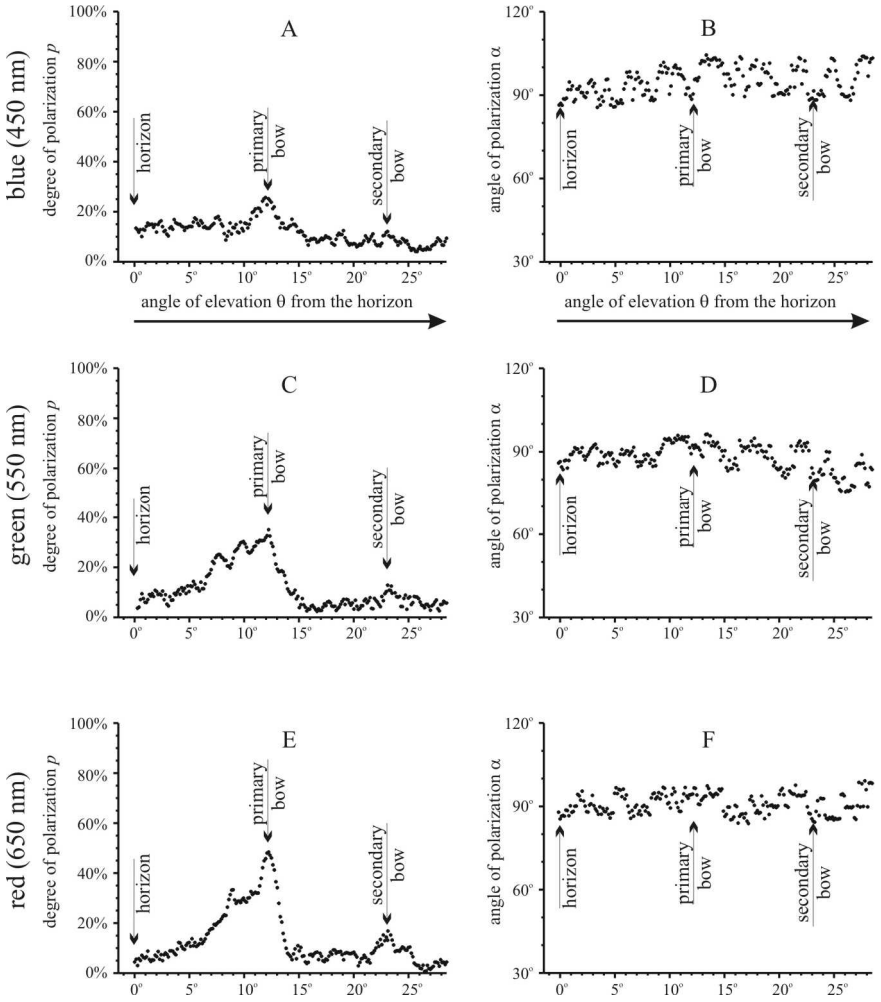

Fig. 7.9.2. Degree of linear polarization p and angle of polarization α at 450, 550 and 650 nm as a function of the angle of elevation θ along the vertical arrows shown in Fig. 7.9.1 (pointing from down $\theta = 0^o$ to up $\theta = 28^o$) after subtracting the contribution of the weakly polarized light from the sky background. (After Fig. 4 of Barta et al., 2003, p. 404).

8 Which Part of the Spectrum is Optimal for Perception of Skylight Polarization?

In many insect species the perception of skylight polarization is mediated by a group of anatomically and physiologically specialized ommatidia in an upward-pointing narrow dorsal rim area (DRA) of the compound eye. The ommatidia in the DRA contain two sets of monochromatic and highly polarization-sensitive photoreceptors with orthogonal microvilli. The spectral type of the receptors in the DRA is ultraviolet (UV) in flies, honeybees, desert ants, scarab beetles and spiders, blue in crickets, desert locusts and cockroaches, while green in the beetles *Melolontha melolontha* and *Parastizopus armaticeps* (Table 8.1).

However, the perception of skylight polarization in the UV is rather surprising, because both the radiance I and the degree of linear polarization p of skylight in the UV are considerably lower than in the blue and green (Figs. 8.1 and 8.2), furthermore the atmospheric absorption of light is much higher in the UV than for longer wavelengths (e.g. Henderson 1970). We call this the "ultraviolet paradox of perception of skylight polarization", simply "UV-sky-pol paradox" further on. In the opinion of Wehner (1994a, p. 110), there is no particular region of the spectrum predestined to be used preferentially for detection of the E-vector of skylight under all possible sky conditions.

8.1 A Common Misbelief Concerning the Dependence of the Degree of Skylight Polarization on Wavelength

Some researchers are not aware of the UV-sky-pol paradox due to an erroneous belief considering the wavelength dependency of polarization of light from the clear sky. In the literature of animal polarization sensitivity a frequently occurring misbelief is that p of scattered blue skylight is the highest in the UV. Several biologists tried to explain by this misinformation why certain animal species detect the skylight polarization in the UV. We mention here the following typical examples for this delusion:

1. Waldvogel (1990, p. 352): "In insects, the visual cells that are responsive to the **ultraviolet** - where **skylight polarization is most pronounced** - are also sensitive to polarization."
2. Beason and Semm (1991, p. 107): "Polarized light detection probably occurs in the **UV wavelengths**, because **the greatest degree of polarization occurs at those frequencies**."
3. Helbig (1991, p. 288): "Since **natural skylight is most strongly polarized in the UV**, much of the natural polarization is taken away by the cage covers with increasing absorption below 400 nm."
4. Tovée (1995, p. 456): "So shorter wavelengths, such as **UV light**, are scattered and **polarized more than longer wavelengths**."
5. Shashar et al. (1995b, p. 215): "A growing portion of the literature shows that vision in the **ultraviolet (UV) range** (300-400 nm) is closely related to sensitivity to **partially linearly polarized light** (PLPL) … Further, the characteristics of PLPL are expected to change according to the wavelength observed, and should be **especially strong in the short end of the spectrum**."

From the context it was always obvious that these researchers wrote about polarization of light from the clear sky rather than about light from clouds. However, polarization measurements (e.g. Coulson 1988, p. 285) have shown that under clear atmospheric conditions p of scattered skylight decreases with decreasing wavelength λ (Fig. 8.1A). The reason for this has already been explained in Chapter 7. Figure 8.1B shows the dispersion of $p_{max}(\lambda)$ of skylight for a turbid, dusty atmosphere. Dust considerably reduces p_{max} in the long-wavelength (orange, red, infrared) range, while in the short-wavelength (blue, UV) range it has only a minor effect, p in the UV being essentially the same as that for the clear atmosphere. Due to this reduction, p_{max} in the UV is about as low as p_{max} for $\lambda >$ 650 nm. However, for $\lambda <$ 650 nm, p_{max} is the lowest in the UV.

8.2 Why do Many Insects Perceive Skylight Polarization in the UV?

Several hypotheses have been published which tried to solve the UV-sky-pol paradox. In this section we describe these hypotheses and give their criticism, finally we expound a convincing solution of the paradox. However, we should emphasize that several insect species perceive the skylight polarization in the blue or green (Table 8.1). Why do not use these insects UV-sensitive photoreceptors for detection of skylight polarization? Below some arguments are presented for the advantage of perception of celestial polarization in the blue and especially in the UV. However, also another important physical, biological or environmental factors may exist still, which determine the optimal wavelength range of detection of skylight polarization in a particular animal species.

Sometimes it is simply declared without any explanation, that the UV spectral range is the least or the best reliable for perception of skylight polarization. We

mention only one example: "In *Cataglyphis*, polarized light patterns in the ultraviolet apparently provide the primary compass information …, ultraviolet wavelengths are the least reliable for performing these tasks, so why insects use only those wavelengths for polarized light orientation is puzzling in itself" (Able 1989, pp. 252-253). Similar declarations cannot help to solve the UV-sky-pol paradox.

8.2.1 Is the Celestial Polarization Pattern More Stable in the UV?

Zdenek Sekera claimed in his communication to Karl von Frisch (1967, p. 382) that UV wavelengths are the least sensitive to "atmospheric disturbances". Relying on this suggestion, Frisch (1967) postulated that UV polarization patterns of skylight might be more advantageous as cues for orientation not only because the UV E-vector orientation ought to approximate simple theory most precisely, but also because it might be most stable during "marginal sky conditions", unlike patterns in longer wavelengths which may be easily disrupted. In other words, atmospheric disturbances may affect the E-vector direction of skylight, and such disturbances may have an increased effect on the longer wavelengths, and the least influence on UV skylight. Although in the 1960's neither the experimental nor the theoretical basis was available for this assumption and the evidence for this conjecture were very slim, this idea has become widely accepted in the literature, because any strategy that could extend the conditions under which successful orientation is possible would certainly constitute a major selective advantage.

The statement of Sekera (cf. Frisch, 1967, p. 382), that "the celestial polarization pattern might be the least sensitive to atmospheric disturbances in the UV spectral region", has been frequently cited in the literature. Here we refer only to three examples:

- Duelli and Wehner (1973, p. 50): "The **polarization pattern** looks about the same in different spectral regions. With **increasing wavelengths**, however, the pattern is getting more and **more susceptible to atmospheric disturbances**."
- Wehner (1976, p. 110): "It is **in the ultraviolet** range of wavelengths that the **polarization of skylight is least affected by atmospheric disturbances** and is therefore the most stable."
- Dacke et al. (2002, p. 215): "The high polarization sensitivity of the **UV receptors** in *Pachysoma striatum* further supports the use of this spectral class for the analysis of the sky compass. At these short wavelengths the **sky polarization pattern** is also the most stable under different weather conditions."

However, the major problem with such too general statements is, that these "atmospheric disturbances" have never been precisely defined. It remained unclear what do "susceptibility to atmospheric disturbances" or "stability of the celestial polarization pattern under different weather conditions" exactly mean.

8.2.2 Was the UV Component of Skylight Stronger in the Past?

It is a logical assumption that the sensitivity maximum of the monochromatic polarization-sensitive photoreceptors perceiving polarized skylight may be adapted to the wavelength where the radiance of skylight is maximal. Such spectral adaptations of certain receptors to the dominant radiation field of the optical environment are common in visual systems (e.g. Lythgoe 1979). Since in the present atmosphere of the earth the radiance of skylight is maximal in the blue (Fig. 8.2), the receptors detecting polarized skylight should be blue sensitive.

Brines and Gould (1982) suggested that a possible reason why UV wavelengths are used by skylight detectors in certain animals may be that in the era when polarization sensitivity has evolved in these animals, the UV component of skylight might have been stronger than it is today. The reasons could be that the atmosphere might have attenuated the UV flux of sunlight to a lesser degree than it does today, and/or the magnitude of UV radiation of the sun might have been greater during earlier epochs of evolution. Although the total energy emitted by the sun fluctuates by a tiny 0.1% over an 11-year solar cycle, and solar UV radiation changes three times as strongly during a cycle as total radiation (Pearce 1998), furthermore the composition of the earth's atmosphere has dramatically changed during the history of the biosphere, the major problem with this hypothesis is that from the past there are no reliable data about the temporal change of the UV radiation reaching the earth's surface. Thus this idea is hard to evaluate. If we accepted this hypothesis, the period, during which the UV component of skylight might have been stronger than nowadays, should have been in the near past on the time scale of evolution, else the sensitivity maximum of skylight detectors should have been adapted to the present situation, namely to the blue maximum of skylight radiation (Fig. 8.2).

Let us estimate, in which spectral range would function optimally a monochromatic crossed-analyzer in the DRA of insects. If the E-vector of partially linearly polarized incident light is parallel (par) or perpendicular (perp) to the microvilli, the amount Q of skylight absorbed by a polarization-sensitive photoreceptor can be calculated as follows (Horváth et al. 2002c):

$$Q_{par} = c \int_0^{\infty} A(\lambda)\, I(\lambda)\, [PS+1+(PS-1)\, p(\lambda)]\, d\lambda,$$

$$Q_{perp} = c \int_0^{\infty} A(\lambda)\, I(\lambda)\, [PS+1-(PS-1)\, p(\lambda)]\, d\lambda, \qquad (8.1)$$

where c is a constant, λ is the wavelength of light, $A(\lambda)$ is the absorption function of the receptor (Fig. 8.3A), $I(\lambda)$ and $p(\lambda)$ are the radiance (Fig. 8.2) and the degree of linear polarization (Fig. 8.1A) of scattered skylight, PS is the polarization sensitivity describing the fact that if the E-vector of totally linearly polarized light is parallel to the microvilli, then a receptor absorbs PS-times more amount of light than in the case when the E-vector is perpendicular to the microvilli. The difference between $logQ_{par}$ and $logQ_{perp}$ is:

$$\Delta(\log Q) = \log Q_{par} - \log Q_{perp} = \log(Q_{par}/Q_{perp}). \qquad (8.2)$$

The basis of E-vector contrast sensitivity of crossed-analyzers in the DRA is to compare $logQ_{par}$ and $logQ_{perp}$, that is, to evaluate the difference $\Delta(logQ)$. The greater this difference, the better is the functioning of the detection of skylight polarization. Thus, maximizing $\Delta(logQ)$ is optimal for receptors in the DRA. Using Eqns. (8.1) and (8.2), $\Delta[logQ(\lambda_{max})]$ was calculated as a function of λ_{max} for the graphs $p(\lambda)$ and $I(\lambda)$ in Figs. 8.1A and 8.3A, where λ_{max} is the wavelength where the receptor's absorption $A(\lambda)$ (Fig. 8.3A) is maximal. The result is shown by graph 1.0 in Fig. 8.3B for PS = 7, which is a typical value for crickets, for example. One can see that this graph has a maximum at 458 nm. Hence, under the recent atmospheric radiation circumstances the most effective polarization-sensitive photoreceptor has an absorption maximum in the blue. In spite of this fact Hymenoptera and Diptera, for example, use for this purpose UV ($\lambda < 400$ nm) receptors. Thus, the functioning of these receptors is not as effective as could be in this regard.

Following the hypothesis of Brines and Gould (1982), let us estimate the necessary magnitude of the "ancient level" of UV radiation of scattered skylight, which would ensure that the maximum of $\Delta[logQ(\lambda_{max})]$ of photoreceptors in the DRA is shifted to the UV part of the spectrum. $\Delta[logQ(\lambda_{max})]$ was calculated for the series of I_n, n = 1.0, 1.5, 2.0, 2.5, 3.0 shown in Fig. 8.3A, where $I_{1.0}$ is the recent radiance of skylight, while $I_{1.5}$, $I_{2.0}$, $I_{2.5}$ and $I_{3.0}$ are imaginary radiance curves derived in such a way that the UV part ($\lambda < 400$ nm) of $I_{1.0}(\lambda)$ was multiplied by factor n. The results are shown by graphs 1.5, 2.0, 2.5 and 3.0 in Fig. 8.3B (for PS = 7), from which one can read that if the total radiance of UV skylight were about twice as high as today, the maximum of $\Delta[logQ(\lambda_{max})]$ would be shifted to the UV.

Hence, if the ancient UV level of skylight had been at least twice higher than the recent one, it would have been advantageous for the skylight detectors to function in the UV. However, the minuscule periodic variation of the solar flux could not account for a considerable (e.g. twice) increasing of the UV level of skylight in the past. Much greater variations in the UV radiation from the sun are improbable during the evolution in the case of a star like the sun. Thus, it is very unlikely that an earlier enhancement of the solar UV radiation could be the clue of the solution of the UV-sky-pol paradox.

What about the absorption of UV light in the earth's atmosphere? The attenuation of the UV flux of solar radiation in the atmosphere is governed predominantly by the concentration of ozone (O_3) in the stratospheric ozone layer, which is the greater, the higher the oxygen (O_2) level. The link between UV level and atmospheric oxygen concentration is that UV radiation converts oxygen into ozone. However, this cannot be the clue of the solution of the UV-sky-pol paradox, because the detection of skylight polarization in animals functions between 345-400 nm (Table 8.1), and in this range of the spectrum the absorption of ozone is practically zero. In the visible spectrum, the ozone has one absorption maximum at 600 nm, while in the UV range there are three maxima at 255, 314 and 344 nm (Rozenberg 1966). Due to absorption by the ozone layer, practically 300 nm is the effective wavelength cut-off for UV light incident on the earth's

surface. Thus, the change of the oxygen and ozone concentration in the atmosphere does not influence the UV level of sunlight and skylight in that part of the spectrum, where the detection of skylight polarization by animals happens.

8.2.3 Relatively Large Proportion of UV Radiation in Skylight?

According to Hawryshyn (1992, p. 166), "Even though it is potentially harmful, the relatively large proportion of ultraviolet radiation in scattered light at least partially accounts for the use of these wavelengths for the detection of polarization."

However, Fig. 8.2 shows that the radiance of skylight is much lower in the UV than in the blue, where it is maximal. The maximal proportion of blue radiation in scattered skylight could account for the use of blue (rather than UV) wavelengths for the detection of skylight polarization.

8.2.4 Mistaking Skylight for Ground-Reflected Light?

Mazokhin-Porshnyakov (1969) suggested that by using UV wavelengths, animals would be fairly sure that they use polarized skylight for orientation rather than polarized light reflected from the ground, which is richer in long-wavelengths than skylight. In other words, using UV light might help to distinguish phototactically "sky" from "ground". This argumentation was taken over by Wehner in some of his review articles:

- Wehner (1982, p. 88, 89, 123): "The polarization sensitivity of many insect species functions in the UV, because the **light from the radiant sky is rich in UV but light reflected from the surface of the earth is not**. In other words, **the intensity contrast between sky and ground is maximal in the UV**, which is advantageous for **discrimination the sky from the ground**."
- Wehner (1983, pp. 360-361): "As **the scattered light from the radiant sky is rich in ultraviolet components, but reflected light from terrestrial objects is not**, it seems likely that ultraviolet receptors have evolved in the functional context of exploiting skylight cues for one or another type of navigational purpose."
- Wehner (1984, pp. 285-286): "Why do ultraviolet receptors play such a special role in skylight navigation? … As **scattered skylight is rich in ultraviolet, but reflected light from the ground is not** (with the remarkable exception of light reflected from water surfaces), any visual system whose spectral range extends into the ultraviolet is advantageous in **discriminating between sky and ground**, e.g. in detecting the sky when taking off the ground, or in any kind of course control in which skylight is involved."
- Wehner (1994a, p. 125): "... the widespread use of UV receptors for analysing e-vector patterns in the sky might well be an evolutionary heritage derived from

some kind of skylight detecting mechanism. Note that the **light from the sky is the most ubiquitous source of UV radiation** in an insect's environment."

In reality, this idea originates from Frisch and Lindauer (1954), who as first discussed the concurrence of sky and earth in the orientation of honeybees.

Since skylight and ground-reflected light can reach the eye always from above and below, respectively, an appropriate regionalization of photoreceptors in the eye can simply eliminate the confusion of skylight with ground-reflected light (earthlight). The skylight analysers and earthlight detectors should be separately arranged in the eye in such a way, that only the former can see the sky, while the latter can view only towards the ground. Then, both the skylight and earthlight detectors can function in the same, e.g. visible range of the spectrum, and using the UV wavelengths for skylight detection is unnecessary. Hence, the anatomical separation of the adequate photoreceptors can simply solve the problem of distinguishing "sky" from "ground", independently of receptor wavelength sensitivity. Indeed, this is the usual case in insects: It is only the DRA of insect compound eyes, which is sensitive to skylight polarization, and this area is oriented towards the sky, so that the ambiguities envisaged by Mazokhin-Porshnyakov (1969) and Wehner (1982, 1983, 1984, 1994a) do not arise. Thereby, confusion of sky with ground would not occur, because they are viewed by different eye regions.

8.2.5 Confusion of Motion and Form for Celestial Polarization?

In the opinion of Wehner (1976), UV wavelengths may be used for orientation by means of skylight polarization so that polarization can be analysed separately from motion and form, the detection of which is mediated by receptors sensitive for longer wavelengths. However, an appropriate division of labour between receptors in the eye as well as an appropriate eye regionalization can eliminate the confusion of information from motion and form with polarization information from the sky. If there are separate skylight polarization detectors as well as motion/form detectors in separate eye regions, both detector types can function in the same spectral range, and using other (e.g. UV) wavelengths for skylight detection is not necessary. Indeed, the detection of motion and form is mediated by receptors being distinct from receptors in the polarization-sensitive DRA, so that the confusion envisaged by Wehner (1976) does not arise.

On the other hand, longer wavelengths can "mask" the effects of polarized UV light for bees if the source is small (Brines and Gould 1979). In this effect colour-opponent neurons can play an important role (Kien and Menzel 1977). Kirschfeld (1973a) has observed similar "masking" of the effect of polarized UV light by long wavelengths in optomotor experiments, and Edrich et al. (1979) as well as van der Glas (1977) have also shown that longer wavelengths can influence orientation. These results demonstrate that UV receptors are not always involved alone in orientation and in the detection of skylight polarization.

8.2.6 Have been UV Receptors Originally Skylight Detectors and Involved Only Later Into the E-vector Detecting System?

According to Wehner (1989b, p. 80), "It is also very likely indeed that ultraviolet receptors evolved originally as a means of detecting skylight rather than for extending the spectral range of the insect's colour vision system." Wehner (1982, 1994a) hypothesized that UV receptors might have been incorporated into the E-vector detecting system only later. Bees, for example, take an UV but unpolarized beam of light for the sky, particularly for a point lying within the antisolar half of the celestial hemisphere. In contrast, an unpolarized green beam of light is taken for the sun (Brines and Gould 1979; Edrich et al. 1979; Rossel and Wehner 1984). Furthermore, phototactic escape responses exhibited by many insect species have their sensitivity maxima in the UV (Wehner 1981).

The major problem with this hypothesis is that it does not explain why the photoreceptors used originally as simple "photometric" skylight detectors should have been sensitive to UV instead of blue or green, for instance. The radiance of skylight in the UV is much smaller than in the blue and green (Fig. 8.2), which feature should be rather disadvantageous to a photometric skylight detector.

8.2.7 Maximizing "Signal-to-Noise Ratios" by UV Photopigments Under Low Degrees of Skylight Polarization?

In a theoretical approach, Seliger et al. (1994) surmised that rhodopsin absorption spectra with peaks in the blue (450 nm) maximize detection efficiencies under conditions of high p of skylight. On the other hand, rhodopsin absorption spectra peaking in the UV (350 nm) may maximize "signal-to-noise ratios" for the detection of polarized skylight at the other extreme of low p. Photopigments that are most efficient under conditions of high p (under clear skies) would have their maximum sensitivity at 450 nm, whereas UV (350 nm) photopigments would maximize the signal-to-noise ratio under low p (under cloudy skies), where the biologically significant "signal" is the net plane-polarized single-scattered Rayleigh skylight, while the "noise" is the unpolarized, multiply-scattered skylight.

However, we shall see in Chapter 8.2.10 that the degree of linear polarization $p_{sky}(\lambda)$ of skylight given by Eqns. (8.3) and (8.4) should be maximized, rather than the "signal-to-noise ratio" as suggested by Seliger et al. (1994), in order to solve the UV-sky-pol paradox.

8.2.8 In the Spectral and Intensity Domain the Celestial Band of Maximum Polarization is Less Pronounced in the UV than in the Blue

- In the opinion of Wehner (1984, p. 286), "Why do ultraviolet receptors play such a special role in skylight navigation? … It might also be advantageous in exploiting spectral gradients across the sky."
- According to Wehner and Rossel (1985, p. 20), "… within the bee's visual system information about skylight polarization is mediated exclusively by the ultraviolet receptors. Recall that those parts of the (anti-solar) sky that exhibit the most saturated ultraviolet tinge are also the ones that exhibit maximum polarization. Apparently, this important physical property of skylight patterns has been incorporated into the bee's visual system."
- Wehner (1989b, p. 80): "In the ant's POL area there are three times as many ultraviolet receptors per ommatidium as in the remainder of the eye, and the ultraviolet receptors of the POL area exhibit the highest polarization sensitivities of all photoreceptors of bees and ants. In terms of their adaptive significance, these functional properties of the system make a lot of sense. With increasing angular distance from the sun, skylight is increasingly dominated by short-wavelength radiation, and the parts of the sky that exhibit the highest degree of polarization also exhibit the most saturated ultraviolet tinge."

However, the same is true for the blue wavelengths of skylight (e.g. Hess 1939; Nagel et al. 1978; Coulson 1988): Those parts of the sky that exhibit the most saturated blue tinge are also the ones that exhibit maximum p. What is more important, the intensity gradients of skylight are much higher in the blue than in the UV, therefore in the UV the sky is more homogeneous than in the blue (Coemans et al. 1994b). Thus, the cited argument is not sound and is unable to explain why just the UV-sensitive photoreceptors are used for detection of skylight polarization. The UV sensitivity of the polarization-sensitive photoreceptors in the DRA would be rather disadvantageous in detecting the celestial UV intensity gradients. Using the blue part of the spectrum would be more advantageous due to the fact that in the blue the sky is more heterogeneous than in the UV. Consequently, the celestial band of maximum p (at 90^o from the sun) is more pronounced in the blue than in the UV. In the UV this band merges into the homogeneous UV surrounding.

8.2.9 The Proportion of Celestial Polarization Pattern Useful for Animal Orientation is Higher in the Blue than in the Green or Red

Pomozi et al. (2001b) proved experimentally that the proportion q of the celestial polarization pattern available for use in animal navigation measured in the red, green and blue spectral ranges are greater than about 80% for clear skies. Thus, under clear sky conditions there is no selective advantage for the shorter wavelengths, because the extent of the polarized clear sky usable for orientation is great enough in all parts of the visible spectrum (see Chapter 7.6). More serious is

the consequence of the wavelength-dependency of q if the sky is cloudy, because under such frequently occurring meteorological conditions q often can be considerably reduced. Pomozi et al. (2001b) have also proven that in the visible spectrum and under partly cloudy skies, the shorter the wavelength, the greater the proportion q. This phenomenon may have a selective advantage for shorter wavelengths. Hence, the extension of the E-vector pattern of clear sky into celestial areas covered by clouds is more useful for an E-vector compass when the skylight is perceived in the blue rather than in the green or red.

The above features of cloudy and clear skies are demonstrated in Figs. 8.4 and 8.5, where the patterns of the angle of polarization of a partly cloudy sky and a corresponding clear sky measured by full-sky imaging polarimetry in the red, green and blue are shown. We see in these figures that the E-vector pattern of the cloudy sky is most similar to that of the corresponding clear sky in the blue. This conclusion is based on many similar full-sky imaging polarimetric measurements. Figures 8.4 and 8.5 demonstrate quantitatively what Karl von Frisch and Zdenek Sekera could have only suspected (see Chapter 8.2.1): The celestial E-vector pattern at shorter wavelengths is most stable and less disrupted under cloudy conditions. In other words, the shorter the wavelength, the weaker the disturbing effect of clouds on the E-vector distribution of skylight, at least in the visible part of the spectrum.

8.2.10 Perception of Skylight in the UV Maximizes the Extent of the Celestial Polarization Pattern Useful for Compass Orientation Under Cloudy Skies

According to Brines and Gould (1982), under partly cloudy meteorological conditions, or under extensive vegetation[1] UV wavelengths may have advantages over longer ones in animal polarization orientation, because both spuriously polarized and unpolarized light resulting from reflections from the clouds or the vegetation may cause more troublesome interference at longer wavelengths. They proposed that the UV sensitivity of the E-vector detection in many animals may be at least partly an adaptation for perceiving celestial polarization patterns under conditions when useful scattering can occur only relatively close to an animal. They argued that under clear sky conditions there may be no selective advantage for a visual system that detects skylight polarization at wavelengths where p is high. They suggested that the necessary selection pressure to use UV-sensitive skylight polarization detectors has been provided by light scattering beneath the clouds, because these scattering events produce E-vector patterns with nearly the same E-vector orientation seen in a clear sky, and result in higher p in the UV.

[1] Bees must often fly with most of their view of the sky obscured by vegetation. This is a constant problem for the tropical honeybees (the ancestors of all bees) living and dancing on exposed limbs in the dense tropical forests (Wilson 1971, p. 266). Brines and Gould (1982) hypothesized that under many circumstances, typical and biologically significant E-vector patterns may exist against overhead vegetation at UV wavelengths.

Barta and Horváth (2003) formed this idea into a quantitative model, which gave a satisfactory solution of the UV-sky-pol paradox. They have proven that the perception of skylight in the UV maximizes the proportion $q(\lambda)$ of the celestial polarization pattern useful for polarization compass, as suggested by Brines and Gould (1982), who, however, were not able to determine $q(\lambda)$ quantitatively in the full sky. With full-sky imaging polarimetry Pomozi et al. (2001b) could measure celestial polarization patterns and calculate $q(\lambda)$ only in the visible part of the spectrum, because UV light was not transmitted by their fisheye lens. Until full-sky polarization measurements are not available in the UV, model calculations can provide the relation between $q(UV)$ and $q(blue)$ for cloudy skies.

Let us consider the model of Barta and Horváth (2003). Since under partly cloudy conditions the E-vector pattern of cloudy celestial regions is approximately the same as that of the corresponding clear sky regions as shown experimentally by Brines and Gould (1982) as well as Pomozi et al. (2001b), $q(\lambda)$ is essentially determined only by the degree of linear polarization $p_{sky}(\lambda)$ of skylight. If $p_{sky}(\lambda)$ at a particular direction in the sky is higher than the threshold of polarization sensitivity, the skylight from this direction can be used for polarization compass. The higher the $p_{sky}(\lambda)$ in the whole sky, the larger is $q(\lambda)$. The skylight originating from a cloudy celestial region and reaching a ground-based observer is composed of (i) the cloudlight with a wavelength-dependent radiance $I_{cl}(\lambda)$ and degree of linear polarization $p_{cl}(\lambda)$, and (ii) the scattered light with $I_{sc}(\lambda)$ and $p_{sc}(\lambda)$ from the air layer between the clouds and the ground (Fig. 8.6). Since the E-vector direction of both components are approximately the same, the net degree of linear polarization $p_{sky}(\lambda)$ of skylight is the net polarized radiance $a_{cl}(\lambda,h)p_{cl}(\lambda)I_{cl}(\lambda) + a_{sc}(\lambda,h)p_{sc}(\lambda)I_{sc}(\lambda)$ divided by the total radiance $a_{cl}(\lambda,h)I_{cl}(\lambda) + a_{sc}(\lambda,h)I_{sc}(\lambda)$:

$$p_{sky}(\lambda) = [a_{cl}(\lambda,h)p_{cl}(\lambda)I_{cl}(\lambda)+a_{sc}(\lambda,h)\, p_{sc}(\lambda)I_{sc}(\lambda)]/[a_{cl}(\lambda,h)I_{cl}(\lambda)+a_{sc}(\lambda,h)I_{sc}(\lambda)], \qquad (8.3)$$

where $a_{cl}(\lambda,h)$ and $a_{sc}(\lambda,h)$ are factors describing the wavelength-dependent effect of the thickness h of the air layer underneath the clouds. Due to the absorption of cloudlight in the atmosphere, the larger the h, the lower is the relative contribution $a_{cl}(\lambda,h)$ of the radiance $I_{cl}(\lambda)$ of cloudlight reaching the observer. On the other hand, increasing the thickness h of the air layer between a cloud and the observer, the number of scattering events increases resulting in the increase of the relative contribution $a_{sc}(\lambda,h)$ of the radiance $I_{sc}(\lambda)$ of light scattered in the air beneath clouds. Since at all wavelengths the degree of polarization $p_{cl}(\lambda)$ of cloudlight is practically zero due to the diffuse scattering of light by the cloud particles (Können 1985; Coulson 1988), the following approximation can be made:

$$p_{sky}(\lambda, a) \approx a_{sc}(\lambda,h)p_{sc}(\lambda)I_{sc}(\lambda)/[a_{cl}(\lambda,h)I_{cl}(\lambda) + a_{sc}(\lambda,h)I_{sc}(\lambda)] =$$

$$= ap_{sc}(\lambda)I_{sc}(\lambda)/[I_{cl}(\lambda) + aI_{sc}(\lambda)], \quad \text{where} \quad a = a_{sc}(\lambda,h)/a_{cl}(\lambda,h), \quad 0 \le a \le \infty. \qquad (8.4)$$

Since measurements of $a = a_{sc}(\lambda,h)/a_{cl}(\lambda,h)$ are not available yet, as a first approximation we assume that the quotient $a(h)$ is independent of λ. Although the

dependence of $a(h)$ on h is also unknown, it is clear that a increases with increasing h:

- If a cloud would be in the immediate vicinity of the observer, then the contribution of light scattered in air beneath the cloud would be zero, thus $a(h=0) = 0$.
- When a cloud would be at a huge distance from the observer, then the contribution of cloudlight could be neglected in comparison with that of light scattered in the air between the observer and the cloud. This means that $a(h=\infty) = \infty$, and if $a \to \infty$ then $p_{sky} \to p_{sc}(\lambda)$.

Figures 8.1A and 8.2 show the measured functions $p_{sc}(\lambda)$ and $I_{sc}(\lambda)$ of scattered skylight at 90° from the sun. Figure 8.2 shows also the function $I_{cl}(\lambda)$ of cloudlight measured by Coemans et al. (1994b) under a thick cloud deck, when the total intensity $aI_{sc}(\lambda)+I_{cl}(\lambda)$ of skylight is practically the same as the intensity $I_{cl}(\lambda)$ of cloudlight (because $a \approx 0$). Using these particular functions without any loss of generality, Fig. 8.7A shows $p_{sky}(\lambda)$ calculated on the basis of Eqn. (8.4) for different values of the control parameter a. We can see in Fig. 8.7 that

- if $a < 2.5$ (when the cloudlight dominates, that is, the air layer between the clouds and the observer is thinner than a threshold), $p_{sky}(\lambda,a)$ is maximal in the UV;
- if $a > 2.5$, the maximum of $p_{sky}(\lambda,a)$ is in the visible part of the spectrum;
- if $a > 10$, $p_{sky}(\lambda,a)$ approximates $p_{sc}(\lambda)$ of the clear sky (Fig. 8.1A).

The reason for this is the following: Although the polarized radiance $ap_{sc}I_{sc}$ of skylight is more intense in the blue (B) than in the ultraviolet (UV) because $p_{sc}(B) > p_{sc}(UV)$ and $I_{sc}(B) > I_{sc}(UV)$, in the UV the radiance $I_{cl}(UV)$ of cloudlight is much smaller than the radiance $aI_{sc}(UV)$ of light scattered in the air beneath clouds. In other words, changing the wavelength λ from blue to UV, the denominator of the expression of $p_{sky}(\lambda,a)$ given in Eqn. (8.4) decreases more drastically than the nominator, resulting in that $p_{sky}(UV,a)$ becomes higher than $p_{sky}(B,a)$. Figure 8.7B shows the wavelength λ_{max} where $p_{sky}(\lambda,a)$ is maximal as a function of the control parameter a. λ_{max} is optimal for orientation by means of skylight polarization.

The measurements of Brines and Gould (1982) support that the above theoretical prediction is correct. They measured p_{sky} against several isolated cumulus clouds at 350, 500, 600 nm and obtained that p_{sky} was the highest in the UV (Table 8.2).

8.3 Resolution of the UV-Sky-Pol Paradox

The essence of the resolution of the UV-sky-pol paradox proposed by Brines and Gould (1982), Pomozi et al. (2001b) as well as Barta and Horváth (2003) is the following:

1. There is no favoured wavelength for perception of skylight polarization under clear skies, because the proportion of the celestial polarization pattern useful for orientation is large enough at all wavelengths in the UV and visible parts of the spectrum.
2. Under partly cloudy skies, the E-vector patterns characteristic to clear skies approximately continue beneath the clouds, especially for blue and UV wavelengths.
3. If the clouds are near enough to the ground-based observer and the air columns under clouds are partly sunlit, the degree of linear polarization of skylight originating from the cloudy regions is the highest in the UV, because the nearly unpolarized UV-deficient cloudlight dilutes the least the polarized light scattered in the air beneath the clouds. Thus, detection of skylight polarization in the UV maximizes the extent of the celestial polarization pattern useful for polarization compass under cloudy skies.

8.4 E-Vector Detection in the UV also Maximizes the Proportion of the Celestial Polarization Pattern Useful for Orientation Under Canopies

Let us consider the influence of the weighting of unpolarized green light transmitted through a foliage and linearly polarized blue light scattered in the air beneath the foliage on the degree of linear polarization $p_{ca}(\lambda)$ of downwelling light under a canopy, if the air beneath the foliage is illuminated partly by direct sunlight, as usually in forests, for example. This is important for those insects with polarization-sensitive DRA that live under canopies and orient by means of the E-vector pattern of downwelling light. Under canopies, the same calculation can be performed as under clouds, but in the former case the intensity $I_{cl}(\lambda)$ of white cloudlight should be replaced by the intensity $I_{ca}(\lambda)$ of green light transmitted by the canopy, called "canopylight" further on:

$$p_{ca}(\lambda, a) \approx a p_{sc}(\lambda) I_{sc}(\lambda) / [a I_{sc}(\lambda) + I_{ca}(\lambda)]. \quad (8.5)$$

Figure 8.2 shows the intensity $I_{ca}(\lambda)$ of canopylight transmitted through the leaves of cottonwood (*Populus deltoides*). Similarly to the cloudlight, the canopylight is most deficient in the UV and is practically unpolarized due to the diffuse scattering in the leaf tissue (e.g. Gates 1980). Consequently, the same phenomenon occurs as under clouds, as shown in Fig. 8.8: the degree of linear polarization $p_{ca}(\lambda,a)$ of light from the canopy (composed of the partially linearly

polarized bluish light scattered in the air layer beneath the canopy and the UV-deficient unpolarized greenish canopylight) is maximal in the UV if $a < 0.10$. Hence, detection of polarization of downwelling light in the UV also maximizes the extent of the celestial polarization pattern useful for polarization compass under canopies.

In this chapter we showed how the weighting (described by the control parameter a) of unpolarized white cloudlight or unpolarized green canopylight and linearly polarized blue light scattered in the air beneath clouds or canopies affects the degree of linear polarization $p(\lambda,a)$ of downwelling light under clouds or canopies, respectively. The only important difference between the effects of clouds and canopies is that clouds can also be at huge (practically infinite) distances from the ground-based observer (meaning great a-values), while the distance of canopies from the ground can range between 0 m and only about some 10 m (meaning small a-values). Thus, under canopies, $p_{ca}(\lambda,a)$ is maximal always in the UV. However, the question is whether the maximum of $p_{ca}(\lambda,a)$ is higher than the threshold p^* for polarization sensitivity (about 5% for crickets and 10% for honeybees). In other words, the question is if the polarized light scattered in the thin air layer beneath the canopy can be enough intense (relative to the unpolarized canopylight) to ensure that $p_{ca}(\lambda,a) > p^*$. The experimental spectro-polarimetric study of this question could be an interesting task of future work.

8.5 Analogy Between Perception of Skylight Polarization and Polarotactic Water Detection Considering the Optimal Spectral Range

The spectral aspects of the detection of polarization of light reflected from water surfaces are discussed in Chapters 16-20. Here we mention only that the majority of the known polarotactic water-seeking insect species exploit UV wavelengths to seek for water (Table 8.3), because the amount of light originating from the underwater region is minimal in the UV, thus p of light reflected from the water surface is maximal in the UV. However, also some known polarotactic water insect species detect water in the visible part of the spectrum (Table 8.3).

Note that considering the optimal wavelength range, there is an analogy between perception of skylight polarization for orientation and detection of the polarization of light reflected from water surfaces to find water bodies. Both tasks are most efficient in the UV, the reason for which is the same (Figs. 8.6 and 12.1): p of both skylight and water-reflected light is highest in the UV if there is a background – a cloud or canopy in the sky and the bottom or particles suspended in water –, which reflects nearly unpolarized light. The amount of light originating from this background is minimal in the UV, thus the net p of the biologically relevant light (downwelling skylight and water-reflected light) is highest in the UV.

8.6 Analogy of the UV-Sky-Pol Paradox in the Polarization Sensitivity of Aquatic Animals

Interestingly, UV sensitivity is frequently coupled with sensitivity to linear polarization also in aquatic animals. Several fish species (e.g. Hawryshyn 1992) as well as mantis shrimps (Marshall et al. 1991a,b) use their UV photoreceptors to perceive underwater polarization. However, the role of UV polarization sensitivity in the underwater world by these animals is as yet unknown.

What is the unique property of the UV part of the spectrum that has such importance to underwater polarization sensitivity? The common answer to this question sounds: "The underwater UV light field undergoes fewer changes during the day, and was more stable on an evolutionary scale, than other regions of the visible range. This stability is important when polarization sensitivity is used for navigation" (Shashar 1995, p. 203). This recalls the similarly frequently cited opinion that the skylight polarization should be more stable against atmospheric disturbances mentioned in Chapter 8.2.1. Unless these "changes", "stabilities" and "disturbances" are not exactly defined and their existence and importance experimentally are not proven, one can do nothing with such hypotheses.

Note, however, that crustaceans generally perceive polarization between 440 and 580 nm (e.g. Goldsmith 1972; Schwind 1999), and the polarization-sensitive photoreceptors of cephalopods are maximally sensitive near 500 nm. According to Cronin and Shashar (2001), this may be explained by the fact that p of underwater light increases with increasing wavelength, at least above 450 nm (Ivanoff and Waterman 1958b). The question is whether this trend does also continue below 450 nm.

8.7 Why do Crickets Perceive Skylight Polarization in the Blue?

We can see in Fig. 8.7A that $p_{sky}(\lambda,a)$ is always relatively high in the violet and blue (400 nm < λ < 470 nm) for a given a-value. Thus, under partly cloudy conditions the violet-blue wavelength region is the second optimal spectral range to detect skylight polarization for orientation. Crickets perceive the celestial polarization in the blue, the reason for which is still unknown. Using the blue part of the spectrum may have the following advantage against the UV range under clear skies, when the degree of skylight polarization is high enough for all wavelengths: The intensity of the UV component of sunlight and light from the clear sky is low relative to that of the blue and green components (Fig. 8.2). At twilight under clear skies, the absolute light intensity is more likely to fall below the sensitivity threshold of a polarization-sensitive visual system operating in the UV than in the blue.

In the context of the detection of skylight polarization, the finding that the photoreceptors in the DRA of the twilight-active field cricket *Gryllus campestris*

operate in the blue rather than in the UV, has been interpreted in this way by Labhart et al. (1984) as well as Herzmann and Labhart (1989). Crickets (*Acheta domestica*, *Gryllus bimaculatus* and *Gryllus campestris*) are active not only during the day but also during crepuscular periods (dusk and dawn) as well as at night and all have highly polarization-sensitive blue receptors in their DRA specialized to perceive skylight polarization for orientation. According to Zufall et al. (1989), the combination of blue sensitivity and polarization sensitivity in the DRA may be a common adaptation of insects that are active at very low light intensities, as opposed to day-active insects (e.g. honeybees, desert ants and flies) which predominantly use UV receptors as detectors for skylight polarization (Table 8.1).

However, the question is whether this "intensity argument" holds also for cloudy conditions: On the one hand, since under cloudy skies the UV component of skylight is much weaker than under clear skies (Fig. 8.2), detection of skylight may be more disadvantageous in the UV than in the blue. On the other hand, under cloudy skies the degree of linear polarization p_{sky} of skylight is the highest in the UV (Fig. 8.7), thus perception of skylight polarization could be more advantageous in the UV than in the blue. The question is, which effect is the stronger.

8.8 Concluding Remark

The question why insects differ in their spectral channel used for polarization detection cannot be answered at the present time, because too little data are available. One would have to correlate the spectral channels of a large number of insect species with their biology and ecology (e.g. under what sky conditions are they normally active) to obtain an answer. Theory alone will not clarify the situation. Clearly, honeybees, for instance, have an advantage in that they can exploit the weak UV (but stronger than blue) polarization under clouds, whereas under clear skies the polarization is normally strong enough at all wavelengths. But why do other insects not take advantage of this? The explanation of this remains an interesting future task.

Tables

Table 8.1. Wavelengths λ_{max}^{POL} at which the sensitivity of photoreceptors detecting skylight polarization is maximal in insects and spiders.

species	λ_{max}^{POL} **(nm)**	**reference**
Calliphora erythrocephala, *Musca domestica* (flies)	330-350	Smola & Meffert (1978), Hardie et al. (1979), Hardie (1984), Philipsborn & Labhart (1990)
Apis mellifera (honeybee)	345-350	Helversen & Edrich (1974), Labhart (1980)
Cataglyphis bicolor (desert ant)	380-410	Duelli & Wehner (1973)
Cataglyphis setipes (desert ant)	380-400	Frantsevich et al. (1977)
Lethrus apterus, *Lethrus inermis* (scarab beetles)	350	Frantsevich et al. (1977)
Pachysoma striatum (desert dung beetle)	350	Dacke et al. (2002)
Drassodes cupreus (spider)	350	Dacke et al. (1999)
Gryllus campestris (field cricket)	433-435	Labhart et al. (1984), Brunner & Labhart, 1987), Herzmann & Labhart (1989)
Schistocerca gregaria (desert locust)	450	Eggers & Gewecke (1993)
Leucophaea maderae (Madeira cockroach)	< 471	Loesel & Homberg (2001)
Melolontha melolontha (cockchafer)	~520	Labhart et al. (1992)
Parastizopus armaticeps (beetle)	~540	Bisch (1999)

Table 8.2. Average degree of linear polarization p_{sky} of skylight measured by Brines and Gould (1982) at three wavelengths λ against 20 different small cumulus clouds under hazy and clear atmospheric conditions. (After Table 2 of Brines and Gould 1982, p. 88).

p_{sky} **(%)**	λ **(nm)**	**sky condition**
10	350	hazy
7	500	hazy
6	600	hazy
37	350	clear
23	500	clear
17	600	clear

Table 8.3. Polarotactic insects detecting water or moist substrata by means of the horizontal polarization of reflected light studied by multiple-choice field experiments (Schwind 1991, 1995). The known spectral ranges in which the polarization of reflected light is perceived are given in brackets (after Table 1 of Schwind 1995, p. 446).

HETEROPTERA **Corixidae**: *Sigara nigrolineata* (360 nm), *Sigara lateralis* (360 nm) **Pleidae**: *Plea leachi* **Saldidae**: *Saldula saltatoria*
EPHEMERIDAE: *Cloeon* sp. (450-480 nm)
COLEOPTERA **Dytiscidae**: *Agabus bipustulatus* (480-520 nm), *Bidessus nasutus, Guignotus pusillus* (360 nm), *Hydroporus* sp. (390-420 nm), *Laccophilus minutus* (430-450 nm), *Potamonectes* sp., *Rhantus pulverosus* (500 nm), *Scarodytes halensis* **Haliplidae**: *Neohaliplus lineato* (530-550 nm), *Haliplinus lineolatus* (530-550 nm), *Peltodytes caesus* **Hydrophilidae**: *Anacaena limbata* (390-420 nm), *Enochrus quadripuctatus, Helophorus aquaticus* (< 360 nm), *Helophorus brevipalpis* (< 360 nm), *Helophorus flavipes* (< 360 nm), *Helophorus griseus* (< 360 nm), *Helophorus minutua* (< 360 nm), *Helochares lividus* (380-390 nm), *Hydraena* sp., *Hydrobius fuscipes* (370-400 nm), *Laccobius sinatus* (370-390 nm), *Limnoxenus niger* **Hyfraenidae**: *Limnebius crinifer* (360-380 nm) **Sphaeridiinae**: *Megasternum boletophagum, Cryptopleurum minutum, Cercyon* sp.

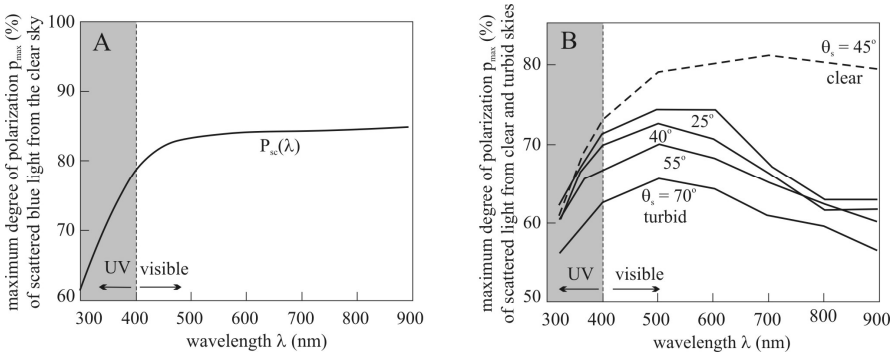

Fig. 8.1. A: Degree of linear polarization p_{sc} versus wavelength λ of scattered blue skylight measured under a clear sky at a solar elevation of 10^o (after Fig. 5.6 of Coulson 1988, p. 285). B: As A measured in an atmosphere when it was turbid, dusty (continuous) and clear (dashed) (after Fig. 5.9 of Coulson 1988, p. 291).

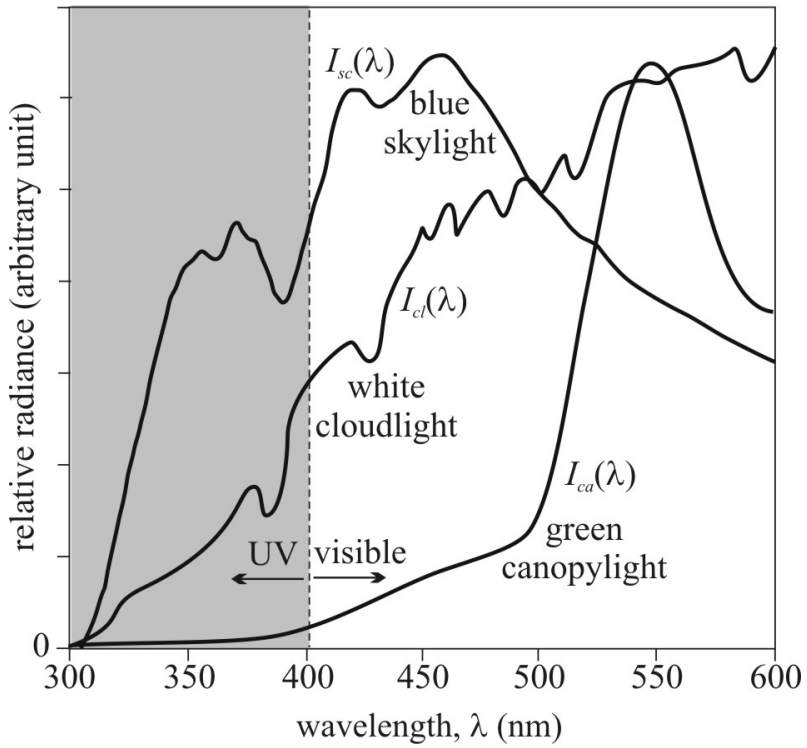

Fig. 8.2. Relative radiances as a function of the wavelength λ. $I_{sc}(\lambda)$: radiance of scattered blue skylight measured by Hess (1939) at 90° from the sun under clear sky conditions (after Fig. 4 of Seliger et al. 1994, p. 481). $I_{cl}(\lambda)$: radiance of white cloudlight measured by Coemans et al. (1994b) at an elevation of 40° under a thick cloud deck (after Fig. 4b of Coemans et al. 1994b, p. 1464). $I_{ca}(\lambda)$: radiance of green canopylight transmitted through the leaves of cottonwood (*Populus deltoides*) (after Fig. 8.20 of Gates 1980, p. 216).

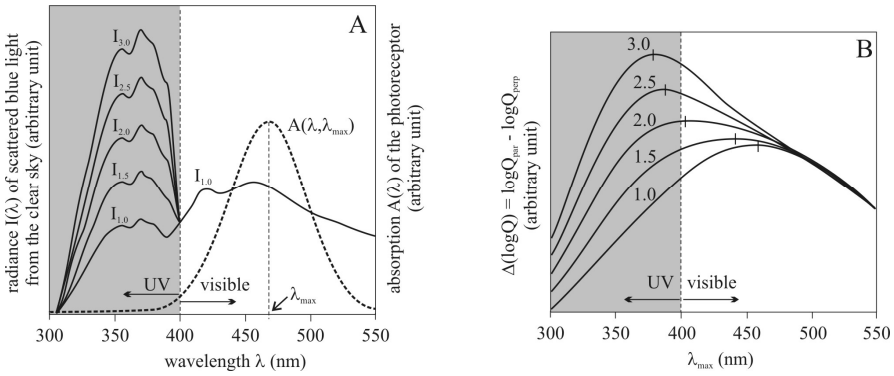

Fig. 8.3. A: Real and imaginary relative radiances $I_n(\lambda)$, n = 1.0, 1.5, 2.0, 2.5, 3.0 of scattered blue light from the clear sky as a function of the wavelength λ. The Gaussian function $A(\lambda,\lambda_{max})$ with 50 nm half bandwidth is the absorption function of a photoreceptor, the sensitivity maximum of which is at λ_{max}. $I_{1.0}(\lambda)$: The radiance of blue skylight today (after Fig. 4 of Seliger et al. 1994, p. 481). $I_n(\lambda)$, n = 1.5–3.0: Imaginary radiances of blue skylight obtained in such a way, that the UV part (λ < 400 nm) of $I_{1.0}(\lambda)$ is multiplied by a factor n ranging from 1.5 to 3.0. B: The difference $\Delta(logQ) = logQ_{par} - logQ_{perp}$ of the logarithms of the amounts of skylight absorbed by a polarization-sensitive (PS = 7) photoreceptor with microvilli direction parallel (par) and perpendicular (perp) to the E-vector of polarized skylight as a function of λ_{max} calculated for the series of $I_n(\lambda)$ shown in A. The maxima (marked by vertical bars) of $\Delta(logQ)_{1.0}$, $\Delta(logQ)_{1.5}$, $\Delta(logQ)_{2.0}$, $\Delta(logQ)_{2.5}$ and $\Delta(logQ)_{3.0}$ are at λ_{max} = 458, 442, 404, 390 and 380 nm, respectively.

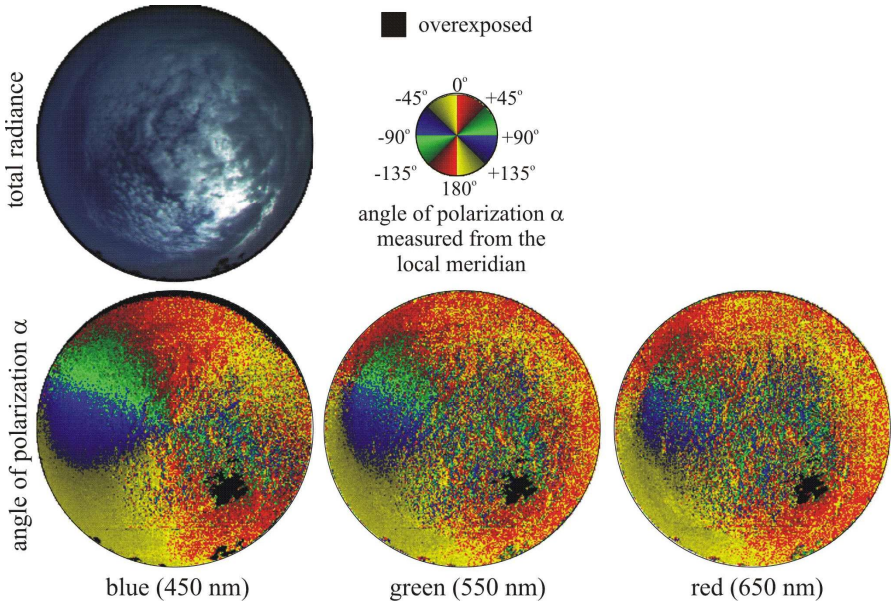

Fig. 8.4. Patterns of the angle of polarization of a partly cloudy sky measured by full-sky imaging polarimetry in Tunisia in August 1999. The sun is occluded by clouds, but its approximate position is within the overexposed (chequered) region of the sky.

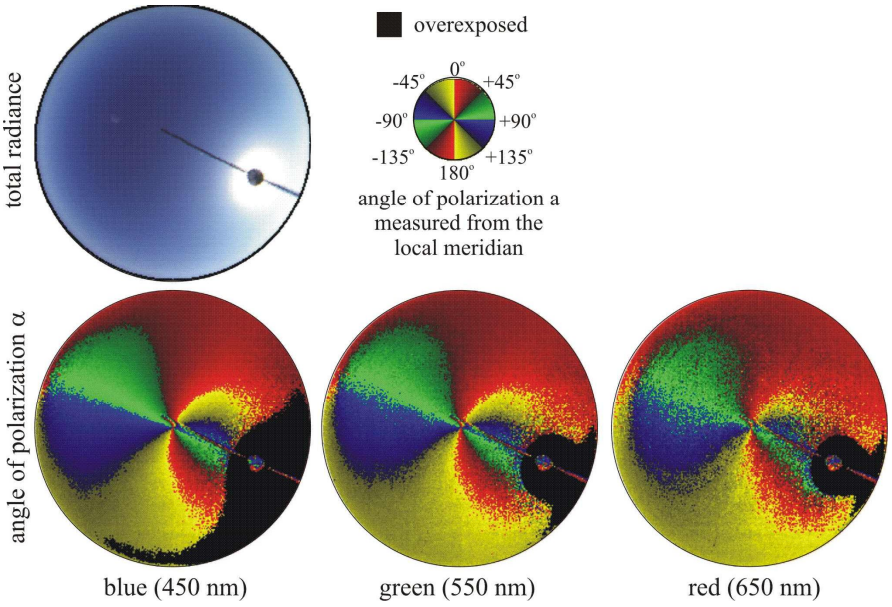

Fig. 8.5. Patterns of the angle of polarization of a clear sky measured by full-sky imaging polarimetry in Tunisia in August 1999 approximately at the same solar zenith angle as in the case of the cloudy sky in Fig. 8.4. In the circular pictures the radial bar with a small disk is the sun occulter. The sun is positioned behind the disk.

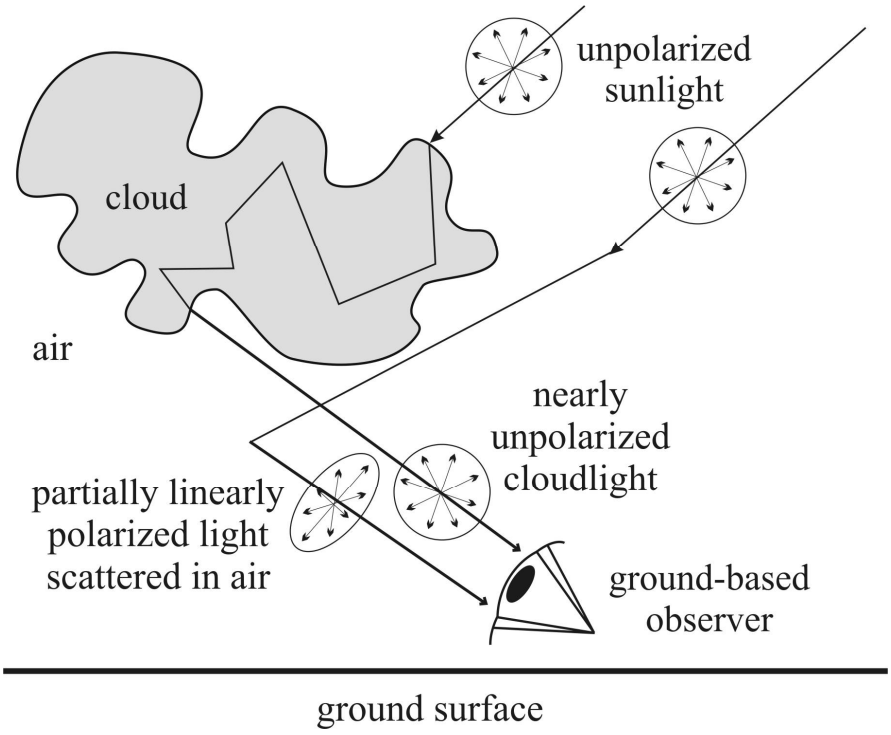

Fig. 8.6. Schematic representation of the two components of cloudlight reaching a ground-based observer. Unpolarized sunlight is scattered in the air and/or in a cloud. Direct cloudlight is nearly unpolarized, while light scattered in air is partially linearly polarized. (After Fig. 3 of Barta and Horváth 2003).

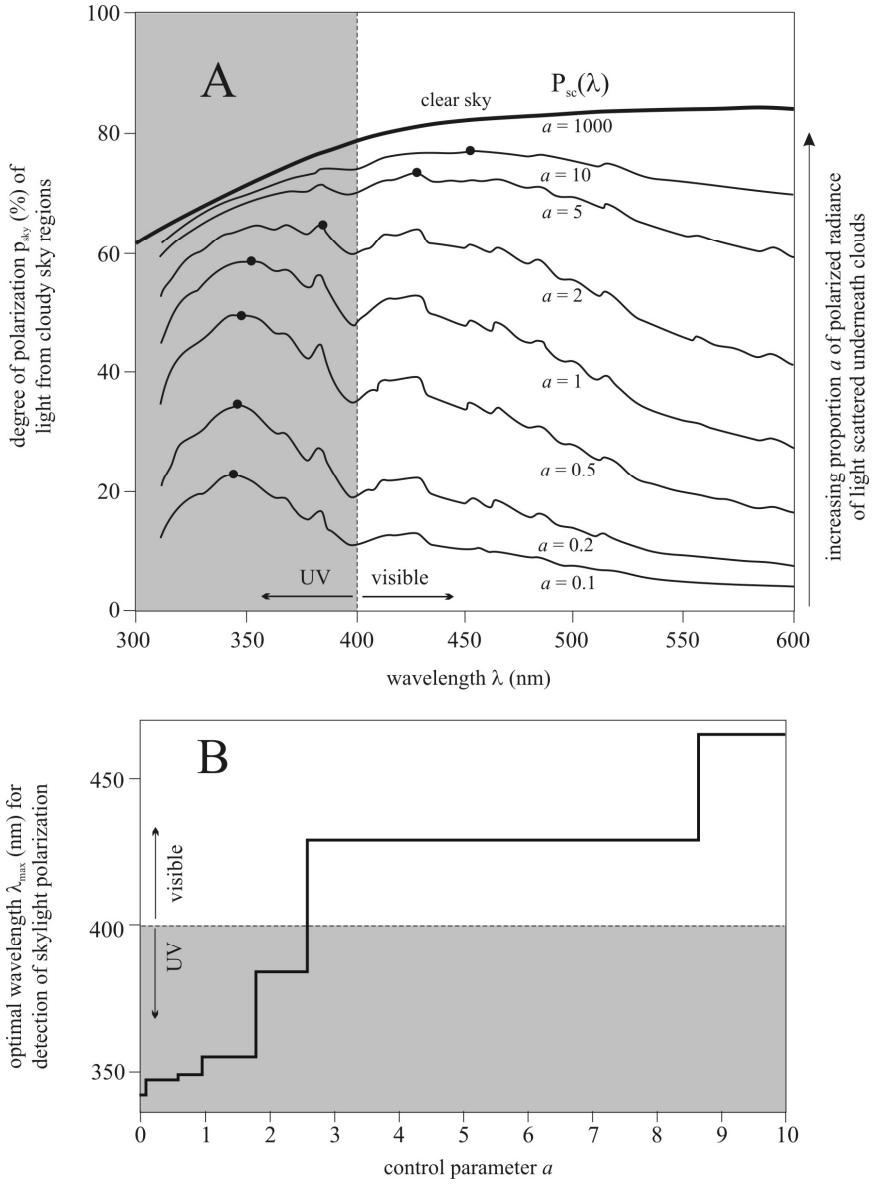

Fig. 8.7. A: The degree of polarization $p_{sky}(\lambda,a)$ of light from cloudy sky regions calculated on the basis of Eqn. (8.4) for different values of the control parameter a, using the functions $p_{sc}(\lambda)$ in Fig. 8.1A, and $I_{sc}(\lambda)$ and $I_{cl}(\lambda)$ in Fig. 8.2. Increasing a-values mean increasing proportion of the polarized radiance of light scattered underneath clouds. The positions of the local maxima of the curves are marked by dots. B: Wavelength λ_{max} where $p_{sky}(\lambda,a)$ is maximal as a function of the control parameter a. λ_{max} is optimal for orientation by means of skylight polarization. (After Fig. 4 of Barta and Horváth 2003).

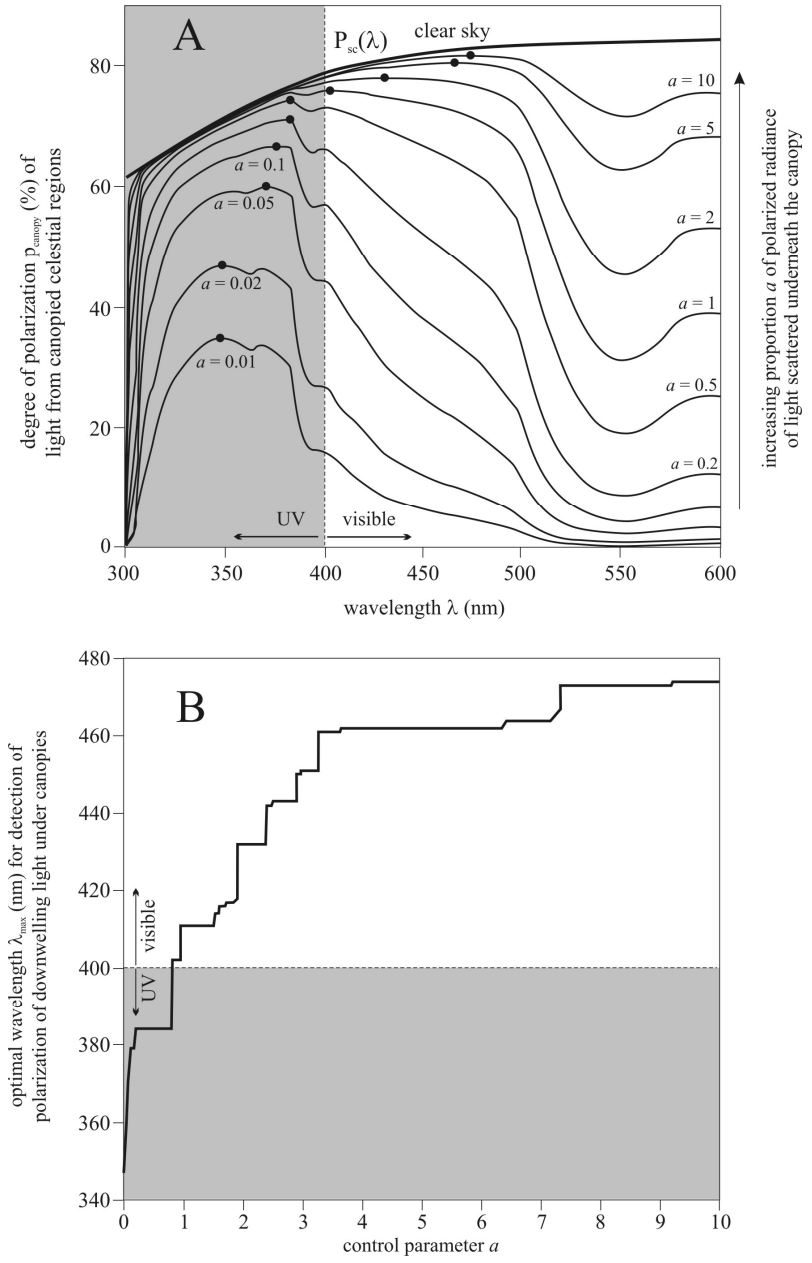

Fig. 8.8. As Fig. 8.7 for the downwelling light under a canopy calculated on the basis of the expression of $p_{ca}(\lambda,a)$ given in Eqn. (8.5) using the functions $p_{sc}(\lambda)$ in Fig. 8.1A, as well as $I_{sc}(\lambda)$ and $I_{ca}(\lambda)$ in Fig. 8.2. Increasing a means increasing proportion of the polarized light scattered underneath the green foliage. (After Fig. 5 of Barta and Horváth 2003).

9 Polarization of the Sky and the Solar Corona During Total Solar Eclipses

9.1 Structure of the Celestial Polarization Pattern and its Temporal Change During the Eclipse of 11 August 1999

During a total solar eclipse the sun is completely covered by the moon for some minutes, and this immediately transforms the aspect of the sky completely. Then the sky is not lit up by the radiance of the solar corona alone; the main source of skylight is light coming from outside the area where the totality is taking place and where the sun is still shining (Können 1985). During a total eclipse a particular type of twilight occurs: most light is seen near the horizon where parts of the atmosphere are still lit by the partially eclipsed sun outside the zone of totality, and the sky is darkest in the zenith.

Since the beginning of the 1960's several atmospheric optical phenomena associated with total solar eclipses have been the subject of extensive studies (e.g. Coulson 1988): The rapid change in light intensity of the sky, the apparent sudden darkening at totality, and the change in sky colour during totality have frequently been described and measured. As the radiance and colour distribution of light of the sky is immediately transformed at totality, so also is the polarization of skylight. Apart from the very scant light of the solar corona, the skylight is then produced almost entirely by secondary and higher order scattering (Fig. 9.1.6A), in which case the degree of linear polarization p of skylight is very low.

The knowledge accumulated about the celestial polarization during total solar eclipses is rather modest. The reason for this is that earlier it was not possible to measure the polarization pattern of the entire sky during the few minutes of a total eclipse. The few skylight polarization measurements performed before 1999 during total solar eclipses are summarized in Table 9.1.1. These measurements were done by point-source polarimeters with fields of view not wider than a few degrees and oriented in a given direction of view along the solar or antisolar meridian (Piltschikoff 1906; de Bary et al. 1961; Moore and Rao 1966; Dandekar and Turtle 1971; Rao et al. 1972; Miller and Fastie 1972; Coulson 1988).

It has been known since the observation by Piltschikoff (1906) that at the beginning of the totality of a solar eclipse the polarization of the sky decreases drastically at 90^{o} from the sun. Subsequently this phenomenon has been sporadically studied. De Bary et al. (1961) measured the temporal change of p of

skylight at 90° from the obscured sun during the total solar eclipse of 15 February 1961 in Viareggio (Italy). Dandekar and Turtle (1971) performed skylight polarization measurements in the blue and red spectral ranges at a point 90° from the sun during the total eclipse of 7 March 1970 in Kinston (USA).

There were great technical bravura when Shaw (1975) was able to scan the sky with a single-channel (400 nm) rotating-analyzer point-source polarimeter with a field of view of 1.44° × 5.44° along the solar and antisolar meridian during the total eclipse on 30 June 1973 in Northern Kenya. He observed the approximate cylindrical symmetry of the distribution of p of the eclipse sky and near the zenith a local minimum of p. Using two polarimeters oriented in the direction of the zenith and at 90° from the sun along the antisolar meridian, Coulson (1988) observed a virtual lack of polarization response during a partial (approximately 80%) eclipse of the sun at Davies (USA) on 26 February 1979. Using a numerical model, Können (1987) explained quantitatively several polarizational characteristics of the eclipse sky.

The forerunner of imaging polarimetric studies of the eclipse sky was Gerharz (1976), who took photographs about the celestial circumsolar area of 12° × 15° through a modified Savart filter and a green (535 nm) interference filter during the total solar eclipse of 7 March 1970 near Williamston (USA). From the photographed interference bands he deduced the degree and angle of polarization of light scattered from the circumsolar region of the eclipse sky and demonstrated a slight (0.5%) polarization asymmetry around the eclipsed sun.

Although the main characteristics of the normal polarization of the firmament are well-known (e.g. Können 1985; Coulson 1988; North and Duggin 1997; Horváth et al. 1998b; Horváth and Wehner 1999; Gál et al. 2001b), the same cannot be said about the fine structure of the celestial polarization pattern and its temporal change during total solar eclipses. This gap was partially filled by the measurements and observations of Pomozi et al. (2001a). Using full-sky imaging polarimetry, they measured the temporal change of the polarization pattern of the entire celestial hemisphere during the total solar eclipse of 11 August 1999 occurred in Hungary from the beginning of the partial eclipse through the totality to the end of the partial eclipse (Fig. 9.1.1). They compared these patterns with the normal celestial polarization patterns measured at the same times on the subsequent day to the total eclipse. As a second control sky, the celestial polarization pattern measured on 26 August 1999 in Tunisia was chosen with the same solar zenith angle as that at the Hungarian eclipse.

9.1.1 Temporal Change of the Celestial Polarization Pattern During the Eclipse

Although the celestial polarization patterns were measured from the beginning (first contact, 11:28:35) to the end (fourth contact, 14:15:35) of the partial eclipse, we present in this chapter only the patterns from 12:50:00 (preeclipse, 98% obscuration) to 13:01:00 (posteclipse, 89% obscuration), because practically only

in this time interval occurred detectable differences in the degree p and angle α of linear polarization of skylight in comparison with the normal (control) skylight.

Figures 9.1.2B,C show the temporal change of the celestial pattern of p and α measured at 450 nm during the total eclipse on 11 August 1999. From Figs. 9.1.2B and 9.1.2C it is evident that the celestial polarization pattern suffers a sudden and dramatic change at the moment of the beginning and the end of totality. Immediately prior to and after the totality the qualitative characteristics of the polarization pattern of the sky are very similar to those of the normal sky. During totality, however, the distribution of p of skylight becomes roughly cylindrically symmetric with respect to the zenith (Figs. 9.1.2B3-5). p gradually increases from the horizon, then reaching a maximum it gradually decreases towards the zenith where it is approximately zero. During totality, the distribution of α of skylight remains asymmetric with respect to the zenith (Figs. 9.1.2C3-5). But comparing with the preeclipse (Figs. 9.1.2C1,2) and posteclipse (Figs. 9.1.2C6,7) α-patterns, during totality the region of negative polarization (where $-45^o \le \alpha \le +45^o$ relative to the local meridian) considerably extends at cost of the area of positive polarization (where $45^o < \alpha \le 135^o$).

Figures 9.1.2D,E show the differences between the subsequent polarization patterns in Figs. 9.1.2B,C calculated for the entire sky apart from the overexposed areas and landmarks/vegetation. The change of p was not greater than ±24% within a few minutes immediately prior to and after totality (Figs. 9.1.2D2, 9.1.2D7). The same was true for the period of totality (Figs. 9.1.2D4,5). After the second (Fig. 9.1.2D3) and third (Fig. 9.1.2D6) contacts, however, on a considerable area of the sky (for angular distances from the sun greater than about 55^o) $|\Delta p| > 24\%$ differences occurred.

We can see that the sign of Δp was approximately mirror symmetrical to the time of about 12:52:15 in patterns D3-6 in Fig. 9.1.2: where positive or negative Δp values occur in patterns D3 and D4, there negative or positive Δp values occur in patterns D5 and D6, respectively. This can be explained in the following way: From the first contact to about 12:52:15 the deviations of skylight polarization from the normal celestial polarization gradually increased. From about 12:52:15 to the fourth contact, however, the sign of these deviations reverted and their absolute value gradually decreased. Thus, the skylight polarization reverted to its normal state after 12:52:15.

The change of the α-pattern of skylight seen in Fig. 9.1.2E was qualitatively similar to that of p: the α-pattern suddenly changed at the moment of the second (Fig. 9.1.2E3) and third (Fig. 9.1.2E6) contacts, otherwise its change was rather modest (Figs. 9.1.2E2,4,5,7), the sign of $\Delta\alpha$ was again more or less mirror symmetrical to 12:52:15 (Figs. 9.1.2E3-6). For zenith angles greater than about 20^o the values of $|\Delta\alpha|$ were smaller than 38^o. Greater changes of α than $\pm 38^o$ occurred only around the zenith at the second (Fig. 9.1.2E3) and third (Fig. 9.1.2E6) contacts.

Figures 9.1.2F,G show the frequencies of Δp and $\Delta\alpha$ calculated for the entire sky apart from the overexposed areas and landmarks/vegetation. In these diagrams small or great polarization differences are characterized by narrow or wide

distribution functions, respectively, around the zero difference marked by a vertical broken line. Here we can see again how relatively small was the change of skylight polarization during the preeclipse (Figs. 9.1.2F2 and 9.1.2G2), eclipse (Figs. 9.1.2F4,5 and 9.1.2G4,5) and posteclipse (Figs. 9.1.2F7 and 9.1.2G7) periods, and how great changes occurred in the state of skylight polarization at the moment of the second (Figs. 9.1.2F3 and 9.1.2G3) and third (Figs. 9.1.2F6 and 9.1.2G6) contacts. The distribution functions of Δp and $\Delta\alpha$ possess two peaks at the second and third contacts: one of these peaks is placed in the positive range and the other peak in the negative range. The maximal value of $|\Delta p|$ was about 55%. The approximate mirror symmetry of the distribution functions to 12:52:15 can be seen in Figs. 9.1.2F,G too.

Figures 9.1.3B,C show the spatial change of p and α of skylight as a function of time along four differently oriented meridians of the Hungarian eclipse skies measured at 450 nm. We can see in Figs. 9.1.3B1,2,6,7 that during the preeclipse and posteclipse periods the celestial distribution of p was not rotationally symmetric: in the antisolar half of the celestial hemisphere always higher p-values occurred than in the solar half. At the second contact the p-pattern became approximately rotationally symmetric, a feature which remained throughout the totality as can be seen in Figs. 9.1.3B3-5, especially in Fig. 9.1.3B5. The celestial distribution of p was, however, not exactly cylindrically symmetric to the zenith during totality. Smaller deviations from the rotational symmetry occurred especially along the meridian marked with a triangle (Figs. 9.1.3B3,4).

The change of α along the different meridians of the sky was rather complex (Fig. 9.1.3C), but it can be clearly seen that the change of α along all meridians during totality (Figs. 9.1.3C3-5) was substantially different from that during the preeclipse (Figs. 9.1.3C1,2) and posteclipse (Figs. 9.1.3C6,7) periods.

Figures 9.1.2A3-5 and 9.1.3E demonstrate that although the distribution of the radiance of skylight during totality was remarkably smooth and tended to be approximately symmetrical around the zenith, the same cannot be said for the distribution of α of skylight (Figs. 9.1.2C3-5, 9.1.3C3-5). On the other hand, there is no tendency for the normal p-pattern to be symmetrical about the zenith (Fig. 9.1.3A), in distinct contrast to the approximately symmetrical distribution of p observed during totality (Figs. 9.1.2B3-5, 9.1.3B3-5).

Earlier investigators of total eclipses could measure the skylight polarization averaged only in relatively small windows of the sky (generally at the zenith, or at 90^o from the sun on the antisolar meridian, or at the cross-section of the almucantar[1] and the solar and antisolar meridians, or perpendicularly to the solar meridian), because they had point-source polarimeters with a field of view of a few degrees. In order to compare the results of Pomozi et al. (2001a) with the observations of earlier authors, in Fig. 9.1.4 the temporal change of p and α of skylight measured at 450 nm are plotted within four different small celestial windows with a field of view of about $5^o \times 5^o$. The four windows designated by A, B, C and D are represented in the bottom right inset of Fig. 9.1.4 and correspond

[1] Almucantar is the horizontal circle in the celestial hemisphere passing through the sun.

with the windows generally chosen by earlier authors. Considering the temporal variation of p and α at the beginning and the end of totality, we can see in Fig. 9.1.4 that all possible combinations could be observed in the sky:

- remarkable changes of p associated with almost no change of α in window A,
- considerable changes of p associated with moderate variations of α in window B,
- small variations of p associated with considerable changes of α in window C,
- small variations of p associated with modest variations of α in window D.

This high diversity of the changes of p and α of skylight is the consequence of the spatio-temporal complexity of the celestial polarization pattern observed during the total eclipse (Fig. 9.1.2). Figure 9.1.4 demonstrates well how strongly dependent is the temporal change of p and α on the direction of view in the sky. Due to this strong dependence the interpretation and comparison of observations on the temporal change of skylight polarization during total eclipses are difficult and problematic if the observations by different authors were performed at different angles of view in the sky.

We can see in Figs. 9.1.2, 9.1.3 and 9.1.4 that as the umbra moved across the observation point, the celestial polarization varied somewhat during totality due to the changing geometry of atmospheric light scattering.

9.1.2 Spectral Characteristics of Skylight Polarization During Totality

Figure 9.1.5 shows the spectral characteristics of skylight polarization measured in the red (650 nm), green (550 nm) and blue (450 nm) during the total eclipse of 11 August 1999 at 12:52:30. Apart from a reddish-orange narrow annular zone at the horizon, during totality the skylight was the brightest and the darkest in the blue and red, respectively. These can be explained by the Rayleigh scattering, which results in higher intensities of scattered light for shorter wavelengths and higher intensities of "semi-direct" light for longer wavelengths. During totality "semi-direct" light means the light, which is scattered into the umbral area from the directly illuminated regions of the atmosphere outside the umbra.

Figures 9.1.5B,E,G show that during totality the longer the wavelength of skylight, the higher is its p. This observation contradicts with certain earlier (erroneous) observations. Contrary to the relatively great dispersion of p of skylight, the wavelength-dependence of α of skylight was rather modest during totality as can be seen in Figs. 9.1.5C,D,F,H.

9.1.3 Origin of the E-vector Pattern During Totality

Let us consider the origin of the sudden change of α of skylight when the zenith is crossed along the solar/antisolar meridian observed during totality (Fig. 9.1.6B2).

This switch of α occurs at the border of the regions of positive and negative polarization. Figure 9.1.6A represents schematically how the originally unpolarized sunlight illuminating the atmosphere reaches an observer after primary and higher order scattering events during totality. Light from a first order scattering event (A) can reach the observer only at very small angles of view with respect to the horizon. At greater viewing angles light can reach the observer only due to second (B_2) or higher order scattering events. The observed celestial polarization is the result of these higher order scattering events. The magnitude of the very scant direct light of the solar corona can be neglected in comparison with the intensity of scattered light coming from outside the umbral region of the atmosphere.

As a first approximation, α of skylight during totality can be qualitatively explained solely on the basis of first (A, B_1) and second (B_2) order scattering events. First order scattering would result in the well-known Rayleigh pattern of skylight polarization. This is a relatively good description of the celestial polarization pattern apart from the regions of the sky surrounding the Arago, Babinet and Brewster neutral points. In Figs. 9.1.6B1 and 9.1.6B3 the theoretical single-scattering Rayleigh pattern calculated for a solar zenith angle of 32^o (corresponding with the solar zenith angle during totality on 11 August 1999 in Hungary) can be seen.

In the model, during totality the atmosphere is illuminated only by the single-scattering Rayleigh skylight from outside the umbral region. The atmospheric scattering centres (B_2) in the umbra scatter the rays of this Rayleigh skylight towards the observer (Fig. 9.1.6A). If the observer views towards the antisolar half of the umbra (Fig. 9.1.6B1), this region of the atmosphere is illuminated mainly by highly polarized scattered Rayleigh skylight (B_1), the E-vectors of which are approximately perpendicular to the scattering plane (the local meridian). This more or less perpendicularly polarized skylight is scattered (B_2) towards the observer. This is the reason for the fact that during totality mainly positive (E-vectors more or less normal to the scattering plane) skylight polarization was observed in the antisolar half of the sky (top half of Fig. 9.1.6B2).

If the observer views towards the solar half of the umbra (Fig. 9.1.6B3), this region of the atmosphere is illuminated mainly by highly polarized scattered Rayleigh skylight (B_1), the E-vectors of which are approximately parallel to the local meridian. This more or less parallelly polarized skylight is scattered (B_2) towards the observer. This is the reason for the fact that during totality mainly negative (E-vectors more or less parallel to the scattering plane) skylight polarization was observed in the solar half of the sky (bottom half of Fig. 9.1.6B2). In Fig. 9.1.6B2 we can see that α suffers a sudden change when the zenith is crossed, and $|\Delta\alpha|$ is about 90^o if we cross the zenith parallel to the solar/antisolar meridian.

Although during a total eclipse higher than second order scattering events also play an important role in the formation of the celestial polarization pattern, the above qualitative derivation can explain well the gross characteristics of the observed E-vector pattern of skylight during totality. Previous studies (e.g. Sharp et al. 1971; Coulson 1988) have indicated that up to approximately 98% geometric

obscuration of the solar disk eclipse phenomenology can be interpreted in terms of attenuated, but otherwise essentially unchanged, sunlight. For high obscuration ratios, greater than about 98%, multiple scattering predominates, and the distribution of colour, intensity and polarization over the sky hemisphere changes rapidly and dramatically. The *p*-pattern tends to be rather symmetric about the zenith. The observations of Pomozi et al. (2001a) are in accordance with these. Full-sky imaging polarimetry can help to gather as much information as needed for a comprehensive theory and computer simulations of the polarizational characteristics of multiply scattered skylight during eclipses.

Table

Table 9.1.1. Summary of instrumental observations of the degree of linear polarization p of skylight at mideclipse measured [apart from Gerharz 1976] at 90° from the eclipsed sun along the antisolar meridian. Pomozi et al. (2001a) measured the p-pattern of the full eclipse sky in several hundred thousands of different directions of view, which data cannot be given here. Y: year of eclipse, θ: zenith angle of the observed point(s), λ: wavelength. (After Table 1 of Horváth et al. 2003).

observer(s)/reference	Y	θ	altitude	λ	p
E. de Bary, K. Bullrich, D. Lorenz (1961)	1961	12°	ground-borne	green	0%
J.G. Moore, C.R.N. Rao (1966)	1965	41° 41°	air-borne	475 nm 601 nm	0.5% 4.5%
R.E. Miller, W.G. Fastie (1972)	1965	65° 65° 65° 65°	air-borne	558 nm 578 nm 610 nm 630 nm	31% 35% 28% 26%
C.R.N. Rao, T. Takashima, J.G. Moore (1972)	1966	70° 70°	air-borne	475 nm 601 nm	19% 21%
B.S. Dandekar, J.P. Turtle (1971)	1970	46° 46°	ground-borne	475 nm 600 nm	4% < 0.5%
R. Gerharz (1976)	1970	38°–53°	ground-borne	535 nm	< 2.5%
G.E. Shaw (1975)	1973	37°	ground-borne	400 nm	4%
I. Pomozi, J. Gál, G. Horváth, R. Wehner (2001a); G. Horváth, I. Pomozi, J. Gál (2003)	1999	full sky	ground-borne	450 nm 550 nm 650 nm	– – –

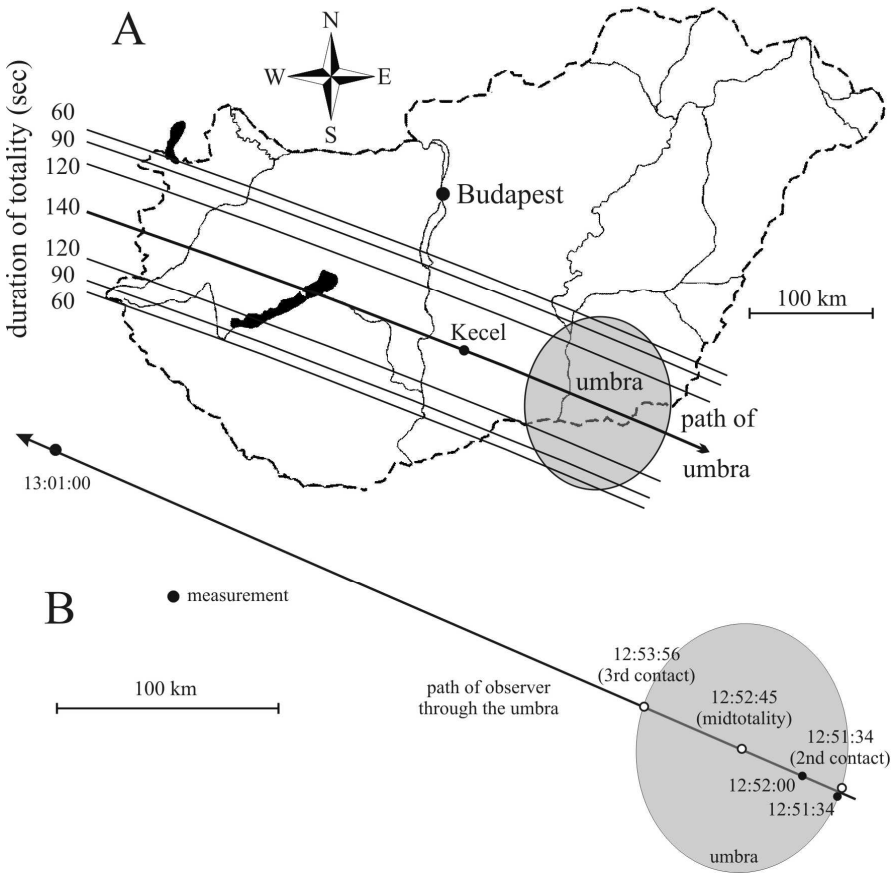

Fig. 9.1.1. A: Map of Hungary showing the path and shape of the umbra during the total solar eclipse on 11 August 1999. The full-sky imaging polarimetric measurements of Pomozi et al. (2001a) and Horváth et al. (2003) were performed at Kecel (46°32'N, 19°16'E). B: Trajectory of the observer through the umbra of the total eclipse on 11 August 1999 with black dots where and when the polarimetric measurements were taken. White dots represent the 2nd and 3rd contact as well as the midtotality. (After Figs. 1 and 2 of Horváth et al. 2003).

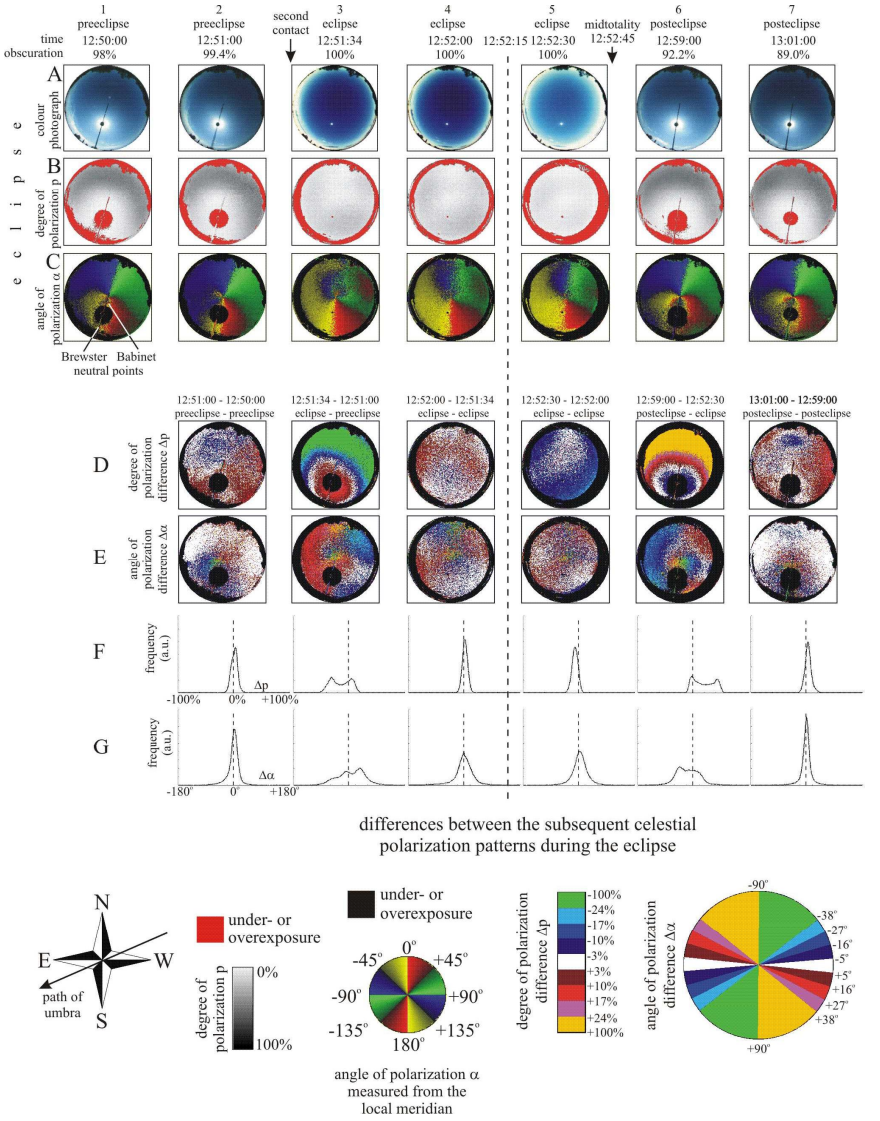

Fig. 9.1.2. Temporal change of the celestial pattern of radiance I (A), degree of linear polarization p (B) and angle of polarization α with respect to the local meridian (C) measured at 450 nm in Kecel (Hungary) during the total solar eclipse on 11 August 1999. Values of time and percent geometric obscuration of the solar disk are given above every column. D-G: Differences between the subsequent polarization patterns calculated for the entire sky apart from the overexposed areas and the landmarks/vegetation near the horizon. D: Difference of the p-patterns. E: Difference of the α-patterns. F, G: Frequencies (measured in arbitrary unit) of differences Δp and $\Delta\alpha$. The colour photographs of the sky in row A do not represent correctly the real radiance of skylight, because they were taken with different times of exposure and apertures. (After Fig. 2 of Pomozi et al. 2001a, p. 185).

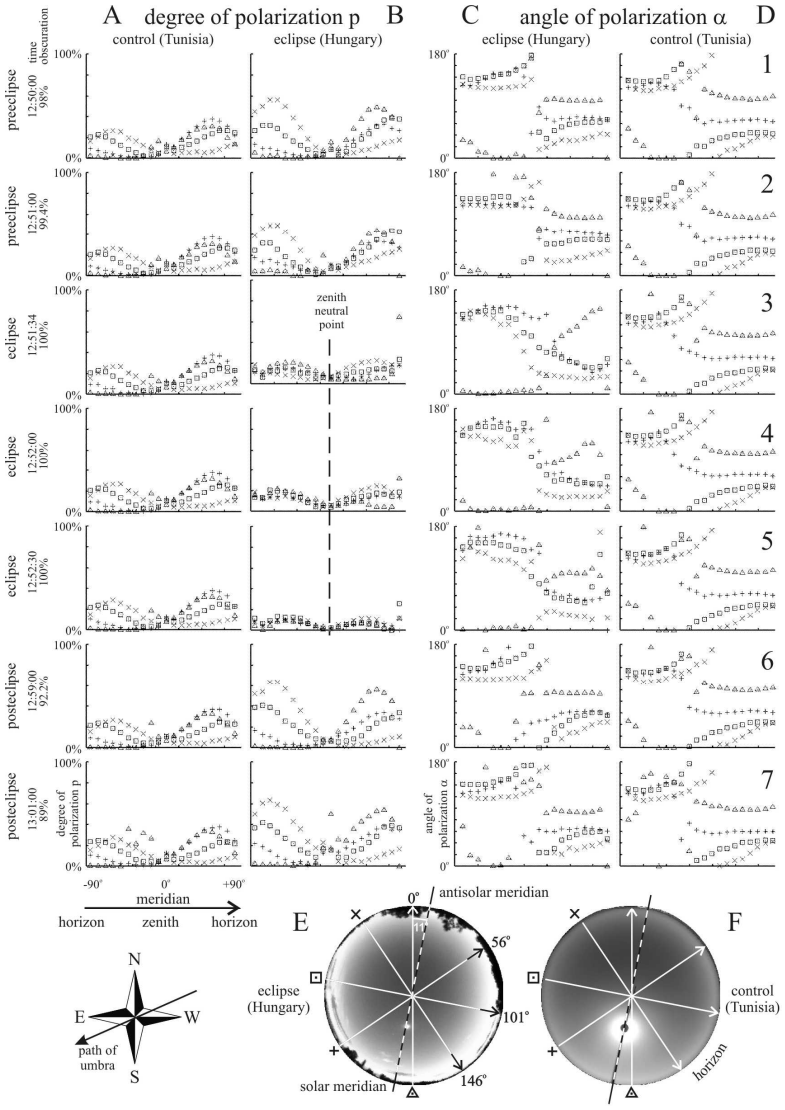

Fig. 9.1.3. Spatial change of p and α (measured from the local meridian) of skylight as a function of time (1-7) along four differently oriented meridians (coded with ×, square, + and triangle in E and F) of the Hungarian eclipse skies (B, C) and the Tunisian control skies (A, D) measured at 450 nm. The shape of the data points in the diagrams coincides with the shape of the symbols coding the different meridians indicated in E and F. Every data point represents a value averaged on p- or α-values measured in 33 neighbouring celestial points along a given meridian. The position of the neutral point near the zenith occurring during totality is marked by a vertical dashed line in diagrams B3-B5. (After Fig. 5 of Pomozi et al. 2001a, p. 191).

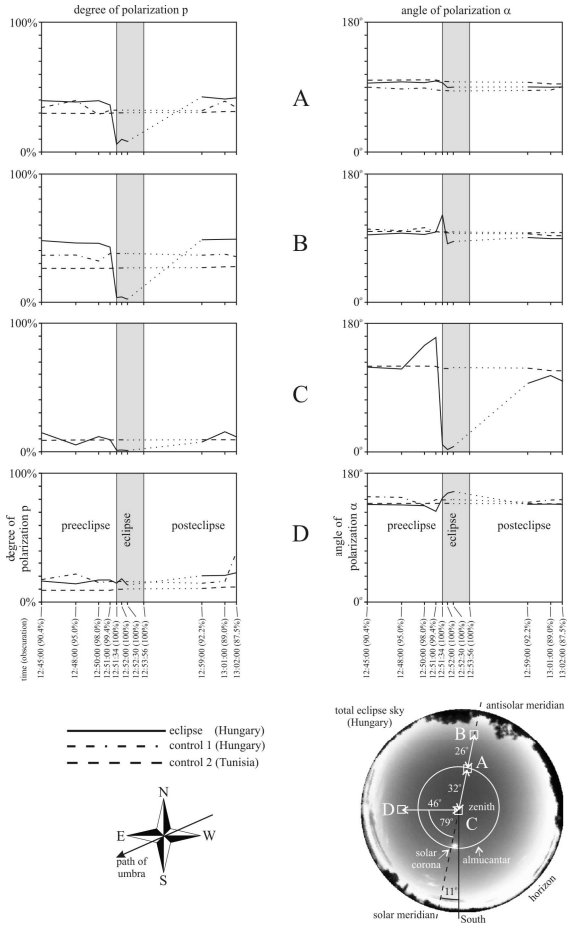

Fig. 9.1.4. Temporal change of p and α within four different windows (A-D) of the Hungarian eclipse skies (continuous line), Hungarian control skies (dashed and dotted line) and Tunisian control skies (dashed line) measured at 450 nm. The diameter of the entire sky is 700 pixels, and the dimensions of the celestial windows are 20 pixels × 20 pixels. A: Window in the cross-section of the almucantar and the antisolar meridian positioned at the same zenith angle of 32° as the eclipsed sun. B: Window on the antisolar meridian at 90° from the eclipsed sun. C: Window at the zenith. D: Window at an angle of 79° from the solar meridian with a zenith angle of 46°. Windows A, B and D were cloudless during all measurements. The zenith window C was not always cloudless during the Hungarian control measurements, thus control 1 (dashed and dotted line) was omitted for window C. The data points in the diagrams were simply connected with each other by straight lines (linear interpolation). The error bars were omitted for the sake of perspicuousness (the values of the standard deviation were not greater than 1-5% due to the small dimension of the celestial windows). The linear interpolation between the polarization values measured at 12:52:30 and 12:59:00 was represented by dotted lines in order to distinguish this relatively long period (in which the photographic film was changed in the camera after totality) from the others. (After Fig. 6 of Pomozi et al. 2001a, p. 193).

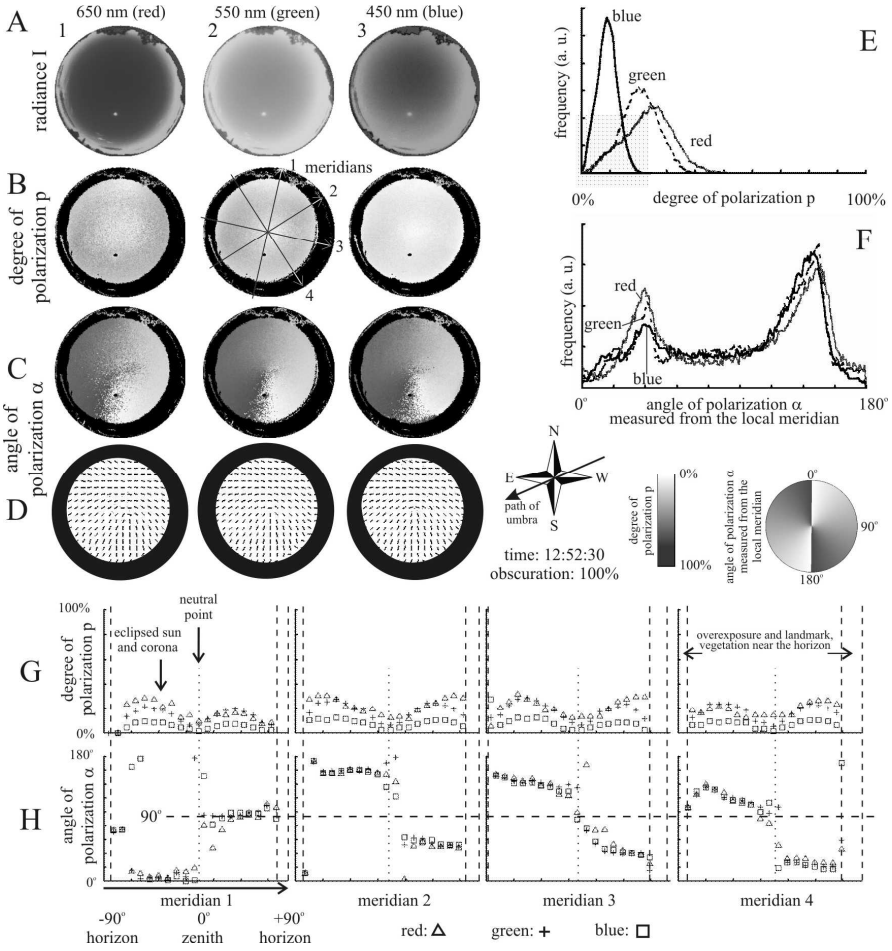

Fig. 9.1.5. Spectral characteristics of *I*, *p* and α of skylight measured at 650, 550 and 450 nm during the totality of the eclipse of 11 August 1999 at 12:52:30. A: *I*-patterns. B: *p*-atterns. C: α-patterns. D: Patterns of α, where the direction of the bars represents the local orientation of the E-vector. E, F: Frequencies of *p* and α calculated for the entire sky apart from overexposed areas and landmarks/vegetation. G, H: Spatial change of *p* and α along four differently oriented meridians (designated by 1-4 in B2) of the sky. The shape of the data points in diagrams G and H is a triangle, + or square for the red, green or blue spectral range, respectively. Every data point represents a value averaged on *p*- or α- values measured in 33 neighbouring celestial points along a given meridian. The position of the neutral point is marked by a vertical dotted line in diagrams G and H. The areas of the sky with overexposure and landmarks/vegetation are shaded by black in rows B-D. (After Fig. 7 of Pomozi et al. 2001a, p. 194).

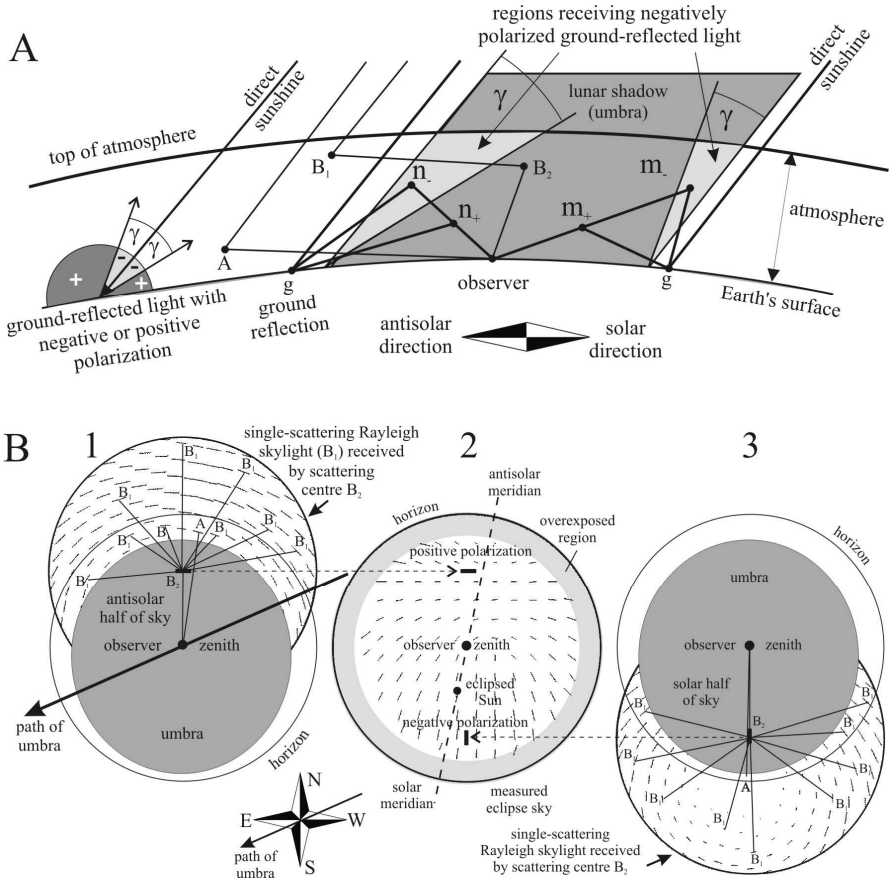

Fig. 9.1.6. A: Schematic representation of the geometry of primary (A, B_1) and secondary (B_2) scattering as well as ground reflection of sunlight in the atmosphere during a total solar eclipse. For the qualitative explanation of the origin of the local minimum of p and the neutral points observed approximately along the antisolar meridian near the horizon during totality if primary scattering events of negatively (n_-, m_-) or positively (n_+, m_+) polarized ground-reflected light are taken into account. B: For the qualitative explanation of the origin of the regions of positive (B1, B2) and negative (B2, B3) polarization in the sky observed during totality. The single-scattering Rayleigh pattern was calculated for the position of the sun during totality (solar zenith angle = 32°); the alignment of the bars represent the local direction of polarization and their length is proportional to p. (After Fig. 8 of Pomozi et al. 2001a, p. 196).

9.2 Neutral Points of Skylight Polarization Observed During the Totality of the Eclipse on 11 August 1999

In spite of the scientific popularity of total solar eclipses, appearing almost every year somewhere on the earth, the empirical knowledge accumulated about the polarization pattern and neutral points of eclipse skies is rather limited, since the earlier polarization measurements were restricted to one single point in the sky or at most to the solar and antisolar meridian. Due to the methods of full-sky imaging polarimetry (North and Duggin 1997; Voss and Liu 1997; Liu and Voss 1997; Gál et al. 2001a,b,c; Pomozi et al. 2001a,b; Horváth et al. 2002a,b) the last difficulty was cleared away to measure the polarization pattern of the entire skydome under the extreme illumination conditions occurring during the short period of a total solar eclipse. Horváth et al. (2003) reported on the neutral points of the eclipse sky observed on 11 August 1999 in Hungary.

In this chapter observational material is presented about the neutral points and local minima of the degree of linear polarization p of the eclipse sky collected by Horváth et al. (2003). Earlier only de Bary et al. (1961) observed exactly zero p of skylight during totality at 90^o from the obscured sun on the antisolar meridian. Numerical calculations of the atmospheric scattering phenomena under the complex illumination conditions of the eclipse on 11 August 1999 with the use of an improved version of the quantitative model of Können (1987) could be an interesting task of future work. We refer to the sky observed immediately before or after totality (immediately before the second contact or after the third contact) of the solar eclipse as "preeclipse sky" or "posteclipse sky", respectively. Under "normal sky" we mean the sky observed under normal illumination conditions when the sun was not eclipsed by the moon, but its zenith angle was the same (32^o) as that during totality on 11 August 1999.

Figures 9.2.1 and 9.2.2 show the celestial patterns of p and α of skylight measured at two different moments (see Fig. 9.1.1B) at 450 and 550 nm during totality. Figures 9.2.3 and 9.2.4 represent the graphs of p and α measured along different meridians crossing the zenith and the neutral points or the local minima of p listed in Table 9.2.1. One of the most striking features of the α-pattern of the eclipse sky (Fig. 9.2.2) is that α changes from 0^o (or from 180^o because of the 180^o periodicity of α) to 90^o near the zenith if the direction of view moves approximately along the solar and antisolar meridian. Other remarkable phenomenon in the eclipse sky is the occurrence of points, where p is zero or has a local minimum (Figs. 9.2.1 and 9.2.3). Table 9.2.1 summarizes the zenith angles θ and azimuth angles φ (measured counter-clockwise from West) of these celestial points.

On the p-patterns measured at 12:51:34 (Figs. 9.2.1A, 9.2.3B) and 12:52:00 (Figs. 9.2.1B, 9.2.3D) at 450 nm a point is discernible near the zenith where p = 0%. This point is called "zenith neutral point of type-2". It is called neutral point,

because p is zero at it; and it is classified as "type-2", because it can be considered a point where p passes through a minimum, rather than a real neutral point as the well-known Arago, Babinet and Brewster neutral points of the normal sky classified as "type-1" further on. In the type-2 zenith neutral point of the eclipse sky the absence of polarization is analogous to the absence of polarization of the sunlit sky straight in the direction of the sun. At 12:52:00 approximately at the position of the zenith neutral point a local minimum of p occurred at 550 nm (Figs. 9.2.1C, 9.2.3F). The local minimum of p in the immediate vicinity of the zenith can also be seen in the graphs of Figs. 9.2.3A, 9.2.3C and 9.2.3E.

At 12:51:34 at 450 nm (Figs. 9.2.1A and 9.2.3A) two neutral points of type-1 occurred approximately along the antisolar meridian near the horizon. They arise because the Stokes parameter Q (if $U = 0$) for single and multiple (double) scattering cancels out, that occurs also in the usual Arago, Babinet and Brewster neutral points (Coulson 1988; Gál et al. 2001a,c; Horváth et al. 1998b; Horváth and Wehner 1999).

At 12:52:00 a neutral point of type-3 was observed at 450 nm (Figs. 9.2.1B, 9.2.3C) and a local minimum of p occurred at 550 nm (Figs. 9.2.1C, 9.2.3E) approximately at the position of the two type-1 neutral points. Note that there was no switch of α crossing the type-3 neutral point along a meridian: this celestial point is characterized by the abolition of p (Figs. 9.2.1B, 9.2.3C) in a celestial area where the α-pattern is homogeneous, that is, the E-vectors are approximately horizontal on both sides of the neutral point (Figs. 9.2.2B, 9.2.4C). The latter feature distinguishes the neutral point of type-3 from the neutral points of type-1 and type-2, which are characterized by a sudden change of 90^o of α (Figs. 9.2.2A, 9.2.2B, 9.2.4A, 9.2.4B, 9.2.4D).

9.2.1 Origin of the Zenith Neutral Point During Totality

Figure 9.2.5 explains qualitatively the origin of the neutral point or local minimum of p observed near the zenith during totality of the eclipse on 11 August 1999. This qualitative model is similar to that discussed in Chapter 9.1. If only primary (B_1) and second order (B_2) scattering events are taken into account, the situation is shown in Fig. 9.2.5A. Since the atmospheric scattering centres (B_2) at or near the zenith (above the observer in the umbra) are illuminated by single-scattered Rayleigh skylight with all possible directions of the E-vector coming from outside the umbra (B_1), the atmosphere at or near the zenith scatters E-vectors with all possible alignments towards the observer. This results in a zero or almost zero net p, that is, unpolarized skylight or skylight with very low p near the zenith. If beside first (B_1) and second (B_2) order scattering also third order scattering events (B_3) are taken into account, the situation is shown in Fig. 9.2.5B. In the umbra, from the northern (Fig. 9.2.5B4) or southern (Fig. 9.2.5B2) part of the sky (B_2) the atmospheric scattering centres (B_3) above the observer (at or near the zenith) are illuminated mainly by highly polarized scattered Rayleigh skylight (B_1), the E-vectors of which are approximately perpendicular or parallel to the local meridian, respectively. From the western (Fig. 9.2.5B1) or eastern (Fig. 9.2.5B3) part of the

sky (B_2) the atmospheric scattering centres at or near the zenith (B_3) are illuminated mainly by more or less polarized scattered Rayleigh skylight (B_1), the E-vectors of which are more or less diagonal relative to the local meridian. These more or less perpendicularly, parallelly and diagonally polarized rays of skylight are scattered from the zenith (B_3) towards the observer (Fig. 9.2.5B5) resulting in all possible directions of the E-vector. This results in again unpolarized skylight or skylight with very low p at or near the zenith.

The exact position of the zenith neutral point or local minimum of p near the zenith depends on the wavelength (due to the dispersion of polarization of scattered skylight) as well as on the time-dependent geometry of the lunar shadow with respect to the earth's surface and the observer's position. Shaw (1975) observed a similar minimum of p in the eclipse sky, which phenomenon was quantitatively explained by Können (1987).

9.2.2 Origin of Another Neutral Points at Totality

The prerequisite of formation of a neutral point or a local reduction of p in the positively polarized antisolar half of the sky during totality is a mechanism that introduces negatively polarized light into the umbral region of the atmosphere. One of such mechanisms is the reflection of light from the ground. Natural soil surfaces reflect more or less partially linearly polarized light, the p of which depends on the type (roughness, albedo and spectral characteristics) of the surface (Coulson 1974). It is a general rule that the higher the albedo of a rough reflecting surface in a given spectral range, the lower the p of reflected light. This phenomenon is called the Umov effect (Coulson 1988). The polarization of the ground-reflected light is negative or positive if the angle of reflection measured from the direction of incidence is smaller or greater than a threshold angle γ, respectively (Fig. 9.1.6A). Angle γ is dependent on the characteristics of the reflecting surface, but its typical value is about 20^o for bright sandy and grassy terrains, as was the terrain at the place of the polarimetric measurements of Horváth et al. (2003) in the surroundings of Kecel (Hungary). The degree of negative polarization of light reflected from such a surface changes from zero to several percents if the angle of reflection with respect to the direction of incidence decreases from γ to zero.

Figure 9.1.6A shows schematically the situation when such negatively or positively polarized ground-reflected light is introduced into the atmosphere during the total eclipse. The degree of positive polarization of multiply scattered skylight from the antisolar half of the sky in the umbra is more or less reduced by the negatively and enhanced by the positively polarized light reflected by the ground from outside the umbral region if it is scattered towards the observer by umbral atmospheric scattering centres (n_- and n_+ in Fig. 9.1.6A). At a given direction of view depending on the relative intensity of the positively and negatively polarized skylight (the Stokes parameter Q if $U = 0$), the following three different situations can be imagined:

1. If at wavelength λ the negatively polarized skylight intensity $I_{-}(\lambda)$ is smaller than the positively polarized skylight intensity $I_{+}(\lambda)$ in all directions of view, a local minimum of the celestial degree of positive polarization can be observed at the zenith angle of the maximum reduction of p (Figs. 9.2.1C, 9.2.3E).
2. If $I_{-}(\lambda) = I_{+}(\lambda)$ at a certain zenith distance, a neutral point occurs in this direction (Figs. 9.2.1B, 9.2.3C).
3. If $I_{-}(\lambda) > I_{+}(\lambda)$, a negatively polarized "island" is seen in the region of positive polarization (Figs. 9.2.1A, 9.2.2A, 9.2.3A, 9.2.4A). Then two neutral points appear at the border of this celestial island of negative polarization. In these neutral points the positive polarization switches to negative polarization as in the case of the neutral point observed near the zenith during totality, or of the normal Arago, Babinet and Brewster neutral points.

Due to the moving lunar shadow both the p- and α-patterns change during totality for any location of the observer while the eclipse proceeds from 2nd to 3rd contact. These changes depend on the wavelength and are determined by the observer's view through a varying slant range of air in the umbra, before the directly scattered sunlight is encountered. The site and points of time of the measurements of Horváth et al. (2003) in relation to the moving umbra as well as the wavelengths (450, 550 nm) of their observations were so fortunate during the totality of the eclipse on 11 August 1999 that they could observe all the above-mentioned three different situations (Figs. 9.2.1-9.2.4). In these cases the maximum reduction of p happened approximately along the antisolar meridian, because the thickness of the umbral region of the atmosphere receiving negatively polarized ground-reflected light was the greatest in this direction at the time of recording.

It is interesting that in the special case when condition 1 was satisfied there was no switch of α crossing the neutral point of type-3 along a meridian. This unique celestial point is characterized by the abolition of p in a celestial area where the α-pattern is homogeneous, that is, positive polarization occurs on both sides of the neutral point. The latter feature distinguishes this unique neutral point of type-3 from the other neutral points of type-1 and type-2 of the eclipse sky as well as from the normal Arago, Babinet, Brewster and fourth neutral points, which are characterized by a sudden change of 90^{o} of α.

During the total eclipse on 11 August 1999 in Kecel the degree of negative polarization of multiply scattered skylight from the solar half of the sky in the umbra was more or less enhanced by the negatively and reduced by the positively polarized light reflected by the ground from outside the umbral region and scattered towards the observer by umbral atmospheric scattering centres (m_{-} and m_{+} in Fig. 9.1.6A). During totality the negatively polarized light dominated in the solar half of the firmament, thus here negatively polarized skylight with slightly greater p than in the antisolar half was observed.

The main cause of the slight drift of the neutral points from the solar-antisolar meridian (Table 9.2.1) may be the changing geometry of the umbra with respect to the observer as the eclipse proceeded. A second cause may be distant clouds,

which may disturb the distribution of singly scattered light around the observer. A third factor is the polarization of singly scattered light. Such effects may be capable to explain the observed double neutral points, but calculations should prove this conjecture in the future.

9.2.3 Relation of the Unique Neutral Point Observed During the Eclipse on 11 August 1999 to Earlier Observations on Anomalous Neutral Points

The oldest report on an anomalous neutral point dates back to Brewster (1864), who on 22 occasions observed a dark purple band extending to 1.5^{o} above the sea horizon at the azimuth of the antisun. This band had positive polarization, instead of the usual negative polarization existing between the Arago point and horizon. Due to this positively polarized horizontal band a secondary Arago point occurred at the edge of the band. Generally, the normal Arago point and the band of positive polarization near the horizon were separated by a band of negative polarization with the primary and secondary Arago points well defined. This phenomenon was most often seen above a sea horizon, it occasionally occurred above a land horizon as well. In one special case when the primary Arago point coincided with the edge of the band, a strange situation occurred in which the Arago point had positive polarization on both sides of it.

The latter observation of Brewster (1864) recalls the celestial distribution of polarization around the unique neutral point of type-3 observed by Horváth et al. (2003) on 11 August 1999 in the eclipsed sky: also this unique neutral point occurred in a positively polarized celestial region near the (land) horizon, approximately along the antisolar meridian. Both neutral points observed by Brewster and Horváth et al. (2003) differ from the normal Arago, Babinet and Brewster points, because the latter occur always at the edge of positively and negatively polarized neighbouring regions rather than in a positively polarized area of the sky.

The change of sky polarization that occurs during totality is complex and depends on the distribution and magnitude of numerous parameters: e.g. variations in ground albedo, solar zenith angle, shape and diameter of the eclipse shadow (umbra) and optical thickness of the atmosphere. Due to the complex geometry and the great number of control parameters, apart from the quantitative model of skylight polarization developed by Können (1987) for solar eclipses, at present does not exist any in-depth computation for determining the celestial polarization during an eclipse. According to Können (1987, p. 607): "Within the limited set of existing observations there is no possibility to test the model further at present. This has to wait until more detailed observations are available. Such observations should include the polarization distribution of the eclipse sky, preferably in the solar vertical plane and in the plane perpendicular to the solar vertical containing the zenith, together with simultaneous almucantar scans of radiance and polarization near the horizon, all of them preferably at various wavelengths. Only if such a complete set of measurements is available will a rigorous test of models

like the present one be possible." Full-sky imaging polarimetry meets these requirements, and the polarimetric data gathered by Pomozi et al. (2001a) and Horváth et al. (2003) make possible to test any quantitative model of the polarization of eclipsed skies.

The ground-based observation of total solar eclipses is regarded by many scientists as the fuss of amateurs and its scientific importance is frequently querried too. The results obtained by full-sky imaging polarimetry (Pomozi et al. 2001a; Horváth et al. 2003) demonstrate, however, that the ground-based study of eclipses can even nowadays yield new scientific issues.

Table

Table 9.2.1. Zenith angles θ and azimuth angles φ (measured counter-clockwise from West; for the antisolar meridian: $\varphi_{a.m.} = 79^o$) of the local minima of the degree of linear polarization p and the neutral points of skylight polarization observed during the total solar eclipse on 11 August 1999 in Kecel (Hungary). The numerical values are given in format $a \pm b$, where a is the average and b is its standard deviation. (After Table 2 of Horváth et al. 2003, p. 474).

circular patterns in Figs.	9.2.1A, 9.2.2A	9.2.1B, 9.2.2B	9.2.1C, 9.2.2C
graphs in Figs.	9.2.3A, 9.2.3B, 9.2.4A, 9.2.4B	9.2.3C, 9.2.3D, 9.2.4C, 9.2.4D	9.2.3E, 9.2.3F, 9.2.4E, 9.2.4F
recording time	12:51:34	12:52:00	12:52:00
wavelength	450 nm (blue)	450 nm (blue)	550 nm (green)
neutral point N2 of type-2 near the zenith	$\theta = 14^o \pm 2^o$ $\varphi = 76^o \pm 3^o$	$\theta = 5^o \pm 2^o$ $\varphi = 74^o \pm 3^o$	– –
first neutral point N1 of type-1 near the horizon	$\theta = 60^o \pm 2^o$ $\varphi = 74^o \pm 3^o$	– –	– –
second neutral point N1 of type-1 near the horizon	$\theta = 66^o \pm 2^o$ $\varphi = 74^o \pm 3^o$	– –	– –
neutral point N3 of type-3 near the horizon	– –	$\theta = 64^o \pm 2^o$ $\varphi = 85^o \pm 2^o$	– –
local minimum MH of p near the horizon	– –	– –	$\theta = 67^o \pm 2^o$ $\varphi = 83^o \pm 2^o$
local minimum MZ of p near the zenith	– –	– –	$\theta = 4^o \pm 2^o$ $\varphi = 75^o \pm 2^o$

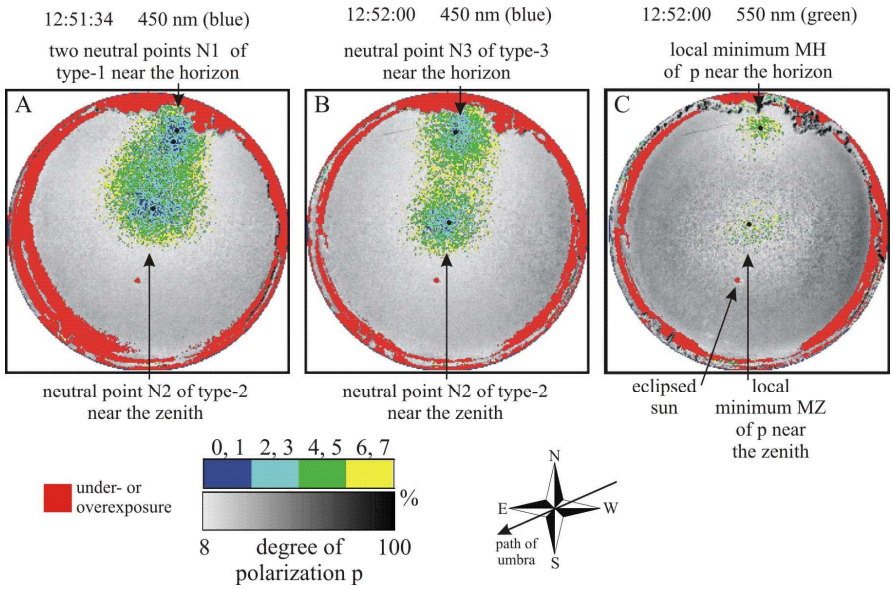

Fig. 9.2.1. Celestial patterns of the degree of linear polarization *p* of skylight measured with full-sky imaging polarimetry during totality of the solar eclipse on 11 August 1999 in Kecel (Hungary) at different times and wavelengths. A: 12:51:34 (local summer time = UTC+2), 450 nm; B: 12:52:00, 450 nm; C: 12:52:00, 550 nm. The values of *p* are rounded to integers (0,1,2,3,...,100%). The neutral points are marked by dots. (After Figs. 7-9 of Horváth et al. 2003, p. 469).

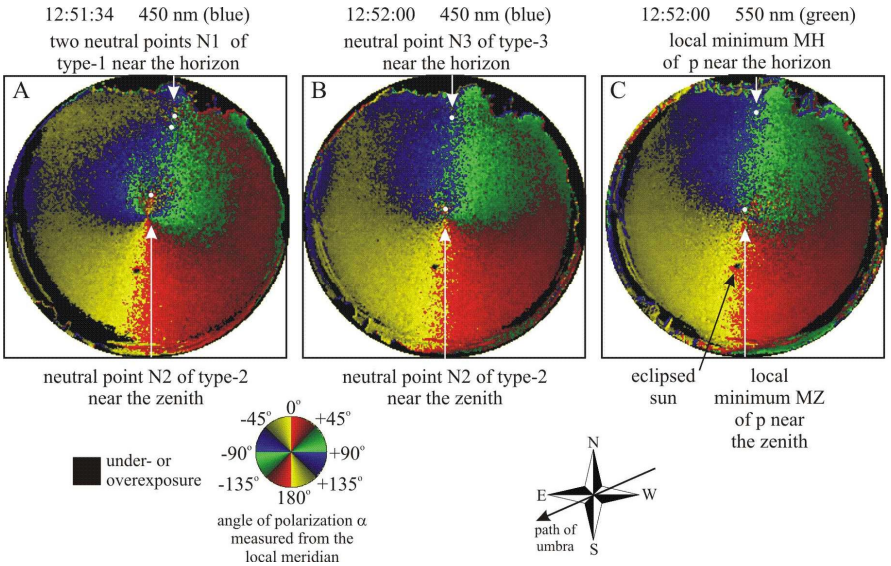

Fig. 9.2.2. As Fig. 9.2.1 for the angle of polarization α of skylight measured from the local meridian. (After Figs. 10-12 of Horváth et al. 2003, p. 469, 470).

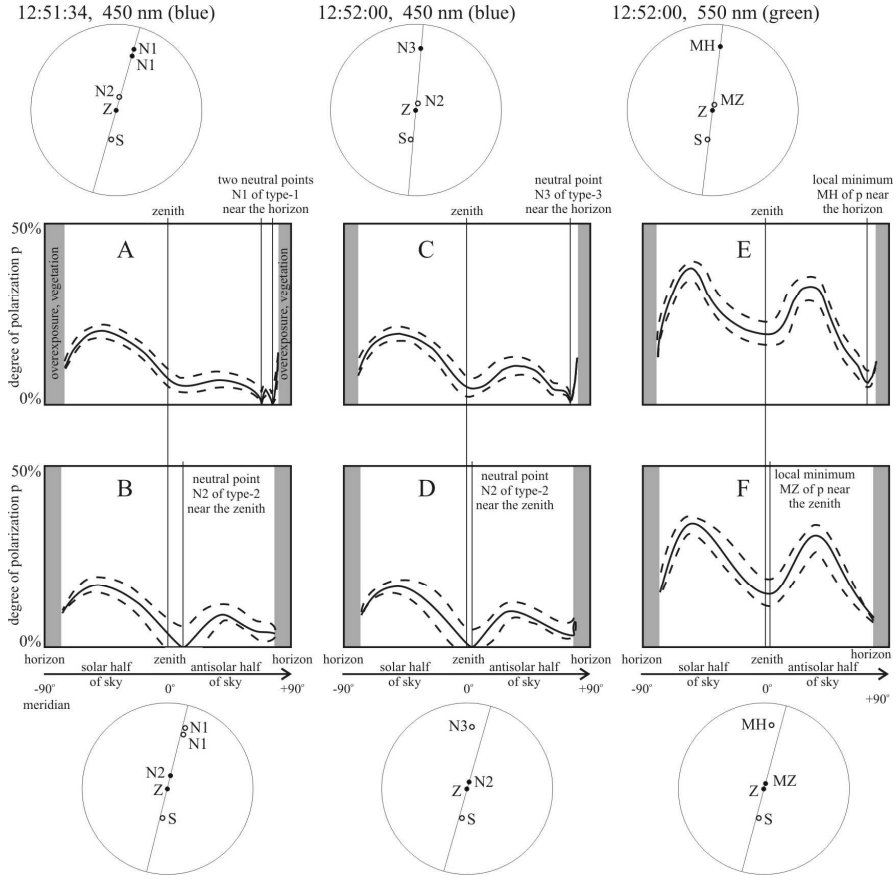

Fig. 9.2.3. Graphs of the degree of linear polarization *p* measured along different meridians crossing the zenith Z of the eclipse sky at different times and wavelengths. A, B: 12:51:34 (UTC+2), 450 nm; C, D: 12:52:00, 450 nm; E, F: 12:52:00, 550 nm. The continuous lines represent the curves fitted by the method of least squares to the measured values of *p*, while the dashed lines show the upper and lower limits, between which 90% of the *p*-values falls. The circular insets show how the scans are located relative to the circular patterns in Fig. 9.2.1. A: Scan through the two neutral points N1 of type-1 near the horizon. B: Scan through the neutral point N2 of type-2 near the zenith. C: Scan through the neutral point N3 of type-3 near the horizon. D: Scan through the neutral point N2 of type-2 near the zenith. E: Scan through the local minimum MH of *p* near the horizon. F: Scan through the local minimum MZ of *p* near the zenith. (After Figs. 13-15 of Horváth et al. 2003, p. 470, 471).

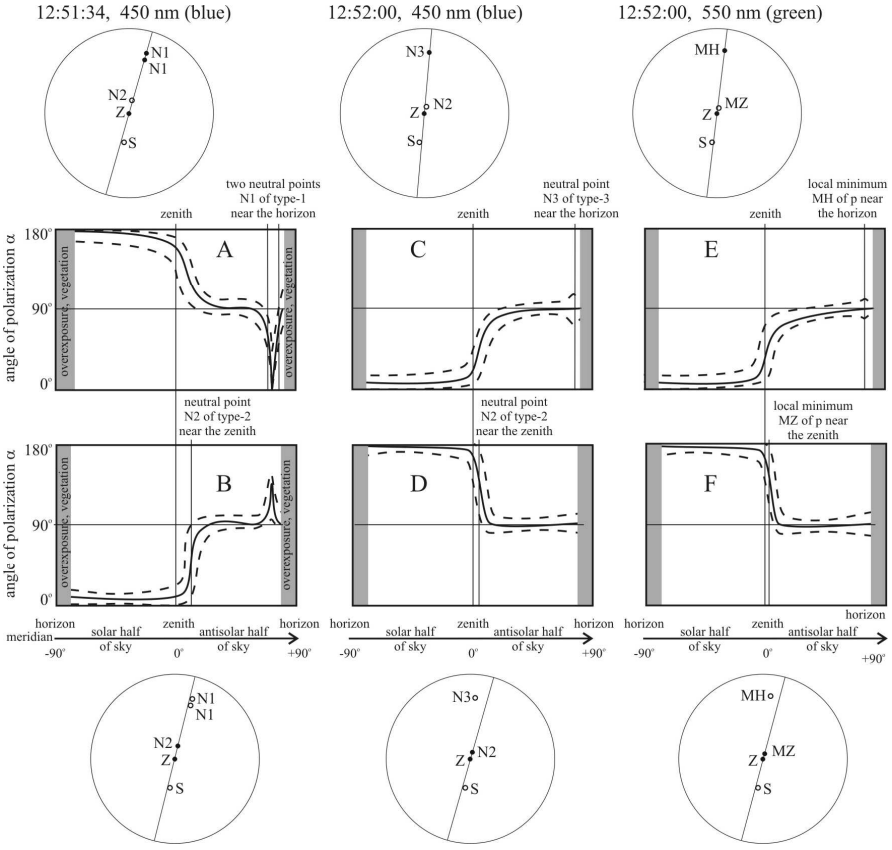

Fig. 9.2.4. As Fig. 9.2.3 for the angle of polarization α measured from the local meridian. (After Figs. 16-18 of Horváth et al. 2003, p. 472, 473).

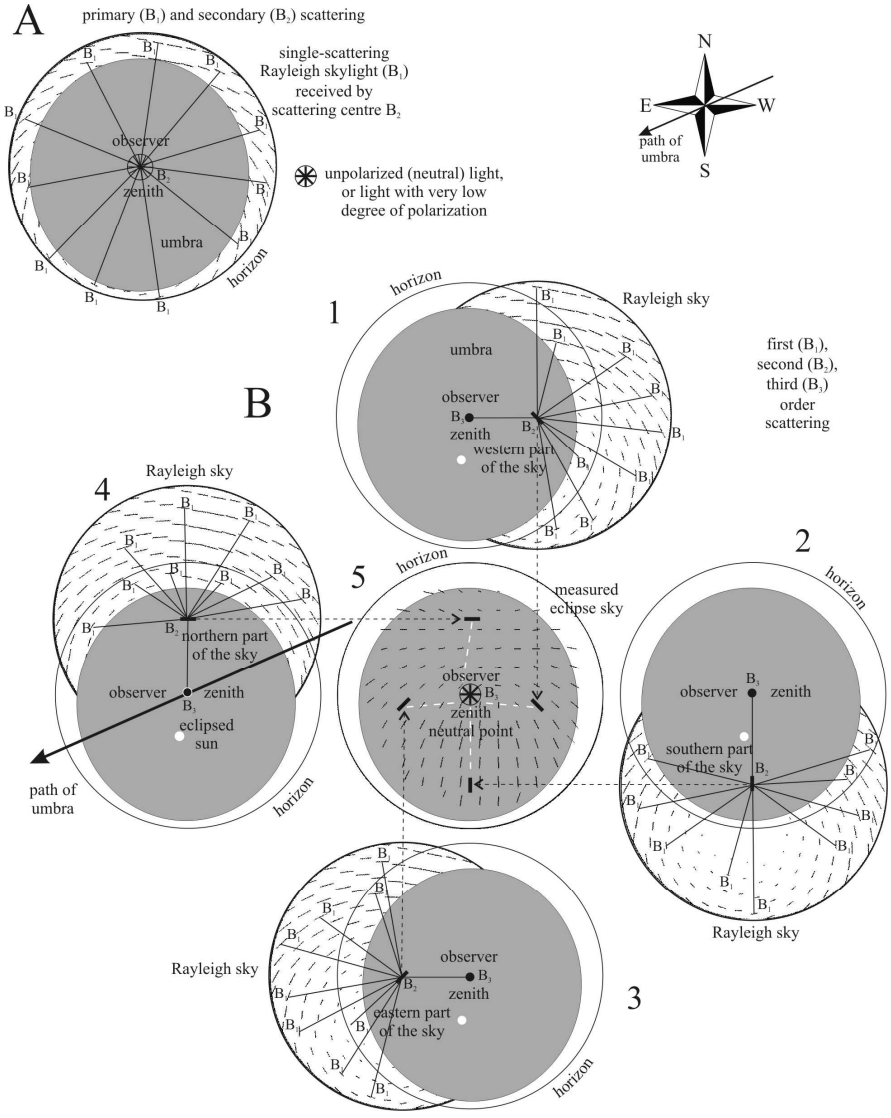

Fig. 9.2.5. For the qualitative explanation of the origin of the neutral point of skylight polarization observed near the zenith during totality if first and second order scattering events (A), or first, second and third order scattering events (B) are taken into account. (After Fig. 9 of Pomozi et al. 2001a, p. 198).

9.3 Imaging Polarimetry of the Solar Corona During the Total Solar Eclipse on 11 August 1999

The observation and investigation of the solar corona has a great popularity both in the scientific and amateur astronomy since the characteristics of the corona allows for conclusions regarding the solar activity, and thus the details of the predictions for sun models derived from different theoretical calculations and numerical simulations can be tested. The light of the corona is scattered sunlight: Thomson scattering takes place on free electrons surrounding the sun like a cloud. The corona visible in the neighbourhood of the sun from the Earth's surface during total eclipses, or through coronographs of high altitude astronomical observatories or satellites has been the subject of many investigations (e.g. Newall 1906; Sivaraman et al. 1984; Gabryl et al. 1998). The scattered corona light is highly polarized with E-vectors approximately perpendicular to the radii from the solar centre. The maximum degree of polarization p is about 40% at a distance of a quarter of the solar diameter from the edge of the sun (Können 1985). Farther away p gradually decreases. Taking the corona as a whole, the directions of polarization more or less neutralize each other with the result that the total radiance is very weakly polarized, if at all. On the basis of the polarization pattern of the solar corona the astronomers and solar physicists can calculate the electron density around the sun (e.g. Sivaraman et al. 1984), which is an important parameter in solar physics. The net p of the corona, if not zero, is also an important quantity characterizing the solar atmosphere. Since the polarization pattern of the solar corona changes from eclipse to eclipse, and may vary also during a given eclipse, it is always worth to measure these patterns and to compare them with each other. These patterns are an important part of the data basis related with the history of the sun.

Taking a pair of photographs of the solar corona through two linearly polarizing filters, the transmission axes of which were perpendicular to each other, Können (1985, p. 39, Plates 16 and 17) demonstrated that the solar corona is polarized. Other authors (e.g. Sivaraman et al. 1984; Gabryl et al. 1998; Horváth et al. 2001) have imaged the polarization pattern of the corona in form of high-resolution maps of the spatial distribution of the degree and angle of linear polarization of the corona light. Recently, Horváth et al. (2001) have studied the polarizational characteristics of the corona during the total eclipse on 11 August 1999 in Kecel (46°32'N, 19°16'E, Hungary). Using rotating-analyzer video and photo polarimetry, they measured the polarization pattern of the corona at 650, 550 and 450 nm. In this chapter some of their results are presented.

Figures 9.3.1A-C show the picture of the corona and the spatial distribution of p and α of corona light measured by rotating-analyzer photo polarimetry at 550 nm. The polarization patterns were quite similar at 650 and 450 nm (Fig. 9.3.1D). In the immediate vicinity of the sun the photoemulsion was overexposed, while at the periphery of the pictures the film was underexposed. In these over- or

underexposed areas the evaluated p- and α-values are false. This is the reason for the random distribution of p and α at the periphery of the patterns. There is a relatively narrow annular zone around the solar disc where the radiance of the corona is neither too high nor too low. p and α of corona light can be evaluated only within this annular region, which could be made wider with the use of a grey filter, the rotation symmetric absorption of which decreases from the centre to the periphery in a similar way as the radiance of the corona decreases radially.

Figure 9.3.1D shows the radial change of p of corona light along a relative radius ρ directed at an angle $\beta = 185^{o}$ clockwise from the vertical measured at 650, 550 and 450 nm, where ρ is the quotient of the radius r measured from the solar centre and the radius r_{sun} of the solar disc. We can see that, depending slightly on the wavelength, the maximum of p is about 30-35% at a relative radial distance of about $\rho = 1.70$-1.75. Figure 9.3.1E represents the tangential change of α of the corona light along a circle shown in the inset measured at 650, 550 and 450 nm. Here we can see that α depends slightly on wavelength and the E-vectors of corona light are approximately perpendicular to the radial direction. The slight tangential change of α is due to the non-homogeneous structure of the corona.

Analysing qualitatively Fig. 9.3.1, we can establish the following: The light of the solar corona is partially polarized, and the polarization pattern of the corona possesses approximately a rotational symmetry. The polarizational characteristics of the corona are practically independent of the wavelength in the visible part of the spectrum. p first increases from zero with the radial distance from the solar disc, then reaches its maximum, and decreases gradually to zero. The E-vector alignment of corona light is approximately tangential with respect to the centre of the solar disc. In August 1999 the activity of the sun was high. Therefore the structure of the solar corona was relatively homogeneous and rotation symmetric, which is clearly seen in Figs. 9.3.1A-C.

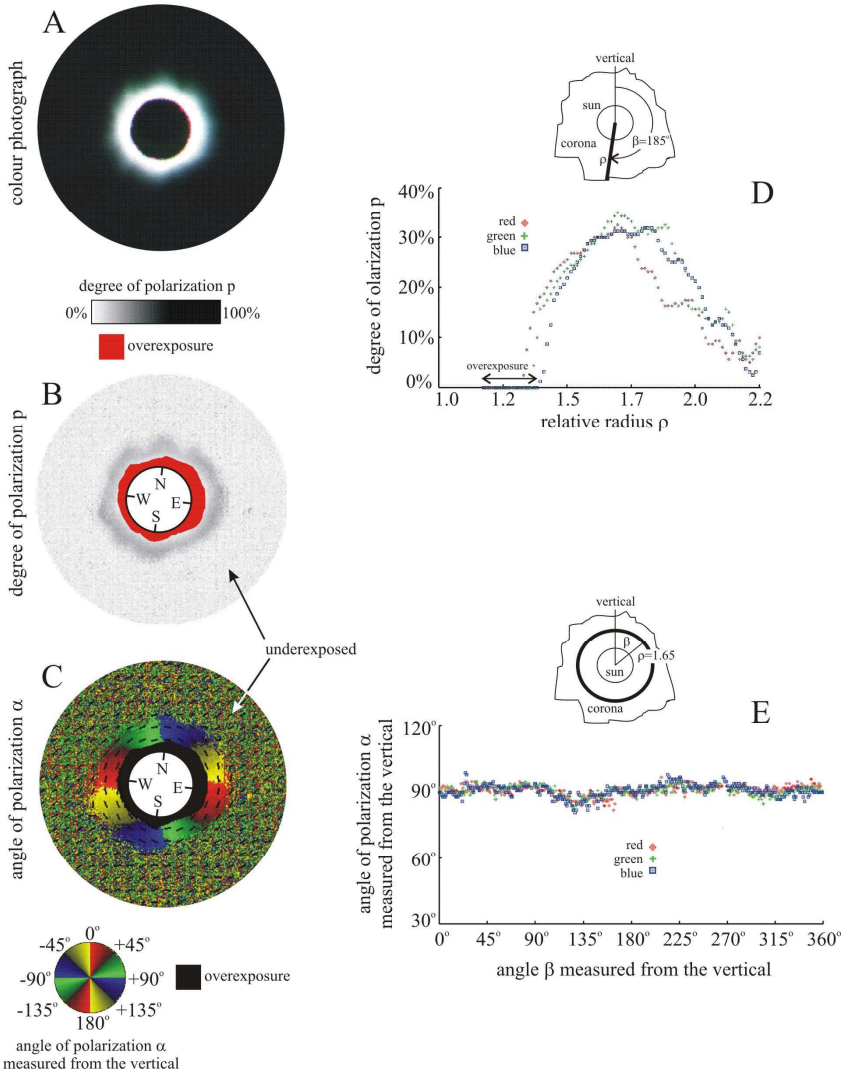

Fig. 9.3.1. A: Photograph of the solar corona taken during the total solar eclipse on 11 August 1999 in Kecel (46°32'N, 19°16'E, Hungary). B, C: Patterns of the degree of linear polarization p and the angle of polarization α measured at 550 nm with rotating-analyzer photopolarimetry. α is measured from the vertical. The black bars in the α–pattern show the local directions of the E-vectors. The obscured solar disc is replaced by a white disc, in which the North and South poles of the sun are marked. D: Radial change of p of the corona light along the radius (thick line) shown in the inset measured at 650, 550 and 450 nm. $\rho = r/r_{sun}$ is the relative radius, where r is the radius from the center of the sun and r_{sun} is the radius of the solar disc. E: Tangential change of α of the corona light along the circle shown in the inset (thick line) measured at 650, 550 and 450 nm. (After Fig. 5 of Horváth et al. 2001, p. 237).

10 How the Polarization of Skylight Changes due to Reflection from the Deflector Panels in Deflector Loft and Mirror Experiments Studying Avian Orientation

The deflector loft technique utilizes a pinwheel arrangement of glass panels that deflect wind and light in either a clockwise or counter-clockwise direction (Figs. 10.1A,B). Such deflector lofts are commonly used in behavioural experiments to investigate avian navigation (e.g. Schmidt-Koenig 1979; Helbig 1991). Homing pigeons *Columba livia* raised in normal lofts and then housed in deflector lofts change their site orientation corresponding to the direction of wind and light deflection. This is called the "deflector loft effect" (e.g. Papi 1991). Phillips and Waldvogel (1988) showed that the biased orientation of short-term deflector loft birds is due to the reflection of light from the glass portions of the deflector panels, rather than being the result of rotation of wind-borne olfactory cues.

Also metal or metal-glass mirrors have been used in some behavioural experiments to investigate the role of the view of setting sun, sunset glow, skylight polarization in the migratory orientation of birds (e.g. Kramer 1950a,b, 1951; Kramer and St. Paul 1950; Walcott and Michener 1971; Moore 1982, 1985; Moore and Phillips 1988; Phillips and Waldvogel 1988; Sandberg 1991). In these experiments the shift of the direction of sunset cues with mirrors produces a predictable shift in the migrant's orientation. This mirror technique was first applied by Santschi (1911), who studied the visual orientation of desert ants. These experiments and others (e.g. Helbig and Wiltschko 1989; Able 1989, 1993; Helbig 1990; Able and Able 1993) demonstrated that the celestial polarization pattern is one of the most important visual information in the orientation of certain birds, whose visual system is sensitive to polarization.

Considering the deflector loft and mirror experiments on avian navigation and polarization sensitivity, it is important to know how the skylight polarization changes due to reflection from these deflector panels and mirrors. Phillips and Waldvogel (1988) have made an attempt to investigate the effect that a Plexiglas deflector panel has on the distribution of celestial polarization cues visible at a deflector loft. Since the acceptance angle of the sensor of their polarimeter was too wide, about 20^{o}, they could not determine the fine structure of the reflection-polarization pattern induced by the deflector panel.

To quantify the influence of a deflector panel on the celestial polarization, Horváth and Pomozi (1997) calculated the polarization pattern of skylight reflected

from four different deflector panels as a function of the solar elevation. On the basis of these computations those deflector types can be selected, which modify the celestial polarization pattern only slightly, that is, which can be used without significant "reflection-polarization complication" in behavioural experiments with polarization-sensitive birds. Figures 10.1C,D show the geometry of reflection of polarized skylight from a vertical deflector panel, which is perpendicular to the plane of the solar meridian. Since the polarizational characteristics of the deflector depend only slightly on the colour of light, all reflection-polarization patterns were computed for wavelengths in the middle of the visible range of the spectrum. The polarization of skylight was described by the single-scattering Rayleigh model. Using the Fresnel formulae (Azzam and Bashara 1992), the reflection-polarizational characteristics were derived for the following four different types of deflector panel: (i) glass on a white substratum, (ii) glass on a black background, (iii) metal mirror, (iv) metal-glass mirror.

Figure 10.2 shows the pattern of the degree p and angle α of linear polarization of skylight reflected from a vertical glass deflector panel calculated for four different solar elevations. Figure 10.3 displays the corresponding differences $\Delta p = p_{sky} - p_{deflector}$ and $\Delta\alpha = \alpha_{sky} - \alpha_{deflector}$ between the degrees and angles of linear polarization of skylight and reflected skylight. These figures demonstrate well that the glass deflector panel has a considerable influence on the celestial polarization pattern: Δp can be as large as -100%, and $\Delta\alpha$ can approximate -90°.

On the one hand, in the mirrored celestial polarization pattern there are several neutral points from which unpolarized light is reflected (Figs. 10.2A-D). Crossing these neutral points, the alignment of the reflected E-vector changes from parallel to perpendicular relative to the panel surface (Figs. 10.2E-G). On the other hand, the glass panel possesses a characteristic annular zone, where the reflected skylight is totally linearly polarized (black half rings in Fig. 10.2A-D) and its E-vector is parallel to the glass surface (black areas in Fig. 10.2E-H). Although the direction of polarization of the glass-reflected skylight is predominantly more or less parallel to the glass plate (dark areas in Fig. 10.2E-H), there are also regions where the reflected E-vector is perpendicular to it (brighter areas). One can see that the difference $\Delta\alpha = \alpha_{sky} - \alpha_{deflector}$ is always negative along the entire deflector panel (Fig. 10.3E-H), that is, the reflected E-vector becomes more parallel to the panel than the E-vector of incident light. On the basis of Fig. 10.3 we can establish that a simple glass plate cannot mimic the real celestial polarization pattern because of the strong reflection polarization.

Similarly to Figs. 10.2 and 10.3, Horváth and Pomozi (1997) calculated the polarization pattern of skylight reflected from a silver-glass mirror. Contrary to the glass deflector, they established that such a mirror has practically no influence on the linear polarizational characteristics of incident light. The differences Δp and $\Delta\alpha$ between skylight and reflected skylight were lower than 2% and 2°. Thus, the reflected celestial polarization pattern of light deflected by a common metal-glass mirror can be considered realistic in the deflector loft or mirror experiments investigating avian orientation.

The latter conclusion is also supported by Fig. 10.4A which shows p of light reflected from different deflector panels as a function of the incident angle θ measured from the normal vector of the panel calculated for unpolarized incident light. In the case of a deflector panel composed of an aluminium plate or a silver-glass mirror the maximum of p reaches only a few %, that is, the unpolarized incident light remains almost unpolarized after reflection. The light reflected from the aluminium mirror is slightly more polarized than the light reflected by the silver-glass mirror. Contrary to this, a deflector panel made of glass on a black substratum or on a white background polarizes significantly the reflected light. As θ increases from 0^o to 90^o, p increases from 0% to 100% up to the Brewster angle $\theta_B \approx 56^o$ from the vertical, then it decreases to 0%, but remains always positive, that is, the E-vector of reflected light is always parallel to the panel.

The situation is quite different in the case of a deflector made of glass on a white substratum. Here the light component penetrating into the glass is diffusely scattered backwards by the white background, then it is refracted at the upper glass surface. The light emanating from the glass is always perpendicularly polarized to the surface due to refraction at the glass-air interface. This perpendicularly polarized light is superimposed with the parallelly polarized light reflected from the upper glass surface. Apart from quite grazing angles ($\theta \approx 90^o$) the former component dominates, thus the net E-vector is perpendicular to the panel. If $\theta \approx 90^o$ the parallel polarized reflected light controls the net p, as we can see on the corresponding curve in Fig. 10.4A. Figure 10.4B shows the change of p versus θ as a function of the albedo A of the white background. The albedo has a considerable influence on the reflection-polarizational characteristics of the panel. Increasing A, the E-vector of reflected light becomes more and more perpendicular to the panel, that is, the region of the incident angle characterized by parallel polarized reflected light becomes gradually narrower. The larger the albedo A, the weaker is the reflected light polarized with perpendicular E-vector.

Hence, a glass deflector panel modifies considerably the polarization pattern of reflected skylight in the deflector loft or mirror experiments studying avian orientation. Thus, such deflector panels might induce a conflict situation for the test birds in such a way, that the intensity and spectral features of reflected skylight contradict to its polarizational characteristics. A glass plate modifies the colour and intensity of incident skylight only slightly. However, it changes significantly the polarization of reflected skylight. Thus, in this case a polarization-sensitive test bird is confronted with such a deflected view of the sky, where the spatial distribution of intensity and colour is similar to the real one but the polarization pattern is quite different from the expected pattern. Since many birds prefer the celestial polarization pattern against other optical cues from the sky (e.g. Able 1993), they may solve this conflict in such a way, that they begin to orient not by means of skylight polarization, but on the basis of other cues, e.g. stars or geomagnetism, or they orient randomly or ambiguously. This might be one of the reasons for the frequently observed ambivalent responses of test birds during the deflector loft or mirror experiments using deflector panels, which change significantly the polarization of skylight.

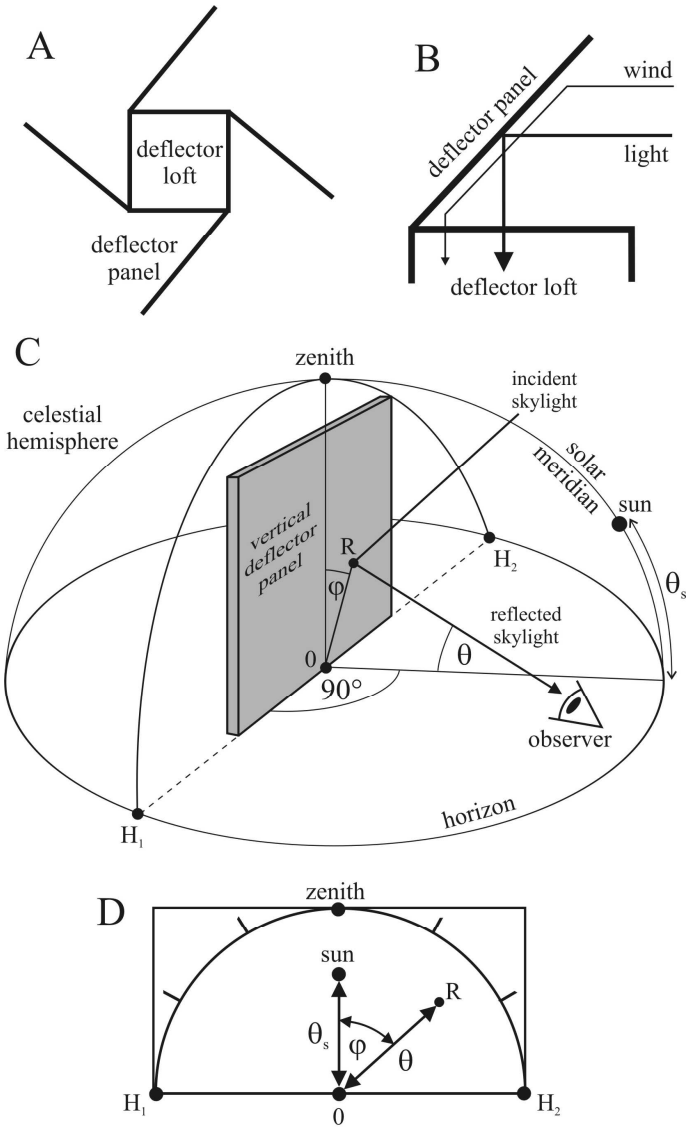

Fig. 10.1. A: Top view of a common deflector loft used in the experiments to investigate the visual and olfactory navigation of birds. The mirroring portion of each deflector panels consists of a glass-metal mirror or a glass plate with a bright or dark background. B: The deflector panel changes both wind and light in the same direction either clockwise or counter-clockwise. C: The geometry of reflection of polarized skylight from a vertical deflector panel, which is perpendicular to the plane of the solar meridian. D: The polar-coordinate system used to represent the reflected celestial polarization patterns. (After Fig. 1 of Horváth and Pomozi 1997, p. 292).

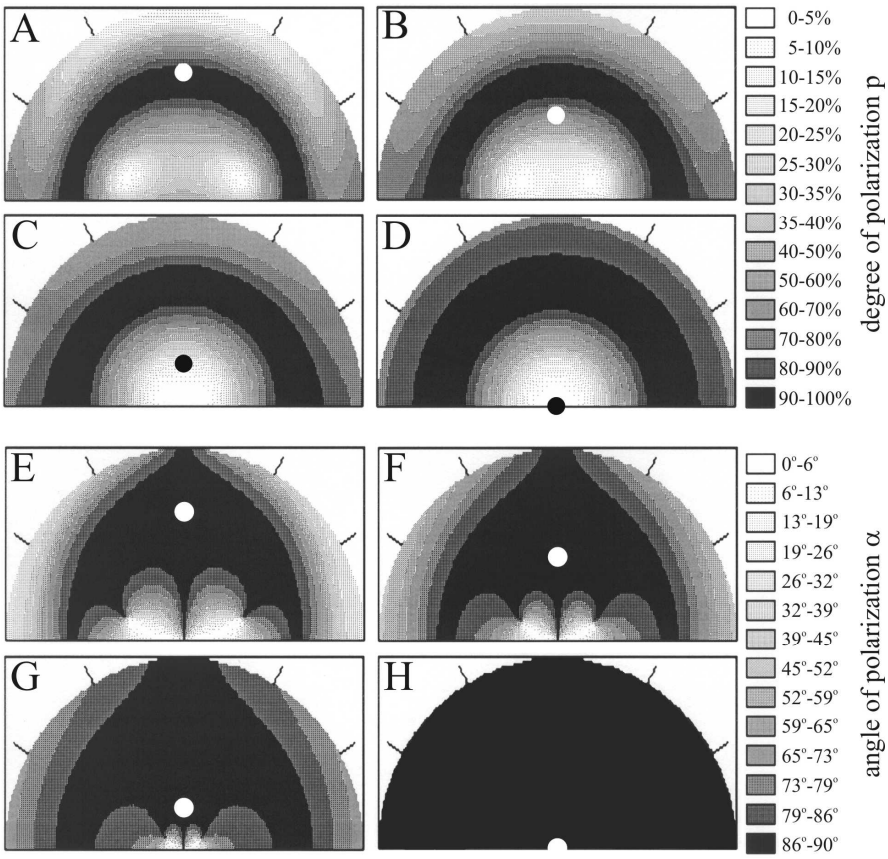

Fig. 10.2. A-D: The pattern of the degree of linear polarization p of skylight reflected from a vertical glass deflector panel calculated for four different solar elevations θ_s. The mirror image of the sun is represented by a dot. (After Fig. 2 of Horváth and Pomozi 1997, p. 294). E-H: The angle of polarization α of reflected skylight measured from the normal vector of the panel. Brighter shades represent regions where the E-vector is more or less perpendicular to the panel, while darker tones mean E-vectors more or less parallel to it. (After Fig. 3 of Horváth and Pomozi 1997, p. 294).

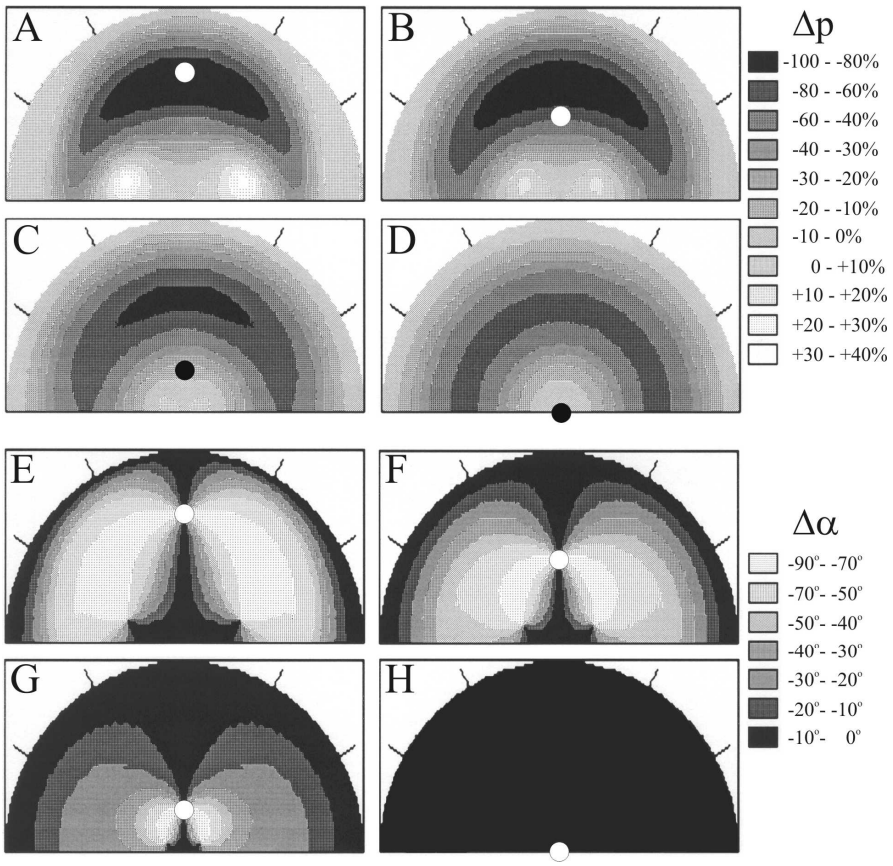

Fig. 10.3. A-D: Difference $\Delta p = p_{sky} - p_{deflector}$ between p_{sky} of skylight and $p_{deflector}$ of skylight reflected from a vertical glass deflector panel calculated for four different solar elevations θ_s. The mirror image of the sun is represented by a dot. (After Fig. 4 of Horváth and Pomozi 1997, p. 295). E-H: Difference $\Delta\alpha = \alpha_{sky} - \alpha_{deflector}$ between α_{sky} of skylight and $\alpha_{deflector}$ of skylight reflected from a vertical glass deflector panel. Since $\alpha_{sky} < \alpha_{deflector}$, $\Delta\alpha < 0$ in every point of the deflector. (After Fig. 5 of Horváth and Pomozi 1997, p. 295).

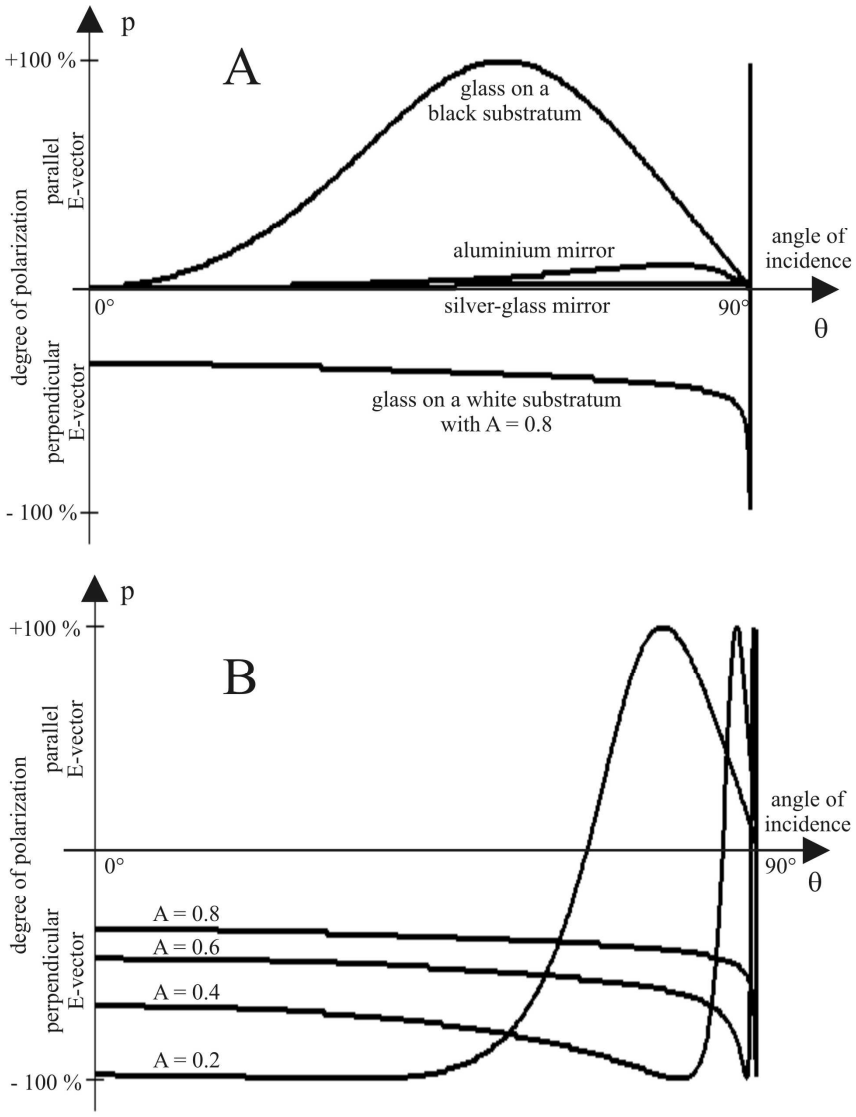

Fig. 10.4. A: The degree of linear polarization p of light reflected from different deflector panels as a function of the incident angle θ measured from the normal vector of the panel calculated for unpolarized incident light. The albedo of the white substratum is $A = 0.8$. Positive or negative p-values mean E-vectors parallel or perpendicular to the panel, respectively. (After Fig. 6 of Horváth and Pomozi 1997, p. 296). B: p of light reflected from a glass deflector panel as a function of the incident angle θ from the normal of the panel calculated for unpolarized incident light in the case of four different values of the albedo A of the underlying white substratum. (After Fig. 7 of Horváth and Pomozi 1997, p. 297).

11 Reflection Polarization of Rayleigh Skylight at the Air-Water Interface

In the optical environment one of the main sources of partially linearly polarized light is that reflected from water surfaces. The reflection-polarization pattern of water surfaces is a striking cue and plays an important role in the habitat search of insects associated with water.

In this chapter a quantitative account is given of the physics of polarization of single-scattered Rayleigh skylight due to reflection from the water surface on the basis of the results of Schwind and Horváth (1993) and Horváth (1995a). The light arising from the bottom or reflected by particles suspended in water is neglected. Spectral and intensity characteristics of the skylight and the wavelength-dependence of the refractive index of water are not taken into consideration.

11.1 Reflectivity, Reflection-Polarization Ellipse, Degree and Angle of Linear Polarization of Light Reflected from the Water Surface

The amplitude reflection coefficients $\rho_{hor}(\theta_i)$ and $\rho_{ver}(\theta_i)$ versus the angle of incidence θ_i (Guenther 1990) describe how the horizontal and vertical components of the electric field vector $\underline{E}$ change after reflection from the water surface. Figure 11.1A shows $\rho_{hor}(\theta_i)$ and $\rho_{ver}(\theta_i)$ for the air-water interface. There is a sign change in ρ_{ver} at the Brewster angle $\theta_{Brewster} = 53^o$ measured from the vertical. Vertically polarized light is considerably weakened when reflected from the water surface and at the Brewster angle its intensity even falls to zero, while horizontally polarized light is much less weakened. Thus the water surface reflects vertically polarized light much less effectively than horizontally polarized light.

In general, partially linearly polarized light with an arbitrary direction of polarization can be decomposed into a horizontally and a vertically polarized component which vibrate coherently. As the horizontal component is less weakened after reflection, the plane of polarization of the sum of the components will become more horizontal, that is, the E-vector rotates after reflection towards the water surface. The sign change of ρ_{ver} at the Brewster angle has the consequence that the reflected electric field vector is exactly horizontal, if $\theta_i = \theta_{Brewster}$. If $\theta_i < \theta_{Brewster}$, the plane of polarization is also mirrored besides the rotation towards the water surface. This mirroring is caused by an additional

phase-shift of 180° of the vertically polarized component after reflection, because ρ_{ver} is then negative, which does not occur for horizontally polarized light. For $\theta_i > \theta_{Brewster}$ this phase-shift is absent, because ρ_{ver} is then positive. The dependence of the reflectivity R of the water surface on θ_i and the angle of polarization α_i of totally linearly polarized incident light is shown in Figs. 11.1B and 11.1C.

The direct sunlight, the light coming from the neutral points of the sky and the light from the heavily overcast sky are unpolarized, that is, their polarization ellipse is a circle. After reflection from the water surface this unpolarized incident light becomes partially linearly polarized with horizontal E-vector irrespective of θ_i. The change of the degree of linear polarization p of reflected light versus θ_i can be read qualitatively from the shape of the reflection-polarization ellipses in Figs. 11.2A and 11.2B, and quantitatively in Fig. 11.2C. Figure 11.2D shows the reflectivity of the water surface versus θ_i for unpolarized incident light. The horizontal dimension of the reflection-polarization ellipse increases monotonously with increasing θ_i, because $\rho_{hor}(\theta_i)$ increases monotonously and has always positive values (Fig. 11.1A). However, the vertical dimension of the reflection-polarization ellipse decreases with increasing θ_i up to the Brewster angle $\theta_{Brewster}$, then it increases with θ_i because of the sign change of $\rho_{ver}(\theta_i)$ (Fig. 11.1A). Representing the series of the reflection-polarization ellipses in three dimensions versus θ_i, the quasi-exponential increase of ρ_{ver} and ρ_{hor} for $\theta_i > \theta_{Brewster}$ results in a special trumpet-like form, which is horizontally flattened at the Brewster angle (Fig. 11.2B).

The degree of linear polarization p_r of reflected light for unpolarized incident light increases from 0% to 100% as θ_i increases from 0° to $\theta_{Brewster}$, then it decreases from 100% to 0% as θ_i increases from $\theta_{Brewster}$ to 90° (Fig. 11.2C). This change of p_r means that the shape of the reflection-polarization ellipse is circular at $\theta_i = 0°$ and $\theta_i = 90°$, and it becomes horizontally more flattened with increasing θ_i, and at the Brewster angle it is distorted to a straight horizontal line, which means that the reflected light is totally linearly polarized. Similar but opposite change occurs in the shape of the reflection-polarization ellipse when θ_i increases from $\theta_{Brewster}$ to 90° (Figs. 11.2A and 11.2B). The reflectivity of the water surface for unpolarized incident light increases quasi-exponentially with θ_i (Fig. 11.2D).

Figure 11.3 shows the reflection-polarization ellipses, p_r and α_r of light reflected from the water surface versus θ_i for partially linearly polarized incident light with $p_i = 50\%$ and four different α_i-values. Due to the sign change of $\rho_{ver}(\theta_i)$ (Fig. 11.1A), also α_r has a sign change at the Brewster angle as can be seen in the plots of $\alpha_r(\theta_i)$ in Fig. 11.3. Figures 11.4 and 11.5 show the dependence of p_r and α_r of light reflected from the water surface as functions of θ_i, α_i and p_i of the incident light.

Hence, if the incident light is partially linearly polarized, as the skylight for instance, the effects of reflection of the unpolarized and totally linearly polarized parts of the incident light can be summed. The unpolarized component is partially converted into horizontally polarized light and the totally polarized part rotates its plane of vibration towards the water surface, while in addition this plane is or is

not mirrored if the angle of incidence is smaller or larger than the Brewster angle, respectively (Figs. 11.3-11.5). The net effect is an increase in the degree of polarization and a stronger rotation of the polarization plane towards the water surface than is the case when the incident light is totally linearly polarized.

11.2 Polarization Patterns of Single-Scattered Rayleigh Skylight Reflected from the Flat Water Surface as a Function of the Solar Zenith Angle

A possible way of displaying polarization patterns is to represent the direction of polarization by the orientation of a bar, the width of which is proportional to p. Such polarization patterns of the clear single-scattering Rayleigh sky are shown in Fig. 11.6 for four solar zenith angles. Figure 11.7 shows the polarization patterns of single-scattered Rayleigh skylight reflected from the flat water surface for the same solar zenith angles. In Figs. 11.8A-D the pattern of reflectivity R of the water surface versus the solar zenith angle is seen for the single-scattered Rayleigh skylight. Figure 11.8E shows the R-pattern of the water surface for unpolarized light from a totally overcast sky.

The disadvantage of these representations of the distribution of polarization is that due to the relatively large dimensions of the bars and polarization ellipses the spatial resolution of these patterns is low. This disadavantage is eliminated in Figs. 7.6.1D,E; 7.6.2D,E and 11.9, 11.10 showing the colour-coded patterns of p and α of single-scattered Rayleigh skylight and Rayleigh skylight reflected from the water surface for different solar zenith angles. The most important features of the water-surface-reflected polarization patterns are the following:

- At or near the Brewster angle the polarization ellipses are distorted to horizontal lines tangential in circular two-dimensional representation or become horizontally very flattened, because p_r of reflected light is approximately 100%. Hence there is a characteristic, nearly totally and horizontally polarized annular Brewster zone on the water surface (Figs. 11.7, 11.9, 11.10).
- At lower solar elevations the E-vectors of reflected light are mainly horizontal towards the sun and opposite to it (Figs. 11.7C,D and 11.10C,D). Apart from the annular Brewster zone, at 90^o from the sun, the E-vectors of reflected light are mainly vertical i.e. radial in two-dimensional representation. This band, visible at the water surface and interrupted twice by the Brewster zone (Figs. 11.7C,D and 11.10C,D), is the counterpart of the maximally polarized continuous band in the clear sky at 90^o from the sun (Figs. 11.6C,D).

Comparing the R-patterns of the water surface calculated for clear skies (Figs. 11.8A-D) with the R-pattern for unpolarized light from a heavily overcast sky (Fig. 11.8E), we can establish that there is no significant difference between them and they all have quasi-cylindrical symmetry for $R > 7\%$, that is, for directions of

observations larger than 65° from the vertical. The *R*-pattern calculated for the clear sky with sun at the zenith (Fig. 11.8A) and that for unpolarized skylight (Fig. 11.8E) have exact cylindrical symmetry. As the sun nears the horizon, the contour lines of equal reflectivity become gradually elliptical being flattened perpendicularly to the solar meridian.

The two central black spots in Figs. 11.8C and 11.8D are regions of the water surface where $R < 2\%$. The water surface is clearly more transparent at these dark spots, because there is hardly any reflection-gloss. In ditches, even with slightly rippling water, these dark spots are also distinctly visible. Then the spots make the impression of being more or less triangular, that can be deduced from the shape of these spots (Figs. 11.8C and 11.8D). These dark spots can be photographed without a polarizing filter, too (see e.g. Plate 10 of Können 1985, p. 30).

11.3 Effect of Clouds on the Reflection-Polarization Pattern of the Water Surface

When the sky is partly cloudy, some regions of the celestial polarization pattern are hidden. Figure 11.11 demonstrates this situation. Here, the celestial *p*-patterns are partly covered by simulated clouds. For the sake of simplicity, the light radiated by clouds[1] is supposed to be unpolarized, so the depolarizing clouds are represented by white in Fig. 11.11.

Figure 11.12 shows the *p*-pattern of skylight reflected from the water surface as a function of the solar zenith angle for the cloudy Rayleigh skies in Fig. 11.11. Contrary to the uniformly white shade of the clouds in Fig. 11.11, the mirror clouds in Fig. 11.12 are heterogeneously grey, because the unpolarized incident cloud light becomes horizontally polarized after reflection from the water surface with *p* depending on the direction of view from the nadir as shown in Fig. 11.9E. In Fig. 11.12 the patterns of Figs. 11.9A-D are combined with the pattern of Fig. 11.9E in such a way, that in the patches of the mirror clouds the pattern of Fig. 11.9E is seen.

[1] The polarizational characteristics of clouds are diverse. There are many kinds of clouds, and the polarization of their light depends on their illumination, composition, height, density and the size of their elements. α of light from higher clouds is the same as that of the blue sky, its *p*, however, differs considerably (see Chapters 7.6 and 7.7). The maximum *p* of ice-clouds and water-clouds is not higher than about 40%. Their polarization decreases in directions closer to or further away from the sun. In water-clouds the light is strongly polarized at 90° from the sun and due to the rainbow-scattering it is most strongly polarized at about 145° from the sun, which can be as high as 60%. *p* of cloudlight is generally lower if the clouds are denser.

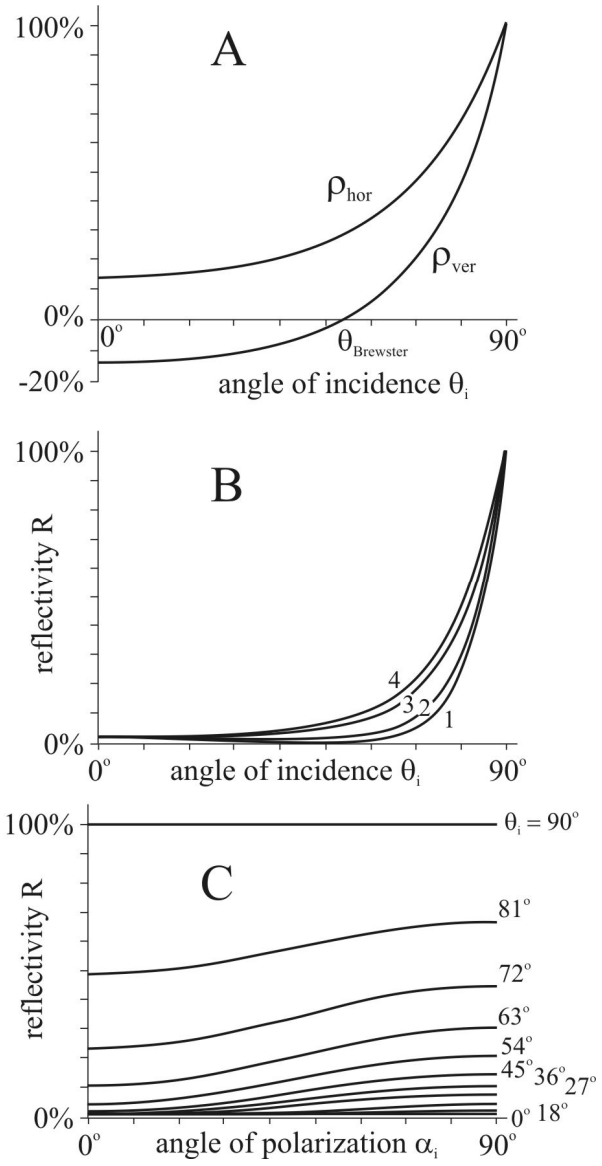

Fig. 11.1. A: Amplitude reflection coefficients ρ_{hor} and ρ_{ver} as a function of the incident angle θ_i measured from the vertical for horizontal and vertical E-vector of totally linearly polarized incident light calculated for the air-water interface with indices of refraction n_{air} = 1 and n_{water} = 1.33. B: Reflectivity $R(\theta_i)$ of the water surface for totally linearly polarized incident light with different angles of polarization α_i measured from the vertical. 1: $\alpha_i = 0^o$, 2: $\alpha_i = 30^o$, 3: $\alpha_i = 60^o$, 4: $\alpha_i = 90^o$. C: Reflectivity $R(\alpha_i)$ of the water surface for different θ_i of totally linearly polarized incident light. θ_i changes from 90^o to 0^o with a step of $\Delta\theta_i = 9^o$. (After Fig. 5.1 of Horváth 1993, p. 77).

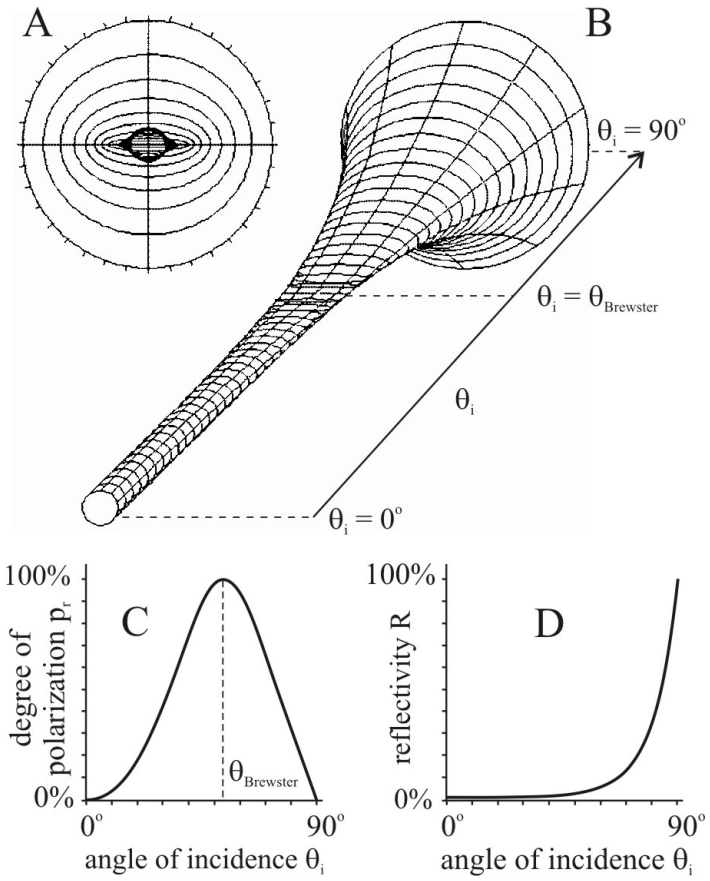

Fig. 11.2. A: Reflection-polarization ellipses calculated for the water surface for unpolarized incident light as a function of the angle of incidence θ_i measured from the vertical and increasing from the Brewster angle $\theta_{Brewster}$ to 90° in steps of $\Delta\theta_i = 6°$ from the center towards the periphery. The outermost circle with a graduation scale of 10° represents the polarization circle of the neutral incident light. B: Three-dimensional representation of the reflection-polarization ellipses versus θ_i. For $\theta_i = \theta_{Brewster} = 53°$ the reflected light is totally and horizontally polarized. C: Degree of linear polarization p_r of light reflected from the water surface versus θ_i calculated for unpolarized incident light. D: Reflectivity R of the water surface versus θ_i for unpolarized incident light. (After Fig. 5.2 of Horváth 1993, p. 78).

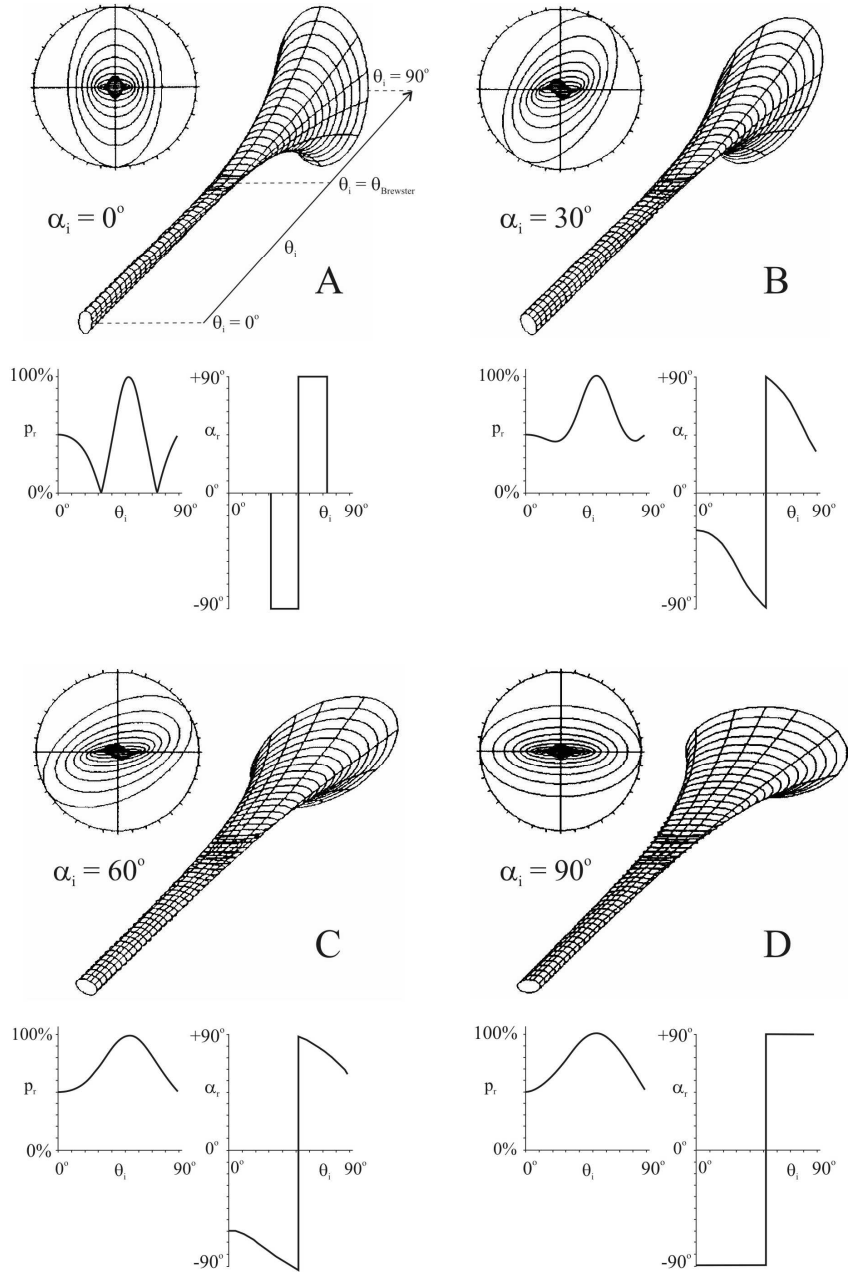

Fig. 11.3. Reflection-polarization ellipses, degree p_r and angle α_r of linear polarization of light reflected from the water surface versus the angle of incidence θ_i for partially linearly polarized incident light with p_i = 50% and four different α_i measured from the vertical. (After Fig. 5.3 of Horváth 1993, p. 80).

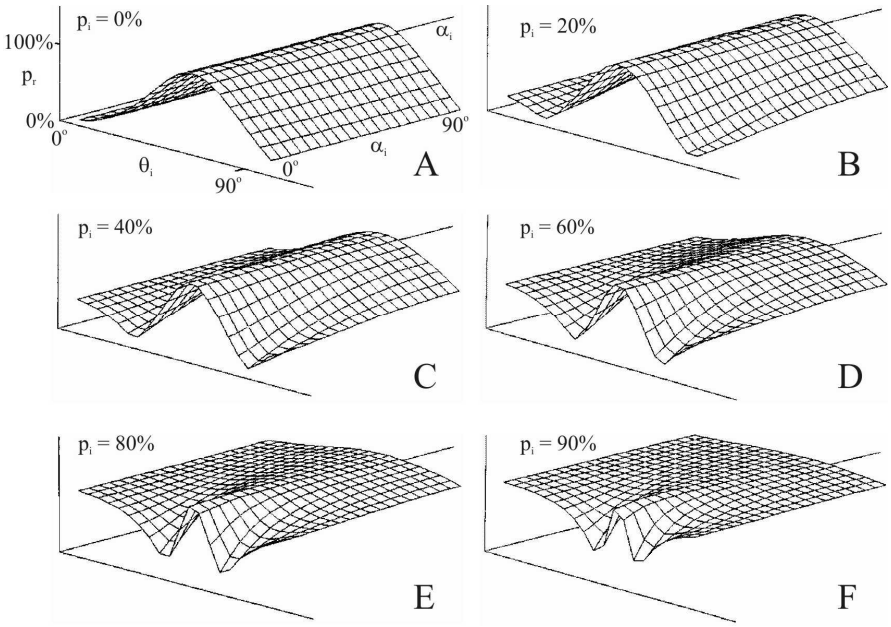

Fig. 11.4. Degree of linear polarization p_r of light reflected from the water surface as functions of the incident angle θ_i and angle of polarization α_i of partially linearly polarized incident light with six different p_i. (After Fig. 5.4 of Horváth 1993, p. 81).

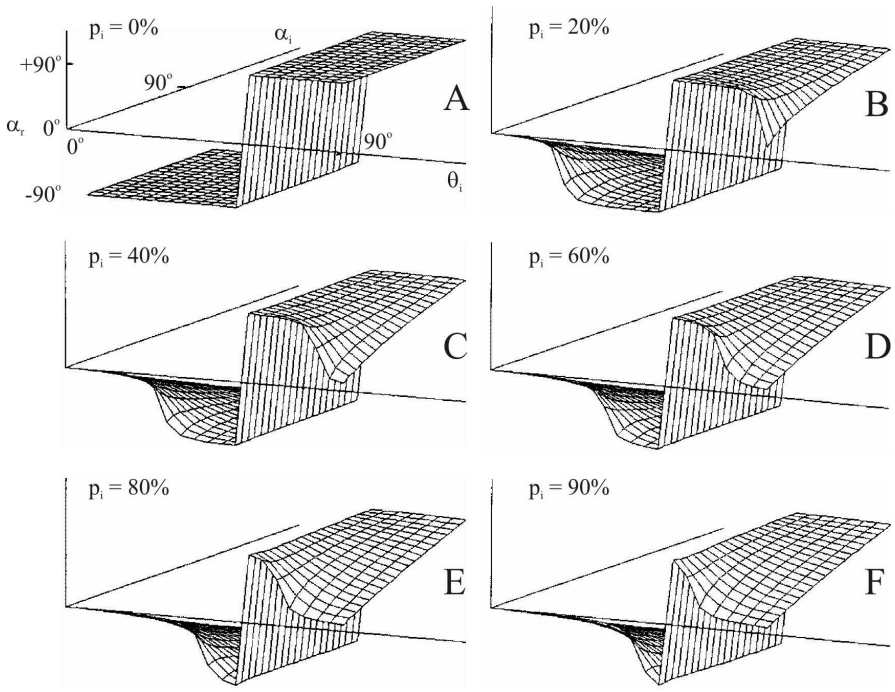

Fig. 11.5. Angle of polarization α_r of light reflected from the water surface as functions of the incident angle θ_i and angle of polarization α_i of partially linearly polarized incident light with six different p_i. (After Fig. 5.5 of Horváth 1993, p. 81).

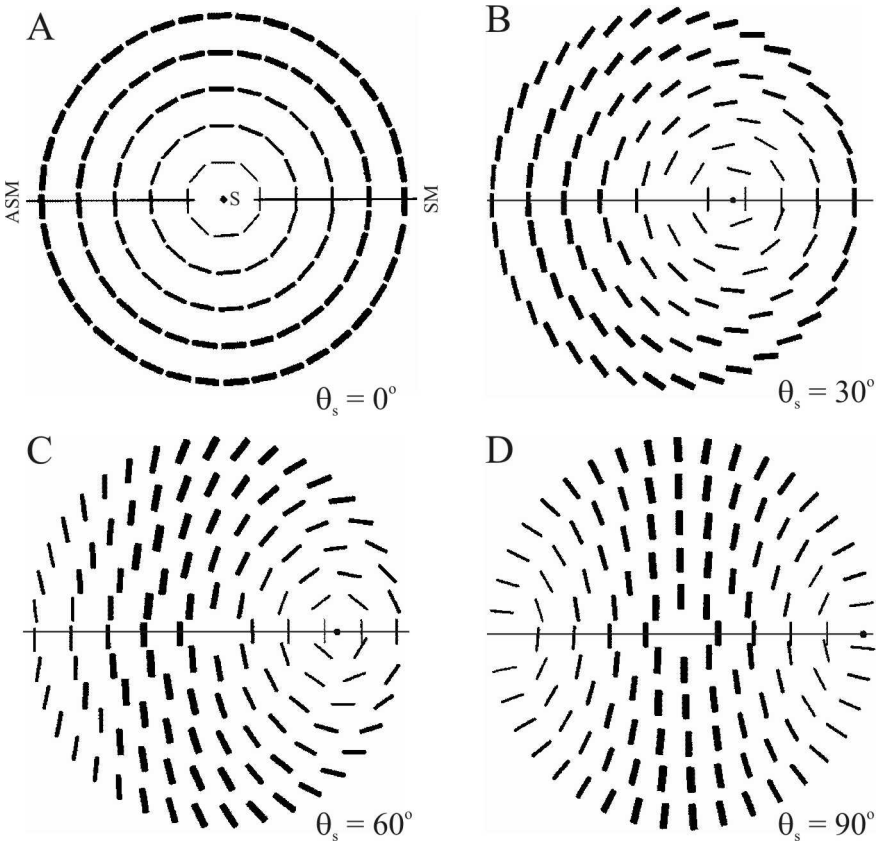

Fig. 11.6. Polarization pattern of the clear single-scattering Rayleigh sky for four different solar zenith angles θ_s. The alignment of the bars represents the direction of polarization and their width is proportional to the degree of linear polarization. The patterns represent the celestial hemisphere in two dimensions. The zenith is at the center, the position of the sun *S* is shown by a dot, the horizon is the outermost circle. ASM: antisolar meridian, SM: solar meridian. The zenith angle θ is measured radially (e.g. zenith: $\theta_z = 0^o$, horizon: $\theta_h = 90^o$) in such a way that the radius is proportional to θ. The azimuth angle φ is measured from the solar meridian (e.g. solar meridian: $\varphi_{SM} = 0^o$, antisolar meridian: $\varphi_{ASM} = 180^o$). (After Fig. 5.6 of Horváth 1993, p. 82).

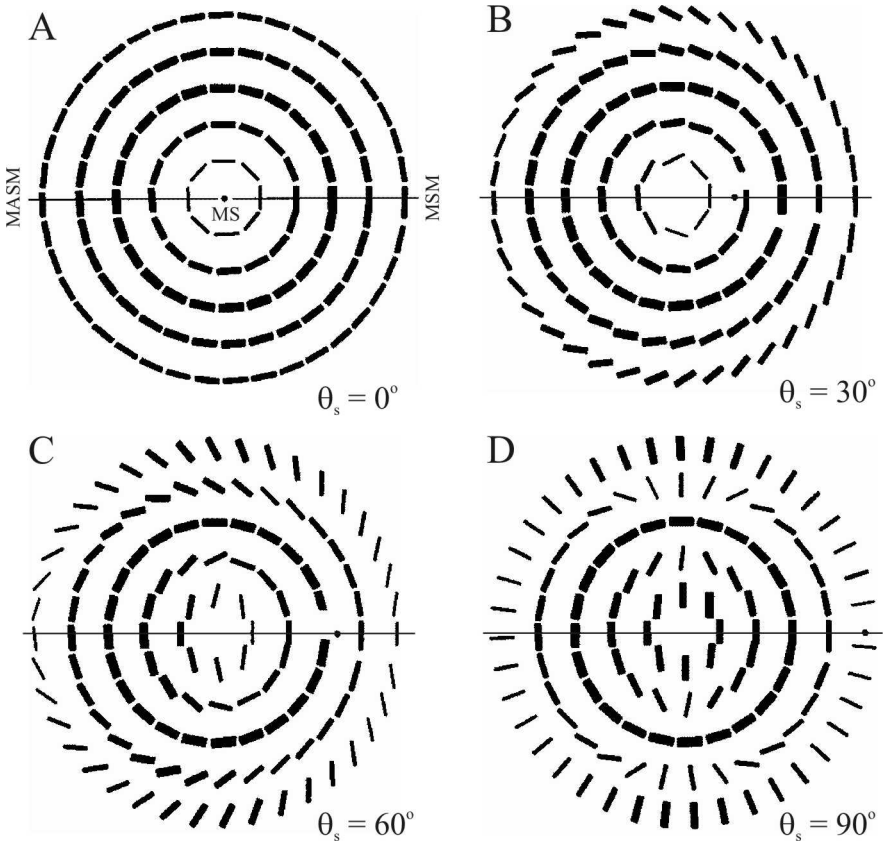

Fig. 11.7. As Fig. 11.6 for the reflection-polarization patterns of skylight at the flat water surface. MS: mirror sun, MSM: mirror solar meridian, MASM: mirror antisolar meridian. (After Fig. 5.7 of Horváth 1993, p. 83).

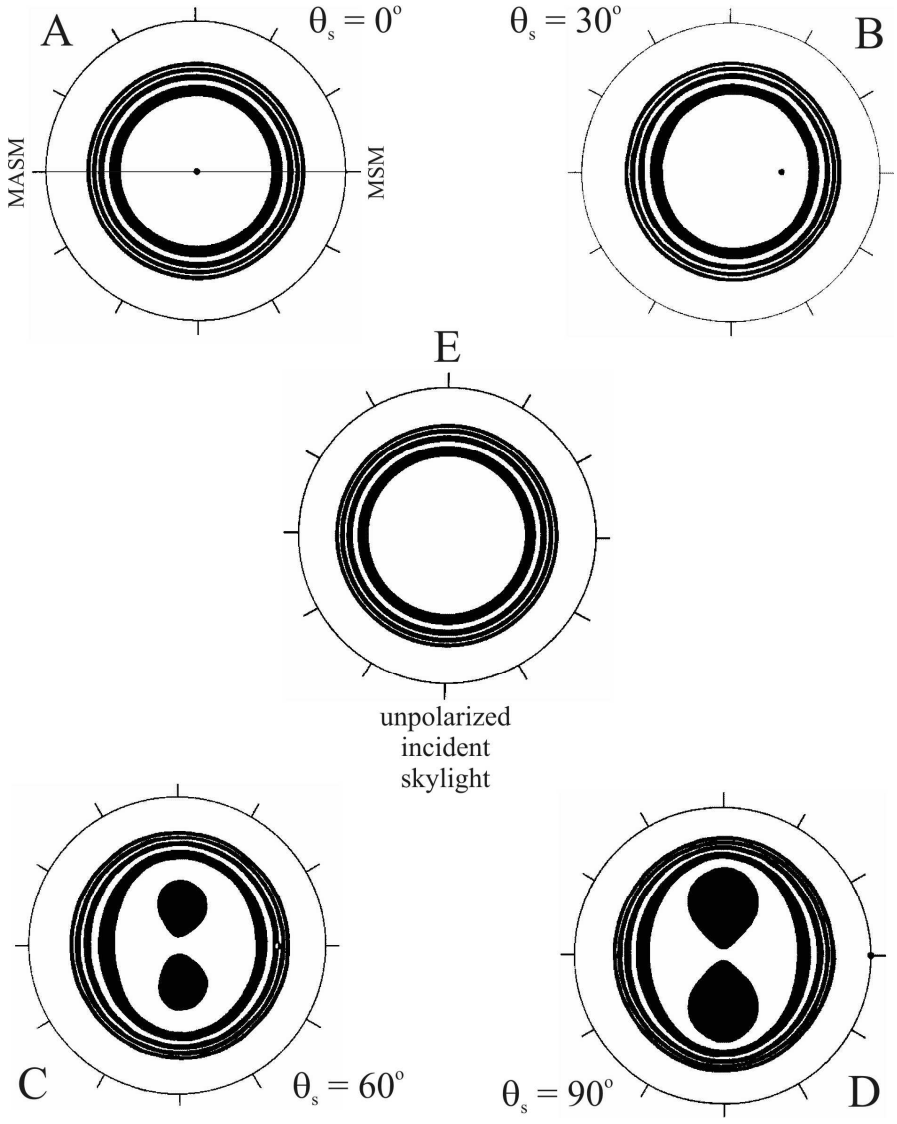

Fig. 11.8. Contour lines of equal reflectivity R for single-scattered Rayleigh skylight reflected from the water surface versus the solar zenith angle θ_s calculated for clear skies (A-D) and a totally clouded sky emitting unpolarized light (E). The positions of the sun are shown by dots. In patterns C and D the two central black spots represent the regions of the water surface where $R < 2\%$. In all patterns the elliptical or circular contour lines belong to $R = 3, 4, ..., 9, 10\%$ from the center towards the periphery, and the outermost circle at the horizon, with a graduation scale represents $R = 100\%$. For the sake of a better visualization every second reflectivity region is black. MSM: mirror solar meridian; MASM: mirror antisolar meridian. (After Fig. 5.10 of Horváth 1993, p. 87).

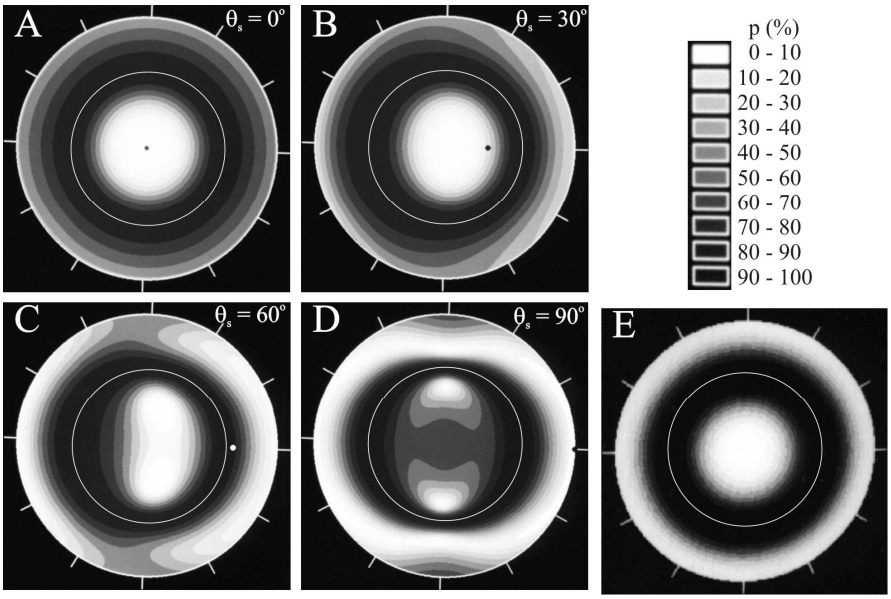

Fig. 11.9. A-D: Patterns of the degree of linear polarization p of light from the clear single-scattering Rayleigh sky reflected from the flat water surface for different solar zenith angles θ_s. The positions of the mirror sun are represented by dots. E: As A-D for unpolarized incident light from a totally cloudy sky. The white central circle in the strongly polarized annular zone in the patterns represents the Brewster angle $\theta_{Brewster} = 53^\circ$ from the vertical. (After Fig. 6.3 of Horváth 1993, p. 103).

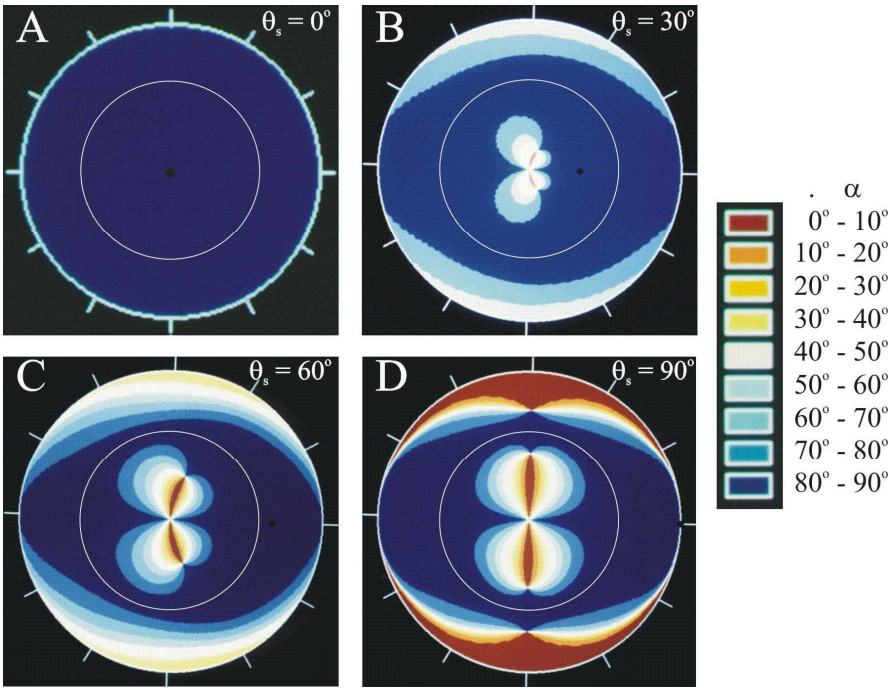

Fig. 11.10. As Fig. 11.9 for the angle of polarization α_r of reflected single-scattered Rayleigh skylight measured from the vertical. Since the E-vectors of skylight reflected from the water surface are horizontal when the sun is at the zenith, pattern A is homogeneously dark blue. (After Fig. 6.6 of Horváth 1993, p. 106).

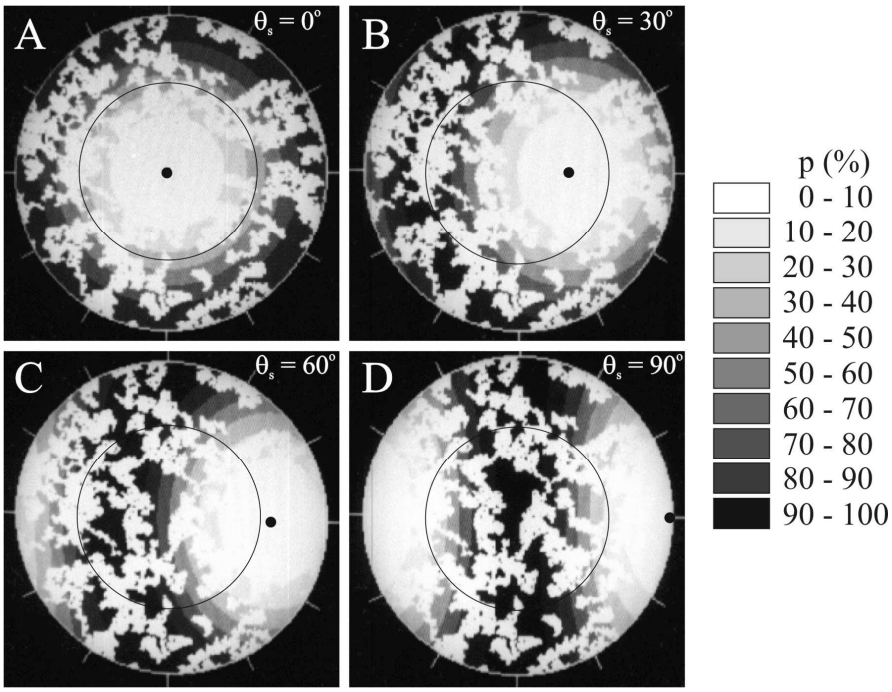

Fig. 11.11. Patterns of the degree of linear polarization p of light from the cloudy single-scattering Rayleigh sky for different solar zenith angles θ_s. The positions of the sun are represented by dots. The simulated clouds are white, because it was supposed that the light emitted by them is unpolarized (p = 0%). (After Fig. 6.2 of Horváth 1993, p. 102).

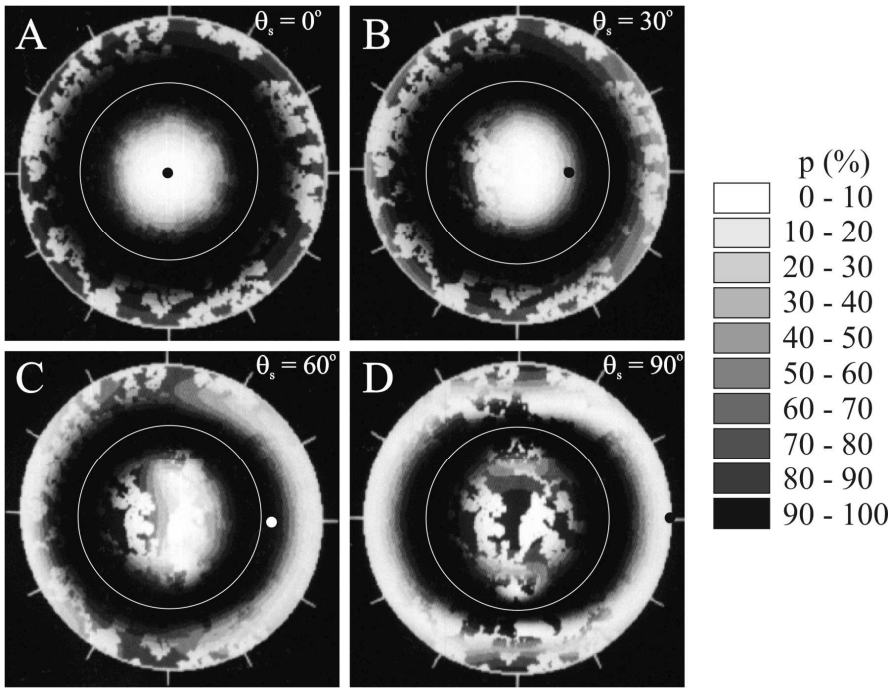

Fig. 11.12. As Figs. 11.9A-D with the same patterns of clouds as in Fig. 11.11. The mirror clouds visible at the smooth water surface are heterogeneously shaded by grey, because the unpolarized incident cloud light becomes horizontally polarized after reflection from the water surface with degree of polarization depending on the direction of view from the nadir as shown in Fig. 11.9E. (After Fig. 6.4 of Horváth 1993, p. 104).

12 Reflection-Polarization Patterns of the Flat Water Surface Measured by Imaging Polarimetry

12.1 Reflection-Polarization Patterns of Freshwater Habitats Measured by Video Polarimetry

Horváth and Varjú (1997) measured the reflection-polarization patterns of two typical freshwater habitats under clear skies by video polarimetry in the red, green and blue ranges of the spectrum. They have shown that the polarization patterns of small water bodies are very variable depending on the illumination conditions. Under clear skies and in the visible range of the spectrum, flat water surfaces reflecting light from the sky are most strongly polarized in the blue. Under an overcast sky radiating diffuse white light, small freshwater habitats are characterized by a high horizontal polarization at or near the Brewster angle in all spectral ranges except those in which the contribution of subsurface reflection is large. In a given spectral range and at a given angle of view, the direction of polarization is horizontal if the surface reflection and vertical if the subsurface reflection dominates (Fig. 12.1). The greater this dominance, the higher the net degree of linear polarization p, the theoretical maximum of which is 100% at the Brewster angle for the horizontal E-vector component and approximately 30% at grazing viewing angles for the vertical E-vector component.

Figures 12.2-12.5 illustrate the reflection-polarization patterns of two small ponds of different types recorded from an angle of view of 50^{o} with respect to the vertical on a sunny day under a clear sky. In Fig. 12.2 the patterns of a dark pond with clear water and a dense growth of aquatic plants are presented. In the red the water reflects only a small amount of light, unlike the plants in and around it. In the green the amount of surface-reflected light is slightly higher, and in the blue it dominates and the pond appears quite bright, because the incident light from the sky is predominantly blue. In the red and green the water surface is less polarizing than in the blue. This is especially true at and near the Brewster angle (53^{o} from the vertical), where a dark patch appears in the centre of Fig. 12.2C3. The maps in column D indicate that the surface of the pond reflects horizontally polarized light.

The histograms in Fig. 12.3 show the distribution of the angle α and degree p of linear polarization in the red, green and blue computed for the central region of the dark pond in Fig. 12.2. In the blue the most frequent p-values are concentrated around 60%, while in the red and green these values are approximately 40%. In all

three spectral regions, the most frequent α-values are between 90° and 100° from the vertical; that is, the reflected E-vectors are concentrated about the horizontal. However, in the blue the reflected E-vectors are more narrowly distributed around the main peak than in the red and green.

In Fig. 12.4 the polarization patterns of a bright pond are shown. From the right-hand side of the water surface blue skylight was reflected, which was occluded on the left side by a bush. The water was clear and transparent, and its yellowish-green bottom reflected a relatively high proportion of light. In the red and especially in the green, the shadowed bottom of the pond is brighter than in the blue. In the red and green the whole pond appears only slightly polarizing. Only in the blue and only in the skylight-reflecting region of the surface is the reflected light highly polarized.

The E-vector of light emanating from the water is more or less vertical in the shadowed area and horizontal where skylight is reflected from the water surface. This is illustrated quantitatively in Fig. 12.5. In the blue the histogram of p has two peaks: one at 10% and the other at 38%. The former peak is the contribution of the shadowed left-hand side of the pond, and the latter peak originates from the right-hand side, which is reflecting blue skylight. In the green these two peaks virtually coincide between 8% and 12% (Fig. 12.5B3), and in the red there is a single peak at 10% (Fig. 12.5A3), because the difference in p between the left- and right-hand sides of the pond gradually disappears at longer wavelengths. Here again, in the red and green the E-vector directions of reflected light are more widely distributed around the main peak than in the blue.

12.2 Reflection-Polarization Pattern of the Flat Water Surface Measured by 180° Field-of-View Imaging Polarimetry

Using 180° field-of-view imaging polarimetry, Gál et al. (2001b) measured the reflection-polarization pattern of the flat water surface under a clear sky at sunset. Owing to this technique, they could experimentally test and prove the validity of the theoretical predictions of Schwind and Horváth (1993) and Horváth (1995a).

Figures 12.6A and 12.6B show the spatial distribution of the degree of linear polarization p and angle of polarization α of single-scattered Rayleigh skylight calculated for sunset. Figures 12.6C and 12.6D show the p- and α-pattern of the sunset sky in Fig. 12.6E measured by 180° field-of-view imaging polarimetry at 550 nm. Figures 12.7B,C,D represent the theoretical patterns of p, α and reflectivity R of the flat water surface calculated for the single-scattered Rayleigh skylight (Figs. 12.6A,B) with the use of the Fresnel formulae. Figures 12.7E,F,G show the same reflection-polarization patterns of the flat water surface computed for the measured skylight (Figs. 12.6C-E) with the use of the Fresnel formulae. The reflection-polarization patterns in Figs. 12.7E-G are semi-empirical, because the incident light was the measured polarized skylight, while the optical

parameters of reflected skylight were calculated theoretically on the basis of the Fresnel formulae.

Figures 12.7H,I,J show the patterns of p, α and R of the flat water surface measured by 180^o field-of-view imaging polarimetry at 550 nm. Figure 12.7A illustrates the mirror image of the sky reflected from the flat water surface. The triangular region on the right hand side of these pictures is the railing at the end of the jetty from which the recording was taken. Although the mirror image of the railing screens out the mirror image of the sky in the vicinity of the setting sun, this does not matter because of the axial symmetry of the reflection-polarization pattern at sunset. The (red/black) narrow annular region in Figs. 12.7H-J were overexposed due to the large amount of light reflected from the water surface near the horizon, the reflectivity of which approximates 100% if the angle of reflection measured from the vertical nears 90^o. The reflection-polarization patterns in the red (650 nm) and blue (450 nm) were practically the same as those in the green (550 nm) in Figs. 12.7B-J.

Comparing the theoretical, semi-empirical and measured reflection-polarization patterns of the flat water surface in Figs. 12.7B-D, 12.7E-G and 12.7H-J, respectively, a remarkable resemblance can be established between them. The reason for this close similarity is that the strong repolarization ability of the water surface overwhelms the slight differences between the polarization of the single-scattered Rayleigh skylight and the real skylight (see Fig. 12.6). Apart from the overexposed regions and the mirror image of the railing of the jetty, the reason for the small, irrelevant differences between the measured (Figs. 12.7H-J) and predicted (Figs. 12.7E-G) reflection-polarization patterns are that the water surface was slightly undulating, and some light was scattered inside the water, then returned (this re-emitted radiation from the water was not taken into consideration in the prediction).

Analysing the fine details of the reflection-polarization patterns in Fig. 12.7 we can establish the following: The maximum (approximately 100%) p of reflected skylight is located in a characteristic annular band, called the Brewster zone, from which the light is reflected with an angle of reflection of 53^o, called the Brewster angle (Figs. 12.7B,E,H). When the sun is on the horizon the Brewster zone with a strong horizontal polarization is maximally extended towards and away from the sun and becomes narrowest perpendicular to this direction.

At sunset or sunrise the light reflected from the flat water surface is mainly horizontally polarized. The angle of polarization is $45^o \leq \alpha \leq 135^o$ with respect to the vertical, both in the direction of the sun and opposite to it. Apart from the horizontally polarized Brewster zone it is mainly vertically polarized, i.e. $0^o \leq \alpha < 45^o$ or $135^o \leq \alpha \leq 180^o$ at right angles to the mirror solar meridian (Figs. 12.7C,F,I) just like the blue sky itself (Figs. 12.6B,D). At twilight the mainly vertically polarized region of the water surface is 8-shaped within the Brewster zone and takes an extended bow-shape outside the Brewster zone.

At twilight under a clear sky there are several neutral points on the water surface (Figs. 12.7B,E,H). Inside the Brewster zone (*Bz*) there exist two neutral points (*a, b*) positioned at about 45^o from the nadir at right angles to the mirror solar meridian. There are two additional neutral points (*c, d*) outside the Brewster

zone perpendicularly to the mirror solar meridian, and two further neutral points, the position of which coincides with the mirror sun (*e*) and the mirror antisun (*f*). The neutral points *c*, *d* and *e*, *f* are not clearly visible in Figs. 12.7B,E. These neutral points are the regions of the water surface where the horizontal polarization of reflected skylight switches to vertical.

The reflectivity pattern of the flat water surface has a quasi-cylindrical symmetry for $R > 7\%$, i.e. for directions of observation larger than 65^o from the vertical. The contour lines of equal R are elongated perpendicularly to the mirror solar meridian. The two central patches in Figs. 12.7D,G,J show those regions of the water surface where $R < 2\%$. These two dark patches can be seen on the water surface at 90^o from the sun when it is near the horizon. The surface is clearly more transparent at these patches. The occurrence of these patches is the result of the fact that R of the water surface is lower for vertically polarized incident light than for horizontally polarized light.

The reflection-polarization patterns visible over the flat water surface under a clear sky at sunset or sunrise have characteristic gradients of R, p and α. These different gradients are associated with the same regions of the water surface: where the gradient of R is high, so too are the gradients of p and α. This can be seen, for example, in the case of the characteristic 8-shaped pattern inside the Brewster zone in Figs. 12.7C,F,I. The tips of this 8-shaped pattern coincide with the two neutral points (*a, b*) of the *p*-pattern (Figs. 12.7B,E,H) and with the centre of the two dark patches of the *R*-pattern (Figs. 12.7D,G,J).

The fact that the measured polarization pattern agreed so closely with that predicted by Schwind and Horváth (1993) and Horváth (1995a) indicates that the simple single-scattering Rayleigh theory and Fresnel theory can accurately describe the reflection of polarized skylight at a flat air-water interface.

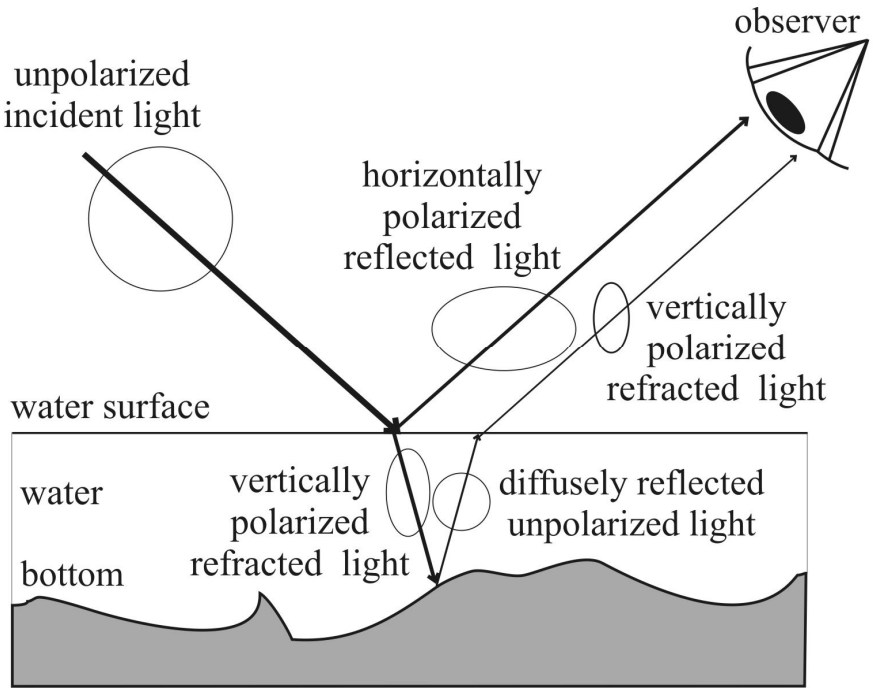

Fig. 12.1. Polarization of unpolarized incident light returned from a body of water. The returned light has two components: (i) the partially horizontally polarized light reflected from the water surface and (ii) the partially vertically polarized refracted light coming from the water.

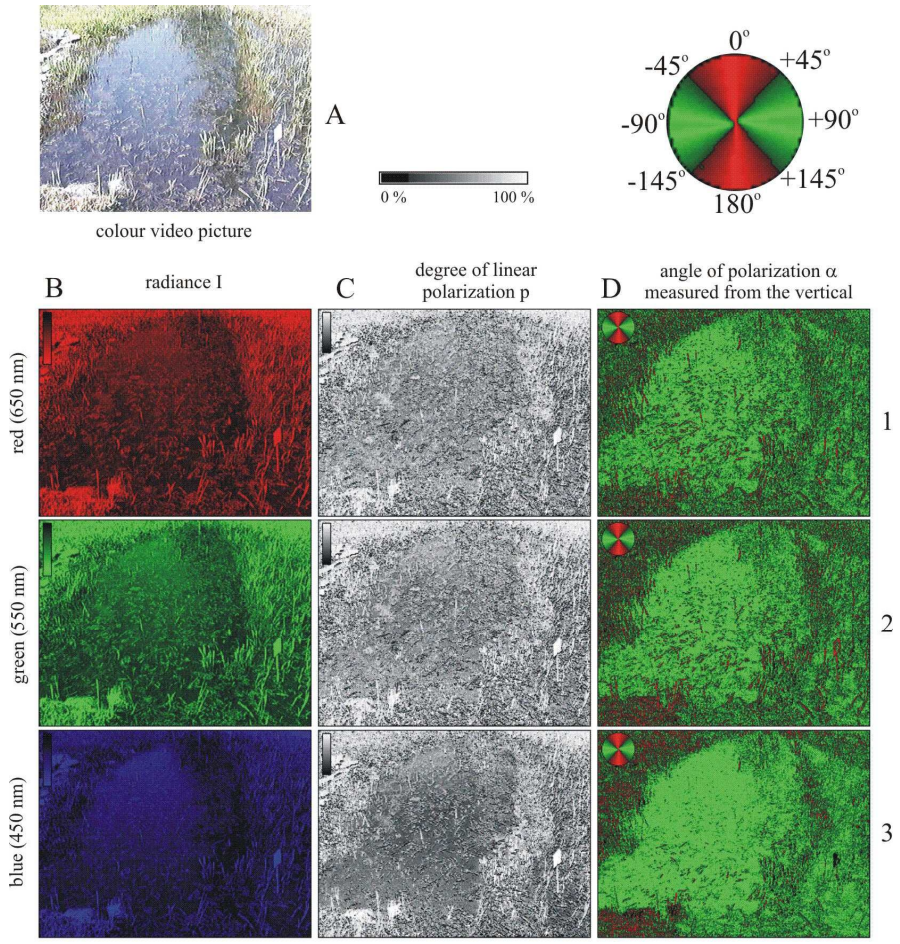

Fig. 12.2. A: Photograph of a small dark pond with clear water and a dense growth of aquatic plants under a clear sky on a sunny day. B-D: Maps of the radiance *I*, degree of linear polarization *p* and angle of polarization α (from the vertical) of the pond measured in the red (650 nm), green (550 nm) and blue (450 nm). (After Fig. 3 of Horváth and Varjú, 1997, p. 1158).

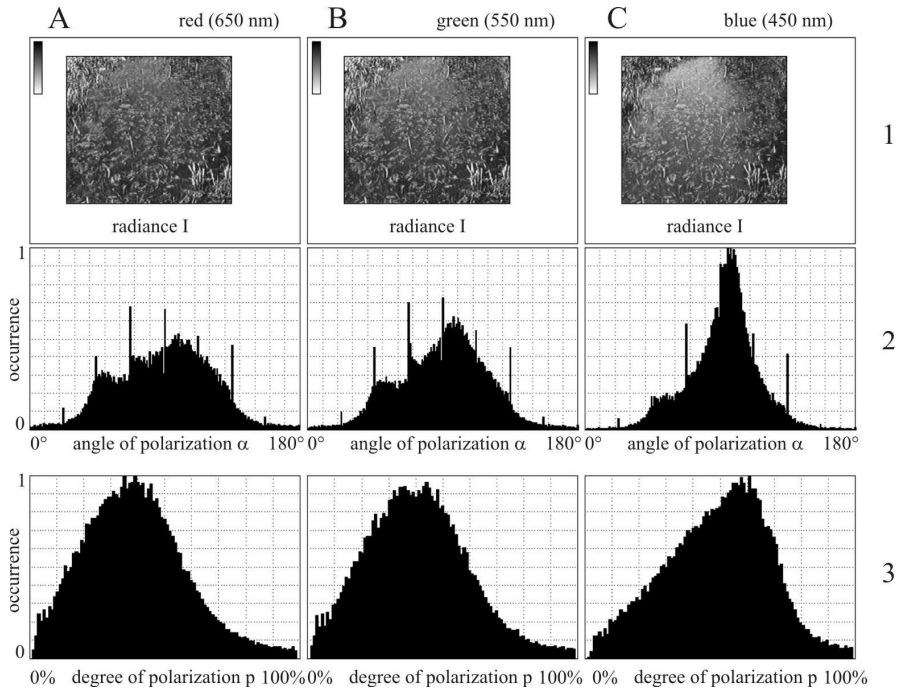

Fig. 12.3. The radiance map, histograms of the distribution of the angle of polarization α and the degree of linear polarization *p* in the red (650 nm), green (550 nm) and blue (450 nm) calculated for the central region of the dark pond in Fig. 12.2A. (After Fig. 4 of Horváth and Varjú, 1997, 1159).

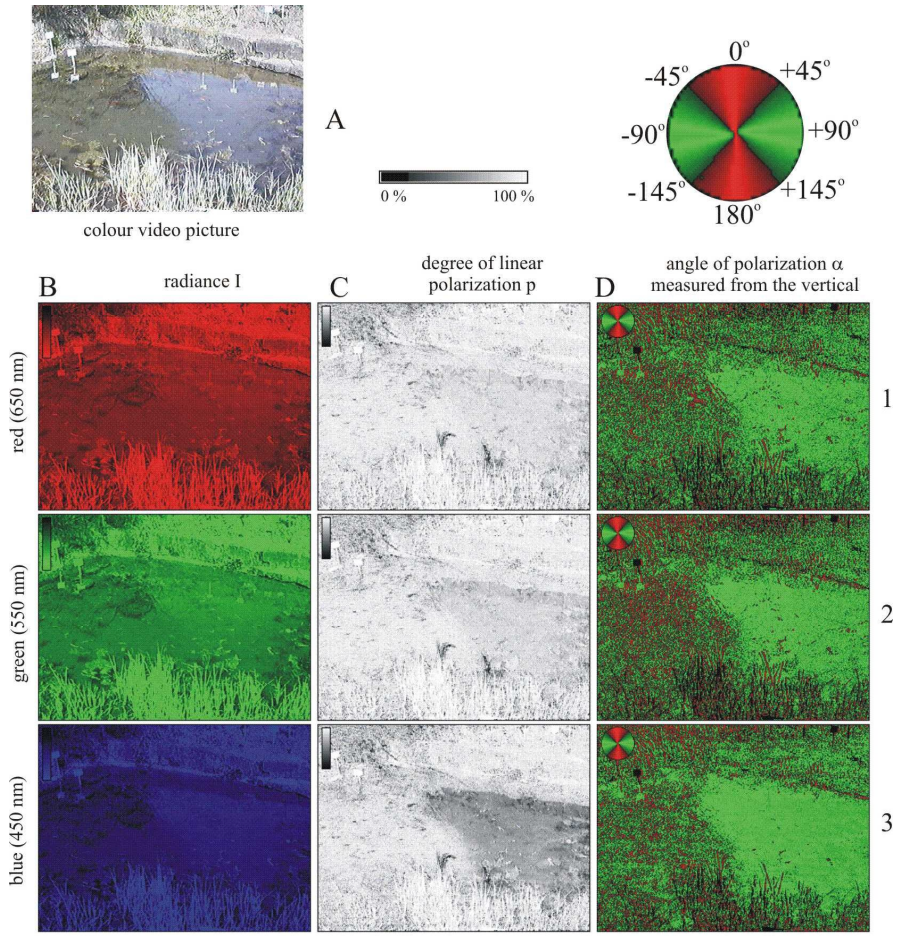

Fig. 12.4. As Fig. 12.2 for another pond, the right side of which was illuminated by skylight, while its left-hand side was in the shadow of a bush. From the right-hand side of the water surface blue skylight was reflected. The water was clear and transparent, and the yellowish-green bottom of the pond reflected a relatively large amount of light. (After Fig. 5 of Horváth and Varjú, 1997, p. 1160).

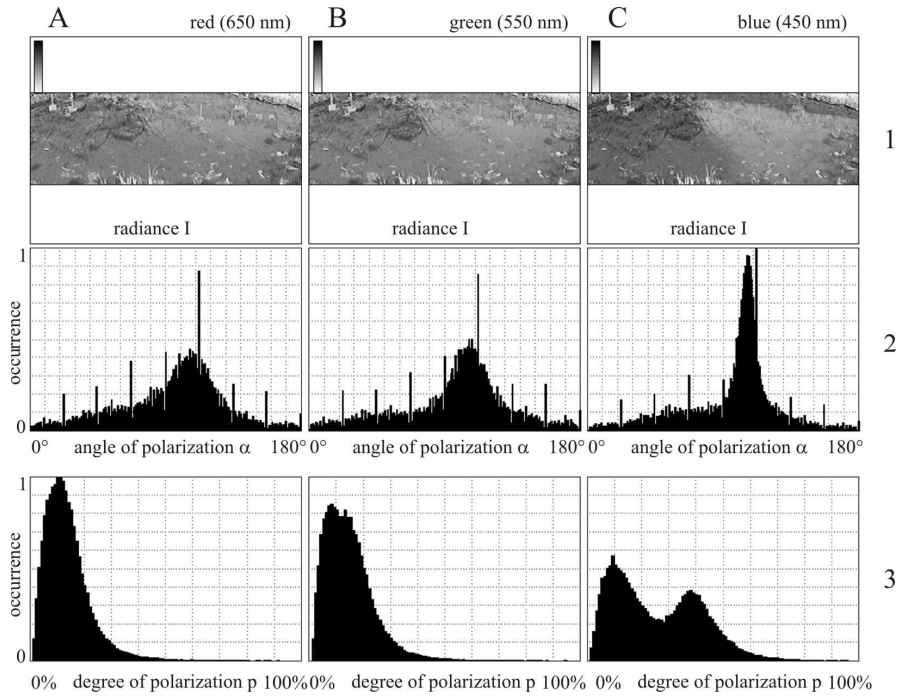

Fig. 12.5. As Fig. 12.3 for the pond in Fig. 12.4A. (After Fig. 6 of Horváth and Varjú, 1997, p. 1161).

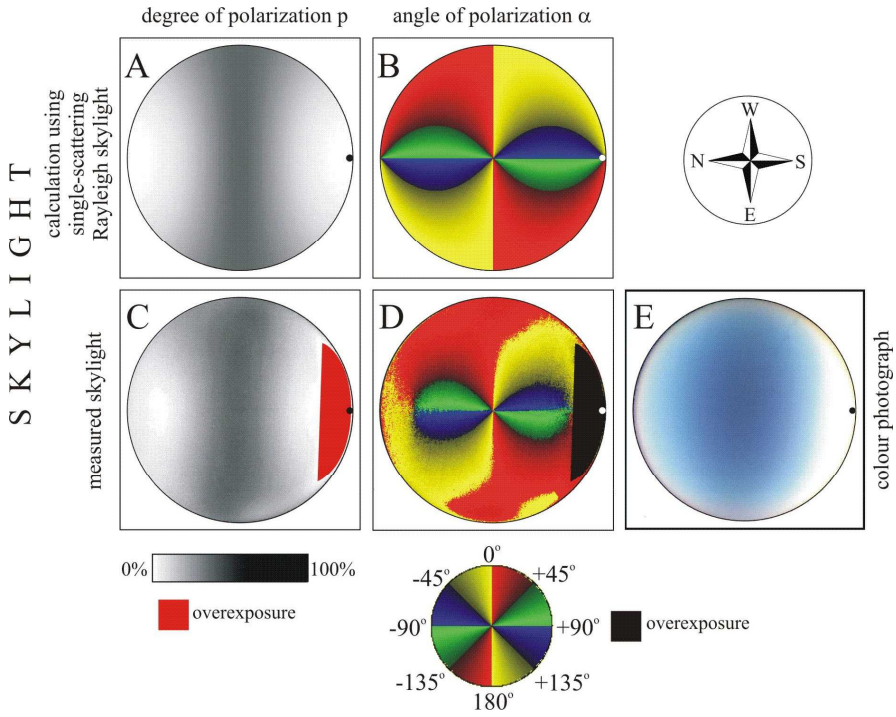

Fig. 12.6. A, B: Spatial distribution of the degree p and angle α of linear polarization of skylight calculated on the basis of the single-scattering Rayleigh theory for sunset. C, D: Patterns of p and α of skylight measured by 180° field-of-view imaging polarimetry at 550 nm at sunset. E: Photograph of the sunset sky during the measurement of patterns C and D. α is measured from the local meridian. The position of the setting sun is represented by a dot and the horizon is the perimeter of the circular patterns. (After Fig. 2 of Gál et al. 2001b, p. 108).

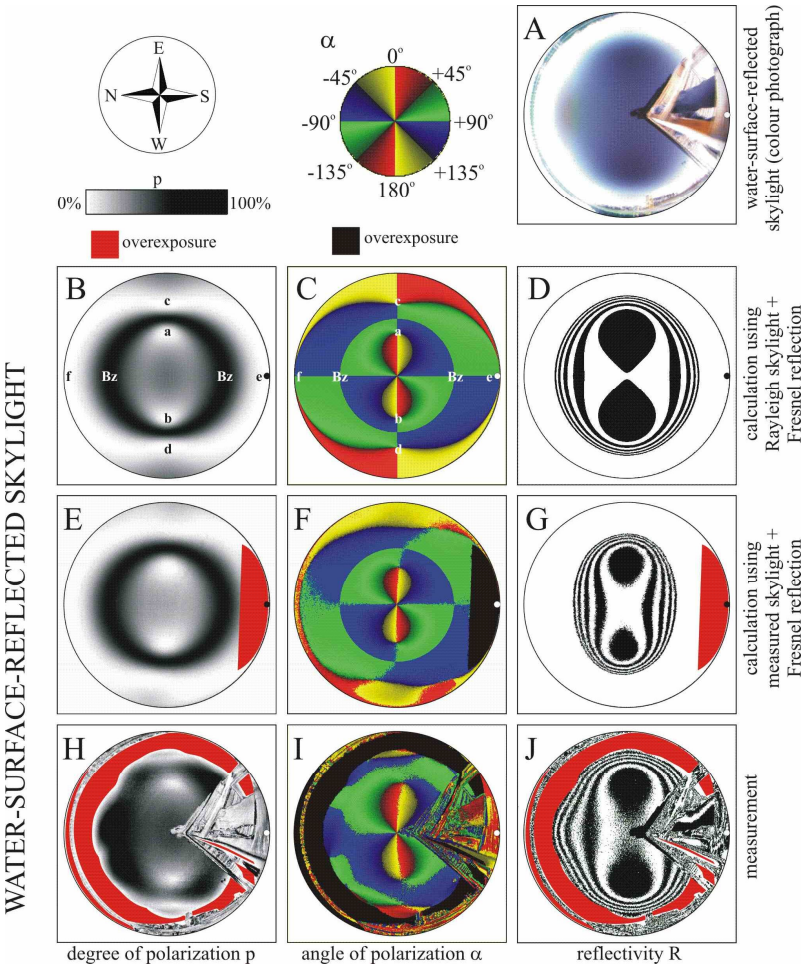

Fig. 12.7. A: Photograph of the mirror image of the sky reflected from the flat water surface at sunset. B, C, D: Theoretical patterns of the degree of linear polarization p, the angle of polarization α and the reflectivity R of the flat water surface calculated for single-scattered Rayleigh skylight (Figs. 12.6A,B) with the use of the Fresnel formulae. a, b, c, d, e, f: neutral points on the water surface. Bz: Brewster zone. E, F, G: Reflection-polarization patterns of the flat water surface calculated for the measured real skylight pattern (at 550 nm; Figs. 12.6C,D,E) with the use of the Fresnel formulae. H, I, J: Reflection-polarization patterns of the flat water surface measured by 180° field-of-view imaging polarimetry at 550 nm. The coding of the reflectivity values R is the following: The two central 8-shaped black patches in patterns D, G and J represent $R \leq 2\%$. The concentric oval and annular, alternately black and white narrow zones around these patches represent $R = 3, 4,..., 9, 10\%$ towards the periphery. The outermost annular red or black zone represents $R > 10\%$. α of light reflected from the water surface is measured from the vertical. The position of the mirror image of the sun is represented by a dot and the horizon is the perimeter of the circular patterns. (After Fig. 3 of Gál et al. 2001b, p. 109).

13 Polarization of Light Reflected by Cow-Dung and its Biological Relevance

Schwind (1991) observed that certain insects living on moist substrata or dung detect polarization of reflected light in a way similar to the water bug *Notonecta glauca* (Schwind 1985b) and many other water insects (Schwind 1995). The beetles *Megasternum boletophagum*, *Cryptopleurum minutum* and a *Cercyon* species of the subfamily Sphaeridiinae of the family Hydrophilidae were also attracted by the polarization of reflected light. Sphaeridiinae inhabit moist substrata such as plant debris and cow-dung. The polarization sensitivity of these insects operates in the UV. They are attracted whenever the degree of linear polarization p is high in the UV, irrespective of p in other wavelength ranges, and irrespective of colour and brightness of the background beneath a transparent polarizing, reflecting surface.

Horváth (unpublished) demonstrated how strong the reflection polarization of fresh cow-dung can be under different illumination conditions (direct sunlight or light from partially clouded skies) in the field (Fig. 13.1). Such investigations form the basis of the ecological problem how dung-loving insects can detect and find fresh dung. The cues attracting these insects to dung can be optical and olfactory. Ecologists dealing with this problem investigate the different insect species landing on a cow-dung and search a correlation between their number and the physical/chemical characteristics of the dung as a function of time elapsed after defecation. From a remote distance the smell of dung, even if it is quite fresh, may be not intensive enough to attract a large number of insects. In this case optical cues are more effective for the explanation of the observed high attractiveness of fresh dung to certain insects.

Figure 13.1 shows the reflection-polarizational characteristics of a sunlit greenish brown fresh cow-dung in a meadow recorded by video polarimetry at 650, 550 and 450 nm under a clear sky. We can see that the dung has similar brightness and colour as the ground of the grassy surrounding. However, the dung differs from the ground strikingly in the patterns of the degree p and angle α of polarization, especially in the blue because of the blueness of the incident skylight. Therefore the dung can efficiently be detected on the basis of the polarization of reflected light. p of light reflected specularly from fresh dung is higher than that reflected from the background with rough surface. Furthermore, the distribution of α of light reflected from fresh dung is more homogeneous than that reflected diffusely from the rough background surface. However, p of light reflected by dung decreases versus time as the moisture of dung is gradually lost (Horváth,

unpublished). Dry dung possesses a rough surface reflecting light diffusely, thus p of reflected light is low and the distribution of α is heterogeneous. Therefore it has similar reflection-polarizational characteristics as the surrounding. Dung insects prefer fresh dung, because they (i) can feed on it, suck its liquid components or lick its wet surface, (ii) can lay their eggs easily into the wet and soft substratum, where (iii) their larvae can develop before the dung becomes dry and hard. Thus, dung insects must find fresh dung as soon as possible. Fresh dung can be detected on the basis of the strong polarization of light reflected by its wet surface as shown in this chapter.

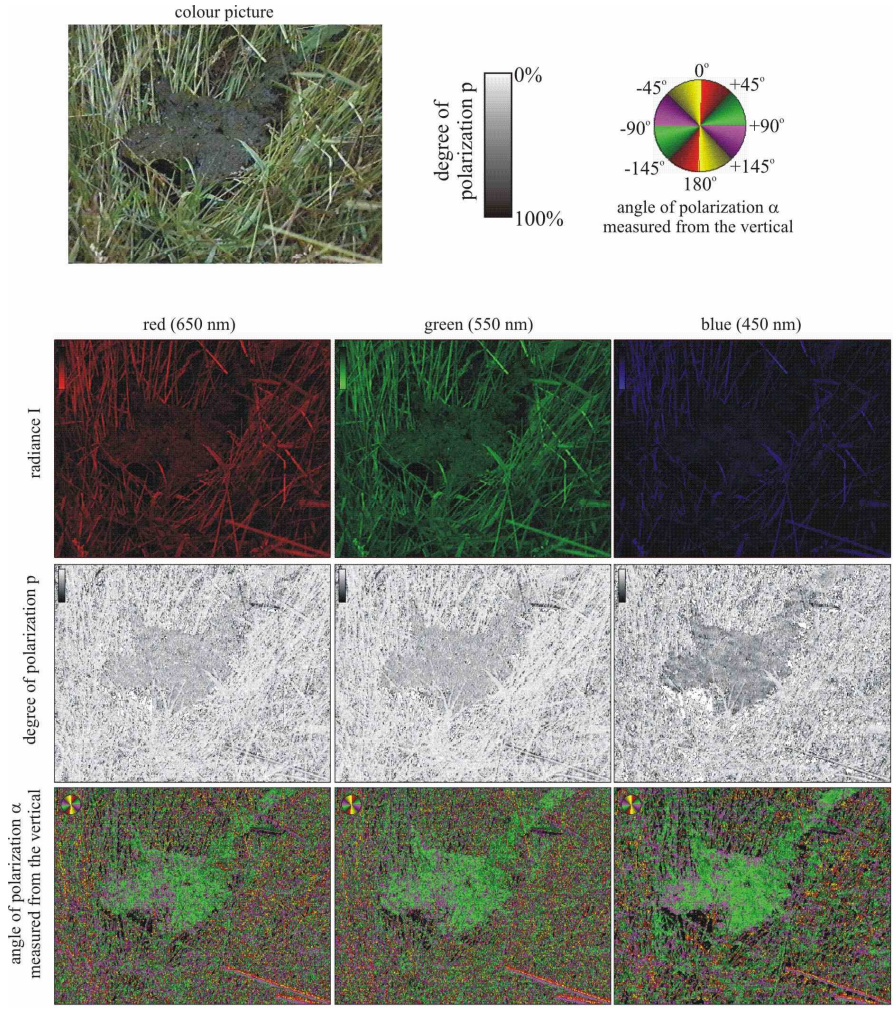

Fig. 13.1. Reflection-polarizational characteristics of a sunlit greenish brown fresh cow-dung in a meadow measured by video polarimetry in the red (650 nm), green (550 nm) and blue (450 nm) under a clear sky.

14 Polarization Pattern of a Fata Morgana: Why Aquatic Insects are not Attracted by Mirages?

It is a well-known phenomenon that on hot days mirages, called also Fata Morgana, may appear on roads. Such mirages are also seen on hot plains. There seems to be a pool of shiny water in the distance, which dissolves on approach. The sky, different landmarks and objects are mirrored in this ”pool”. In addition, the chaotic vibration of a mirage due to the turbulent flows of hot air imitates the wind-generated undulation of a water surface. Water insects, however, do not detect water on the basis of its brightness and colour but by means of the horizontal polarization of reflected light. Hence, the question arises, whether mirages can deceive water-seeking polarotactic insects.

To answer this question, Horváth et al. (1997) investigated and compared the polarizational characteristics of a mirage and a real water surface. They studied a mirage on a sunny hot day under clear sky conditions in the Tunisian desert within a salt pan. As at the study site the salt pan was totally dried out, a beautiful mirage could be observed near the horizon. The polarization pattern of the mirage and the landscape was measured by video polarimetry (Horváth and Varjú 1997). In addition, the reflection-polarization pattern of the surface of a sea was measured by video polarimetry on a sunny day under clear sky on the beach of Maharés in central Tunisia. Both the mirage and the sea were seen near the horizon at a great distance from the observer. Thus, the direction of view of the video camera recorder was always horizontal.

Figure 14.1A provides a view of a salt pan landscape over which a mirage has developed. The top half of the landscape is covered by clear sky. The darker, cone-shaped band in the middle of the picture is a mountain and its mirror image. The height of the mountain decreases gradually from right to left. Below the mountain the shiny, water-mimicking region is the sky's mirage merging into the sky at the left-hand side. Note that as the mirror-effect of a mirage is optically equivalent to total reflection of light, the horizontal area of the sky's mirage appears as bright as the sky itself. Thus, due to the mirage of the sky the mountain seems to be elevated above the apparent horizon, i.e. above the sandy bottom of the salt pan.

Figures 14.1B and 14.1C represent the spatial distributions of the degree of linear polarization p and angle of polarization α occurring within the same areas of the landscape as in Fig. 14.1A. The light reflected from the sandy bottom of the salt pan is slightly polarized. The skylight is partially polarized with $\alpha \approx 120^{o}$, measured clockwise from the vertical. Since the light from the sky and the sky's

mirage coincide in their p and α, there is no contrast between the sky and its mirage. In Fig. 14.2A histograms of α and p are shown for the rectangular area outlined in Figs. 14.1A-C. This area includes part of the sky and its mirage. As these histograms have only single peaks, there are no differences in the mean α- and p-values between the sky and its mirage.

Figures 14.1D, E and F provide the picture as well as the p- and α-patterns of another type of landscape, the muddy beach near the village of Maharés. The top half of the landscape as shown in Fig. 14.1D is occupied by clear sky. The darker band in the middle represents the sea. Note the undulating surface of the sea and, at the horizon, the two sailing boats with their vertical yards. There is a sharp brightness contrast between the sea and the sky. Similarly sharp contrast occurs in the maps of p and α in Figs.14.1E and F. The light reflected from the sea surface is partially horizontally polarized with an average $p = 19\%$. This low p is due to the small angle between the sea surface and the line of sight. The light coming from the clear sky is partially linearly polarized. At the time of day at which the measurement was performed $p \approx 8\%$ of the skylight near the horizon was even lower than that of light reflected from the sea surface. α in the strip of sky shown here is about 125^{o}. Figure 14.2B depicts quantitative data about α and p as measured for the rectangular area demarcated in Figs. 14.1D-F. In these histograms the double peaks again illustrate the polarization contrast between sky and sea.

These video-polarimetric measurements make it quite clear that there are significant differences between the polarizational characteristics of water-imitating mirages and real water surfaces. Flat water surfaces reflect usually more or less horizontally polarized light, while undulating water surfaces reflect light, the E-vector of which is perpendicular to the line between the point of reflection and the sun. The p of reflected light depends upon the direction of view and the undulation of the surface. If the water surface is far away from the observer, p is relatively low due to the grazing direction of view. If the horizon is defined by the border between the water surface and the sky, there is, in general, a high polarization contrast between water and sky in both p and α (Figs. 14.1D-F). The reason for this is that due to its reflection from water surfaces skylight gets repolarized (Fig. 14.3A).

On the other hand, in the desert landscape there are no contrasts of brightness, p and α between the sky and its mirage (Figs. 14.1A-C). Mirages are not usual reflections but are formed by gradual refraction and a total reflection of light (Fig. 14.3B). Fata Morganas are generated above hot plains. The nearer to the ground, the warmer the air and the smaller its index of refraction. Thus, the direction of grazing rays of light gradually changes to such an extent that the rays do not reach the ground, but after total reflection they are deflected upward (Fig. 14.3B). This gradual deflection provides an observer with the same impression as mirroring does. Such gradual refractions and total reflection of light do not change the polarization (Können 1985). This can be seen in Fig. 14.1. In comparison, if unpolarized incident light is reflected from a flat water surface under angles of incidence larger than 89.4^{o}, p of horizontally polarized reflected light is not higher

than about 2% (Guenther 1990). However, if one approaches the water surface, the p of reflected light increases abruptly as the angle of observation approaches the Brewster angle. In contrast, a mirage can never be reached by an observer, so that the direction of observation remains always the same, i.e. nearly horizontal.

Contrary to the calculated $p \approx 2\%$ of light reflected from a distant, flat water surface, p of light reflected from the sea surface in Fig. 14.2B is on average 19% and reaches a maximum of about 40%. The reason for this difference is twofold: On the one hand, the incident skylight is partially polarized ($p \approx 8\%$). On the other hand, due to wind the sea surface is undulating. Thus, the average angle of incidence of skylight reflected from the wavy water surface is lower than for an ideally flat, exactly horizontal water surface. As the angle of incidence gets smaller than 90^o, p of reflected light increases. In the case of unpolarized incident light the observed average and maximum p of reflected light (19% and 40%, respectively) indicates that the average and maximum angles of incidence are 84^o and 77^o, respectively.

Water insects detect water surfaces polarotactically, that is, by means of the horizontally polarized reflected light, rather than phototactically, that is, by means of the intensity of reflected light. Horváth et al. (1997) proposed that Fata Morganas can imitate water surfaces only for those animals, whose visual system is polarization-blind, but sensitive to brightness and colour differences. A polarization-sensitive water-seeking insect is able to detect the polarizational characteristics of a mirage. Since these characteristics differ considerably from those of real water surfaces, these animals cannot be deceived by and attracted to Fata Morganas.

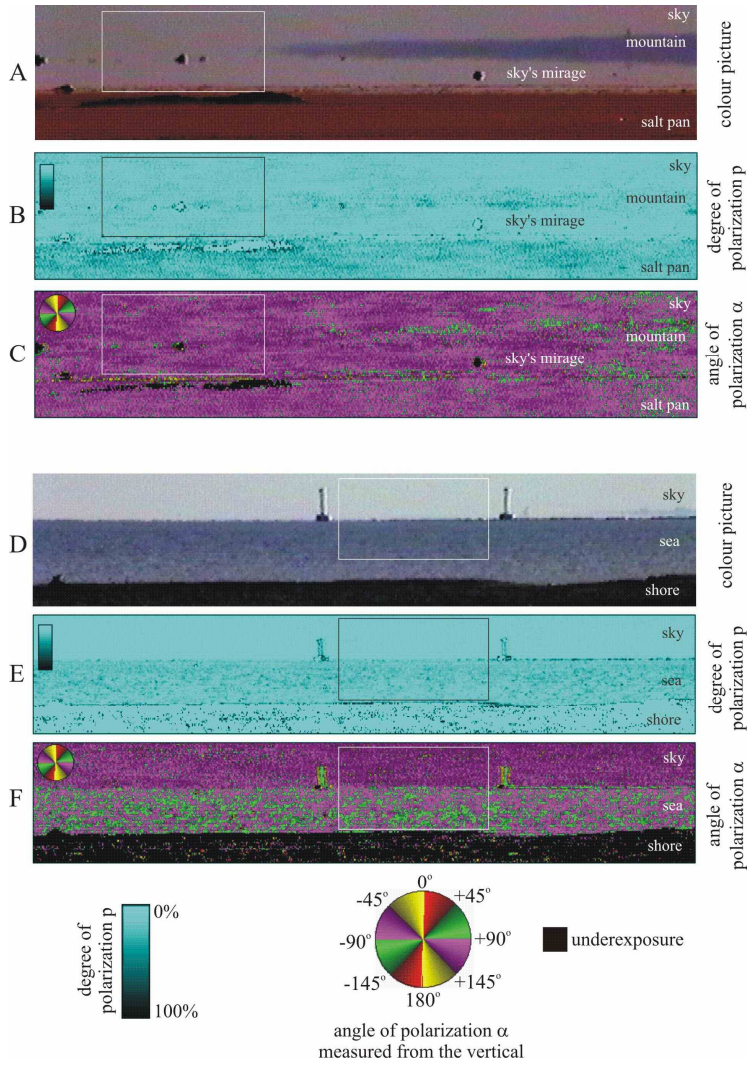

Fig. 14.1. A: Colour picture of a mirage occurring above a desert landscape, the salt pan Chott el Djerid in southern Tunisia. The dark cone-shaped band in the middle right is a mountain, tapering to the left. Below the mountain, the shiny stripe represents the mirage of the sky which merges in the real sky on the left. The lower half of the picture is occupied by the sandy floor of the salt pan. The vertical angular extension of the landscape shown is about 1.5°. The areas demarcated with rectangular windows represent the regions, for which the histograms of the degree p and angle α of linear polarization are given in Fig. 14.2. B, C: Spatial distribution of p and α of the landscape portrayed in A and measured by video polarimetry at 550 nm. D-F: Same as A-C, but now for a seaside landscape near Maharés, Tunisia. The uppermost part of the picture is filled with clear sky, the middle part is occupied by the sea and the lowermost part by the shore. (After Fig. 1 of Horváth et al., 1997, p. 301).

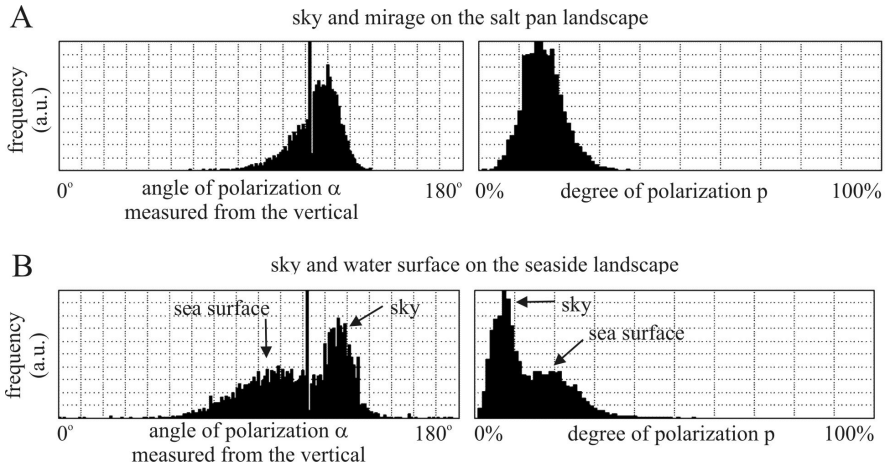

Fig. 14.2. Histograms (frequency in arbitrary units) of the angle of polarization α and the degree of linear polarization p computed for the areas demarcated with rectangular windows in Fig. 14.1. A: Mirage occurring above the desert plain of the salt pan. B: Seaside landscape at Maharés. (After Fig. 2 of Horváth et al., 1997, p. 302).

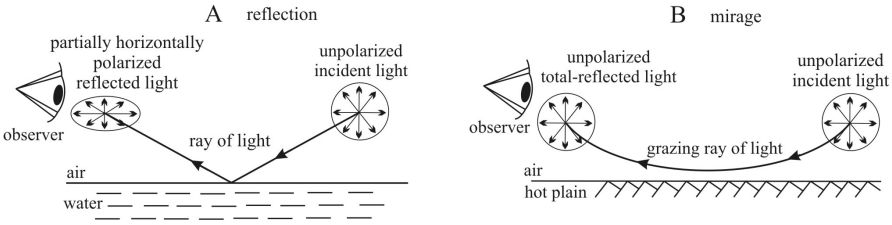

Fig. 14.3. A: Unpolarized incident light becomes partially horizontally linearly polarized when reflected from a water surface. B: Formation of a mirage above a hot plain, where the air temperature decreases exponentially as height above ground increases. As a consequence, the refractive index of air increases abruptly with height above ground, and grazing rays of light refract and after total reflection bend gradually into the eye of the observer. This gradual refraction and the total reflection do not alter the polarization of light. The inset figures represent polarization ellipses. The E-vector orientations are shown by double-headed arrows. (After Fig. 3 of Horváth et al., 1997, p. 302).

15 Polarizational Characteristics of the Underwater World

15.1 Underwater Polarized Light Field

In qualitative submarine visual observations down to 15 m Waterman (1954a) found that aquatic animals of the photic zone are surrounded by complex polarization patterns. He used a diving helmet and a hand-held polarization analyser, in which the light first passed through a plate of a uniaxial crystal cut perpendicularly to its optical axis, then through a quarter-wave plate and a linearly polarizing filter. The intensity of unpolarized light passing through this polariscope simply decreases. If the incident light is partially linearly polarized, a brightly coloured interference pattern of concentric, broken rings appears in the polariscope, from which the presence of polarization, the E-vector direction as well as a rough estimate of the degree of linear polarization p can be deduced. The interruptions of the broken rings occur in orthogonal quadrants, and the axis of one of the pairs of these opposed quadrants is parallel to the E-vector of incident light. The intensity of the pattern and the number of concentric rings vary with p. With this polariscope the E-vector direction could be obtained with an accuracy of about $\pm 3^{\circ}$.

Waterman (1954a) found the following characteristics of the submarine polarized light field (Fig. 15.1): Underwater there are two polarization patterns, one inside and one outside the Snell window, which is visible within the critical angle of the refractive cone.[1] Due to refraction at the water surface, the entire 180°

[1] The boundary of Snell window extends up to $\beta_{SW} = arc\ tan\ [n_a/(n_w^2 - n_a^2)^{1/2}] = 48.5^{\circ}$ measured from the zenith, where $n_a = 1$ and $n_w = 1.333$ are the refractive indices of air and water, respectively. Due to refraction the abovewater world visible through the Snell window is distorted (Horváth and Varjú 1991). A point of the firmament with a zenith angle β is apparently seen in direction $\beta^* = arc\ tan\ [n_a sin\beta/(n_w^2 - n_a^2 sin^2\beta)^{1/2}]$ from the vertical. The apparent horizon corresponds to the boundary of Snell window. Light from Snell window in shallow waters contains most of the components of the spectrum available to terrestrial animals. Outside Snell window the light from deeper water layers is reflected and it is dim and its spectral range is restricted especially in open waters. At the boundary of Snell window light from near the abovewater horizon is split into a rainbow due to dispersion (Jerlov 1976). An abovewater object directly overhead suffers

field of view above the water is compressed into a cone with 48.2° half-angle. The polarization pattern of the sky is visible within the Snell window. Chapter 15.3 deals in detail with this pattern. Outside the Snell window is another polarization pattern created by the scattering of sunlight entering the water. Both of these underwater polarization patterns are complex and contain information about the location of the sun. An aquatic animal able to maintain a stable spatial orientation relative to the gravitation and capable of analyzing E-vector direction would have a sun compass available even if the glitter pattern at the depth of the animal would prevent it from seeing the sun directly.

The underwater polarization pattern forms a virtual sphere that surrounds the observer. The highest p occurs in a band along a great circle of this sphere perpendicularly to the refracted sunlight, and the E-vector is always perpendicular to the scattering plane (Fig. 15.1). On cloudy days most of the underwater polarization can be attributed to the scattering of light by water molecules, with little contribution from the polarized skylight.

Small particles suspended in the water scatter most strongly the UV and blue light, while water molecules have absorption bands in the UV and red (Jerlov 1976). Dissolved organic materials absorb UV light extensively, thus the UV light is most attenuated. Attenuation of the blue and red wavelengths can be accredited mostly to absorption by various chlorophylls (Wetzel 1975). p is highest near the water surface (Ivanoff and Waterman 1958b) and decreases rapidly with depth within the first 40 m. The underwater polarization is influenced above a critical depth by the sky as well as the relation between the observer's line of sight and the direction of the underwater rays. Waterman (1954a) hypothesized that under totally overcast skies the E-vector of the underwater polarized light is overall horizontal and the polarization pattern in deep waters is similar to that near the surface on a heavily overcast day.

After the pioneering observations of light polarization in the ocean (Waterman 1954a), a huge amount of experimental (e.g. Ivanoff and Waterman 1958a,b; Waterman and Westell 1956; Timofeeva 1961, 1962, 1969, 1974; Jerlov 1963, 1976; Ivanoff 1974; Loew and McFarland 1990; Novales Flamarique and Hawryshyn 1997a) and theoretical (e.g. Kattawar and Adams 1989; Adams and Kattawar 1993; Kattawar 1994) information has been accumulated about the underwater polarized light field. Submersible point-source scanning polarimeters with different colour filters made possible to collect data in shallow as well as deep marine waters (e.g. Ivanoff and Waterman 1958b; Tyler 1963; Ivanoff 1974).

---

little refractive distortion when seen from the water, but the image of objects near the horizon is substantially compressed (Horváth and Varjú 1991). When the water is flat, the boundary of Snell window is sharp, and there is a strong contrast between the bright scene above and the darker reflections from deep water. Some plankton-feeding fishes living near the surface have an area of enhanced acuity on that part of their retinae where the boundary of Snell window comes to lie (Munk 1970). One of the two foveae of the compound eye in the water bug *Notonecta glauca* also looks in the direction of the edge of Snell window when the animal rests upside down below the water surface (Schwind 1983b, 1985b).

These results are reviewed and discussed thoroughly by Jerlov (1976). The most complete description of underwater polarization in the visible part of the spectrum combining laboratory and field experiments was given by Timofeeva (1961, 1962, 1969, 1974). In milky solutions in the laboratory, she studied p and α of underwater scattered light as functions of the direction of observation and the azimuth angle of the light source. Ivanoff and Waterman (1958b) as well as Timofeeva (1961) found that p was highest for both milky solutions and ocean waters with the highest absorption and lowest dispersion, regardless of the azimut angle of the source. Timofeeva (1969, 1974) observed also submarine neutral points in the vertical plane through the observer and the sun. Waterman (1955), Waterman and Westell (1956), Ivanoff and Waterman (1958b) as well as Timofeeva (1969, 1974) found that p decreases with increasing depth, and at a critical depth it reaches a constant maximum value horizontally, when the radiance distribution no longer varies with direction of observation and the downwelling light becomes more vertical. This critical depth depends on the optical properties of the medium and varies from 40 m (Ivanoff and Waterman 1958b) to 200 m (Waterman 1955) in very clear waters. p near the surface of clear water was found to reach 60% depending on the solar azimuth, but at greater depths p dropped to 30% (Ivanoff and Waterman 1958b). Tyler (1963) calculated that even under cloudy skies, p of light in deep water can reach 30-40%. The lowest p occurs approximately at 470 nm, at which light is least attenuated in clear seawater (Hawryshyn 1992).

Lythgoe and Hemmings (1967) reported that when the transmission axis of a linearly polarizing filter was oriented in front of their eyes to exclude the maximally polarized underwater spacelight, the apparent brightness of small fishes (Sparidae and *Atherina*) was reduced less than the background spacelight, and thus fishes had a higher contrast against their background. Furthermore, distant fishes, invisible to the naked eye became visible using the polarizer. Photographing underwater white, black and grey panels through a linear polarizer with two orthogonal transmission axes from different distances and at various depths under cloudless skies, Lythgoe and Hemmings observed that the unobstructed water background has undergone a greater brightness change than the targets. One target, which was brighter than its background with a given orientation of the polarizer, became darker when the polarizer was rotated by 90^{o}. In another experiment, a polarizer was fixed to the outer surface of a diving helmet and oriented to exclude the maximally polarized underwater light. The horizontal distances at which different grey underwater targets just became invisible seen through the helmet with and without the polarizer were measured. Lythgoe and Hemmings found that the polarizer increased or decreased the range at which underwater objects brighter or darker than the water background could be seen. They suggested that polarization sensitivity could enable aquatic animals to see distant objects in clear waters. However, Luria and Kinney (1974) argued that there are so many drawbacks in using polarizers as means of enhancing contrast that underwater vision with polarizers is not reliably superior to vision without them.

The above-mentioned pioneering results of Waterman (1954a) were confirmed also by the polarimetric investigations of Cronin and Shashar (2001). They measured the spatial and temporal variation of the radiance I, p and α of light in clear, tropical marine waters under partly cloudy skies from 350 to 600 nm throughout the day on a coral reef at a depth of 15 m. They used a submersible rotating-analyzer, point-source (15^{o} field-of-view) sequential polarimeter based on a spectrometer with sensitivity in the UV and visible spectral ranges. Light entering a collector aperture and passing through a rotatable linearly polarizing filter was conducted to the spectrometer by a 10 m optical fibre. Polarizational characteristics of the downwelling light were investigated in different directions in the upper hemisphere. They found that both p and α varied only slightly with wavelength. Light was sometimes less polarized in the UV and maximally polarized in the visible range, or *vice versa*, depending on the viewing direction, solar elevation and sky cloudyness. Thus, they could find no particular optimum wavelength range for polarization-sensitive photoreceptors of underwater animals. p was always less than 50%.

The complex underwater intensity and polarization patterns are modified by spatio-temporal variations of light distribution due to surface waves (Jelley 1989), which focus sunlight at different depths depending on the wavelength. Surface ripples focus light at depths of few centimetres, longer waves at greater depths (Schenck 1957). Wave-focusing causes flicker, the frequency of which decreases with increasing depth.

15.2 Underwater Polarized UV Light and the UV Polarization Sensitivity in Fishes

The ability to utilize UV light (UV-A: 320 nm < λ < 400 nm) is widespread among terrestrial and aquatic arthropods, fresh- and saltwater fishes (e.g. Tovée 1995), reptiles (e.g. Fleishman et al. 1993), birds (e.g. Bennett et al. 1996) and some amphibians and tiny mammals (e.g. Goldsmith 1994). In fishes, UV sensitivity can persist throughout most of the animal's lifetime as in the goldfish *Carassius auratus* (Neumeyer 1985; Fratzer et al. 1994), or it may be restricted primarily to specific periods such as the presmolting and reproductive stages of salmons (Beaudet et al. 1993; Novales Flamarique and Hawryshyn 1996; Beaudet et al. 1997).

There are several possible functions of UV sensitivity in fishes, e.g. contrast enhancement of planktonic targets that absorb or scatter UV light differently from the water background (Loew et al. 1993; Browman et al. 1994), or reflective communication, especially among schooling fishes (e.g. Denton and Rowe 1994), or polarization sensitivity (e.g. Coughlin and Hawryshyn 1995). Because shorter wavelengths are scattered most strongly in water (McFarland and Munz 1975; Novales Flamarique and Hawryshyn 1997a) and UV cones are primarily located in areas of low photoreceptor density of the retinae in various fishes (e.g. Beaudet et al. 1997), furthermore since involving the near-UV part of the spectrum to

vision enhances the chromatic aberration of the dioptric apparatus (e.g. Sivak and Mandelman 1982), it is believed that UV sensitivity does not enhance the visual acuity in fishes in contrast to sensitivity in other parts of the spectrum.

The UV-sensitive neural pathways are usually polarization sensitive in fishes (e.g. Hawryshyn and McFarland 1987; Parkyn and Hawryshyn 1993; Coughlin and Hawryshyn 1995). This is not always the case for the neural mechanisms mediating sensitivity in other parts of the spectrum, e.g. the blue cones in certain cyprinids and salmonids (Hawryshyn and McFarland 1987; Coughlin and Hawryshyn 1995) and the green and red cones in green sunfishes (Cameron and Pugh 1991; Novales Flamarique and Hawryshyn 1997b) are polarization-blind.

Studying the photic environment of a salmonid nursery lake, Novales Flamarique et al. (1992) found that although strongest attenuation of light occurred in the UV, there was enough light to stimulate all UV-sensitive photoreceptors in juvenile salmonid retinae from a depth of 18 m to the surface. This depth restriction may be linked to the observed salmonid movements close to the surface during crepuscular periods, when the relative proportion of UV, blue and green light with respect to the entire spectrum was maximal while that of red light was minimal. UV polarization sensitivity may enable juvenile salmonids to detect zooplankton which absorb and polarize UV light due to their pigments and birefringent skeletons.

Novales Flamarique and Hawryshyn (1997a) measured the spectral distribution of the underwater polarized light field at a depth of 4 m under clear skies in the upper photic zone of meso-eutrophic waters, i.e. blue-green waters containing medium to high chlorophyll-A concentrations. They found that the maximum degree of polarization p_{max} during the day was 35-40%, but at dawn and dusk it increased to 67%. The reason for this is that during the crepuscular period underwater polarization is mainly determined by the incident light from the sky, which is maximally polarized when the sun is on the horizon. At dawn and dusk also the relative contribution of blue and UV wavelengths to the total spectrum increased. In blue oligotrophic waters, where smaller particles create higher Rayleigh scattering, p_{max} = 60% was measured for daylight hours by Waterman and Westell (1956) as well as Ivanoff and Waterman (1958b). Electrophysiological recordings from the optic nerve of young rainbow trouts (*Oncorhynchus mykiss*) stimulated by partially linearly polarized light with spectral characteristics mimicking that of the natural underwater light field indicated that the threshold of p for detection of polarization is between 63% and 72%. This threshold value is very high compared with those as low as 5-10% in field crickets and honeybees. These physiological findings suggest that the use of underwater polarization by rainbow trouts should be restricted to crepuscular periods and only to regions near (< 7 m) the water surface.

15.3 Underwater Refraction-Polarization Patterns of Skylight Perceived by Aquatic Animals through the Snell Window of the Flat Water Surface

In this chapter we give a quantitative account of the physics of repolarization of skylight transmitted through the flat water surface on the basis of Horváth and Varjú (1995). The polarizational characteristics of skylight are described by the single-scattering Rayleigh model (Coulson 1988). It is assumed that the air-water interface is without ripples and the refraction polarization of light at the water surface is governed by the Fresnel formulae (Guenther 1990). The contribution of underwater polarization due to scattering in water is neglected. This approximation is reasonable if the underwater observer is near the water surface.

15.3.1 Refraction-Polarization Ellipses, Degree and Angle of Linear Polarization of Refracted Light

In Fig. 15.2 the amplitude transmission coefficients σ_{par} and σ_{perp} for parallel and perpendicular E-vector of totally linearly polarized incident light are shown as a function of the incident angle θ_i at the air-water interface. The vertically polarized light is slightly less attenuated than the horizontally polarized light at all θ_i except $\theta_i = 0^o$ and $\theta_i = 90^o$. When the E-vector direction of totally polarized light is oblique, it can be decomposed into a horizontally and a vertically polarized component both of which oscillate coherently. Since the vertical component is less attenuated, the plane of polarization of the sum of the components will become more vertical, so that the E-vector rotates towards the vertical after refraction if $\theta_i \neq 0^o$ and $\theta_i \neq 90^o$.

The refractive indices of air and water vary slightly with the wavelength of light, such that less light is transmitted in the UV than in the visible range of the spectrum (Guenther 1990). This dispersion, however, is not strong. The refractive index of red (656.3 nm) light amounts to 1.3312, that of UV (308.2 nm) light to 1.3567. Therefore one can omit the spectral character of skylight and use in the calculations the refractive indices $n_{air} = 1$ and $n_{water} = 1.333$, that correspond to wavelengths in the middle range (587.6 nm) of the visible spectrum.

After refraction at the water surface unpolarized incident light becomes partially linearly polarized with vertical E-vector at any θ_i. In Figs. 15.3A,B the shape of the refraction-polarization ellipses (RPE's) are depicted as a function of θ_i of unpolarized incoming light. Figures 15.3C,D show the degree of linear polarization p_r of refracted light and the transmissivity T of the water surface for unpolarized incident light versus θ_i. The greater the θ_i, the larger the p_r of refracted light (Fig. 15.3C). As θ_i increases, the size of the RPE decreases (Figs. 15.3A,B) due to the decrease of T (Fig. 15.3D). Since $\sigma_{par} \leq \sigma_{perp}$ (Fig. 15.2) the RPE for unpolarized incident light is slightly elongated (Figs. 15.3A,B).

If the incident light is partially linearly polarized, as is skylight, the spatial distribution of the incident E-vectors is characterized by a polarization ellipse. In this case the influence of refraction on the unpolarized and totally polarized parts of incident light can be superimposed. The unpolarized component is partially converted into vertically polarized light (Fig. 15.3) and the totally polarized part rotates its plane of oscillation towards the vertical, unless its E-vector is horizontal or vertical. Figure 15.4 illustrates the RPE's, p_r and α_r of refracted light as a function of θ_i for $p_i = 0.5$ and different α_i of the incident light. Since the vertical component of the incident electric field vectors is less attenuated than the horizontal one (Fig. 15.2), the RPE rotates towards the vertical, i.e. α_r decreases as θ_i increases, whenever the incident E-vector is oblique relative to the water surface (Figs. 15.4B,C), but not when the incident E-vector is vertical (Fig. 15.4A) or horizontal (Fig. 15.4D). Figure 15.4 also demonstrates that p_r of refracted light increases with increasing θ_i when α_i is less than 30^o (Figs. 15.4A,B). The opposite is true when α_i is larger than 60^o (Figs. 15.4C,D).

15.3.2 Refraction-Polarization Patterns of Skylight Visible Through Snell Window Versus the Solar Zenith Angle

One of the possible ways of displaying the celestial polarization pattern is to represent the distribution of polarization ellipses of skylight in two dimensions. This is shown in Fig. 15.5 for four different solar zenith angles. Figures. 15.6A-D show the corresponding patterns of RPE's, and Fig. 15.6E represents the refraction-polarization pattern calculated for unpolarized light of a totally overcast sky. Spectral and intensity differences in skylight were not taken into consideration.

Another way of displaying is to plot lines along which p and α of incident and refracted skylight are constant. For a better visualization we shaded the areas between neighbouring isolines with different grey tones. Figure 15.7 shows the distribution of p of skylight for different solar zenith angles θ_S. Figures 15.8A-D demonstrate the corresponding patterns after refraction at the flat water surface under clear skies. Figure 15.8E was calculated for unpolarized light of an overcast sky. In Fig. 15.9 some contour lines of equal p of skylight refracted within the Snell window are shown for different θ_S to represent the neutral points near the apparent sun and antisun. In Fig. 15.7 the celestial neutral points coincide with the solar and antisolar points. Figure 15.9 demonstrates, however, that the neutral points within the Snell window do not correspond to the position of the apparent sun and antisun but they are shifted further away from the latter, except when the sun is at the zenith (Fig. 15.9A).

In addition to the distortion of the contour lines of p by refraction, there are also some qualitative differences between the celestial polarization patterns in Fig. 15.7 and the corresponding refraction-polarization patterns in Figs. 15.8 and 15.9. When the sun approaches the zenith, the band of maximum p of the firmament with nearly horizontally polarized skylight lies near the horizon (Figs. 15.7A,B).

Since p of refracted light for nearly horizontally polarized incoming light decreases with increasing incident angle (Figs. 15.4C,D), the contour lines of equal p of refracted light move further away from the solar point, i.e. they are shifted towards the boundary of Snell window (Figs. 15.8A,B and 15.9A,B). However, when the sun approaches the horizon, the celestial maximally polarized band with nearly vertically polarized skylight lies near the zenith (Figs. 15.7C,D). Since p of refracted light for nearly vertically polarized incoming light increases with increasing incident angle (Figs. 15.4A,B), the contour lines of equal p of refracted light are shifted towards the solar and antisolar points (Figs. 15.8C,D and 15.9C,D). This results in two strongly polarized wedge-shaped patches near the boundary of Snell window perpendicularly to the solar meridian (Figs. 15.8C,D and 15.9C,D).

The α-patterns of skylight are shown in Fig. 15.10 as a function of the solar zenith angle θ_s. Since all celestial E-vectors are directed horizontally when the sun is at the zenith, the pattern in Fig. 15.10A is uniformly dark blue. The corresponding patterns of refracted skylight are shown in Fig. 15.11. The E-vector of refracted light is also always horizontal when the sun is at the zenith, the pattern in Fig. 15.11A is, therefore, also homogeneously black. In this two-dimensional representation the contour lines of equal α in Figs. 15.10B-D converge. One of the celestial points of convergence is always the zenith, and the other ones are the solar and antisolar points (Figs. 15.10B-D).

The most prominent difference between the patterns in Figs. 15.10 and 15.11 is that the point of convergence at the sun (Fig. 15.10B) is split into two points of convergence positioned around the apparent sun along the solar meridian (Fig. 15.11B). The skylight from the solar meridian is always horizontally polarized and its p decreases gradually towards the sun, where it is unpolarized. The unpolarized direct sunlight becomes slightly vertically polarized after refraction (Fig. 15.3). As the direction of view moves off the sun, p of skylight gradually increases along the solar meridian (Fig. 15.7). If p of this light is low, i.e. the angular distance from the sun is short, then the refracted light also becomes partially vertically polarized. However, if it is polarized over a certain threshold, the refracted light remains partially horizontally polarized but its p is slightly reduced (Fig. 15.4D). Hence there are two distinct points along the solar meridian and near the apparent sun where the direction of polarization of refracted skylight switches from vertical to horizontal. These points coincide with the two points of convergence around the apparent sun (Fig. 15.11B) and they constitute the two neutral points there (Fig. 15.9B).

In Figs. 15.12A-D the two-dimensional patterns of transmissivity T of the flat air-water interface are shown for different θ_S. The T-pattern in Fig. 15.12E is computed for unpolarized light of an overcast sky. These patterns have in all cases approximately a cylindrical symmetry for $T < 95\%$. The T-pattern calculated for clear sky with the sun at the zenith (Fig. 15.12A) and that for unpolarized skylight (Fig. 15.12E) have an exact cylindrical symmetry. As the sun approaches the horizon, the contour lines of equal T gradually become elongated, they are flattened perpendicularly to the solar meridian. The patches in Figs. 15.12C,D represent those regions where $T > 98\%$. These bright patches correspond to the

two dark patches of the water surface visible from air, where the surface is particularly transparent (see Figs. 11.8C,D and 12.7D,G,J).

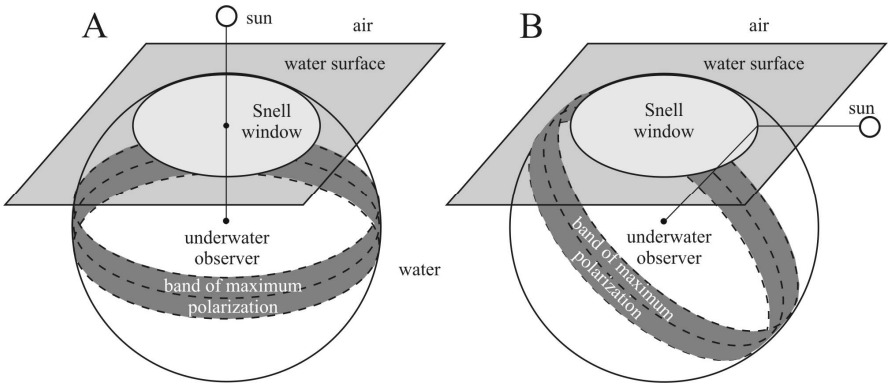

Fig. 15.1. The underwater polarization pattern forms a virtual sphere that surrounds the observer. The distribution of polarization underwater depends on the position of the sun and the relative stillness of the water surface. The highest degree of linear polarization occurs in a band that runs along a great circle of this sphere perpendicularly to the refracted sunlight, and the E-vector is always perpendicular to the scattering plane. (After Fig. 3 of Hawryshyn 1992, p. 167).

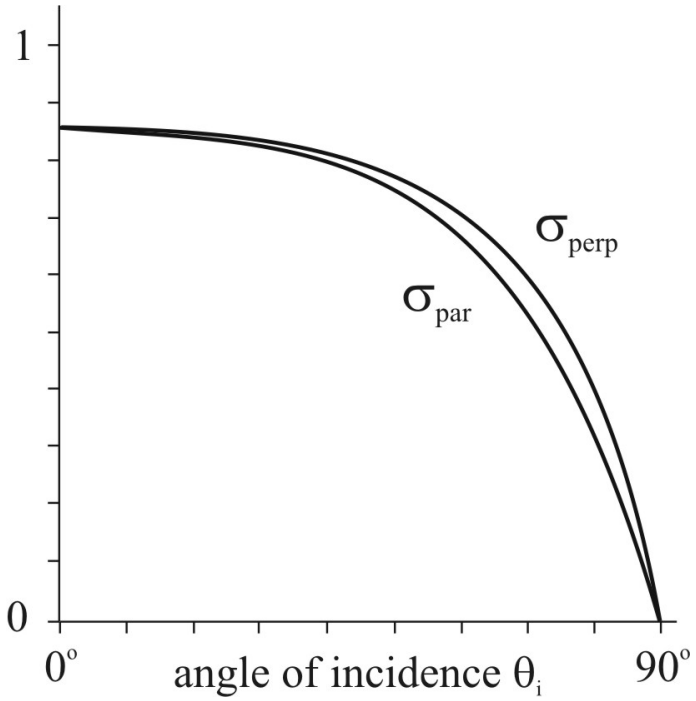

Fig. 15.2. Amplitude transmission coefficients σ_{par} and σ_{perp} as a function of the incident angle θ_i measured from the vertical for parallel and perpendicular E-vector of totally linearly polarized incoming light with respect to the water surface calculated for the flat air-water interface with $n_{air} = 1$ and $n_{water} = 1.333$. (After Fig. 1 of Horváth and Varjú 1995, p. 1653).

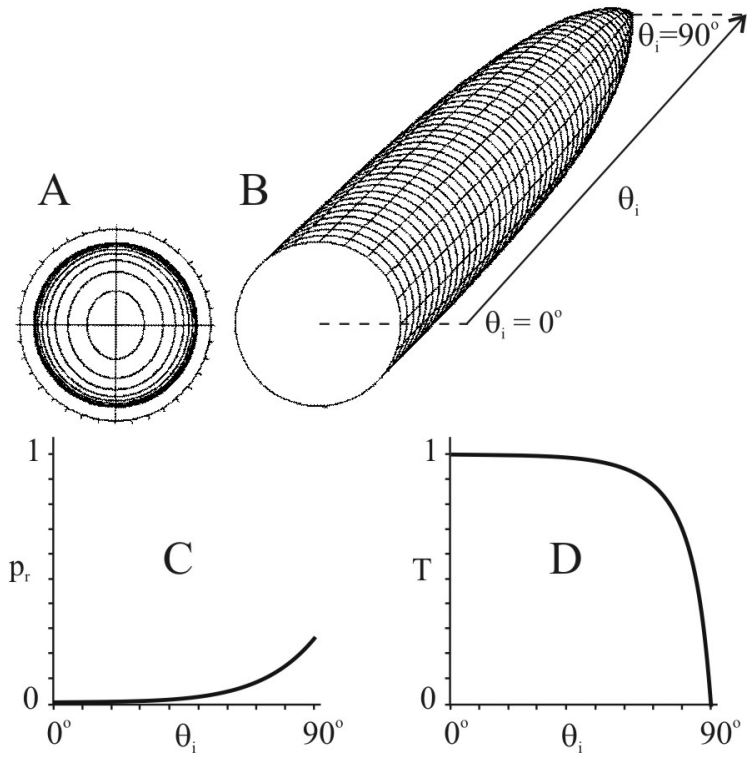

Fig. 15.3. A: Refraction-polarization ellipses for unpolarized (p_i = 0) incident light as a function of the incident angle θ_i increasing from 0° to 90° in steps of $\Delta\theta_i$ = 9° from the centre towards the periphery. The outermost circle with a graduated scale shows the spatial distribution of the electric field vector of unpolarized light. B: Representation of the refraction-polarization ellipses versus θ_i in a perspectivic view. C, D: Degree of linear polarization p_r of refracted light, and transmissivity T of the flat air-water interface versus θ_i for unpolarized incoming light. (After Fig. 2 of Horváth and Varjú 1995, p. 1653).

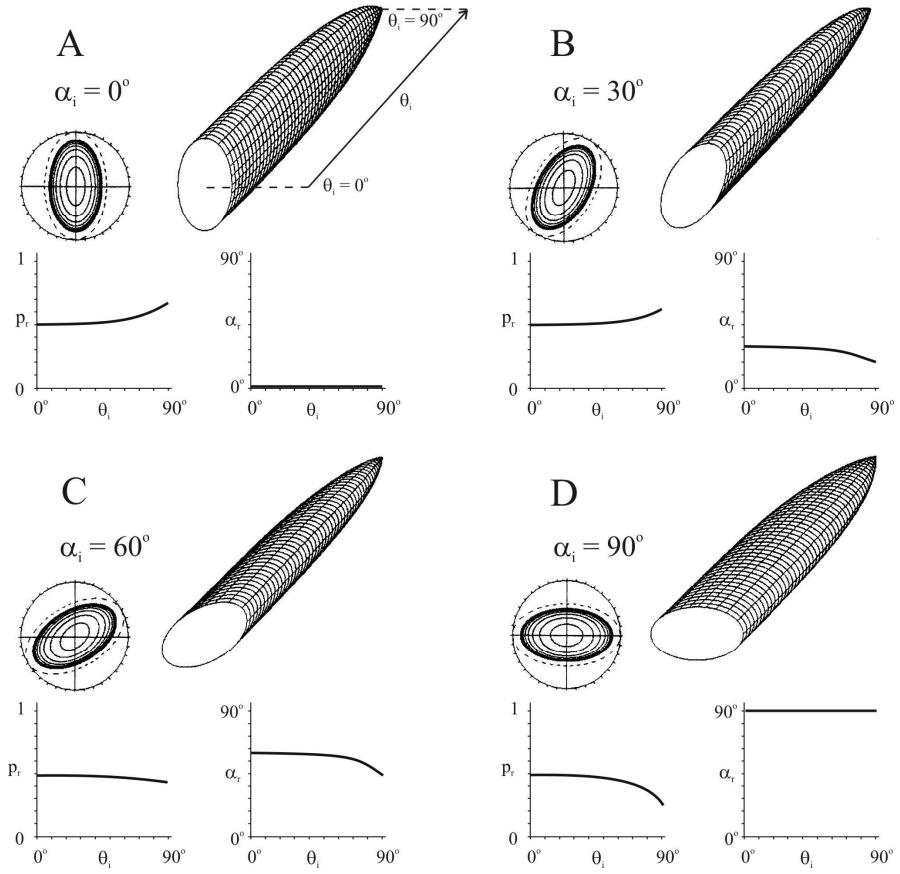

Fig. 15.4. Refraction-polarization ellipses, degree p_r and angle α_r of linear polarization of refracted light as a function of the incident angle θ_i of partially linearly polarized incident light with $p_i = 0.5$ for different α_i measured from the vertical. The dashed ellipses illustrate the polarization ellipses of incident light. (After Fig. 3 of Horváth and Varjú 1995, p. 1654).

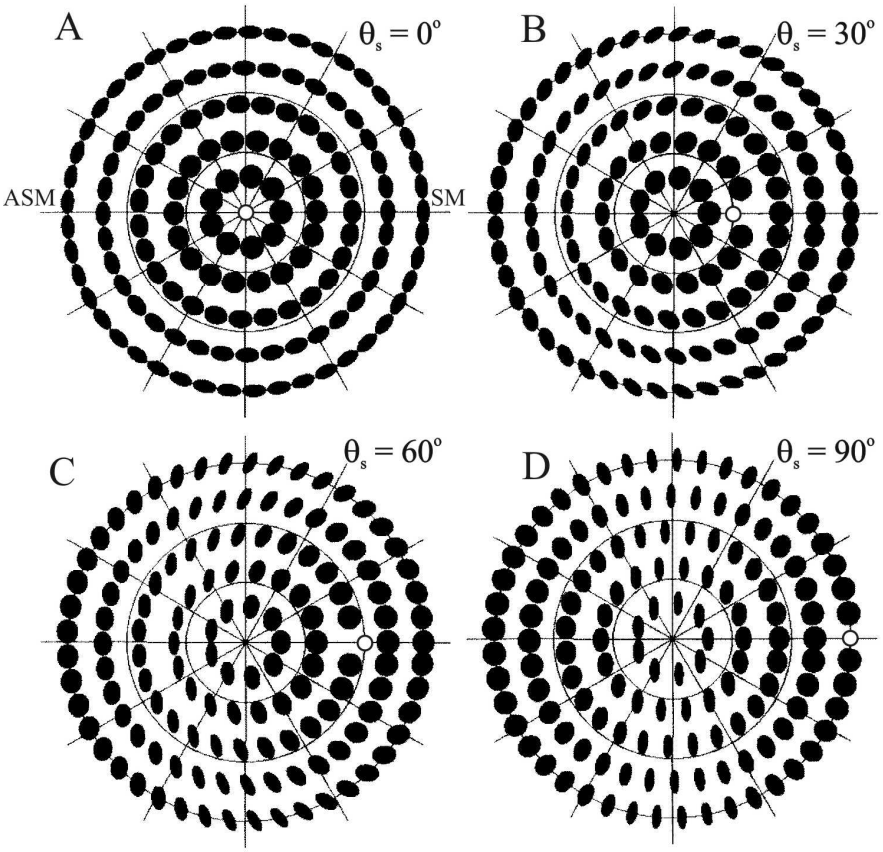

Fig. 15.5. Two-dimensional representation of the pattern of polarization ellipses of skylight for different solar zenith angles θ_s. The polar-coordinate system represents the celestial hemisphere. The zenith is at the centre, the sun is indicated by a dot, the horizon is the outermost circle; SM: solar meridian; ASM: antisolar meridian. The direction of observation θ from the zenith changes radially (zenith: $\theta_z = 0^o$, horizon: $\theta_h = 90^o$). The azimuth angle φ is the angle between the solar meridian SM and the meridian of the point observed (solar meridian: $\varphi_{SM} = 0^o$, antisolar meridian: $\varphi_{ASM} = 180^o$). (After Fig. 4 of Horváth and Varjú 1995, p. 1655).

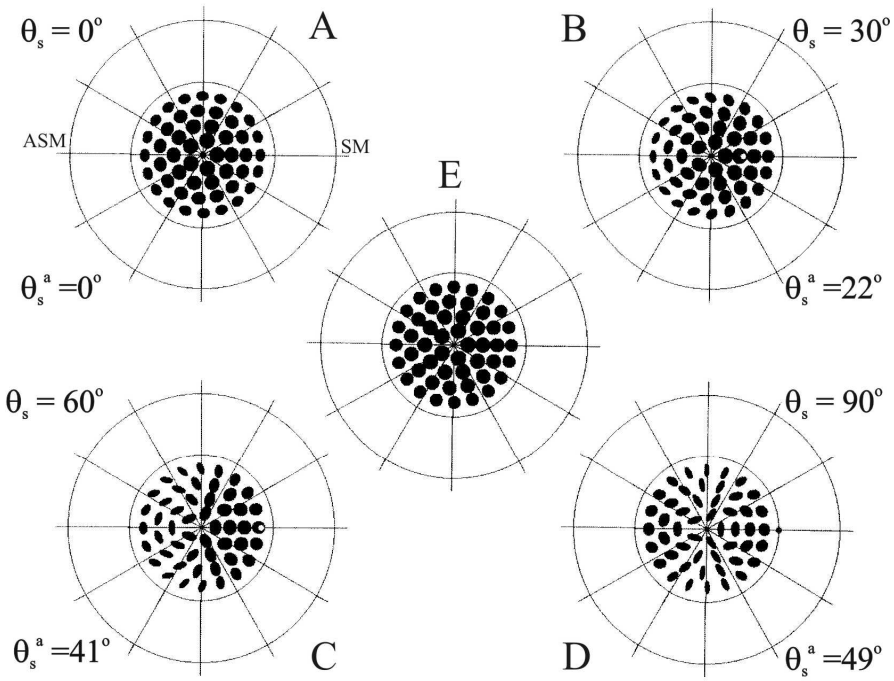

Fig. 15.6. A-D: Two-dimensional representation of the pattern of refraction-polarization ellipses of skylight visible from water through Snell window of the flat water surface for different solar zenith angles θ_s and for the corresponding apparent zenith angles θ_s^a within the Snell window. The large circles correspond to the abovewater horizon, the smaller ones represent the boundary of Snell window with an angular diameter of 97°. Other conventions as in Fig. 15.5. E: Pattern of the refraction-polarization ellipses within Snell window for unpolarized light from a totally overcast sky. (After Fig. 5 of Horváth and Varjú 1995, p. 1656).

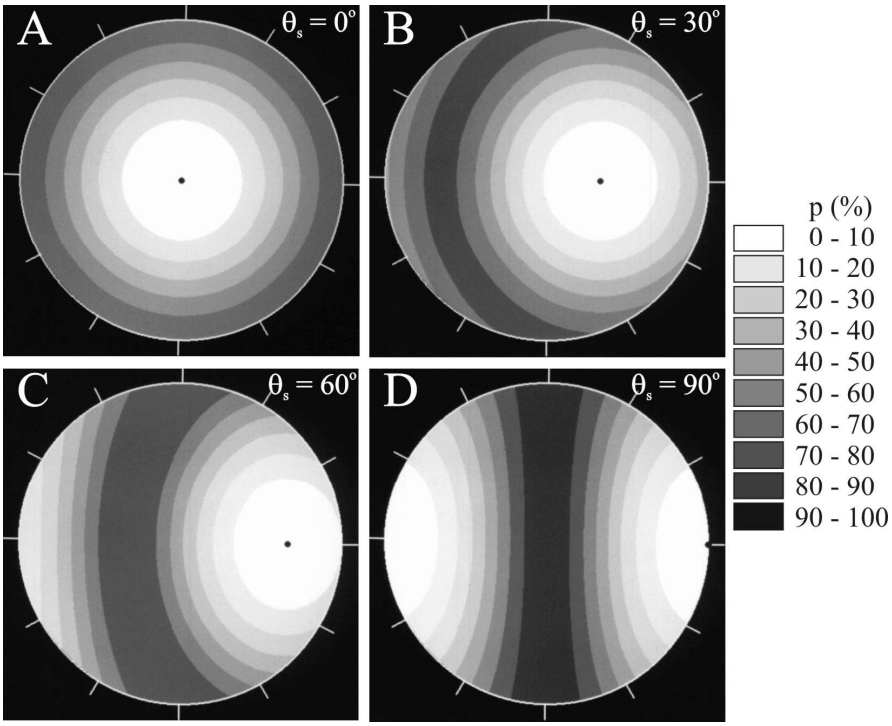

Fig. 15.7. Two-dimensional pattern of the degree of linear polarization p of skylight for different solar zenith angles θ_s. Other conventions and parameters as in Fig. 15.5. (After Fig. 6 of Horváth and Varjú 1995, p. 1657).

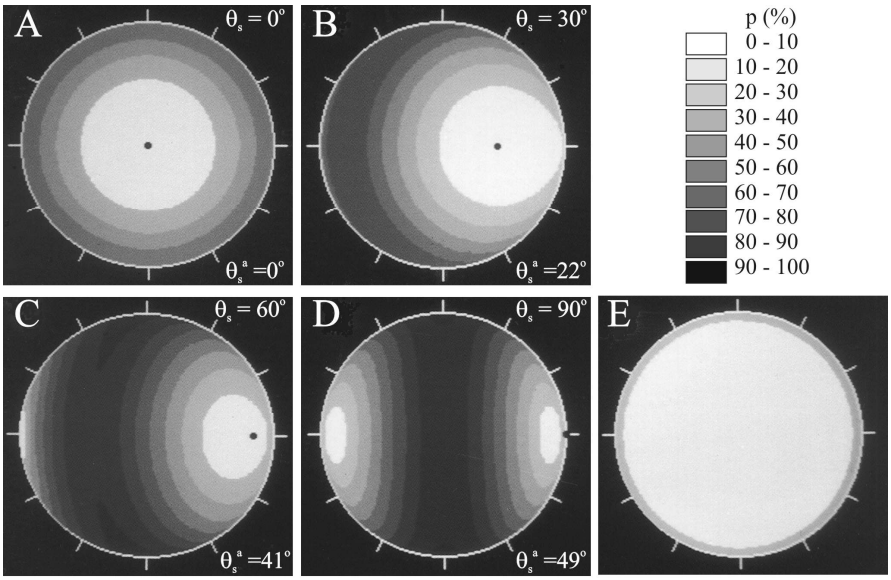

Fig. 15.8. A-D: Pattern of the degree of linear polarization p of skylight refracted within Snell window of the flat water surface under clear skies for different solar zenith angles θ_s and for the corresponding apparent zenith angles θ_s^a within the Snell window. θ_s and θ_s^a as in Fig. 15.6. E: As A-D for unpolarized light from a totally overcast sky. The outermost circles represent the boundary of Snell window. (After Fig. 7 of Horváth and Varjú 1995, p. 1658).

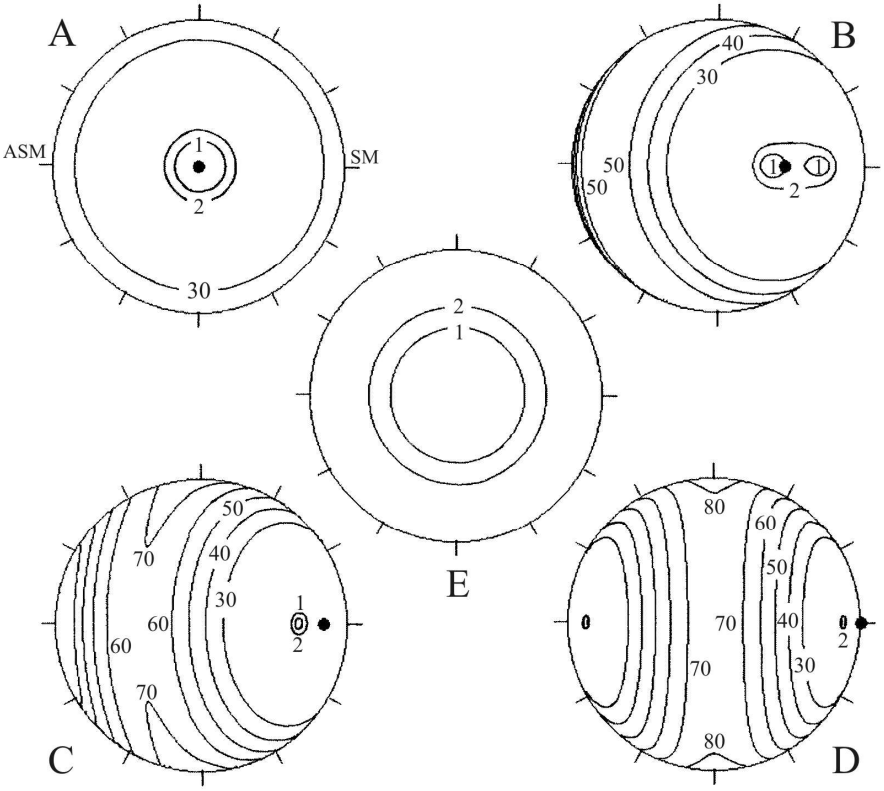

Fig. 15.9. A-D: Contour lines of equal degree of linear polarization p of skylight refracted within the Snell window of the flat water surface for different solar zenith angles θ_s and for the corresponding apparent zenith angles θ_s^a within the Snell window. θ_s and θ_s^a as in Fig. 15.6. E: As A-D for unpolarized light from a totally overcast sky. The apparent position of the sun is indicated by a dot. The outermost circles represent the boundary of Snell window. The p-values of refracted light in % are indicated at the corresponding contour lines. (After Fig. 8 of Horváth and Varjú 1995, p. 1659).

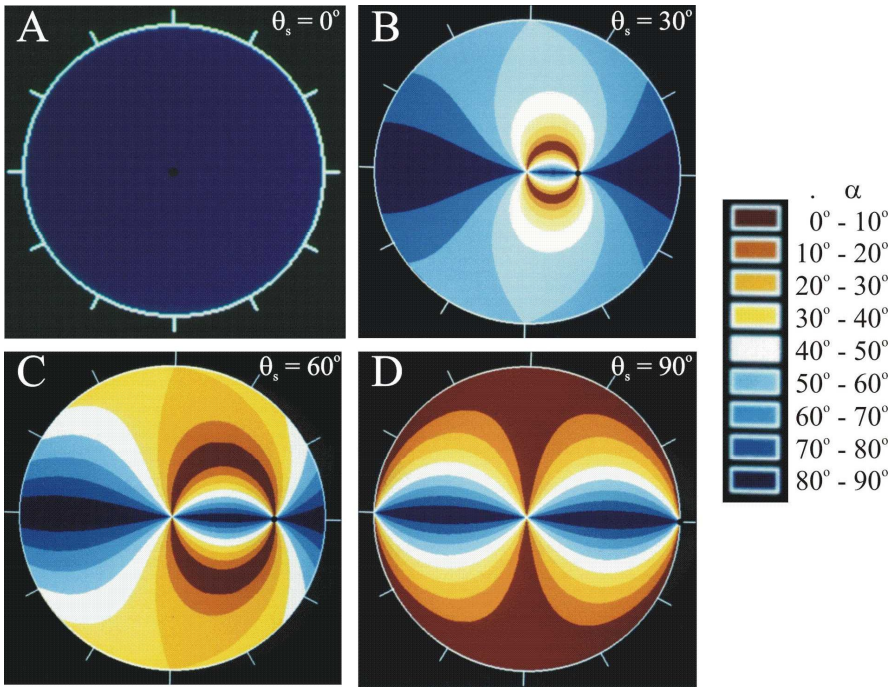

Fig. 15.10. As Fig. 15.7 for the angle of polarization α of skylight measured from the meridian of the point observed in the clear sky. Since all E-vectors of the celestial polarization pattern are horizontal when the sun is at the zenith, pattern A is homogeneous dark blue. (After Fig. 9 of Horváth and Varjú 1995, p. 1660).

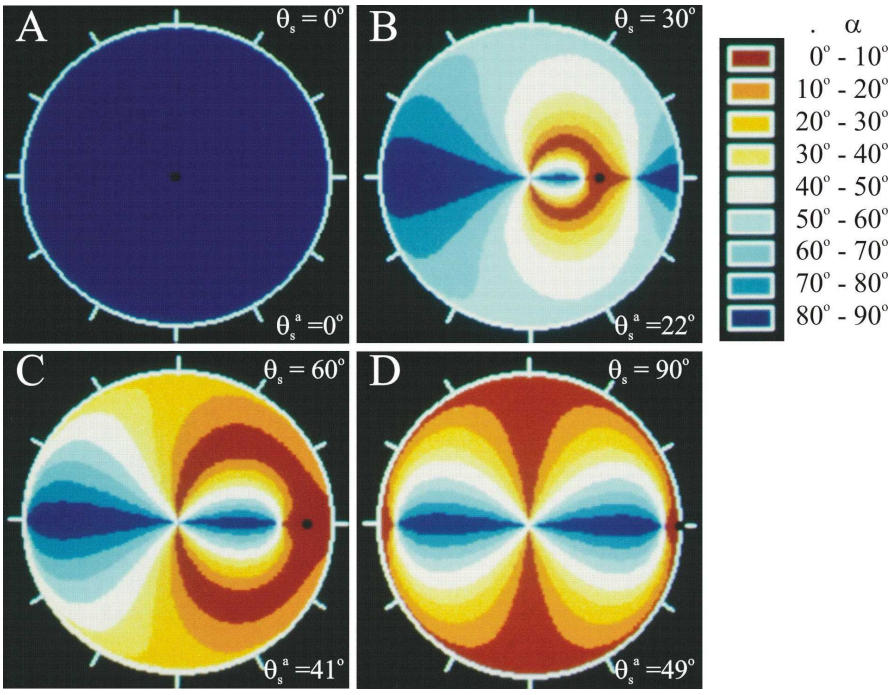

Fig. 15.11. Patterns of the angle of polarization α of refracted skylight within Snell window of the flat water surface under clear skies for different solar zenith angles θ_s. α is measured from the meridian of the celestial point observed through the Snell window. Since all refracted E-vectors are horizontal when the sun is at the zenith, pattern A is homogeneous dark blue. The outermost circles represent the boundary of Snell window. (After Fig. 10 of Horváth and Varjú 1995, p. 1661).

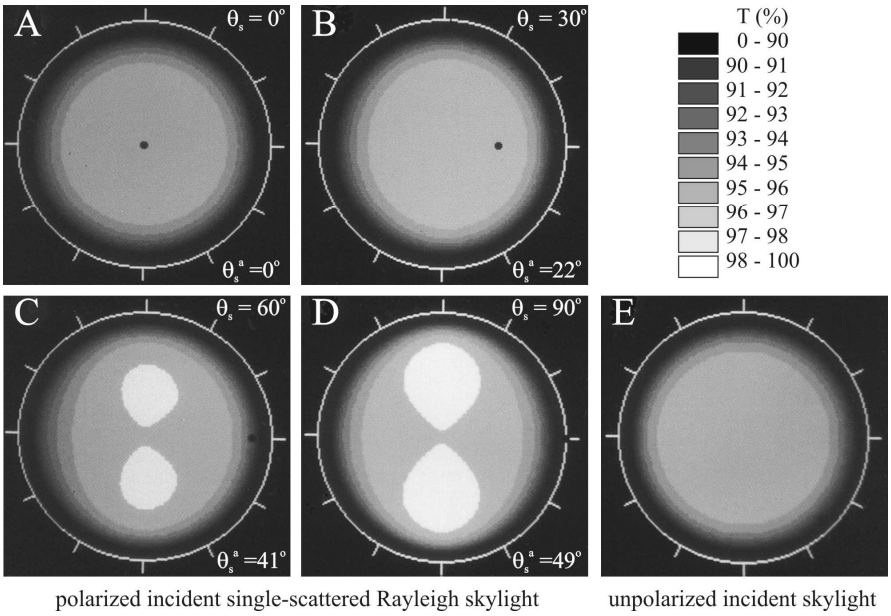

Fig. 15.12. A-D: Patterns of transmissivity T of the flat air-water interface under clear skies visible from water through the Snell window for different solar zenith angles θ_s. E: As A-D for unpolarized light of a totally overcast sky. In patterns C and D the two bright patches show the regions of Snell window where $T > 98\%$. The outermost circles represent the boundary of Snell window. (After Fig. 11 of Horváth and Varjú 1995, p. 1662).

16 Multiple-Choice Experiments on Dragonfly Polarotaxis: Dragonflies Find Crude Oil Visually More Attractive than Water

Kennedy (1917) gave an account of many individuals of the dragonfly *Anax junius* having been killed as a result of mistaking an open surface of crude oil for water. Puschnig (1926), Fraser (1936) and Whitehouse (1941) reported that dragonflies *Ophiogomphus forcipatus, Ictinogomphus ferox, Macromia magnifica* and several species of *Chlorogomphus* patrolled along asphalt roads instead of rivers and showed a typical water-touching behaviour above the asphalt surface. Kennedy (1938) cited cases in which dragonflies were attracted to pools of petroleum. Horváth and Zeil (1996) reported that dragonflies were deceived, attracted and trapped in large numbers by crude oil lakes in the desert of Kuwait. Horváth et al. (1998a) observed the same behaviour of dragonflies at a waste oil lake in Budapest (Fig. 16.1).

Such examples demonstrate that dragonflies[1] respond to shiny black oil or dark grey asphalt surfaces, and also that their response is elicited by particular misleading cues. Horváth and Zeil (1996) suggested that the reason why crude oil deceive, lure and trap insects on a large scale might be that an oil surface looks like an "exaggerated", strongly horizontally polarizing water surface, making oil visually more attractive than water to water-loving insects, the visual system of which is sensitive to the polarization of reflected light.

Horváth et al. (1998a) tested and supported this hypothesis in multiple-choice field experiments with dragonflies. They compared the numbers of dragonflies being caught in water, crude oil (Fig. 16.2) and salad-oil (Fig. 16.3) traps with different reflection-polarizational characteristics. They demonstrated that polarotaxis is the most important mechanism which guides dragonflies during their habitat choice and oviposition site selection, and this is the reason why dragonflies can be deceived by and attracted to crude and waste oil, tar or asphalt (Kennedy 1917, 1938; Puschnig 1926; Fraser 1936; Whitehouse 1941; Angus 1973; Akersten et al. 1983; Horváth and Zeil 1996; Kowalski 1999).

In the first choice experiment of Horváth et al. (1998a), two matt aluminium trays of 0.5 m^2 area were filled with water respectively black crude oil. They were placed on a large field about 500 m away from a small lake. Matt aluminium trays

[1] Dragonflies: all members of Odonata, including both Anisoptera and Zygoptera; the latter commonly known as damselflies.

were chosen to mimic the bright grey colour of the ground of the alkaline field. The bottom of the water-filled tray was covered by a thin layer of grey, sandy soil to imitate the typical bottom of alkaline puddles in the biotope. In order to trap all insects that touched the water, the common ecological method of catching and monitoring insects was used (Southwood 1966): the surface tension of water was reduced with a detergent. In a pilot-experiment it was proven that both crude oil and detergent-treated water were efficient insect traps. Any insect that touched either surface was entrapped at once. These traps were left in the field for two weeks and checked every day. The dragonflies trapped by the trays were collected and identified. The distance between the traps was 0.5 meter. The position and orientation of the trays was changed randomly. The evaporated crude oil and water were continuously replenished. The reflection-polarizational characteristics of the traps were measured by video polarimetry (Horváth and Varjú 1997) on a typical sunny day under a clear sky.

We can see in Table 16.1 that male dragonflies were trapped about twice as frequently as females, and black crude oil was significantly more attractive than water on a light grey background. This observation constitutes the experimental evidence for the hypothesis put forward by Horváth and Zeil (1996). The light reflected from the oil had a degree of linear polarization p = 33% with horizontal E-vector (Table 16.1, Fig. 16.2). The light reflected from the water had p = 4% with vertical E-vector, since a slightly greater amount of light with vertical polarization came from the bottom than horizontally polarized light from the water surface. Although the reflection-polarizational characteristics of the trays depend on the angle of view, solar zenith angle and meteorological conditions, Fig. 16.2 demonstrates well the fact that crude oil is a more effective polarizer than water with a bright bottom, even relatively far away from the Brewster angle (57^o from the vertical for crude oil and 53^o for water). Thus, the light reflected from crude oil is a supernormally polarized stimulus for water seeking dragonflies.

In the first choice experiment of Horváth et al. (1998a), the bottom of water was much lighter than the black crude oil, like in the desert of Kuwait, where there occurred bright sand-bottomed water ponds and dark brown or black crude oil lakes and ponds (Horváth and Zeil 1996). Horváth et al. (1998a) performed also a second multiple-choice experiment: Five white plastic trays were filled with transparent, slightly yellowish salad-oil. The bottom of four traps was covered by shiny plastic sheets with different grey shades ranging from black, through dark and light grey to white. The bottom of the fifth trap was a shiny aluminium foil. In this experiment differences of the trapping efficiency of the salad-oil filled in five traps were surely not due to smell. We can see in Table 16.2 and Fig. 16.3 that the relative radiance I gradually increased while p gradually decreased from the black trap (S5) through the dark (S3) and light (S6) grey to the white trap (S4). The aluminium trap possessed a relatively high p = 20.2%, but because shiny aluminium surfaces reflect the linearly polarized light with practically no change (Horváth and Pomozi 1997), the reflection-polarizational characteristics of this trap was very variable depending on the solar zenith angle. Apart from the white

and aluminium traps, the direction of polarization of the light reflected from the traps was always horizontal. The E-vector of reflected light was more or less vertical for the white and very variable for the aluminium trap.

Although the black trap reflected about twice so highly polarized light (p = 69.6%) as the dark grey trap (p = 33.7%), there was no significant difference between the number of dragonflies trapped by them. The light grey and white traps with low p trapped significantly fewer dragonflies and the aluminium trap with very variable polarization was the least attractive. Males were trapped again much more frequently than females.

In full sunshine, the black crude oil and the salad-oil in the black-bottomed tray heated up considerably, maximum of about 70°C, unlike the water and the salad-oil in the white- and aluminium-bottomed trays, the temperature of which followed the temperature of the surroundings, maximum of ca. 35°C. Similarly to Horváth et al. (1998a), Wildermuth (1993) also observed that dragonflies (*Aeshna juncea*) do not land when the test surface composed of black plastic sheet or cloth heated up too much in full sunshine.

To exclude the role of temperature and radiance of the surfaces in the choice of dragonflies, Horváth et al. (1998a) performed a third experiment. They laid six odourless sheets measuring 1 m × 1 m covered by different materials, non-transparent black, grey and white shiny plastic sheets, shiny aluminium foil, matt black and white cloths with the same temperature and with different reflection-polarizational characteristics on the ground (Fig. 16.4). In the experiments the surfaces were positioned along a rectangle, and their order was changed randomly. The response of flying dragonflies to these test surfaces was studied by visual observation. The following main behaviour types were differentiated:

- air fight, hovering and protection of the territory against intruders;
- surface touching;
- settling down;
- egg-laying.

The relative frequency of these behaviour types have been counted and compared, and the reflection-polarization patterns of the test surfaces were recorded (Table 16.3, Fig. 16.4).

The number of egg-laying was very low (Table 16.3), thus one cannot draw any firm conclusion considering the oviposition. Egg-laying occurred only on the shiny surfaces. Settling down occurred also only sporadically, but significantly more often than egg-laying. For settling down the brighter test surfaces, matt white cloth, shiny white plastic, shiny aluminium with low p were preferred independently of their shiny or matt appearance and of the angle of polarization of reflected light. This reaction recalls the settling down behaviour onto the matt light grey ground observed frequently in the study site. This behaviour is apparently different from the water-seeking behaviour, because dragonflies never settle down directly onto the water surface. According to Corbet (1999), settling

down to a brighter surface may serve thermoregulation or simply resting. Many dragonfly species must warm their thorax to a temperature well above the ambient temperature before they can fly, and they do this by behavioural and physiological means. Behavioural warming occurs as basking in sunlight, sometimes gaining additional heat by sitting on hot rocks or the ground (Corbet 1999).

Surface touching was the second more frequent behaviour type observed at the test surfaces. This is a reaction, which is typical above water surfaces when dragonflies inspect the surface to select the optimal oviposition site. The shiny black plastic sheet with the highest degree (p = 73.5%) of horizontal polarization was the most attractive (46.3%). The shiny grey plastic sheet with a much lower degree (p = 9.1%) of horizontal polarization was less attractive (25.6%). Since the direction of polarization was not horizontal, the matt white and black cloths, independently of their low or high p, and the shiny aluminium were practically unattractive.

The most frequently observed types of behaviour were the air fight, hovering and protection. These are typical again only above water surfaces. Males frequently hover in their territories, or when they search for females elsewhere. Hovering serves to advertise the presence of a male in his territory. Females also hover when they inspect oviposition sites (Corbet 1999). Both females and males inspect the surface, or males protect their territory during air fights against intruders. Considering these aerial territorial behaviours, the shiny black plastic sheet was again the most attractive (40.1%). The shiny grey plastic sheet was less attractive (21.2%). The matt white and black cloths furthermore the shiny aluminium were practically unattractive. The shiny white plastic sheet was only slightly attractive (17.3%). Hence, for air fight, hovering and protection the relative attractiveness of the different test surfaces was similar to that obtained for the surface touching behaviour. These reactions demonstrate that the higher the degree of horizontal polarization, the greater is its attractiveness to dragonflies.

Analysing Table 16.3, we can establish that the radiance I does not play an important role in the choice of surfaces. The dragonflies were attracted predominantly to the shiny black plastic sheet, and the very dark matt black and too bright white and aluminium surfaces were unattractive. The preferred shiny black plastic sheet reflected highly and horizontally polarized light. The matt test surfaces scattered light diffusely due to their roughness, and the reflected light was practically unpolarized. Thus, the strong reflection polarization of light remains as the only explanation for the fact that dragonflies preferred exclusively the black plastic surface. This conclusion is in agreement with the results of Wildermuth and Spinner (1991) and Wildermuth (1993, 1998).

Since the smell of the salad-oil traps was the same and the test surfaces used in the third choice experiment were odourless, one can conclude that olfaction is not relevant for detection of water by dragonflies. Because the temperature of the black shiny plastic and matt cloth, like the temperature of the white plastic and cloth, were approximately the same, the dragonflies trapped by the crude oil and salad-oil traps were presumably not be attracted by the heat, that is, the

temperature was not relevant in their choice. It can also be established, that the radiance of reflected light did not play an important role in their choice, as otherwise either the darkest matt black cloth, the white cloth, or the brightest aluminium would have been the most attractive.

To confirm that strongly polarized reflected light is very attractive to water-seeking dragonflies, Horváth et al. (1998a) performed a fourth field experiment. One half (0.2 m^2) of a shiny aluminium test surface was covered by a common linearly polarizing filter, while the other half was uncovered. The two halves were separated by a narrow matt black cloth, which was unattractive. The polarizing filter was neutral grey with a transmissivity of 80% in the visible range of the spectrum and absorbed entirely UV light. The number of the different behaviour types above the two different halves of the aluminium test surface have been counted and compared. The results are presented in Table 16.4.

The light reflected from the filter-covered half of the aluminium was totally linearly polarized (p = 100%) in the visible spectral range and its E-vector was horizontal for dragonflies flying from the proper directions towards the filter. Since the uncovered half of the aluminium was only slightly polarized and its E-vector was generally not horizontal, there was a strong polarization contrast between the two halves. The number of egg-laying and settling down was very low on both halves (2:1 and 6:3, respectively). About 60% of the most frequent reactions, the air fight and hovering, happened above the polarizing filter, which thus was not significantly more attractive than the aluminium surface. The reason for this is that the territories of the observed small dragonflies are usually less than 1 m^2 (Corbet 1999). Thus, both halves of the aluminium belonged to their territory. About 86% of the surface touching, the second most frequent reaction, happened on the polarizing filter. This difference is highly significant and demonstrates that both males and females select strongly horizontally polarizing surfaces as habitats and oviposition sites.

One can conclude that dragonflies detect water by means of polarotaxis, like many other water insects (Schwind 1985b, 1991, 1995). The spectral range in which this water detection functions in dragonflies is still unknown. Some dragonflies have UV receptors looking downwards (Corbet 1999) which respond perhaps to the polarization of UV light reflected from water. In the choice experiments of Horváth et al. (1998a) chiefly males were trapped. Wildermuth and Spinner (1991) and Wildermuth (1993) have also observed that female dragonflies visited black, shiny plastic sheets and natural oviposition sites less frequently. This can be explained by the operational sex ratio at breeding sites which is strongly biased towards males, because females spend much time elsewhere (Corbet 1999).

The first experiment of Horváth et al. (1998a) with the crude-oil- and water-filled trays closely mimicked the "natural" situation in the desert of Kuwait from late autumn to late spring, when some of the oil lakes were partially covered by sand and rain water (Horváth and Zeil 1996). Then water-seeking dragonflies had to choose between the dark crude oil ponds and the bright sand-bottomed water

bodies. The crude or waste oil lakes in nature as well as the crude-oil- and salad-oil-filled trays in the choice experiments of Horváth et al. (1998a) entrapped the dragonflies when the males or females performed a water-touching manoeuvre or when the females tried to deposit their eggs. Monitoring the waste oil lake in Budapest (Fig. 16.1), Horváth et al. (1998a) could observe that the dragonflies exhibited the complete repertoire of behavioural elements which belong to reproduction including site defence and oviposition. These dragonflies behaved at the strongly horizontally polarizing shiny black surface of the waste oil lake very much like at natural water surfaces or above water-imitating dummies as reported by Wildermuth and Spinner (1991) and Wildermuth (1993, 1998).

Muller (1937) observed the females of *Orthetrum* dragonflies laying eggs on a shiny cement floor and *Copera marginipes* made repeated egg-laying movements in a dirty seam on a shiny black bench. Wyniger (1955) has reported on the egg-laying of *Libellula depressa* onto a glass pane of a greenhouse. Neville (1960) experienced that mature individuals of *Pantala flavescens* performed sexual behaviour and oviposition movements over shiny roofs of tents. Kennedy (1938) reported on instances in which dragonflies were attracted to shiny roofs of automobiles. These authors experienced that the dragonflies performed sexual behaviour and oviposition movements over these shiny surfaces. Noordwijk (1980) found that the flight activity of dragonflies above shiny plastic sheets (2 m × 3 m) laid on *Sphagnum* bog was significantly higher than above control plots without plastic.

Fränzel (1985) laid out transparent plastic sheets at the edge of a creek and observed that both female and male dragonflies *Cordulegaster bidentatus* were attracted to the plastic, and the females performed oviposition movements while males patrolled predominantly over those plastic pieces which covered dark regions of the ground. These authors, however, did not recognize the important role of polarotaxis in the habitat choice or in the deceiving by different artificial shiny black surfaces.

Using different breeding site dummies in multiple-choice experiments, Wildermuth and Spinner (1991) and Wildermuth (1993) found that a shiny black plastic sheet was highly attractive to both sexes of *Somatochlora arctica* and *Aeshna juncea*, and they exhibited the complete repertoire of behavioural elements which belong to reproduction including site defence and oviposition. Matt white or black tulle and cotton cloths, even when covered with glass splinters proved to be completely unattractive, and when glass splinters providing a great number of reflecting light spots were added to a black shiny plastic sheet no enhancement of the responses was recorded (Wildermuth and Spinner 1991; Wildermuth 1993). According to Steiner (1948), matt black paper had almost no effect on *Leucorrhinia dubia*, and Wildermuth and Spinner (1991) noticed similar weak reactions towards matt black cotton also by *Somatochlora alpestris*.

Tables

Table 16.1. Row 2: The total number and sex (F: female, M: male) of dragonflies (*Sympetrum vulgatum, Ischnura pumilio, Enallagma cyathigerum*) trapped by the crude-oil- and water-filled trays during the first choice experiment of Horváth et al. (1998a). Rows 3-5: The relative radiance *I*, degree of linear polarization *p* and direction of polarization of light reflected from the trays and measured by video polarimetry at 450 nm from a direction of view of 70° relative to the vertical. (After Table 1 of Horváth et al. 1998a, p. 292).

	crude oil-filled tray S1	**water-filled tray S2**
number of trapped dragonflies	16 F + 34 M	2 M
relative radiance *I*	20%	100%
degree of linear polarization *p*	33%	4%
direction of polarization	horizontal	vertical

Table 16.2. Row 2: The total number (J: juvenile) and sex (F: female, M: male) of dragonflies (Ischnura elegans, Erythromma viridulum, Lestes macrostigma, Enallagma cyathigerum, Orthetrum cancellatum, Libellula quadrimaculata, Sympetrum sanguineum) trapped by the salad-oil-filled trays during the multiple-choice experiment of Horváth et al. (1998a). Rows 3-5: The relative radiance I, degree of linear polarization p and direction of polarization of light reflected from the trays and measured by video polarimetry at 450 nm from a direction of view of 70° from the vertical. The trays are designated by S3-S7 as in Fig. 16.3. (After Table 2 of Horváth et al. 1998a, p. 294).

	black tray S5	**dark grey tray S3**	**light grey tray S6**	**white tray S4**	**aluminium tray S7**
number of trapped dragonflies	8 F (5 J) + 62 M (7 J)	12 F (3 J) + 63 M (9 J)	11 F (7 J) + 32 M (3 J)	7 F (5 J) + 21 M (2 J)	5 F (4 J) + 10 M (2 J)
relative radiance *I*	22.1%	35.6%	52.4%	100%	42.3% (variable)
degree of linear polarization *p*	69.6%	33.7%	10.3%	4.6%	20.2% (variable)
E-vector direction	horizontal	horizontal	horizontal	vertical	horizontal (variable)

Table 16.3. The total number and the frequencies relative to the total number of a given reaction counted above all six test surfaces of the different behaviour types of dragonflies (*Ischnura elegans, Erythromma vividulum, Lestes macrostigma, Enallagma cyathiqerum, Orthetrum cancellatum, Sympetrum sanquimum*) in the choice experiment, repeated 11 times. The relative radiance *I*, degree of linear polarization *p* and angle of polarization with respect to the vertical of the light reflected from the test surfaces and measured by video polarimetry at 470 nm from a direction of view of 70° relative to the vertical.

behaviour type	**shiny black plastic S8**	**shiny grey plastic S9**	**matt white cloth S13**	**shiny white plastic S11**	**matt black cloth S12**	**shiny aluminium S10**
air fight, hovering, protection	922 (40.1%)	486 (21.2%)	189 (8.2%)	397 (17.3%)	91 (4.0%)	212 (9.2%)
surface touching	343 (46.3%)	190 (25.6%)	22 (3%)	120 (16.2%)	13 (1.8%)	53 (7.1%)
settling down	5 (6.3%)	9 (11.4%)	30 (38%)	20 (25.3%)	1 (1.3%)	14 (17.7%)
egg-laying	4 (20%)	8 (40%)	0	4 (20%)	0	4 (20%)
relative radiance *I*	52.9%	63.5%	99.7%	100%	22.2%	78.8% variable
degree of polarization	73.5%	9.1%	3.4%	2.8%	21.5%	7.0% variable
angle of polarization	90° horizontal	90° horizontal	51.3° variable	0° vertical	51.6° variable	80.3° variable

Table 16.4. Rows 2-5: The total number of the different behaviour types of dragonflies (*Ischnura elegans, Erythromma viridulum, Lestes macrostigma, Enallagma cyathigerum, Orthetrum cancellatum, Sympetrum sanguineum*) above the two test surfaces in the fourth choice experiment repeated five times. Rows 7-9: The relative radiance, degree of linear polarization and angle of polarization with respect to the vertical of the light reflected from the test surfaces and measured by video polarimetry at 450 nm from a direction of view of 70° relative to the vertical. (After Table 3 of Horváth et al. 1998a, p. 296).

1	**behaviour type**	**polarizing filter on shiny aluminium**	**shiny aluminium**
2	air fight and hovering	412 (59.6%)	279 (40.4%)
3	surface touching	115 (85.8%)	19 (14.2%)
4	settling down	6	3
5	egg-laying	2	1
6	**optical characteristics**		
7	relative radiance *I*	40%	100%
8	degree of polarization *p*	100%	30% (variable)
9	angle of polarization α	90° (horizontal)	65° (variable)

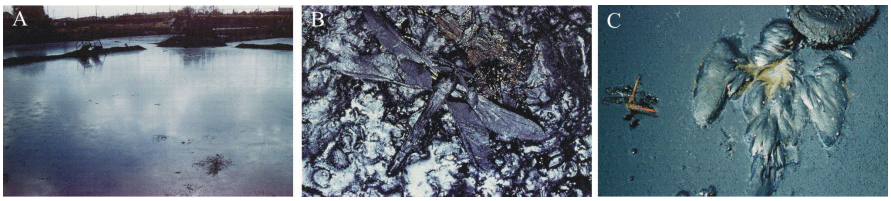

Fig. 16.1. The shiny, strongly horizontally polarizing, water-imitating surface of the waste oil lake in Budapest (A) has deceived, attracted and trapped a dragonfly *Anax imperator* (B) and a copulating pair of *Sympetrum sanguineum* (C, left hand side).

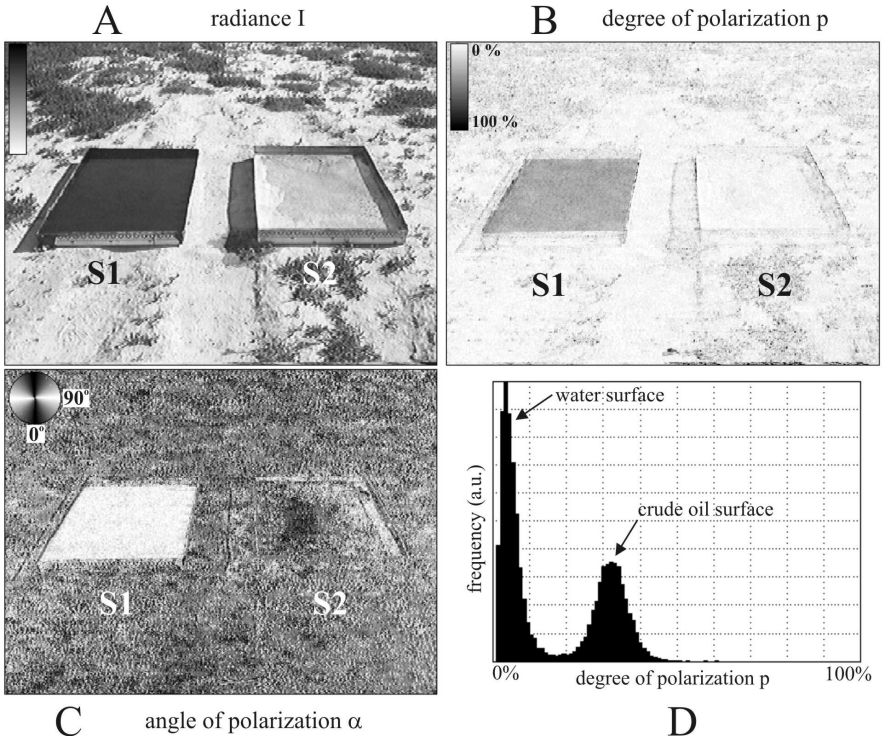

Fig. 16.2. The reflection-polarizational characteristics of the two trays used by Horváth et al. (1998a) in the first choice experiment, filled with black crude oil (S1) and detergent-treated water (S2) measured by video polarimetry at 450 nm under a clear sky. A: Distribution of the radiance *I*. B: Pattern of the degree of linear polarization *p*. C: Pattern of the angle of polarization α. (Black: vertical E-vector, white: horizontal E-vector). D: Histogram of *p* calculated for the surface area of the two trays. The left (p = 4%) and right (p = 33%) peak of the distribution corresponds to the water and crude oil surface, respectively. Viewing direction was 70° from the vertical and at a right angle to the solar meridian. (After Fig. 2 of Horváth et al. 1998a, p. 294).

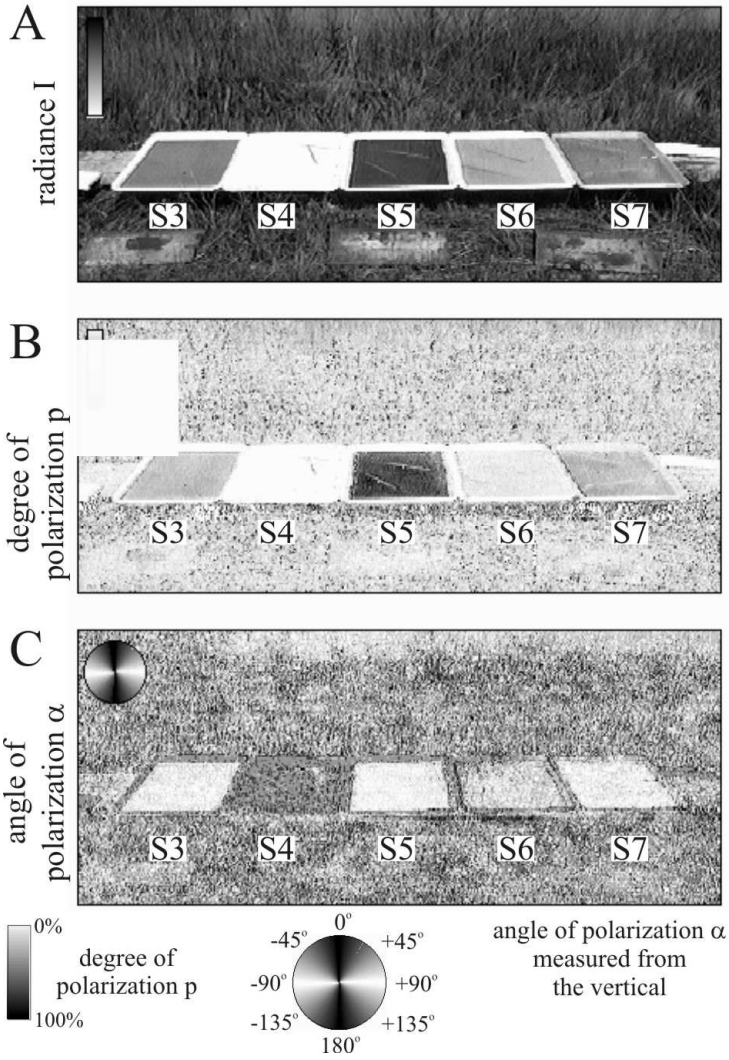

Fig. 16.3. The reflection-polarizational characteristics of the salad-oil-filled traps used by Horváth et al. (1998a) in the multiple-choice experiment measured by video polarimetry at 450 nm from a direction of view of 70° with respect to the vertical and at a right angle to the solar meridian under a clear sky. The bottom of the salad-oil-filled trays were covered by dark grey (S3), white (S4), black (S5), light grey (S6) plastic sheets and aluminium foil (S7). The trays were positioned farther away from each other during the experiment than seen here. They are placed in this picture as close as possible in order to image them at the same time. A: Distribution of the radiance *I*. B: Pattern of the degree of linear polarization *p*. C: Pattern of the angle of polarization α from the vertical. (After Fig. 3 of Horváth et al. 1998a, p. 295).

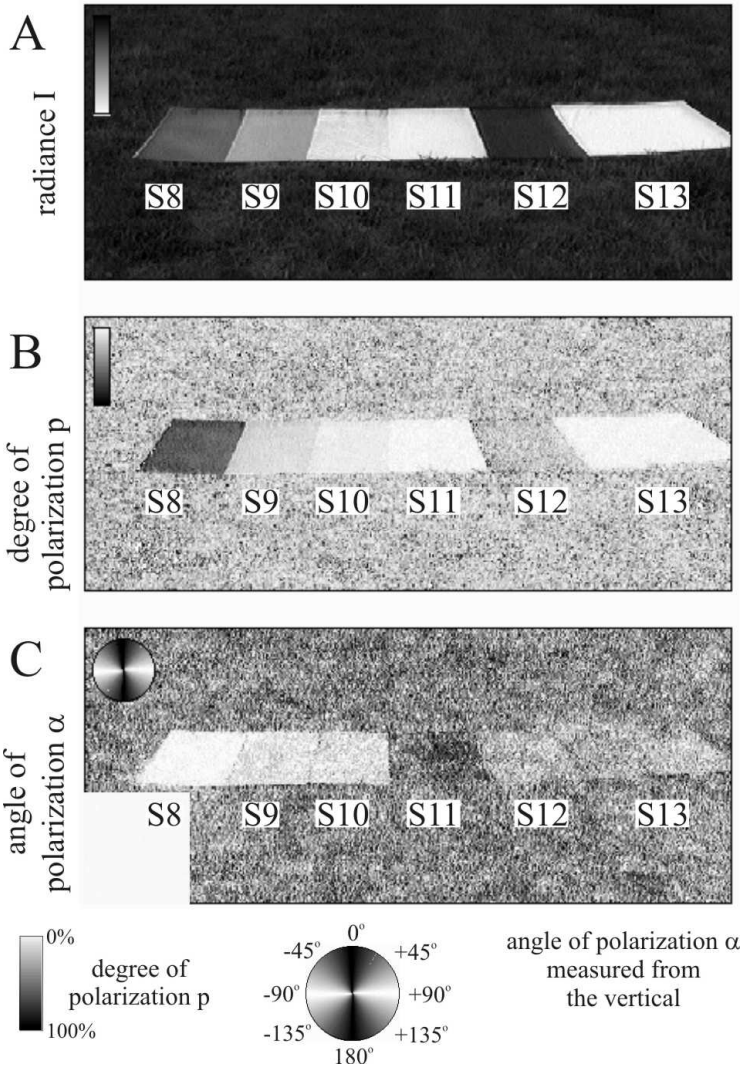

Fig. 16.4. The reflection-polarizational characteristics of the different test surfaces used in the third experiment by Horváth et al. (1998a) and measured by video polarimetry at 450 nm under a clear sky from a direction of view of 70° with respect to the vertical at a right angle to the solar meridian. The test surfaces were shiny black plastic sheet (S8), shiny grey plastic sheet (S9), shiny aluminium foil (S10), shiny white plastic sheet (S11), matt black cloth (S12) and matt white cloth (S13). These test surfaces were positioned farther away from each other during the experiment than seen here. They are placed here as close as possible in order to image them at the same time.

17 How can Dragonflies Discern Bright and Dark Waters from a Distance? The Degree of Linear Polarization of Reflected Light as a Possible Cue for Dragonfly Habitat Selection

The females of many insects associated with water, e.g. dragonflies, must return to water to lay their eggs. Water bodies also often serve as meeting places for both sexes. In Odonata many species are habitat generalists, while others are highly specific in their ecological requirements (Corbet 1999). Since orientation in dragonflies is predominantly visual, one may ask for the cues by which specific water bodies are recognized (Wildermuth 1994). Depth, turbidity, transparency, colour, surface roughness of the water and substratum composition strongly influence the reflection-polarizational characteristics of water bodies. The polarization of light reflected by water provides important information on the quality of freshwater habitats for polarotactic insects and can aid the orientation of these insects from a distance when other cues, e.g. atmospheric humidity, dimension and shape of the water body, undulation of the water surface, water plants on the surface and on the shore, temperature and odour, are ineffective.

While monitoring the fauna of dark ponds in peatland and bright ponds in gravel pits in the Swiss midlands, Bernáth et al. (2002) observed that some dragonflies preferred dark or bright ponds, whereas others were found in both types. It is a well-known optical phenomenon that two water bodies, being bright and dark to the human eye viewing downwards perpendicularly to their surface, cannot be distinguished from each other from a distance. Then the angle of view with respect to the water surface is very narrow, called "grazing" angle, and the amount of light reflected from the surface is equal for both dark and bright waters (definition see below). Thus, the main question is to find how dragonflies distinguish a bright from a dark pond before they get sufficiently close to perceive brightness differences.

Since many dragonfly species find their aquatic habitat by polarotaxis (Horváth et al. 1998a; Wildermuth 1998; Bernáth et al. 2001b), one can hypothesize that certain dragonflies can select from far away their preferred dark or bright water bodies, at least partly on the basis of reflection-polarization information. In order to answer this question, Bernáth et al. (2002) investigated the reflection-polarizational characteristics of a number of dark and bright ponds inhabited by different dragonfly species. Their field studies were carried out at two localities: (1) a former gravel pit, and (2) a moorland area with former peat diggings; the two

sites being situated 22 km apart from each other. The Odonata fauna was monitored in a sample of six ponds at each locality. The water bodies at study site 1 appeared bright to the human eye viewing downwards perpendicularly to their surface, those at site 2 dark. "Bright" means shallow and clear water with a bright substratum, "dark" refers to shallow and clear water with a dark substratum, from which light reflection is limited. The bright ponds had a diameter of 5-10 m and a maximum depth of 0.3-0.4 m. Their surface was sparsely covered by aquatic vegetation. The colour was bright beige and the bottom consisted of gravel and clay. All dark ponds were situated in peatland. Their diameter ranged from 4 to 8 m and they had a maximum depth of 0.4-0.8 m. The ponds were sparsely or moderately overgrown with emergent vegetation. Their colour was dark brown and the substratum consisted of peaty mud.

17.1 Comparison of the Dragonfly Fauna in Dark and Bright Waters

The dragonfly faunae of six bright and six dark ponds are summarized in Table 17.1. Five species, *Enallagma cyathigerum*, *Anax imperator*, *Libellula depressa*, *Orthetrum cancellatum* and *Orthetrum brunneum*, were common only in bright ponds, although three of them, *E. cyathigerum*, *L. depressa* and *A. imperator*, also appeared sparsely at one or the other of the peat diggings. Successful development, that is, finding of a few exuviae, was observed only in *A. imperator*. By comparison, nine species, *Lestes virens*, *Lestes sponsa*, *Lestes viridis*, *Coenagrion pulchellum*, *Aeshna juncea*, *Cordulia aenea*, *Somatochlora flavomaculata*, *Leucorrhinia pectoralis* and *Sympetrum sanguineum*, occurred regularly only at dark ponds. Five further species, *Pyrrhosoma nymphula*, *Coenagrion puella*, *Aeshna cyanea*, *Libellula quadrimaculata* and *Sympetrum striolatum*, were common in both types of ponds. Species recorded only exceptionally as adults were considered to be guest species and are omitted from this analysis. In general, earlier findings concerning the species composition of small water bodies in peatland, gravel pits and other secondary biotopes in the Swiss midlands were confirmed (Wildermuth 1980, 1992a,b; Wildermuth and Krebs 1983, 1987).

17.2 Comparison of the Reflection-Polarizational Characteristics of Dark and Bright Waters

In the visible (red, green, blue) part of the spectrum there were no significant differences in radiance I between dark and bright water bodies towards the sun (Fig. 17.1A). The same was true in the UV away from the sun and perpendicularly to it (Figs. 17.2A,B). In the green and red, however, I of light reflected from bright waters was significantly higher than that reflected from dark ponds away from the sun (Fig. 17.1B) and perpendicularly to it (Fig. 17.1C).

The degree of linear polarization p of light coming from bright or dark waters was the highest in the blue for any direction of view (Figs. 17.1D-F, 17.2C,D). Independently of the wavelength and the viewing direction, p of light reflected from dark water bodies was significantly higher than that from bright waters (Figs. 17.1D-F, 17.2C,D). The differences were smallest in the blue.

Independently of the wavelength as well as the viewing direction, the average direction of polarization of reflected light was horizontal for both bright and dark water bodies (Figs. 17.1G-I, 17.2E,F). However, its standard deviation was small towards (Fig. 17.1G) and away from the sun (Figs. 17.1H, 17.2E), while it was large perpendicularly to it (Figs. 17.1I, 17.2F).

The direction of polarization of light reflected from bright waters changes from horizontal to vertical from the shorter wavelengths towards the longer ones (Fig. 17.3), since the amount of vertically polarized light emanating from the subsurface overwhelms the amount of horizontally polarized surface-reflected light for longer wavelengths. Similar change in the direction of polarization does not occur in the case of dark water bodies (Fig. 17.4).

Shadows also have a considerable effect on the reflection-polarizational characteristics of water bodies. In the case of dark waters, the horizontally polarized surface-reflected light always dominates, and thus the direction of polarization is always horizontal for both the shaded and sunlit regions (right column in Fig. 17.4). The middle column in Fig. 17.4 shows that p of light reflected from the shaded regions of dark waters is lower than that reflected from the sunlit regions, because in the shaded areas the amount of horizontally polarized surface-reflected light is reduced. Figure 17.5 shows an example for a bright pond, in the sunlit or shaded regions of which the E-vector is horizontal or vertical, and p is higher or lower, respectively. Figure 17.6 presents another bright pond, where the contrasts of α and p are contrary to those in Fig. 17.5. In Fig. 17.6 in the sunlit or shady regions of the bright pond the E-vector is vertical or horizontal, and p is lower or higher, respectively. p of bright water bodies is always much less than that of dark waters. The reflection-polarizational characteristics of dark and bright water bodies are also influenced by the roughness of the water surface. Under windy conditions the water surface undulates, which more or less distorts the reflection-polarization patterns (Mobley 1994; Shaw 1999) as seen in Fig. 17.7.

17.3 The Degree of Linear Polarization of Reflected Light as a Possible Cue for Dragonfly Habitat Selection

On the basis of the above findings the following can be concluded: Dragonflies in the study of Bernáth et al. (2002) belong to three groups:

1. certain species prefer exclusively bright water bodies, while
2. other species prefer only dark water bodies, and
3. some species are ubiquitous, choosing dark and bright waters with equal frequencies.

From long distances, that is, at a small angle of view with respect to the water surface, dark water bodies cannot be distinguished from bright ones on the basis of the radiance of reflected light or its direction of polarization. However, even at such small angles of view dark waters reflect light with a significantly higher degree of linear polarization than bright waters in any range of the visible spectrum and in any direction of view with respect to the sun. Although in the UV the reflection-polarizational characteristics are presented here for only one dark and one bright pond as an example, this conclusion may also be extended to the UV region of the spectrum, because we do not know any optical argument against it. It does not contradict the fact that the human visual system discriminates between dark and bright waters by intensity differences. But this distinction can be done only if the water bodies are relatively close to the observer, so that the viewing angle with respect to the horizontal is large.

Water bodies possess many physical, chemical and biotic features. Although mechanical (Wildermuth 1992b), thermal (Sternberg 1990) and even olfactory (Steiner 1948) characteristics can be used in the localization of oviposition sites, dragonflies recognize their habitat mainly by visual cues (Wildermuth and Spinner 1991; Wildermuth 1993), one of them being the partially and horizontally linearly polarized light (Horváth et al. 1998a; Wildermuth 1998). The degree of polarization of reflected light is a physical property that can be perceived from great distances and provides some information about the quality of the habitat. Thus, it may be the visual cue for polarization-sensitive dragonflies enabling them to discern dark and bright water bodies from a distance. Future studies applying structural manipulations of natural substrata and choice experiments using dummies should prove whether dragonflies indeed use p of reflected light in their habitat selection.

However, one should bear in mind that polarized light is only one of the visual cues guiding dragonflies in the search of water habitats. In *Coenagrion mercuriale*, *Platycnemis pennipes* and *Leucorrhinia pectoralis* it was shown experimentally that structural features of the habitat, such as emergent vegetation, are also important for the choice (Buchwald 1989; Martens 1996; Wildermuth 1992a).

Table

Table 17.1. Dragonflies inhabiting bright and/or dark ponds as adults and/or larvae. Abundance classes: ++ = common, + = regular, (+) = sparse, – = absent. (After Table 1 of Bernáth et al. 2002, p. 1710).

	six bright ponds in gravel pits		six dark ponds in peatland	
	adults	**exuviae**	**adults**	**exuviae**
Enallagma cyathigerum	++	++	(+)	–
Anax imperator	++	++	+	(+)
Libellula depressa	++	++	(+)	–
Orthetrum cancellatum	++	++	–	–
Orthetrum brunneum	++	++	–	–
Pyrrhosoma nymphula	+	+	+	+
Coenagrion puella	++	++	++	++
Aeshna cyanea	++	++	++	++
Libellula quadrimaculata	++	++	++	++
Sympetrum striolatum	++	++	+	+
Lestes virens	–	–	++	++
Lestes sponsa	–	–	++	++
Lestes viridis	–	–	+	+
Coenagrion pulchellum	–	–	+	+
Aeshna juncea	–	–	+	+
Cordulia aenea	–	–	+	+
Somatochlora flavomaculata	–	–	+	+
Leucorrhinia pectoralis	–	–	++	++
Sympetrum sanguineum	–	–	+	+

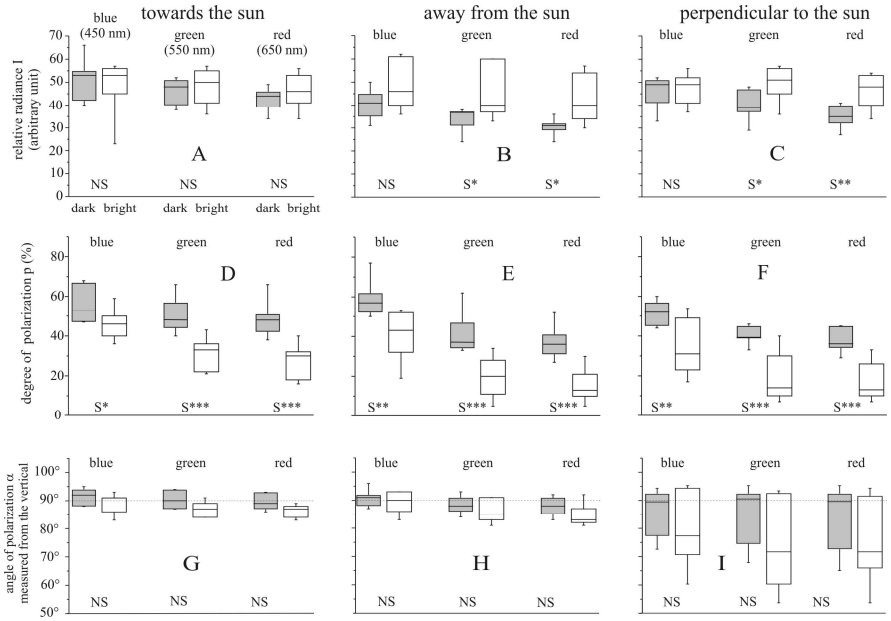

Fig. 17.1. Means (horizontal bars in boxes), quartiles (boxes), 5th and 95th percentile values (vertical bars protruding from boxes) of the relative radiance I, degree of linear polarization p and angle of polarization α with respect to the vertical measured by video polarimetry at sunlit surfaces of six bright and six dark Swiss ponds in three different viewing directions: towards the sun, away from the sun and perpendicular to the sun at 650, 550 and 450 nm. Data for dark or bright ponds are shown by dark grey or white boxes, respectively. t-test (Sachs 1974) was used, S*: $p<0.05$, S**: $p<0.01$, S***: $p<0.001$, NS: not significant. (After Fig. 1 of Bernáth et al. 2002, p. 1711).

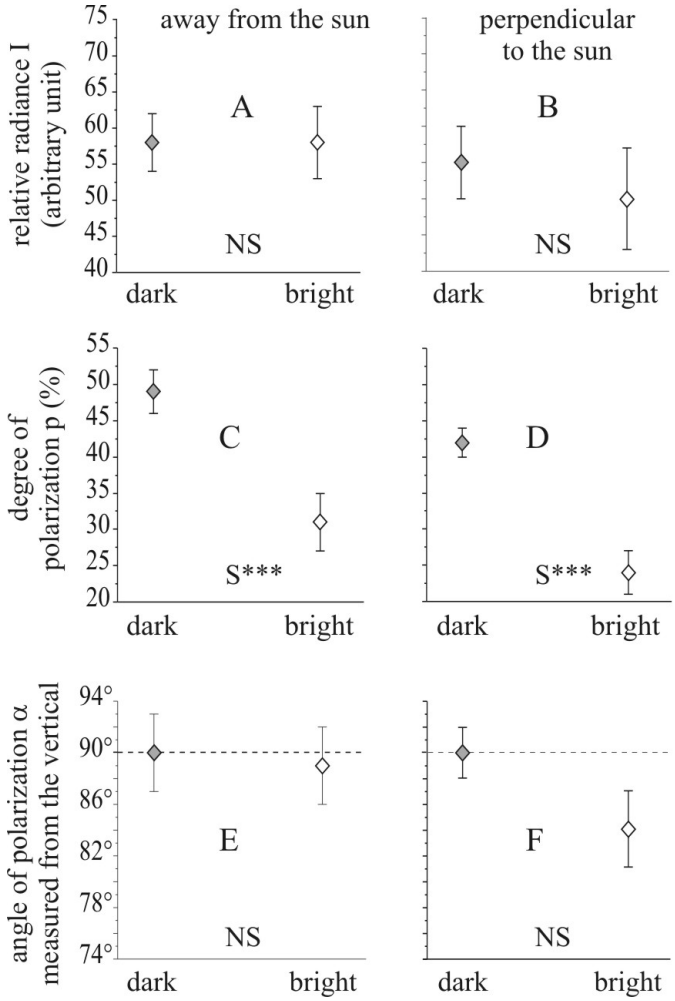

Fig. 17.2. *I*, *p* and α in two different viewing directions away from the sun and perpendicular to the sun at 360 nm. Other conventions as in Fig. 17.1. (After Fig. 2 of Bernáth et al. 2002, p. 1712).

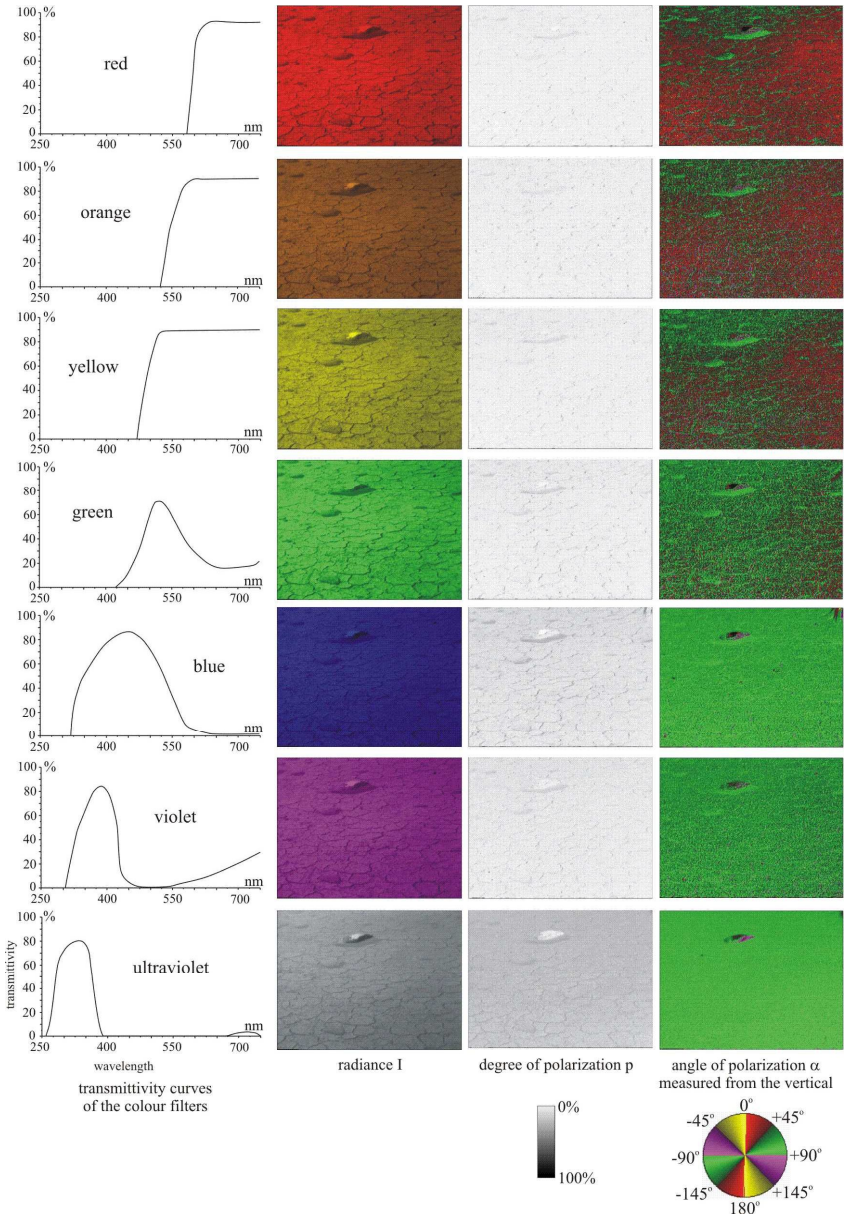

Fig. 17.3. Transmittivity $T(\lambda)$ versus wavelength λ of the colour filters used in the video-polarimetric measurements (left column) and reflection-polarization patterns (relative radiance I, degree of linear polarization p and angle of polarization α from the vertical) of light reflected from a bright pond in a gravel pit measured by video polarimetry in seven different ranges of the spectrum perpendicular to the sun with a viewing angle of 20° from the horizontal. (After Fig. 3 of Bernáth et al. 2002, p. 1713).

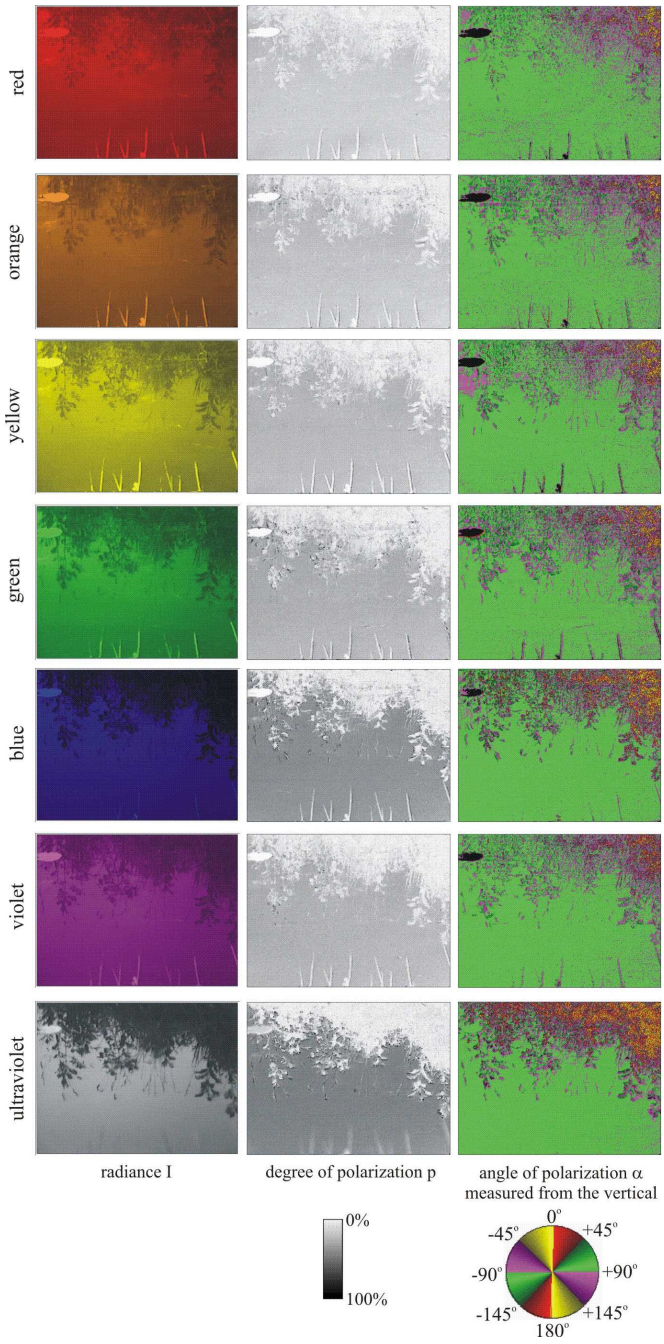

Fig. 17.4. As Fig. 17.3 for a dark pond in a peat digging measured away from the sun. (After Fig. 4 of Bernáth et al. 2002, p. 1714).

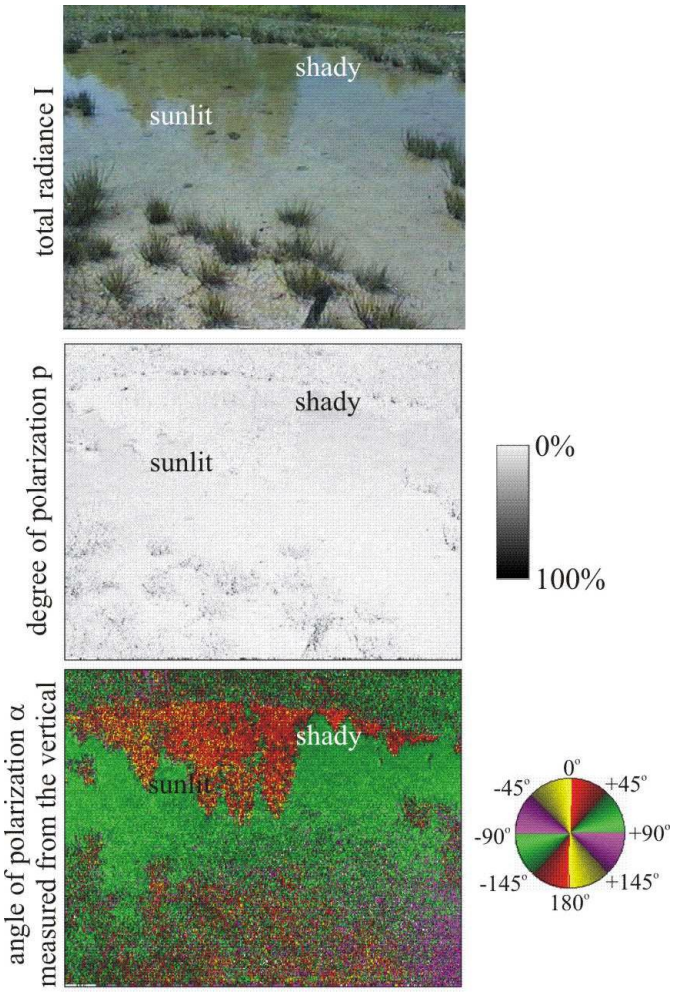

Fig. 17.5. Reflection-polarization patterns of a sunlit bright pond with shady regions measured by video polarimetry at 550 nm perpendicular to the sun with a viewing angle of 20° from the horizontal. (After Fig. 5 of Bernáth et al. 2002, p. 1715).

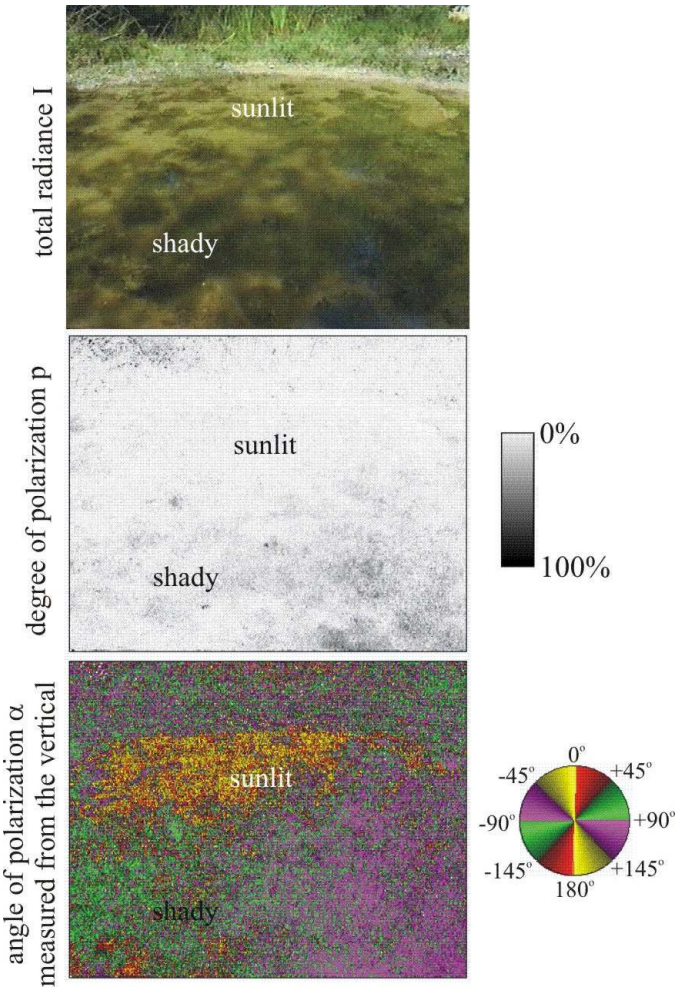

Fig. 17.6. As Fig. 17.5 for another shady bright pond with sunlit regions measured away from the sun. (After Fig. 6 of Bernáth et al., 2002, p. 1716).

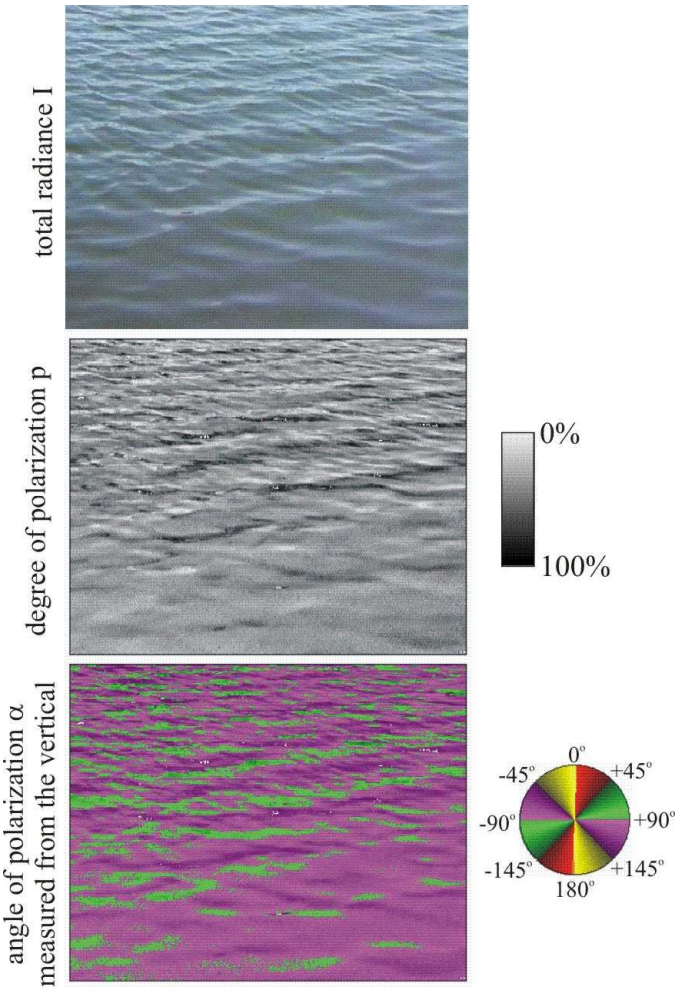

Fig. 17.7. As Fig. 17.5 for a dark lake with undulating surface measured away from the sun.

18 Oil Reservoirs and Plastic Sheets as Polarizing Insect Traps

18.1 Oil Lakes in the Desert of Kuwait as Massive Insect Traps

During the Gulf War in early 1991, Iraqi occupation forces blasted oil wells and pipelines in the desert of Kuwait, forming more than 900 oil ponds. Several years later, the majority of these oil lakes (Figs. 18.1A,B) still existed (Pearce 1995) and continued to trap a variety of animals, mainly insects (Pilcher and Sexton 1993; Horváth and Zeil 1996). Reductions in the oil level due to evaporation and percolation into the ground created distinct bands of insect carcasses at their edges (Fig. 18.2). Bands of dead dragonflies, damselflies and ground-beetles reflected arrivals of migrating insects in autumn and spring. Mass arrivals of aeschnid dragonflies were witnessed by Jochen Zeil in October 1994 and February 1995, many females being trapped while attempting to lay eggs in the oil. Different species of water beetles (Dytiscidae, Coleoptera), giant water scorpions (*Belostoma* sp., Nepidae, Heteroptera), mole crickets (Gryllotalpidae, Orthoptera) as well as sphingid moths, *Vanessa* butterflies, solifugid spiders, scorpions, reptiles, birds and mammals were found at the edge of the oil ponds.

In summer and early autumn, when maximum air temperature ranges between 40 and 50 ^{o}C in the desert of Kuwait, the viscosity of the oil is so low that wind transported sand sinks to the bottom thus leaving the surface flat and shiny. The winter rains and the seasonal drop in temperature have two effects on the appearance and consistency of the oil lakes: the oil becomes more viscous, sand settles on and remains on the oil surface, and the sand-covered oil is pushed to the bottom by accumulating rain water. As the temperature rises in spring, tar domes appear at the bottom of the water lakes and in contact with the surface disperse into a thin oil film. By May, when the water has evaporated, the surface of the ponds again consists of smooth and shiny, low-viscosity oil.

These oil lakes trap different animals in different ways. In summer and autumn, when water has already evaporated, terrestrial animals (e.g. ground beetles, solifugid spiders, lizards and rodents) become entrapped by chance at the edges of the ponds during foraging or migration. During winter and spring they may have been attracted to the water that overlies the tar. Water-seeking birds (e.g. herons, egrets) and many flying insects (e.g. butterflies, dragonflies) land directly on the

surface or at the edge of the oil lakes also during times of the year when the surface is completely covered by oil. While some insects might have crashed into the oil, others have been clearly attracted to the oil lakes.

Horváth and Zeil (1996) suggested that certain insects were attracted by the strong horizontal polarization of light reflected from the surface of the oil ponds. There are a number of reasons, why oil surfaces may be even more attractive than water surfaces to animals sensitive to the polarization of reflected light:

1. Crude oil is a better polarizing reflector, because it has a higher refractive index than water. The index of refraction of clear water is 1.33 for the middle range of the visible spectrum. Oil has a refractive index of 1.39-1.49 depending on its composition, but the refractive index of tar can be as large as 1.57 (Levorsen 1967).
2. The higher viscosity of oil has the effect that the reflection polarization of light is less distorted by wind-induced ripples.
3. Since crude oil is not transparent, the light reflected from flat oil surfaces is always horizontally and more strongly polarized than that reflected from transparent water bodies.

To demonstrate the stronger polarizing ability of an oil surface relative to that of a water surface, Horváth and Zeil (1996) compared the reflection-polarizational characteristics of crude oil and transparent/translucent water surfaces by video polarimetry. Figure 18.3 shows the patterns of radiance I, degree of linear polarization p and angle of polarization α of light reflected from a crude oil surface (left dish) from the surface of clear, transparent water (middle dish) and milky, translucent water (right dish). The dishes were positioned so that the lower half of their surface (closest to the observer) reflected specularly incident diffuse light from an overcast sky while the upper half was in shadow. Note the great radiance contrast between the top and bottom half of the oil surface in the left dish. The light reflected from the bottom half is almost totally polarized and the E-vector is perfectly horizontal. The top half of the oil surface reflects little and almost unpolarized ambient light with horizontal E-vector. In comparison with the oil surface, the contrast between the top and bottom half of the water surfaces in the middle and right dishes is small. The top half returns mainly refracted light that is scattered and reflected from the subsurface layer of the liquid, while the bottom half returns a mixture of refracted and surface-reflected light. The specular surface reflection dominates in the bottom half of the water-filled dishes and has polarizational characteristics similar to the oil surface: high p with horizontal E-vector. In the top half of the water surfaces, however, the returned light is vertically polarized because of refraction at the water surface. Refraction polarization also reduces the net p in the bottom half of the water surface.

The water-filled dishes demonstrate that light emanating from water is vertically polarized whenever the refracted light dominates (top half) and that the light is horizontally polarized when the main contribution stems from surface-reflected light (bottom half). A similar effect cannot occur in an oil pond, because the penetrating light is entirely absorbed by the dark pigments of oil. The E-vector

reflected from a flat oil surface is therefore always horizontal. The larger the p and the smaller the deviation of the E-vector of reflected light from the horizontal, the greater is the attractiveness of the surface to water insects. The consequence is, that a crude oil pond can be even more attractive to water insects than a water lake. Thus, for animals sensitive to polarization, oil lakes could appear as an exaggerated water surface acting as a supernormal optical stimulus.

Figure 18.4 shows the reflection-polarizational characteristics of a Kuwait oil lake in summer when the surface consisted of flat, low-viscosity oil. Figure 18.5 displays the same patterns for another oil lake in winter when rainwater and oil formed complex surface features. In the foreground of the picture in Fig. 18.5 there is a clear water surface; the dark oil surface beyond is broken by wind into bands and channels. The tar bands have a rough texture and reflect light diffusely because sand has settled on the surface. Water and clean oil surfaces are highly polarizing, whereas p of light from the sand-covered tar is very low. The direction of polarization of light from both flat water and oil surfaces is horizontal, while areas with rough surface reflect tangentially polarized light with respect to the sun. The high p of light from the region where oil and water meet (Fig. 18.5) again demonstrates the effect of transparency: the sandy bottom lies in the shadow of a floating oil slab and horizontally polarized surface reflection thus dominates in the blue (Fig. 18.6) due to the blueness of skylight. As with the water-filled dishes, however, p is reduced in the bright areas of water puddles, because the polarization of surface-reflected light is degraded by the refracted, vertically polarized light returning from the sandy bottom.

18.2 The Waste Oil Reservoir in Budapest as a Disastrous Insect Trap for Half a Century

Unfortunately, in many countries plenty of temporary inland oil spills exist as a by-product of the oil industry (exploitation, transport, storage and refinery of the oil). Figure 18.1 shows some typical representatives of such ponds and reservoirs of crude, refused, spent or waste oil in Kuwait (Figs. 18.1A,B) and Hungary (Figs. 18.1C-G). At warm weather the surface of these oil lakes is flat, shiny and acts as an efficient reflector of sunlight and skylight, like a water surface. Since 1951 there has existed an open-air waste oil reservoir (Fig. 18.7) in a suburb of Budapest. Bernáth et al. (2001a,b) observed that this oil reservoir deceived, attracted and trapped insects (Figs. 18.8 and 18.9A) in large numbers. They also measured the reflection-polarizational characteristics of the waste oil surface versus time (Fig. 18.10).

This oil reservoir acted as a disastrous insect trap for 50 years. The uniqueness of this oil reservoir is that it has existed for half a century in a densely populated suburb of a city (Fig. 18.7A), where there was no any natural water surface within 3 kilometres. One must not underestimate the ecological impact of such man-made oil reservoirs on the fauna. Bernáth et al. (2001a,b) observed that even a quite

small and shallow oil spill with an area of a few dm^2 and a depth of a few mm can attract, trap and kill water insects.

Also some ancient natural asphalt seeps in the Earth's history have acted as massive animal traps, and their fossil remains play an important role in palaeontology. Cases in point are the famous Rancho La Brea tar pits at Hancock Park in Los Angeles (Miller 1925; Akersten et al. 1983; Harris and Jefferson 1985). Paleontological excavations in Rancho La Brea began in 1901. Since that time more than 660 species of plants and animals were found in 13 localities. 95% of the entrapped animal species belong to insects. Similar fossil deposits associated with natural oil reservoirs are the tar pools at Starunia in Western Ukraine, the Talara tar seeps in Peru, and the tar pits in Binagadin near Baku in Azerbaidjan (Angus 1973; Kowalski 1999). Most of the insect fossil remains found in Starunia were water beetles belonging to the genus *Helophorus* (Angus 1973). The carcasses of water beetles are better preserved than those of soft-bodied species. Thus one may assume that many other insects associated with water (e.g. nematocerans, ephemeropterans, trichopterans, heteropterans and odonates) were also trapped by these Pleistocene tar seeps, but their carcasses decayed quickly.

It is a general view in palaeontology that Rancho La Brea and Starunia animals might have stumbled accidentally across these tar pools, which may have been camouflaged by dust or leaves (e.g. Miller 1925; Burchak-Abramovich 1975; Akersten et al. 1983; Harris and Jefferson 1985). Alternatively, these asphalt seeps may have been covered by rain-water from time to time, thus attracted animals which then sank into the underlying tar, became entrapped and fossilized (Kowalski 1999). Horváth and Zeil (1996) suggested another possible scenario: Some polarotactic animals were deceived by and attracted to the tar pits, even in the absence of water, by the horizontal polarization of light reflected from the oil surface mimicking a supernormally attractive body of water.

18.2.1 Surface Characteristics of Waste Oil Reservoirs

The waste oil reservoir in Budapest was positioned in the 18th district of the Hungarian capital (47°27'N, 19°17'E) and consisted of seven oil pools situated within an approximately 220 m × 110 m area (Figs. 18.7A-C). Before the Second World War this area was a mine of pebble. During the war the mining operations were stopped, then from 1951 the remained pits were used to store waste, spent and refused oil. The pebble pits were separated by hindrances resulting in the lakes. After appropriate recycling the oil was consumed as fuel, but according to the decrease of demand the plant was closed. Its final removal happened between 1988 and 2001. Figures 18.7A and 18.7C show a satellite and an aerial photograph of the waste oil reservoir, respectively.

The reflectivity of the surface of the oil had a characteristic seasonal cycle: Similarly to the crude oil lakes in Kuwait (Pilcher and Sexton 1993; Horváth and Zeil 1996), in summer the surface of the waste oil was usually mirror flat and shiny (Fig. 18.7D). This was disturbed only rarely by rainfall or cool weather. The

viscosity of the oil remained low due to the great thermal inertia of the oil mass. The oil kept its fluidity also in cooler periods, consequently, the denser rain-water sank down in the lighter oil. Thus the shiny and flat appearance of the black oil surface remained a characteristic feature throughout the warm months (from April to September). Using colour photographs of the waste oil reservoir taken in the warm months (like Fig. 18.7D), many people have been asked: What do these pictures display? The answer was always the same: These picture show water reservoirs or dark water lakes. Hence, men apparently could be deceived by the shiny surface of the waste oil, which could be mistaken for water. In autumn the oil surface became gradually dull (Fig. 18.7E) as the air temperature dropped and the oil became more viscous. In winter the surface of the oil became matt and wrinkled, and rain-water accumulated in small pools on it (Fig. 18.7F). Then the oil surface looked like gluey asphalt if it was not covered by snow.

Figures 18.10A-C show the pictures as well as the degree of linear polarization p and angle of polarization α of light reflected from the surface of the waste oil reservoir versus time. In Fig. 18.10D the daily maximal air temperature T in Budapest and the average $p_{average}$ of light reflected from the oil surface are shown as a function of time. $p_{average}$ is calculated for the entire oil surface visible in the pictures. Due to the relatively wide field of view of the camera ($50^o \times 40^o$), the angle of reflection changes vertically on a picture, thus p changes too. On the other hand, p changes from point to point in a picture if the oil surface is not smooth and homogeneous. This was the case in the cooler and colder months when the oil surface was dull, matt or even wrinkled sometimes.

It is clear from Fig. 18.10 that also the reflection-polarizational characteristics of the surface of the waste oil reservoir had a seasonal cycle: In summer (from June to August) the oil surface reflected highly and horizontally polarized light (rows 1 and 6 in Fig. 18.10), which remained a characteristic feature throughout the summer. In autumn (from September to November) the average p of reflected light gradually decreased as the air temperature decreased (row 2 in Fig. 18.10). The average E-vector direction of reflected light differed considerably from the horizontal in the dull regions of the gradually stiffening oil surface. In winter (from December to February) the average p of reflected light was very low, and the average E-vector direction was not horizontal and changed from point to point (row 3 in Fig. 18.10). In spring (from March to May) as the temperature gradually increased, the average p increased and the average direction of polarization approximated the horizontal (rows 4 and 5 in Fig. 18.10).

18.2.2 Insects Trapped by the Waste Oil

Figure 18.8 shows some typical representatives of the insects collected by Bernáth et al. (2001b) from the waste oil reservoir and on the oily shore and the oil surface in Budapest. Table 18.1 summarizes the names of insect species, the carcasses of which were collected from the waste oil and could be identified. Dragonflies, mayflies, water bugs, water beetles and butterflies were trapped *en masse* by the oil in spring, summer and autumn at the time of their swarming and migration.

Usually, the insects landed or plunged directly on the sticky oil surface and became immediately entrapped. Pairs of insects, e.g. dragonflies and mayflies, were trapped frequently by the oil during copulation and/or egg-laying. Depending on the viscosity of the oil, the trapped insects sank within more or less time. The greater the oil temperature, the lower the oil viscosity, and the shorter the time interval (ranging from 5-10 seconds to 1-3 months) between landing and submergence of an insect.

Most of the insect carcasses filtered from the oil were in very bad condition, so that it was not possible to identify them. Insects with softer bodies decayed almost completely; in most cases only their wings remained, and carcasses of coleopterans were preserved in the best condition. Bernáth et al. (2001b) assumed that the insects found in the oil may have been trapped during the last year before the sampling. To estimate the number of insect carcasses in the oil lake, fragments of the bodies were counted separately. The minimum number of insects allowed by the number of body parts was calculated, although they could have belonged to more individuals.

Filtrates contained insects associated with water in large numbers (Table 18.1). Ephemeropterans and Trichopterans could be identified only on the basis of their wing remains. Species of Corixidae were abundant (although in most cases only their wings remained). Nematocerans were found most frequently; 44% of them could be classified as Chironomids. Hymenopterans were found in large numbers, many of them were swarming ants. An estimate was made of the numbers of different aquatic insect groups identified in the waste oil (Table 18.2). Although these numbers should be considered as a gross approximation, it is clear that the waste oil reservoir trapped a huge number of insects during its existence of half a century. Certain insects, e.g. *Mantis religiosa* and *Oryctes nasicornis holdhausi*, probably became entrapped by the oil during their walk when they reached the shore of the oil reservoir, where the soil and the pebbles were covered by the sticky oil. Although some of the larger insects, like great silver diving beetles (*Hydrophilus piceus*), were able to crawl out from the oil to the shore or to a pebble (Fig. 18.8E), they soon perished because their trachea openings became filled by oil. This is one of the reasons why so many carcasses of large insects could be found on the shore of the waste oil. The other reason is that the level of the oil gradually decreased from year to year, so that many insect carcasses became exposed on the shore (Figs. 18.8A,B,F).

18.2.3 Behaviour of Dragonflies Above Oil Surfaces

Several dragonfly species are on a list of protected insects in many countries. Unfortunately, in practice they receive no protection from several environmental damages; they are entrapped in large numbers by the natural tar seeps or artificial open-air oil reservoirs, for instance. Studying their reaction to the water-imitating black oil surfaces could help in suggesting necessary measures to be taken for the prevention of their mass trapping by these oil surfaces.

Horváth and Zeil (1996) as well as Bernáth et al. (2001b) observed also the behaviour of larger dragonflies above the crude oil lakes in Kuwait and the waste oil reservoir in Budapest, respectively. Male dragonflies frequently patrolled above the flat oil surface and protected their territory against all intruders (Fig. 18.9A). They tried to attack all flying objects (e.g. other dragonflies and larger insects, birds, and even helicopters and airplanes). Male dragonflies often sat guard on the tip of perches at the shore (Fig. 18.9B). Copulating pairs of dragonflies were frequently observed flying above the oil surface or trying to lay eggs into the oil. They became trapped during water-touching manoeuvres or egg-laying. In the latter case sometimes only the female became entrapped when the tip of her abdomen was dipped into the oil (Fig. 18.9C). In many cases, however, the male was also carried along with the female into the oil (Fig. 16.1C). Touching the surface by dragonflies observed often at oil lakes is a reaction, which is typical only above water surfaces when dragonflies inspect the surface to select the optimal habitat or oviposition site (Wildermuth 1993; Corbet 1999). The most frequently observed behaviour types of dragonflies above the oil surface were the air fight, hovering and protection, which again are typical only above water surfaces (Horváth et al. 1998a; Wildermuth 1998; Corbet 1999).

After rain, pools of water formed on the shore of the waste oil reservoir. The surface of these pools was covered by a thin iridescent oil layer. Dragonflies or other insects that touched the surface of a water pool with a thin oil layer frequently became entrapped and drowned because the oil wets the wings.[1] Even if the insect could crawl out from the water, its trachea openings were blocked by the oil. The same was observed by Horváth and Zeil (1996) at the crude oil lakes in the desert of Kuwait (Figs. 18.9D-F). In the case of unpolluted water bodies dragonflies and larger water beetles can fly out easily from the water if they are dropped into water (Corbet 1999).

18.3 Dual-Choice Field Experiments Using Huge Plastic Sheets

Bernáth and Horváth (1999) as well as Bernáth et al. (2001a,b) performed dual-choice field experiments with insects and birds. Two huge plastic (polyethylene) sheets (Fig. 18.14) measuring 20 m × 30 m were laid on the ground in a large alkaline field at about 500 m from a smaller alkaline lake. Such plastic sheets are commonly used in agriculture against weeds, and/or to keep the soil warm in order to speed up the sprouting, or simply to cover produce and to protect it against rain (Fig. 18.11). One of the sheets was black (Figs. 18.14A,C,E) and the other milky translucent (Figs. 18.14B,D,F). The lower surface of the latter dimmed in some minutes following unfolding. Since billions of tiny condensed water droplets

[1] That is why a thin layer of oil has been used for many decades for mosquito control, for example.

scattered the incident light diffusely, the translucent plastic sheet became brilliant white (Fig. 18.14F).

The black plastic sheet was used to imitate the shiny dark surface of oil or tar surfaces, and the white plastic sheet mimicked the surface of brighter bodies of water. The distance between the two plastic sheets was 30 m. In every experiment in the first half of the period the white plastic sheet was closer to the lake, and in the second half of the period the two sheets were transposed with each other. The vegetation beneath the sheets was mown. The sheets were streched out horizontally as tightly as possible and were pinned down by bricks at the edges. Because of wind-generated wrinkles and thermal dilatation in sunshine the surface of the sheets became sometimes uneven, which was compensated by repeated spanning of the sheets, usually at sunrise, noon and sunset. After rains the water was removed from the plastic sheets. During the experiments the insects and birds attracted to the plastic sheets were observed from a hide (Figs. 18.14E,F).

18.3.1 Reflection-Polarizational Characteristics of the Plastic Sheets

Figure 18.15 shows the reflection-polarizational characteristics of a white and a black plastic sheet used in the dual-choice field experiments and measured by video polarimetry. The light reflected from the black plastic sheet has much higher p than the light reflected from the white plastic sheet (Figs. 18.15 and 10.4A). On the other hand, the white plastic sheet reflects a much greater amount of light. The direction of polarization of the black plastic sheet is always parallel to the surface, that is, more or less horizontal. On the other hand, the white plastic sheet reflects more or less vertically or obliquely polarized light. Fig. 18.15 demonstrates well that the shiny black plastic sheet is a more effective polarizer than the white plastic sheet, even relatively far away from the Brewster angle. Thus, the light reflected from the shiny black plastic sheet acts as a supernormally polarized stimulus for polarotactic water-seeking insects.

Comparing the reflection-polarizational characteristics of the plastic sheets (Horváth et al. 1998a; Horváth and Pomozi 1997; Kriska et al. 1998) with those of crude and waste oil (Horváth and Zeil 1996; Horváth et al. 1998a; Bernáth et al. 2001b), asphalt (Kriska et al. 1998) and natural water bodies (Horváth et al. 1998a; Horváth and Varjú 1997; Horváth and Zeil 1996; Kriska et al. 1998; Bernáth et al. 2002a) the following can be established: The optical characteristics of the shiny black plastic sheet are practically the same as those of wet, marshy soil; dark, deep water bodies and black crude/waste oil or asphalt surfaces. The reflection-polarizational characteristics of the shiny white plastic sheet are very similar to those of bright-bottomed shallow clear water bodies and turbid white (e.g. alkaline) water. Because the oil surface and the plastic sheets are colourless, their reflection-polarizational characteristics are practically independent of the wavelength.

18.3.2 Insects Attracted to the Shiny Black Plastic Sheets and their Behaviour

Figure 18.12 shows some examples how water-loving insects can be deceived by and attracted to different artificial shiny dry surfaces such as the body-work of cars, black plastic sheets and asphalt roads. Figure 18.13 shows examples for the behaviour of a great diving beetle (*Dytiscus marginalis*) on a shiny dry black plastic sheet at sunset: The water beetle landed on the plastic sheet, touched and probed the surface. Then flew up from the plastic sheet and looked for another place. After landing again, the beetle tried to swim, crawl or creep on the smooth plastic sheet. After half an hour the beetle got entirely exhausted, it could not fly away, although it tried to fly up several times. Within an hour the beetle perished.

Bernáth et al. (2001b) found that only the black plastic sheet laid onto the ground attracted insects associated with water (Table 18.3), and the white plastic sheet was totally unattractive to them. Although they checked both plastic sheets every day, they found water insect carcasses exclusively on the black plastic sheet. The carcasses of insects larger than 5 mm collected during 10 days included 86 Hydrophiliidae, 42 Dytiscidae, 23 Corixidae and 21 Notonectidae. There was no any carcass on the white plastic sheet. All these aquatic insects showed similar behavioural elements on and above the black plastic sheet: landing, flying up, touching, crawling, egg-laying, copulating, reproductive activity. Finally, all of them dried out and perished within some hours. Butterflies, flies, bees, wasps and dragonflies were also attracted to both plastic sheets, but they did not perish on them. Sometimes Bernáth et al. (2001b) searched the plastic sheets by eye and using binoculars for 3-4 hours and checked the insects that landed on them. They found no aquatic insects crashing on the white plastic sheet. At sunset the black plastic sheet was as cool as the white one. Thus one must conclude that the higher temperature of the black plastic sheet was not the reason why only the black plastic sheet trapped aquatic insects. Apparently, the black plastic sheet was visually more attractive to water-seeking insects than the white one.

When the plastic sheets were laid onto the ground in the vicinity of an alkaline lake near Kunfehértó, almost at every sunset Bernáth et al. (2001b) heard the black plastic sheet rattle sounding like the pattering of raindrops. The reason for this was thousands of Corixidae landing on and crashing into the black plastic sheet, then jumping repeatedly up and down. They did not leave the optical trap, and did not fly away from the visually attractive black plastic sheet; they remained on it throughout the night and perished. At the white plastic sheet similar effect was not observed.

18.4 The Possible Large-Scale Hazard of "Shiny Black Anthropogenic Products" for Aquatic Insects

Horváth and Zeil (1996) as well as Bernáth et al. (2001a,b) identified a seldom addressed conservation and animal welfare issue, the possible large-scale hazard of all "shiny black anthropogenic products" including oil reservoirs (Figs. 18.1, 18.2, 18.4, 18.5 and 18.7) as well as asphalt and plastic sheets used in agriculture for aquatic insects (Fig. 18.11). From the study of the impacts of the crude oil lakes in Kuwait and the waste oil reservoir in Budapest to the insect fauna they recognized a more general problem, the attraction of aquatic insects to oil lakes, black plastic sheets and other black and shiny surfaces. These insects show the same behaviour at these surfaces (Figs. 18.9, 18.12 and 18.13) as at real water surfaces; these typical water-specific behavioural elements involve touching the water surface (e.g. at egg-laying or probing the oviposition site), or landing on the water surface, or plunging into the water. All these reactions are fatal for insects in the case of oil surfaces, because the sticky oil traps the insects. Even a thin oil layer on the water surface can hinder insects from escaping, the consequence of which can be drowning (Figs. 18.9D-F). It is important to emphasis that water insects laid their eggs on the surface of plastic sheets, so these surfaces may endanger the renewal of their populations too (Kriska et al. 1998). Although the dry shiny black plastic sheets used frequently in agriculture cannot mechanically trap the attracted insects as does the sticky oil, they can be very dangerous to aquatic insects, because the polarization of light reflected from such smooth, shiny surfaces are so strong that polarotactic insects associated with water are visually compelled to remain on the dry plastic sheets in spite of the fact that other senses signal that these surfaces are not water (Figs. 18.12 and 18.13). The consequence of this reaction is drying out and perishing.

Bernáth et al. (2001b) called the attention to the dangerous visual deceiving capability of the huge shiny black plastic sheets to insects and demonstrated that the attracted insects can perish *en masse* on these plastic sheets. The visual ecological impacts of these plastic sheets to the insect fauna must not be underestimated in those habitats and biotopes, in the vicinity of which such huge shiny black plastic sheets are used in agricultural production (Fig. 18.11). The impact of oil reservoirs on the fauna is well-known, and problems with oil spills have been well documented especially for the marine fauna (e.g. Pilcher and Sexton 1993; Pearce 1995). Much less attention has been paid to the possible global impact of oil wastes and other black and shiny products on the continental aquatic fauna.

On the basis of the above it is clear that if the degree of linear polarization p of reflected light could be somehow reduced and it could someway be ensured that the direction of polarization of reflected light differs from the horizontal, then the dangerous visual attractiveness of "shiny black anthropogenic products" to polarotactic insects could be reduced or even eliminated. A general rule is that the brighter and rougher a surface, the lower is p of reflected light (Umov effect) and the more can deviate the direction of polarization from the horizontal. Thus, Bernáth et al. (2001b) suggested the following environmental protective

arrangements that should be taken in the vicinity of habitats of insects associated with water:

- In agriculture, the huge shiny black plastic sheets should be replaced by matt grey or white plastic sheets. It has to be investigated still whether these sheets would perform their agricultural function as properly as black sheets, and therefore be acceptable by farmers.
- Until their removal, the surfaces of open-air oil reservoirs, spills and seeps should be covered by a thin layer composed of finely granulated white polystirol spheres, for example. This layer may require frequent renewal, because the spheres themselves can become coated all over.

These measures would be relatively inexpensive and could save countless members of the insect fauna in the vicinity of open-air oil reservoirs and areas where huge plastic sheets are used in agriculture.

Tables

Table 18.1. Insect species, the carcasses of which were collected from the waste oil lake in Budapest and could be identified. (After Table 1 of Bernáth et al. 2001b, p. 97).

ODONATA: *Aeshna mixta, Anax imperator, Sympetrum vulgatum*
HETEROPTERA: *Callicorixa concinna, Corixa punctata, Gerris lacustris, Gerris pallidus, Hesperocorixa linnei, Notonecta glauca, Ranatra linearis, Sigara falleni, Sigara lateralis, Sigara striata*
COLEOPTERA: *Acilius sulcatus, Coelambus impressopunctatus, Colimbetes fuscus, Copelatus ruficollis, Cybister laterimarginalis, Dytiscus circumflexus, Dytiscus marginalis, Elaphrus riparius, Hydaticus transversalis, Hydrophilus atterinus, Hydrophilus piceus, Hyphydrus ovatus, Ilybius subaenus, Oryctes nasicornis, Longitasrus tabidus, Rhanatus punctatus,*
MANTODEA: *Mantis religiosa*

Table 18.2. Numbers of insects of different groups associated with water identified in the 3000 m^3 of the waste oil lake in Budapest and estimated for 1 year and 50 years. (After Table 2 of Bernáth et al. 2001b, p. 97).

	Odonata	Trichoptera	Ephemeroptera	Nematocera	Corixidae	Dytiscidae
1 y	$150 \cdot 10^3$	$100 \cdot 10^3$	$50 \cdot 10^3$	$17.9 \cdot 10^6$	$1.4 \cdot 10^6$	$600 \cdot 10^3$
50 ys	$7.5 \cdot 10^6$	$5 \cdot 10^6$	$2.5 \cdot 10^6$	$895 \cdot 10^6$	$70 \cdot 10^6$	$30 \cdot 10^6$

Table 18.3. Insect species attracted to the shiny black plastic sheet used in the dual-choice field experiments. (After Table 3 of Bernáth et al. 2001b, p. 99).

EPHEMEROPTERA: *Baetis rhodani, Cloeon dipterum, Ecdyonurus venosus, Epeorus silvicola, Ephemera danica, Haproleptoides confusa, Rhitrogena semicolorata,*
PLECOPTERA: *Perla burmeisteriana*
COLEOPTERA: *Acilius sulcatus, Anacaena limbata, Besorus luridus, Copelatus ruficollis, Cybister laterimargnalis, Cymbiodita marginella, Dytiscus dimidatus, Hydaticus transversalis, Hydrobius fusipes, Hydrochara caraboides, Hydrochara flavipes, Hydrophilus piceus, Hyphydrus ovatus, Laccophilus obscurus, Phylidrus bicolor, Rhanatus punctatus, Spercheus emarginatus*
HETEROPTERA: *Aigara assimilis, Corixa affinis, Cymatia rogenhofferi, Hesperocorixa linnei, Notonecta glauca, Sigara falleni, Sigara lateralis, Sigara striata*

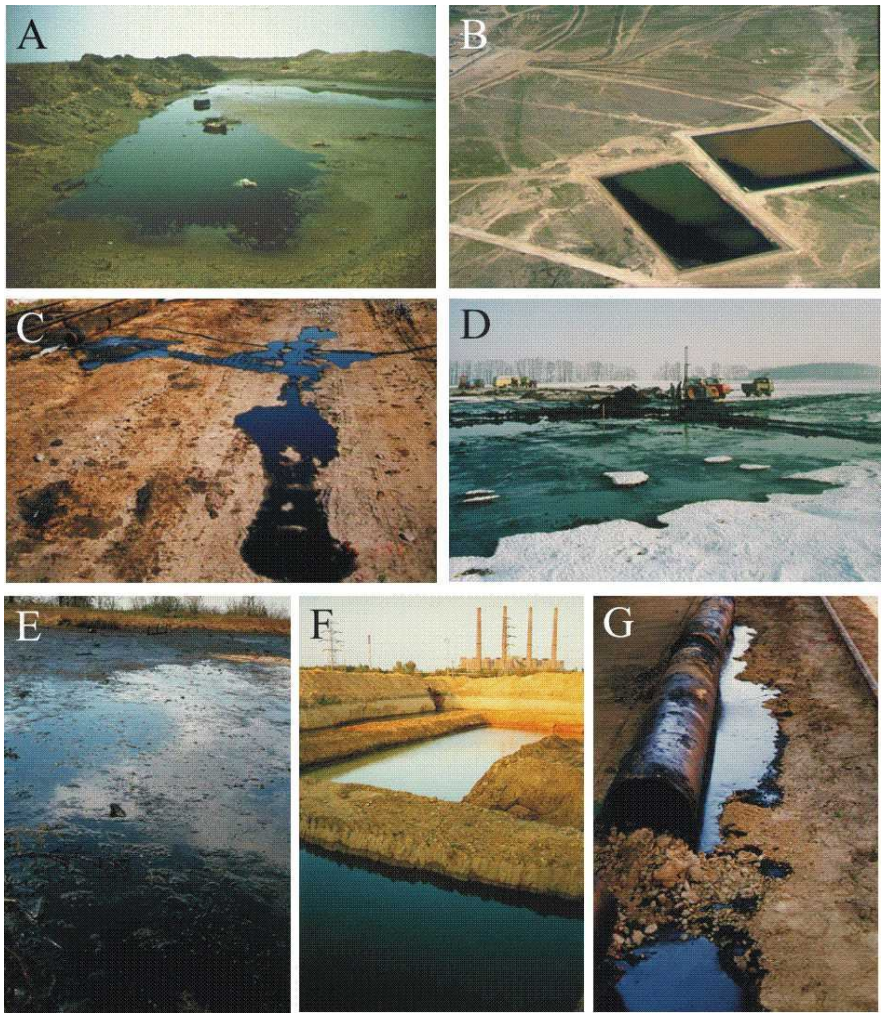

Fig. 18.1. Some typical representatives of small and great open-air reservoirs of crude, refused, spent or waste oil in the desert of Kuwait (A, B) and in Hungary (C-G). A: a crude oil pond in Kuwait photographed in September 1995 by Dr. Jochen Zeil; B: two rectangular reservoirs filled with crude oil (left, bottom) and water (right, top) in Kuwait photographed from an airplane in September 1995 by J. Zeil; C: a puddle composed of crude oil spilled during pouring from railway tanks into another tanks; D: a crude oil spill around an oil well in a snow-covered field; E: a refused oil lake in an oil refinery; F: two reservoirs filled with spent oil (bottom) and rain water (top) in a thermal power-station; G: waste oil puddles around percolating rusty barrels at a railway station.

Fig. 18.2. The edge of an oil lake in the vicinity of Kuwait City photographed in September 1995 by J. Zeil. Two distinct bands of mainly aeschnid dragonfly carcasses are visible on the old tar deposits high up at the bank of the lake.

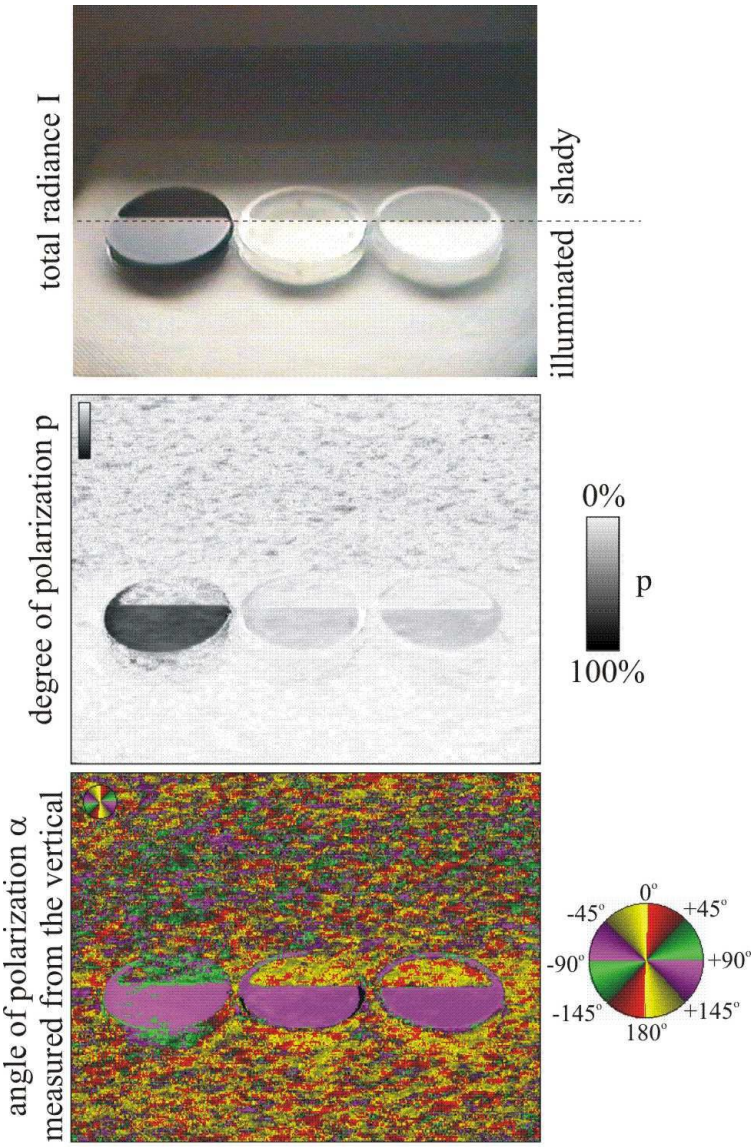

Fig. 18.3. The reflection-polarizational characteristics of three Petri dishes filled with black crude oil (left), clear water (middle) and milky water (right) measured by video polarimetry at 450 nm. The top half of the dishes is in shadow, the bottom half is illuminated by unpolarized diffuse light from an overcast sky. Viewing direction is 55° relative to the vertical. (After Fig. 1A of Horváth and Zeil 1996, p. 303).

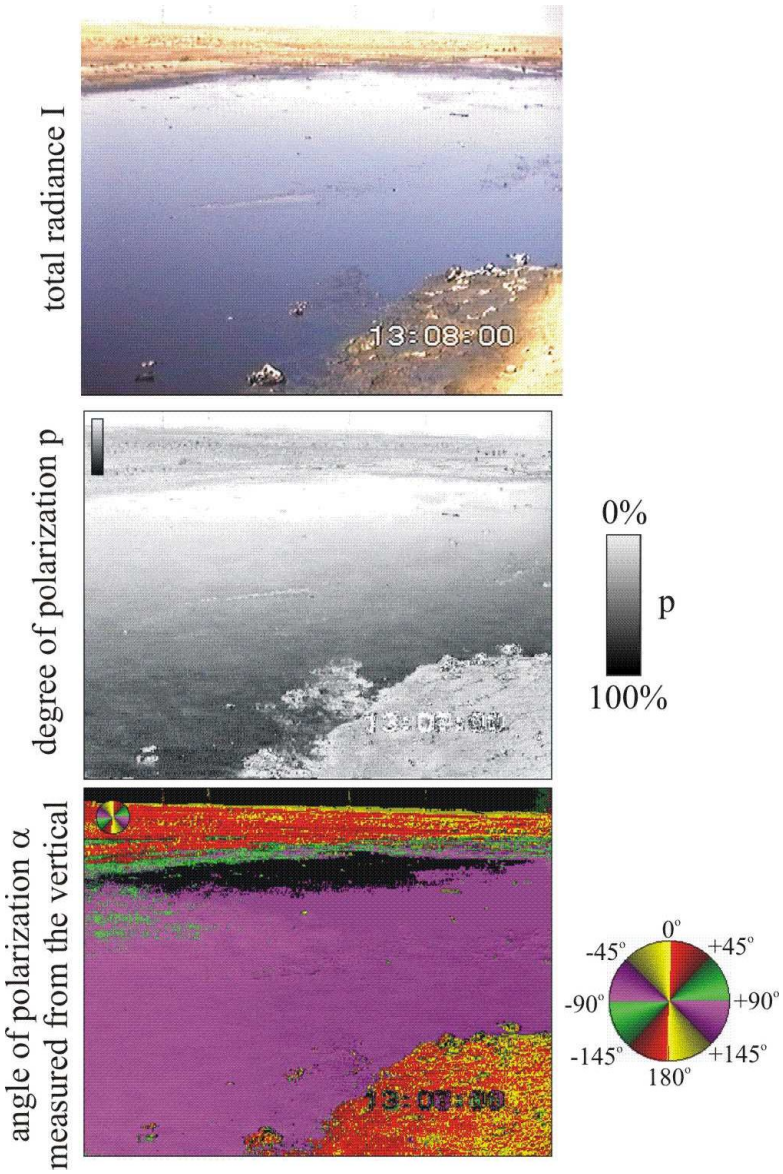

Fig. 18.4. The reflection-polarization patterns of an oil lake in the desert of Kuwait measured on 9 May 1995 at 450 nm. The polarimeter viewed towards North from a direction of 75° relative to the vertical. The surface of the lake was flat due to the low viscosity of oil because of the high air temperature. (After Fig. 1B of Horváth and Zeil 1996, p. 303).

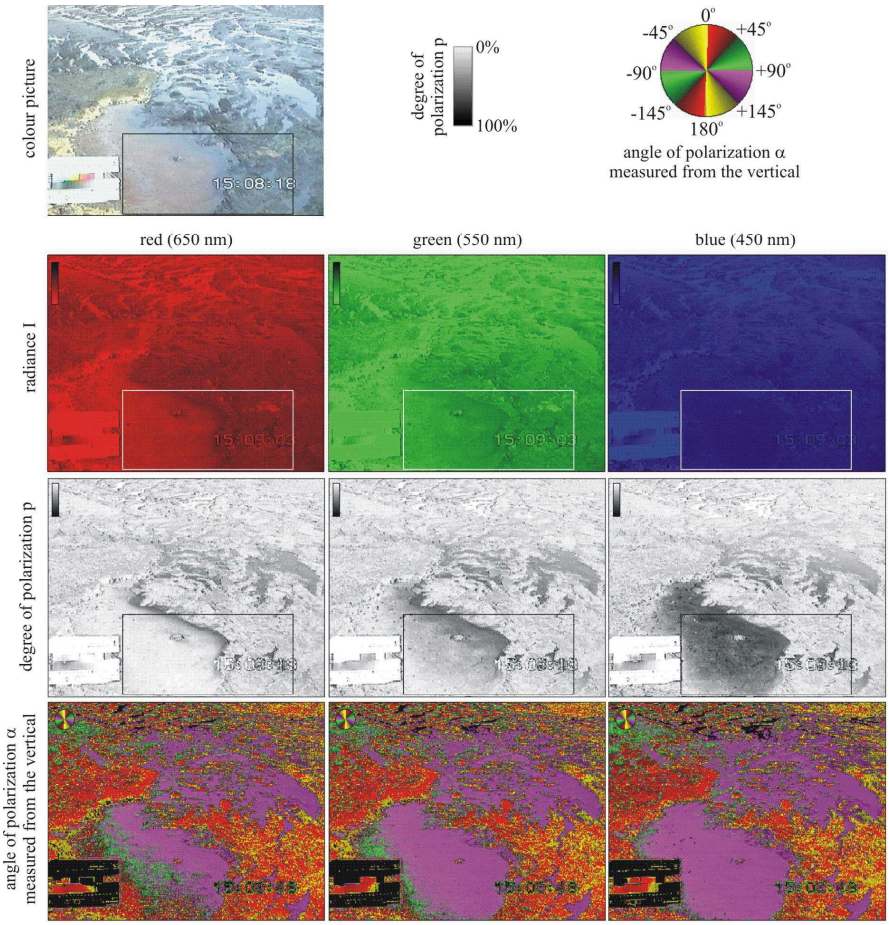

Fig. 18.5. As Fig. 18.4 measured on 15 January 1995 towards East and from 70° relative to the vertical at 650, 550 and 450 nm. Rain water accumulated on the high-viscosity oil during the winter months. Slabs of oil swam on the water surface and sand has settled on it. The areas demarcated with rectangular windows represent the regions, for which the frequency of p is given in Fig. 18.6. The left and right half of the windows contains water and oil surfaces, respectively. (After Fig. 1C of Horváth and Zeil 1996, p. 303).

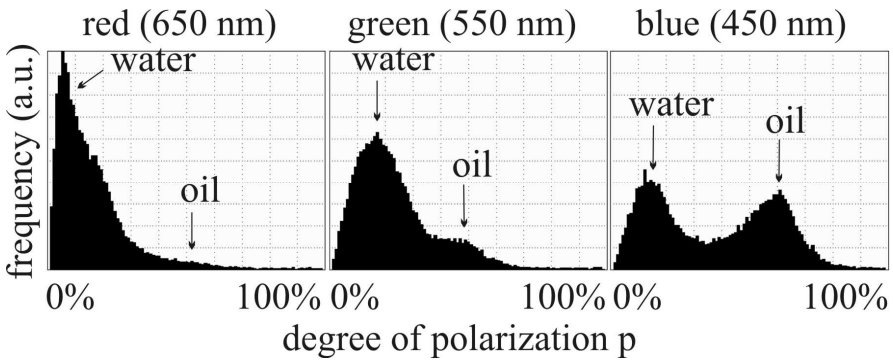

Fig. 18.6. Frequency (in arbitrary unit) of the degree of linear polarization *p* computed for the areas demarcated with rectangular windows in Fig. 18.5.

Fig. 18.7. The waste oil reservoir in Budapest in 1997. A: On this satellite photograph the oil reservoir is the black poligonal patch at the right-hand side marked with a white arrow. B: Schematic map of the reservoir composed of seven smaller oil lakes. C: Aerial photograph of the oil reservoir. D: In summer (July) the oil surface was flat and shiny. E: In Autumn (September) the oil surface became gradually dull as the air temperature decreased. F: In Winter (December) the oil surface became matt and wrinkled, and rainwater accumulated in small pools on it. (After Fig. 1 of Bernáth et al. 2001a, p. 3).

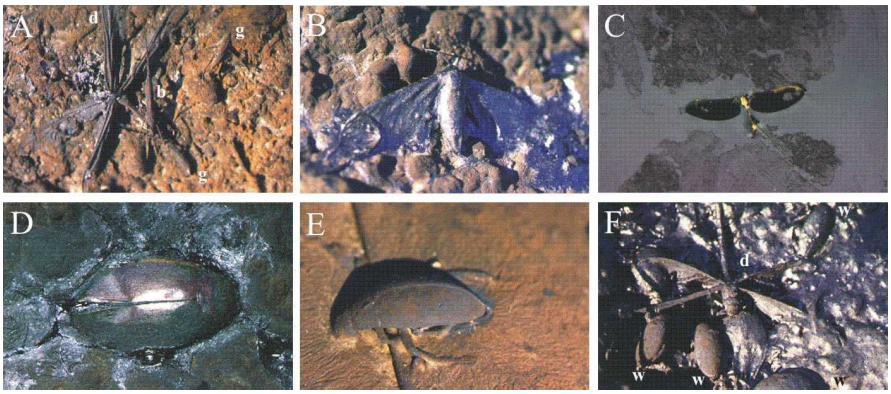

Fig. 18.8. Some typical representatives of the insects collected from the waste oil reservoir in Budapest and photographed on the oily shore (A, B, E, F) and on the oil surface (C, D). A: a dragonfly (d, *Anax imperator*), a long-bodied water scorpion (b, *Ranatra linearis*) and two waterstriders (g, *Gerris lacustris*); B: a moth (Lepidoptera sp.); C: a mayfly (*Cloeon dipterum*); D: a water beetle (*Dytiscus* sp.); E: a great silver diving beetle (*Hydrous piceus*); F: a dragonfly (d, *Sympetrum vulgatum*), and scavenger beetles (w, Hydrophiliidae sp.). (After Fig. 1 of Bernáth et al. 2001b, p. 90).

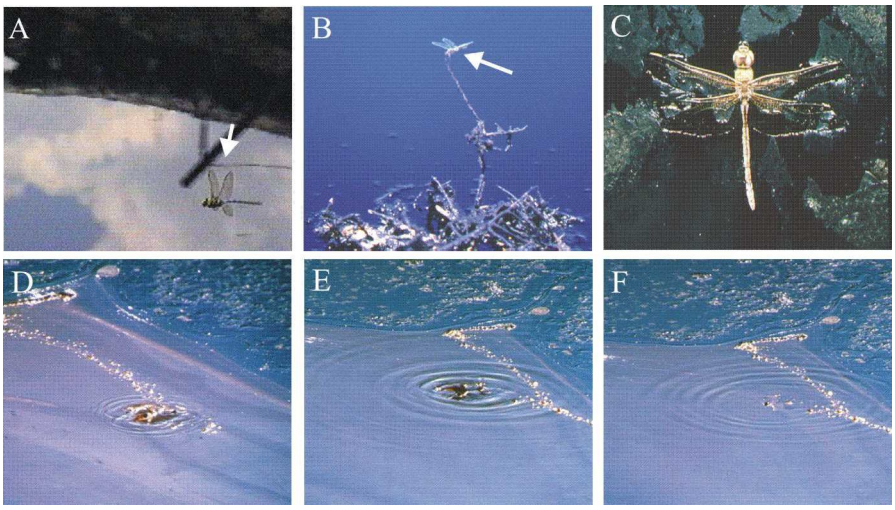

Fig. 18.9. Dragonflies observed at different oil surfaces and trapped by oil. A: A male dragonfly (*Anax imperator*) patrolling above the shiny flat surface of the waste oil reservoir in Budapest. B: A male dragonfly sitting guard on the tip of a perch at the shore of a crude oil lake in the desert of Kuwait photographed in September 1995 by J. Zeil. C: A dragonfly (*Anax parthenope*), that was trapped in the oil moments before the picture was taken in Kuwait in September 1995 by J. Zeil. D-F: When a large dragonfly touched the surface of a water pool with a thin oil layer in the desert of Kuwait (D), it was entrapped (E) and drowned (F; by courtesy of J. Zeil).

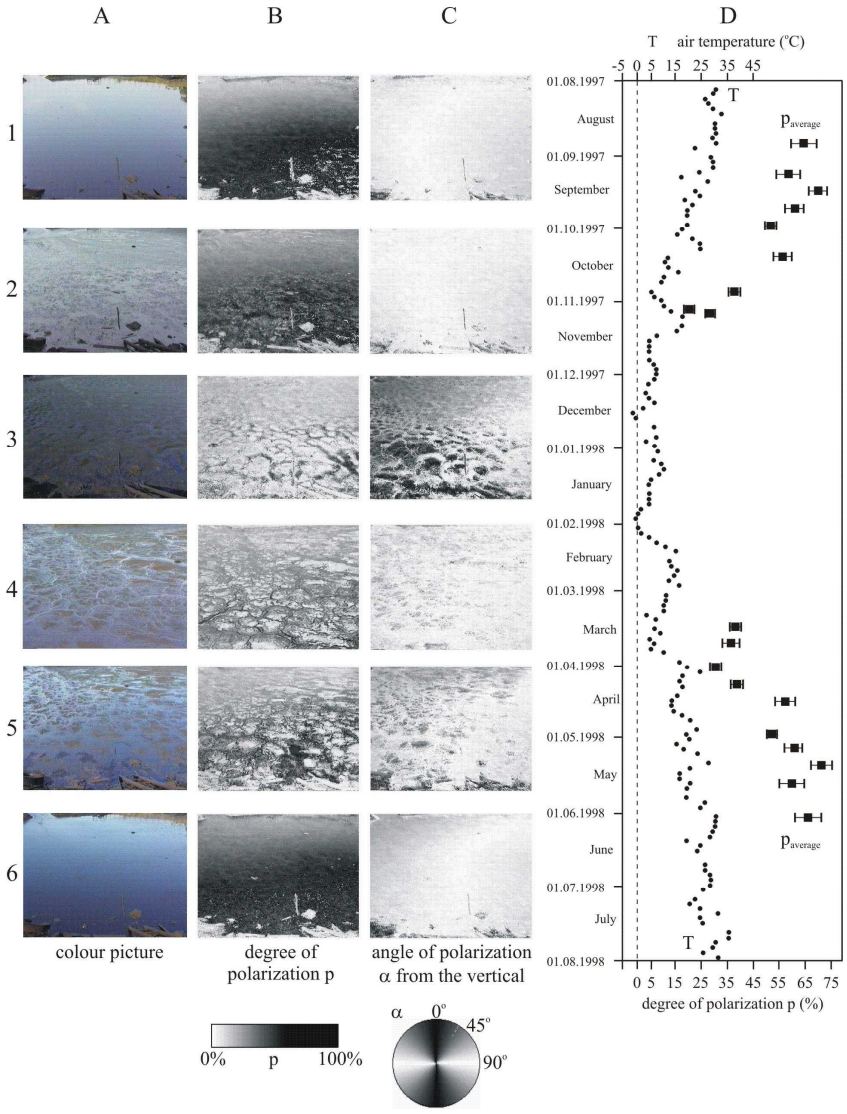

Fig. 18.10. Reflection-polarizational characteristics of the surface of the waste oil reservoir in Budapest versus time measured by video polarimetry at 450 nm under clear skies for a solar zenith angle of 60°. A: Colour picture of the oil surface; B: degree of linear polarization p of reflected light; C: angle of polarization α of reflected light measured from the vertical (black: vertical, $\alpha = 0°$, white: horizontal, $\alpha = 90°$); D: the daily maximal air temperature T in Budapest and the average (calculated for the entire picture) $p_{average}$ of light reflected from the oil surface as a function of time. The horizontal bars represent the standard deviation of p; sample size (= number of pixels in the p-pattern) = 560 × 736 = 412160. Viewing direction of the camera was 60° relative to the vertical and perpendicular to the solar meridian. (After Fig. 4 of Bernáth et al. 2001b, p. 101).

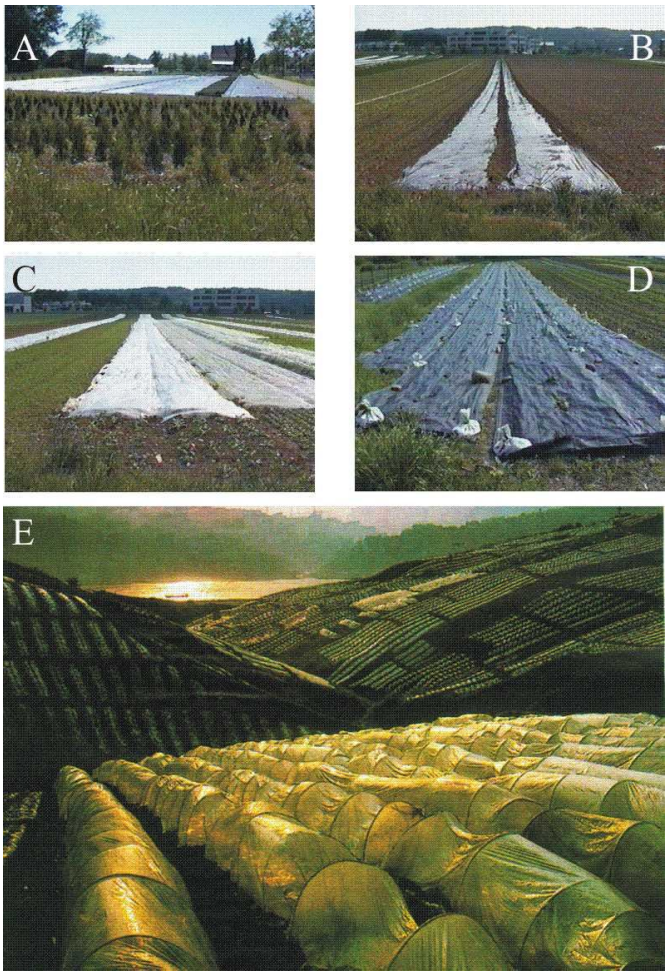

Fig. 18.11. Some examples for huge black (A-C) and white (D, E) plastic sheets used in the agriculture. A: Black plastic sheets cover the ground in this nursery-garden to control the microclimate and to protect against weed. B, C: Black plastic sheets laid on the ground keep warm the soil to accelerate sprouting. D: Air- and water-permeable white plastic meshes protect the underlying plants against frost. E: Thousands of green-houses composed of white plastic sheet in a hilly country.

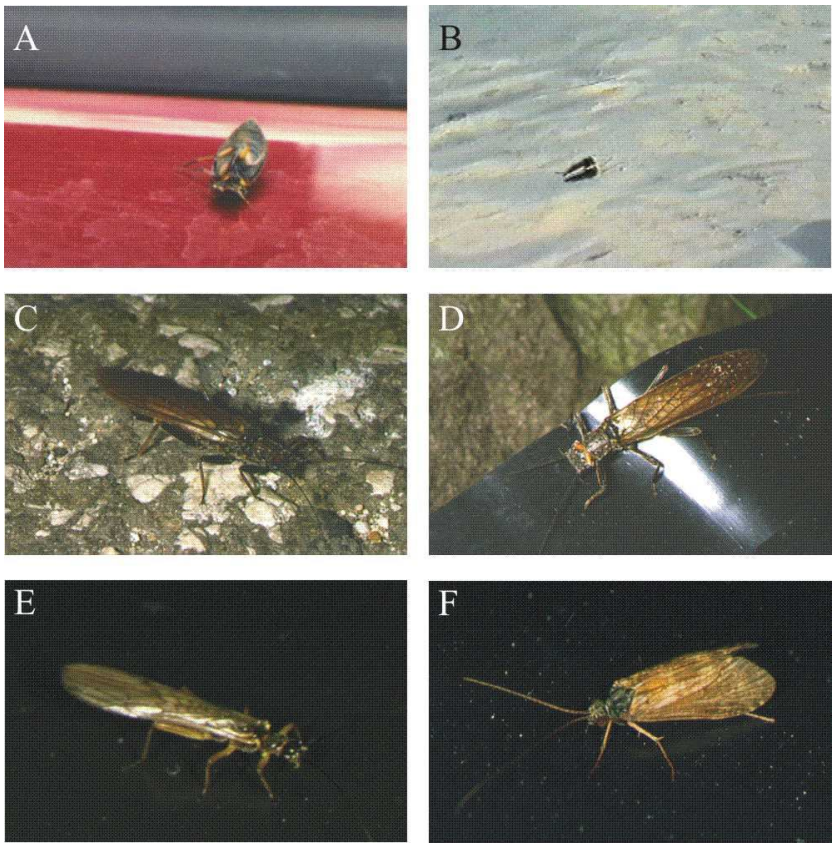

Fig. 18.12. Some examples how insects associated with water can be deceived by and attracted to different artificial shiny dry surfaces such as the bodywork of cars (A), black plastic sheets used in the agriculture (B, D-F) and asphalt roads (C). A: a scavenger beetle (*Hydrochara* sp.); B: a mosquito; C, D: a female large stonefly (*Perla burmeisteriana*); E: a male stone fly (*Nemoura cinerea*); F: a female caddish fly (Trichoptera sp.). (After Fig. 2 of Bernáth et al. 2001b, p. 91).

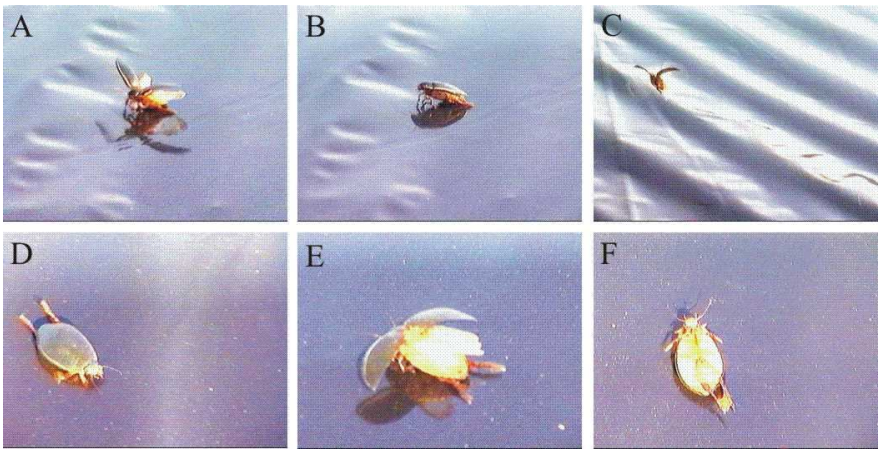

Fig. 18.13. Behaviour of a great diving beetle (*Dytiscus marginalis*) on a shiny dry black plastic sheet at sunset. A: landing on the plastic sheet; B: touching, trying and probing the sheet; C: flying up from the plastic sheet and looking for another place; D: after landing again, the beetle tried to swim, crawled, or crept on the smooth plastic sheet; E: after half an hour the beetle got entirely exhausted, it could not fly away, although it tried to fly up several times; F: after an hour the beetle perished. (After Fig. 3 of Bernáth et al. 2001b, p. 92).

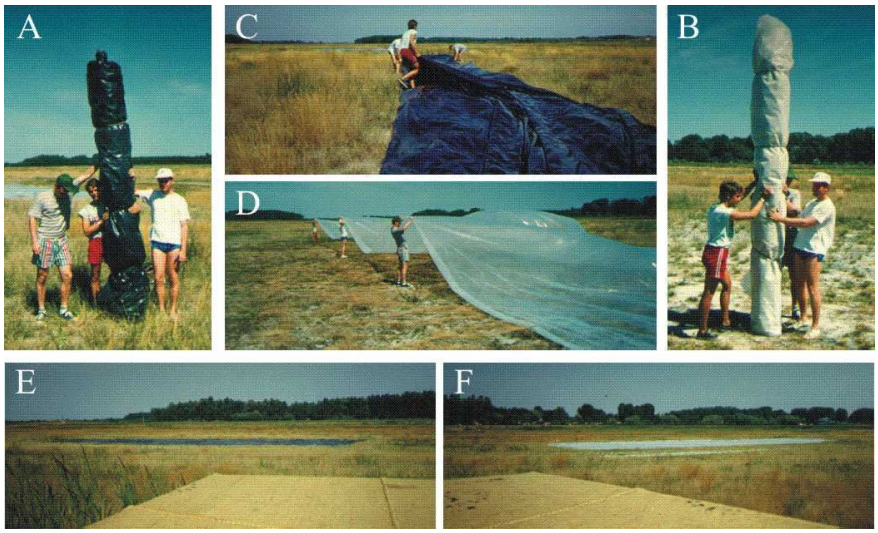

Fig. 18.14. A, B: Rolls of the black and the white plastic sheets used in the dual-choice field experiments. C, D: Unfolding the black and the white plastic sheets. E, F: The oil-lake-imitating black plastic sheet (E) and the water-mimicking white plastic sheet (F) laid out in the field and viewed from a hide, the top of which is seen in the bottom part of the pictures. (After Fig. 3 of Bernáth et al. 2001a, p. 6).

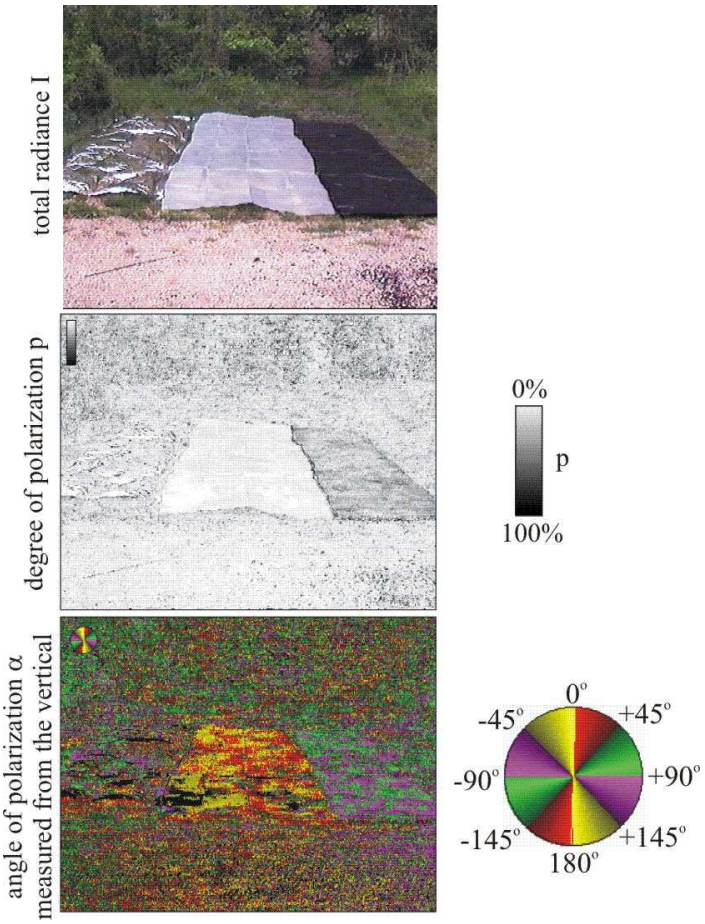

Fig. 18.15. The reflection-polarization patterns of an aluminium foil (left), a white plastic sheet (middle) and a black plastic sheet (right) laid on the ground and measured by video polarimetry at 450 nm under a clear sky at sunset. The viewing direction of the camera was 70° relative to the vertical and perpendicular to the solar meridian.

19 Why do Mayflies Lay Eggs on Dry Asphalt Roads? Water-Imitating Horizontally Polarized Light Reflected from Asphalt Attracts Ephemeroptera

Kriska et al. (1998) observed near sunsets that individuals of several mayfly (Ephemeroptera) species swarmed and mated above and landed on dry asphalt roads (Figs. 19.1A-C), shiny black plastic sheets used in agriculture (Figs. 19.1D-I) and windscreens and roofs of cars (Figs. 19.1J,K) in the immediate vicinity of their emergence sites (mountain streamlets), and that after copulation the females laid their eggs *en masse* on dry asphalt roads (Figs. 19.1A-C) instead of laying them on the water surface. These mayflies showed the same behaviour above the more or less horizontal regions of the surface of cars as above asphalt roads, black plastic sheets and water surfaces. Such behaviour was, however, observed only when the colour of the car was red, black or dark grey. White or light cars (metallic coloured or not) did not attract any mayflies. These observations, especially the egg-laying by females, suggest that the mayflies were apparently deceived by and attracted to these shiny surfaces. Previous descriptions of ephemeropteran swarming, mating and egg-laying behaviour have largely ignored or misinterpreted this phenomenon. Although such observations on Ephemeroptera are known to entomologists, they have been mentioned only sporadically as marginal notes in publications or lectures. There were two different interpretations of this phenomenon:

1. It has generally been assumed, that asphalt roads serve as markers for swarming mayflies.
2. Oviposition by mayflies on asphalt roads has been simply explained by the shiny appearance of wet roads which may lure the insects like the surface of real water bodies.

The first interpretation, however, cannot apply to the observed egg-laying on asphalt roads, because normally mayflies oviposit exclusively onto the water surface and not onto objects serving as markers. However, the behaviour of males and females swarming and mating above asphalt roads are similar to that above water surfaces. The second interpretation cannot explain why egg-laying by Ephemeroptera frequently occurs also on totally dry asphalt surfaces. Kriska et al. (1998) gave a correct and convincing explanation of this surprising behaviour.

In the life cycle of mayflies, only one function is important during the adult stage, the production of progeny. Flight is virtually the only form of locomotion in winged mayflies, therefore the finding of the female, her capture and mating take place in the air. Mating is preceded by peculiar swarming behaviour, during which a group of insects maintains a stationary position with respect to an object of the landscape (Edmunds and Edmunds 1980; Harker 1992). The concentration of males in the swarm and its stationary position are vital conditions for the meeting with females. The maintenance of these conditions is particularly important since the sexually mature stage of mayflies is very short (Brodskiy 1973). Flight in the swarm requires the control of velocity both in relation to a striking visible object of the landscape called the "marker" and, in the presence of wind, relative to the air. Control of the position relative to the marker involves also an optomotor reaction. Markers can be larger objects, the shores of lakes, roads, rows of plants on the littoral, for example (Savolainen 1978). Because of the very short adult stage and the fact that the newly moulted mayflies can dry out quickly, during swarming the mayflies remain relatively close to the water, in which the nymphs develop. Thus, it is essential for the markers to be near water. This is why the role of markers in ephemeropteran swarming has been intensively studied.

Discovering the causes of the above-mentioned strange behaviour of mayflies is important not only for scientific studies of Ephemeroptera, but also for the protection of this insect group since the 6000-9000 eggs laid onto the asphalt roads do not survive. Mayflies are in great danger, because their aquatic habitat is becoming more polluted with herbicides, pesticides, excess fertilisers and industrial waste. Almost all mayfly species are threatened, and many of them have suffered a severe decline during the last decades as a result of habitat destruction by agricultural and urban development and land drainage. As a consequence, mass swarming of Ephemeroptera is now a rare phenomenon. Thus, it is particularly important to determine whether the egg-laying of mayflies on asphalt roads can be prevented. Little attention has been paid to this aspect of ephemeropteran swarming behaviour despite the considerable attention regarding swarm formation.

In an attempt to clarify the causes of reproductive behaviour of mayflies over asphalt roads, Kriska et al. (1998) conducted a 2-year study on six species of mayfies, using visual observations, video recordings, multiple-choice experiments and video-polarimetric measurements in the field. On the basis of these investigations, they proposed a new interpretation for the peculiar behaviour of Ephemeroptera over asphalt roads. Their explanation was that asphalt surfaces near sunset mimic a highly and horizontally polarizing water surface to water-seeking mayflies which, as Kriska et al. (1998) showed, detect water by means of the horizontal polarization of reflected light.

19.1 Multiple-Choice Experiments with Different Test Surfaces

Although Kriska et al. (1998) frequently observed the reproductive behaviour of *Ephemera danica*, *Ecdyonurus venosus*, *Epeorus silvicola*, *Baetis rhodani*, *Rhithrogena semicolorata* and *Haproleptoides confusa* over dry asphalt roads near sunset, they performed multiple-choice experiments only with *Epeorus silvicola* and *Rhithrogena semicolorata*. These experiments were carried out in late May and early June of 1996 and 1997 in Hungary. The study site was the bank of a section of a mountain creek, from which mayflies emerged in large numbers and where they swarmed near sunset during May and June (Andrikovics 1991; Andrikovics and Kéri 1991). In the immediate vicinity, at a distance of 1-5 m from the creek, an asphalt road ran between trees and bushes almost parallel to the water, and in some places it crossed the stream over small bridges. The creek itself ran in a valley under trees and bushes and was usually completely shadowed by riparian vegetation, except where the road crossed it. The road was several metres higher than the creek, and above it the sky was open. The surface of the asphalt road was relatively smooth and dark grey, but there were several lighter grey patches with a rougher surface.

In the multiple-choice experiments, rectangular test surfaces of different types were laid on the asphalt road near different reaches of the creek where mayflies swarmed near sunset. The 1 m × 2 m test surfaces placed 0.5 m apart were: (i) shiny black plastic sheet, (ii) shiny white plastic sheet, (iii) shiny aluminium foil, (iv) slightly shiny black cloth, (v) matt black cloth and (vi) matt white cloth. In order to avoid the influence of colour on the choice of mayflies, the test surfaces were composed of colourless materials. The number of mayflies landing on and swarming immediately above the test surfaces at a height of no more than 0.1 m within a 0.1 m × 0.1 m rectangular region were counted. The position of the test surfaces relative to each other was changed randomly. These experiments were always carried out under clear skies at sunset. At the beginning of an experiment, the landscape was illuminated by the setting sun and, after sunset, by skylight from above.

19.2 Swarming Behaviour of Mayflies

At the study site, depending on species, the swarming of mayflies began prior to and after sunset every evening from the beginning of May until the end of June. After the emergence of the newly hatched insects from the mountain creek, the males gathered in several diffuse swarms in the air at a distance of approximately 4-5 m from the ground. At the beginning of swarming, these relatively diffuse swarms were observed everywhere above the streamlet, asphalt road, dirt roads and clearings in the vicinity of the emergence sites. Generally, these swarms developed at places where the sky was visible. As time elapsed, the swarms

gradually approached the ground and more females flew through them in order to copulate with the males. After mating, the females returned to the streamlet or landed on the asphalt road and laid their eggs on the water or asphalt surface.

Later, as the air temperature and intensity of ambient light decreased, the swarms gradually left the dirt roads and clearings. Thereafter swarming mayflies were observed exclusively above the asphalt road and the reaches of the creek open to the sky. In these swarms, both the males and females flew periodically up and down displaying the species-specific nuptial dances (Fischer 1992), or flew parallel to the water or asphalt surface against the prevailing breeze. They frequently touched the water or asphalt surface, or dropped onto it for a few seconds. When the air temperature decreased below 14-15 ^{o}C and the light intensity became too low, mayfly swarming suddenly ceased, and the insects disappeared from both the water and asphalt surfaces. They then landed on the leaves of neighbouring trees, bushes and grass to roost.

All six mayfly species observed behaved similarly above and on the asphalt road as at the water surface. The density of swarming, mating and ovipositing mayflies was highest above those patches of the asphalt road where the surface was smoother and darker than the surrounding regions. No courting and egg-laying occurred above the relatively light grey or rough spots of the asphalt. One of the most typical reactions of female mayflies to the black and smooth asphalt patches was the following: After aerial copulation the females arrived above one of these patches. First, they flew over the patch, then suddenly turned back at its border, and in the presence of a gentle breeze all of them flew into the breeze. Females touched the patch several times and landed on it to lay their eggs. Thus, Kriska et al. (1998) concluded that the darker and smoother the asphalt, the greater is its attractiveness to water-seeking mayflies. Above the asphalt road Kriska et al. (1998) observed the following two flight types for the six Ephemeroptera species, which are typical flight maneouvres usually found only above water surfaces:

1. **Egg-laying flight of females:** The females, generally facing into the slight breeze, flew to and fro parallel to and immediately above the asphalt surface, dancing up and down in a zig-zag pattern and sometimes touching the asphalt. This type of flight was performed only by females above the middle part of the asphalt road. During egg-laying flight, the females performed a typical, species-specific stereotypical flight pattern (Fischer 1992), which resembled the nuptial dance of the swarming males and occurred simultaneously with it. As egg-laying flight progressed, an increasing number of eggs was pressed out from the genitalia of the females in the air. At the end of this flight, the females landed on the asphalt and laid their egg-packet (Fig. 19.1H). In the case of *Ephemera danica*, the females landed on the asphalt and remained on it until their elongated egg-packet was pressed out and laid (Fig. 19.1I). The functions of egg-laying flight are finding an optimal site for oviposition, and/or allowing a larger number of eggs to be pressed out, and/or acting as a defence against attacks by swarming males (Fischer 1992).

2. **Surface-touching maneouvres of males:** The males also periodically touched the asphalt surface during their flight, usually facing into the wind. Some of the individuals touched the asphalt periodically only with their cerci while flying up and down immediately above the road. Others landed on the asphalt, stayed on it for 1 s and then took off, to land again some seconds later. Similar water touching by male mayflies (e.g. *Baetis vernus, Ecdyonurus venosus, Rhithrogena semicolorata* and *Ephemera danica*) was observed by Fischer (1992) above water surfaces at ephemeropteran emergence sites. According to Fischer (1992), such touching of the water surface by male Ephemeroptera allows them either to drink or to test the height above the water surface using their cerci.

19.3 Multiple-Choice Experiments with Swarming Mayflies

Table 19.1 shows the air temperature and the number of *Rhithrogena semicolorata* landing on a given region of three different test surfaces. *Rhithrogena semicolorata* was attracted almost exclusively to the shiny black plastic sheet. At the beginning of swarming above the asphalt road at approximately 19:00 h, only a few mayflies landed on the black plastic, but their number increased rapidly over time. At 20:40 the reproductive activity reached its maximum. The swarming ceased suddenly approximately 20-30 min after this maximum because of the decreasing temperature and the low light intensity. The shiny white plastic sheet and the aluminium foil were not attractive to *Rhithrogena semicolorata*. The very small number of mayflies landing on these test surfaces was negligible.

As Table 19.2 demonstrates, similar results were obtained for *Epeorus silvicola*. In order to preclude the possibility that temperature differences between the test surfaces resulted in the observed patterns, the temperature of the test surfaces was measured, but no temperature difference was found between the three different surfaces. The temperature of the test surfaces was always significantly higher than the air temperature above the asphalt road. Both temperatures decreased gradually.

In the first series of multiple-choice experiments, Kriska et al. (1998) found that the shiny black plastic sheet reflecting light specularly was the only attractive surface for all six mayfly species. In a control experiment, slightly shining matt black and matt white clothes were used, which reflected light diffusely. The results of this control experiment are presented in Table 19.3 for *Rhithrogena semicolorata*. Again, the shiny black plastic sheet was significantly more attractive than the cloths. The white cloth was unattractive. The black cloth attracted a small number of mayflies. The reason for this was that the matt black cloth was slightly shiny.

In the second series of multiple-choice experiments, Kriska et al. (1998) used totally matt black cloth as one of the control surfaces. The other two test surfaces were a shiny black plastic sheet and a matt white cloth. The matt black and white surfaces were unattractive to mayflies; the shiny black plastic sheet was the only

attractive one. A similar result was obtained for *Rhithrogena semicolorata*. In this species, the majority of mayflies observed on the cloths and the aluminium foil were copulating pairs; they began to mate while in the air, and dropped accidentally onto these surfaces. The mayflies observed on the black plastic sheet were mainly single male or egg-laying female insects, but copula were also abundant. At the beginning of swarming only a few mayflies landed on the shiny black plastic sheet, but later practically every member of the swarm landed on it periodically. At the end of swarming more individuals had settled onto the plastic than remained flying above it.

The landing of mayflies on the black plastic sheet was so intensive that one could hear the loud strikes of the insect bodies similar to rain drops rattling on the plastic. If any part of the black plastic sheet was covered by a piece of any other test surface, the reproductive activity of mayflies ceased above this region. When the piece of the other test surface was removed, reproductive behaviour of the insects above this part of the black plastic sheet recommenced.

To demonstrate the strong preference of swarming mayflies for the shiny black plastic sheet, the black plastic sheet above which mayflies swarmed in large numbers was lifted and moved slowly such that its surface remained horizontal. The swarming mayflies followed the slowly moving plastic. When the black plastic sheet with the cloud of swarming mayflies was moved above one of the other test surfaces and then the black plastic was quickly removed, the mayfly cloud dissipated rapidly. When the unattractive test surface was quickly covered by the black plastic sheet, the mayflies returned and the swarm developed again. If the black plastic was held vertically, the mayflies did not swarm over or next to it, nor did they follow its movement. The same was true for all other test surfaces in this experiment.

Using a hand net, mayflies (single males and females, egg-laying females, copula) swarming above the black plastic sheet were captured and released onto one of the other test surfaces. These mayflies did not continue their reproductive activity on the new test surface, but they left it and returned to the black plastic. However, if these mayflies were transferred to another black plastic sheet, they began their reproductive behaviour again, showing that the captured mayflies did not fly away from the new test surface because of the netting procedure, but because of the unattractive or repellant nature of the test surface.

19.4 Influence of Temperature on the Reaction of Mayflies to the Test Surfaces

The water temperature of the creek was between 12 and 14 ^{o}C, and did not change during swarming on a given day. The air temperature above the creek (at a distance of 1 m from the water surface) was significantly higher than that of the water and decreased from approximately 20-22 ^{o}C to 14-15 ^{o}C between the start and end of swarming each day. The air temperature above the asphalt road (at a distance of 1 m from the surface) was still significantly higher and decreased from

approximately 25-26 °C to 16-17 °C during swarming (Table 19.1). The warmest location was always the asphalt road and the test surfaces on it (Table 19.2).

The swarming of mayflies began immediately prior to or after sunset when the air temperature was still relatively high above both the asphalt surface and the creek. The swarming ceased when the air temperature decreased below 14-16 °C. The higher air temperature above the asphalt road prolonged the reproductive behaviour of mayflies by approximately 15 min in comparison to the reaches of the creek from which the sky was visible, presumably making the asphalt more attractive to mayflies than the creek. However, since there was no temperature difference among the test surfaces, the different reactions of mayflies to the different test surfaces cannot be explained by their thermal perception. Similarly, a role of olfaction in the choice of the test surfaces by mayflies can be excluded (see below). Mayflies must have preferred the asphalt road and the black plastic sheet and avoided the other test surfaces because these surfaces were visually attractive, non-attractive, or even repellant.

Mayflies roosted on the leaves of trees and bushes after their reproductive activity. To study the role of the substratum chosen by the insects as a roosting place, Kriska et al. (1998) used again the test surfaces, which were laid onto the ground beneath trees and bushes on the bank of the creek. After swarming, the mayflies landed *en masse* not only on the shiny black plastic sheet, but also on other test surfaces independently of their type. The behaviour of roosting mayflies was, however, quite different from that observed during their swarming. Roosting mayflies did not dance, fly up and down, or oviposit on the test surfaces, but simply settled on them and remained motionless, apparently using the test surfaces as roosting places and not as reproduction sites. Because of the lower temperature, the roosting of mayflies on the shore of the creek began earlier than at the border of the warmer asphalt road.

19.5 Reflection-Polarizational Characteristics of the Swarming Sites of Mayflies

19.5.1 Reaches of a Mountain Creek

Figure 19.2 shows the measured reflection-polarizational characteristics of three different reaches of a mountain creek from which mayflies emerged and where they swarmed, mated and oviposited yearly in large numbers at sunset. All three scenes had a slightly undulating water surface and were recorded from a direction of view of the camera of 60° measured from the vertical, which is slightly larger than the Brewster angle of asphalt (57.5°) and water (53°) with refractive indices of 1.57 and 1.33, respectively.

In the first reach of the creek (Fig. 19.2A1), the water was relatively slow and calm and a small pond was present in the shadow of trees. Through the foliage,

skylight illuminated the water surface from above and to the right. The degree of linear polarization p was high only in those regions of the water surface that were illuminated by skylight (Fig. 19.2A2). The other regions of the water and the shore reflected practically unpolarized light. Because of the undulation of the water surface, the degree p and angle α of polarization (Fig. 19.2A3) changed strongly from site to site on the water surface, giving a relatively wide distribution of these variables (Fig. 19.2A4,5). The E-vectors of light reflected from the water surface were approximately horizontal but, because of the ripples on the water surface, they could diverge strongly from this direction (Fig. 19.2A3,5).

The second reach of the mountain creek was exposed to skylight from above (Fig. 19.2B). The water flowed slowly among stones and pebbles. Here, p of light reflected from the undulating surface of the turbulent water was also relatively low, and the dry stones and pebbles were largely unpolarized (Fig. 19.2B2). Thus, the spatial distributions of p (Fig. 19.2B2) and α (Fig. 19.2B3) were patchy and the histograms of these variables were again relatively wide (Fig. 19.2B4,5).

In the case of the third reach (Fig. 19.2C), the creek flowed under trees, but its surface was illuminated by skylight from the side. Consequently, p of light reflected from the water surface was relatively high (Fig. 19.2C2,4). However, similarly to the first and second reaches, both p and α of the water-surface-reflected light changed strongly because of ripples (Fig. 19.2C2,3) and their histograms were again wide (Fig. 19.2C4,5).

19.5.2 Sections of an Asphalt Road

Figure 19.3 shows the measured reflection-polarizational characteristics of three different sections of the asphalt road above and on which mayflies swarmed, mated and oviposited. Analysing the patterns and histograms of p and α of the three sections of the asphalt road in Fig. 19.3 and comparing them to those of the reaches of the mountain creek in Fig. 19.2, we can establish several important points. The distribution of p and α of light reflected from the asphalt road is narrow; the E-vector of reflected light is predominantly horizontal and, apart from the lighter and rougher patches of the asphalt surface, p is relatively high, in spite of the fact that the surface was dry. The reflection-polarizational characteristics of wet sections of the asphalt road after rain were also measured with similar results as for the dry asphalt road; however, p was significantly higher when the asphalt was wet (see Table 19.4).

19.5.3 Test Surfaces Used in the Multiple-Choice Experiments

Table 19.4 shows the measured relative radiance I, degree of linear polarization p and angle of polarization α of light reflected from the test surfaces. The shiny black plastic sheet ($p = 55\%$) and the wet asphalt ($p \approx 51\%$) possessed the highest p. The degree of polarization of the dry asphalt ($p \approx 31\%$) was still high and much

higher than that of the slightly shiny black cloth ($p \approx 15\%$), matt black cloth ($p \approx 9\%$) and shiny white plastic sheet ($p = 7.7\%$). The matt white cloth ($p = 3.3\%$) and the shiny aluminium foil ($p = 3.2\%$) reflected practically unpolarized light.

Because of the approximately smooth and horizontal reflecting surfaces, the direction of polarization of light reflected from the wet and dry asphalt and the shiny black and white plastic sheets was not significantly different from horizontal. The E-vectors of light reflected from the cloths differed significantly from the horizontal because of the surface roughness of these cloths. The shiny aluminium foil reflected the light such that it did not change p and α of the incident light. Since the surroundings (sky and randomly oriented leaf blades of the vegetation) of the swarming sites and the site of the multiple-choice experiments possessed randomly oriented E-vectors, α of light reflected from the shiny aluminium foil was also random and the relatively low p changed strongly from site to site depending on the direction of view.

19.6 Role of Different Cues in the Reproductive Behaviour of Mayflies Above Asphalt Roads

19.6.1 Olfaction, Wind and Air Humidity

The asphalt road and the test surfaces did not possess any characteristic smell detectable by the human olfactory system. The black and white plastic sheets were composed of the same polyethylene, consequently their odour must be the same, as in the case of the matt black and white cloths. Similarly, there might not be any significant difference between the smell of the smooth/dark and light/rough regions of the asphalt surface. It is, therefore, improbable that olfaction plays a role in the attractiveness of the shiny black plastic sheet and the asphalt surface to mayflies.

Mayflies generally avoid those sites where the wind is strong and the air humidity is low (Brodskiy 1973). Any small possible differences in wind velocity and relative humidity among the test surfaces were compensated for by their random positioning. Thus, a role of wind and air humidity in the attractiveness of the shiny black plastic sheet can be excluded.

19.6.2 Temperature

Since there was no temperature difference between the different regions of the asphalt road and the test surfaces laying on it, the attractiveness of the smoother and darker regions of the asphalt surface and the shiny black plastic sheet cannot be explained in terms of temperature. Mayflies must have thermal sensitivity in order to perceive the optimal temperature range for their swarming (Savolainen

1978). When the air becomes colder than approximately 14-15 °C after sunset, the swarming ceases and the mayflies roost on the leaves of grass, trees and bushes on the shore of their emergence site. The air above asphalt roads is always warmer than that above the water surface. This higher temperature is advantageous for mayflies as it prolongs their reproductive activity. Note, however, that it is unlikely to be the higher temperature that attracts mayflies to asphalt roads. The higher temperature only affects the duration of the swarming period (approximately 15 min longer) above the asphalt road compared to the cooler water surface. For species swarming at dusk over water, a gradual increase in swarming altitude has been reported (Brodskiy 1973) as the insects avoid cold air near the ground. Kriska et al. (1998) observed the reverse of this phenomenon above asphalt roads.

19.6.3 Colour and Radiance

Based on the above arguments, the high attractiveness of asphalt roads to mayflies can be explained only by optical cues, i.e. by the colour, radiance or polarization of reflected light. Because a black or grey asphalt surface reflects the whole spectrum of the incident light and its reflectivity is almost independent of the wavelength, as for the colourless test surfaces used in the experiments, the role of colour in the choice by mayflies can be excluded. The shiny aluminium foil and the plastic sheets reflected the light specularly, the matt cloths reflected it diffusely. Among the test surfaces, the brightest was the aluminium foil; the white plastic sheet and the white matt cloth reflected a slightly but not significantly smaller amount of light; and the black plastic sheet and the black cloths were the darkest (Table 19.4).

If mayflies were attracted to the asphalt surface by positive phototaxis, then the shiny aluminium foil, the shiny white plastic sheet and the matt white cloth should have been the most attractive to them. Since the reverse was found, one can conclude that mayflies were not guided by phototaxis to the asphalt surface. Mayflies were attracted only to the shiny black plastic sheet among the test surfaces. This cannot be explained by the relatively small amount of reflected light of this plastic sheet, because the matt black cloth which had a similar relative radiance (there is no any significant difference in radiance; Table 19.4) was not attractive at all. In a specular direction, a shiny black surface reflects more light than a matt black one, however, it was established above that the amount of light reflected is not the cue used by mayflies.

19.6.4 Reflection Polarization

Aluminium foil does not change p and α of the incident light after reflection (Horváth and Pomozi 1997). The light reflected from the plastic sheets became polarized parallel to their surface, but p of the white plastic sheet (p = 7.7%) was much smaller than that of the black one (p = 55%) (Table 19.4). The cloths also

possessed very low p; furthermore, the E-vector of light reflected by them was not horizontal. Thus, polarization of reflected light is the most important variable explaining the attractiveness of the shiny black plastic sheet. The black plastic sheet was attractive only if its surface was horizontal; the vertically oriented black plastic sheet, for which the E-vectors would have been vertical, was not attractive at all to mayflies. Thus, one can conclude that only horizontally polarized reflected light attracts mayflies. This is also supported by the fact that the shiny aluminium foil, which did not change p and α, was unattractive to mayflies. The polarization distribution of the surroundings of the sites of the choice experiments was generally characterized by random orientation of the E-vectors, and by relatively low p (e.g. see Fig. 19.3A). Thus, the light reflected from the aluminium foil was relatively unpolarized in comparison with the black plastic sheet and its E-vector was not horizontal (Table 19.4).

The shiny black plastic sheet was more attractive to mayflies than the dry asphalt surface, and the latter was much more attractive than the slightly shiny black cloth. However, the smoother and darker regions of the asphalt road were much more attractive than the rougher and lighter patches. p = 55% was the highest for the shiny black plastic sheet; the dry asphalt road possessed a smaller p ≈ 31%, but higher than that of the slightly shiny black cloth (p ≈ 15%). p of the rougher and lighter patches of the asphalt was lower than that of the smoother and darker regions of the asphalt road (Fig. 19.3C1,2). Therefore, the higher the p of reflected light, the greater is its attractiveness to mayflies. Hence, mayflies swarming, mating and egg-laying on asphalt roads are predominantly visually deceived by and attracted to the asphalt surface because the strongly and horizontally polarized reflected light imitates a water surface.

This is in accordance with the results of Schwind (1985b, 1991, 1995), whose test surfaces attracted also *Cloeon* species (Ephemeroptera). He found that the probable spectral range where *Cloeon* is sensitive to polarization is between 450 and 480 nm. In the experiments of Kriska et al. (1998), the slightly shiny black cloth with p = 15% was slightly attractive while the matt black cloth (p = 9.1%) was relatively unattractive to the six mayfly species investigated. This indicates that the threshold of polarization sensitivity of their visual system is between 9% and 15%.

Kriska et al. (1998) could not determine the spectral range in which the studied mayflies are sensitive to polarization. These Ephmeroptera swarm at dusk when the only light source is the sky. Thus, they can detect the water surface by means of the polarization of reflected skylight, in which the short wavelength range (UV and blue) of the spectrum dominates (Coulson 1988). Both asphalt and water surfaces reflect the entire spectrum of the skylight. Kriska et al. (1998) observed that mayflies were deceived by and attracted to asphalt roads not only under clear skies (when skylight is rich in the UV component beside the blue one), but also under partially cloudy skies or even at total overcast (when the UV component of skylight is strongly reduced or even absent). From this one can expect that the polarotactic water detection of the Ephemeroptera studied functions in the blue, as in *Cloeon*.

The best known fact about the visual system of Ephemeroptera is the presence of large dorsal eyes, called turban eyes, in the male of some families. The eyes of these insects are characterized by a strong sexual dimorphism. In addition, these insects also have lateral eyes just as the females do. The males of one of the mayfly species studied by Kriska et al. (1998), *Ephemera danica*, however, do not possess turban eyes, the morphology of their eyes is very similar to that of the females. Most works published on the ephemeropteran visual system deal predominantly or entirely with the dorsal eyes (e.g. Horridge 1976; Horridge and McLean 1978). The function of the dorsal eyes is to distinguish the female in flight (the female usually enters the top of a swarm, and the turban eyes allow the male to search the area above it), while with the lateral eyes the male and female orients itself in relation to the elements of the landscape, to the water surface, for instance. Although in some mayfly species the microvilli structure of the retina in the dorsal as well as lateral eye has already been investigated (e.g. Burghause 1981), unfortunately nothing is known about the polarization sensitivity of the visual system in mayflies. The observations of Kriska et al. (1998) show that mayflies are polarization sensitive and detect the water by means of the horizontal polarization of reflected light.

19.7 Comparison of the Attractiveness of Asphalt Roads and Water Surfaces to Mayflies

Since the asphalt is black or dark grey and non-transparent, an asphalt road is an efficient specular reflector and polarizer if its surface is smooth. At sunset it always reflects horizontally polarized light, the p of which is almost 100% near the Brewster angle (57.5^{o}). Light penetrating into the asphalt has no effect on the polarization, because it is totally absorbed. The situation in the case of a streamlet, however, is different, because light reflected specularly from the water surface is horizontally polarized, whereas light penetrating into water and emanating from it is vertically polarized due to refraction. This vertically polarized component reduces the net p. Thus, a brook is horizontally polarized when the surface-reflected light dominates and vertically polarized if the light returning from the water dominates. The greater the proportion of light returning from the water in comparison to that reflected from the water surface, the lower is the net p (Figs. 19.2A,B). In Fig. 19.2C, p of the water surface is relatively high, because only a small amount of light is coming from the water (due to the sheltering vegetation), and the amount of water-surface-reflected light is great (due to the bright illumination from the side).

The highly and at sunset always horizontally polarized asphalt roads with a relatively homogeneous distribution of p and α (Fig. 19.3) can therefore be much more attractive to mayflies than the surface of a streamlet (Fig. 19.2). An asphalt road can reflect and polarize the incident light in such a way that the reflected light becomes a supernormal stimulus for water-seeking mayflies in comparison to the light reflected from water. This was also observed in the multiple-choice

experiments of Kriska et al. (1998), when mayflies swarming above the asphalt road were attracted to the highly polarized shiny black plastic sheet after it was laid onto the road. A relatively small black plastic sheet (a few m^2) attracted all the mayflies swarming above the asphalt road within several tens metres.

According to Schwind (1991), insects inhabiting running waters, e.g. plecopterans living near brooks (Zwick 1990), may not locate their habitats using polarization, because polarization is reduced or even distorted by waves (see Fig. 19.2B). Nevertheless, the observations and multiple-choice experiments of Kriska et al. (1998) show that this is not true of the Ephemeroptera, at least for the six species studied.

According to Brodskiy (1973), considering swarming site, mayflies form three groups:

1. species swarming over water,
2. species swarming over the littorial but maintaining visual contact with the water,
3. species swarming in conditions where there is no visual contact with water.

It is clear that the fertilized eggs of the mayfly species belonging to groups 2 and 3 can be exposed to the danger that they are laid on the surface of a highly polarized asphalt road running near the emergence site of their parents. Similar danger may not be expected in the case of the species of group 1, because these mayflies cannot be attracted by a surface (in spite of its high p and horizontal E-vector) which is positioned farther away from the water.

The mayfly species observed by Kriska et al. (1998) possess the following typical behaviour, which is considered the most generalized one in Ephemeroptera (Brodskiy 1973): At the time of the nuptial flight the males are spread out along the shore line of the water basin and under optimal weather conditions they collect together in a swarm. The females fly from the water over the row of plants on the littorial intersecting it at a right angle and, when no swarm is encountered, fly back again with a change in altitude. This continues until the females fly through a swarm. They are visually detected and then captured by the males. Mating usually takes place in flight, after which the male again returns to the swarm. A single female can be repeatedly fertilized, after which she lays her eggs into the water. From this behaviour it follows that one of the prerequisites of mayfly mating is to swarm above places where the sky is visible, because the females usually are detected visually and captured by the males from below (Brodskiy 1973). One of the few exceptions is *Ephemera danica* without turban-like dorsal eyes and with a ventrally oriented chasing flight. The sky is generally open above highways and asphalt or dirt roads; thus, in this respect roads near the emergence site of mayflies provide a good swarming place. After mating, the polarotactic females return to water to oviposit. Among roads, highly and horizontally polarizing asphalt roads with a smooth and dark surface can deceive and attract them. Hence, asphalt roads are visually attractive on several levels to mayflies:

– the sky above them is visible,
– their strong and horizontal polarization at sunset mimics a water surface, and
– at sunset they have a slightly higher temperature than the surrounding areas.

Asphalt roads can be much more attractive to mayflies than real creeks, because the latter run frequently under trees and bushes. Mayflies do not swarm or mate above those reaches of the creek which are in the shelter of trees, that is, from which the sky is not visible. Egg-laying also takes place on the reaches of streamlets where the sky is visible, and from which polarized skylight can be reflected to guide the mayflies to the water surface.

In the attractiveness of asphalt roads to mayflies at sunset it is of particular importance that at dusk the E-vector of polarized light reflected from the rough asphalt surface is always horizontal due to the diffuse illumination from the sky. Mayflies (like many polarotactic water-seeking insects) are attracted only by horizontal E-vector. If the asphalt surface is illuminated by direct sunlight during the day when the sun is above the horizon, the E-vector of light reflected from the asphalt is not horizontal, and thus, asphalt roads are no longer attractive to mayflies, even if p of reflected light is high.

19.8 An Efficient Method to Study Ephemeropteran Swarming Behaviour in the Field

The experiments of Kriska et al. (1998) suggest that a shiny black plastic sheet can be used for the investigation of reproductive behaviour in Ephemeroptera. In the field, under natural conditions it is often difficult to observe mayfly swarms, because they are formed in unapproachable sites, above the water surface, or at high altitudes, for instance. The placement of a shiny black plastic sheet of some square metres would attract the whole swarm, allowing the study of mayflies, or their capture. This simple method could facilitate field studies on Ephemeroptera.

19.9 Possible Measures to Prevent Mayfly Egg-Laying onto Asphalt Roads

After the discovery of the causes of the reproductive behaviour of mayflies above asphalt roads, the experts of protection of animals and the environment could take the necessary measures to prevent the egg-laying by mayflies and to reduce the amount of eggs laid and perished on asphalt surfaces. One could, for example treat the sections of the asphalt roads running near the emergence sites of Ephemeroptera in such a way that their surface becomes relatively light and rough to reduce their reflection polarization. This could be performed by rolling down of small-sized lighter gravel on the asphalt surface. This treatment of the asphalt surface reduces significantly p of reflected light, which abolishes its attractiveness

to mayflies. Not only the highly polarizing asphalt roads, but also the huge shiny black plastic sheets used in the agriculture can deceive and attract mayflies in a large number, if they are laid on the ground near the ephemeropteran emergence sites. Thus, also these black plastic sheets can be dangerous to mayflies. It would be advisable to forbid the farmers to use such black plastic sheets near the swarming and egg-laying sites of Ephemeroptera.

Tables

Table 19.1. Observation time t (local summer time = UTC + 2), air temperature T_{air} (°C) and the number N of *Rhithrogena semicolorata* landing within 30 s on a 0.1 m × 0.1 m area of three test surfaces. S7: shiny black plastic sheet; S4: shiny white plastic sheet; S3: shiny aluminium foil. (After Table 1 of Kriska et al., 1998, p. 2276).

t	T_{air} (°C)	N (S7)	N (S4)	N (S3)
19:06	25.5	1	0	0
19:09	25.5	3	1	0
19:12	25.0	4	0	0
19:32	24.0	8	0	0
19:35	24.0	9	2	0
19:41	23.5	13	1	0
20:09	21.5	16	0	0
20:20	21.0	33	1	0
20:25	20.5	57	1	2
20:33	20.0	97	1	0
20:40	19.0	166	0	0
20:48	18.0	85	0	2
20:56	17.0	29	2	0
21:02	16.0	9	1	0

Table 19.2. As Table 19.1 for *Epeorus silvicola*. Here also the temperature T_{sur} (°C) of the test surfaces is given. (After Table 2 of Kriska et al. 1998, p. 2277).

t	T_{air} (°C)	T_{sur} (°C)	N (S7)	N (S4)	N (S3)
19:10	25.0	27.5	11	0	0
19:12	25.0	27	9	0	0
19:15	24.5	27	9	0	0
19:19	24.0	26.5	24	0	0
19:22	23.5	26	26	1	0
19:25	23.0	25.5	19	1	0
19:29	22.0	24.5	16	0	0
20:03	21.5	23.5	3	0	0

Table 19.3. As Table 19.1 for *Rhithrogena semicolorata,* without air temperature. S7: shiny black plastic sheet; S6: slightly shiny black cloth; S2: matt white cloth. The slightly shiny black cloth reflected partially horizontally polarized light. Its degree of polarization was much lower than that of the shiny black plastic sheet (Table 19.4). (After Table 3 of Kriska et al. 1998, p. 2277).

t	*N* (S7)	*N* (S6)	*N* (S2)
19:33	25	6	0
19:38	18	3	0
19:43	20	3	2
19:48	25	2	0
19:53	23	5	1
19:58	22	4	0
20:03	24	4	0
20:08	16	3	0
20:13	23	4	0
20:18	21	4	0

Table 19.4. The relative radiance I, degree of linear polarization p and angle of polarization α of light reflected from the test surfaces measured by video polarimetry. I is calculated relative to the shiny aluminium foil; α is measured from the vertical. Values are mean ± standard deviation ($N = 560 \times 736$ = number of pixels in a video picture). S1: wet asphalt; S2: matt white cloth; S3: shiny aluminium foil; S4: shiny white plastic sheet; S5: matt black cloth; S6: slightly shiny black cloth; S7: shiny black plastic sheet; S8: dry asphalt. (After Table 6 of Kriska et al. 1998, p. 2281).

	S1	S2	S3	S4	S5	S6	S7	S8
I (%)	38.8 ± 3.4	99.7 ± 5.4	100 ± 5.7	97.6 ± 4.3	24.4 ± 2.8	17.6 ± 3.2	22.6 ± 2.4	26.0 ± 3.1
p (%)	50.9 ± 3.4	3.3 ± 0.9	3.2 ± 1.1	7.7 ± 1.5	9.1 ± 2.1	15.1 ± 2.8	55.0 ± 5.4	30.6 ± 3.4
α (°)	89.1 ± 1.4	58.8 ± 4.3	57.7 ± 2.1	91.3 ± 1.1	81.9 ± 5.4	73.1 ± 4.9	90.5 ± 1.2	90.9 ± 1.3

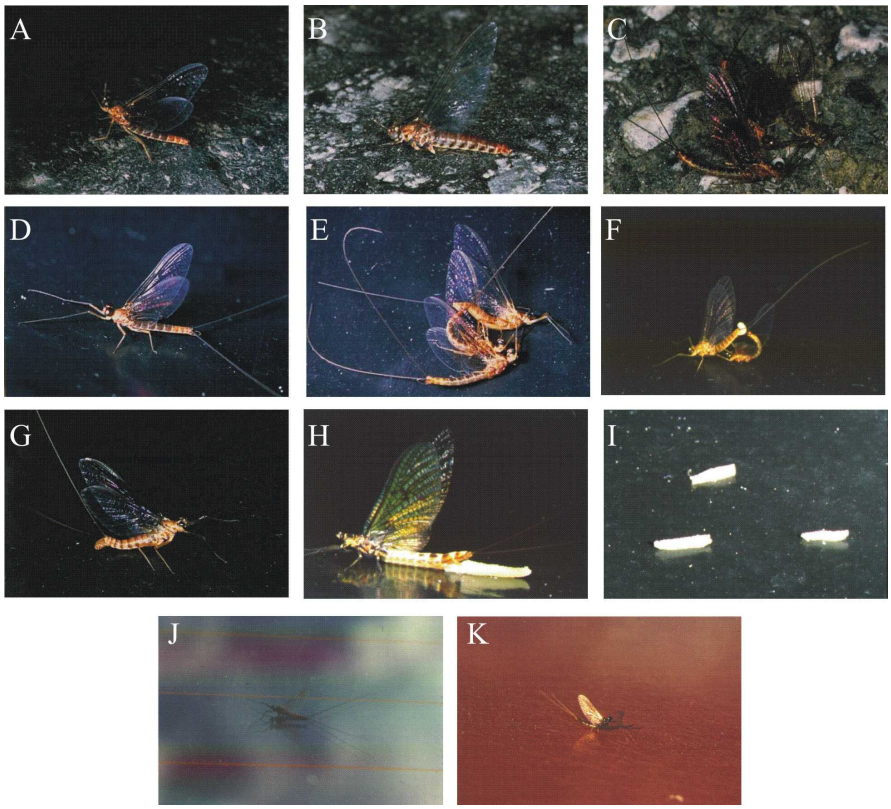

Fig. 19.1. Examples of mayflies deceived by and attracted to a dry asphalt road (A-C), a shiny black plastic sheet used in agriculture (D-I), the windscreen (J) and the red bodywork (K) of a car in the immediate vicinity of a mountain creek near Budapest during May/June 1997. A: a male *Rhithrogena semicolorata*; B: a female *Epeorus silvicola*; C: a female and two male *Epeorus silvicola* attempting to mate; D: a male *Rhithrogena semicolorata*; E: a copulating pair of *Rhithrogena semicolorata*; F: a female and two male *Rhithrogena semicolorata* attempting to mate; G: an ovipositing *Rhithrogena semicolorata*; H: an ovipositing *Ephemera danica*; I: egg-packets of *Ephemera danica*, J,K: a male *Baetis rhodani*. (After Fig. 1 of Kriska et al. 1998, p. 2274).

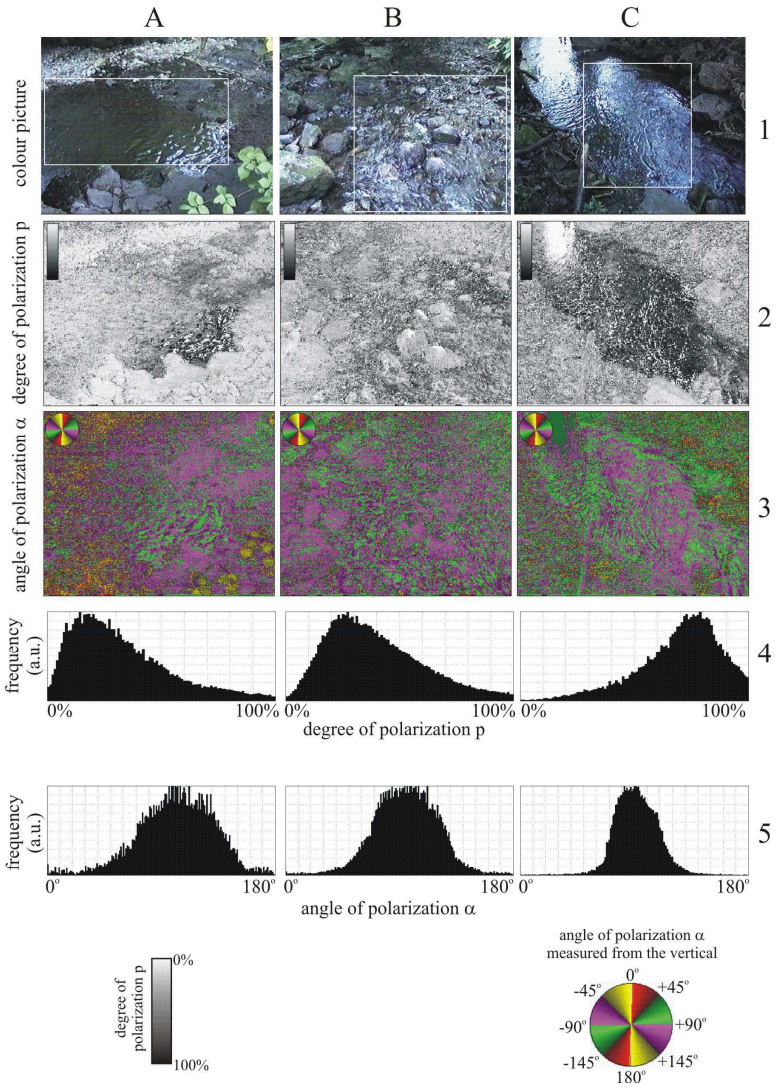

Fig. 19.2. The reflection-polarizational characteristics of three different reaches of a mountain creek (a typical emergence and swarming site of the mayflies studied) measured by video polarimetry at 450 nm. All three scenes with a slightly undulating water surface were recorded from a direction of view of the camera of 60° relative to the vertical. A: In this relatively slow and calm reach of the creek a small pond was shadowed by trees. Through the foliage skylight illuminated the water surface from above and from the right. B: A reach of the creek illuminated from above by the clear sky where the water flowed slowly among stones and pebbles. C: A reach where the creek flowed under trees, but its surface was illuminated by skylight from the side. Rows 4 and 5 show the frequencies (in arbitrary units) of p and α calculated for the rectangular windows in row 1. (After Fig. 2 of Kriska et al. 1998, p. 2280).

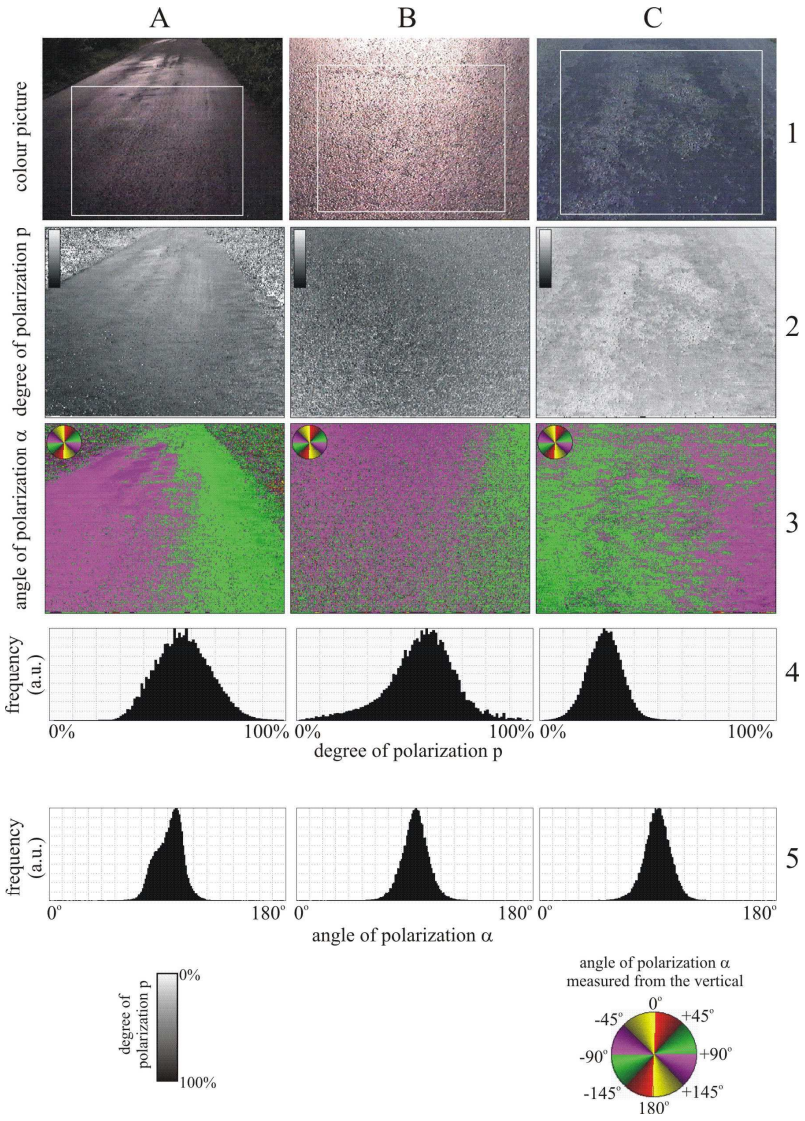

Fig. 19.3. The reflection-polarizational characteristics of three different sections of the asphalt road above and on which mayflies swarmed, mated and oviposited. In each case, the asphalt surface was dry, and the scenes were recorded from a direction of view of the camera of 60° with respect to the vertical. A: A long section of the asphalt road illuminated by direct light from the setting sun under a clear sky. The camera viewed towards the solar meridian. B: A short, smooth and dark section of the asphalt road illuminated by direct sunlight prior to sunset. The camera viewed towards the solar meridian. C: A short section of the asphalt road with smooth and rough, bright and dark patches illuminated by skylight from above after sunset. Other details as in Fig. 19.2. (After Fig. 3 of Kriska et al. 1998, p. 2282).

20 Reflection-Polarizational Characteristics of Car-Bodies: Why are Water-Seeking Insects Attracted to the Bodywork of Cars?

20.1 Attractiveness of the Bodywork of Cars to Certain Insects

Figure 3.4 demonstrates that light reflected from the shiny bodywork of cars may be strongly linearly polarized. The smooth surface of bodyworks reflects the whole spectrum of light, while the paint beneath it returns light only in a certain spectral range, apart from the case when this paint is grey. The light returning from the underlying paint becomes vertically polarized after refraction at the surface. This vertically polarized light reduces the degree of linear polarization p of the horizontally polarized light reflected by the surface itself. Thus, the net p is low or even abolished in that spectral range in which the pigment reflects light efficiently. The bodywork of cars possesses regions, from which strongly and horizontally polarized light is reflected. These regions are very attractive to polarotactic water-seeking insects, because they mimic a water surface. There are many observations (e.g. Fernando 1958; Popham 1964; Watson 1992; Mizera et al. 2001) that insects associated with water are deceived by and attracted to the shiny bodywork of cars.

20.2 Automotive Clearcoat Damage by Dragonfly Eggs

Stevani et al. (2000a,b, 2001) observed that certain common Brazilian dragonflies are attracted by the reflecting surface of cars and lay eggs on them. At the high temperatures of the car surface exposed to sun the eggs can cause damage (Fig. 20.1), the chemical mechanism of which is similar to that caused by acid rains. In experiments on resin-coated plates, Stevani et al. (2000a,b, 2001) showed that cysteine and cystine residues present in dragonfly eggs are oxidized during the egg hardening process (sclerotization) which releases hydrogen peroxide, a cysteic acid derivative, a strong acid capable to catalyse the hydrolysis of acrylo/melamine clearcoat polymer. Cysteic acid was indeed identified in

dragonfly egg extracts submitted to oxidation by H_2O_2 followed by acid digestion. These acids, destroying the clearcoat above 70°C, originate from proteins of the egg-shell, chorion, as products of chemical reactions. The temperature of car-bodies can often rise above 70°C in sunshine. Then, eggs laid onto the car surface can damage the resin just like acid rain (Fig. 20.1).

20.3 Influence of Colour of Paint

Beyond the polarization of light reflected from the bodywork of cars also the colour of the paintwork may strongly influence the attractiveness of the automotive clearcoat to insects. The light reflected from cars with shiny, smooth clearcoat and red paintwork, for example, is less polarized in the red but highly in the blue and possibly also in the UV part of the spectrum, if the paint layer absorbs UV light. Many insects do not perceive red but UV light. Their colour sensitivity is shifted towards the shorter wavelengths in comparison with the human colour sensitivity. Thus, red cars are highly attractive to water-seeking polarotactic red-blind insects, due to the high degree of polarization of reflected light in the blue and UV spectral ranges. The bodywork of cars with metallized paint reflects light with low p in a wide region of the spectrum, where the metall particles reflect light efficiently.

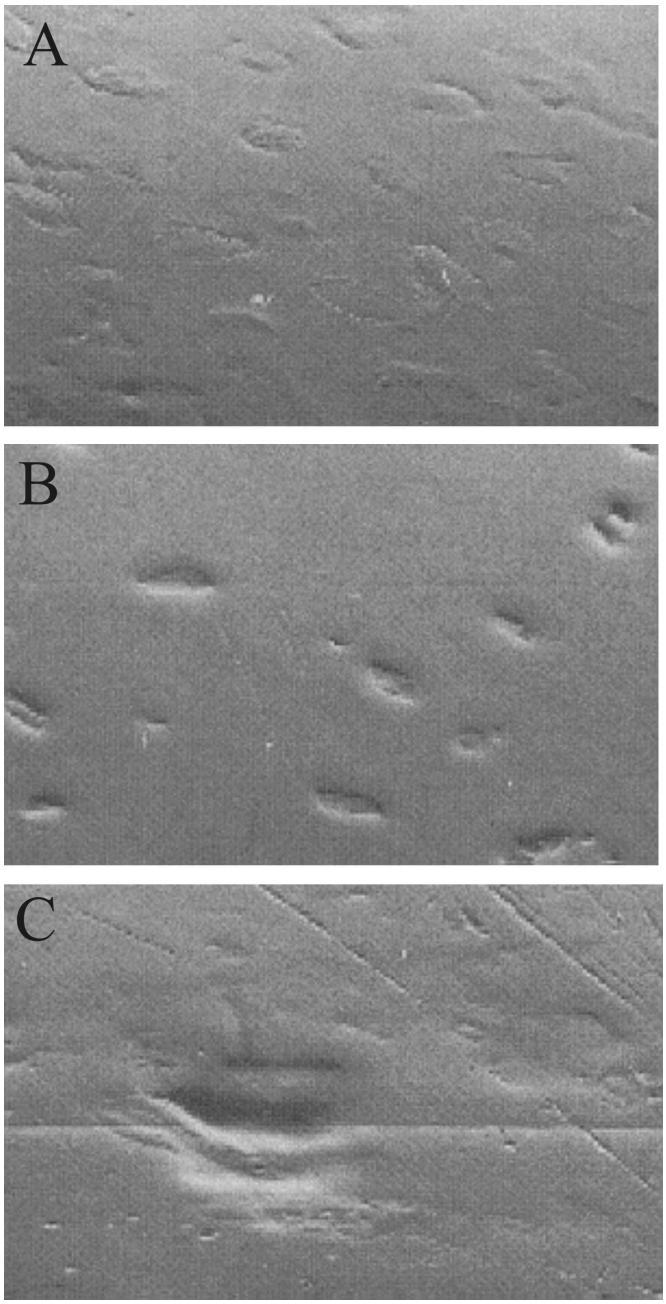

Fig. 20.1. Scanning electron-microscopic photographs of the acrylic/melamine resin after 3 h at 90 °C in contact with dragonfly eggs (A), cysteine of 10 mmol/L (B), and cystine of 10 mmol/L (C) (after Fig. 3 of Stevani et al. 2000b, p. 1636).

21 Polarization-Sensitive Optomotor Reaction in Invertebrates

If a cylindrical pattern of vertical black and white stripes is rotated around an animal, it usually displays a turning reaction. The tendency for the animal to turn in the direction of motion of a pattern is called "optomotor response", which demonstrates that the animal is able to detect the movement of the optical environment on the basis of brightness cues. This behaviour serves to stabilize the animal's orientation with respect to the environment, and helps it to maintain a straight course during locomotion. The optomotor reaction of insects to black-and-white (B&W) patterns has been intensively studied (e.g. Hassenstein and Reichardt 1956; Hassenstein 1959; Varjú 1959). Studies of the dependence of motion perception on the wavelength of light demonstrated, that the visual subsystem performing directionally-selective movement detection is usually colour-blind (e.g. Kaiser and Liske 1974; Kaiser 1974, 1975; Tinbergen and Abeln 1983; Lehrer et al. 1990; Srinivasan and Guy 1990; Schaerer and Neumeyer 1994).

If this visual subsystem is sensitive to polarization, it is to be expected that an optomotor response can also be elicited by movement of stripes of linearly polarizing filters with alternating orientations of their transmission axes. The strength and phase difference of the optomotor response to rotating B&W patterns should depend on the orientation of the transmission axis of a polarizing filter positioned between the animal and the pattern. Such experiments with crabs, honeybees, flies, backswimmers and waterstriders have shown that depending on the orientation of the polarization-sensitive microvilli system in the eyes of these animals, optomotor responses can be elicited by different E-vector patterns. In this chapter first the published results are briefly surveyed. Then the results of the experiments performed by Horváth and Varjú (2003) are presented, who studied the polarization sensitivity of the optomotor response of the backswimmer *Notonecta glauca* and the waterstrider *Gerris lacustris*.

21.1 Crabs

Korte (1965) observed polarization-induced optomotor response in the European fiddler crab *Uca tangeri*. According to Kirschfeld (1973b, p. 291), optomotor response can be elicited in the crabs *Carcinus* with white, blue or orange light, if the alternating E-vectors of the moving polarization pattern are parallel and perpendicular to the dorso-ventral plane of the eyes. However, if the E-vector directions were $\pm 45^{o}$ with respect to the dorso-ventral plane, optomotor response was not observed.

21.2 Honeybees

De Vries and Kuiper (1958) investigated the optomotor reaction of honeybees *Apis mellifera* to a moving pattern of stripes of linear polarizers with alternating vertical and horizontal E-vectors. In this experiment the bees did not show optomotor response to the E-vector contrast, since the polarization-insensitive lateral and frontal eye regions were stimulated. In *Apis mellifera* the optomotor response appeared only when the E-vectors were oriented $\pm 45^{o}$ from the dorso-ventral plane of the eyes (Kirschfeld 1973a). In this reaction the blue- and/or UV-sensitive receptors participate. Alternating parallel and perpendicular E-vectors in the frontal eye region did not elicite optomotor response.

21.3 Flies

Kirschfeld and Reichardt (1970) recorded optomotor reactions under open-loop conditions of walking houseflies *Musca domestica* as a function of the E-vector orientation of the stimulus light and found a sinusoidal modulation of the strength of the response. The E-vectors of the stimulating white, blue or orange light had to be $\pm 45^{o}$ from the dorso-ventral plane of the eyes to produce this reaction. Alternating E-vectors parallel and perpendicular to the dorso-ventral plane in the lateral eye region produced no optomotor response. Using electrophysiological recordings and optomotor experiments, McCann and Arnett (1972) studied the spectral and polarization sensitivity of wild-type adult *Musca domestica*, *Calliphora erythrocephala* and *Phaenicia sericata*.

Polarization sensitivity of the optomotor response in flying fruitflies *Drosophila melanogaster* was investigated by Heisenberg (1972) in an experiment, in which a rotating cylinder composed of two polarizing filters with E-vectors $\pm 45^{o}$ to the vertical was used as a stimulus. Repeating the optomotor experiment of Kirschfeld and Reichardt (1970) with *Drosophila*, Wolf et al. (1980) studied thoroughly the polarization sensitivity of course control and optomotor reaction of fruitflies. They found that polarization sensitivity is mediated by the peripheral retinula cells R1-R6 in the ommatidia. Although the

amplitude of the optomotor response of walking *Drosophila* was a sinusoidal function of the E-vector orientation, the phase and amplitude did not reflect directly the polarization sensitivity of the photoreceptors mediating the reaction. This suggests that *Drosophila* has an inner representation of the E-vector orientation, which is abstracted from the alignment of the dichroic microvilli. According to the original interpretation of Kirschfeld and Reichardt (1970), the modulation of the optomotor response due to the change of E-vector orientation should correspond to the change in the perceived brightness and thus to the polarization sensitivity of the receptors. Obviously, this is not the case in *Drosophila*, for which the polarization sensitivity estimated on the basis of the optomotor response is *PS* = 20-60, values considerably larger than typical *PS*-values in insect photoreceptors.

In a closed-loop situation, in which the fruitflies were illuminated from above by linearly polarized light and were allowed to turn the orientation of the E-vector relative to their body axes by their yaw torque, the animals could maintain their optomotor balance, i.e. they could use the polarization to fly straight. Above a rotating polarizer covering a fraction of the visual field with an angular diameter of 45^{o} just underneath the animal, *Drosophila* showed a significant optomotor response at 550 nm.

In the opinion of Wolf et al. (1980), at least under clear skies flying *Drosophila* could use the celestial polarization pattern for orientation. The threshold of the degree of linear polarization is about 15%. Since polarization sensitivity is not restricted to the dorsal part of the eye, *Drosophila* seems to possess polarization-sensitive receptors in most, if not in all, parts of its visual field. It might utilize polarization sensitivity to distinguish different surface properties on the ground, when searching for or trying to avoid water, distinguishing wet and dry surfaces which is a vital function for such a small insect. Alternatively, also with its ventral eye region *Drosophila* could use a polarization pattern for course control. Note, that Wolf et al. (1980) suggested as first that an animal could use the polarization sensitivity of its ventral eye region for water detection. This capability was later demonstrated by Schwind (1983a) in the backswimmer *Notonecta glauca*.

Considering the polarization sensitivity of the R1-R6 retinula cells in flies, there is a controversial problem. On the one hand, the polarization sensitivity of receptors mediating the optomotor response has been demonstrated for both *Musca* (Kirschfeld and Reichardt 1970) and *Drosophila* (Heisenberg 1972; Wolf et al. 1980; Coombe et al. 1989). On the other hand, it was argued that due to neural superposition in the dipteran *lamina ganglionaris* behavioural responses mediated by retinula cells R1-R6 should be almost invariant to the rotation of the E-vector of polarized light (Kirschfeld 1971). Each of these six cells, which superimpose their activity onto the same monopolar cells in the lamina, differ in their preferred E-vector direction by about 60^{o} from the neighbouring cells. Thus polarization sensitivity should be lost at the level of the lamina if the six retinula cells contribute equally to the activity of the monopolar cells. In light of this argument Kirschfeld (1973c) suggested that receptors R1-R6 may not be involved in the polarization-sensitive optomotor response. However, this is not the case in *Drosophila*. Coombe et al. (1989) have shown that although the optomotor

response of *Drosophila*, mediated unambiguously by the retinula cells R1-R6, is strongly polarization sensitive, the large monopolar neurons in the lamina are not sensitive to polarization.

21.4 Rose Chafers

Mischke (1984) investigated the polarization sensitivity of the optomotor reaction in the African rose chafer *Pachnoda marginata*. The lateral middle regions of the superposition eyes were stimulated by different oscillating (6 Hz) patterns containing intensity and/or colour and/or E-vector contrasts. The scarab beetle showed optomotor response exclusively to intensity contrasts. Mischke concluded, that *Pachnoda* is insensitive to polarization contrasts and was surprised, because the related scarab beetle *Lethrus* can orient menotactically by means of polarization (Frantsevich et al. 1977). Since in the experiment of Mischke the dorsal rim area of the eye of *Pachnoda marginata* was not stimulated, only the polarization insensitivity of the lateral middle eye regions can be concluded.

21.5 Optomotor Reaction to Over- and Underwater Brightness and Polarization Patterns in the Waterstrider *Gerris lacustris*

Waterstriders (Gerrids) have trichromatic colour vision (Hamann and Langer 1980; Bartsch 1991) and polarization sensitivity (Bohn and Täuber 1971; Bartsch 1995). The high polarization sensitivity of their photoreceptors to vertically and horizontally polarized light is not restricted to a special eye region or to a distinguished spectral region. One of the functions of this polarization sensitivity is to find the aquatic habitat by means of the partially and horizontally polarized light reflected from the water surface (Schwind 1991). This task requires a ventral polarization-sensitive eye region. Schwind (1985b) proposed that this ventral polarization-sensitive visual pathway is UV-sensitive in Gerrids. The high polarization sensitivity in the whole eye of waterstriders (Bartsch 1991, 1995) raises the question of its functional significance in the dorsal and lateral eye regions.

Waterstriders compensate for displacement and rotation of their body due to water flow or wind by two distinct types of behaviour (Junger and Varjú 1990; Junger 1991; Junger and Dahmen 1991):

1. To compensate for linear displacement they periodically jump against the direction of drift such that they maintain in average their position relative to the surroundings over a long time.
2. For rotation they compensate by a precisely combined rotation of the head and body, such that the gaze is stabilized in space.

Both behaviour types are visually controlled. With this in mind, the function of the polarization sensitivity of the lateral and dorsal eye regions in waterstriders could be to enhance the contrast of objects in the optical environment used for motion detection. The optical environment of waterstriders, composed of the water surface below the animal, the vegetation on the shore and the sky above the animal, is rich in polarization patterns with different degrees and angles of polarization, which could serve for contrast enhancement. To test whether these polarization patterns can be exploited for motion detection, Horváth and Varjú (2003) investigated the optomotor response of *Gerris lacustris* to different polarization patterns and compared it with the optomotor reaction to B&W patterns.

Male and female *Gerris lacustris* were collected from ponds and kept in a watertank. They were fed on wingless *Drosophila* from a culture. Before an experiment the animals were narcotised by CO_2 for some seconds. Then they were fixed by a wax drop on their pronotum to a 2 mm long vertical piece of a needle, which was glued to one end of a horizontal thin plastic stripe of about 2.5 cm length and 5 mm width. The other end of the stripe was adjusted by a holder to a proper height above the water surface. In this way the animals on the water surface were allowed to roll, pitch and raise to some degree in order to accommodate themselves, but were prevented from yaw and displacement of their body. On the head of the animal a pin, a hair of about 1 cm length of a shaving brush, was fixed by a wax droplet. The function of this pin was to display the head orientation during video recording (Fig. 21.1).

The animals were placed in the centre of a plexi cylinder (diameter 9.4 cm, height 12 cm), which was connected to a second one by a silicone tube (Fig. 21.1A). After the system was filled half with water, the water level in the first cylinder could be changed by lowering or raising the second cylinder. For stimulation of the ventral and dorsal eye regions a horizontal disc consisting of 12, e.g. black and white, sectors was oscillated sinusoidally with an amplitude of 5^o and a frequency of 1 Hz around its vertical symmetry axis immediately below (Fig. 21.1B) and above the animal (Fig. 21.1C). Ventrally and dorsally, this disc occupied a cone with an aperture of 120^o and 90^o, respectively (Fig. 21.2). The black and white sector pattern B&Wsec (Fig. 21.2) consisted of matt black and thin semitransparent white paper providing a brightness contrast of 80%. The polarizing sector pattern POLsec consisted of sectors cut from a neutral density linearly polarizing filter (HN32, Polaroid) with the transmission axes of adjacent sectors perpendicular to each other (Fig. 21.2).

For stimulation of the lateral eye region $\pm 30^o$ from the horizontal direction (Fig. 21.2) a vertical cylindrical pattern holder with two different patterns, one on the top and another below, composed of 12 segments in a panoramic arrangement, was sinusoidally oscillated around the animal (Fig. 21.1A). Two pattern holders with four different patterns were used (Fig. 21.2). In an experiment one of the two patterns on a given pattern holder was occluded by a cylindrical matt black occulter, which could be vertically lowered and raised (Fig. 21.1A). The water level with the animal on it was adjusted in such a way, that the non-occluded stimulus pattern on the holder was seen by the animal at 0^o–30^o above the horizon.

Due to reflection at the water surface the animal could also see the mirror image of the pattern at 0^o–30^o below the horizon (Fig. 21.2). A change between the two stimulus patterns could be achieved by cautiously lowering or raising the water level together with the animal within 10-15 seconds without larger disturbance of the animal. This was important, because thus reactions of the animal to two different patterns could be recorded while the physiological state of the animal did not change. The experiments were performed in white, green and blue light. In the latter two cases cylindrical colour filters (Käsemann, Germany) were used around the animal (Fig. 21.1A). The intensity of light emitted by the white lamps was adjusted in such a way that the intensities transmitted by these two colour filters were the same (Fig. 21.3).

The oscillation of the stimulus patterns and the reactions of the animals were video recorded from above or below through tilted plane and conical mirrors (Fig. 21.1). After a frame-by-frame analysis, the orientations φ of the stimulus pattern and the pin fixed onto the head of the animal were determined as a function of time. The resulting stimulus and response data were fitted by sinusoid functions with amplitude A, from which the closed-loop gain $g_c = A_{response}/A_{stimulus}$ and the closed-loop phase difference $\Delta\varphi_c = \varphi_{response} - \varphi_{stimulus}$ were determined. Then the open-loop gain $g_o = g_c/[1+g_c^2-2g_c cos\Delta\varphi_c]^{1/2}$ and the open-loop phase difference $\Delta\varphi_o = arc\ tan(sin\Delta\varphi_c/cos\Delta\varphi_c - g_c)$ were calculated.

The stimulation of the ventral eye region of *Gerris* from nadir angle 0^o to $\pm60^o$ (Fig. 21. 2) in white light did not induce optomotor reaction for both the B&Wsec and POLsec patterns, although about 30% of the ommatidia look into these directions and see the underwater world (Varjú and Horváth 1989; Dahmen 1991; Horváth 1995a). This corresponds to the finding that *Velia caprai* does not respond to underwater brightness stimuli at all (Meyer 1970, 1971). When the dorsal eye region of *Gerris* from zenith angle 0^o to $\pm45^o$ (Fig. 21.2) was stimulated in white light, a weak optomotor response (with an open-loop gain $g_o = 25\pm3\%$ and phase difference $\Delta\varphi_o = 62^o\pm5^o$ averaged for 8 animals) was elicited by the B&Wsec pattern but none by the POLsec pattern.

Stimulating the lateral eye region between 0^o and 30^o above the horizon and because of reflection at the water surface also from 0^o to 30^o below the horizon in white light, *Gerris* exhibited an optomotor response to the B&W pattern (Fig. 21.4A) and the vhPOL pattern (Fig. 21.4B), but it did not respond to the ±45POL pattern (Fig. 21.4C) and the vvPOL pattern (Fig. 21.4D). The vvPOL pattern was used as a control to test whether the small inevitable brightness contrast at the borders of adjacent polarizing filters elicited a response. As we can see in Fig. 21.4D, there was no such a reaction, even if the amplitude of the stimulus was sometimes quite large. The spatial resolution of the compound eyes of *Gerris* (Dahmen 1991) was apparently not high enough to perceive the low brightness contrast at the borders of the polarizing filters. The optomotor response to the vhPOL pattern (Fig. 21.4B) is, therefore, exclusively due to the E-vector contrast.

As we mentioned, in the experiments waterstriders could also see the mirror image of the vhPOL pattern (Fig. 21.2). The intensity of vertically polarized light reflected from the water surface is slightly smaller than that of horizontally

polarized light, because the reflectivity of water is slightly smaller for vertical polarization (Guenther 1990). Thus after reflection the vhPOL pattern should have been partially transformed to a brightness pattern with a weak contrast. Using the same experimental setup (Fig. 21.1A), Horváth and Varjú (2003) repeated the experiment without water beneath the animals and with a double-height vhPOL pattern stimulating the lateral eye region at $\pm 30^{o}$ from the horizon. Then the average gain and phase difference of the optomotor response to this modified vhPOL pattern were the same as in the original case. Thus, the weak brightness contrast in the mirror image of the vhPOL pattern did not affect the optomotor response of *Gerris*.

The open-loop gain and phase difference of the optomotor response of *Gerris* to vhPOL and B&W patterns in white, green and blue light averaged over 8 animals are shown in Fig. 21.5 together with their standard deviations. In Fig. 21.6A the open-loop gain of responses to the B&W pattern in white, green and blue light is plotted versus that to the vhPOL pattern. The strongest response is found in white light, the weakest in blue. The ratio $gain_{B\&W}/gain_{vhPOL}$ is relatively constant independently of colour and physiological state of the animal (the latter varied only slightly between subsequent stimulations). Figure 21.6B shows the average open-loop gains for the three different light fields. The open-loop gain ratio, as indicated by the regression line, is $gain_{B\&W}/gain_{vhPOL} = 2.564$. It is clear from Fig. 21.5B that waterstriders followed the lateral stimuli with the smallest delay in white light and with the largest delay in blue light, furthermore the phase difference for the vhPOL pattern was always larger than that for the corresponding B&W pattern.

In order to interpret the above findings, we refer to the ultrastructure of the ommatidia in *Gerris lacutris* shown in Fig. 21.7. Since the light sources used in the optomotor experiments did not emit UV light and the polarizing filters did not transmit UV light, the UV-receptors could not be involved in the registered optomotor responses of *Gerris*. This and the result that waterstiders did not respond to ventral rotating brightness or polarization patterns suggest that self-rotation is detected by a visual pathway, which is separate from that mediating polarotactic water detection. The contrast of the vhPOL pattern is

$$C_{vhPOL} = (PS-1)/(PS+1) \approx 75\% \qquad (21.1)$$

both for the green and blue receptors due to the similar *PS*-values of about 7. The intensity of the stimulating green and blue light was adjusted to be the same (Fig. 21.3). In his electrophysiological recordings Bartsch (1991, 1995) found a great variation of the absolute sensitivity. Nevertheless the blue receptors tend to be slightly more sensitive than the green ones. If the blue receptors contributed remarkably to the optomotor response, a similar or even a somewhat higher gain could be expected for the blue compared to the green stimuli used in the experiments of Horváth and Varjú (2003). Instead, they found a gain ratio

$$gain_{B\&W}{}^{green}/gain_{B\&W}{}^{blue} = 2.82. \qquad (21.2)$$

The green receptors were also stimulated by the blue light used in the experiments (Fig. 21.3). The ratio of the amounts of green and blue light absorbed by the green receptor (calculated from the spectral sensitivity of the green receptor and the equal transmitted light intensity of the green and blue filters, Fig. 21.3) is

$$I_{green}/I_{blue} = 1.58. \quad (21.3)$$

Although nothing is known about the relation between stimulus intensity and gain of the optomotor response of *Gerris*, comparison of the ratios given in Eqns. (21.2) and (21.3) suggests that the blue receptor may not contribute to the optomotor reaction, otherwise the gain ratio $gain_{B\&W}{}^{green}/gain_{B\&W}{}^{blue}$ should be less than 1.58. Thus, the optomotor response of *Gerris* are mediated by the R1-R6 green receptors, and the motion-sensitive visual pathway is colour-blind. This agrees well with the findings that in many insect species the primary input to the optomotor pathway is via receptors R1-R6 (Coombe et al. 1989), and in honeybees and butterflies, for example, the optomotor response is green sensitive (Kaiser 1974; Kaiser and Liske 1974; Horridge et al. 1983). For waterstriders, living in an optical environment dominated by green foliage on the shore, green receptors seem to be optimal to the task of detecting self-motion (e.g. compensation for drift and rotation of the body), or motion of dark objects (e.g. enemies) against a green background.

Since in *Gerris* the ±45POL pattern did not elicit optomotor response, whereas the vhPOL pattern did (Fig. 21.4), all rhabdomeres involved in this reaction should have either horizontal or vertical microvilli in the normal posture of the animal. This conclusion is in accordance with the anatomical findings of Schneider and Langer (1969) and with the electrophysiological findings of Bartsch (1991, 1995).

21.6 Optomotor Response to Over- and Underwater Brightness and Polarization Patterns in the Backswimmer *Notonecta glauca*

The backswimmer *Notonecta glauca* is polarization sensitive and detects water by means of the horizontally polarized light reflected from the water surface (Schwind 1983a,b, 1984a,b, 1985a,b). Both of its above- and underwater optical environments are rich in polarization patterns:

- viewing from water through the Snell window, the celestial polarization pattern is seen, which is modified by refraction polarization (see Chapter 15.3);
- the foliage on the shore reflects strongly polarized light, which also can be seen through the Snell window;
- the light scattered in turbid water is strongly polarized.

The last phenomenon was demonstrated by Horváth and Varjú (2003) in the following way: A small aquarium was filled with turbid water from a pond with a dense growth of green-yellowish phytoplankton inhabited by backswimmers. The middle part of the aquarium was illuminated by a vertical, slightly divergent white light beam of an incandescent lamp. The polarization of light scattered by the suspended particles in water was measured by video polarimetry from the side. Figure 21.8 shows the obtained polarization patterns. The light scattered by the suspended phytoplankton is strongly polarized, and its E-vector is horizontal, i.e. perpendicular to the incident light beam. Thus, in small turbid ponds the spatial distribution of scattering polarization is quite similar to that in lakes and seas.

In turbid waters the characteristic strongly polarized ring at 90^o from the refracted sun light (see Fig. 15.1) develops within some centimetres around a backswimmer, the light intensity progressively decreases due to absorption, and the brightness contrasts are significantly reduced due to scattering (Lythgoe 1979). In such a contrast-poor, dimly lit, turbid optical environment the mentioned highly polarized ring around backswimmers could be well exploited for orientation. In their natural habitat backswimmers are often hanging upside-down at the water surface in such a way that the angle of their longitudinal body axis is 31^o from the surface. In this position they precisely compensate for passive translations and rotations of their body induced by water flow or wind. In this behaviour they rely mainly on visual cues (Blanke and Varjú 1995; Blanke 1996). To elucidate whether the overwater and underwater polarization patterns can be exploited for motion detection in backswimmers, Horváth and Varjú (2003) investigated the optomotor response of *Notonecta glauca* to different above- and underwater polarization patterns and compared it with the optomotor reaction to B&W patterns.

Backswimmers *Notonecta glauca* were collected from ponds, and were placed in the centre of a vertical plexi cylinder (diameter: 9.5 cm, height: 12 cm) half-filled with water. Translation of the animal's body was prevented by means of a small water-filled plexi cylinder (diameter: 3 cm, height: 6 cm) within the large one. In the small cylinder the animal could rotate freely around the vertical axis. The stimulation of the ventral, dorsal and lateral eye regions happened in white light with the same apparatuses and patterns used in the optomotor experiments with waterstriders (Fig. 21.1). Figure 21.9 shows the angular extensions of the stimuli within the visual field of *Notonecta*. The patterns were sinusoidally oscillated with 5^o amplitude and 0.2 Hz frequency. The orientation of the longitudinal body axis and the angular position of the stimulus pattern were evaluated frame by frame, from which the closed- and open-loop gains and phase differences were calculated.

Stimulation of the dorsal and ventral eye regions of *Notonecta* induced optomotor reaction only to the B&Wsec pattern. To the ventral B&Wsec pattern there were only weak responses (g_o = 7±2.7%, $\Delta\varphi_o$ = 43^o±21.7^o). The responses were relatively strong (g_o = 54±28.7%, $\Delta\varphi_o$ = 33^o±18.3^o) to the dorsal B&Wsec pattern. Backswimmers did not respond to the ventral and dorsal POLsec patterns.

The open-loop gain and phase difference of the optomotor response of *Notonecta* to lateral B&W, vhPOL and vvPOL patterns are shown in Fig. 21.10.

Stimulating the lateral eye region, backswimmers exhibited strong optomotor responses to the B&W pattern and a considerably weaker reaction to the vhPOL pattern. The optomotor responses to vvPOL and ±45POL patterns were the same and very weak. The vvPOL pattern was used to control the weak response induced by the small inevitable brightness contrast at the border lines between adjacent polarizing filters. Although the response to the vvPOL pattern was very weak, it was not zero, like in the case of waterstriders. Due to the higher spatial resolution of their compound eyes (Schwind 1978, 1980, 1983b) backswimmers could perceive the low brightness contrast at the borders of the polarizing filters. In order to obtain the real gains of the optomotor response of *Notonecta* to the vhPOL and ±45POL patterns, the gain of this "border response" to the vvPOL pattern must be subtracted from them. After this subtraction we obtain that *Notonecta* did not respond to the ±45POL pattern, while its response to the vhPOL pattern was weak, but definitely significantly larger than zero. Backswimmers followed the lateral B&W stimulus pattern with shorter delay than the vhPOL pattern (Fig. 21.10B).

The responses to overwater lateral stimulations were always slightly weaker than those for the corresponding underwater stimulations. Due to total-reflection of light at the water surface, backswimmers could also see the mirror image of the underwater stimulus pattern at 0^o-30^o above their horizon (Fig. 21.9). Thus, the underwater stimulus patterns were doubled in their vertical angular extension. On the other hand, because of refraction of light at the water surface the apparent vertical angular extension of the overwater stimulus patterns was compressed to about 8^o. These two effects explain, why backswimmers had a weaker optomotor response to overwater patterns in comparison with that to underwater ones.

According to Schwind (1985b), in the ommatidia of *Notonecta glauca* the six peripheral rhabdomeres R1-R6 are open and grouped around the two central fused rhabdomeres R7 and R8 (Fig. 21.11). In the medial eye region, with optical axes from 60^o ventrally to 80^o dorsally from the horizontal direction, the microvilli of the central rhabdomeres are horizontal. In the ventral eye region, 70^o or more ventrally from the horizontal, the microvilli of receptors R7 and R8 are horizontally and vertically aligned. We call this part of the eye the "ventral POL-area". Both in the dorsal and ventral eye regions, receptors R1-R6 are green sensitive. In the dorsal eye region, cells R7 and R8 are either UV or blue sensitive, while in the ventral POL-area they are exclusively UV sensitive. In the normal resting position, like in our experiments, the direction of the longitudinal body axis of *Notonecta* is 30^o relative to the water surface with head down. In this position the visual field of the animal is subdivided in three different regions (Schwind 1985b):

- the ventral POL-area looks into the air through the Snell window;
- the eye region directly below the ventral POL-area looks at the region of total reflection on the water-air interface;
- the remaining part of the eye looks at the underwater world.

In our optomotor experiments the light sources did not emit UV light, and the polarizing filters did not transmit UV light. Therefore in the ventral POL-area only the peripheral green receptors R1-R6 were stimulated, while in the lateral and dorsal eye regions also the central blue receptors. Thus, in the optomotor response of *Notonecta* to overwater stimuli the green receptors of the ventral part of the eye must have been involved. Since it is very unlikely that in the other eye regions the motion perception would be mediated by another receptor type than in the ventral POL-area, we conclude that in backswimmers only the green-sensitive visual pathway is responsible for motion detection, which is distinct from the UV-sensitive pathway involved in polarotactic water detection. In blowflies, droneflies, honeybees and goldfishes (Kaiser and Liske 1974; Tinbergen and Abeln 1983; Srinivasan and Guy 1990; Schaerer and Neumeyer 1994), for example, the visual subsystem performing directionally-selective movement detection responds also only in the green.

Since the microvilli of the central receptors R7 and R8 in the ventral POL-area of *Notonecta* are always vertical or horizontal (Fig. 21.11), the contrast of the vhPOL pattern is $C_{vhPOL}^{blue} = (PS-1)/(PS+1) \approx 75\%$. In *Notonecta PS*-values are unknown, therefore $PS = 7$ measured in waterstriders (Bartsch 1991, 1995) was assumed for the blue receptors of *Notonecta*. Because the B&W pattern provided a contrast of about $C_{B\&W} = 90\%$, the ratio of the contrast of the vhPOL and B&W patterns is $C_{vhPOL}^{blue}/C_{B\&W} = 0.83$.

On the other hand, the effective contrast of the vhPOL pattern perceived by the green-sensitive visual pathway is reduced, because the microvilli orientations of the peripheral green receptors are slightly disordered (Fig. 21.11). The perceived contrast of the vhPOL pattern is $C_{vhPOL}^{green}(\beta) = |cos2\beta|(PS-1)/(PS+1)$ for a green receptor, where β is the angle of the microvilli axis measured from the vertical. In the ventral POL-area of the *Notonecta* eye the mean values of β for the peripheral green receptors R1-R6 are (Fig. 21.11) $\beta_1 = 56^o$, $\beta_2 = 15^o$, $\beta_3 = 71^o$, $\beta_4 = 68^o$, $\beta_5 = 20^o$, $\beta_6 = 30^o$, and the relative cross-sections of the corresponding rhabdomeres are $A_1 = 0.17$, $A_2 = 0.83$, $A_3 = 0.83$, $A_4 = 1$, $A_5 = 1$, $A_6 = 0.17$ (Schwind 1985b). Supposing that the contribution of the green receptors to the effective contrast is proportional to their cross-section and to the perceived contrast, the average effective contrast of the vhPOL pattern is $C^*_{vhPOL}^{green} = {}_{n=1}\Sigma^6 A_n C_{vhPOL}^{green}(\beta_n)/ {}_{n=1}\Sigma^6 A_n = 56\%$. From here the ratio of the contrasts of the vhPOL and B&W patterns perceived by the green receptors is $C^*_{vhPOL}^{green}/C_{B\&W} = 0.62$. The contrast of the vhPOL pattern perceived by both the blue and green receptors is, thus lower than that of the B&W pattern. This is in accordance with our findings that backswimmers responded stronger to the B&W stimulation. In the case of the ±45POL stimulation the green-sensitive subsystem perceived a considerably reduced contrast, and this is the reason why *Notonecta* possessed practically no optomotor reaction in this situation.

The role of the UV-sensitive ventral POL-area in the eye of *Notonecta* in water detection is well understood (Schwind 1985b). In the opinion of Schwind (1983b), the special pattern of the central microvilli in the ventral part of the eye might not be related to the ability of the animal to orient itself by polarization below the

water surface. On the other hand, our results suggest the functional significance of polarization sensitivity of the lateral eye region in the optomotor reaction to polarization patterns in the green range of the spectrum. Horváth and Varjú (2003) proposed that the function of this polarization sensitivity may be a slight contrast enhancement for motion perception in the course of compensation for passive drift and rotation of the body of *Notonecta*. They admitted that the relatively disoriented microvilli structure of the peripheral green receptors (Fig. 21.11) is not ideal for this task, because the effective polarization sensitivity of this subsystem is not as good as it could be. The consequence is that the effective contrast of polarization patterns perceived by the green-sensitive visual pathway is generally reduced in comparison with the contrast perceived by the UV- or blue-sensitive central receptors. In spite of this, in *Notonecta* the motion perception is mediated by the green receptors, perhaps because in the aquatic habitat of backswimmers brightness and polarization contrasts occur mainly in the visible, especially in the green part of the spectrum, e.g. foliage on the shore, water plants and phytoplankton in water.

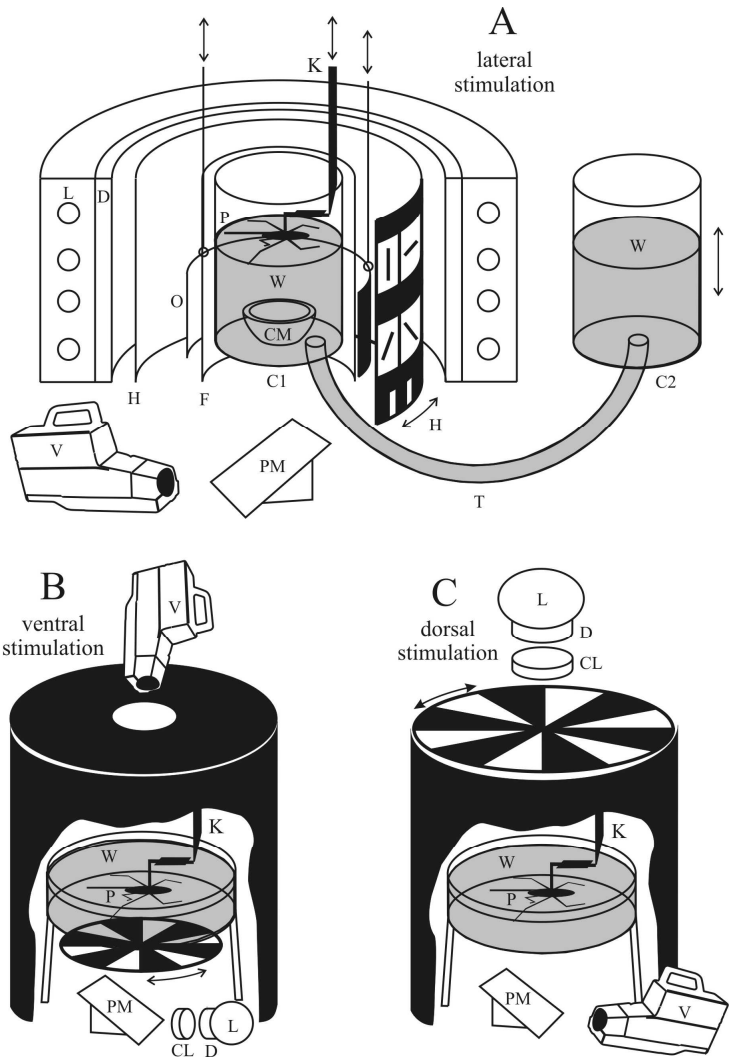

Fig. 21.1. Schematic diagrams of the arrangement of the optomotor experiments for stimulation of the lateral (A), ventral (B) and dorsal (C) eye regions in waterstriders *Gerris lacustris*. V: video camera; W: water; PM: plane mirror; P: pin (on the head of the animal); CM: conical mirror; T: tube; C1: first plexi cylinder (fixed); C2: second plexi cylinder (vertically moveable, to alter the water level in C1); H: oscillating cylindrical holder with two different stimulus patterns above (in a given experiment only one of them is visible to the animal) and a black and white stripe pattern below (invisible to the animal); O: occulter (vertically moveable by strings, to occlude one of the two stimulus patterns on the holder); F: colour filter (green or blue); K: moveable keeping (to change the vertical position of the animal following the change of the water level); L: incandescent lamps emitting white light; D: diffusor (white milky plexi glass); CL: condensor lens. (After Fig. 27.1 of Horváth and Varjú 2003).

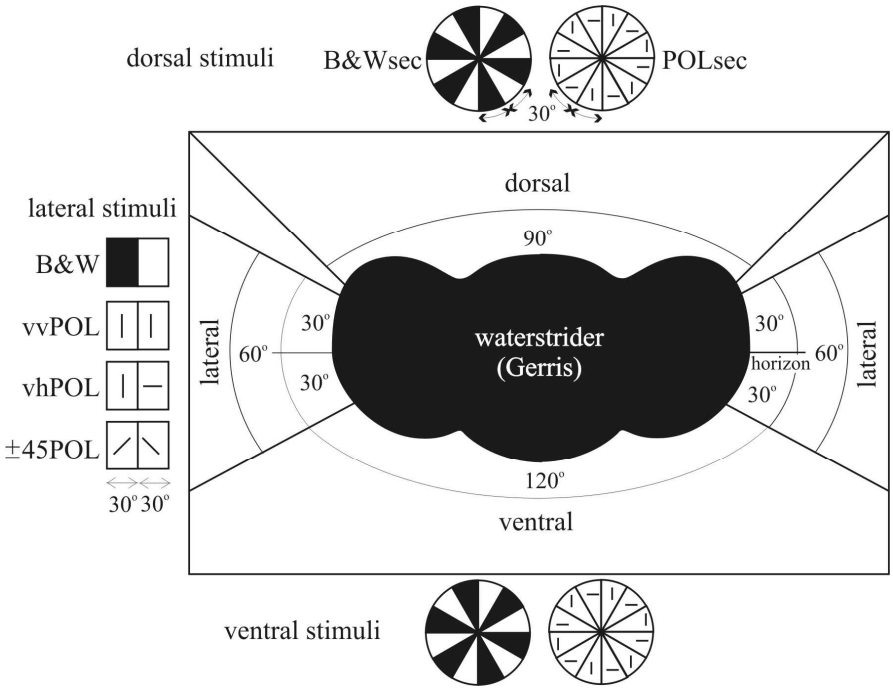

Fig. 21.2. Frontal view of the visual field of the eyes of *Gerris lacustris* (black: eyes and head) showing the different eye regions stimulated by various patterns. One of the two patterns on a given cylindrical pattern holder (Fig. 21.1A) stimulate the lateral eye region ±30° from the horizon due to the mirror image of the pattern at the water surface. The symbols outside the rectangle represent the different stimuli. B&Wsec: horizontal disc with alternating black and white sectors; POLsec: horizontal disc composed of sectors of linearly polarizing filters with alternating orthogonal transmission axes; B&W: vertical alternating black and white stripes; vvPOL: vertical stripes of polarizers with vertical transmission axes; vhPOL: vertical stripes of polarizers with alternating vertical and horizontal transmission axes; ±45POL: vertical stripes of polarizers with transmission axes alternating ±45° to the vertical. The orientation of the transmission axes of the polarizers is shown by bars. (After Fig. 27.2 of Horváth and Varjú 2003).

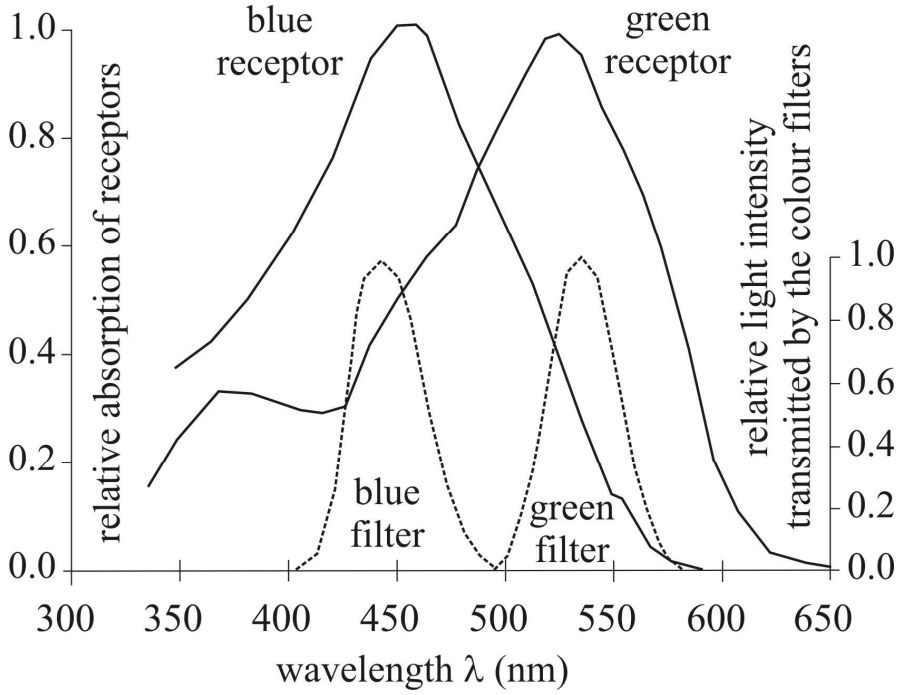

Fig. 21.3. Relative light intensities (dashed lines) transmitted through the blue and green filters versus wavelength λ used in the optomotor experiments, as well as the relative absorption curves $A(\lambda)$ (continuous lines) of the blue and green receptors R1-R6 in the eye of *Gerris lacustris*. (After Fig. 27.3 of Horváth and Varjú 2003).

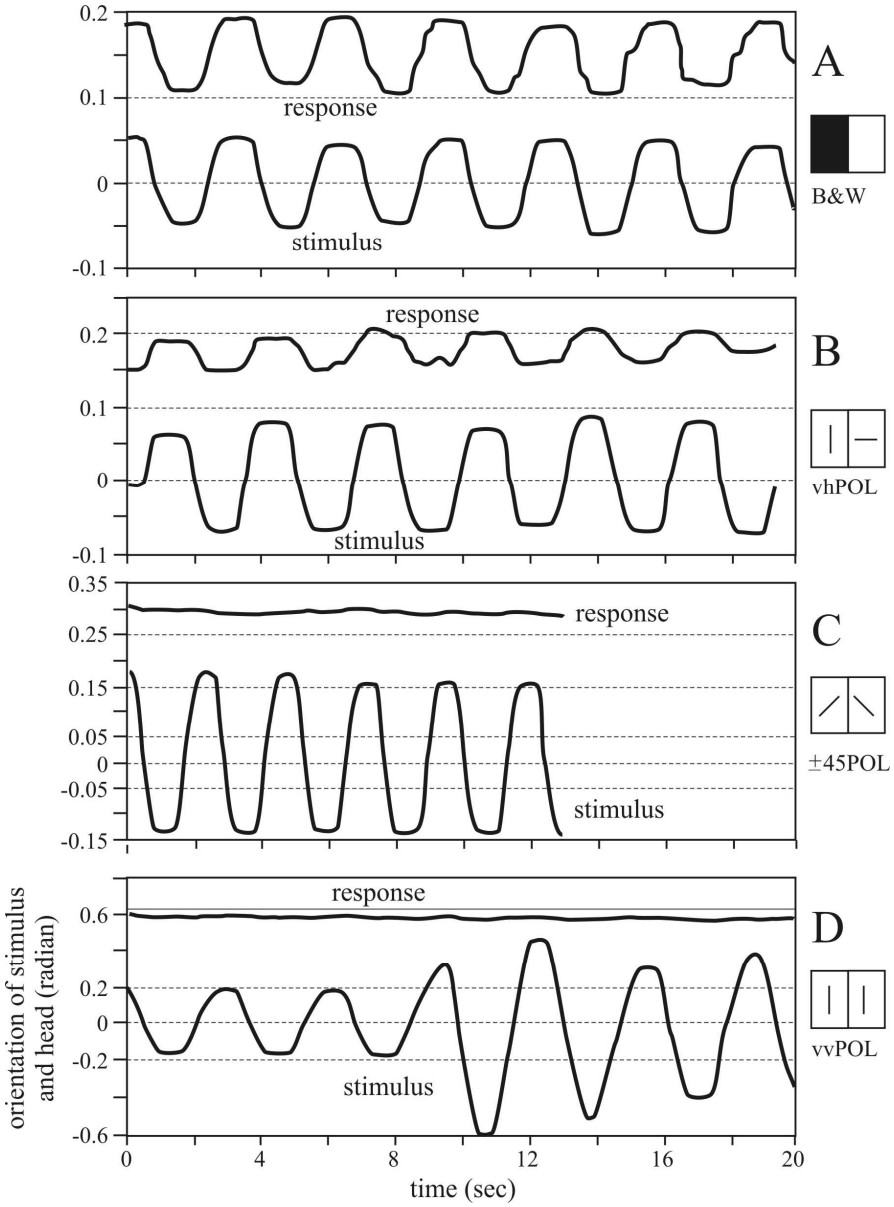

Fig. 21.4. Typical examples of the optomotor response of *Gerris lacustris* for different lateral stimuli in white light. The stimulus type is indicated by its symbol defined in Fig. 21.2. The abscissa is the time (measured in second) and the ordinate is the oscillating orientation (in radian) of the stimulus and the head. The response is practically zero to the ±45POL and vvPOL stimuli. (After Fig. 27.4 of Horváth and Varjú 2003).

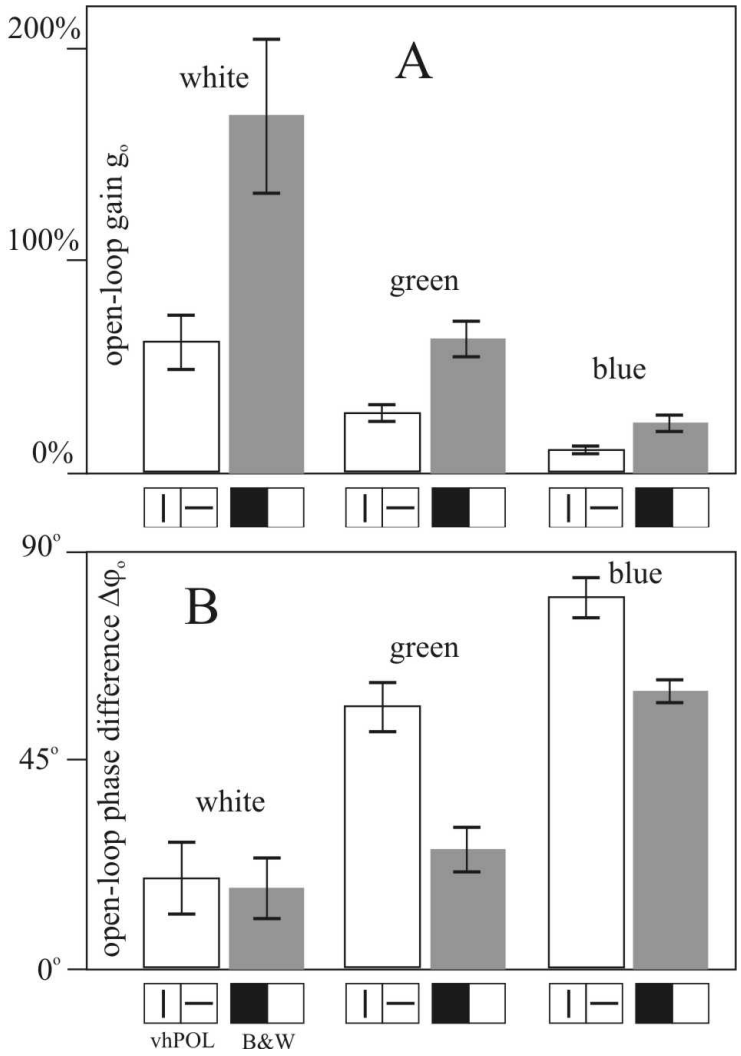

Fig. 21.5. The open-loop gain g_o (A) and phase difference $\Delta\varphi_o$ (B) of the optomotor response of *Gerris lacustris* to the vhPOL (white columns) and B&W (grey columns) stimulus in white, green and blue light averaged over 8 animals. The bars show the standard deviations. (After Fig. 27.5 of Horváth and Varjú 2003).

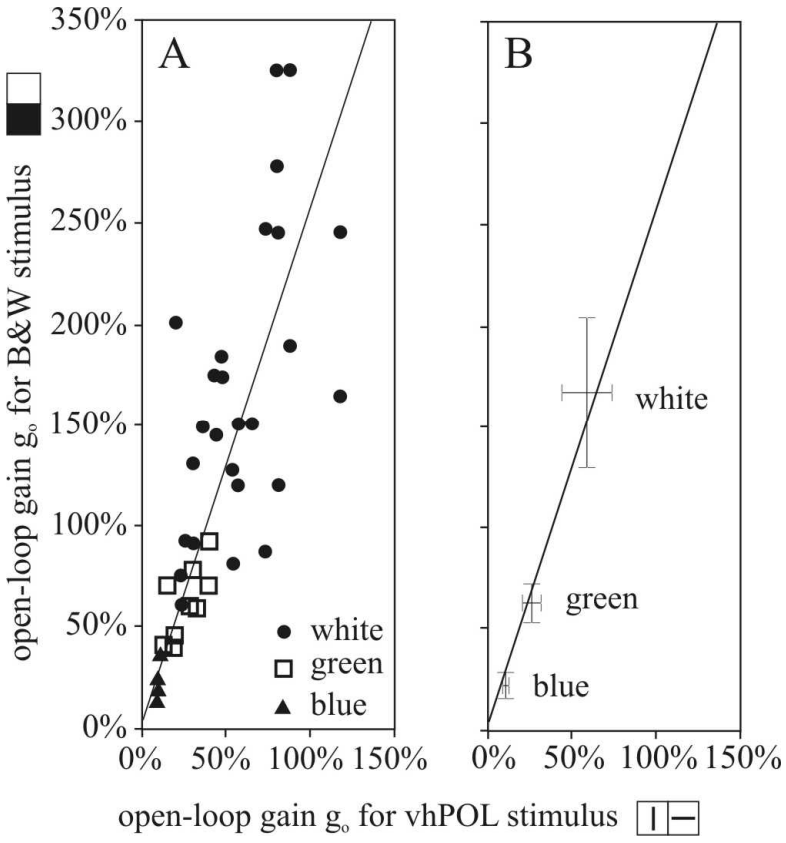

Fig. 21.6. A: The open-loop gain g_o for B&W stimulus versus g_o for vhPOL stimulus of the optomotor response of *Gerris lacustris* in white (dots), green (rectangles) and blue (triangles) light for 8 animals. Every symbol represents two subsequent optomotor responses to vhPOL and B&W stimuli. B: The average of the above-mentioned data. The horizontal and vertical bars show the standard deviation of the open-loop gains for the vhPOL and B&W stimuli, respectively. The slop of the regression line passing through the origin and fitted to the data points is $gain_{B\&W}/gain_{vhPOL} = 2.564$. (After Fig. 27.6 of Horváth and Varjú 2003).

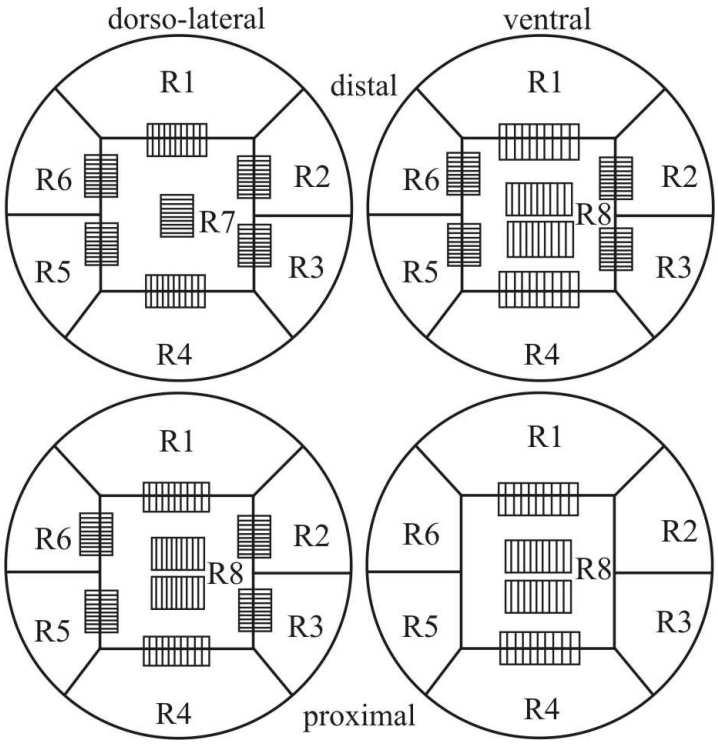

Fig. 21.7. Schematic cross-section of the ommatidium in different regions of the compound eye of the waterstrider *Gerris lacustris*. The hatched areas represent the microvilli of retinula cells R1-R8 and their orientation in the open rhabdom. (After Fig. 18.2 of Horváth and Varjú 2003).

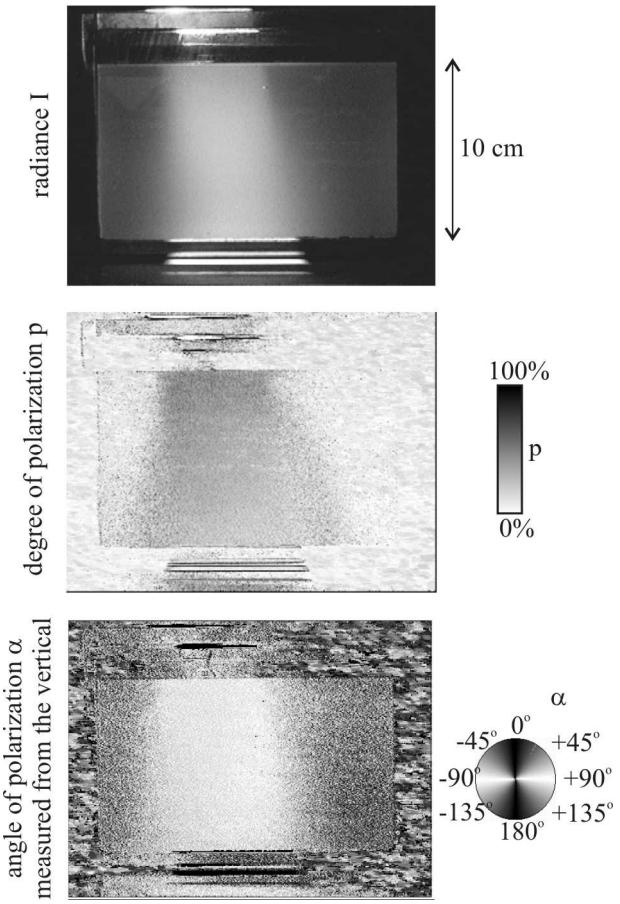

Fig. 21.8. Scattering-polarizational characteristics of turbid water in an aquarium, the middle part of which was illuminated by a slightly divergent vertical white light beam and the polarized light scattered by suspended particles in water was measured from the side by video polarimetry at 550 nm in such a way that the optical axis of the video camera was horizontal (perpendicular to the incident light beam). Demonstration of the strong scattering polarization of light within some centimetres in turbid water with a dense growth of green-yellowish phytoplankton from a pond inhabited by backswimmers *Notonecta glauca*. (After Fig. 27.7 of Horváth and Varjú 2003).

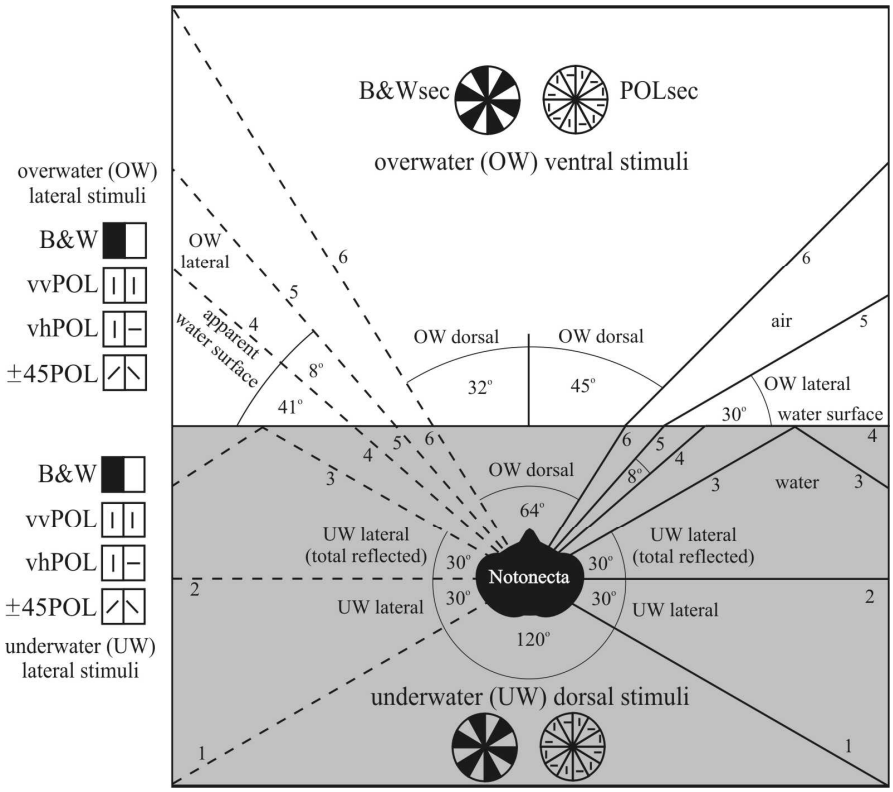

Fig. 21.9. Frontal view of the visual field of the eyes of *Notonecta glauca* (black: eyes and head) showing the different eye regions stimulated by various patterns. The patterns on the cylindrical pattern holder (Fig. 21.1A) stimulate the lateral eye region ±30° from the horizon due to total reflection at the water-air interface. The symbols outside the rectangle represent the different stimuli, which are the same as in Fig. 21.2. At the right hand side of the figure the incident, refracted and reflected rays of light from the borders of the different stimulus patterns are traced by continuous lines, while at the left hand side the dashed lines show the corresponding directions of view perceived by the eye of *Notonecta*. (After Fig. 27.8 of Horváth and Varjú 2003).

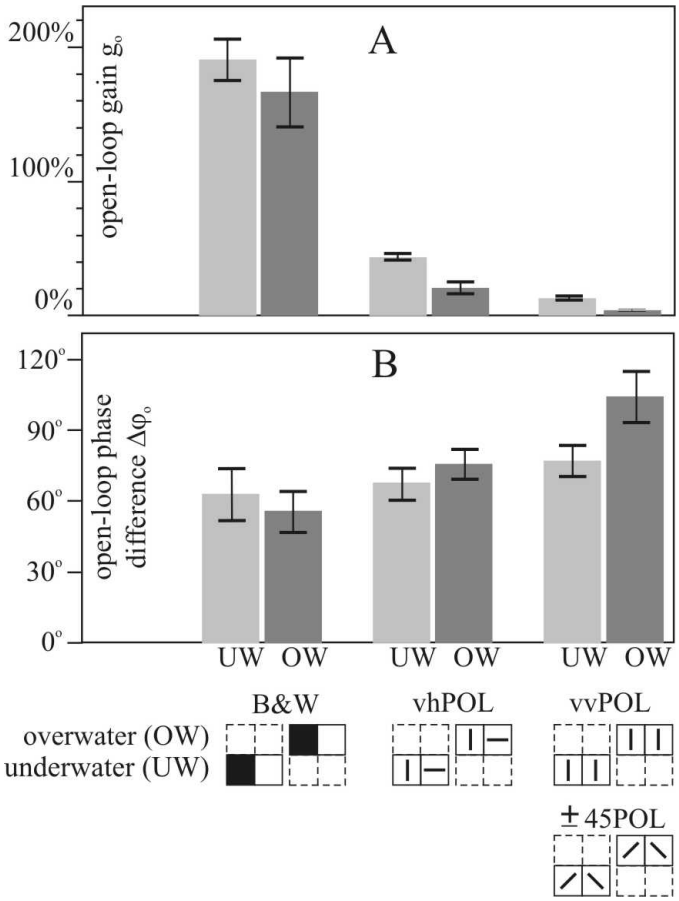

Fig. 21.10. The open-loop gain g_o (A) and open-loop phase difference $\Delta\varphi_o$ (B) of the optomotor response of *Notonecta glauca* to the B&W, vhPOL and vvPOL patterns stimulating the lateral eye region under (UW) and over (OW) the water surface. Columns: average data obtained with 8 animals. Bars: standard deviations. (After Fig. 27.9 of Horváth and Varjú 2003).

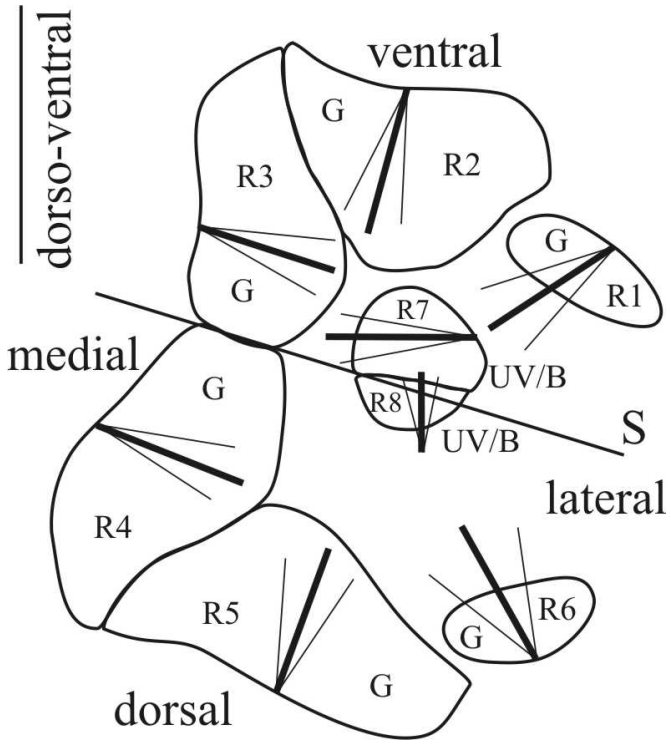

Fig. 21.11. Schematic representation of the cross-section of rhabdoms in the ventral POL-area of the compound eye of *Notonecta glauca* with the average orientations of the microvilli (thick bars) and their standard deviations (thin bars). These ommatidia look immediately above the water surface through the Snell window at its margin. The contours of retinula cells R1-R8 are also shown. Vertical bar at left: orientation of the dorso-ventral plane of the animal. S: average direction of the symmetry axis of the rhabdoms. G: green receptor, UV/B: ultraviolet or blue receptor. (After Fig. 18.4 of Horváth and Varjú 2003).

22 Polarization-Induced False Colours

22.1 Polarization-Dependent Colour Sensitivity and Colour-Dependent Polarization Sensitivity

Glas (1975, 1976, 1980) was the first, who has hypothesized that false colours could be induced in an insect visual system by polarized light. He proposed that the honeybee *Apis mellifera* may perceive the polarization of skylight not as a distinct entity, but rather as "polarizational false colours". In his model, all UV, blue and green photoreceptors are involved in the perception of polarization. Since, according to the model, the UV and blue receptors are polarization sensitive, their output signals depend on the degree and direction of linear polarization. Consequently, the model retina should perceive "polarization-induced false colours".

Glas (1975, 1976, 1980) suggested that bees perceive such false colours when they are looking at the sky, and the resulting false colour pattern, the symmetry axis of which is the solar-antisolar meridian, could be used for orientation. He tested this hypothesis in behavioural laboratory experiments, in which honeybees oriented under differently coloured linear polarizers. He observed that the spontaneous orientation of bees relative to the artificial overhead E-vector direction depended on colour. From these experiments he concluded that the observed changes in the distribution of the running directions of bees can only be understood by assuming that integration of the contributions of receptors with different spectral types occurs in polarization perception. Although later studies did not confirm several details of the anatomical and receptor physiological assumptions of this model, and the results of the mentioned behavioural experiments with bees could have been interpreted otherwise (see e.g. Wehner 1982, p. 121), the relevance of this model is obvious in the study of polarization-induced false colours.

Honeybees *Apis mellifera* respond to skylight polarization and use it for navigation. The polarization-sensitive UV photoreceptors concerned are gathered in an upward-pointing narrow dorsal rim area of the eye. Except for this specialized eye region, the retina of honeybees is composed of photoreceptors that are twisted about their longitudinal axes (Wehner et al. 1975), so that their polarization sensitivity is almost abolished (Labhart 1980). Lau (1976) observed that honeybees fail to discriminate polarization patterns that mark a food source,

i.e. are presented to the frontal part of their eyes. The reason for this is that the frontal part of the eye is polarization-blind due to rhabdomeric twist. Similar twisted photoreceptors, or receptors in which the microvilli of the rhabdomeres are not aligned consistently in a single particular direction, were found also in many other insects. In these photoreceptors the polarization sensitivity is weak, whereas the untwisted receptors located at the dorsal rim of the eye and used exclusively for detecting skylight polarization exhibit high polarization sensitivity.

Wehner and Bernard (1993) proposed that the functional significance of the photoreceptor twist is to avoid the "polarization-induced (or simply polarizational) false colours" of natural surfaces such as leaves and petals of flowers, which reflect partially linearly polarized light. The degree and angle of linear polarization of reflected light depend on how smooth the plant surfaces are and how they are oriented with respect to the incoming light at the direction of view. For a flower-visitor this could cause difficulties, because the absorbing photopigments responsible for colour vision are contained in receptors with different microvillar orientations. Thus, each receptor gives a signal that depends not only on intensity and wavelength but also on the angle and degree of polarization. If the sensors of a colour vision system are also polarization sensitive, the system generates false colours that may obscure the real colours defined by the spectral properties of the object.

As Wehner and Bernard (1993) pointed out: "... when zig-zagging over a meadow with all its differently inclined surfaces of leaves, the bee would experience pointillistic fireworks of false colors that would make it difficult to impossible to detect the real colors of the flowers". The twist of photoreceptors of the colour vision system abolishes the ability to respond selectively to the plane of polarization. This allows each type of receptor to take part unambiguously in the bee's trichromatic colour vision system. To demonstrate the false colour problem Wehner and Bernard (1993) computed the shift of perceived colour caused in the bee's colour triangle when it views reflections from a dandelion leaf at different angles.

Marshall (1988) suggested that each of rows 5 and 6 of the midband in the compound eyes of mantis shrimps may contain a separate three-channel polarization-analyzer system with output comparisons: In row 5 between retinula cells R8, R1-R2-R5-R6 and R3-R4-R7; in row 6 between R8, R1-R2-R5 and R3-R4-R6-R7, which receptor triplets have different microvilli directions. Since the spectral sensitivities of R8 and R1-R7 cells are maximal at 350 and 500 nm, respectively (Cronin and Marshall 2001), in both types of the three-channel polarization-sensitive system suggested by Marshall (1988) polarization-induced false colours would be inevitably generated. However, to prevent such confusion between polarization and spectral information, in the ommatidia specialized for colour vision the rhabdoms are polarization-insensitive due to randomly oriented microvilli (Marshall et al. 1991b).

Mammals represent an extrema in the solution of the problem of polarization-induced false colours: they eliminate polarizational false colours in such a way that they have colour vision but are polarization-blind. Certain cephalopod (squid, cuttlefish and octopus) species are the other extrema: they are colour-blind but

polarization sensitive (Hanlon and Messenger 1996). Hypotheses about salmon polarization sensitivity also predict an interaction between colour and polarization (Novales Flamarique et al. 1998). Ultraviolet-, green- and red-sensitive cones appear to contribute to both spectral and polarization sensitivity in several salmonid fishes (Parkyn and Hawryshyn 2000). Thus, also these fishes may perceive polarization-induced false colours. The counterpart of polarization-dependent colour vision, namely colour-dependent polarization sensitivity has been found in *Daphnia pulex* (Novales Flamarique and Browman 2000).

Horváth et al. (2002c) gave a quantitative model to calculate such polarizational false colours with the use of polarization patterns measured by imaging polarimetry. In this chapter some results obtained with this model are presented.

22.2 Polarizational False Colours of Leaves and Flowers Perceived by *Papilio* Butterflies

Kelber (1999) and Kelber et al. (2001) suggested that the butterflies *Papilio aegeus* and *Papilio xuthus* do not process polarization and colour separately, and thus they may perceive polarization-induced false colours due to their weakly polarization-sensitive photoreceptors. Since Kelber and collaborators worked with artificial stimuli having an unnaturally high degree of linear polarization $p = 100\%$ which is not characteristic for light reflected from plant surfaces, no published behavioural data so far support that there is a significant influence of polarization on butterfly colour vision under natural conditions, when the receptors are stimulated by partially linearly polarized light with frequently low p. Since the polarization sensitivity of photoreceptors in *Papilio* species, ranging between $PS = 1.3$ and 2 (Bandai et al. 1992; Kelber et al. 2001), is very low[1], the questions arise:

- Can the often low p of light reflected from plant surfaces induce sufficiently strong polarizational false colours in *Papilio* butterflies to influence their colour vision significantly?
- How do these polarization-induced false colours depend on the different parameters of the butterfly retina (microvillar directions, polarization sensitivity, orientation of the eye), on the characteristics of the optical stimuli (degree and angle of polarization of reflected light) and on the illumination conditions (alignment of the plant surface with respect to the direction of view and to the solar direction; plant surface in direct sunshine or in shadow)?

[1] Note that $PS = 1$ for polarization-insensitive receptors, and $PS = 1.3$-2 are such low values that many researchers consider a photoreceptor with such PS-values as polarization insensitive. Laughlin (1976, p. 227), for example, wrote about the polarization-insensitive photoreceptors of the dragonfly *Hemicordulia tau*: "All linked pigment cells and the single pigment green cells are notable for their lack of PS (< 2.5) at peak wavelength."

Shashar et al. (1998) investigated the polarization of light in a tropical rain forest and demonstrated some polarizational features of light reflected from certain leaves. Continuing the analysis done by Wehner and Bernard (1993), Horváth et al. (2002c) quantitatively estimated the influence of polarization sensitivity on the perception of natural surface colours by *Papilio* butterflies.

22.2.1 Computation of the Spectral Loci of Colours Perceived by a Polarization- and Colour-Sensitive Retina

The numerical values of the retina model of Horváth et al. (2002c) (Fig. 22.1) described in this chapter are characteristic to the butterfly *Papilio xuthus* (Fig. 1B and Table 1 of Kelber et al. 2001, pp. 2470-2471). The model retina contains polarization-sensitive photoreceptors of spectral types red (R), green (G) and blue (B), with sensitivity maxima at λ_R^r = 600 nm, λ_G^r = 520 nm and λ_B^r = 460 nm. The relative absorption functions of the receptors are shown in Fig. 22.1A. In the retina model, angle β is the direction of the microvilli measured clockwise from the dorso-ventral meridian of the compound eye (Fig. 22.1C). For the microvilli of the blue photoreceptors $\beta_B = 0^o$, in the green receptors $\beta_G = 0^o$, 35^o, 90^o, 145^o and in the red receptors $\beta_R = 0^o$, 35^o, 145^o (Fig. 22.1B). The colour vision system of *Papilio* butterflies is pentachromatic (Arikawa et al. 1987). Treating the short-wavelength receptors (UV, violet, blue) as one receptor type, allows to demonstrate false colour effects in a plausible way by indicating the shifts of colour loci in the equilateral colour triangle (Fig. 22.1E). No principally different false colour effects are expected by including all five receptor types in the retina model.

If the electric field vector E of totally linearly polarized incident light is parallel (par) to the longitudinal axes of the microvilli, a polarization-sensitive photoreceptor of type *r (=R,G,B)* absorbs P_r-times the number of photons (in the following called quantum absorption) as in the case when the E-vector is perpendicular (perp) to the microvilli. Thus, the relationship between the numbers of absorbed quanta is: $q_r^{par} = P_r q_r^{perp}$, where P_r is the polarization sensitivity ("*PS*-value") of the receptor, and q_r is the quantum absorption. The polarization sensitivity of the photoreceptors in *Papilio xuthus* ranges from 1.3 to 2 at peak wavelengths (Kelber et al. 2001, p. 2471, Table 1). In the retina model $P_B = P_G = P_R = 2$ are chosen, by which the average polarization sensitivity is slightly overestimated.

Let the angle of the eye's dorso-ventral meridian be χ clockwise from the vertical (Fig. 22.1C). If receptor r receives partially linearly polarized light with intensity $I(\lambda)$, degree of linear polarization $p(\lambda)$, angle of polarization $\alpha(\lambda)$ (clockwise from the vertical), minimum and maximum E-vectors $E_{min}(\lambda)$ and $E_{max}(\lambda)$, respectively, the quantum absorption q_r can be calculated as follows:

$$q_r = k \int_0^\infty A_r(\lambda) \left[P_r E^{par}{}_{max}(\lambda)^2 + E^{perp}{}_{max}(\lambda)^2 + P_r E^{par}{}_{min}(\lambda)^2 + E^{perp}{}_{min}(\lambda)^2\right] d\lambda, \qquad (22.1)$$

where k is a constant, λ is the wavelength of light, $A_r(\lambda)$ is the relative absorption of the receptor (Fig. 22.1A), $E^{par}{}_{max}(\lambda)$, $E^{perp}{}_{max}(\lambda)$ and $E^{par}{}_{min}(\lambda)$, $E^{perp}{}_{min}(\lambda)$ are the parallel and perpendicular components of the electric field vectors $E_{max}(\lambda)$ and $E_{min}(\lambda)$ with respect to the microvillar direction. From Fig. 22.1C one can read:

$$E^{par}{}_{max}(\lambda) = E_{max}(\lambda)\cos[\alpha(\lambda) - \chi - \beta_r], \quad E^{perp}{}_{max}(\lambda) = E_{max}(\lambda)\sin[\alpha(\lambda) - \chi - \beta_r],$$

$$E^{par}{}_{min}(\lambda) = -E_{min}(\lambda)\sin[\alpha(\lambda) - \chi - \beta_r], \quad E^{perp}{}_{min}(\lambda) = E_{min}(\lambda)\cos[\alpha(\lambda) - \chi - \beta_r]. \tag{22.2}$$

The relationship between $E^2{}_{min}(\lambda)$, $E^2{}_{max}(\lambda)$ and $p(\lambda)$ is:

$$E^2{}_{min}(\lambda) = E^2{}_{max}(\lambda)\,[1-p(\lambda)]/[1+p(\lambda)]. \tag{22.3}$$

The intensity $I(\lambda)$ can be expressed with $E_{min}(\lambda)$ and $E_{max}(\lambda)$ as follows:

$$I(\lambda) = k'\,[E^2{}_{max}(\lambda) + E^2{}_{min}(\lambda)]/2 = k'\,E^2{}_{max}(\lambda)/[1+p(\lambda)], \quad k' = \text{constant}. \tag{22.4}$$

Using Eqns. (22.1)-(22.4), one can obtain:

$$q_r = k''\int_0^{\infty} A_r(\lambda)\, I(\lambda)\, \{P_r[1+p(\lambda)] + 1 - p(\lambda) - 2p(\lambda)(P_r-1)\sin^2[\alpha(\lambda) - \chi - \beta_r]\}\,d\lambda,$$

$$r = R, G, B; \quad k'' = \text{constant}. \tag{22.5}$$

The expressions for k, k' and k'' involve different electrodynamical constants. Using them, one could calculate the absolute value of the absorbed quantum absorption q_r. We omit to give the expressions of k, k' and k'', because they all are eliminated in the final expressions describing the spectral loci of colours perceived by a polarization- and colour-sensitive retina.

Since using video polarimetry (Horváth and Varjú 1997), one can measure the spatial distribution of I, p and α of light reflected from plant surfaces only at wavelengths $\lambda_B{}^c = 450$ nm, $\lambda_G{}^c = 550$ nm and $\lambda_R{}^c = 650$ nm, in the calculations the following approximations are taken (Fig. 22.1D):

$$f(400\text{ nm} \le \lambda \le 500\text{ nm}) = f(\lambda_B{}^c) = f_{blue},$$

$$f(500\text{ nm} < \lambda < 600\text{ nm}) = f(\lambda_G{}^c) = f_{green},$$

$$f(600\text{ nm} \le \lambda \le 700\text{ nm}) = f(\lambda_R{}^c) = f_{red}, \qquad f = I,\ p,\ \alpha, \tag{22.6}$$

that is, in the spectral range s = red, green, blue the values of I, p and α are considered to be constant. This approximation can be applied, because the maxima and half bandwidths of the red, green and blue relative sensitivity functions of the camera of the used imaging polarimeter fall close to those of the corresponding

red, green and blue relative absorption functions $A(\lambda)$ (Fig. 22.1A) of the butterfly retina modelled. Then:

$$q_r = k'' \Sigma_s I_s[P_r(1+p_s) + 1 - p_s - 2p_s(P_r-1)\sin^2(\alpha_s - \chi - \beta_r)] \int_{\lambda s1}^{\lambda s2} A_r(\lambda)d\lambda,$$

$$r = R, G, B; \quad s = \text{red, green, blue;}$$

$$\lambda_{blue1} = 400 \text{ nm}, \quad \lambda_{blue2} = \lambda_{green1} = 500 \text{ nm},$$

$$\lambda_{green2} = \lambda_{red1} = 600 \text{ nm}, \quad \lambda_{red2} = 700 \text{ nm}. \tag{22.7}$$

In the literature of colour vision, there are two different conventions to give the relative absorption functions $A(\lambda)$ of photoreceptors: they possess either (i) equal amplitude $A_{max}(\lambda) = 1$ (e.g. Przyrembel et al. 1995; Fig. 12, p. 584), or equal integrals $\int_0^\infty A(\lambda)d\lambda = 1$ (e.g. Lunau and Maier 1995; Fig. 1A, p. 3). Kelber et al. (2001), for example, used the first convention, as Fig. 22.1A gives also the $A(\lambda)$ curves with the same amplitudes. This convention is called "amplitude normalization". The second convention, called "integral normalization", corresponds to the assumption that the quantum absorptions of receptors of different spectral types are the same if the incident light is unpolarized [$p(\lambda) = 0$] and physically white [$I(\lambda)$ = constant]. This has the consequence that "physical (or optical) white" coincides with "physiological (or perceptional) white"; in other words, the locus of both physical and physiological white is positioned at the colourless centre of the equilateral colour triangle of a colour vision system (Fig. 22.1E). In this case the receptor absorption curves are normalized by setting their integral to 1, that is, the quantum absorption q_r of receptor type r is divided by the quantum absorption

$$q_r^{white} = k'' I_{white} (P_r + 1) \Sigma_s \int_{\lambda s1}^{\lambda s2} A_r(\lambda)d\lambda \tag{22.8}$$

of the receptor for unpolarized ($p_s = 0$) and physically white light ($I_s = I_{white}$ = arbitrary constant). Then, the normalized quantum absorption is:

$$m_r = q_r/q_r^{white} = \{k''\Sigma_s I_s [P_r(1+p_s)+1-p_s-2p_s(P_r-1)\sin^2(\alpha_s-\chi-\beta_r)] \int_{\lambda s1}^{\lambda s2} A_r(\lambda)d\lambda\}/$$

$$/[k'' I_{white}(P_r+1) \Sigma_s \int_{\lambda s1}^{\lambda s2} A_r(\lambda)d\lambda]. \tag{22.9}$$

The three coordinates of the spectral locus of the perceived colour within an equilateral colour triangle (Fig. 22.1E) are

$$M_R = q_R/(q_R+q_G+q_B), \quad M_G = q_G/(q_R+q_G+q_B), \quad M_B = q_B/(q_R+q_G+q_B) \tag{22.10}$$

for amplitude normalization, and

$$M_R = m_R/(m_R+m_G+m_B), \quad M_G = m_G/(m_R+m_G+m_B), \quad M_B = m_B/(m_R+m_G+m_B) \qquad (22.11)$$

for integral normalization. Note that the constants k'' and I_{white} are eliminated from the expressions of M_R, M_G and M_B, as mentioned above. The calculations were performed for both amplitude and integral normalizations, but both conventions provided very similar results. The only significant difference between them is that for integral normalization the colour loci remain close to the white point (centre of the colour triangle), i.e. the colours are extremely pale, while for amplitude normalization all colour loci slightly shift towards the red-green border of the colour triangle. The reason for the latter shift is that the integral of $A_G(\lambda)$ is the greatest among the integrals of the absorption curves of the red, green and blue receptors (see Fig. 22.1A). Hence, when amplitude normalization is used, the quantum absorption q_G of the green receptors is the largest resulting in that the component M_G will be the greatest. If integral normalization is used, the relative differences in the quantum absorptions q_R, q_G and q_B of the R, G and B receptors are reduced, which decreases the colour saturation. In this chapter only the results are presented that were obtained using the more common integral normalization, which puts white in the intuitively correct location in the middle of the colour triangle. The values of I_s, p_s and α_s originate from the reflection-polarization patterns measured by imaging polarimetry in the s = red, green, blue ranges of the spectrum.

Using Eqns. (22.10) and (22.11), the coordinates M_r (r=R,G,B) of the colour locus are computed for every pixel of a given picture of plant surfaces. The calculated spectral coordinates M_r are plotted within the equilateral colour triangle (Fig. 22.1E). Note that the peak wavelengths of the colour receptors in the human eye differ significantly from those of the *Papilio* retina. Thus the false colour pictures given in this chapter merely serve to visualize the effect of polarization-induced colour changes for the reader. The false colours will look differently to a butterfly.

22.2.2 Polarization-Induced False Colours Perceived by the Polarization- and Colour-Sensitive Model Retina

Figure 22.2 shows the reflection-polarizational characteristics of the red flower petals and green leaves of *Campsis radicans* (trumpet vine, Bigniniaceae). In Fig. 22.3A the colours of *Campsis radicans* are shown as perceived by a polarization-blind retina. They are considered as "real" colours and serve as reference: the shifts of the polarization-induced false colour loci in the colour triangle are measured from the loci of these real colours. Figures 22.3B-E show the false colours of the plant perceived by the weakly polarization-sensitive retina of *Papilio xuthus* as a function of the alignment χ of the dorso-ventral symmetry plane of the eye with respect to the vertical, when a given set of photoreceptors rotates in front of the plant. Rotating the polarization-sensitive receptor set by 180^o, the perceived false colours shift continuously in the colour triangle passing within an approximately elliptical chromatic area: in cases B, C, D and E of Fig.

22.3 the false colour of the leaves, for example, is slightly blue-greenish, bluish, reddish and greenish, respectively. These colours are, however, more or less masked by the whitish reflected light (see Fig. 22.2A). Similar shifts of the perceived colour occur if the relative position of the plant surface with respect to the receptor set (orientation of the dorso-ventral meridian of the eye) changes because of rotation and/or translation. In the case of *Papilio xuthus* the chromatic distances of the polarization-induced false colours from the real colour are small due to the relatively small *PS*-value of 2 of the retina. These chromatic distances are smaller for the matt petals reflecting light with lower p than for the shiny leaves reflecting light with much higher p.

Figure 22.3 also demonstrates how the real and the polarization-induced false colours of leaves depend on the orientation of leaf blades. Although the average alignment of leaf blades is approximately horizontal, there are considerable deviations from this direction (see Fig. 22.2A; the E-vector alignment of specularly reflected light is always perpendicular to the plane of reflection determined by the incident ray, reflected ray and the normal vector of the reflecting surface). The more or less randomly curved leaf blades are more or less randomly oriented around the horizontal direction, thus both p and α change from site to site. The consequence is that the homogeneously green real colour of the leaves being independent of p and α (see the narrow colour distribution around the most frequent real green colour of leaves in the right colour triangle of Fig. 22.3A of the leaves) becomes more heterogeneous for a polarization-sensitive retina resulting in different colour hues ranging from (although partly white-masked) violet through blue, green, yellow, orange to red (see the relatively wide false colour distribution around the most frequent green false colour of leaves in the colour triangles of Figs. 22.3B-E). This shows one of the consequences of the polarization sensitivity of colour vision: due to the high diversity of p and α of light reflected from plant surfaces, the perceived polarizational false colours are more diverse than the real colours. This phenomenon makes more difficult to recognize a given real colour and demonstrates a disadvantage of the perception of polarization-induced false colours.

In *Papilio xuthus*, the microvilli in the red and green receptors can have three or four different directions as given in Fig. 22.1B, and at present it is not known how the receptors contribute to the net neural polarizational signal. It is only known that in the blue receptors the microvillar direction is $\beta_B = 0^o$. Apart from the contribution of $\beta_R = 145^o$, $\beta_G = 35^o$ and $\beta_B = 0^o$ (Fig. 22.3), other possible combinations of β_R and β_G (together with $\beta_B = 0^o$) are also used. Figure 22.4D shows how the polarization-induced false colours of an *Epipremnum aureum* plant (golden pothos, Aracea) perceived by *Papilio xuthus* depend on β_R and β_G. In the foreground of the colour picture in Fig. 22.4A the inflorescence of *E. aureum* can be seen which possesses a large, shiny, petal-imitating red leaf called spathe, while the background is composed of the shiny green leaves of the plant. Figures 22.4B and 22.4C show the patterns of p and α of the plant measured at 450 nm.

Figure 22.4D demonstrates the chromatic diversity of the polarizational false colours versus the microvillar direction. Depending on β_G and β_R, all false colours

b-m perceived by *Papilio xuthus* shift slightly towards the red and/or green hues with respect to the real colour *a* possessing the largest blue component M_B. This is because (i) the light reflected from the investigated areas of the plant was approximately horizontally polarized (Fig. 22.4C), and (ii) the microvillar direction of the blue receptor is dorso-ventrally (vertically) fixed. The false colours are scattered within areas, the dimensions of which are similar for both the spathe and the leaf, because both are shiny and reflect strongly polarized light (Fig. 22.4B).

Having based the previous considerations on a low polarization sensitivity of $PS = 2$, let us now consider visual systems with high *PS*. Figure 22.5 shows the dependence of the polarization-induced false colours on $P_B = P_G = P_R = P$ as a function of β_G and β_R. When *P* increases from 1 to 20, all false colours shift to some degree from the real unsaturated, bluish-green colour (locus *a*) of the leaf towards relatively saturated red, orange, yellow or green colours. The chromatic distance of the false colours from the real colour can be considerable if the polarization sensitivity is strong enough.

p of light reflected from plant surfaces depends on the angle of incidence, the surface roughness and the wavelength. At wavelengths, where the amount of light coming from the subsurface layers is negligible in comparison with the amount of light reflected from the surface, the reflected light can be almost totally polarized if the angle of incidence is near the Brewster angle (Horváth and Varjú 1997). This is the situation for shiny green leaves in the blue or red (Fig. 22.2), for instance. The increasing surface roughness decreases *p*. Hence, in nature *p* of light reflected from plant surfaces can vary between 0% and almost 100%. Figure 22.6 shows the dependence of the polarization-induced false colour on *p* of reflected light as functions of β_G and β_R. The dependence of the polarization-induced false colours on *p* (Fig. 22.6) is qualitatively the same as that on the polarization sensitivity *P* of the photoreceptors (Fig. 22.5). The only essential quantitative difference between Figs. 22.5 and 22.6 is that in the latter case the chromatic shifts (the lengths of the arrows) are much smaller than in the former case in spite of the very high *p*-values of 78%, 75%, 99% (Table 22.1).

Figure 22.7 shows how the spectral and reflection-polarizational characteristics of a sunlit leaf of a *Ficus benjamina* tree (weeping fig, Ficaceae) depend on the direction of sunlight at a given solar elevation, and how they change if the leaf is shaded from direct sunlight. The colours as well as *p* and α of light reflected from the leaf depend on the orientation of the leaf blade with respect to the sun. For a given position of the sun there are chromatic and polarizational differences between the sunlit and the shaded leaf. The colour of the sunlit leaf is always greenish (Figs. 22.7A,C,E,G) due to the diffuse scattering and selective absorption of white sunlight in the green subcuticular leaf tissue. This greenish hue is, however, more or less masked by strong specular reflection of white sunlight, if the leaf is viewed in the direction of the sun (Fig. 22.7G). The colour of the shaded leaf (Figs. 22.7B,D,F,H) is always bluish, because it is illuminated by blue skylight. Due to the non-planar curved shape of the leaf blade *p* and α of reflected light changes from point to point. In Fig. 22.7 the leaf blade in the small rectangular left and right window is approximately horizontal and vertical,

respectively. Note that although in Fig. 22.7G the entire leaf is lit by direct sunshine, both the left and right windows are placed in a local shaded region due to the curved leaf blade. Thus, both the left and right windows in case G represent a shaded situation.

In Fig. 22.8 we can see that under the clear blue sky the hues of shaded leaves are always nearer to the blue-green parts of the colour triangle than those of sunlit leaves. In the left window of the leaf in Fig. 22.7 the false colour shifts (represented by arrows) towards red, orange, yellow or green hues for both shaded and sunlit leaves. Since in the right window of the leaf in Fig. 22.7 the orientation of the leaf blade is different (vertical) from that (horizontal) in the left window, the colour shifts in the right window differ from those in the left window. Apart from case E, in the right window the false colours shift toward the green hues for both shaded and sunlit leaves. In case E the colour shift is very small.

22.2.3 Reflection-Polarizational Characteristics of Plant Surfaces

As we have seen above, the higher the p, the stronger is the colour shift, the direction of which depends on the viewing direction, the alignment of the dorso-ventral meridian of the eye, the polarization sensitivity, the microvillar orientation of the photoreceptors and the illumination conditions. Rough surfaces reflect light diffusely, which reduces polarization. Thus, the rougher a plant surface (e.g. due to a waxy layer or other microstructures), the lower the p of reflected light. The E-vector reflected from a plant surface follows its curvature, because the reflected light becomes partially linearly polarized perpendicularly to the plane of reflection for any dielectric reflector.

The darker a plant surface in a given spectral range, the higher the p of reflected light. The reason for this is the following: p of light reflected by the cuticle or epidermis of plants depends on the incident angle, but is almost independent of the wavelength. The direction of polarization of reflected light is parallel to the surface. The colour of plant surfaces arises from the selective absorption and diffuse scattering of light in the tissue below the transparent cuticle. The diffuse light emanating from this tissue is originally unpolarized, but it becomes partially polarized after transmission and refraction at the epidermis. The E-vector of the tissue-scattered light is perpendicular to the cuticle because of refraction polarization. Hence, the net degree and direction of polarization of a plant surface are determined by the superposition of the epidermis-reflected and the subcuticle-scattered light. If the former dominates (e.g. in sunlit shiny leaves observed from the direction of specular reflection), the direction of polarization is parallel to the cuticle; otherwise, the E-vector is perpendicular to it (e.g. sunlit leaves observed from behind, when the leaf-transmitted light is perceived). In those spectral regions where the subcuticle-scattered light has a considerable contribution, the net p of returned light is reduced or even abolished.

These general rules are demonstrated in Fig. 22.2: The considerably reduced amount of subcuticle-scattered light in the blue causes the red flowers to be dark and relatively strongly polarized at 450 and 550 nm. At 650 nm the amount of

light emanating from the red tissue below the epidermis of the flower is greater, thus, the net p is reduced. This is the physical reason for the general rule that in a given spectral region the darker objects polarize light to a higher degree if the illuminating light is unpolarized and white. Thus, green leaves are less polarized in the green than in the blue and the red, as can be well seen in Fig. 22.2.

Surfaces of petals have a matt finish, making them much better diffuse reflectors than leaves, which have a shiny, smooth cuticle (Kay et al. 1981). Thus, petals usually reflect diffuse and only weakly polarized light, while leaves reflect more specularly and the reflected light is generally highly polarized if the direction of view is near the Brewster angle.

Horváth et al. (2002c) proposed that the major function of the surface roughness of petals is not the reduction of p of reflected light (and thus the reduction of polarization-induced false colours), but to reduce the white glare of the surface, which would overwhelm the petal-tissue-backscattered coloured light and would make more difficult to perceive the real, attractive and striking colour of the petal. An appropriately rough petal surface functions as a Lambertian reflector, which reflects light uniformly in all directions independently of the angle of incidence. As a byproduct, the light reflected by a Lambertian surface is unpolarized. The intensity and colour of such a (matt) Lambertian surface is the same from all directions of view. If the surface of a petal were smooth, like the red spathe in Fig. 22.4A, it would function as a Fresnel reflector, which reflects light specularly. Then the intensity and colour of the petal-tissue-backscattered coloured light would be overwhelmed by the white glare (that is, by the specularly reflected white light) from the smooth cuticle if the direction of view coincides with the angle of reflection. This problem would not occur for other directions of view. Hence, the reduction of p of reflected light seems to be the consequence, and not the main aim of the surface roughness of petals. The roughness of petal surfaces is of great importance for all colour vision systems, independently of polarization-blindness or polarization-sensitivity, which must efficiently detect and distinguish the colours of flowers.

In columns 2 and 3 of Fig. 22.7, we can see that at a given illumination direction and in a given (e.g. blue) part of the spectrum the gross features of the patterns of p and α of the *Ficus* leaf are similar for both the sunlit and the shaded cases, although the colours of the sunlit and shaded leaf differ considerably. The reason for this is that the smooth *Ficus* leaf is similar to a Fresnel reflector, and the leaf blade is tilted so that sunlight cannot be reflected specularly from it towards the camera (apart from certain small curved areas). Thus, the sunlight reflected specularly from the leaf blade is not visible and does not add to the leaf-tissue-backscattered light. Large differences between the reflection-polarizational characteristics of sunlit and shaded leaves occur only if the direction of view coincides with or is near the direction of specular reflection. This is seen at those regions of the *Ficus* leaf in rows G and H of Fig. 22.7 where due to the appropriate local orientation of the curved leaf blade the sunlight is specularly reflected, the consequence of which is that in a considerable portion of these areas the leaf blade is overexposed due to the too intense reflected sunlight.

All these findings are in accord with the earlier results of Shul'gin and Moldau (1964), Vanderbilt and Grant (1985a,b), Vanderbilt et al. (1985a,b), Grant (1987), Grant et al. (1987a,b, 1993) and Sarto et al. (1989), who measured the polarized, non-polarized and specular reflectance of leaves of many different plant species as functions of the leaf surface features in the visible and near-infrared parts of the spectrum by point-source polarimetry. They found that in some viewing directions the surface reflection is so large that leaves appear white instead of green. In this case the strong specularly surface-reflected white light overwhelms the much smaller amount of green light scattered diffusely by the interior leaf tissue. They showed that the reflectance of the colourless and transparent leaf epidermis is practically independent of the wavelength of light, and in the visible part of the spectrum p of light reflected from green leaves is always the lowest in the green. They also demonstrated that the whitish light reflected specularly from leaves is always strongly polarized, while the green light reflected diffusely and non-specularly is practically unpolarized.

22.2.4 Do Polarization-Induced False Colours Influence the Weakly Polarization-Sensitive Colour Vision of *Papilio* Butterflies Under Natural Conditions?

Figures 22.3-22.6 and 22.8 clearly show that for the weakly polarization-sensitive model retina the polarization-induced false colours of plants fall near the real colours perceived by a polarization-blind retina even if they reflect strongly polarized light. Another effect of specular reflection is that whitish glare strongly masks the colour hue. Is the colour vision system of *Papilio* butterflies sensitive enough to perceive the tiny polarization-induced colour shifts in Figs. 22.3-22.6 and 22.8 under these circumstances? Behavioural studies on the discrimination of weakly saturated colours by insects are scarce. Honeybees seem to be able to discriminate pure white from white mixed with just a few percent of spectral light (Daumer 1963; Lieke 1984). Such stimuli differ in their locus position to a comparable degree as the loci of the real colours differ from some of the polarizational false colours calculated in this study. However, how well *Papilio* discriminates unsaturated colours remains to be demonstrated.

Horváth et al. (2002c) showed that in plant parts with dominating diffuse reflection, the colour saturation is relatively high but p is low. Although in this case hue discrimination will be good, the false colour effect is minute. On the other hand, plant surfaces with high p possess low colour saturation due to the white specularly reflected light. Thus, under natural conditions the weak polarization sensitivity of the photoreceptors might not interfere with the colour vision at all. This may be the reason why the average PS of the photoreceptors in proven colour-sensitive insects is not reduced to 1.0 but was found to be about 2.0-2.5 (*Cataglyphis bicolor*: Labhart 1986; *Papilio*: Kelber et al. 2001; *Drosophila melanogaster*: Speck and Labhart 2001; other fly species: Hardie 1985). Only in honeybees is the PS significantly smaller than 2 (Labhart 1980).

The complete destruction of the polarization sensitivity in a microvillar photoreceptor is not a trivial task but calls for a systematic misalignment of the microvilli along the rhabdom, in which complicated optical effects such as self-screening and lateral filtering within the rhabdom must be considered. The microvilli are misaligned by random or continuous direction changes (twist) along the rhabdom, but in most photoreceptors certain microvillar directions still dominate (Labhart and Meyer 1999). In honeybees, the rhabdom twists by about 180^{o} which reduces the *PS* to lower values than in other insects (Wehner et al. 1975; Labhart 1980). This might be taken as an indication that the exquisite colour vision system of honeybees might be more sensitive to small colour differences than that of other insect species and, thus, more compelled to avoid polarizational false colours.

Kelber (1999) and Kelber et al. (2001) showed that the colour choices of butterflies *Papilio aegeus* and *Papilio xuthus* is influenced by the E-vector orientation of linearly polarized light emitted by the colour stimuli to which the butterflies are exposed. They suggested that the interaction between colour and polarization might help the butterfly to find the best oviposition sites. Thus, they found that horizontally polarized green stimuli (mimicking horizontally oriented green leaves) were more attractive than vertically polarized stimuli of the same colour. At first glance, the findings of Kelber and collaborators, that polarization influences the colour choices of *Papilio* butterflies, seems to contradict the conclusion of Horváth et al. (2002c) that colour vision is quite insensitive to reflection polarization. However, in their behavioural tests, Kelber and collaborators used stimuli that had both a very high p ($\approx 100\%$) and a high degree of colour saturation, a situation that does not occur under natural conditions. Using this hyperstrong polarization/colour saturation combination, Kelber (1999) and Kelber et al. (2001) confirmed behaviorally the polarization sensitivity of *Papilio* photoreceptors that was previously measured electrophysiologically by Bandai et al. (1992). Thus, one can assume that this receptor property plays only a minor role in real life.

To demonstrate that the polarization sensitivity of the colour vision system can indeed ease certain vital tasks in a butterfly's life, further behavioural experiments with *Papilio* exposed to stimuli with natural combinations of p and colour saturation are needed. For an eye with $PS = 2$, even for almost totally polarized light reflected from a leaf of *Campsis radicans*, the false colour shifts in Fig. 22.6 should be smaller than those induced by the totally polarized and highly colour saturated stimuli of Kelber and co-workers, because the light reflected from leaves has rather low colour saturation. At the moment it is unknown how large a false colour shift needs to be in order to be just detectable, and thus useful in a behavioural context. Although Horváth et al. (2002c) did not claim that their calculations prove *Papilio* is incapable of detecting false colours under natural conditions, they did predict that the calculated colour shifts in the simulated *Papilio* retina may not large enough to be seen. The question, if *Papilio* might be equally sensitive to colours as bees and could perceive spectral shifts comparable to the calculated polarizational false colour shifts, can be answered only by further studies of the colour sensitivity of *Papilio*.

Another finding that seems to contradict the thesis of Horváth et al. (2002c) is that in plants the petals are usually less shiny than the leaves (Kay et al. 1981), i.e. specular reflection is reduced relative to diffuse reflection and, therefore, they exhibit less polarization. One might argue that this is to reduce false colour effects and, thus, to improve flower recognition. However, matter petals also avoid masking of the hue of a flower by whitish glare. The avoidance of glare alone may already be reason enough to reduce specular reflection in petals: the matter the petals, the more constant the appearence of flower colour when seen from different directions.

22.3 Polarizational False Colours Perceived by a Highly Polarization-Sensitive Retina Rotating in Front of Flowers and Leaves

It occurs frequently that insects hover in front of flowers and leaves, or approach the landing site on plant surfaces along oscillating flight paths, and their body axis more or less rotates to and fro simultaneously. Figures 22.9, 22.10, 22.11 and 22.12 demonstrate how the polarization-induced false colours perceived by a highly polarization-sensitive visual system (PS = 20) change in this situation. Figure 22.9 demonstrates well that the polarizational false colours of shiny leaves usually much more differ from their real colours than in the case of matt flower petals. The reason for this is that matt petals reflect light with lower p than shiny leaves. Rotating the head, the false colours of the leaves change more drastically than those of the petals: If the head's alignment χ with respect to the vertical changes from 0^o through 45^o and 90^o to 135^o, the false colours of the leaf in Fig. 22.9 change from violet through bluish and greenish to orange, while the false colours of the petals remain in the reddish-orange spectral range. There is no colour change in those regions of the flower where the reflected light is unpolarized. Here the colours perceived by the polarization-sensitive retina are the same as the real colours.

Figure 22.10 demonstrates how the polarization and the false colours induced by it change as a function of the orientation of the plant surface. In Fig. 22.10 the reflection-polarizational and spectral characteristics of green grass leaves in a meadow can be seen. The leaf blades are randomly oriented and curved, thus both p and α of reflected light change gradually from site to site. The consequence is that the real green colour of the grass becomes very heterogeneous resulting in practically all possible colour shades and hues ranging from violet through blue, yellow, orange to red. Thus, the originally relatively homogeneous green grass surface looks kaleidoscopic with randomly altering tiny false-coloured patches for a polarization-sensitive visual system, and what is more, the colours of the spots in this kaleidoscope change chaotically as the head rotates or the viewing direction alters.

Figure 22.11 shows the colours as well as the colours and brightness of *Epipremnum aureum*, the reflection-polarizational characteristics of which are

given in Fig. 22.4A, perceived by a polarization-blind ($P_R = P_B = P_G = 1$, β_R, β_G, β_B = arbitrary) and a highly polarization-sensitive ($P_R = P_B = P_G = 20$, $\beta_R = 0^o$, $\beta_G = 90^o$, $\beta_B = -45^o$) retina as a function of the alignment χ of the eye's dorso-ventral meridian with respect to the vertical. Here, both the shiny green leaves and the flower-imitating shiny red spathe reflect highly polarized light, induce striking false colours, the hues of which change drastically as the eye rotates in front of the plant.

If the eye regions viewing the flowers in flower visitors were polarization-sensitive, then colour-related behaviour, innate colour preferences, learned associations between nectar and flower colours, flower fidelity, colour constancy, chromaticity contrast between flowers and their background, nectar guides and other flower-pattern components, floral colour changes, true colour vision, or colour mimicry of flowers would lose their sense because of the disturbing effect of polarization-induced false colours. The consequence of these false colours would be that such flower visitors could not distinguish visually the flowers from other non-floral objects or the vegetable background.

22.4 Camouflage Breaking via Polarization-Induced False Colours and Reflection Polarization

We have seen above that generally polarization-induced false colours may be disadvantageous for perception of colour signals in the plant-pollinator interaction. However, Fig. 22.12A presents an example, when polarizational false colours could be advantageous in camouflage breaking for a predator. Figure 22.12A shows the colours as well as the colours and brightness of a beetle with shiny black carapace on a green leaf blade of *Helianthus annuus* perceived by a polarization-blind ($P_R = P_B = P_G = 1$, β_R, β_G, β_B = arbitrary) and a highly polarization-sensitive ($P_R = P_B = P_G = 20$, $\beta_R = 0^o$, $\beta_G = 90^o$, $\beta_B = -45^o$) retina as a function of the alignment χ of the eye's dorso-ventral meridian with respect to the vertical. The recording was taken under a clear sky, the scene was illuminated by direct sunlight and the originally colourless carapace of the beetle reflected green light from the surrounding vegetation and blue light from the sky. Thus, the carapace has a greenish-bluish appearance, which reduces the colour contrast between the beetle and the green leaf. This effect results in a moderate colour camouflage of the carapace for a polarization-blind visual system. However, this camouflage is broken for a highly polarization-sensitive visual system perceiving the striking polarizational false colours of the carapace, which differ considerably from those of the leaf blade. The polarization-induced false colours change dramatically as the eye rotates, which further enhances the break of the colour camouflage.

Figure 22.12B shows the patterns of p and α of the beetle and the underlying leaf measured by video polarimetry in the green (550 nm), which patterns are practically the same also in the red (650 nm) and blue (450 nm). We can see that

there is also a remarkable p- and α-contrast between the carapace and the leaf blade, because the horizontal and slightly rough surface of the leaf reflects horizontally polarized light with relatively low p, while the strongly curved and smooth carapace reflects highly polarized light with spatially changing α. Hence, break of the camouflage of the carapace occurs not only for a highly polarization-sensitive colour vision system, but also for a visual system with true polarization vision, which is able to perceive the large p- and α–contrasts between the beetle and the substratum.

Camouflage breaking via polarization-induced false colours or reflection-polarization is a possible visual phenomenon, which would be worth testing in the future. The possible breaking of the brightness and colour camouflage of hidden animals (e.g. caterpillars or frogs on leaves) by means of reflection polarization was suggested by Shashar et al. (1995a).

22.5 Is Colour Perception or Polarization Sensitivity the more Ancient?

Honeybees need accurate colour vision in order to find properly the flowers to gather nectar and pollen. They also need polarization sensitivity (PS) to orient by means of the celestial polarization pattern. The perception of polarization is ensured by the dorsal rim area (DRA) of the compound eye, where monochromatic and highly polarization-sensitive photoreceptors are gathered. Horváth and Varjú (2003) proposed that the polarization-sensitive receptors with non-twisted microvilli in the DRA and the polarization-insensitive receptors with twisted microvilli in other eye regions of honeybees and many other insects support the hypothesis that perception of polarization is a more ancient visual capability than perception of colours.

We have seen above that unambiguous colour vision can be ensured only by means of polarization-insensitive photoreceptors. In a compound eye composed of photoreceptors with microvilli such polarization insensitivity can be ensured by a random orientation of the microvilli. Morphologically, this would be the simplest and easiest way to abolish the inherent PS of the microvilli. Using exclusively such polarization-blind photoreceptors, bees could precisely discriminate the colours and find the adequate flowers in a meadow, but they could not find the way backwards to their nest if the sun is occluded by clouds. The latter would be lethal for them.

Contrary to this, however, if the non-twisted photoreceptors were polarization sensitive due to the parallel orientation of the microvilli in the entire eye, bees could orient by means of the celestial polarization even if the sun is not visible, and could navigate back to their nest. The cost of this would be, that the colour perception would be ambiguous because of the polarization-induced false colours. Although in this case bees could not find easily the proper flowers on the basis of their characteristic colour patterns, this imperfection could be partly compensated by using other sensory cues, such as the characteristic shape or odour of flowers.

Although polarization-sensitive compound eyes could be frequently deceived by the polarizational false colours, the resulting wrong landing on plant leaves or inappropriate flowers instead of landing on the sought flower petals with given colours would not be deadly. This would only decrease more or less the efficiency of nectar and pollen gathering in bees. On the basis of the above we propose the following evolutionary scenario:

1. In the compound eyes of the ancestors of bees polarization-sensitive, non-twisted photoreceptors with parallel microvilli evolved in the whole eye in order to orient by means of the celestial polarization pattern.
2. Since the absorption spectrum of photopigments is relatively narrow, receptors with different spectral sensitivities were needed to perceive the near-UV and visible ranges of the spectrum. Thus, UV-, blue- and green-sensitive receptors evolved in the ancestors of bees.
3. In a later stage of evolution, apart from the DRA of the eye, the polarization-induced false colours of plant surfaces were eliminated by the proper twist of photoreceptors. Polarization-sensitivity remained only in the DRA of the eye, where polarizational false colours do not cause any problem, because here only UV receptors occur.

The regular twist of the photoreceptors in bee eyes may hint that polarization sensitivity is more ancient than colour perception. Polarization-sensitive receptors need only to be twisted in order to abolish their inherent polarization sensitivity. Would the colour perception be the more ancient, the microvilli of ancient photoreceptors would have originally been randomly oriented to ensure polarization-blindness and unambiguous colour discrimination. Later, polarization-sensitive receptors with parallel microvilli should have been gradually evolved from such receptors, if the ancestors of bees could have survived the lack of the capability of orientation by means of celestial polarization.

The above proposal is consistent with the findings of Chittka (1996) that the essential components of bee's colour vision predated the evolution of flower colour, because the spectral receptor sets of bees are indistinguishable from those of many members of arthropod taxa, whose evolutionary lineages diverge from those of bees before there were flowers. The Cambrian ancestors of extant insects and crustaceans possessed already UV, blue and green receptors. Insects were well preadapted for flower colour coding more than 500 million years ago, about 400 million years before the extensive radiation of the angiosperm plants which started in the middle Cretaceous (100 million years ago), although the origin of the angiosperms might have to be placed in the Triassic. According to Chittka (1996), flower colours had no impact on wavelength positioning of bee photoreceptors. In contrary, because bee colour vision is optimally suited to code flower colour, flower colours should adapted to insect vision.

Table

Table 22.1. Intensity I, degree of linear polarization p and angle of polarization α (measured from the vertical) of a pixel of a leaf in Fig. 22.2 measured by video polarimetry at 650 nm (R), 550 nm (G) and 450 nm (B). The data in rows 1-3 are used in the calculations of Fig. 22.5. Using the original degrees of polarization p_0 in row 3, the other degrees of polarization are derived as follows: $p_i = n_i \cdot p_0$, i = 1,2,...,8. These data are used in the calculations of Fig. 22.6. (After Table 2 of Horváth et al. 2002c, p. 3290).

row		**R**	**G**	**B**
1	I (%)	78	87	100
2	α	105°	107°	108°
3	$p_0(R,G,B)$ (%)	61	59	78
	$p_i(R,G,B) = n_i \cdot p_0(R,G,B)$ (%)			
4	$n_1 = 0$	0	0	0
5	$n_2 = 0.18$	11	10	14
6	$n_3 = 0.36$	22	21	28
7	$n_4 = 0.55$	33	32	42
8	$n_5 = 0.73$	44	43	57
9	$n_6 = 0.91$	55	53	71
10	$n_7 = 1.09$	66	64	85
11	$n_8 = 1.28$	78	75	99

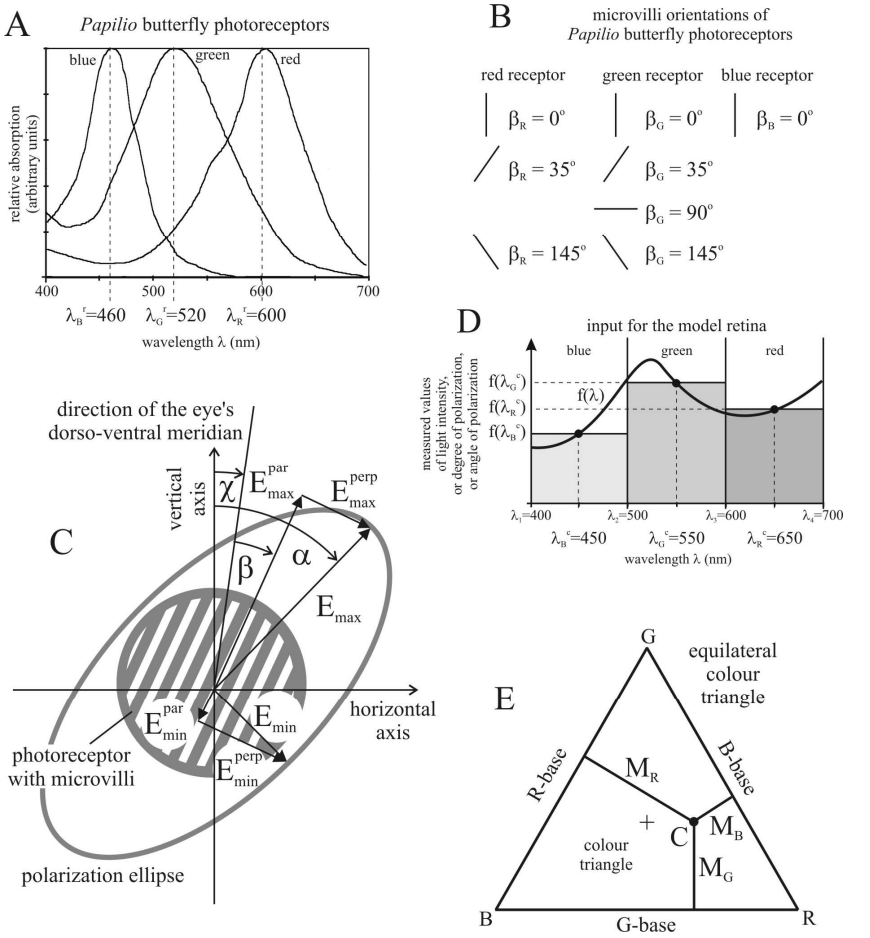

Fig. 22.1. A: Relative absorption functions of the blue, green and red photoreceptors of *Papilio xuthus*. B: Microvilli orientations β measured clockwise from the eye's dorso-ventral meridian in the photoreceptors of different spectral types in *Papilio xuthus*. C: Definition of the different parameters of partially linearly polarized light and a polarization-sensitive photoreceptor. The direction of hatching indicates the microvilli orientation β. The angle of the eye's dorso-ventral meridian is χ clockwise from the vertical. α is the angle of polarization of light measured clockwise from the vertical. The arrows represent the maximum (E_{max}) and minimum (E_{min}) of the electric field vector (the major and minor axes of the polarization ellipse) and their components that are parallel (E^{par}_{min}, E^{par}_{max}) or perpendicular (E^{perp}_{min}, E^{perp}_{max}) to the microvilli. D: Replacement of the blue (400–500 nm), green (500–600 nm) and red (600–700 nm) parts of function $f(\lambda)$ [$f = I$ (intensity), or $f = p$ (degree of linear polarization), or $f = \alpha$ (angle of polarization)] by discrete constant values $f(\lambda_r^c)$ $(r=B,G,R)$ measured by video polarimetry at wavelengths λ_r^c. E: Position of a visual stimulus C with spectral components M_R, M_G and M_B within the equilateral colour triangle of a colour-sensitive visual system with photoreceptor types R, G and B. The centre of the triangle is marked by +. (After Fig. 1 of Horváth et al. 2002c, p. 3283).

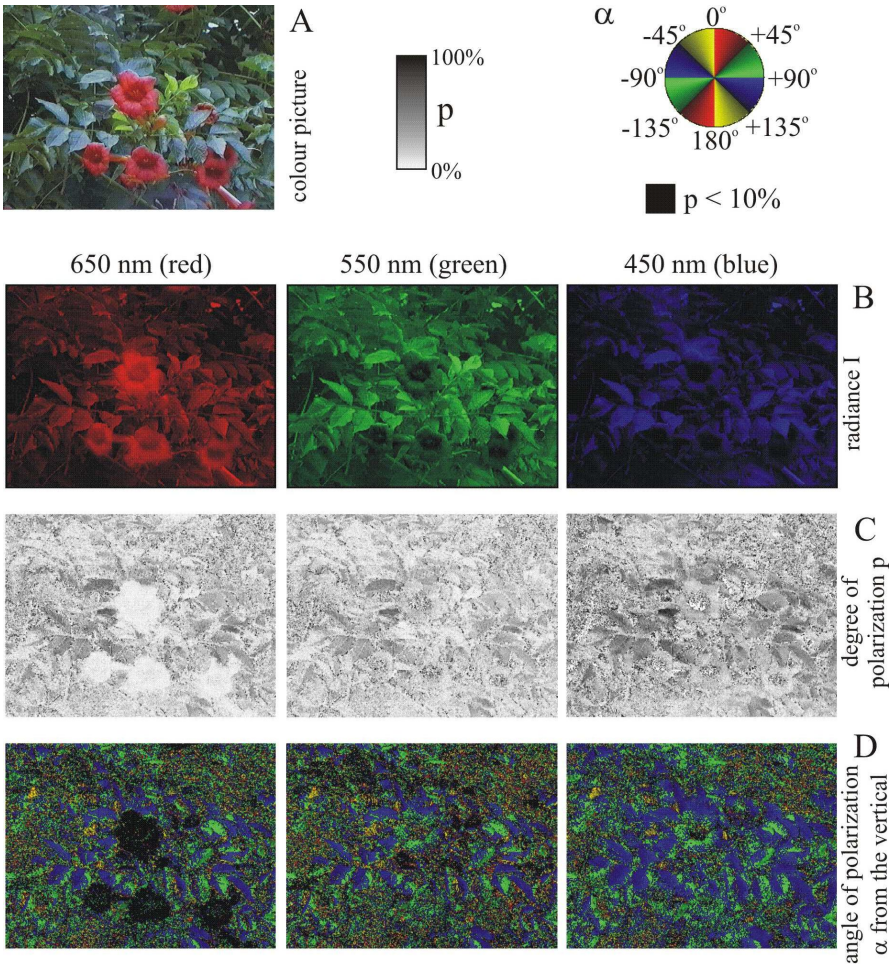

Fig. 22.2. A: Colour picture of red flowers and green leaves of *Campsis radicans* (trumpet vine, Bigniniaceae). B-D: Patterns of radiance I, degree of linear polarization p and angle of polarization α (measured from the vertical) of the plant surfaces in A measured by video polarimetry at 650, 550 and 450 nm. Number of pixels = 560×736 = 412160. In row C regions are black where $p < 10\%$. (After Fig. 3 of Horváth et al. 2002c, p. 3286).

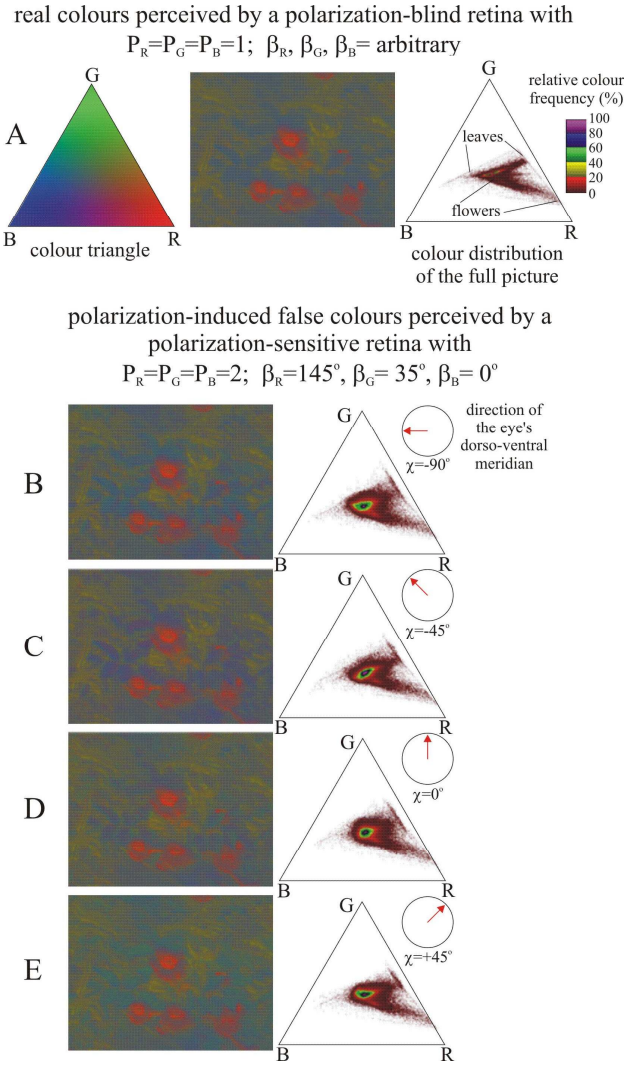

Fig. 22.3. A: Left: Equilateral R-G-B colour triangle filled with the isoluminant colour shades used. Middle: Real colours of *Campsis radicans* in Fig. 22.2A as perceived by a polarization-blind retina with polarization sensitivity $P_R = P_G = P_B = 1$ and microvillar directions β_R, β_G, β_B = arbitrary. Right: Relative frequency distribution of perceived colours (M_R, M_G, M_B) within the colour triangle calculated for the full rectangular picture. B-E: Polarization-induced false colours of *C. radicans* perceived by a polarization-sensitive retina with $P_R = P_G = P_B = 2$, $\beta_R = 145^\circ$, $\beta_G = 35^\circ$, $\beta_B = 0^\circ$ and their relative frequency distribution in the colour triangle as a function of the alignment χ of the eye's dorso-ventral symmetry plane (indicated by red arrows in the circular insets) measured from the vertical. Note that the isoluminant rectangular images and the isoluminant colour triangle on the left in row A give information on colour alone; intensity information is missing. (After Fig. 4 of Horváth et al. 2002c, p. 3288).

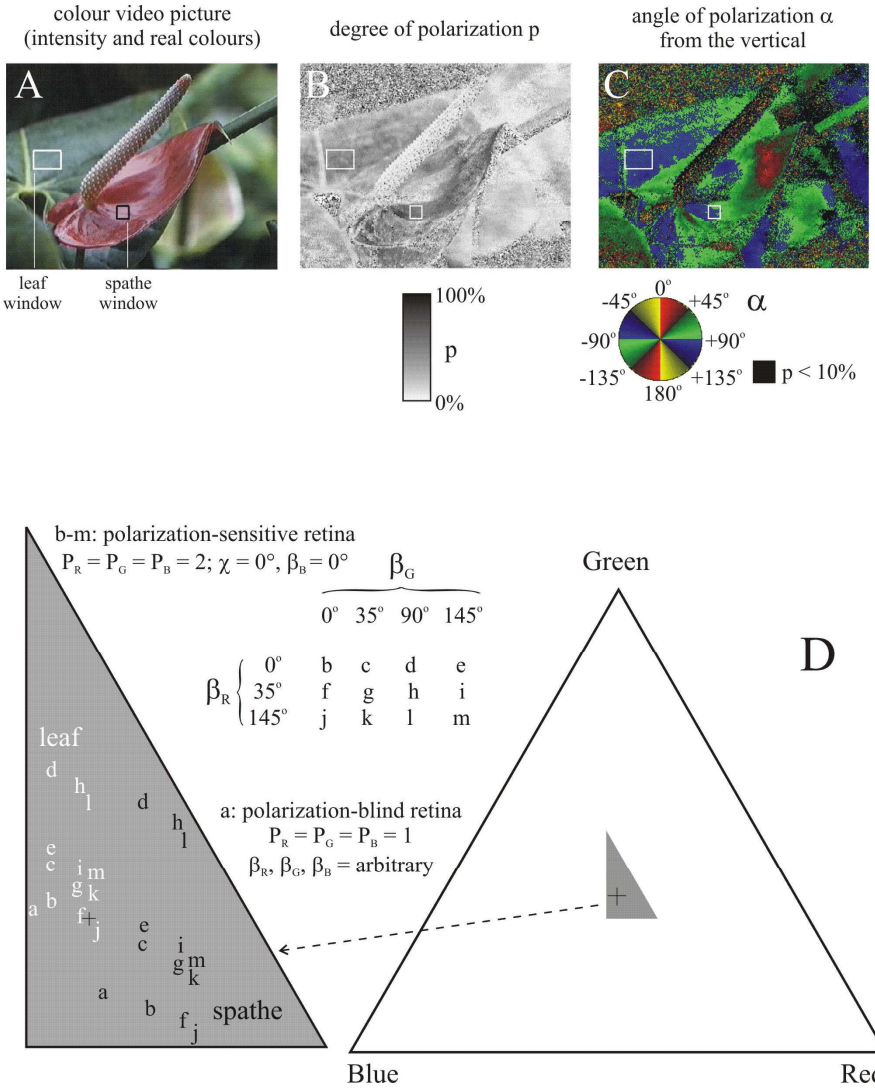

Fig. 22.4. A-C: Colour picture and patterns of the degree p and angle α of linear polarization of *Epipremnum aureum* (golden pothos, Aracea) measured by video polarimetry at 450 nm. D: Colours (M_R, M_G, M_B) of *E. aureum* perceived by a polarization-blind retina with $P_B = P_G = P_R = 1$, and β_R, β_G, β_B = arbitrary (*a*), and by a polarization-sensitive retina with $P_B = P_G = P_R = 2$, $\chi = 0^o$, $\beta_B = 0^o$ as a function of the microvillar directions β_G and β_R of the green and red receptors (*b-m*). Every microvilli situation is designated by a lower case letter ranging from *a* to *m*. The corresponding spectral loci (designated by letters *a-m*) of two details of the picture, one on a leaf blade (white) and one on the spathe (black) marked by rectangular windows in patterns A-C, are plotted within the equilateral R-G-B colour triangle, the colourless centre of which is represented by +. (After Fig. 6 of Horváth et al. 2002c, p. 3291).

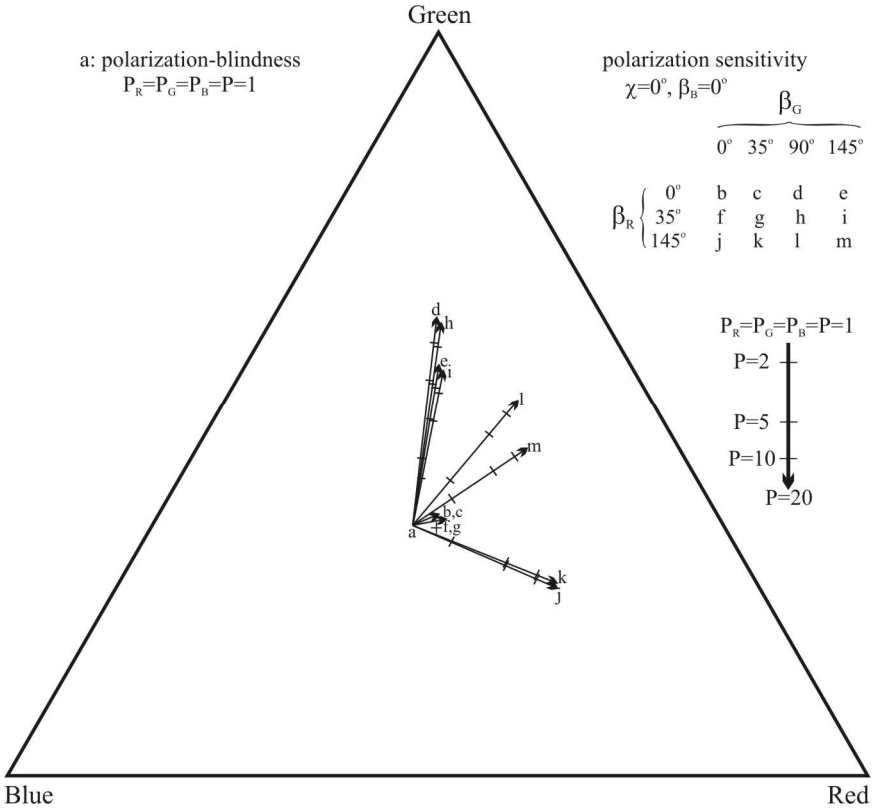

Fig. 22.5. Dependence of the polarization-induced false colour (M_R, M_G, M_B) perceived by a retina with $\chi = 0^o$, $\beta_B = 0^o$ on the polarization sensitivity $P_B = P_G = P_R = P$ as a function of the microvillar directions β_G and β_R of the green and red receptors (designated by lower case letters *b*-*m*) plotted within the equilateral R-G-B colour triangle, the colourless centre of which is represented by +. The colours are calculated for a point on a leaf of *Campsis radicans*, the reflection-polarizational characteristics of which are given in Table 22.1. The arrows start from the spectral locus *a* of the real colour when $P_B = P_G = P_R = P = 1$, meaning polarization-blindness, while the arrowheads point to the spectral locus of perceived false colours if $P_B = P_G = P_R = P = 20$. The spectral loci of false colours for P ranging between 1 and 20 are placed along the straight arrows, on which the loci for $P = 2$, 5 and 10 are marked by bars. (After Fig. 7 of Horváth et al. 2002c, p. 3292).

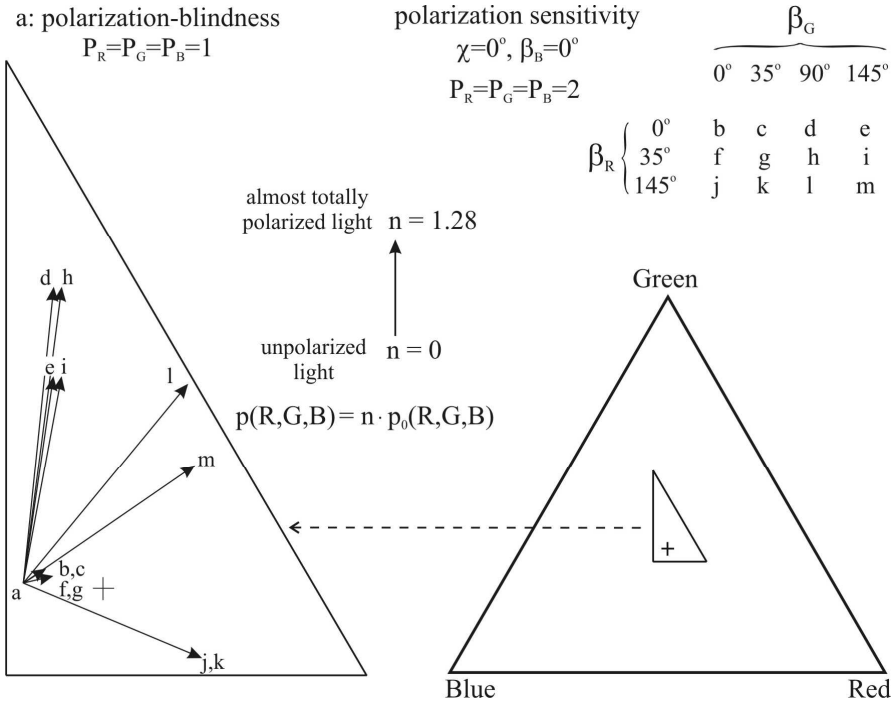

Fig. 22.6. Dependence of the polarization-induced false colour (M_R, M_G, M_B) perceived by a polarization-sensitive retina with $P_B = P_G = P_R = 2$, $\chi = 0^o$, $\beta_B = 0^o$ on the degree of linear polarization $p(R,G,B)$ of reflected light as a function of the microvillar directions β_G and β_R of the green and red receptors (designated by lower case letters *b*-*m*) plotted within the equilateral R-G-B colour triangle, the colourless centre of which is represented by +. The colours are calculated for the point of a leaf of *Campsis radicans*, the original reflection-polarizational characteristics of which are given in Table 22.1. The degrees of linear polarization of reflected light are calculated as $p(R,G,B) = n \cdot p_0(R,G,B)$ and given in Table 22.1, where n is an arbitrary factor. The arrows start from the spectral locus *a* of the real colour when $n = 0$ (unpolarized light) and $P_B = P_G = P_R = P = 1$ (polarization-blindness), while the arrowheads point to the spectral locus of perceived false colours for $n = 1.28$ (almost totally polarized light in all three spectral ranges). The spectral loci of false colours for n ranging between 0 and 1.28 are placed approximately equidistant along the straight arrows. (After Fig. 8 of Horváth et al. 2002c, p. 3293).

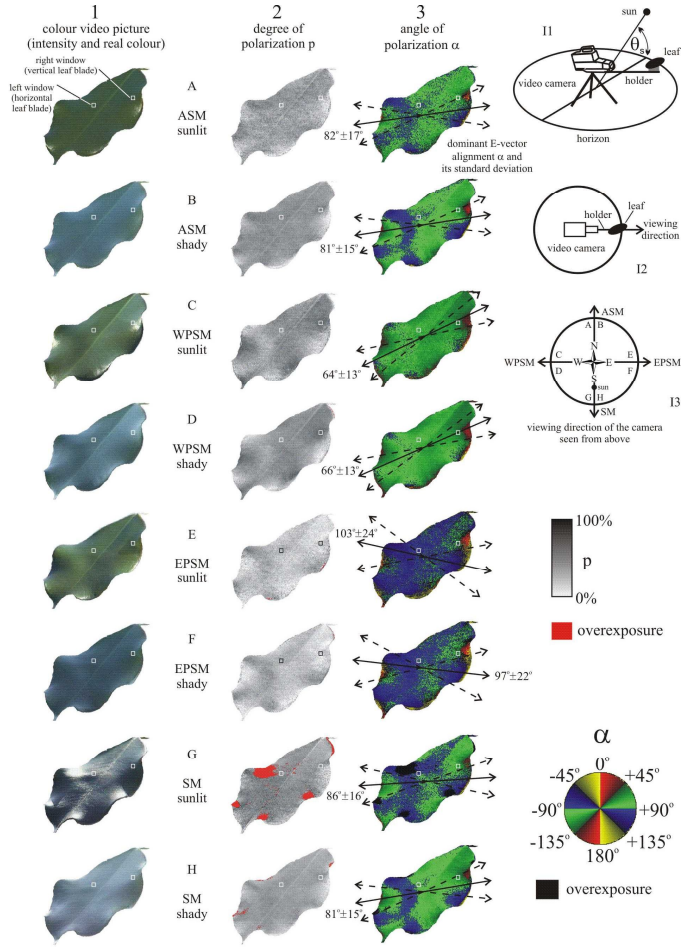

Fig. 22.7. Spectral and reflection-polarizational characteristics of a leaf of a *Ficus benjamina* tree (weeping fig, Ficaceae) as functions of the illumination conditions in the open. The leaf was mounted in front of the camera on a horizontal rod, which rotated in a horizontal plane along a vertical axis together with the camera (insets I1 and I2). The solar elevation was $\theta_S = 55^o$ and the leaf was illuminated by direct sunlight (A,C,E,G) or shaded with a small screen (B,D,F,H) which just occluded the sun and exposed the leaf to the full clear sky. In the small rectangular left and right window, the leaf blade is approximately horizontal and vertical, respectively. Inset I3 shows the four different horizontal directions of view of the camera with respect to the solar azimuth. ASM: antisolar meridian, SM: solar meridian, EPSM: eastwardly perpendicular to the solar meridian, WPSM: westwardly perpendicular to the solar meridian. *Column 1*: Colour pictures of the leaf. *Column 2*: Patterns of the degree of linear polarization p of the leaf measured by video polarimetry at 450 nm. *Column 3*: Patterns of the angle of polarization α (measured from the vertical) of the leaf at 450 nm, where the dominant (average) E-vector alignment of the leaf blade is represented by a double-headed solid arrow, while the standard deviations are shown by double-headed dashed arrows. (After Fig. 9 of Horváth et al. 2002c, p. 3294).

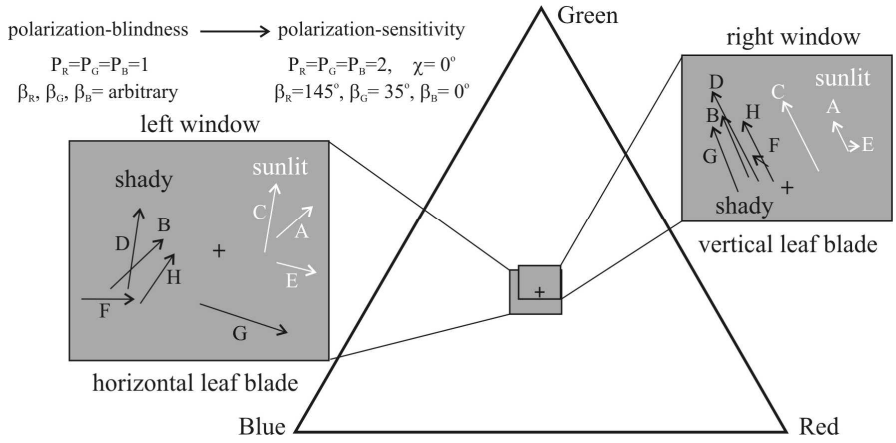

Fig. 22.8. Spectral loci (designated by capitals A-H, representing the situations A-H in Fig. 22.7) of the leaf areas marked with a left and a right small rectangular window in Fig. 22.7 plotted within the equilateral R-G-B colour triangle, the colourless centre of which is represented by +. The arrows start from the spectral locus of real colours perceived by a polarization-blind retina with $P_B = P_G = P_R = 1$ and β_R, β_G, β_B = arbitrary, while the arrowheads point to the spectral locus of false colours perceived by a polarization-sensitive retina with $P_B = P_G = P_R = 2$, $\chi = 0^o$, $\beta_R = 145^o$, $\beta_G = 35^o$, $\beta_B = 0^o$. (After Fig. 10 of Horváth et al. 2002c, p. 3295).

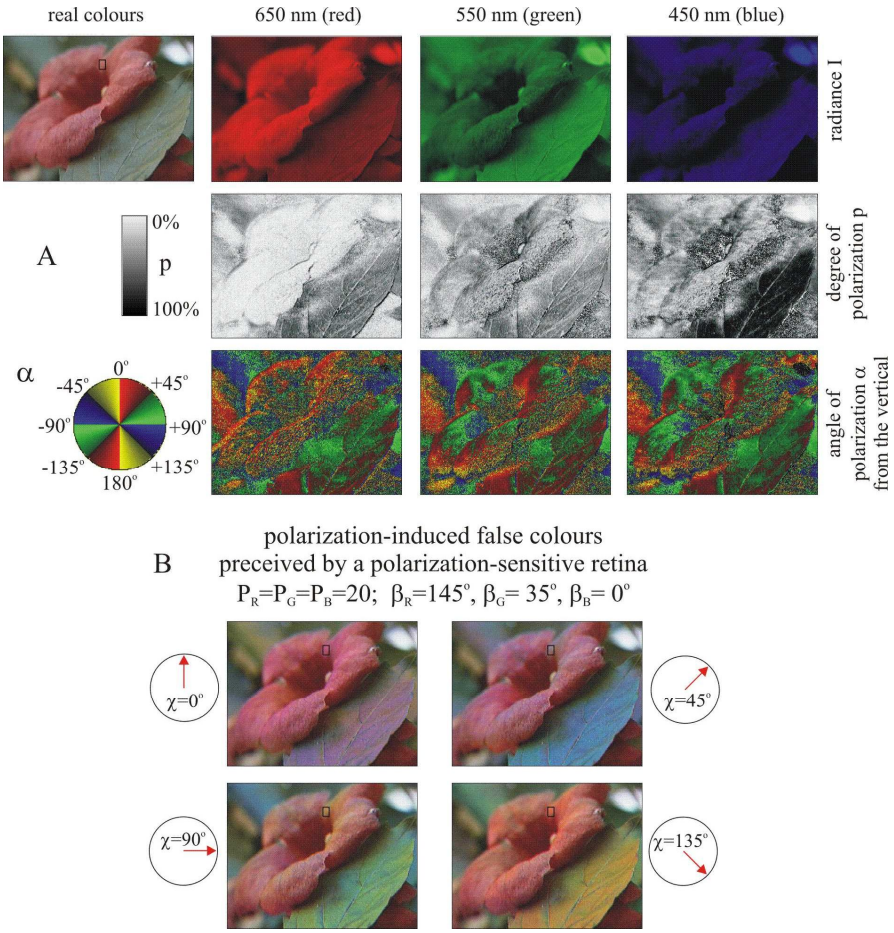

Fig. 22.9. A: Reflection-polarizational characteristics of a reddish flower and a green leaf of *Campsis radicans* measured by video polarimetry in the red, green and blue. B: Brightness and polarization-induced false colours of the same plant perceived by a highly polarization-sensitive retina with $P_R = P_B = P_G = 20$, $\beta_R = 0^o$, $\beta_G = 90^o$, $\beta_B = -45^o$ as a function of the alignment χ of the eye's dorso-ventral meridian with respect to the vertical. In the circular insets the red arrow shows the actual value of χ.

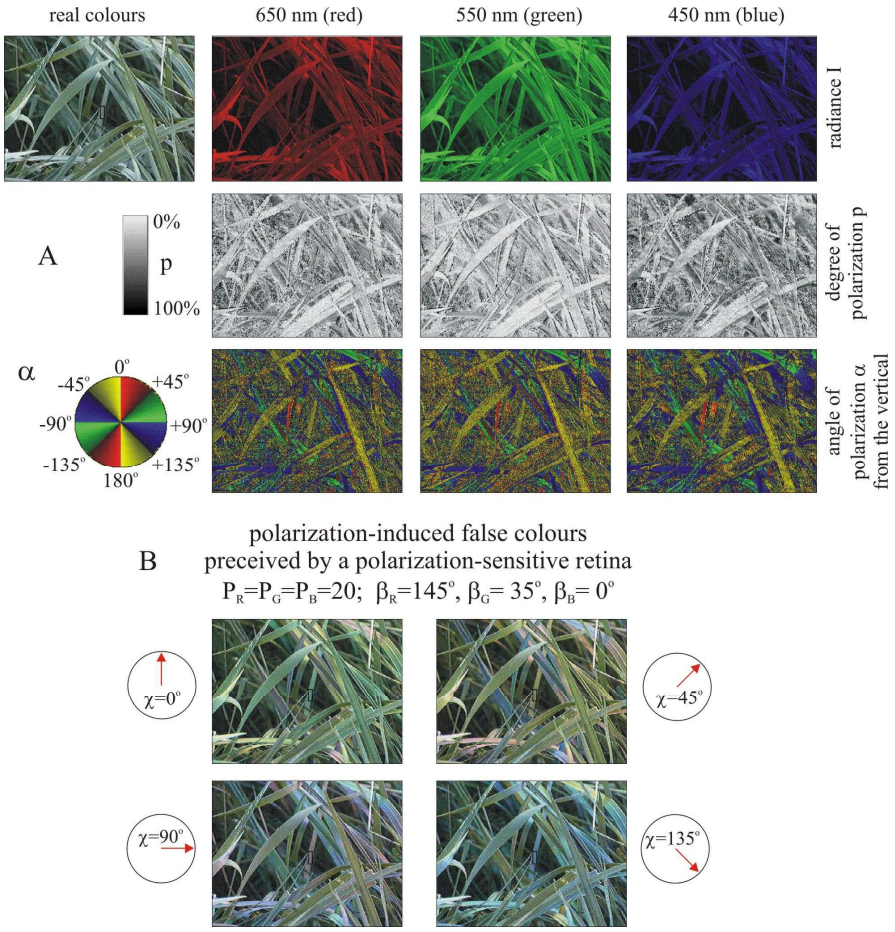

Fig. 22.10. As Fig. 22.9 for shiny green grass leaves in a meadow.

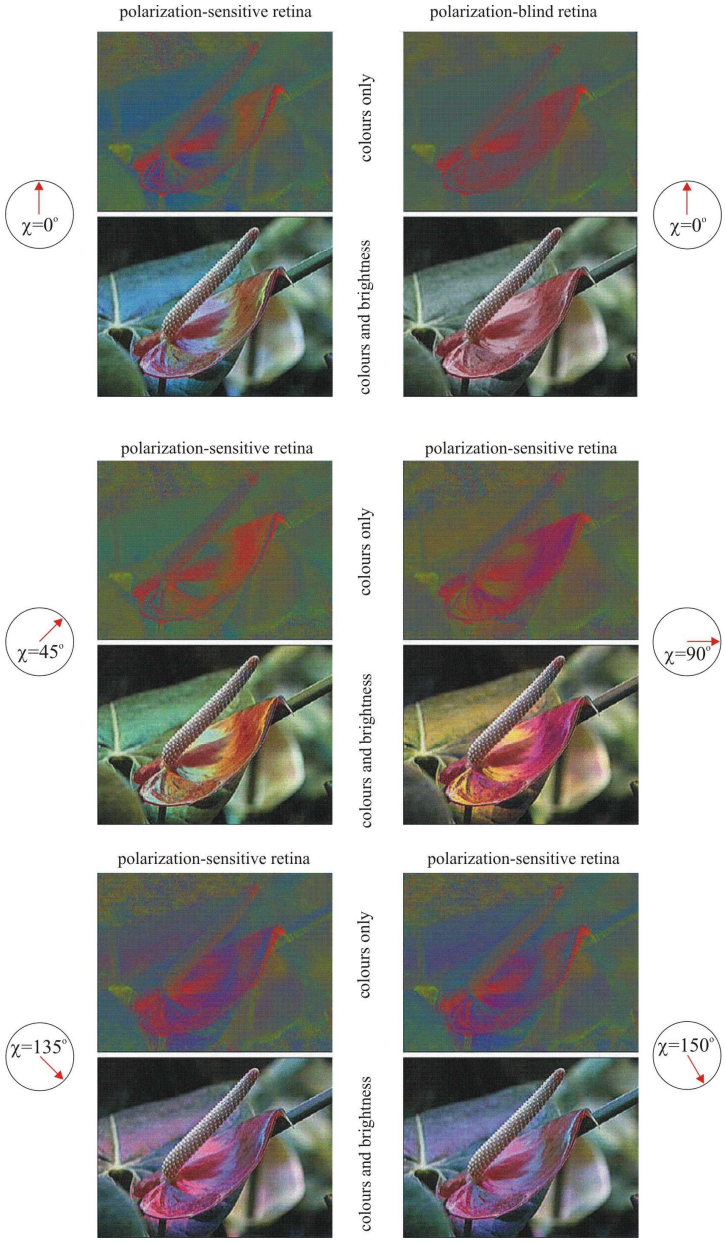

Fig. 22.11. Colours as well as colours and brightness of *Epipremnum aureum* perceived by a polarization-blind ($P_R = P_B = P_G = 1$, β_R, β_G, β_B = arbitrary) and a highly polarization-sensitive ($P_R = P_B = P_G = 20$, $\beta_R = 0^o$, $\beta_G = 90^o$, $\beta_B = -45^o$) retina as a function of the alignment χ of the eye's dorso-ventral meridian with respect to the vertical. In the circular insets the red arrow shows the actual value of χ.

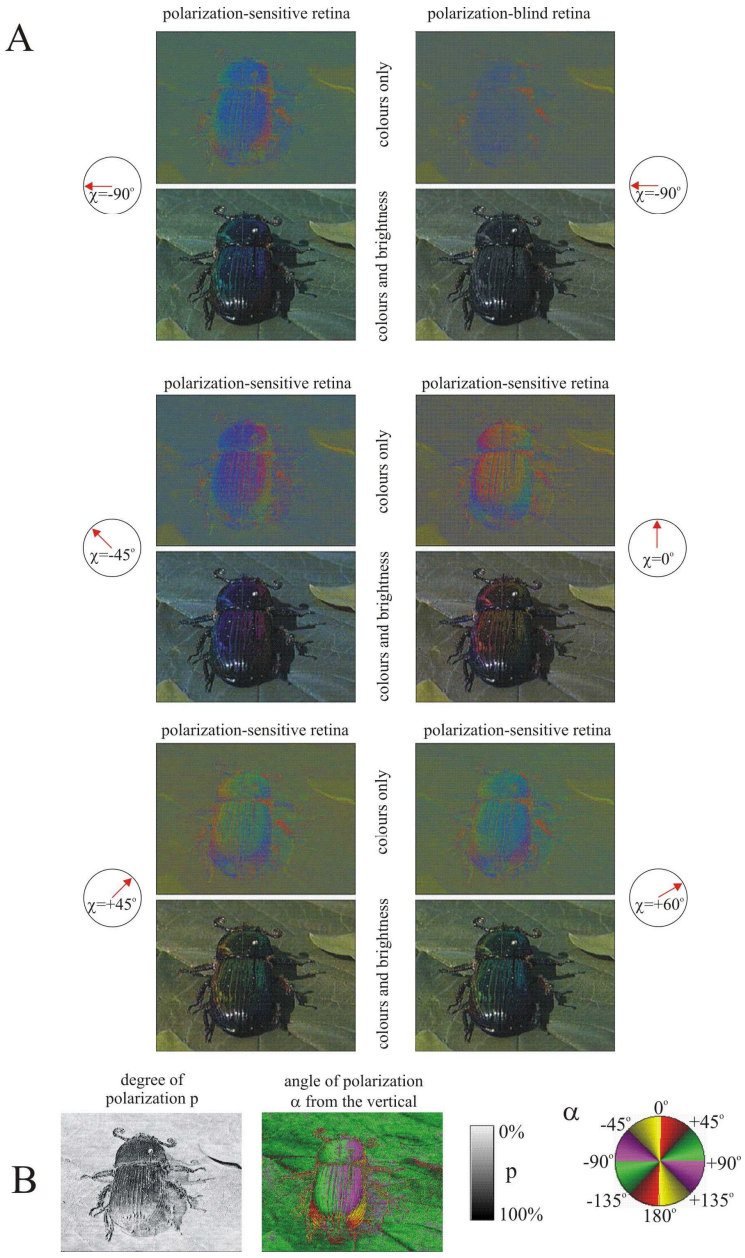

Fig. 22.12. A: As Fig. 22.11 for a beetle with shiny black carapace on a green leaf blade of *Helianthus annuus*. The recording was taken under a clear sky. The scene is illuminated by direct sunlight and the originally colourless (shiny black) carapace of the beetle reflects blue skylight and green light from the surrounding vegetation. B: Patterns of the degree p and angle α of linear polarization of the scene measured by video polarimetry at 550 nm.

23 Why is it Worth Flying at Dusk for Aquatic Insects? Polarotactic Water Detection is most Efficient at Low Solar Elevations

It is a well-documented phenomenon that aquatic insects, especially the small-bodied ones, seek for new habitats during their migration and dispersal generally at dusk (e.g. Popham 1964; Danilevskii 1965; Johnson 1969; Fernando and Galbraith 1973; Zalom et al. 1979, 1980; Saunders 1981; Danthanarayana 1986). From an ecological point of view this is explained conventionally by the reduced risk of both predation and dehydration as well as by the period of calm and optimal air temperature at twilight (e.g. Landin 1968; Landin and Stark 1973). At sunset the intensity of ambient light decreases rapidly with time rendering more difficult the visual detection of flying preys by birds (e.g. King and Wrubleski 1998). Furthermore, at nightfall the lower temperature, higher humidity and calmness of air relative to those in daytime are optimal for small-bodied aquatic insects (Landin and Stark 1973), which can be drifted away by wind and can easily become dehydrated during flight if they cannot find a water body within about one hour.

Bernáth et al. (2003) showed that a further visual ecological factor could also play an important role in the preference of twilight period for habitat finding by polarotactic water insects detecting water by means of the horizontally polarized light reflected from the water surface (Schwind 1991, 1995). They presented experimental and computational evidence for the phenomenon that polarotactic water detection is most efficient at low solar elevations. To prove this, the reflection-polarizational characteristics of the full surface of water bodies of different optical types should be measured and compared as a function of the solar elevation. Although imaging polarimetric measurements of these characteristics have been performed previously (e.g. Horváth and Zeil 1996; Horváth and Varjú 1997; Horváth et al. 1997, 1998a; Kriska et al. 1998; Bernáth et al. 2002), they were restricted to relatively small (maximum about $40^o \times 50^o$) fields of view. The method of 180^o field-of-view imaging polarimetry developed by Gál et al. (2001b,c) and Horváth et al. (2002a) made it possible to measure the reflection-polarization patterns of the whole water surface in a hemispherical field of view, the half aperture of which ranges from the nadir to the horizon.

Since the down-facing polarimeter must be suspended somehow above the water surface which must not undulate during recording, it is enormously difficult to perform such comparative measurements above real water surfaces versus time. The requirement of cloudless sky and completely windless weather ensuring flat

water surfaces without ripples throughout the day makes comparative polarimetric measurements almost impossible. Thus, Bernáth et al. (2003) decided to use water-imitating artificial surfaces, called "water-dummies". These dummies were composed of a horizontal glass pane underlain by either a black or a grey substratum in order to eliminate the inevitable rippling of natural water surfaces. Such reflecting surfaces with manipulated reflection-polarizational and spectral characteristics were successfully applied by Schwind (1991, 1995) to study the polarotaxis of water insects. Bernáth et al. (2003) compared the reflection-polarization patterns of both water-dummies measured in the red (650 nm), green (550 nm) and blue (450 nm) spectral ranges under clear skies from sunrise to sunset as a function of the solar elevation.

Bernáth et al. (2003) calculated the percentage Q of the lower hemispherical visual field, in which the two water-dummies are considered as water by a hypothetical polarotactic water insect versus the solar elevation θ_S. The reflection-polarization patterns and the derived Q-values were also calculated as a function of θ_S for a perfectly black horizontal reflector absorbing all penetrating light for both indices of refraction n_w=1.33 and n_g=1.5 of water and glass, respectively. Bernáth et al. (2003) showed that the difference between the Q-values calculated for water and glass are smaller than 4%, which is practically negligible. Thus the conclusions drawn from the data obtained for the glass water-dummies also hold for flat water surfaces.

23.1. Measurement and Computation of the Reflection-Polarizational Characteristics of the Water Dummies

One of the two water-dummies of Bernáth et al. (2003) was composed of a horizontal glass pane (1m × 1m) underlain by a ply-wood covered with a matt black cloth. This imitated dark water bodies with transparent water and black bottom, or deep waters, from the subsurface layers of which only small amount of light is returned. The other water-dummy was a horizontal glass pane (1m × 1m) underlain with a ply-wood covered by a matt light grey cloth. It mimicked bright waters with transparent shallow water and bright bottom, or waters with bright suspended particles, from which considerable amount of light is returned in comparison with the amount of surface-reflected light. The relative reflectivity of the black and grey cloths (Fig. 23.1A) and the water dummies (Fig. 23.1B) versus the wavelength was measured with a Jobin Yvon-Spex Fluoromax-2 spectrofluorimeter. The water-dummies were laid horizontally on levelled metal holders 30 cm above the ground (Fig. 23.2A) on a hill top in order to minimise the disturbing mirroring of landmarks near the horizon. The horizontality of the dummies was checked by water levels.

Bernáth et al. (2003) used the 180° field-of-view imaging polarimeter described by Gál et al. (2001b,c). The polarimeter with down-facing fisheye lens was suspended on a holder above the centre of the water-dummy in such a way, that the vertical optical axis of the lens pointed towards the nadir (Fig. 23.2A). In order

to minimise the disturbance of the shadow of the holder on the dummy surface, different holder orientations relative to magnetic north were chosen as shown in Figs. 23.2B and 23.2C. The distance between the outermost surface of the fisheye lens and the glass surface was as small as possible (7 cm) in order to measure the reflection-polarizational characteristics of the water-dummies in a conical field of view as wide as possible (about 160^o). The fisheye lens was focused into infinity to record the mirror image of the sky reflected from the glass surface. For a complete measurement three photographs were taken through the polarizers with three different transmission axes. This needed about 10 seconds, during which the operator triggered the expositions by a remote cord and turned the filter wheel of the polarimeter three-times. During measurements the operator lay on the ground below the level of the glass pane to avoid unwanted reflections (Fig. 23.2A). After the measurement of the reflection-polarization pattern of a water-dummy, the dummy was replaced by the other one within about 1 minute and the procedure was repeated. This allowed to measure the reflection-polarization patterns of both dummies within about a few minutes, that is, practically under the same illumination conditions and at the same solar elevation θ_S.

Measurements were carried out near the time of the summer solstice under sunny, partly cloudy skies on 17 July 2002 and on 18 July 2002 under sunny, cloudless clear skies near Kunfehértó in Hungary (46°23'N, 19°24'E) from sunrise (4:49, local summer time = UTC+2) to sunset (20:37) at different θ_S shown in Figs. 23.2B and 23.2C, respectively. The maximum of θ_S was 67° at noon (12:56). Because of disturbing early morning dewfall, reflection-polarization patterns at low solar elevations are presented here only for the sunset and dusk period.

Although during measurements the direction of the polarimeter holder relative to the fixed dummies below the polarimeter changed and the sun moved along its celestial arc (Figs. 23.2B and 23.2C), for the sake of a better visualization in Figs. 23.3-23.5 we present all circular pictures rotated in such a way, that the actual solar meridian points always vertically upward, since these patterns are symmetrical to the solar-antisolar meridian under clear skies.

The mirror image of the polarimeter, its holder and the remote cord as well as their shadows (Fig. 23.2A) moved counter-clockwise with respect to the solar meridian versus time (Figs. 23.3 and 23.4). Since the major aim was to compare the reflection-polarization patterns of the two water-dummies and the numerical values of a derived quantity Q, from comparative analysis the regions (chequered in Figs. 23.3 and 23.4) were excluded, in which landscape near the horizon, or unwanted overexposure, or disturbing shadows and mirror images of the polarimeter, its holder and remote cord occurred in the individual pictures taken at a given θ_S. Thus for both dummies at a particular θ_S a mask was obtained, the area of which was inappropriate for comparative analysis: directions of view within the time-dependent mask were not taken into account. Hence, in comparative analysis only those viewing directions were considered, where the mirror image of the sky and the polarizational characteristics of reflected skylight could be registered without any disturbance.

The reflection-polarization patterns of a perfectly black water-dummy, absorbing the penetrating component of incident light, shown in Fig. 23.5 were calculated with the mathematical method developed by Schwind and Horváth (1993), Horváth (1995a) and Gál et al. (2001b) for incident single-scattered Rayleigh skylight.

23.2. Calculation of the Area of the Water Dummies in which they are Considered as Water by a Hypothetical Polarotactic Insect

Schwind (1985b) showed that backswimmers (*Notonecta glauca*) avoid a light source emitting vertically polarized light. The same was demonstrated in dragonflies (Horváth et al. 1998a; Wildermuth 1998), mayflies and many other water-loving insects (Schwind 1991, 1995; Kriska et al. 1998; Bernáth et al. 2001b). Thus, it is logical to assume, that polarotactic water insects consider any surface as water, if the degree of linear polarization p of reflected light is higher than the threshold p_{tr} of polarization sensitivity and the deviation $\Delta\alpha$ of the angle of polarization of reflected light from the horizontal is smaller than a threshold $\Delta\alpha_{tr}$ in that part of the spectrum in which the polarization of reflected light is perceived. An imaginary polarotactic water insect levitating above the center of the water-dummies was assumed to take those areas of the dummies for water from which skylight is reflected with the following two characteristics: $p > p_{tr}$ and $|\alpha–90^{o}| < \Delta\alpha_{tr}$. The "percentage Q detected as water" was introduced, which is the angular proportion Q of the viewing directions for which both criteria are satisfied relative to the angular extension of 2π steradians of the whole lower hemisphere of the field of view of the insect. In other words, Q gives the relative proportion of the entire ventral field of view in which the water-dummies are considered polarotactically as water. The percentages Q detected as water calculated for the grey water-dummy were compared with those of the black dummy in the blue (450 nm), green (550 nm) and red (650 nm) parts of the spectrum.

23.3. The Reflection-Polarization Patterns of the Water Dummies

Column 1 in Figs. 23.3 and 23.4 shows the colour photographs (without polarizers) of the mirror image of the clear sky reflected from the grey and black water-dummies, respectively, as a function of the solar elevation θ_S. We can see the unavoidable disturbing mirror images of the fisheye lens of the polarimeter, its holder and remote cord as well as their inevitable shadows opposite to the mirror image of the sun. Several photographs are overexposed in the vicinity of the mirror sun and in some cases also near the horizon due to the great amount of light

reflected from the glass surface. In some cases also a bright spot occurs opposite to the mirror sun due to the internal reflection of sunlight from the refractive surfaces of the fisheye optics composed of several individual lenses. Although the water-dummies fill the major part of the field of view of the polarimeter due to its small distance from the glass surface, at the periphery of the pictures the landscape is seen near the horizon. All areas of the pictures with these unwanted disturbances (chequered in Figs. 23.3 and 23.4) were recognized during the computer evaluation and they were considered as regions inappropriate for comparative analysis. Since these colour photographs were taken with different times of exposure, they do not display correctly the relative intensity of reflected light. They serve only for demonstration of the mirror images of the clear skies, under which the reflection-polarization patterns of the water-dummies were recorded. Nevertheless, it is clear from these photographs, that the amount of light reflected from the glass surface dominates relative to the cloth-reflected amount of light in the case of the black water-dummy (Fig. 23.4), while at the grey dummy (Fig. 23.3) the latter component also contributes significantly to the net amount of returned light.

Column 2 in Figs. 23.3 and 23.4 shows the patterns of the degree of linear polarization p of skylight reflected from the grey and black water-dummies in the blue (450 nm) versus θ_S. Comparing the p-patterns of the two dummies, we see that the grey water-dummy is less polarizing than the black one. The light reflected from the grey dummy is almost unpolarized in many directions of view, and its maximum p is only about 30%. At the Brewster angle (56° from the nadir for glass) very low p-values occur in many azimuth angles. On the other hand, the black water-dummy is an effective polarizer reflecting highly polarized skylight from many directions of view. At the Brewster angle a continuous annular zone occurs with maximum p. Depending on θ_S, two neutral points with unpolarized reflected skylight appear within the Brewster zone perpendicularly to the solar meridian.

Column 3 in Figs. 23.3 and 23.4 shows the patterns of the angle of polarization α of skylight reflected from the water-dummies in the blue (450 nm) as a function of θ_S. There are again considerable differences in the α-patterns between the two water-dummies. At the grey dummy as θ_S increases the proportion of the nearly vertically polarized reflected skylight with $-45^o < \alpha < +45^o$ shaded by red and yellow becomes dominant over the nearly horizontally polarized reflected skylight with $45^o < \alpha < 135^o$ shaded by green and blue, especially perpendicularly to the solar meridian. However, from regions of the grey water-dummy toward the mirror sun always approximately horizontally polarized light is reflected. At near-zero solar elevations this is the case also for regions toward the mirror antisun. From the Brewster zone of the grey dummy always nearly vertically polarized light is reflected perpendicularly to the solar meridian. From the black water-dummy always predominatly nearly horizontally polarized skylight is reflected irrespectively of θ_S. However, approximately vertically polarized skylight is reflected from 8-shaped regions with long axes perpendicular to the solar-antisolar meridian within the Brewster zone as well as from crescent-shaped areas near the

horizon perpendicularly to the solar meridian. From the Brewster zone of the black dummy always horizontally polarized skylight is reflected. Note that the mirror images of the polarimeter, its holder and remote cord disturb the α-patterns only slightly. Therefore in these regions we omitted the chequered pattern in the α-maps of Figs. 23.3 and 23.4. These regions were, however, not taken into account in comparative analysis.

23.4. Areas of the Dummies Detected as Water

In column 4 of Figs. 23.3 and 23.4, the regions of the water-dummies are shaded by black, where $p > p_{tr} = 5\%$ and $|\alpha - 90^o| < \Delta\alpha_{tr} = 5^o$, assuming that the imaginary polarotactic insect detects the water in the blue (450 nm). Analysing these patterns, we can see that at $\theta_S \approx 0^o$ the grey water-dummy is taken for water only in areas towards the mirror sun and mirror antisun and partly in the Brewster zone. As θ_S increases, the area detected as water gradually decreases and the grey dummy is considered as water only in small spots around the mirror sun and opposite to it. At higher θ_S the grey dummy is not taken as water in the Brewster zone. On the other hand, the black water-dummy is always considered as water at and near the Brewster angle. Farther away from the Brewster angle the black dummy is not taken for water perpendicularly to the solar meridian. Since in the green (550 nm) and red (650 nm) quite similar patterns were obtained as those in Figs. 23.3 and 23.4, we omit to present them.

Figure 23.5 shows the p- and α-patterns and the areas detected as water of a perfectly black glass (index of refraction $n_g = 1.5$) reflector absorbing all penetrating light computed for the same θ_S as in Figs. 23.3 and 23.4 and for incident single-scattered Rayleigh skylight. We can see that the patterns in Fig. 23.5 are very similar to those in Fig. 23.4, hence the reflection-polarizational characteristics of the black water dummy approximate those of a perfectly black glass reflector. The same patterns were also computed for a perfectly black water reflector with an index of refraction $n_w = 1.33$, and practically the same results were obtained. Hence the slightly higher index of refraction of glass makes the reflection-polarizational characteristics of glass surfaces only a little different from those of water: p of light reflected from the glass is slightly higher and the Brewster angle $\theta_B = 56°$ of glass is slightly larger than that of the water ($\theta_B = 53°$), for example. Thus the conclusions drawn from the data obtained for the glass water-dummies also hold for flat water surfaces.

Since in the literature there are no reliable data about the thresholds p_{tr} and $\Delta\alpha_{tr}$ of polarization sensitivity in any water insect, one has to set their numerical values arbitrarily. To study how the percentage Q detected as water depends on these thresholds, Q was calculated as functions of them for both water-dummies. The results are shown in Fig. 23.6 in the intervals $0\% < p_{tr} < 10\%$ and $0^o < |\Delta\alpha_{tr}| < 10^o$ for the blue (450 nm) spectral range. Since the $Q(d_{tr})$ and $Q(\Delta\alpha_{tr})$ curves continued similarly outside these intervals and very similar curves were obtained

for both the green (550 nm) and red (650 nm) spectral ranges, we omit to display these curves outside these intervals and in other parts of the spectrum. It is clear from Fig. 23.6 that increasing the threshold p_{tr}, Q decreases monotonously, and the increase of threshold $\Delta\alpha_{tr}$ results in the monotonous increase of Q. Since there are no sudden changes, or local extrema, or breaking points, or plateaus, for instance, in the $Q(p_{tr})$ and $Q(\Delta\alpha_{tr})$ curves, one could not establish any criterion for a threshold value which could be preferred. This fact has the important consequence, that the values of these two thresholds can indeed be chosen arbitrarily, and the actual choice concerns neither the relative values of Q calculated for different θ_S nor the conclusions drawn from them. Selecting other values of p_{tr} and $\Delta\alpha_{tr}$ would change only the absolute Q-values but not the qualitative shape of the $Q(p_{tr})$ and $Q(\Delta\alpha_{tr})$ curves versus θ_S. Thus the arbitrary use of $p_{tr} = 5\%$ and $|\Delta\alpha_{tr}| = 5°$ is not a serious restriction.

The left column in Figs. 23.7 and 23.8 shows the percentage Q detected as water calculated for the grey and black water-dummies under a clear and a partly cloudy sky as well as for the perfectly black glass ($n_g = 1.5$) and water ($n_w = 1.33$) reflectors as a function of θ_S in the blue (450 nm), green (550 nm) and red (650 nm). The $Q(\theta_S)$ curves of the perfectly black reflectors are approximately the same in all three spectral ranges, since the slight wavelength-dependency of the refractive indices of glass and water can be neglected in the visible part of the spectrum. The $Q(\theta_S)$ curves of the perfectly black reflectors were calculated for the full surface of the reflectors (dashed curves) as well as for the masked surface, that is, for regions appropriate for comparative analysis (individual data points displayed with triangles). The right column in Figs. 23.7 and 23.8 shows the difference ΔQ between the grey and black water-dummies as well as between the perfectly black glass and water reflectors. In Figs. 23.7 and 23.8 the following are seen:

- The differences ΔQ between the perfectly black glass and water reflectors are smaller than a few percents, the maximum difference is $\Delta Q_{max} = 4\%$ for $\theta_S \approx 0^o$ and $\Delta Q = 2\%$ for higher θ_S. This also shows that the conclusions drawn from the data obtained with the glass water-dummies can be extended also to flat water surfaces.
- The differences ΔQ between the full and masked surfaces of the perfectly black reflectors are smaller than 5%. From this one can conclude that the use of the masks (e.g. chequered in Figs. 23.3 and 23.4) in comparative analysis does not change significantly the Q-values calculated for different θ_S and for the two water-dummies. In other words, disregarding from the regions being inappropriate for comparative analysis does not concern the conclusions drawn from the remaining parts of the measured reflection-polarization patterns of the water-dummies.
- At $\theta_S \approx 0^o$ the percentage Q detected as water is maximal for the grey water-dummy and has a local maximum for the black dummy in all three spectral ranges. Thus in the visible part of the spectrum, polarotactic detection of brighter water bodies is most efficient when the sun is approximately at the

horizon. The $Q(\theta_S)$ curve of the black water-dummy has a local minimum at $\theta_S \approx 30^o$ in all three spectral ranges. For higher solar elevations $Q(\theta_S)$ of the black dummy is as high as or even higher than that at $\theta_S \approx 0^o$. Thus in the visible part of the spectrum, polarotactic detection of dark water bodies is most efficient when the sun is either approximately at the horizon or near the zenith.

- The difference ΔQ between the grey and black water-dummies is minimal at low solar elevations in all three parts of the spectrum.

For both water-dummies, more than 85% of the region appropriate for comparative analysis satisfies the degree of polarization criterion $p > p_{tr} = 5\%$. Q of the grey water-dummy is significantly smaller than that of the black dummy. However, according to the angle of polarization criterion $|\alpha–90^o| < \Delta\alpha_{tr} = 5^o$ alone, maximum 40% of the region appropriate for comparative analysis is detected as water for both water-dummies, and Q of the grey dummy is significantly smaller again than that of the black dummy. Since in any direction of view the α-criterion is always satisfied if the p-criterion is satisfied, polarotatic water detection is limited by the α-criterion in the case of the used thresholds $p_{tr} = 5\%$ and $\Delta\alpha_{tr} = 5^o$.

23.5. Discussion

The reflection-polarizational characteristics of water surfaces depend on the illumination conditions, material composition of the bottom, dissolved organic materials, angle of view measured from the nadir and the direction of observation relative to the sun. Aquatic insects can identify their water habitat by perceiving the partial linear polarization of light reflected from the water surface if the degree of linear polarization is high enough and the direction of polarization approximates the horizontal. These two criteria are satisfied predominantly in the Brewster zone, which is continuous throughout the day at dark water bodies, but for bright waters this is true only towards the sun and antisun and in the time of sunrise and sunset. During the day the percentage Q detected as water is such low at bright water bodies, that they can be easily overlooked by water insects. In the case of bright water surfaces the shape and direction of the regions suitable for polarotactic water detection change considerably with the changing solar elevation (column 4 in Figs. 23.3 and 23.4). Therefore bright aquatic habitats can be recognised polarotactically only from certain directions of view with respect to the sun.

If the polarization of light reflected from water is analyzed in the whole lower hemisphere of the visual field of a flying and water-seeking imaginary polarotactic insect, the percentage Q detected as water is proportional to the chance a water body is recognized as water in the optical environment. Then in the visible part of the spectrum, polarotactic water detection is most efficient in the sunrise and sunset periods, when Q is maximal, the reflection-polarizational characteristics of dark and bright waters are most similar and the risk of escaping the attention of polarotactic water-seeking insects is minimal. This conclusion is valid also for a

visual field of the ventral polarization-sensitive eye region which is much narrower than the whole lower hemisphere, because the areas detected as water are centred at or near the Brewster angle (see column 4 of Figs. 23.3, 23.4 and column 3 of Fig. 23.5).

In field experiments, in which huge white and black shiny plastic sheets were laid onto the ground in summer as water dummies Bernáth et al. (2001a,b) observed that during daytime only large- or medium-bodied (1-5 cm) aquatic insects (e.g. *Dytiscidae, Hydrophilidae, Notonectidae*) were attracted to the black plastic sheet. These beetles can fly for a few hours also daytime at higher temperature and lower humidity of the air due to their larger size with a smaller surface/volume ratio and to their thick sclerotized cuticle, which slows down the dangerous dehydration of the body. Small-bodied water bugs (1-5 mm, e.g. *Sigara* sp.) were lured to the black plastic sheet *en masse* exclusively at and after sunset. These insects possess such a large surface/volume ratio and thin chitinuous cuticle, that they can become easily dehydrated during flight of a few tens minutes. Their flight can also be hindered by wind, which usually abates at sunset when direct solar radiation quickly decreases to zero (Landin and Stark 1973). The sunrise period is less optimal for dispersal of aquatic insects than the sunset period, because at dawn the air temperature is much lower than at dusk (Landin 1968; Landin and Stark 1973). This may be one of the reasons why small-bodied aquatic insects generally migrate *en masse* in the sunset and dusk period.

However, the medium-bodied backswimmer *Notonecta glauca* seems to be an exception from this rule. Apart from *Notonecta glauca*, the angular extension of the ventral eye region, in which the polarization of light reflected from water is analyzed, is unknown in aquatic insects. In *Notonecta* the ventral eye region, in which the microvilli of the UV-sensitive central photoreceptors R7 and R8 are orthogonal, extends up to a nadir angle of about 35^o (Schwind 1983b). This eye region is optimal for the analysis of the horizontal polarization of water-reflected light. According to Schwind (1983b, 1985b), in *Notonecta* the reflection polarization of water surfaces may be analyzed by an approximately 3^o wide narrow annular zone ranging from nadir angles 32^o to 35^o. Figure 23.9 shows the $Q(\theta_S)$ curves of the perfectly black water and glass reflectors in the red, green and blue spectral ranges calculated for the circular region with nadir angle 35^o and for the annular region between nadir angles 32^o and 35^o (see also column 3 in Fig. 23.5). Similar calculations cannot be performed for the measured patterns of the black and grey water-dummies, because around the nadir they are not appropriate for evaluation due to the mirror image and the shadow of the polarimeter (see the central chequered areas in the circular patterns of Figs. 23.3 and 23.4). From Fig. 23.9 we can see that in the case of the regions around the nadir, corresponding with the field of view of the mentioned ventral circular and annular eye regions in *Notonecta*, Q increases with increasing θ_S. Hence, for *Notonecta* the polarotactic detection of dark waters is most efficient for higher solar elevations. This could be the reason why Bernáth et al. (2001b) observed frequently the landing of *Notonecta* on the black plastic sheet during the day rather than at dusk.

Bernáth et al. (2003) used p_{tr} = 5% as the p-threshold of the imaginary polarotactic insect. The threshold of the highly polarization-sensitive

monochromatic photoreceptors in the specialized dorsal rim area of the compound eye in the honeybee *Apis mellifera* is about p_{tr} = 10% and in the field cricket *Gryllus campestris* p_{tr} = 5% (Labhart 1980; Labhart et al. 1984). In insects associated with water the value of this threshold is completely unknown, and it could be species-specific. When Schwind (1995) determined the spectral regions in which some aquatic insect species perceive the polarization of reflected light, he assumed rather arbitrarily a threshold p_{tr} = 35%. However, he has also emphasized that the assumed threshold value did not crucially affect his conclusions.

Under clear skies at a given θ_S the reflection-polarizational characteristics of the water-dummies as well as real water bodies depend on two components of returned light: (1) The first component is the light reflected from the glass/water surface. The direction of polarization (E-vector direction) of this partially polarized component is always horizontal except in small regions within the Brewster zone, and if the angle of reflection is equal to the Brewster angle, it is totally polarized (p = 100%). (2) The second component is the light originating from below the surface due to reflection from the underlying substratum or from the bottom of water, or to backscattering from particles suspended in water. This component is always vertically polarized due to refraction at the surface (Horváth and Pomozi 1997). The net degree and direction of polarization of the returned light are determined by the polarizational features and relative intensities of these two components. Since these two components have orthogonal directions of polarization, their superposition reduces the net p. If the intensity of the first component is greater than that of the second one, the returned light is partially linearly polarized with horizontal E-vector. When the second component is the more intense, the returned light is partially vertically polarized. Finally, if the intensities of these two components are approximately equal, the returned light is nearly unpolarized.

In the case of a perfectly black reflector only the surface-reflected first component exists. The resulting reflection-polarization patterns under clear skies versus θ_S are shown in Fig. 23.5, where the following trend is seen: the lower the θ_S, the smaller is the proportion of the nearly horizontally polarized ($45^o < \alpha < 135^o$) reflected skylight. Since the percentage Q detected as water is determined predominantly by α of reflected skylight, the same trend occurs for the change of Q versus θ_S: the lower the θ_S, the smaller is Q, as seen in the left column of Figs. 23.7 and 23.8. The $Q(\theta_S)$ curve has a flat local maximum at $\theta_S = 5^o$, due to the interference of the θ_S-dependent complex p- and α-patterns in the determination of the value of Q. Q is maximal (about 96%) when the sun is at the zenith. Although then both the incident and reflected skylight are horizontally polarized, regions of the surface within and outside the Brewster zone reflect light with almost zero degrees of polarization, and due to the criterion $p > p_{tr}$ = 5% for successful water detection, Q cannot be as high as 100%.

Although in the case of the black water-dummy also the subsurface-reflected second component exists, the reflection-polarizational characteristics and the shape of the $Q(\theta_S)$ curve are similar to those of the perfectly black reflector, since

the intensity of the second component is small relative to that of the surface-reflected first component. The major difference is that the skylight reflected from the black water-dummy is less polarized (column 2 in Fig. 23.4) than the skylight reflected from the perfectly black reflector (column 1 in Fig. 23.5) due to the depolarising effect of the second component. This lower p is the reason for the lower Q of the black water-dummy relative to that of the perfectly black reflector (left column in Figs. 23.7 and 23.8).

For the grey water-dummy the vertically polarized second component from the subsurface is such intense that it depolarises considerably the horizontally polarized surface-reflected first component (column 2 in Fig. 23.3). At lower θ_S the first component is the more intense towards the mirror sun and mirror antisun resulting in nearly horizontally polarized reflected light, while perpendicularly to the solar-antisolar meridian the second component is the more intense causing nearly vertically polarized reflected light (column 3 in Fig. 23.3). As θ_S increases, the relative intensity of the second component increases, thus the proportion of the nearly horizontally polarized reflected light decreases, resulting in the decrease of the percentage Q detected as water (column 4 in Fig. 23.3). For $\theta_S > 20^o$ the amount of subsurface-reflected light is such enhanced that Q becomes smaller than 10% (left column in Figs. 23.7 and 23.8).

The polarimetric technique of Bernáth et al. (2003) used a fisheye lens including numerous optical elements made of ultraviolet-absorbing glasses. For polarimetric measurements in the ultraviolet (UV) spectral range, a UV-transmitting fisheye lens composed of quartz would be needed, but such an objective is not available in the market. In the UV, the second component of returned light originating from below the water surface is considerably reduced in natural water bodies due to the great absorption by the dissolved organic materials and to the low reflectivity of the bottom (Schwind 1995; Bernáth et al. 2002). Thus in the UV, the majority of natural water bodies has similar reflection-polarizational characteristics and $Q(\theta_S)$ curve as the black water-dummy has in the blue (Figs. 23.4, 23.7 and 23.8). Consequently, although Bernáth et al. (2003) could not measure the reflection-polarization patterns of the water-dummies in the UV, the conclusions hold also for this part of the spectrum.

Comparing Figs. 23.7 and 23.8, we can establish that the $Q(\theta_S)$ curves of the water-dummies possess the same qualitative features under clear and partly cloudy skies. The light emitted by clouds is usually almost unpolarized (Können 1985). If this unpolarized cloudlight is reflected from the horizontal glass surface of the water-dummies, it becomes partially polarized with always horizontal direction of polarization. Thus clouds can enhance the relative proportion of horizontally polarized reflected light in those regions of the reflector, from which nearly vertically polarized light would be reflected if the sky were clear. Since the percentage Q detected as water is predominantly governed by α of reflected light, the final consequence of clouds will be a slight increase of Q; the more extended the cloud cover, the larger is Q. This is clearly seen in Figs. 23.7 and 23.8. Thus, under a cloudy sky polarotactic water detection is slightly more efficient than under a clear sky with the same θ_S. Due to the frequent or durable occlusion of the

sun, under cloudy sky conditions the air temperature is usually lower than under clear sunny skies, which is advantageous for small-bodied flying aquatic insects, though the risk of predation is higher than at dusk. From this one can conclude that beside the sunset, the second most optimal period for polarotactic water seeking are the periods when the daytime sky is partly or totally cloudy.

For $\theta_S > 30^o$ the $Q(\theta_S)$ curve increases with θ_S in the case of the black water-dummy (Figs. 23.7 and 23.8). Therefore, at high θ_S Q of black waters could be as great as that at $\theta_S \approx 0^o$. This means that at high θ_S the polarimetric detection of dark waters can be as efficient or even more efficient than at sunset. However, when θ_S is high (near noon), the air temperature can be much higher, the air humidity much lower and the wind speed much greater than at dusk, which conditions are disadvantageous to small-bodied insects. Consequently, only certain large-bodied water-seeking polarotactic insects could take advantage of the large Q of dark waters at high θ_S. This may be the reason why have been such insects attracted to horizontal black plastic sheets not only at dusk, but also at noon (Bernáth et al. 2001b).

The shadows and mirror images influence only slightly the α-pattern of reflected skylight, especially for the black water-dummy (column 3 in Figs. 23.3 and 23.4). On the other hand, the p-pattern is strongly affected by these disturbances. Similar effect was observed by Pomozi et al. (2001b), who showed that the clear-sky α-pattern continues underneath many clouds. This phenomenon is of great biological importance, because the stability of the α-pattern against optical disturbances explains why the orientation of polarization-sensitive insects is governed predominantly by the α-pattern rather than the p-pattern: many terrestrial insects orient by means of the E-vector pattern of skylight (e.g. Wehner 1976) and water insects find their aquatic habitat by means of the horizontal polarization of reflected light (Schwind 1991).

Finally, the question arises, how the light reflected from the back surface of the glass pane of the water-dummies influenced the measured reflection-polarizational characteristics. Figure 23.10 shows the change of the intensity I of totally horizontally ($\perp$) or vertically ($||$) polarized light reflected from the front (I_1) or back (I_2) surface of a glass pane versus the angle of incident γ. Since $I_1^{\perp} \approx I_2^{\perp}$ for $\gamma < 55^o$ and $I_1^{||} \approx I_2^{||}$ for $\gamma < 75^o$, the back-reflection has practically no influence on the net polarization of reflected light for smaller angles of incidence (it only increases the net intensity by a factor of about 2). On the other hand, $I_1^{\perp} >> I_2^{\perp}$ for $\gamma > 65^o$ and $I_1^{||} >> I_2^{||}$ for $\gamma > 80^o$. Hence the intensity of back-reflection is negligible relative to that of the front reflection for larger angles of incidence, therefore the influence of back-reflection on the net polarization of reflected light is also negligible. Furthermore, Horváth and Pomozi (1997) calculated the polarizing characteristics of different reflectors composed of glass panes underlain by a metal mirror or various grey substrata. Their results also support that the back-reflection from the second glass surface affects only slightly the net polarization of reflected light. The patterns in Fig. 23.4 measured at the black water-dummy with back-reflection from the second glass surface are practically the same as those in Fig. 23.5 calculated for a perfectly black water without back-

reflection from a second surface. Gál et al. (2001a) measured the reflection-polarization patterns of the flat water surface under a clear sky at sunset. Comparing these patterns of a real dark water surface with the measured pattern of the black water-dummy, we can establish that they are practically the same. All these support that the back-reflection from the second surface of the glass affects only slightly the measurement of polarization.

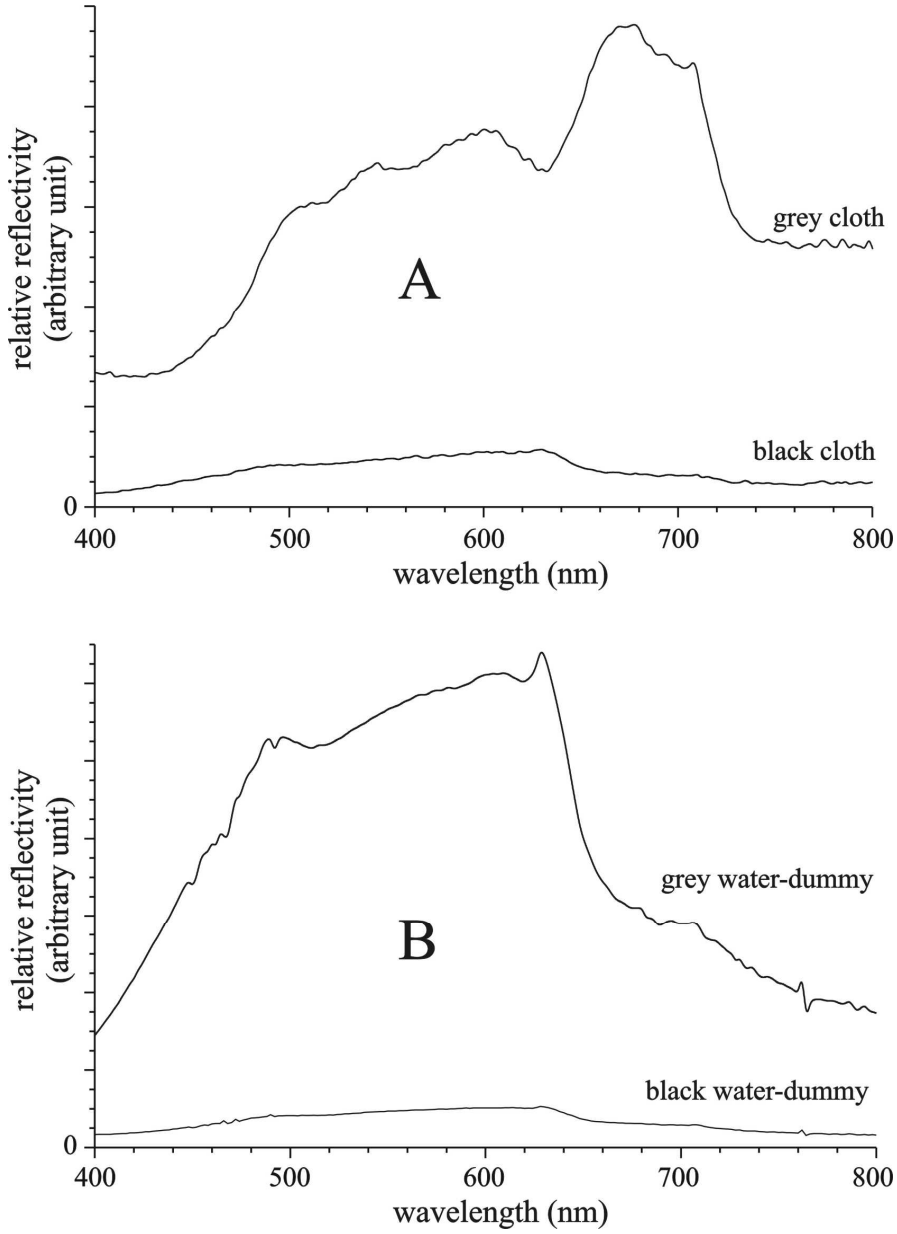

Fig. 23.1. (A) Relative reflectivity of the matt black and grey cloths used as substrata of the glass panes in the water-dummies. (B) Relative reflectivity of the black and grey water-dummies. (After Fig. 1 of Bernáth et al. 2003).

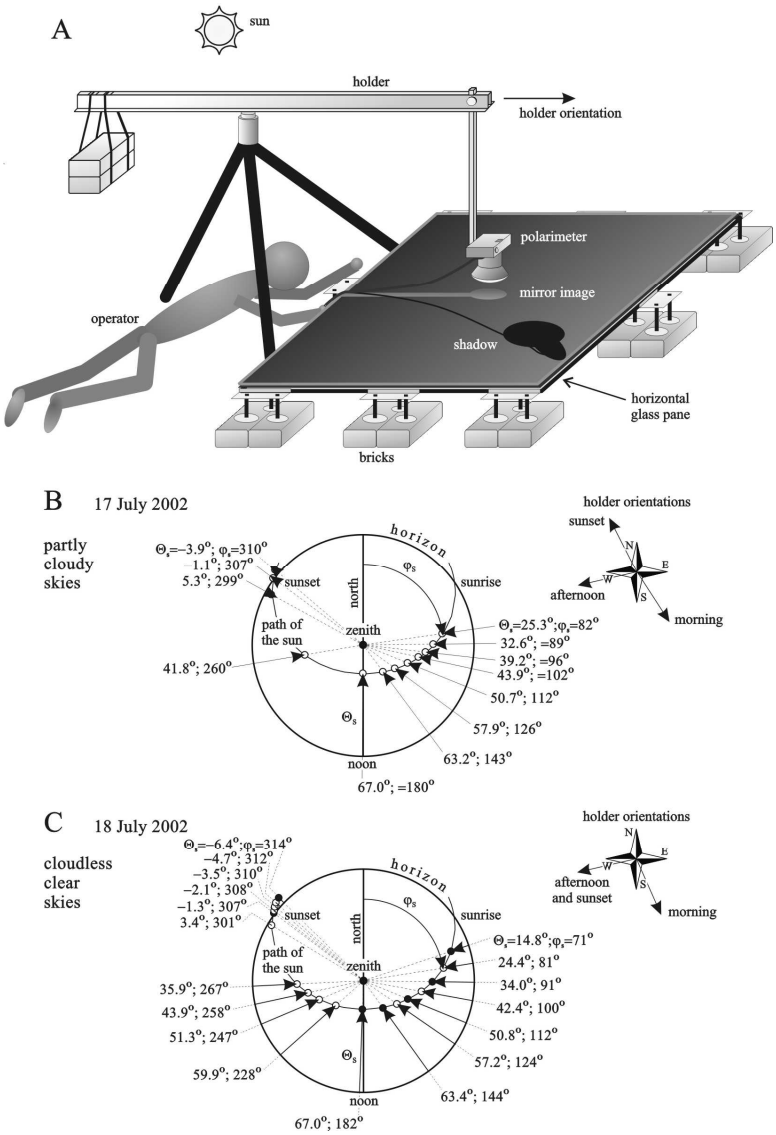

Fig. 23.2. (A) Experimental arrangement of the measurement of the reflection-polarizational characteristics of horizontal water-dummies. (B, C) The apparent celestial path of the sun during the measurements on 17 (partly cloudy skies) and 18 (clear, cloudless skies) July 2002 at the Hungarian Kunfehértó (46°23'N, 19°24'E) in a system of polar coordinates, where the solar azimuth angle φ_S is measured clockwise from the magnetic north, and the solar elevation θ_S is measured radially from the horizon. Dots show the solar positions when the measurements were performed. Black dots represent the solar positions when the patterns in Figs. 23.3 and 23.4 were measured. (After Fig. 2 of Bernáth et al. 2003).

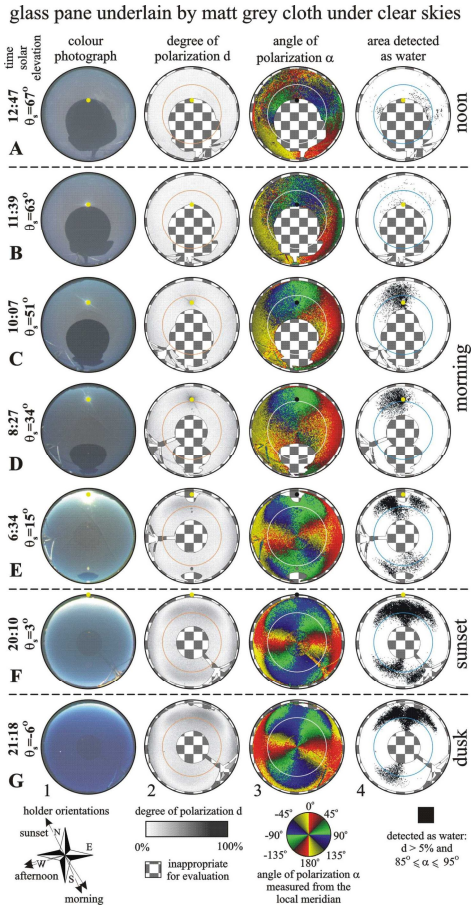

Fig. 23.3. Colour photographs (without polarizers) of the mirror image of the clear sky reflected from the grey water-dummy, patterns of the degree p and angle α (measured from the local meridian) of linear polarization of reflected skylight, and the area detected polarotactically as water as a function of the solar elevation θ_S. The grey water-dummy is composed of a horizontal glass pane underlain by a matt grey cloth, the reflection characteristics of which is shown in Fig. 23.1. The polarization patterns are measured by 180° field-of-view imaging polarimetry in the blue (450 nm). Chequered areas show those regions of the pictures, which are inappropriate for comparative analysis due to unwanted overexposure, shadows and mirror images of the polarimeter, its holder and remote cord. In column 4, regions are shaded by black, where $p > p_{tr} = 5\%$ and $85^\circ \le \alpha \le 95^\circ$. An imaginary polarotactic water insect is assumed to consider a surface as water if these two conditions are satisfied for the partially linearly polarized reflected light. In column 4 the regions where these criteria are not satisfied remained blank. The positions of the mirror image of the sun are shown by dots, the Brewster angle (56° from the nadir for glass with index of refraction $n_g = 1.5$) is represented by an inner circle within the circular patterns. Because of disturbing early morning dewfall, reflection-polarization patterns at low solar elevations are presented here only for the sunset and dusk period. (After Fig. 3 of Bernáth et al. 2003).

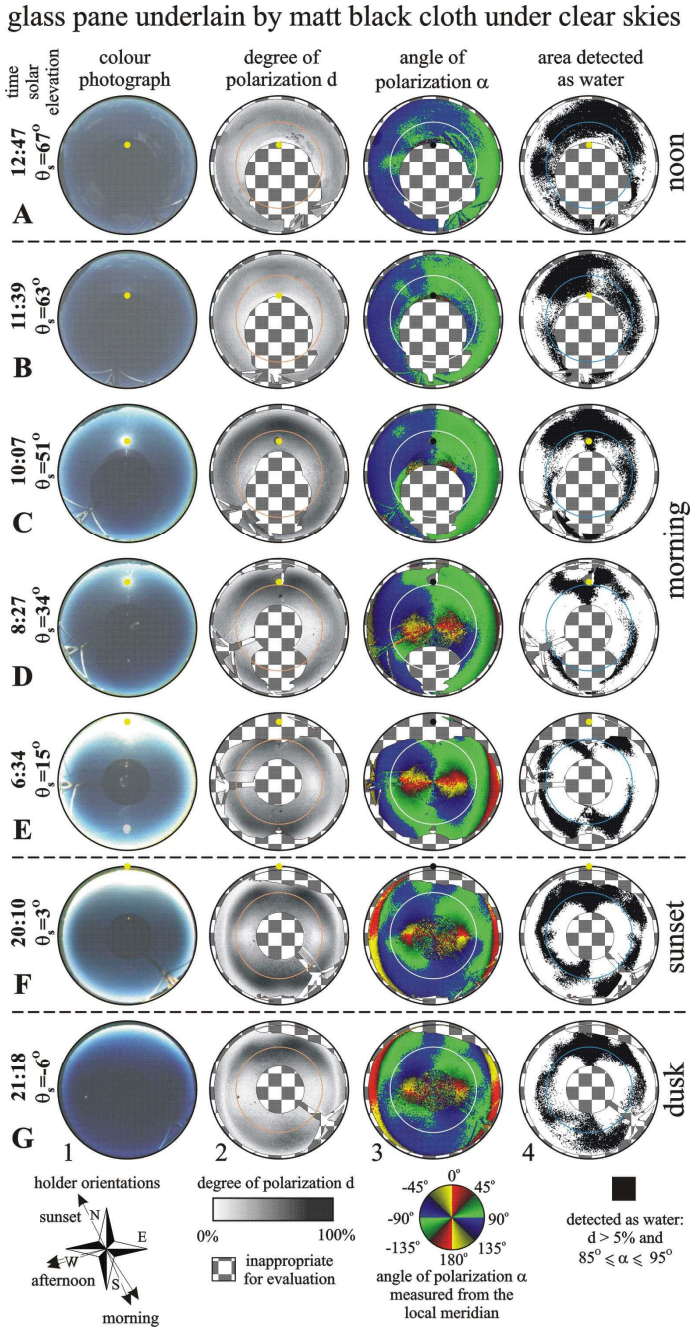

Fig. 23.4. As Fig. 23.3 for the black water-dummy composed of a horizontal glass pane underlain by a matt black cloth. (After Fig. 4 of Bernáth et al. 2003).

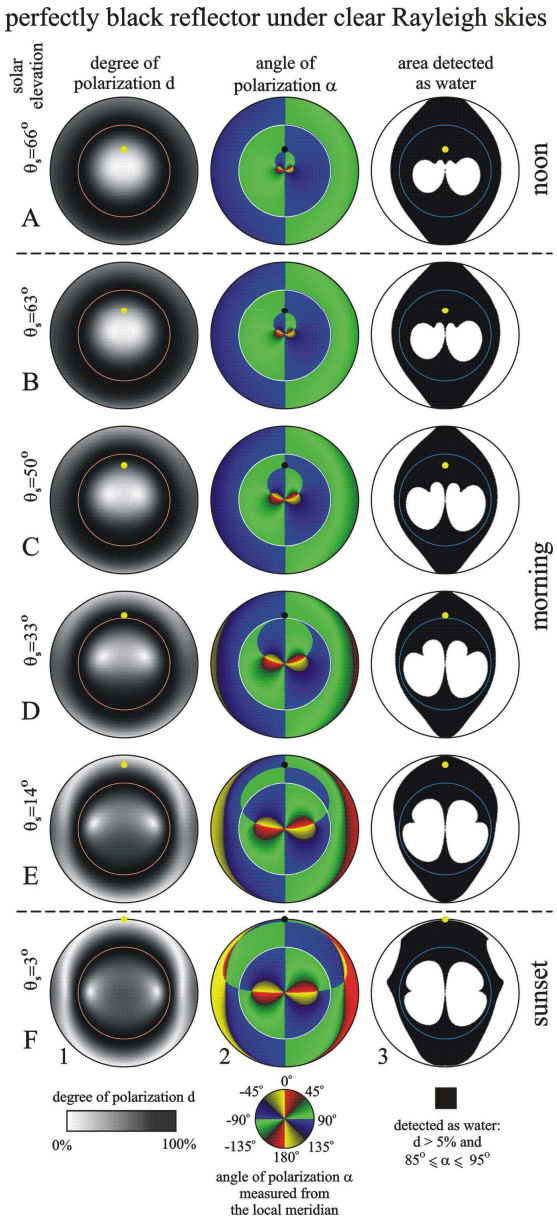

Fig. 23.5. As Fig. 23.3 (without colour photographs) for a perfectly black glass (with an index of refraction n_g = 1.5) reflector absorbing all penetrating light. Here the patterns of the degree p and angle α of linear polarization of reflected skylight are not measured, but they are calculated for incident single-scattered Rayleigh skylight with the use of the Fresnel formulae. The Brewster angle 56° (from the nadir for glass) is represented by a circle within the circular patterns. (After Fig. 5 of Bernáth et al. 2003).

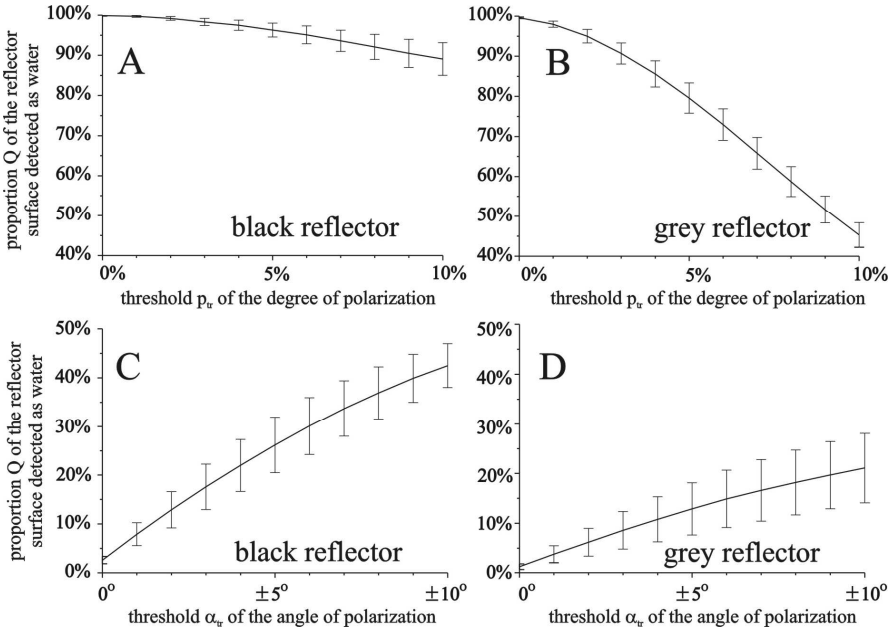

Fig. 23.6. Percentage Q of the whole lower hemispherical field of view (of an imaginary polarotactic water insect) in which the black (A, C) and grey (B, D) water-dummies are detected as water versus p_{tr} and $\Delta\alpha_{tr}$. It is assumed that the insect takes those regions of the dummies for water, from which partially linearly polarized light is reflected with degrees of linear polarization $p > p_{tr}$ or with angles of polarization α for which $|\alpha - 90^{\circ}| < \Delta\alpha_{tr}$, where α is measured from the local meridian. Q was calculated for the p- and α-patterns of the water-dummies measured in the blue (450 nm) and shown in Figs. 23.3 and 23.4. Q gives the proportion of the black areas in column 4 of Figs. 23.3 and 23.4 relative to the entire area of the region appropriate for comparative analysis (non-chequered regions in Figs. 23.3 and 23.4). Vertical bars show the intervals in which Q changed during the day from zero to the maximum (67°) solar elevation at given values of p_{tr} and $\Delta\alpha_{tr}$. The continuous curves are fitted to the centres of these vertical bars by the method of least squares. (After Fig. 6 of Bernáth et al. 2003).

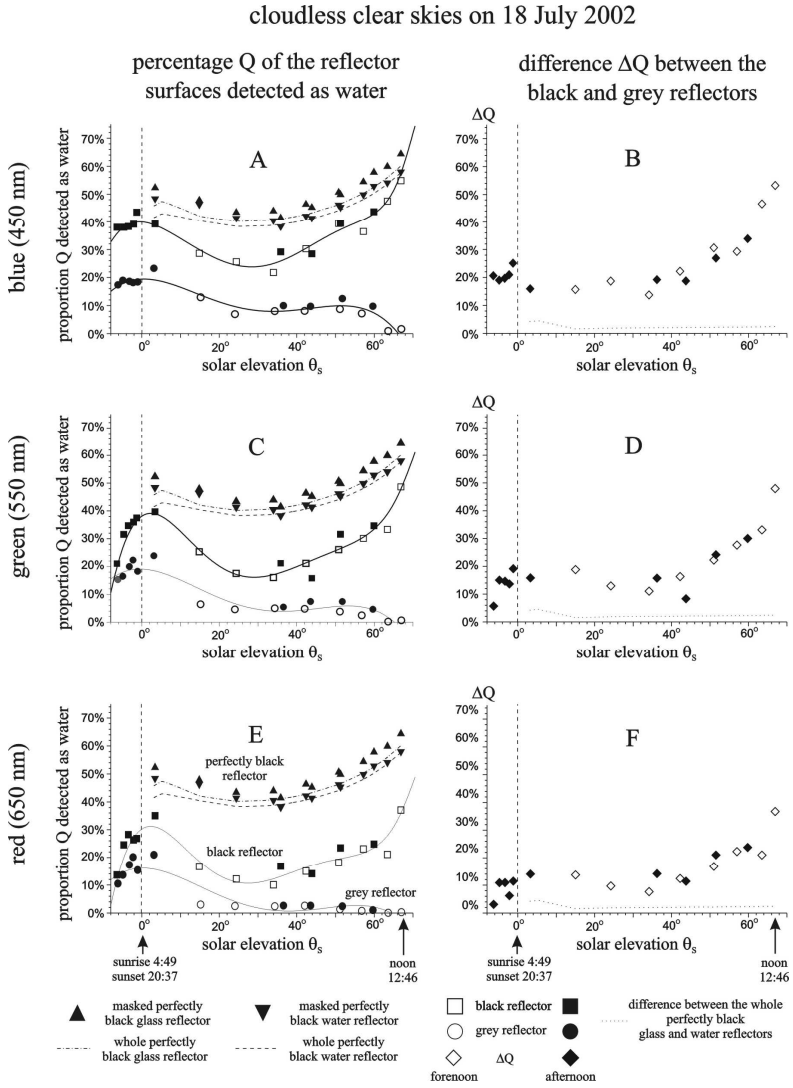

Fig. 23.7. Percentage Q detected as water for the black (squares) and grey (dots) water-dummies (A, C, E) and difference ΔQ between the black and grey water-dummies (rhombi) (B, D, F) as a function of the solar elevation θ_S in the blue (450 nm), green (550 nm) and red (650 nm). Data points measured forenoon and afternoon are symbolized by empty and filled squares/dots, respectively. The continuous curves are fitted to these data points by the method of least squares. The dashed/dashed-dotted $Q(\theta_S)$ curves are computed for the full area of a perfectly black glass (index of refraction $n_g = 1.5$) and water ($n_w = 1.33$) reflector absorbing all penetrating light. Triangles show the Q-values calculated for the perfectly black glass and water reflectors within the masked regions of the field of view appropriate for comparative analysis (non-chequered regions in the p- and α-patterns of Figs. 23.3 and 23.4). (After Fig. 7 of Bernáth et al. 2003).

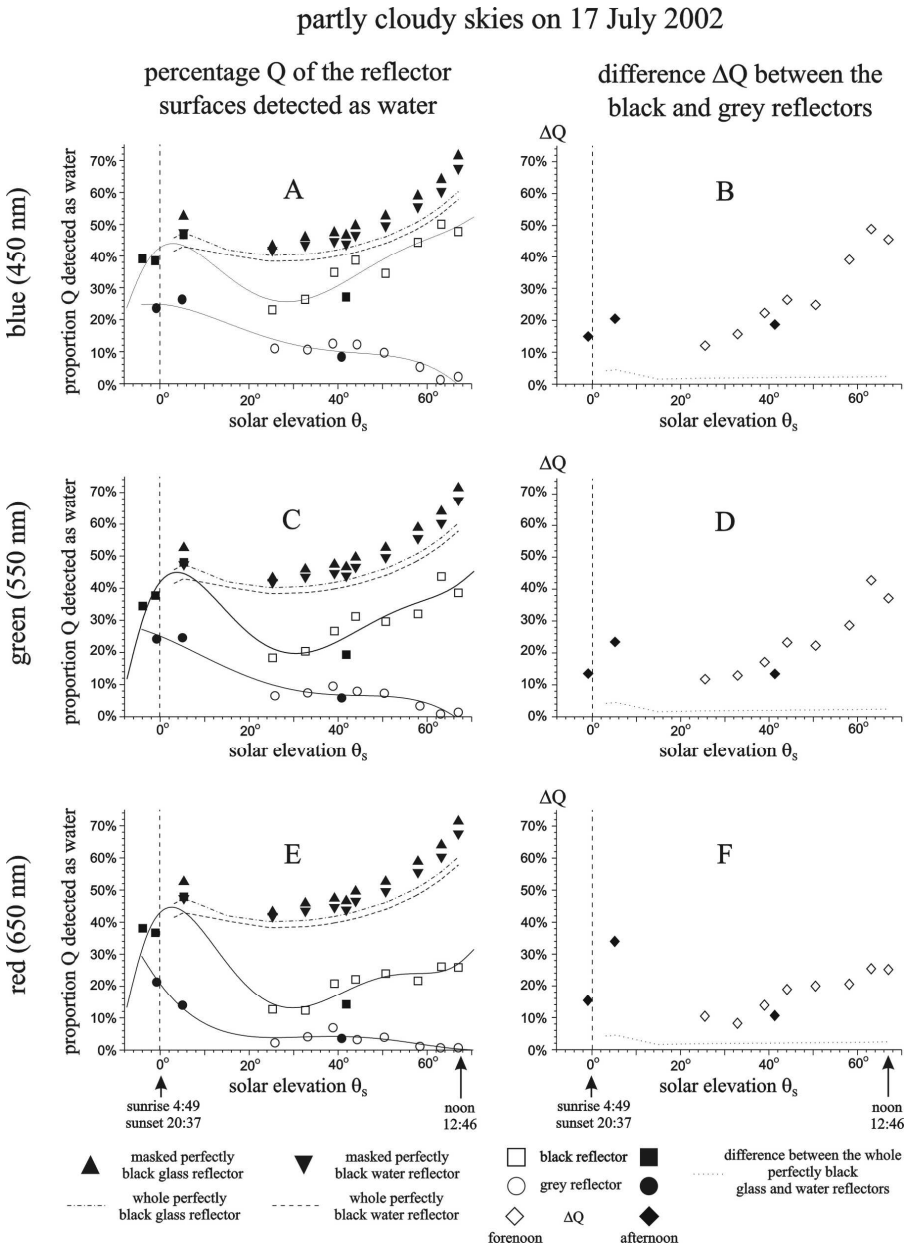

Fig. 23.8. As Fig 23.7 for partly cloudy skies on 18 July 2002. (After Fig. 8 of Bernáth et al. 2003).

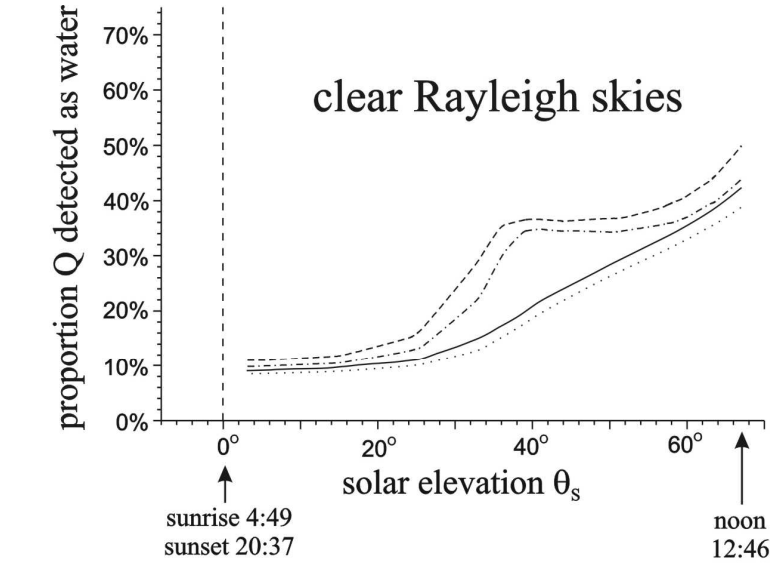

Fig. 23.9. As the left column in Fig. 23.7 calculated for the circular field of view within the nadir angle 35° and for the annular field of view between nadir angles 32° and 35° (representing the field of view of the polarization-sensitive ventral eye region of the backswimmer *Notonecta glauca*) of the patterns in column 3 of Fig. 23.5. (After Fig. 9 of Bernáth et al. 2003).

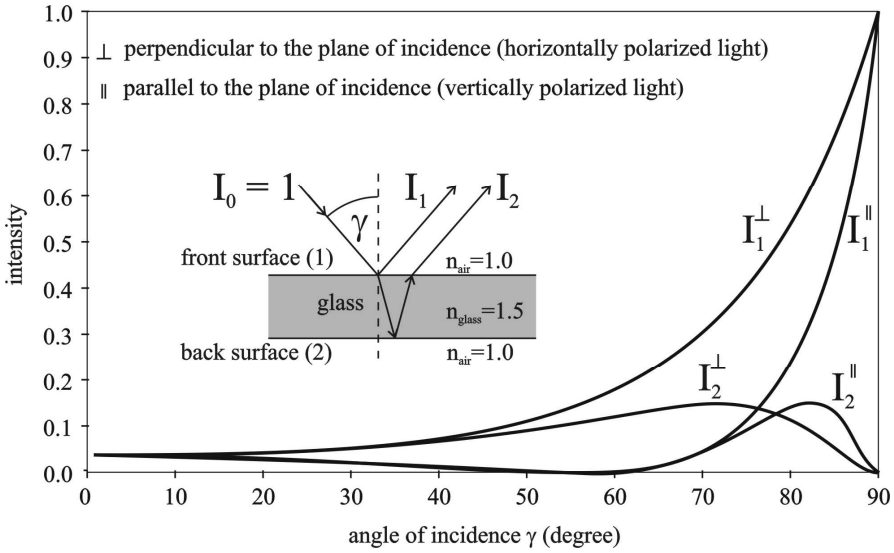

Fig. 23.10. Change of the intensity I of totally (with degree of linear polarization d = 100%) horizontally (⊥) or vertically (||) polarized light reflected from the front (1) or back (2) surface of a glass pane versus the angle of incident γ measured from the normal of the surface calculated with the use of the Fresnel formulae (Guenther, 1990), when the intensity of incident light is I_0 = 1. (After Fig. 10 of Bernáth et al. 2003).

24 Correction of Some Misinterpretations, Misleading Nomenclatures, Misbelieves and Errors Concerning Polarized Light and Polarization Sensitivity

In this chapter I deal with some common misbelieves, misleading nomenclatures, errors and misinterpretations concerning polarized light and polarization sensitivity I found during surveying the literature. The majority of these mistakes occur in publications of biologists. I would like to emphasize that although these misbelieves, errors or misleading usage of technical terms never have concerned the correctness of the final conclusions drawn. However, it is worth correcting them in order to avoid their possible repeated occurance in future publications. The common misbelief that the degree of linear polarization of light from the clear sky is highest in the UV is treated in Chapter 8.1.

24.1 The Relative Positions of the Arago, Babinet and Brewster Neutral Points

A frequently occurring error in text-books is that the relative positions of the Arago, Babinet and Brewster neutral points of skylight polarization are represented as if all three unpolarized points were observable at the same time in the sky. Figure 24.1 shows two examples for such erroneous representations. As we have seen in Chapter 7.4, in the sky only two neutral points can be observed simultaneously, either the Arago and Babinet points for lower solar elevations, or the Babinet and Brewster points for lower solar zenith angles. The reason for this is that the angular distance of the Arago point from the antisun is approximately the same as that of the Babinet and Brewster points from the sun. Thus, when the Brewster point rises above the horizon, the Arago point sets below the horizon. Consequently, all three neutral points can never be seen at the same time under normal atmospheric conditions.

The reason for such erroneous representations (e.g. Fig. 24.1) is probably the lack of space for voluminous figures rather than incorrect knowledge. To display correctly the relative positions of the neutral points, two figures are necessary, like Figs. 7.4.1A,B. Several authors spare one of these two figures and simply merge them into a single one, which leads to the mentioned error. Budó and Mátrai (1980) has known that at a particular time the angular distance of the Arago point

is about 160° from the Brewster point, and thus, the Arago point should already be below the horizon at higher solar elevations, but in their figure (Fig. 24.1A) they displayed the Arago point above the horizon with a much shorter angular distance from the Brewster point. Although Czelnai (1979), as an outstanding Hungarian meteorologist, has also been aware of the correct relative positions of the neutral points, in his meteorology text-book one of the figures comprises erroneously all three neutral points (Fig. 24.1B).

24.2 Correction of Some Misleading Representations of the Celestial E-vector Pattern

In the literature dealing with animal polarization sensitivity, there are some frequently cited figures of the celestial polarization pattern, which are erroneous or at least misleading. The drawing of the sky polarization pattern of Stockhammer (1959, p. 35) reproduced in Fig. 24.2A as well as the two-dimensional representations of the celestial polarization patterns presented by Wehner (e.g. 1989a, figs. 1b,c, p. 354; 1989b, figs. 1b,c on p. 67 and figs. 8A,B on p. 75; 1991, fig. 4A, p. 94; 1992, figs. 3.24a,b, p. 88) contain an error concerning the directions of the E-vectors. The mentioned figure of Stockhammer has been reproduced in many articles and text-books (e.g. Frisch 1965, fig. 328, p. 387; Grzimeks 1974; Duelli 1975, fig. 1, p. 45; Czihak et al. 1990; Frisch 1993, fig. 330, p. 382; Frisch and Lindauer 1993, fig. 88, p. 135) without any criticism. Schwind and Horváth (1993) corrected this error and presented a revised figure of the polarization of skylight (Fig. 24.2B).

Stockhammer based his polarization pattern on the data of Sekera (1957b), who represented the E-vector directions as isolines of the angle of polarization relative to the vertical. In transferring the angles so indicated to the radii of a polar-coordinate system, Stockhammer (1959) reversed the E-vector directions. As a result, all E-vectors appeared mirrored about the radii corresponding to the meridians through the zenith (Fig. 24.2A). Although Wehner presented the sky polarization patterns correctly in three-dimensional representation (e.g. Wehner 1982, fig. 13, p. 34; 1989a fig. 1a, p. 354; 1989b fig. 1a, p. 67), all of his earlier two-dimensional E-vector patterns mentioned above have the same error as the Stockhammer's (1959) pattern. Here the error was that the E-vector directions were determined by looking up at the skydome, but then plotted in a polar-coordinate system viewing the sky vault from above. Again, the result is a mirroring of the E-vector directions at the local meridian. The aim of these figures was to represent the E-vector distribution of the single-scattered Rayleigh skylight. However, in this case the E-vectors should always be aligned perpendicularly to the great circle passing through the sun and the investigated celestial point, irrespectively of whether the map displays the skydome from the point of view of an airborne or a ground-based observer. The mentioned figures are erroneous and/or misleading, because the E-vectors are not perpendicular to the scattering plane due to the incorrect mirroring relative to the local meridian.

Fortunately, inferences regarding the orientation mechanism of honeybees and desert ants have been not affected by this misleading plotting in any way, because the bee's and ant's internal representation of the celestial E-vector pattern has been represented in the same erroneous way (e.g. Wehner and Rossel 1985, fig. 2b on p. 19, fig. 6 on p. 28 and fig. 16 on p. 47; Wehner 1989a, fig. 3B on p. 355 and fig. 9 on p. 358; 1989b, fig. 8, p. 75; 1991, fig. 4B, p. 94; 1992, fig. 3.24c, p. 88).

There are two problems with these E-vector maps: (i) It has not been defined either in the text or in the figure legend whether the E-vector pattern displayed on the two-dimensional representation of the skydome is seen by a ground-based observer or by an observer who looks from above toward the skydome like an astronaut. Only from the figure legend of Duelli (1975, fig. 1, p. 45) was clear that his E-vector map, taken over simply from Frisch (1965), is seen by an ant from the ground. However, also in this case the E-vector map is erroneous. (ii) It has never been mentioned that the E-vectors are displayed in such a strange way that they are mirrored with respect to the local meridian.

Although Wehner (1994b, p. 36) did not acknowledge his mistake, all his two-dimensional representations of the celestial E-vector pattern as well as the honeybee's and desert ant's simplified internal representations of this pattern published after 1993 in a plethora of review articles (e.g. Wehner 1994a, fig. 3, p. 108; 1997, fig. 1b on p. 147 and fig. 9a,b on p. 160; 1998, inserted figs., p. 60 and fig. 7a on p. 66; 1999, fig. 9, p. 11; 2001, fig. 4 on p. 2593 and figs. 5A,B on p. 2594) follow already the correct scheme of Schwind and Horváth (1993) (see Fig. 24.1B). But henceforward the exact position of the observer has not been defined in these figures.

24.3 Misleading Nomenclatures

24.3.1 "Perception of Polarized Light" versus "Perception of Light Polarization"

In numerous publications dealing with polarization sensitivity the misleading terms 'perception/detection of polarized light' or 'sensitive to polarized light' are used, when the authors want to express that a visual system is able to perceive the E-vector direction. Wehner and Strasser (1985, p. 337), for example, wrote: "The photoreceptors of these ommatidia are characterized by a number of anatomical and physiological pecularities which suggest that they have functional significance for the *detection of polarized skylight*". And the next sentence sounds "Here, we show by painting out different parts of the eye and recording the bee's behavioural responses that the specialized photoreceptors at the dorsal margin of the eye are indeed necessary for *detecting polarized skylight*", or "The ultraviolet receptors of the DORS MARG ommatidia are highly *sensitive to polarized light*". I would like to emphasize that these careless terms are misleading, because any visual system

is sensitive to polarized light, even if it cannot perceive the direction of the E-vector. The correct formulation would be e.g. 'perception/detection of light polarization', or 'sensitive to polarization of light'.

24.3.2 "Linear Polarization" versus "Totally Linear Polarization" and "Partial Polarization" versus "Partial Linear Polarization"

It is a common misleading nomenclature that 'linearly polarized light' is used to describe 'totally/completely linearly polarized light', and 'partially polarized light' instead of 'partially linearly polarized light' (e.g. Bernard and Wehner 1977, pp. 1019-1020). Note, however, that linearly polarized light is either partially ($p < 100\%$) or totally/completely ($p = 100\%$) polarized. Furthermore, partially polarized light can be either linearly (Stokes parameter $V = 0$) or elliptical ($V \neq 0$).

24.4 The Celestial Hemisphere Rotates Around the Pole-Point Rather than Around the Zenith

A wide-spread misbelief is that the celestial hemisphere together with the sun and the polarization pattern of skylight rotates around the zenith. For instance, according to Wehner (1989b, pp. 66-67), "… due to the westward movement of the sun, the symmetry plane, and with it the whole e-vector pattern, rotates about the zenith", or "Since the sun changes its azimuth position during the day, the symmetry axis of the pattern in Fig. 4A and with it the distribution of all skylight parameter rotates around the zenith" (Wehner 1991, p. 97)[1]. An example for a misleading formulation is: "Owing to the daily westward movement of the sun across the sky (by some 15 degrees per hour), the entire e-vector pattern rotates about the zenith, thus changing its orientation with respect to geography" (Lambrinos et al. 1997, p. 134, 135). A somewhat less misleading description of the rotation of the celestial pattern sounds: "In a horizon system of coordinates, the pattern of polarization rotates about the zenith, due to the westward movement of the sun. Note, however, that the whole pattern does not merely rotate. Due to the sun's change in elevation mentioned above the pattern changes its intrinsic properties as it rotates about the zenith" (Wehner and Rossel 1985, p. 17).

However, the fact is that the sky rotates around the pole-point (Brines 1980). A ground-based observer can see the pole-point at the zenith only on the geographic north- and south-pole, thus the skydome can rotate around the zenith only at the geographic poles.

---

[1] Translated from the German original: "Da die Sonne im Tagesgang ihre Azimuthposition verändert, rotiert die Symmetrielinie des in Abb. 4A gezeigten Musters und mit ihr die Verteilung aller Himmelslichtparameter um den Zenit."

24.5 The Light Reflected by the Water Surface is not Always Horizontally Polarized

In the biological literature a common naive and too simplified conception is that the light reflected from the flat water surface is always horizontally polarized. For example, according to Wehner (1983, p. 361), "As light reflected from water surfaces is polarised horizontally …", or "The e-vector direction of reflected light is always oriented parallel to the reflecting surface" (Wehner 1994a, p. 111). Another example is the statement of Kelber et al. (2001, p. 2469): "Generally speaking, the polarisation angle is parallel to the reflecting surface and perpendicular to the plane of incidence of the light. Horizontal surfaces therefore reflect horizontally polarised light."

However, these statements are not always true. As Schwind and Horváth (1993), Horváth (1995a,b), Horváth and Zeil (1996), Horváth and Varjú (1997), Horváth et al. (1997), Gál et al. (2001b) and Bernáth et al. (2002, 2003) have shown both theoretically and experimentally, if the incident light is partially linearly polarized with approximately vertical E-vector, as is the case for skylight from the celestial band of maximum degree of polarization when the sun is near the horizon, for example, then also the water-surface-reflected light is approximately vertically polarized outside and inside the strongly and horizontally polarized annular Brewster zone. Consequently, during sunset and sunrise vertically polarized skylight is reflected from a considerable area of the flat water surface, even for perfectly black waters, from the subsurface region of which no light is returned (see e.g. Figs. 10.2E-H, 11.3, 11.7, 11.10, 11.12, 12.7, 23.4, 23.5). The light returned by the subsurface regions influences significantly the reflected E-vector pattern in such a way, that the relative proportion of the water surface reflecting approximately vertically polarized light is remarkably enhanced (see Figs. 12.1, 12.4, 17.3, 17.5, 18.3) depending on the solar elevation and the amount of subsurface-reflected light, which varies with the wavelength. Bernáth et al. (2003) measured the proportion of the area reflecting nearly vertically polarized light from horizontal glass panes underlain by a black or a light grey cloth as a function of the solar elevation. They obtained that at higher solar elevations the vertically polarizing regions of the grey reflecting surface, mimicking bright water bodies, was dominant (Fig. 23.3). This demonstrates well that the light reflected from the water is not always horizontally polarized.

24.6 Arago has Discovered the Skylight Polarization Rather than Malus

In the literature dealing with polarization sensitivity the discoverer of skylight polarization, Dominique Francois Jean Arago (1786-1853) is frequently confused with another French physicist, Etienne Louis Malus (1775-1812), who has also provided discoveries about light polarization. We mention here only four examples demonstrating this confusion:

- "… the French physicist E. Malus (1809) looking through a cordierite crystal accidentally observed … the polarization pattern of the sky ..."[2] (Wehner 1982, p. 25).
- "Owing to the scattering of light within the earth's atmosphere sky-light is partially linearly polarized. In 1809 this phenomenon was discovered accidentally by the French physicist Etienne Malus when he was looking at the sky through a dichroic crystal …" (Wehner 1989a, p. 353).
- "There is, however, an order to the light in the sky that the human eye fails to perceive. It is a phenomenon that was discovered accidentally by the French physicist Etienne Malus in 1809. Malus had looked up at the sky through a special type of crystal and noticed that the light was polarized. Although he did not fully appreciate what he saw, the phenomenon is now well understood" (Hawryshyn 1992, p. 164).
- "This phenomenon was accidentally discovered by the French physicist Etienne Malus in 1809; while looking at the sky through a crystal, Malus recognized that the light was polarized" (Wolken 1995, p. 183).

However, the fact is that the linear polarization of skylight was discovered by the French astronomer, physicist and politician D. F. J. Arago rather than by E. L. Malus. In 1809 Arago observed first that the light from the blue sky is partially polarized. Then he established the general distribution of skylight polarization, observed the maximum of the degree of polarization of skylight at about 90^o from the sun and antisun, as well as discovered the first neutral point, which nowadays bears his name (Coulson 1988, p. 2). On the other hand, in 1808 the Institute of France announced a contest for papers to give a mathematical theory, verified by experiments, of the double refraction of light when transmitted through different crystallized bodies. The prize was awarded in 1810 to E. L. Malus, who was a colonel of the French Imperial Corps of Engineers. During his experiments on the specified subject, Malus looked through a calcite crystal at the light of the setting sun reflected by the windows of a building in Paris, and was surprised to observe the disappearance of one of the two images of the windows as he rotated the crystal. This observation led to his discovery of the laws of reflection by which his

[2] Transleted from the German original: "… der französische Physiker E. Malus (1809) beim Blick durch einen Cordierit-Kristall zufällig am Himmel beobachtet hatte ... das Polarisationmuster des Himmels".

name is immortalized. In fact, Malus was the first to use the term "polarization" as applied to light. He hypothesized that the corpuscles, which made up light were aligned by the process of reflection in a manner similar to the way magnetic bodies are aligned by the poles of a magnet (Coulson 1988, p. 2).

Note, however, that Wehner (1997, p. 150) corrected his earlier misinformation mentioned above: "… it was only in 1809 that the French physicist Etienne-Louis Malus, while looking at a glass through a calcite crystal, discovered and correctly interpreted the phenomenon of the polarization of light. However, the polarization he observed by looking at a glossy surface was produced by the reflection rather than the scattering of light. The first to describe the latter phenomenon was Dominique Arago (1811). Looking at the sky through a rotating dichroic (polarization) filter, he perceived the alternating appearance and disappearance of an impressive dark band extending across the sky at a distance of 90^o from the sun."

24.7 The E-vector Patterns of Real Skies Differ from those of Rayleigh Skies

In the literature dealing with polarization sensitivity, the E-vector patterns of skies are always considered to be the same as those predicted by the single-scattering Rayleigh model. Only seven citations are listed here to demonstrate this wide-spread simplification:

- "The sunlight is polarized linearly by scattering in a direction perpendicular to the plane through the incident solar ray in a celestial point P (with good approximation equivalent to the direction of the sun from the observatory) and the direction of P from the observatory" (Glas 1977, p. 132).
- "In addition to the well-established relationship between the E-vector of sky polarization and the position of the sun (i.e., the E-vector in a given region of the sky is perpendicular to a line drawn by the observer between that point in the sky and sun), …" (Phillips and Waldvogel 1982, p. 197).
- "… the skylight polarization pattern in the natural sky where the E-vector is everywhere perpendicular to the plane containing the sun, the point in the sky being observed and the observer …" (Able and Able 1990, p. 1190).
- "The e vector of the polarized light of the sky is perpendicular to the sun, with the band of maximal polarization at 90^o from the sun's position" (Schmidt-Koenig et al. 1991, p. 5).
- "The only E-vector orientations that reach the surface are those that are perpendicular to both the path of the light from the sun to the atmospheric particle, and also perpendicular to the path of the light from the particle to the earth's surface" (Hawryshyn 1992, p. 166).
- "The natural distribution of linearly polarized light in the sky, …, is closely related to the position of the sun. The orientation of polarization is perpendicular to the direction of the sun, …" (Shashar et al. 1998, p. 276).

– "As light passes through the atmosphere, it is partially polarised, depending on the scattering angle. The electrical (e) vector of each scattered ray exhibits a predominant vibration direction, which is perpendicular to the plane in which the ray was deflected (Rayleigh scattering)" (Freake 1999, p. 1159).

However, there exist relatively great areas in the sky, around the sun, antisolar point and the Arago, Babinet and Brewster neutral points, where the E-vector pattern of real skies differ from those of Rayleigh skies. In these celestial regions the E-vectors are parallel to the plane of scattering (negative polarization) or are neither perpendicular nor parallel to it. In these celestial areas of "anomalous polarization"[3], the degree of polarization is usually lower than the threshold of polarization sensitivity in animals. Thus the skylight from these regions are perceived as unpolarized. Although the polarization patterns of Rayleigh skies are rather a gross approximation of the real ones, they can be considered as a good model for biological purposes. It could be an important task of future research to measure the portion of the sky where the deviation of the E-vector direction from that predicted by the single-scattering Rayleigh model is below a given threshold as a function of the solar elevation and the meteorological conditions.

24.8 Four Measurements are not Enough to Determine the Spectral and Polarizational Characteristics of Linearly Polarized Multichromatic Light

According to Wehner (1989b, p. 65), "How does the insect unambiguously detect particular e-vectors in the sky? … solving the first problem was considered to be analogous to solving a set of four equations with four unknowns (with the four unknowns being intensity, spectral composition, degree of polarization and direction of polarization). To acquire the necessary input data the insect could perform four measurements: either simultaneously by using four different receptors, or successively by employing only one receptor."

However, this formulation is misleading, since the "spectral composition" cannot be simply considered as one of the unknown variables. The spectral composition is actually nothing else as the wavelength-dependent intensity $I(\lambda)$ of light. On the one hand, one can consider the intensity I, degree of linear polarization p and direction of polarization α as unknowns at a given wavelength λ. Then there are only 3 unknowns and only 3 independent measurements should be performed to determine them, if the light is elliptically unpolarized, that is, if the fourth component of the Stokes parameter $V = 0$. On the other hand, one can consider the wavelength-dependent functions $I(\lambda)$, $p(\lambda)$ and $\alpha(\lambda)$ in a given range of λ, and $3n$ ($n = 1, 2, 3,\ldots$) independent measurements are necessary to determine

[3] Anomalous in the sense that the E-vector directions of skylight differ from those predicted by the single-scattering Rayleigh model.

the values of these functions at $3n$ different wavelengths. By means of 4 measurements one cannot unambiguously determine the values of $I(\lambda)$, $p(\lambda)$ and $\alpha(\lambda)$ at different wavelengths. With 4 measurements one can at the very most obtain all four components of the Stokes vector of elliptically and linearly polarized light at a given λ.

24.9 A Common Methodological Error: Brightness Patterns Induced by Selective Reflection of Linearly Polarized Light from Black Surfaces

In behavioural laboratory experiments studying animal orientation, black surfaces are traditionally used to minimize the influence of light reflected from the surfaces surrounding the animal. The same tradition has been adopted by the majority of researchers investigating the polarization sensitivity of animals. However, in these cases the use of black surfaces is the worst choice. The reasons for this are briefly discussed here in a typical case, in which the polarization sensitivity of the rainbow trout (*Oncorhyncus mykiss*) was tested (Hawryshyn et al. 1990; Hawryshyn and Bolger 1990). Although later electrophysiological experiments revealed that juvenile rainbow trouts indeed perceive the linear polarization of light, it is worth criticizing the methodological shortcomings of the experimental technique, which are wide-spread in similar behavioural experiments. Coemans and Vos (1989), Coemans et al. (1990, 1994a) and Vos et al. (1995) called the attention of the scientific community to the need of elimination of such strongly polarizing black surfaces. This has lead to the change of paradigm in behavioural experiments on animal polarization sensitivity.

The forerunners of this subject are Baylor and Smith (1958), Kalmus (1958, 1959) and Waterman (1981). Baylor and Smith (1958) suggested an extra-ocular mechanism of polarization sensitivity in honeybees. According to their hypothesis, an appropriate substratum, serving as dancing place for bees, can function as a polarization analyzer, since vertical beams of linearly polarized light illuminating the substratum give rise to reflections with minimum and maximum intensities parallel and perpendicular to the E-vector direction, respectively. On the other hand, vertical rays of unpolarized light illuminating the substratum give rise to reflections of light with uniform intensities in all directions. Although later anatomical, electrophysiological, behavioural and theoretical studies (e.g. Autrum and Stumpf 1950; Stockhammer 1956; Shaw 1967; Seitz 1969; Skrzipek and Skrzipek 1974) have proven that the rhabdomeres are responsible for polarization sensitivity in bees and many other arthropods, the merit of the hypothesis of Baylor and Smith (1958) was that they as first called the attention of researchers dealing with animal polarization sensitivity to the possibility that spurious unwanted intensity patterns induced by selective reflection of linearly polarized light from the surfaces surrounding the animal can also serve as a cue for orientation. The same was emphasized by Kalmus (1958, 1959), who investigated the responses of insects to linearly polarized light in the presence of dark

reflecting surfaces. He observed that certain optomotor reactions to plane polarized light disappeared when the experimental situation was redesigned so that the unwanted scattering- and reflection-induced intensity patterns could not arise. Waterman (1981) is also one of the few researchers who has taken this problem seriously and pointed out the necessity of testing whether a reaction of an animal to linearly polarized light is not elicited by such unwanted brightness patterns. In spite of these warnings, many experimentators studying the responses of animals to polarized light have left them out of consideration. In these cases the polarization sensitivity of the investigated animals cannot be considered as proven.

Now let us consider the criticism of such an experimental technique. During their experiments, Hawryshyn et al. (1990) and Hawryshyn and Bolger (1990) made the following typical methodical mistakes (written in bold face):

- All experiments were conducted in a room (Fig. 24.3A) with vertical walls **painted flat black** "in order to minimize spurious brightness cues".
- The training tank consisted of **black Plexiglas** with vertical walls (Fig. 24.3A).
- All observations during the test experiments were made from behind a vertical **black curtain** positioned in the immediate vicinity of the test tank (Fig. 24.3B).
- The test tank was a circular plastic pool **painted with flat grey marine paint** with an elevated floor and an approximately vertical, slightly tilted wall (Figs. 24.3A,B) "in order to limit intensity patterns as a potential cue". The fishes could see the curtain as well as the walls of the room, the training tank and the test tank.
- Although the irradiance of the polarized light field was measured along 8 arms in three positions in the test tank at the water surface with a radiometer, it was not mentioned in which range(s) of the spectrum this measurement happened. The **spatial distribution of the UV irradiance** available to the fishes in the training and test tank **was not measured**. Only this measurement could have convincingly excluded the possibility that the fishes oriented to the **brightness cues induced by selective reflection of UV polarized light from the flat black walls** of the experimental room, and/or **from the black curtain**, and/or **from the flat grey Plexiglas wall** of the testing tank, and/or **from the black Plexiglas wall** of the training tank.

In the experiments of Hawryshyn et al. (1990) the training tank was placed on two boards situated on top of the test tank. Above the training and test tanks was an overhead light source fitted with a filter tray for neutral density and cut-off filters and a UV-grade linear polarizer. The fish was placed under the release box (cover: white Plexiglas, sides: **black Plexiglas**) for 20 min prior to every experiment. A trial was initiated by lifting the release box. If a fish did not respond within 5 min the release box was pulled from the test tank completely. The fish was allowed 1-3 min in the release box between trials.

The light reflected from a non-metallic partially transparent material with a flat surface has two components. The first is reflected directly from the surface, the second one originates from the subsurface, that is, from the inner layers of the

material. When a partially linearly polarized light with a given degree of polarization and angle of incidence is reflected from a flat dielectric material, its amount depends on the angle of polarization α measured from the plane of reflection. The smaller the α, the less the amount of reflected light. Thus, more light is reflected from the surface if the E-vector is perpendicular to the plane of reflection than when it is parallel to this plane (Fig. 24.3C). This selective reflection depends only slightly on the wavelength in the near-UV and visible ranges of the spectrum, because the index of refraction of dielectric materials is usually only slightly dependent on the wavelength in these spectral ranges. The light penetrating into the material is randomly, diffusely scattered and absorbed, the consequence of which is depolarisation and decrease of intensity. Both the absorption and the diffuse scattering-induced depolarisation may strongly depend on the wavelength, which results in that the subsurface-returned component will be more or less depolarised and will possess more or less changed spectral composition.

In the case of dark partially transparent materials with smooth surfaces the surface-reflected component dominates in those regions of the spectrum, in which the subsurface-returned component is reduced by strong absorption. If a dark material strongly absorbs UV light, for example, the surface-reflected component will dominate in the UV, where the amount of reflected light will vary with the change of the E-vector direction relative to the plane of reflection. The higher the degree of polarization, the stronger this variation. Then in the UV the dark surface is seen apparently darker or brighter if the E-vector of incident light is perpendicular or parallel to the surface, respectively (Fig. 24.3C). Such reflection-polarization-induced UV-brightness differences can occur in all dark chambers, rooms or tanks, for instance, the walls of which are covered by black or grey UV-absorbing paint, or composed of black UV-absorbing Plexiglas or black UV-absorbing cloth curtain. The walls receiving more or less perpendicularly polarized light reflect less light in the UV than the walls receiving more or less parallel polarized light (Fig. 24.3C). If the E-vector of ambient light in these chambers, rooms or tanks is rotated, the reflection-induced UV-brightness pattern will follow this rotation (Figs. 24.3D,E).

Unfortunately, it cannot be excluded that the rainbow trouts in the experiments described above perceived reflection-polarization-induced UV-brightness cues for orientation, like the homing pigeons in the methodologically erroneous experiments of Delius et al. (1976) and Kreithen and Keeton (1974), because in the UV the spatial distribution of the irradiance of light reflected from the black or grey walls of the room, curtain and training as well as test tanks was not measured. This was admitted also by Hawryshyn et al. (1990, p. 570): "However, this does not fully rule out the possibility that polarization-induced brightness patterns are being utilized…". All results of Hawryshyn et al. (1990) and Hawryshyn and Bolger (1990) can be explained also by these possible UV-brightness differences induced by reflection polarization:

- "Two groups of fishes were trained under a polarized light field with the E-vector parallel and perpendicular to the training tank. During testing, both groups showed orientation consistent with the trained direction". The two groups of fishes could also be trained at a non-homogeneous UV-brightness pattern induced by a polarized light field with the E-vector parallel and perpendicular to the training tank. During testing, both groups would orient consistently with the trained direction (Figs. 24.3D,E).
- "Trouts which were tested at one E-vector orientation performed equally well at an E-vector orientation shifted by 90°". Trouts tested with one non-homogeneous UV-brightness pattern induced by one E-vector orientation could also perform equally well at a shifted non-homogeneous UV-brightness pattern induced by an E-vector orientation shifted by 90°.
- "Trouts which were tested under a polarized light field lacking UV radiation did not orient to the predicted direction". Trouts which would be tested under a polarized light field lacking UV radiation would not orient to the predicted direction, because reflection-polarization-induced brightness differences would occur only in the UV.
- "Trouts at the developmental stage when UV-sensitive cones disappear were not capable of orienting to the polarized light field". Trouts at the developmental stage when UV-sensitive cones disappear would not be capable of orienting to non-homogeneous UV-brightness patterns, because these UV patterns could not be perceived by the photoreceptors sensitive only to longer wavelengths.
- "The lower the degree of polarization p of UV+white light, the smaller the accuracy of the polarotactic orientation of trouts. If p is smaller than a threshold, trouts cannot detect the E-vector and orient polarotactically". The lower the p, the smaller would be the accuracy of the phototactic orientation of trouts, because the weaker would be the UV-brightness differences induced by reflection polarization. If p is lower than a threshold, trouts could not detect these UV-brightness differences and could not orient phototactically.

All these problems could have been avoided if white materials with as rough surfaces as possible would have been used in the above-mentioned experiments with rainbow trouts instead of black or grey materials with flat shiny surfaces. In the case of bright, UV+white-reflective materials with rough surfaces the polarized surface-reflected component, causing all the troubles, would have been strongly depolarised and suppressed by the intense and unpolarized subsurface-returned component, which would have drastically reduced or even eliminated any brightness differences induced by reflection polarization.

24.10 The Alleged Viking Navigation by Skylight Polarization

It has been mentioned in the Icelandic sagas that the Vikings sailed to Greenland by steering a course due west after leaving Bergen on the west coast of Norway. The sun would have been an obvious reference source for keeping a true westerly course during the long daylight of the polar summer (Vebaek and Thirslund 1992). Since the weather at these high latitudes is strongly variable, there have been periods during which the sun was consistently hidden behind clouds. The Danish archaeologist Thorkild Ramskou (1967, 1969) suggested that the Vikings might have used a certain crystal, called "sunstone" as a polarization analyser of skylight for finding the location of the overcast sun. Sunstones are mentioned in the sagas, but without enough detail for a decisive identification (Foote 1956; Schnall 1975). It has been speculated that these enigmatic sunstones might have been composed of calcite or cordierite or turmaline, since these birefringent or dichroic or pleuchroic crystals are common in the areas where the Vikings have lived. However, the fact is that presently it is completely unknown what sort of stone the sunstones were. Furthermore, sunstones are nowhere mentioned in connection with navigation or sailing, nor has any archaeological record of an object with the optical properties of an analyser been discovered (Roslund and Beckman 1994).

Since Ramskou knew that sunlight scattered by clouds is practically unpolarized, he always stressed the importance of a cloudfree sky at the zenith for the successful application of polarimetry as an aid to navigation. In spite of this severe limit to its usefulness at sea and the lack of literary and archaeological evidence for it, Viking navigation by polarimetry has largely been reported in favourable terms as an established fact of Viking achievements. It is so described in text-books (e.g. Barfoed 1967), in scientific essays (e.g. Wehner 1982) and in popular scientific journals such as *National Geographic* (LaFay 1970) or *Scientific American* (Wehner 1976). Experienced deep-sea navigators have considered the sunstone as a remarkably accurate instrument and an essential aid to Viking navigation (Britton 1972; McGrath 1991). All these have led to the widespread misbelief that navigation by skylight polarization is possible under any conditions, from clear to completely overcast skies (Roslund and Beckman 1994). The theory that the Vikings utilized polarized skylight for finding their way across the Atlantic has been uncritically accepted also by many biologists dealing with animal polarization sensitivity. We mention here only five examples:

- Kreithen and Keeton (1974, p. 83): "Instruments that measure the axis of sky polarization are presently used in circumpolar navigation where the magnetic compass is of limited use; for the same reason, early Viking ship captains may have carried polarizing crystals."
- Wehner (1976, pp. 106-107): "It has recently learned, however, that about the year 1000 the Vikings were taking advantage of the polarization of skylight in their voyages west from Iceland and Greenland to Newfoundland. The Danish archaeologist Thorkild Ramskou has pointed out that the 'sunstones' described

in the old sagas were nothing other than birefringent and dichroic crystals that could serve as polarization analysers. As I write this article I have on my table a small crystal of cordierite. When I look through it at any point in the sky, I can determine the direction of polarization by observing the changes of color and brightness as I rotate the crystal around the line of sight. Some years ago an airplane was steered with fair precision from Norway to Sondre Storm Fjord airfield in Greenland with a cordierite crystal as the only navigational aid. These crystals can be found as pebbles on the coast of Norway. Although it is unlikely that the Vikings knew anything about polarized light, they apparently perceived the relation between what they saw through a sunstone and the position of the sun (which was often hidden by clouds in those northern latitudes)."

- Können (1985, p. 18): "About 1000 the Vikings discovered the dichroic properties of crystals like cordierite. With these crystals they observed the polarization of the blue sky and were thus able to navigate in the absence of the sun."
- Wehner (1997, pp. 148, 150): "… humans have only one way to visualize celestial E-vector patterns, namely by using polarization filters as optical aids. This kind of visualization might date back to the times of the Vikings, who used cordierite crystals as polarization filters."
- Shashar et al. (1998a, p. 276): "The natural distribution of linearly polarized light in the sky, …, is closely related to the position of the sun. … This close association between the orientation of polarization and the location of the sun was utilized by the Vikings, who used 'sun stones', probably calcite crystals, as navigational aids."

However, in the opinion of Roslund and Beckman (1994), on most overcast days the Vikings could most certainly not have used the polarization of skylight to determine the location of the sun, since cloudlight is practically unpolarized. Although the Vikings might have been able to do so on partly cloudy days, there would have been no need to. A navigational method that requires patches of blue sky would have been of little interest to the Vikings. Even, when the sun is hidden by clouds, its location can often be found quite accurately for most navigational needs from the pattern of the solar illumination of clouds, from the bright lining of cloud tops and the crepuscular rays emanating from the sun. On overcast days careful observations of the sky may reveal the faint disk of the sun if the cloud cover is not too dense. Nor does polarimetry give clues to the solar position when the sun is below the horizon. The colour and intensity distribution during twilight appears distinct enough for the naked eye to guess the direction of the sun.

On the other hand, according to Roslund and Beckman (1994), simple sun sightings do not directly give meaningful information for steering. The solar positions should have been converted by a Viking navigator into azimuths with reference to geographical north. Today this is done by lengthy calculations with tables of data or by computers. But it is known that the Norsemen possessed a fair amount of knowledge concerning the sun's daily and seasonal movements (Roslund 1989). To convert data from the state of polarization of skylight into

directions for holding the ship's course is a vastly more complicated process. Until compelling new evidence comes forth, the notion that Vikings could have used polarimetry for finding their way across the Atlantic has little scientific basis. The use of skylight polarization for Viking navigation under partly cloudy skies should be treated with extreme caution and scepticism.

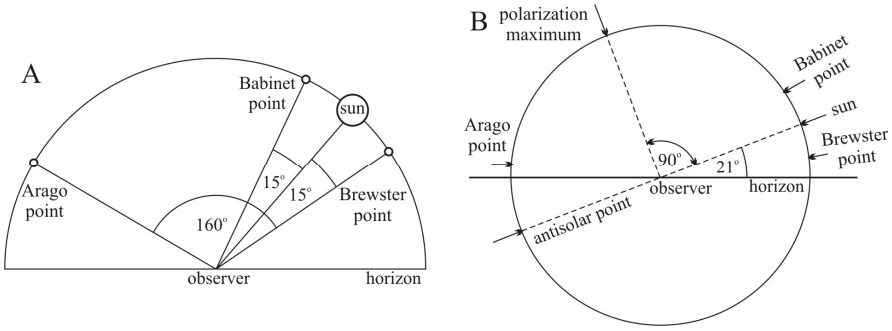

Fig. 24.1. Two erroneous representations of the relative positions of the Arago, Babinet and Brewster neutral points of skylight polarization along the solar-antisolar meridian. In these figures the positions of all three neutral points are shown as if they were observable simultaneously in the sky above the horizon. A: Budó and Mátrai (1980, Fig. 296,3, p. 250). B: Czelnai (1979, Fig. 118, p. 218).

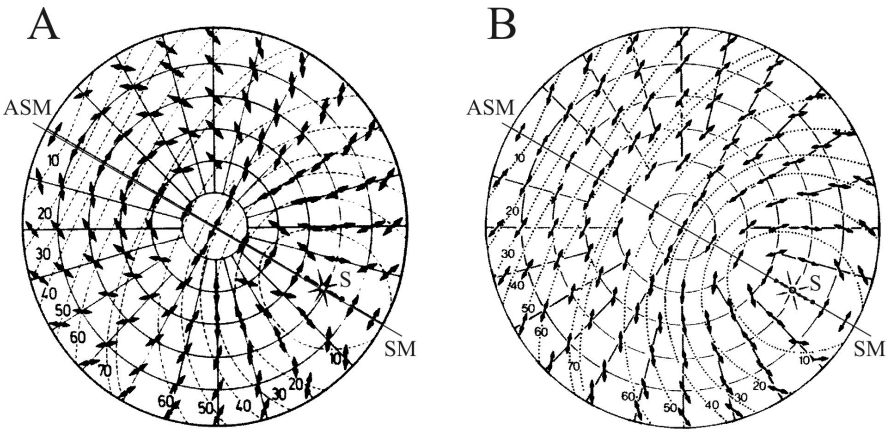

Fig. 24.2. A: The erroneous celestial polarization pattern of Stockhammer (1959) with the E-vector directions mirrored about the local meridians. B: Correct polarization pattern of the sky, with the sun at 30° elevation from the horizon. Circles: elevations at 15° intervals. Dotted: lines of equal degree of linear polarization *p*. Lines of equal *p* pass across the sky approximately concentrically around the sun, and the E-vectors are approximately tangential to these circles. In the two-dimensional representation, therefore, the E-vectors must be approximately parallel to the dotted lines and cannot in some cases lie nearly perpendicular to them, as in the Stockhammer's pattern. S: sun, SM: solar meridian, ASM: antisolar meridian. (After Fig. 2 of Schwind and Horváth, 1993, p. 83).

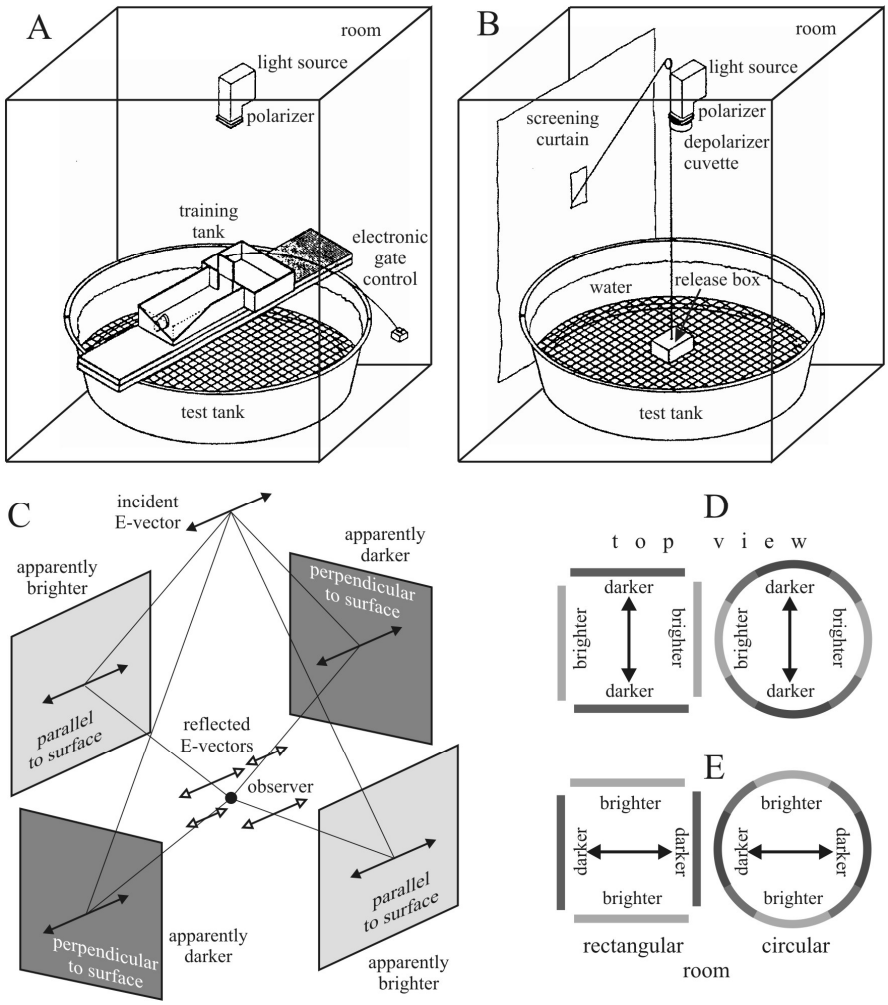

Fig. 24.3. A, B: Arrangements of training (A) and testing (B) of rainbow trouts in the behavioural laboratory experiments of Hawryshyn et al. (1990) and Hawryshyn and Bolger (1990). C: Selective reflection of linearly polarized light from the vertical walls surrounding an imaginary observer. The E-vectors are represented by double-headed arrows, the length of which is proportional to the intensity. The differences in the grey shades demonstrate qualitatively the brightness differences perceived by the observer. D, E: The relative positions of the brighter and darker regions of the walls of a rectangular (left) and circular (right) room as perceived by an observer in the centre for two orthogonal directions of the E-vector of linearly polarized light illuminating the scene from above.

25 REFERENCES

Able KP (1989) Skylight polarization patterns and the orientation of migratory birds. J Exp Biol 141:241-256

Able KP (1993) Orientation cues used by migratory birds: a review of cue-conflict experiments. Trends Ecol Evol 8:367-371

Able KP, Able MA (1990c) Ontogeny of migratory orientation in the Savannah sparrow, Passerculus sandwichensis: mechanisms at sunset. Anim Behav 39:1189-1198

Able KP, Able MA (1993) Daytime calibration of magnetic orientation in a migratory bird requires a view of skylight polarization. Nature 364:523-525

Adams CN, Kattawar GW (1993) Effect of volume-scattering function on the errors induced when polarization is neglected in radiance calculations in an atmosphere-ocean system. Appl Opt 32:4610-4617

Adams JT, Kattawar GW (1997) Neutral points in an atmosphere-ocean system. 1. Upwelling light field. Appl Opt 36:1976-1986

Akersten WA, Shaw CA, Jefferson GT (1983) Rancho La Brea: status and future. Paleobiol 9:211-217

Andrikovics S (1991) On the long-term changes of the invertebrate macrofauna in the creeks of the Pilis-Visegrádi mountains (Hungary). Verhandl Internat Vereins Limnol 24:1969-1972

Andrikovics S, Kéri A (1991) Winter macroinvertebrate investigations along the Bükkös stream (Visegrádi Mountains, Hungary). Opuscula Zoologica Budapest 24:57-67

Angus PB (1973) Pleistocene Helophorus (Coleoptera, Hydrophilidae) from Borislav and Starunia in the Western Ukraine, with a reinterpretation of M. Somnicki's species, description of a new Siberian species and comparison with British Weichselian faunas. Phil Trans Roy Soc Lond 265:299-326

Arikawa K, Inokuma K, Eguchi E (1987) Pentachromatic visual system in a butterfly. Naturwissenschaften 74:297-298

Autrum H, Stumpf H (1950) Das Bienenauge als Analysator fùr polarisiertes Licht. Z Naturforsch 5b:116-122

Azzam RMA, Bashara NM (1992) Ellipsometry and polarized light. North-Holland, Amsterdam, New York

Babinet J (1840) Sur un nouveau point neutre dans l'atmosphere. Compt Rend 11:618-620

Bandai K, Arikawa K, Eguchi E (1992) Localization of spectral receptors in the ommatidium of butterfly compound eye determined by polarization sensitivity. J Comp Physiol A 171:289-297

Barfoed JHP (1967) Navigation. Kulturhistoriskt Lexikon Nordisk Medeltid 12:261

Barral MJA (1858) Oeuvres de Francois Arago I-V., Gide - Paris, Weigel - Leipzig

Barta A, Horváth G (2004) Why is it advantageous for animals to detect celestial polarization in the ultraviolet? Skylight polarization under clouds and canopies is strongest in the UV. J Theor Biol 226: 429-437

Barta A, Horváth G, Bernáth B, Meyer-Rochow VB (2003) Imaging polarimetry of the rainbow. Appl Opt 42:399-405

Bartsch K (1991) Die funktionelle und strukturelle Regionalisierung des Auges der Wasserläufer. PhD thesis, Univ Tübingen, Germany

Bartsch K (1995) Polarization-sensitive photoreceptors of different spectral types in the compound eye of waterstriders. Naturwissenschaften 82:292-293

Bary E de, Bullrich K, Lorenz D (1961) Messungen der Himmelsstrahlung und deren Polarisationsgrad während der Sonnenfinsternis am 15.2.1961 in Viareggio (Italien). Geofisica Pura et Applicata 48:193-198

Baylor ER, Smith FE (1958) Extra-ocular polarization analysis in the honeybee. Anat Rec 132:411-412

Beach DA, Bustamante C, Wells KS, Fougar KM (1987) Theory confirmation. Patterns of polymerization of hemoglobin S in red blood sickle cells. Biophys J 52:947-954

Beaglehole D, Carter GG (1992) Antarctic skies. 2. Characterization of the intensity and polarization of skylight in a high albedo environment. J Geophys Res D 97:2597-2600

Beason RC, Semm P (1991) Neuroethological aspects of avian orientation. In: Berthold P (ed) Orientation in birds. Birkhäuser, Basel Boston Berlin, pp 106-127

Beaudet L, Browman HI, Hawryshyn CW (1993) Optic nerve response and retinal structure in rainbow trout of different sizes. Vis Res 33:1739-1746

Beaudet L, Novales Flamarique I, Hawryshyn CW (1997) Cone-photoreceptor topography in the retina of sexually mature Pacific salmonid fishes. J Comp Neurol 383:49-59

Beckers JM, Wagner WJ (1970) A photographic polarimeter for solar observations. Appl Opt 9:1933-1934

Bellver C (1987) Influence of particulate pollution on the positions of neutral points in the sky at Seville (Spain). Atmos Environ 21:699-702

Bennett ATD, Cuthill IC, Partridge JC, Maier EJ (1996) Ultraviolet vision and mate choice in zebra finches. Nature 380:433-435

Bernard GD, Wehner R (1977) Functional similarities between polarization vision and color vision. Vis Res 17:1019-1028

Bernáth B, Horváth G (1999) Visual deception of a Great White Egret by shiny plastic sheets. Ornis Hungarica 8/9:57-61

Bernáth B, Szedenics G, Molnár G, Kriska G, Horváth G (2001a) Visual ecological impact of a peculiar waste oil lake on the avifauna: dual-choice field experiments with water-seeking birds using huge shiny black and white plastic sheets. Arch Nat Conserv Landsc Res 40(1):1-28

Bernáth B, Szedenics G, Molnár G, Kriska G, Horváth G (2001b) Visual ecological impact of "shiny black anthropogenic products" on aquatic insects: oil reservoirs and plastic sheets as polarized traps for insects associated with water. Arch Nat Conserv Landsc Res 40(2):89-109

Bernáth B, Szedenics G, Wildermuth H, Horváth G (2002) How can dragonflies discern bright and dark waters from a distance? The degree of polarization of reflected light as a possible cue for dragonfly habitat selection. Freshwater Biol 47:1707-1719

Bernáth B, Gál J, Horváth G (2004) Why is it worth flying at dusk for aquatic insects? Polarotactic water detection is easiest at low solar elevations. J Exp Biol 207: 755-765

Bisch SM (1999) Orientierungsleistungen des nachtaktiven Wüstenkäfers Parastizopus armaticeps Peringuey (Coleoptera: Tenebrionidae). PhD thesis, Univ Bonn, Germany

Blanke H (1996) Visuelle Detektion von Eigenbewegung beim Rückenschwimmer Notonecta glauca. PhD thesis, Univ Tübingen, Germany, p. 79

Blanke H, Varjú D (1995) In: Elsner N, Menzel R (eds) Proc 23rd Göttingen Neurobiol Conf, Thieme G, Stuttgart, vol II, p 427

Boerner WM, Brand H, Cram LA, Holm WA, Stein DE, Wiesbeck W, Keydel W, Giuli D, Gjessing DT, Molinet FA (eds) (1992) Direct and inverse methods in radar polarimetry. Dordrecht, Kluwer

Bohn H, Täuber U (1971) Beziehungen zwischen der Wirkung polarisierten Lichtes auf das Elektroretinogramm und der Ultrastruktur des Auges von Gerris lacustris L. Z vergl Physiol 72:32-53

Bohren C (1987) Multiple scattering of light and some of its observable consequences. Am J Phys 55:524-533

Born M, Wolf E (1999) Priciples of optics. 7th ed, Cambridge Univ Press, Cambridge, UK

Brewster D (1842) On the existence of a new neutral point and two secondary neutral points. Rept British Assoc Adv Sci 2:13

Brewster D (1847) On the polarisation of the atmosphere. Phil Magaz J Sci 31:444-454

Brewster D (1864) Additional observations on the polarisation of the atmosphere, made at St. Andrews in 1841-1845. Trans Roy Soc Edinburgh 24:247-286

Bréon FM, Deuzé JL, Tanré D, Herman M (1997) Validation of spaceborne estimates of aerosol loading from Sun photometer measurements with emphasis on polarization. J Geophys Res D 102:17187-17195

Bréon FM, Tanré D, Lecomte P, Herman M (1995) Polarized reflectance of bare soils and vegetation: measurements and models. IEEE Trans Geosci Rem Sens 33:487-499

Brines ML (1980) Dynamic patterns of skylight polarization as clock and compass. J Theor Biol 86:507-512

Brines ML, Gould JL (1979) Bees have rules. Science 206:571-573

Brines ML, Gould JL (1982) Skylight polarization patterns and animal orientation. J Exp Biol 96:69-91

Britton W (1972) The Britton Viking sun-stone expedition. Nutr Today 7(3):14-22

Brodskiy AK (1973) The swarming behavior of mayflies (Ephemeroptera). Entomol Rev 52:33-39

Browman HI, Novales Flamarique I, Hawryshyn CW (1994) Ultraviolet photoreception contributes to prey search behaviour in two species of zooplanktivorous fishes. J Exp Biol 186:187-198

Brown T (1994) Stereoscopic phenomena of light and sight. London, 1903, a facsimile of the 1903 edition, Reel 3-D Enterprises Historical 3-D Reprint Series, USA, 1994

Brunner D, Labhart T (1987) Behavioural evidence for polarization vision in crickets. Physiol Entomol 12:1-10

Buchwald R (1989) Die Bedeutung der Vegetation für die Habitatbindung einiger Libellenarten der Quellmoore und Fliessgewässer. Phytocoenol 17:307-448

Budó Á, Mátrai T (1980) Experimental physics III. Optics and atomphysics. Tankönyvkiadó, Budapest (in Hungarian)

Bueno JM (2000a) Polarimetry using liquid-crystal variable retarders: theory and calibration. J Opt A (Pure Appl Opt) 2:216-222

Bueno JM (2000b) Measurement of parameters of polarization in the living human eye using imaging polarimetry. Vis Res 40:3791-3799

Bueno JM (2001) Depolarization effects in the human eye. Vis Res 41:2687-2696

Bueno JM, Artal P (1999) Double-pass imaging polarimetry in the human eye. Opt Lett 24:64-66

Bueno JM, Artal P (2001) Polarization and retinal image quality estimates in the human eye. J Opt Soc Am A 18:489-496

Bueno JM, Jaronski J (2001) Spatially resolved polarization properties for in vitro corneas. Ophthalm Physiol Opt 21:384-392

Bullrich K (1964) Scattered radiation in the atmosphere and the natural aerosol. In: Advances in geophysics. Academic Press, New York, vol 10, pp 99-260

Burchak-Abramovich NI (1975) Die pleistozäne Vogelfauna der UdSSR. Quartär Paläon 1:87-105

Burder D, Whitehouse P (1992) Photographing in 3-D. Stereoscopic Society, England

Burghause FMHR (1981) The structure of the double-eyes of Baetis and the uniform eyes of Ecdyonurus (Ephemeroptera). Zoomorphol 98:17-34

Buschmann C (1993) Fernerkundung von Pflanzen – Ausbreitung, Gesundheitszustand und Produktivität. Naturwissenschaften 80:439-453

Cameron DA, Pugh EN Jr (1991) Double cones as a basis for a new type of polarization vision in vertebrates. Nature 353:161-164

Cariou J, Jeune BL, Lotrian J, Guern Y (1990) Polarization effects of seawater and underwater targets. Appl Opt 29:1689-1695

Chamberlain JW (1978) Theory of planetary atmospheres. (vol 22 of International Geophysics Series) Academic Press, New York

Chandrasekhar S (1950) Radiative transfer. Clarendon Press, Oxford

Chittka L (1996) Does bee color vision predate the evolution of flower color? Naturwissenschaften 83:136-138

Clarke D, Grainger JF (1971) Polarized light and optical measurement. Pergamon Press, Oxford

Coemans MAJM, Vos HJJ (1989) On the perception of polarized light by the homing pigeon, Columba livia L. In: Kulikowski JJ, Dickonson CM, Murray IJ (eds) Seeing contour and colour. Pergamon Press, Oxford, pp 632-638

Coemans MAJM, Vos HJJ, Nuboer JFW (1990) No evidence for polarization sensitivity in the pigeon. Naturwissenschaften 77:138-142

Coemans MAJM, Vos HJJ, Nuboer JFW (1994a) The orientation of the E-vector of linearly polarized light does not affect the behaviour of the pigeon Columba livia. J Exp Biol 191:107-123

Coemans MAJM, Vos HJJ, Nuboer JFW (1994b) The relation between celestial colour gradients and the position of the sun, with regard to the sun compass. Vis Res 34:1461-1470

Collett E (1994) Polarized light: fundamentals and applications. Marcel Dekker Inc, New York

Coombe PE, Srinivasan MV, Guy RG (1989) Are the large monopolar cells of the insect lamina on the optomotor pathway? J Comp Physiol A 166:23-35

Corbet PS (1999) Dragonflies: behaviour and ecology of Odonata. Harley Books, Martins, Great Horkesley, Colchester, Essex

Cornu MA (1884) Observations relatives a la couronne visible actuellement autour du Soleil. Compt Rend 99:488-493

Coughlin DJ, Hawryshyn CW (1995) A cellular basis for polarized-light vision in rainbow trout. J Comp Physiol A 176:261-272

Coulson KL (1974) The polarization of light in the environment: polarization by reflection from natural surfaces. In: Gehrels T (ed) Planets, stars and nebulae studied with photopolarimetry. Univ Arizona Press, Tucson, Arizona, pp 444-471

Coulson KL (1980) Characteristics of skylight at the zenith during twilight as indicators of atmospheric turbidity. I. Degree of polarization. Appl Opt 19:3469-3480

Coulson KL (1988) Polarization and intensity of light in the atmosphere. A Deepak Publishing, Hampton, Virginia, USA

Coulson KL, Dave JV, Sekera Z (1960) Tables related to radiation emerging from a planetary atmosphere with Rayleigh scattering. Univ California Press, Berkeley Los Angeles

Coulson KL, Whitehead VS, Campbell C (1986) Polarized views of the earth from orbital altitude. Proc Soc Photo-Optical Instrumentation Engin (SPIE) vol 637 (Ocean Optics VIII):35-41

Craig PC (1971) An analysis of the concept of lunar orientation in Orchestoidea corniculata (Amphipoda). Anim Behav 19:368-374

Cronin TW, Marshall J (2001) Parallel processing and image analysis in the eyes of mantis shrimps. Biol Bull 200:177-183

Cronin TW, Shashar N (2001) The linearly polarized light field in clear, tropical marine waters: spatial and temporal variation of light intensity, degree of polarization and e-vector angle. J Exp Biol 204:2461-2467

Cronin TW, Shashar N, Wolff L (1994) Portable imaging polarimeters. Proc 12th IAPR Int Conf Pattern Recogn. Jerusalem, Israel, October 9-13, 1994, pp 606-609

Curran PJ (1978) A photographic method for the recording of polarized visible light for soil surface moisture indications. Rem Sens Environ 7:305-322

Curran PJ (1979) The use of polarized panchromatic and false-color infrared film for the monitoring of soil surface moisture. Rem Sens Environ 8:249-266

Curran PJ (1982) Polarized visible light as an aid to vegetation classification. Rem Sens Environ 12:491-499

Czelnai R (1979) Introduction to meteorology I. Tankönyvkiadó, Budapest (in Hungarian)

Czihak G, Langer H, Ziegler H (1990) Biologie. Springer, Berlin, Heidelberg, New York

Dacke M, Nilsson DE, Warrant EJ, Blest AD, Land MF, O'Carroll DC (1999) Built-in polarizers form part of a compass organ in spiders. Nature 401:470-473

Dacke M, Nordström P, Scholtz CH, Warrant EJ (2002) A specialized dorsal rim area for polarized light detection in the compound eye of the scarab beetle Pachysoma striatum. J Comp Physiol A 188:211-216

Dahmen HJ (1991) Eye specialisation in waterstriders: an adaptation to life in a flat world. J Comp Physiol A 169:623-632

Dandekar BS, Turtle JP (1971) Day sky brightness and polarization during the total solar eclipse of 7 March 1970. Appl Opt 10:1220-1224

Danilevskii AS (1965) Photoperiodism and seasonal development of insects. Oliver and Boyd, Edinburgh London

Danthanarayana W (ed) (1986) Insect flight: dispersal and migration. Springer, Berlin Heidelberg New York

Daumer K (1963) Kontrastempfindlichkeit der Bienen für Weiss verschiedenen UV-Gehalts. Z vergl Physiol 46:336-350

Dave JV (1969) Scattering of visible light by large water spheres. Appl Opt 8:155-164

Delius JD, Perchard RJ, Emmerton J (1976) Polarized light discrimination by pigeons and an electroretinographic correlate. J Comp Physiol Psychol 90:560-571

Denton EJ, Rowe DM (1994) Reflective communication between fish, with special reference to the greater sand eel, Hyperoplus lanceolatus. Phil Tran Roy Soc Lond B 334:221-237

Derrien M, Farki B, Harang L, LeGléau H, Noyalet A, Pochic D, Sairouni A (1993) Automatic cloud detection applied to NOAA-11/AVHRR imagery. Rem Sens Environ 46:246-267

Deschamps PY, Bréon FM, Leroy M, Podaire A, Bricaud A, Buriez JC, Séze G (1994) The POLDER mission: instrument characteristics and scientific objectives. IEEE Trans Geosci Rem Sens 32:598-615

Descloitres J, Parol F, Buriez JC (1995) On the validity of the plane-parallel approximation for cloud reflectances as measured from POLDER during ASTEX. Ann Geophys 13:108-110

Deuzé JL, Bréon FM, Deschamps PY, Devaux C, Herman M (1993) Analysis of the POLDER (POLarization and Directionality of Earth's Reflectances) airbore instrument observations over land surfaces. Rem Sens Environ 45:137-154

Deuzé JL, Devaux C, Herman M, Santer R, Balois JY, Gonzalez L, Lecomte P, Verwaerde C (1989) Photopolarimetric observations of aerosols and clouds from balloon. Rem Sens Environ 29:93-109

Dollfus A (1961) Polarization studies of planets. In: The solar system. 3. Chap 9, Univ Chicago Press, Chicago

Dreher AW, Reiter K, Weinreb RN (1992) Spatially resolved birefringence of the retinal nerve fiber layer assessed with a retinal laser ellipsometer. Appl Opt 31:3730-3735

Drouin F (1995) The stereoscope and stereoscopic photography. London, 1894, a facsimile of the 1894 second edition, Reel 3-D Enterprises Historical 3-D Reprint Series, USA

Duelli P (1975) A fovea for e-vector orientation in the eye of Cataglyphis bicolor (Formicidae, Hymenoptera). J Comp Physiol 102:43-56

Duelli P, Wehner R (1973) The spectral sensitivity of polarized light orientation in Cataglyphis bicolor (Formicidae, Hymenoptera). J Comp Physiol 86:37-53

Dürst J (1982) Two colour photometry and polarimetry of the solar corona of 16 February 1980. Astronom Astrophys 112:241-250

Edmunds GF, Edmunds CH (1980) Predation, climate and mating of mayflies. In: Flannagan JF, Marshall KE (eds) Advances of ephemera biology. New York, pp 277-285

Edrich W, Helversen O von (1987) Polarized light orientation in honey bees: is time a component in sampling? Biol Cybern 56:89-96

Edrich W, Neumeyer C, Helversen O von (1979) "Anti-sun orientation" of bees with regard to a field of ultraviolet light. J Comp Physiol 134:151-157

Egan WG (1986) Proposed design of an imaging spectropolarimeter/photometer for remote sensing of earth resources. Opt Engin 25:1155-1159

Egan WG, Sidran M (1994) Polarimetric detection of land sediment runoff into the ocean using Space Shuttle imagery. Engineering and Laboratory Notes (Opt Soc Am) 17(3): S17-S19

Eggers A, Gewecke M (1993) The dorsal rim area of the compound eye and polarization vision in the desert locust (Schistocerca gregaria). In: Wiese K, Gribakin FG, Popov AV, Renninger G (eds) Sensory systems of arthropods. Birkhäuser, Basel, pp 101-109

Enright JT (1961) Lunar orientation of Orchestoidea corniculata Stout (Amphipoda). Biol Bull 120:148-156

Enright JT (1972) When the beachhopper looks at the moon: the moon-compass hypothesis. In: Galler SR, Schmidt-Koenig K, Jacobs GJ, Belleville RE (eds) Animal orientation and navigation. NASA SP-262, US Government Printing Office, Washington DC, pp 523-555

Fernando CH (1958) The colonization of small freshwater habitats by aquatic insects. 1. General discussion, methods and colonization in the aquatic Coleoptera. Ceylon J Sci (Biol Sci) 1(2):116-154

Fernando CH, Galbraith D (1973) Seasonality and dynamics of aquatic insects colonizing small habitats. Verhandl Internat Verein Limnol 18:1564-1575

Finzi L, Bustamante C, Garab G, Juang CB (1989) Direct observation of large chiral domains in chloroplast thylacoid membranes by differential polarization microscopy. Proc Natl Acad Sci USA 86:8748-8752

Fischer C (1992) Evolution des Schwarmfluges und Flugverhalten der Ephemeropteren. PhD thesis, 1992/3291, Friedrich Alexander Univ Erlangen-Nürnberg, p 171

Fitch BW, Walraven RL, Bradley DE (1984) Polarization of light reflected from grain crops during the heading growth stage. Rem Sens Environ 15:263-268

Fleishman LJ, Loew ER, Leal M (1993) Ultraviolet vision in lizards. Nature 365:397

Foote PG (1956) Icelandic Sólarsteinn and the medieval background. Arv 12:26-40

Frantsevich L, Govardovski V, Gribakin F, Nikolajev G, Pichka V, Polanovsky A, Shevchenko V, Zolotov V (1977) Astroorientation in Lethrus (Coleoptera, Scarabaeidae). J Comp Physiol A 121:253-271

Fraser FC (1936) The fauna of British India. Odonata vol 3, London, Taylor and Francis

Fraser RS (1968) Atmospheric neutral points over water. J Opt Soc Am 58:1029-1031

Fraser RS (1981) Atmospheric neutral points outside of the principal plane. Contrib Atmos Phys 54:286-297

Fratzer C, Dörr S, Neumeyer C (1994) Wavelength discrimination of the goldfish in the ultraviolet spectral range. Vis Res 34:1515-1520

Fränzel U (1985) Öko-ethologische Untersuchungen an Cordulegaster bidentatus Selys, 1843 (Insecta: Odonata) im Bonner Raum. Diploma thesis, Univ Bonn

Freake MJ (1999) Evidence for orientation using the e-vector direction of polarised light in the sleepy lizard Tiliqua rugosa. J Exp Biol 202:1159-1166

Frisch K von (1949) Die Polarisation des Himmelslichtes als orientierender Faktor bei den Tänzen der Bienen. Experientia 5:142-148

Frisch K von (1953) Aus dem Leben der Bienen (5th ed) Springer, Berlin Göttingen Heidelberg

Frisch K von (1965) Tanzsprache und Orientierung der Bienen. Springer, Berlin Heidelberg New York

Frisch K von (1967) The dance language and orientation of bees. Harvard Univ Press, Cambridge, Massachusetts (USA)

Frisch K von (1993) The dance language and orientation of bees (2nd ed, foreword by Seeley TD) Harvard Univ Press, Cambridge, Massachusetts (USA)

Frisch K von, Lindauer M (1954) Himmel und Erde in Konkurrenz bei der Orientierung der Bienen. Naturwissenschaften 41:245-253

Frisch K von, Lindauer M (1993) Aus dem Leben der Bienen (10th ed by Lindauer M) Springer, Berlin, Göttingen, Heidelberg

Gabryl JR, Cugnon P, Clette F (1998) Polarization observations and results of the 1998 February 26th solar corona. Contrib Astron Obs Skalnaté Pleso 28:216-223

Garab G, Pomozi I, Jávorfi T, Menczel L, Weiss G, Jürgens R (2003) Differential polarization laser scanning microscope. (submitted)

Gates DM (1980) Biophysical ecology. Springer, Berlin Heidelberg New York

Gál J, Horváth G, Barta A, Wehner R (2001a) Polarization of the moonlit clear night sky measured by full-sky imaging polarimetry at full moon: comparison of the polarization of moonlit and sunlit skies. J Geophys Res D 106:22647-22653

Gál J, Horváth G, Meyer-Rochow WB (2001b) Measurement of the reflection-polarization pattern of the flat water surface under a clear sky at sunset. Rem Sens Environ 76:103-111

Gál J, Horváth G, Meyer-Rochow VB, Wehner R (2001c) Polarization patterns of the summer sky and its neutral points measured by full-sky imaging polarimetry in Finnish Lapland north of the Arctic Circle. Proc Roy Soc Lond A 457:1385-1399

Gedzelman SD (1982) Rainbow brightness. Appl Opt 21:3032-3037

Gehrels T (ed) (1974) Planets, stars and nebulae studied with photopolarimetry. Univ Arizona Press, Tucson, Arizona

Gerharz R (1975) Self-polarization in refractive systems. Optik 43:471-485

Gerharz R (1976) Appearance of the atmospheric scatter field during a solar eclipse. J Geophys 42:163-167

Gerharz R (1977) Polarization of scattered horizon light in inclement weather. Arch Meteorol Geophys, Bioklimatologie Ser A 26:265-273

Glas HW van der (1975) Polarization induced colour patterns: a model of the perception of the polarized skylight by insects. I. Tests in choice experiments with running honey bees, Apis mellifera. Netherlands J Zool 25:476-505

Glas HW van der (1976) Polarization induced colour patterns: a model of the perception of the polarized skylight by insects. II. Experiments with direction trained dancing bees, Apis mellifera. Netherlands J Zool 26:383-413

Glas HW van der (1977) Models for unambiguous E-vector navigation in the bee. J Comp Physiol A 113:129-159

Glas HW van der (1980) Orientation of bees, Apis mellifera, to unpolarized colour patterns, simulating the polarized zenith skylight pattern. J Comp Physiol A 139:225-241

Goldsmith TH (1972) The natural history of invertebrate visual pigments. In: Dartnall HJA (ed) Handbook of sensory physiology. VII/1, Springer, Berlin Heidelberg New York, pp 685-719

Goldsmith TH (1994) Ultraviolet receptors and color vision: evolutionary implications and a dissonance of paradigms. Vis Res 34:1479-1487

Goloub P, Deuzé JL, Herman M, Fouquart Y (1994) Analysis of the POLDER polarization measurements performed over cloud covers. IEEE Trans Geosci Rem Sens 32:78-88

Gordon HR (1978) Removal of atmospheric effects from satellite imagery of the oceans. Appl Opt 17:1631-1636

Gordon HR, Wang M (1992) Surface-roughness considerations for atmospheric correction of ocean color sensors. I. The Rayleigh scattering component. Appl Opt 31:4247-4260

Grant L, (1987) Diffuse and specular characteristics of leaf reflectance. Rem Sens Environ 22:309-322

Grant L, Daughtry CST, Vanderbilt VC (1987a) Polarized and non-polarized leaf reflectances of Coleus blumei. Environ Exp Bot 27:139-145

Grant L, Daughtry CST, Vanderbilt VC (1987b) Variations in the polarized leaf reflectance of Sorghum bicolor. Rem Sens Environ 21:333-339

Grant L, Daughtry CST, Vanderbilt VC (1993) Polarized and specular reflectance variation with leaf surface features. Physiol Plantarum 88:1-9

Greenler RG (1980) Rainbows, halos and glories. Cambridge Univ Press, Cambridge, London

Grzimeks (1974) Tierleben. Sonderband: Verhaltensforschung. Kindler-Verlag, Zürich

Guenther RD (1990) Modern optics. Duke Univ, John Willey and Sons, Inc

Gupta VA, Kornfield V (1994) Controlling molecular order in "Hairy-rod" Langmuir Blodgett films: polarization modulation microscopy study. Science 265:940-942

Hamann B, Langer H (1980) Sehfarbstoffe im Auge des Wasserläufers Gerris lacustris L. Verhandl Dtsch Zool Ges, p 337

Hanlon RT, Maxwell MR, Shashar N, Loew ER, Boyle KL (1999) An ethogram of body patterning behavior in the biomedically and commercially valuable squid Loligo pealei off Cape Cod, Massachusetts. Biol Bull 197:49-62

Hanlon RT, Messenger JB (1996) Cephalopod behaviour. Cambridge Univ Press, Cambridge

Hannemann D, Raschke E (1974) Measurements of the elliptical polarization of sky radiation: preliminary results. In: Gehrels T (ed) Planets, stars and nebulae studied with photopolarimetry. Univ Arizona Press, Tucson, Arizona, pp 510-513

Hardie RC (1984) Properties of photoreceptors R7 and R8 in dorsal marginal ommatidia in the compound eyes of Musca and Calliphora. J Comp Physiol A 154:157-165

Hardie RC (1985) Functional organization of the fly retina. In: Autrum H et al (eds) Progress in sensory physiology. Springer, Berlin Heidelberg New York, vol 5, pp 2-79

Hardie RC, Franceschini N, McIntyre PD (1979) Electrophysiological analysis of fly retina. II. Spectral and polarisation sensitivity in R7 and R8. J Comp Physiol A 133:23-39

Harker JE (1992) Swarm behaviour and mate competition in mayflies (Ephemeroptera). J Zool Lond 228:571-587

Harkness R, Wehner R (1977) Cataglyphis. Endeavour (New Series) 1(3/4):115-121

Harris JM, Jefferson GI (eds) (1985) Rancho La Brea: treasures of the tar pits. Nat Hist Mus Los Angeles County, Los Angeles

Hassenstein B (1959) Optokinetische Wirksamkeit bewegter periodischer Muster nach Messungen am Rüsselkäfer Chlorophanus viridis. Z Naturforsch 14b:659-674

Hassenstein B, Reichardt W (1956) Systemtheoretische Analyse der Zeit-, Reihenfolgen- und Vorzeichenauswertung bei der Bewegungsperzeption des Rüsselkäfers Chlorophanus. Z Naturforsch 11b:513-524

Hawryshyn CW (1992) Polarization vision in fish. Am Sci 80:164-175

Hawryshyn CW, Arnold M. G., Bowering E. and Cole R. L. (1990) Spatial orientation of rainbow trout to plane-polarized light: the ontogeny of E-vector discrimination and spectral sensitivity characteristics. J Comp Physiol A 166:565-574

Hawryshyn CW, Bolger AE (1990) Spatial orientation of trout to partially polarized light. J Comp Physiol A 167:691-697

Hawryshyn CW, McFarland WN (1987) Cone photoreceptor mechanisms and the detection of polarized light in fish. J Comp Physiol A 160:459-465

Heisenberg M (1972) Comparative behavioral studies on two visual mutants of Drosophila. J Comp Physiol 80:119-136

Helbig AJ (1990) Depolarization of natural skylight disrupts orientation of an avian nocturnal migrant. Experientia 46:755-758

Helbig AJ (1991) Experimental and analytical techniques used in bird orientation research. In: Berthold P (ed) Orientation in birds. Birkhäuser, Basel Boston Berlin, pp 270-306

Helbig AJ, Wiltschko W (1989) The skylight polarization patterns at dusk affect the orientation behaviour of blackcaps, Sylvia atricapilla. Naturwissenschaften 76:227-229

Helversen O von, Edrich W (1974) Der Polarisationsempfänger im Bienenauge: ein Ultraviolettrezepor. J Comp Physiol 94:33-47

Henderson ST (1970) Daylight and its spectrum. American Elsevier, New York

Herman M, Balois JY, Gonzalez L, Lecomte P, Lenoble J, Santer R, Verwaerde C (1986) Stratospheric aerosol observations from a balloon-borne polarimetric experiment. Appl Opt 25:3573-3584

Herman M, Deuzé JL, Devaux C, Goloub P, Bréon FM, Tanré D (1997) Remote sensing of aerosols over land surfaces including polarization measurements and application to POLDER measurements. J Geophys Res D 102:17039-17049

Herzmann D, Labhart T (1989) Spectral sensitivity and absolute threshold of polarization vision in crickets: a behavioral study. J Comp Physiol A 165:315-319

Hess P (1939) Die spektrale Energieverteilung der Himmelsstrahlung. Gerlands Beitr Geophys 55:204-220

Holzworth GC, Rao CR (1965) Studies of skylight polarization. J Opt Soc Am 55:403-408

Horridge GA (1976) The ommatidium of the dorsal eye of Cloeon as a specialization for photoreisomerization. Proc Roy Soc Lond B 193:17-29

Horridge GA, Marcelja L, Jahnke R, Matic T (1983) Single electrode studies on the retina of the butterfly Papilio. J Comp Physiol A 150:270-294

Horridge GA, McLean M (1978) The dorsal eye of the mayfly Atalophlebia (Ephemeroptera). Proc Roy Soc Lond B 200:137-150

Horváth G (1993) Computational Visual Optics. Theoretical Physiologic Optical Study of the Optical Environment and Visual System of Animals. Postdoctoral dissertation to take the degree "candidate for biophysical science" awarded by the Hungarian Academy of Sciences, Budapest, pp 1-256

Horváth G (1995a) Reflection-polarization patterns at flat water surfaces and their relevance for insect polarization vision. J Theor Biol 175:27-37

Horváth G (1995b) How do water insects find their aquatic habitat? World of Nature (Természet Világa special issue) 125:44-49

Horváth G, Barta A, Gál J, Suhai B, Haiman O (2002a) Ground-based full-sky imaging polarimetry of rapidly changing skies and its use for polarimetric cloud detection. Appl Opt 41:543-559

Horváth G, Bernáth B, Molnár G (1998a) Dragonflies find crude oil visually more attractive than water: multiple-choice experiments on dragonfly polarotaxis. Naturwissenschaften 85:292-297

Horváth G, Bernáth B, Suhai B, Barta A, Wehner R (2002b) First observation of the fourth neutral polarization point in the atmosphere. J Opt Soc Am A 19:2085-2099

Horváth G, Gál J, Labhart T, Wehner R (2002c) Does reflection polarization by plants influence colour perception in insects? Polarimetric measurements applied to a polarization-sensitive model retina of Papilio butterflies. J Exp Biol 205:3281-3298

Horváth G, Gál J, Pomozi I, Kriska G, Wehner R (2001) Polarized glance at the sky during a total solar eclipse: the peculiar polarization patterns of the sky-dome and the solar corona on 11 August 1999. Fizikai Szemle (Physical Review) 51:229-238 (in Hungarian)

Horváth G, Gál J, Pomozi I, Wehner R (1998b) Polarization portrait of the Arago point: video-polarimetric imaging of the neutral points of skylight polarization. Naturwissenschaften 85:333-339

Horváth G, Gál J, Wehner R (1997) Why are water-seeking insects not attracted by mirages? The polarization pattern of mirages. Naturwissenschaften 84:300-303 [Erratum 85:90 (1998)]

Horváth G, Pomozi I (1997) How celestial polarization changes due to reflection from the deflector panels used in deflector loft and mirror experiments studying avian navigation. J Theor Biol 184:291-300

Horváth G, Pomozi I, Gál J (2003) Neutral points of skylight polarization observed during the total eclipse on 11 August 1999. Appl Opt 42:465-475

Horváth G, Varjú D (1991) On the structure of the aerial visual field of aquatic animals distorted by refraction. Bull Math Biol 53:425-441

Horváth G, Varjú D (1995) Underwater refraction-polarization patterns of skylight perceived by aquatic animals through Snell's window of the flat water surface. Vis Res 35:1651-1666

Horváth G, Varjú D (1997) Polarization pattern of freshwater habitats recorded by video polarimetry in red, green and blue spectral ranges and its relevance for water detection by aquatic insects. J Exp Biol 200:1155-1163

Horváth G, Varjú D (2003) Polarized light in animal vision - polarization patterns in nature. Springer, Berlin Heidelberg New York

Horváth G, Wehner R (1999) Skylight polarization as perceived by desert ants and measured by video polarimetry. J Comp Physiol A 184:1-7 [Erratum 184:347-349 (1999)]

Horváth G, Zeil J (1996) Kuwait oil lakes as insect traps. Nature 379:303-304

Hulst HC van de (1952) Scattering in atmospheres. In: Kniper GP (ed) The atmosphere of the earth and planets. Univ Chicago Press, Chicago

Hulst HC van de (1981) Light scattering by small particles. John Wiley and Sons, Dover, New York

Ivanoff A (1974) Polarization measurements in the sea. In: Jerlov NG, Steemann-Nielsen E (eds) Optical aspects of oceanography. Academic Press, London, pp 151-175

Ivanoff A, Waterman TH (1958a) Elliptical polarization of submarine illumination. J Mar Res 16:255-282

Ivanoff A, Waterman TH (1958b) Factors, mainly depth and wavelength, affecting underwater polarized light. J Mar Res 16:283-307

Jelley JV (1989) Sea waves: their nature, behaviour, and practical importance. Endeavour (New Series) 13:148-156

Jerlov NG (1963) Optical oceanography. Ocean Mar Biol Ann Rev 1:89-114

Jerlov NG (1976) Marine optics. Elsevier, Amsterdam

Johnson GC (1969) Migration and dispersal of insects by flight. Methuen and Co, London

Jones BF, Fairney PT (1989) Recognition of shiny dielectric objects by analysing the polarization of reflected light. Image Vis Comp 7:253-258

Junger W (1991) Waterstriders (Gerris paludum F.) compensate for drift with a discontinuously working visual position servo. J Comp Physiol A 169:633-639

Junger W, Dahmen HJ (1991) Response to self-motion in waterstriders: visual discrimination between rotation and translation. J Comp Physiol A 169:641-646

Junger W, Varjú D (1990) Drift compensation and its sensory basis in waterstriders (Gerris paludum F.). J Comp Physiol A 167:441-446

Kaiser W (1974) The spectral sensitivity of the honeybees's optomotor walking response. J Comp Physiol 90:405-408

Kaiser W (1975) The relationship between movement detection and colour vision in insects. In: Horridge GA (ed) The compound eye and vision of insects. Clarendon Press, Oxford, pp 359-377

Kaiser W, Liske E (1974) Die optomotorischen Reaktionen von fixiert fliegenden Bienen bei Reizung mit Spektrallichtern. J Comp Physiol 89:391-408

Kalayjian ZK, Andreou AG, Wolff LB, Sheppard N (1996) A polarization contrast retina that uses patterned iodine-doped PVA film. In: Proc ESSCIRC '96, Neuchatel, September 1996, pp 1181-1184

Kalmus H (1958) Responses of insects to polarized light in the presence of dark reflecting surfaces. Nature 182:1526-1527

Kalmus H (1959) Orientation of animals to polarized light. Nature 184:228-230

Kattawar GW (1994) Polarization of light in the ocean. In: Spinrad RW, Carder KL, Perry MJ (eds) Ocean optics. Oxford Univ Press, Oxford, pp 203-225

Kattawar GW, Adams CN (1989) Stokes vector calculations of the submarine light field in an atmosphere-ocean with scattering according to a Rayleigh phase matrix: effect of interface refractive index on radiance and polarization. Limnol Oceanogr 34:1453-1472

Kattawar GW, Plass GN, Guinn JA Jr (1973) Monte Carlo calculations of the polarization of radiation in the earth's atmosphere-ocean system. J Phys Oceanog 3:353-372

Kay QON, Daoud HS, Stirton CH (1981). Pigment distribution, light reflection and cell structure in petals. Bot J Linnean Soc 83:57-84

Kelber A (1999) Why 'false' colours are seen by butterflies. Nature 402:251

Kelber A, Thunell C, Arikawa K (2001) Polarisation-dependent colour vision in Papilio butterflies. J Exp Biol 204:2469-2480

Kennedy CH (1917) Notes on the life history and ecology of the dragonflies (Odonata) of central California and Nevada. Proc US Nat Mus 52:483

Kennedy CH (1938) The present status of work on the ecology of aquatic insects as shown by the work on the Odonata. Ohio J Sci 38:267

Kerfoot WB (1967) The lunar periodicity of Sphecodogastra texana, a nocturnal bee (Hymenoptera: Halictidae). Anim Behav 15:479-486

Khare V, Nussenzveig HM (1974) Theory of the rainbow. Phys Rev Lett 33:976-980

Kien J, Menzel R (1977) Chromatic properties in the optic lobes of the bee. J Comp Physiol 121:35-53

Kim M, Keller D, Bustamante C (1987) Differential polarization imaging. I. Theory. Biophys J 52:911-927

Kimball HH (1913) The effect of the atmospheric turbidity of 1912 on solar radiation intensities and skylight polarization. Bull Mt. Weather Observ 5:295-312

King RS, Wrubleski DA (1998) Spatial and diel availability of flying insects as potential duckling food in prairie wetlands. Wetlands 18:100-114

Kirschfeld K (1971) Aufnahme und Verarbeitung optischer Daten im Komplexauge von Insekten. Naturwissenschaften 58:201-209

Kirschfeld K (1973a) Optomotorische Reaktionen der Biene auf bewegte "Polarisations-Muster". Z Naturforsch 28c:329-338

Kirschfeld K (1973b) Vision of polarised light. In: Symp papers 4th int biophys cong, int union pure appl biophys, Acad Sci USSR, Pushchino, 19 zak 181, pp 289-296

Kirschfeld K (1973c) Das neurale Superpositionsauge. Fortschr Zool 21:229-257

Kirschfeld K, Reichardt W (1970) Optomotorische Versuche an Musca mit linear polarisiertem Licht. Z Naturforsch 25b:228

Kliger DS, Lewis JW, Randall CE (1990) Polarized light in optics and spectroscopy. Academic Press, San Diego, USA

Kocsis K, Hyttinen M, Helminen HJ, Aydelotte MB, Módis L (1998) Combination of digital image analysis and polarization microscopy: theoretical considerations and experimental data. Microscop Res Techn 43:511-517

Kondratyev KY, Buznikov AA, Pozdnyakov DV, Ivanyan GA, Lakhtanov GA, Orlov VM, Mikhailova SM (1974) Application of spectrometric and polarization techniques for remote sensing of oil on sea waters. Proc 9th Int Symp Rem Sens Environ, 15-19 April 1974, Ann Arbor, MI, USA, vol 3, pp 1793-1802

Kopal Z (1969) The moon. Dordrecht, Reidel, Holland

Korte R (1965) Durch polarisiertes Licht hervorgerufene Optomotorik bei Uca tangeri. Experientia 21:98

Koshikawa K, Shirai Y (1987) A model-based recognition of glossy objects using their polarimetric properties. Advances in Robotics vol 2, No 2

Kowalski K (1999) Il Pleistocene di Starunia. In: Pina G (ed) Storia naturale d'Europa - Lagerstaetten of Europe. Jaca Book SpA Servizio Lettori, Milano

Können GP (1985) Polarized light in nature. Cambridge Univ Press, Cambridge

Können GP (1986) Viewing our world with polarizing glasses. Endeavour (new series) 10(3):121-124

Können GP (1987) Skylight polarization during a total solar eclipse: a quantitative model. J Opt Soc Am A 4:601-608

Können GP (1992) Polarization in nature. In: Boerner WM, Brand H, Cram LA, Holm WA, Stein DE, Wiesbeck W, Keydel W, Giuli D, Gjessing DT, Molinet FA (eds) Direct and inverse methods in radar polarimetry. Dordrecht, Kluwer Acad Publ, The Netherlands, Part I, pp 33-44

Können GP, de Boer JH (1979) Polarized rainbow. Appl Opt 18:1961-1965

Kramer G (1950a) Orientierte Zugaktivität gekäfigter Singvögel. Naturwissenschaften 37:188

Kramer G (1950b) Weitere Analyse der Faktoren, welche die Zugaktivität des gekäfigten Vogels orientieren. Naturwissenschaften 37:377-378

Kramer G (1951) Eine neue Methode zur Erforschung der Zugorientierung und die bisher damit erzielten Ergebnisse. Proc 10th Ornithol Cong, Uppsala, pp 269-280

Kramer G, St Paul U von (1950) Stare (Sturnus vulgaris L.) lassen sich auf Himmelsrichtung dressieren. Naturwissenschaften 37:526-527

Kreithen ML, Keeton WT (1974) Detection of polarized light by the homing pigeon, Columba livia. J Comp Physiol 89:83-92

Kriska G, Horváth G, Andrikovics S (1998) Why do mayflies lay their eggs en masse on dry asphalt roads? Water-imitating polarized light reflected from asphalt attracts Ephemeroptera. J Exp Biol 201:2273-2286

Labhart T (1980) Specialized photoreceptors at the dorsal rim of the honeybee's compound eye: polarizational and angular sensitivity. J Comp Physiol A 141:19-30

Labhart T (1986) The electrophysiology of photoreceptors in different eye regions of the desert ant, Cataglyphis bicolor. J Comp Physiol A 158:1-7

Labhart T (1988) Polarization-opponent interneurons in the insect visual system. Nature 331:435-437

Labhart T (1996) How polarization-sensitive interneurones of crickets perform at low degrees of polarization. J Exp Biol 199:1467-1475

Labhart T (1999) How polarization-sensitive interneurones of crickets see the polarization pattern of the sky: a field study with an optoelectronic model neurone. J Exp Biol 202:757-770

Labhart T, Hodel B, Valenzuela I (1984) The physiology of the cricket's compound eye with particular reference to the anatomically specialized dorsal rim area. J Comp Physiol A 155:289-296

Labhart T, Meyer EP (1999) Detectors for polarized skylight in insects: a survey of ommatidial specializations in the dorsal rim area of the compound eye. Microsc Res Techn 47:368-379

Labhart T, Meyer EP, Schenker L (1992) Specialized ommatidia for polarization vision in the compound eye of cockchafers, Melolontha melolontha (Coleoptera, Scarabaeidae). Cell Tissue Res 268:419-429

LaFay H (1970) The Vikings. Natl Geogr 137:528-530

Lambrinos D, Maris M, Kobayashi H, Labhart T, Pfeifer R, Wehner R (1997) An autonomous agent navigating with a polarized light compass. Adapt Behav 6:131-161

Land MF (1993) Old twist in a new tale. Nature 363:581-582

Landin J (1968) Weather and diurnal periodicity of flight by Helophorus brevipalpis Bedel (Col. Hydrophilidae). Opusc Entomol 33:28-36

Landin J, Stark E (1973) On flight thresholds for temperature and wind velocity, 24-hour flight periodicity and migration of the water beetle Helophorus brevipalpis. ZOON Suppl 1:105-114

Lau D (1976) Reaktionen von Honigbienen (Apis mellifica) auf Polarisationsmuster an der Futterquelle. Zool Garten NF (Jena) 1:34-38

Lee RL Jr (1991) What are 'all the colors of the rainbow'? Appl Opt 30:3401-3407

Lee RL Jr (1998a) Digital imaging of clear-sky polarization. Appl Opt 37:1465-1476

Lee RL Jr (1998b) Mie theory, Airy theory, and the natural rainbow. Appl Opt 37:1506-1519

Lee RL Jr, Fraser AB (2001) The rainbow bridge: rainbows in art, myth, and science. Pennsylvania State Univ Press

Lehrer M, Srinivasan MV, Zhang SW (1990) Visual edge detection in the honeybee and its chromatic properties. Proc Roy Soc Lond B 238:321-330

Leroy M, Deuzé JL, Bréon FM, Hautecoeur O, Herman M, Buriez JC, Tanré D, Bouffiés S, Chazette P, Roujean JL (1997) Retrieval of atmospheric properties and surface bidirectional reflectances over land from POLDER/ADEOS. J Geophys Res D 102:17023-17037

Levorsen AI (1967) Geology of petroleum. (2nd ed, FAF Berry) Freeman, San Francisco, London

Lieke E (1984) Farbensehen bei Bienen: Wahrnehmung der Farbsättigung. PhD thesis, Freie Univ Berlin, Berlin

Liou KN (1980) An introduction to atmospheric radiation. Academic Press, San Diego, California

Liu Y, Voss KJ (1997) Polarized radiance distribution measurements of skylight. II. Experiment and data. Appl Opt 36:8753-8764

Loesel R, Homberg U (2001) Anatomy and physiology of neurons with processes in the accessory medulla of the cockroach Leucophaea maderae. J Comp Neurol 439:193-207

Loew ER, McFarland WN (1990) The visual environment. In: Douglas RH, Djamgoz MBA (eds) The visual system of fish. Chapman and Hall, London, pp 1-43

Loew ER, McFarland WN, Mills EL, Hunter D (1993) A chromatic action spectrum for planktonic predation by juvenile yellow perch, Perca flavescens. Can J Zool 71:384-386

Lock JA (ed) (1991) Light and color in the open air. Appl Opt (feature issue) 30:3381-3552

Lunau K, Maier EJ (1995) Innate colour preferences of flower visitors. J Comp Physiol A 177:1-19

Luria SM, Kinney JAS (1974) Linear polarising filters and underwater vision. Undersea Biomed Res 1:371-378

Lynch DK, Schwartz P (1991) Rainbows and fogbows. Appl Opt 30:3415-3420

Lythgoe JN (1979) The ecology of vision. Clarendon Press, Oxford

Lythgoe JN, Hemmings CC (1967) Polarized light and underwater vision. Nature 213:893-894

Malus ÉL (1809) Sur une propriété de la lumiére réfléctie par les corps diaphanes. Nouveau Bull d Sci, par la Soc Philomatique (Paris) 1:266-269; Mém de la Soc d'Arcueil, vol 2

Marshall NJ (1988) A unique colour and polarization vision system in mantis shrimps. Nature 333:557-560

Marshall NJ, Land MF, King CA, Cronin TW (1991a) The compound eyes of mantis shrimps (Crustacea, Hoplocarida, Stomatopoda). I. Compound eye structure: the detection of polarized light. Phil Trans Roy Soc Lond B 334:33-56

Marshall NJ, Land MF, King CA, Cronin TW (1991b) The compound eyes of mantis shrimps (Crustacea, Hoplocarida, Stomatopoda). II. Coloured pigments in the eyes of stomatopod crustaceans: polychromatic vision by serial and lateral filtering. Phil Trans Roy Soc Lond B 334:57-84

Martens A (1996) Die Federlibellen Europas. Westarp Wissenschaften, Magedeburg

Mazokhin-Porshnyakov GA (1969) Insect Vision. Plenum Press, New York

McCann GD, Arnett DW (1972) Spectral and polarization sensitivity of the dipteran visual system. J Gen Physiol 59:534-558

McFarland WN, Munz FW (1975) Part III: the evolution of photopic visual pigments in fishes. Vis Res 15:1071-1080

McGrath WH (1991) The stars look down. Navig News 3:15

Meyer HW (1970) Reizwechselfrequenz und Auslösung des Beutefangs beim Bachwasserläufer (Velia caprai). Naturwissenschaften 57:313

Meyer HW (1971) Visuelle Schlüsselreize für die Auslösung der Beutefanghandlung beim Bachwasserläufer Velia caprai (Hemiptera, Heteroptera). I. Untersuchung der räumlichen und zeitlichen Reizparameter mit formverschiedenen Attrappen. Z vergl Physiol 72:260-297

Miller L (1925) The birds of Rancho La Brea. Carnegee Inst Washington, Wash DC, USA

Miller RE, Fastie WG (1972) Skylight intensity, polarization and airglow measurements during the total solar eclipse of 30 May 1965. J Atmos Terrest Phys 34:1541-1546

Minnaert M (1940) Light and colour in the open air. G Bell and Sons, London

Mischke U (1984) The stimulus efficiency of intensity contrast, spectral contrast and polarization contrast in the optomotorics of Pachnoda marginata (Coleoptera: cetoniinae). In: Varjú D, Schnitzler HU (eds) Localization and orientation in biology and engineering. Springer, Berlin Heidelberg, pp 156-159

Mizera F, Bernáth B, Kriska G, Horváth G (2001) Stereo videopolarimetry: measuring and visualizing polarization patterns in three dimensions. J Imag Sci Technol 45:393-399

Mobbs SD (1979) Theory of the rainbow. J Opt Soc Am 69:089-1092

Mobley CD (1994) Light and water. Academic Press, San Diego, USA

Moore FR (1982) Sunset and the orientation of a nocturnal bird migrant: a mirror experiment. Behav Ecol Sociobiol 10:153-155

Moore FR (1985) Integration of environmental stimuli in the migratory orientation of the Savannah sparrow (Passerculus sandwichensis). Anim Behav 33:657-663

Moore FR, Phillips JB (1988) Sunset, skylight polarization and the migratory orientation of yellow-rumped warblers, Dendroica coronata. Anim Behav 36:1770-1778

Moore JG, Rao CRN (1966) Polarization of the daytime sky during the total solar eclipse of 30 May 1965. Annal Geophys 22:147-150

Módis L (1991) Organization of the extracellular matrix: polarization microscopic approach. Boca Raton, FL, CRC Press

Muller HRA (1937) Een zonderlinge vergissing van Copera marginipes. De Troopische Natuur 26:95

Munk O (1970) On the occurrence and significance of horizontal band-shaped retinal areas in teleosts. Vidensk Medd Dan Naturhist Foren 133:85-120

Nagel MR, Quenzel H, Kweta W, Wendling R (1978) Daylight illumination: color-contrast tables for full-form objects. Academic Press, New York

Neuberger H (1950) Arago's neutral point: a neglected tool in meteorological research. Bull Am Meteorol Soc 31:119-125

Neumeyer C (1985) An ultraviolet receptor as a fourth receptor type in goldfish colour vision. Naturwissenschaften 72:162-163

Neville AC (1960) A list of Odonata from Ghana, with notes on their mating, flight, and resting sites. Proc Roy Entomol Soc Lond A 35:124

Newall HF (1906) Polarization phenomena in the solar corona 1905, Aug. 30. Month Not Roy Astronom Soc 66:475-481

Noordwijk MV (1980) Dragonfly behaviour over shining surfaces. Notul Odonatol 1:105

North JA, Duggin MJ (1997) Stokes vector imaging of the polarized sky-dome. Appl Opt 36:723-730

Novales Flamarique I, Browman HI (2000) Wavelength-dependent polarization orientation in Daphnia. J Comp Physiol A 186:1073-1087

Novales Flamarique I, Hawryshyn CW (1996) Retinal development and visual sensitivity of young Pacific sockeye salmon (Oncorhynchus nerka). J Exp Biol 199:869-882

Novales Flamarique I, Hawryshyn CW (1997a) Is the use of underwater polarized light by fish restricted to crepuscular time periods? Vis Res 37:975-989

Novales Flamarique I, Hawryshyn CW (1997b) No evidence of polarization sensitivity in freshwater sunfish from multi-unit optic nerve recordings. Vis Res 37:967-973

Novales Flamarique I, Hawryshyn CW, Hárosi FI (1998) Double-cone internal reflection as a basis for polarization detection in fish. J Opt Soc Am A 15:349-358

Novales Flamarique I, Hendry A, Hawryshyn CW (1992) The photic environment of a salmonid nursery lake. J Exp Biol 169:121-141

Nussenzveig HM (1979) Complex angular momentum theory of the rainbow and the glory. J Opt Soc Am 69:1068-1079

Papi F (1960) Orientation by night: the moon. Cold Spring Harbor Symp Quantit Biol 25:475-480

Papi F (1991) Olfactory navigation. In: Berthold P (ed) Orientation in birds. Birkhäuser, Basel Boston Berlin, pp 52-85

Papi F, Pardi L (1963) On the lunar orientation of sandhoppers (Amphipoda, Talitridae). Biol Bull 124:97-105

Parkyn DC, Hawryshyn CW (1993) Polarized-light sensitivity in rainbow trout (Oncorhynchus mykiss): chracterization from multi-unit responses in the optic nerve. J Comp Physiol A 172:493-500

Parkyn DC, Hawryshyn CW (2000) Spectral and ultraviolet-polarisation sensitivity in juvenile salmonids: a comparative analysis using electrophysiology. J Exp Biol 203:1173-1191

Pearce F (1995) Devastation in the desert. New Scientist 146 (No 1971):40-43

Pearce F (1998) Sunny side up. New Scientist 159 (No 2142):45-48

Pellicori SF (1971) Polarizing properties of pulverized materials with special reference to the lunar surface. Appl Opt 10:270-285

Pezzaniti JL, Chipman RA (1995) Mueller matrix imaging polarimetry. Opt Engin 34:1558-1568

Philipsborn A von, Labhart T (1990) A behavioural study of polarization vision in the fly, Musca domestica. J Comp Physiol A 167:737-743

Phillips JB, Waldvogel JA (1982) Reflected light cues generate the short-term deflector-loft effect. In: Papi F, Wallraff HG (eds) Avian navigation. Springer, Berlin Heidelberg, pp 190-202

Phillips JB, Waldvogel JA (1988) Celestial polarized light patterns as a calibration reference for sun compass of homing pigeons. J Theor Biol 131:55-67

Pilcher CWT, Sexton DB (1993) Effects of the Gulf War oil spills and well-head fires on the avifauna and environment of Kuwait. Sandgrouse 15:6-17

Piltschikoff N (1906) Sur la polarisation du ciel pendant les éclipses du soleil. C. R. Acad. Sci. Paris 142:1449

Plass GN, Kattawar GW (1970) Polarization of the radiation reflected and transmitted by the earth's atmosphere. Appl Opt 9:1122-1130

Pomozi I (2002) Polarization patterns measured by wide and narrow field-of-view imaging polarimetry with atmospheric optical and biological applications. PhD thesis, Eötvös Univ, Dept Biol Phys, Biooptics Lab, Budapest, p 103 (supervisor: Horváth G) (in Hungarian)

Pomozi I, Gál J, Horváth G, Wehner R (2001a) Fine structure of the celestial polarization pattern and its temporal change during the total solar eclipse of 11 August 1999. Rem Sens Environ 76:181-201

Pomozi I, Horváth G, Wehner R (2001b) How the clear-sky angle of polarization pattern continues underneath clouds: full-sky measurements and implications for animal orientation. J Exp Biol 204:2933-2942

Pomozi I, Jávorfi T, Menczel L, Garab G (2003) Birefringence mapping of magnetically oriented chloroplasts, determined by a differential polarization laser scanning microscope. Biophys J (submitted)

Popham EJ (1964) The migration of aquatic bugs with special reference to the Corixidae (Hemiptera Heteroptera). Arch Hydrobiol 60:450-496

Povel H (1995) Imaging Stokes polarimetry with modulators and charge coupled-device image sensors. Opt Engin 34:1870-1878

Priestly EB, Wojtowicz PJ, Sheng P (1975) Introduction to liquid crystals. Plenum Press, New York

Prosch T, Hennings D, Raschke E (1983) Video polarimetry: a new imaging technique in atmospheric science. Appl Opt 22:1360-1363

Przyrembel C, Keller B, Neumeyer C (1995) Trichromatic colour vision in the salamander (Salamandra salamandra). J Comp Physiol A 176:575-586

Puschnig R (1926) Albanische Libellen. Konowia 5:33, 113, 208, 313

Ramskou T (1967) Solstenen. Skalk 2:16-17

Ramskou T (1969) Solstenen. Primitiv Navigation I Norden for Kompasset. Kobenhavn, Rhodos, pp 1-96

Rao NCR (1969) Balloon measurements of the polarization of the light diffusely reflected by the earth's atmosphere. Planet Space Sci 17:1307-1309

Rao CRN, Takashima T, Moore JG (1972) Polarimetry of the daytime sky during solar eclipses. J Atmos Terrest Phys 34:573-576

Robinson PC, Bradbury S (1992) Qualitative polarized-light microscopy. Oxford Sci Publ

Roslund C (1989) Sun tables of Star-Oddi in the Icelandic sagas. In: Aveni AF (ed) World archaeoastronomy. Cambridge Univ Press, Cambridge

Roslund C, Beckman C (1994) Disputing Viking navigation by polarized skylight. Appl Opt 33:4754-4755

Rossel S, Wehner R (1984) Celestial orientation in bees: the use of spectral cues. J Comp Physiol A 155:605-613

Rowe MP, Pugh EN Jr, Tyo JS, Engheta N (1995) Polarization difference imaging: a biologically inspired technique for observation through scattering media. Opt Lett 20:608-610

Rozenberg GV (1966) Twilight: a study in atmospheric optics. Plenum Press, New York

Sandberg R (1991) Sunset orientation of robins, Erithacus rubecula, with different fields of sky vision. Behav Ecol Sociobiol 28:77-83

Santschi F (1911) Observations et remarques critiques sur le mécanisme de l'orientation chez les fourmis. Rev Suisse Zool 19:303-338

Santschi F (1923) L'orientation sidérale des fourmis, et quelques considérations sur leurs différentes possibilités d'orientation. I. Classification des diverses possibilities d'orientation chez les fourmis. Mém Soc Vaudoise Sci Nat 4:137-175

Sarto AW, Woldemar CM, Vanderbilt VC (1989) Polarized light angle reflectance instrument. I. Polarized incidence. SPIE 1166:220-230

Sassen K (1979) Angular scattering and rainbow formation in pendant drops. J Opt Soc Am 69:1083-1089

Saunders DS (1981) Insect photoperiodism. In: Handbook of behavioral neurobiology (J Aschoff, ed) Plenum, New York

Saunders RW (1986) An automated scheme for the removal of cloud contamination from AVHRR radiances over Western Europe. Int J Rem Sens 7:867-886

Saunders RW, Kriebel KT (1988) An improved method for detecting clear sky and cloudy radiances from AVHRR data. Int J Rem Sens 9:123-150

Savolainen E (1978) Swarming in Ephemeroptera: the mechanism of swarming and the effects of illumination and weather. Ann Zool Fennici 15:17-52

Schaerer S, Neumeyer C (1994) Motion perception in goldfish is "color blind". In: Elsner N, Breer H (eds) Proc 22nd Göttingen Neurobiol Conf. G Thieme-Verlag, Stuttgart, vol II, p 484

Schenck H (1957) On the focusing of sunlight by ocean waves. J Opt Soc Am 47:653-657

Schmidt-Koenig K (1979) Avian orientation and navigation. Academic Press, London

Schmidt-Koenig K, Ganzhorn JU, Ranvaud R (1991) The sun compass. In: Berthold P (ed) Orientation in birds. Birkhäuser, Basel Boston Berlin, pp 1-15

Schnall U (1975) Navigation der Wikinger. Schr Dtsch Schiffahrtsmuseums 6:92-115

Schneider L, Langer H (1969) Die Struktur des Rhabdoms im "Doppelauge" des Wasserläufers Gerris lacustris. Z Zellforsch 99:538-559

Schwind R (1978) Visual system of Notonecta glauca: a neuron sensitive to movement in the binocular visual field. J Comp Physiol A 123:315-328

Schwind R (1980) Geometrical optics of the Notonecta eye: adaptations to optical environment and way of life. J Comp Physiol A 140:59-68

Schwind R (1983a) A polarization-sensitive response of the flying water bug Notonecta glauca to UV light. J Comp Physiol 150:87-91

Schwind R (1983b) Zonation of the optical environment and zonation in the rhabdom structure within the eye of the backswimmer, Notonecta glauca. Cell Tissue Res 232:53-63

Schwind R (1984a) Evidence for true polarization vision based on a two-channel analyser system in the eye of the water bug, Notonecta glauca. J Comp Physiol A 154:53-57

Schwind R (1984b) The plunge reaction of the backswimmer Notonecta glauca. J Comp Physiol A 155:319-321

Schwind R (1985a) A further proof of polarization vision of Notonecta glauca and a note on threshold intensity for eliciting the plunge reaction. Experientia 41:466-467

Schwind R (1985b) Sehen unter und über Wasser, Sehen von Wasser. Naturwissenschaften 72:343-352

Schwind R (1991) Polarization vision in water insects and insects living on a moist substrate. J Comp Physiol A 169:531-540

Schwind R (1995) Spectral regions in which aquatic insects see reflected polarized light. J Comp Physiol A 177:439-448

Schwind R (1999) Daphnia pulex swims towards the most strongly polarized light - a response that leads to 'shore flight'. J Exp Biol 202:3631-3635

Schwind R, Horváth G (1993) Reflection-polarization pattern at water surfaces and correction of a common representation of the polarization pattern of the sky. Naturwissenschaften 80:82-83

Seitz G (1969) Polarisationsoptische Untersuchungen am Auge von Calliphora erythrocephala Meig. Z Zellforsch 93:525-529

Sekera Z (1956) Recent developments in the study of the polarization of skylight. In: Landsberg HE (ed) Advances in geophysics. Academic Press, New York, vol 3, pp 43-104

Sekera Z (1957a) Light scattering in the atmosphere and the polarization of skylight. J Opt Soc Am 47:484-490

Sekera Z (1957b) Polarization of skylight. In: Flügge S (ed) Handbuch der Physik/Encyclopedia of Physics. Springer, Berlin Göttingen Heidelberg, vol 48, pp 288-328

Seliger HH, Lall AB, Biggley WH (1994) Blue through UV polarization sensitivities in insects: optimizations for the range of atmospheric polarization conditions. J Comp Physiol A 175:475-486

Sharp WE, Silverman SM, Lloyd JWF (1971) Summary of sky brightness measurements during eclipses of the sun. Appl Opt 10:1207-1210

Shashar N (1995) UV vision by marine animals: mainly questions. In: Ultraviolet Radiation and Coral Reefs (D Gulko, PL Jokiel, eds.) HIMB Techn Rep 41:201-206

Shashar N, Borst DT, Ament SA, Saidel WM, Smolowitz RM, Hanlon RT (2001) Polarization reflecting iridophores in the arms of the squid Loligo pealeii. Biol Bull 201:267-268

Shashar N, Cronin TW, Johnson G, Wolff LB (1995a) Portable imaging polarized light analyzer. Proc Soc Photo-Optical Instrumentation Engineers (SPIE) (9th Meet Opt Engin Israel) 2426:28-35

Shashar N, Cronin TW, Johnson G, Wolff LB (1995b) Designs for submersible imaging polarimeters. In: Gulko D, Jokiel PL (eds) Ultraviolet radiation and coral reefs. HIMB Techn Rep 41:213-218

Shashar N, Cronin TW, Wolff LB, Condon MA (1998) The polarization of light in a tropical rain forest. Biotropica 30:275-285

Shashar N, Rutledge PS, Cronin TW (1996) Polarization vision in cuttlefish. A concealed communication channel? J Exp Biol 199:2077-2084

Shaw GE (1975) Sky brightness and polarization during the 1973 African eclipse. Appl Opt 14:388-394

Shaw JA (1999) Degree of linear polarization in spectral radiances from water-viewing infrared polarimeters. Appl Opt 38:3157-3165

Shaw SR (1967) Simultaneous recording from two cells in the locust retina. Z vergl Physiol 55:183-194

Shul'gin IA, Moldau KA (1964) On coefficients of brightness of leaves in nature and polarized light. Dokl Akad Nauk SSR Bot Sci Sect (English translation) 162:99-101

Shurcliff WA (1962) Polarized light: production and use. Harvard Univ Press, Cambridge, Massachusetts, USA

Sivak JG, Mandelman T (1982) Chromatic dispersion of the ocular media. Vis Res 22:997-1003

Sivaraman KR, Jayachandran M, Scaria KK, Babu GSD, Bagare SP, Jayarajan AP (1984) Brightness, polarization and electron density of the solar corona of 1980 February 16. J Astrophys Astron 5:149-158

Skrzipek KH, Skrzipek H (1974) Die spektrale Transmission und die optische Aktivität des dioptrischen Apparates der Honigbiene (Apis mellifera). Experientia 30:314-315

Smola U, Meffert P (1978) A single UV-receptor in the eye of Calliphora erythrocephala. J Comp Physiol 103:353-357

Soret MJL (1888) Influence des surfaces d'eau sur la polarisation atmospherique et observation de deux points neutres a droite et a gauche de Soleil. Compt Rend 107:867-870

Southwood TRE (1966) Ecological methods. Chapman and Hall, London

Speck M, Labhart T (2001) Carotinoid deprivation and rhodopsin alignment in R1-6 photoreceptors of Drosophila melanogaster. In: Elsner N, Kreutzberg GW (eds) Proc 28th Göttingen Neurobiol Conf. Thieme, Stuttgart, p 514

Srinivasan MV, Guy RG (1990) Spectral properties of movement perception in the dronefly Eristalis. J Comp Physiol A 166:287-295

Steiner H (1948) Die Bindung der Hochmoorlibelle Leucorrhinia dubia Vand. an ihren Biotop. Zool Jhrb, Systematik 78:65-96

Sternberg K (1990) Autökologie von sechs Libellenarten der Moore und Hochmoore des Schwarzwaldes und Ursachen ihrer Moorbindung. PhD thesis, Univ Freiburg, Freiburg, Germany

Stevani CV, de Faria DLA, Porto JS, Trindade DJ, Bechara EJH (2000a) Mechanism of automotive clearcoat damage by dragonfly eggs investigated by surface enhanced Raman scattering. Polym Degrad Stabil 68:61-66

Stevani CV, Liria CW, Miranda MTM, Bechara EJH (2001) Cysteic acid is the chemical mediator of automotive clearcoat damage promoted by dragonfly eggs. J Appl Polym Sci 81:1549-1554

Stevani CV, Porto JS, Trindade DJ, Bechara EJH (2000b) Automotive clearcoat damage due to oviposition of dragonflies. J Appl Polym Sci 75:1632-1639

Stockhammer K (1956) Zur Wahrnehmung der Schwingungsrichtung linear polarisierten Lichtes bei Insekten. Z vergl Physiol 38:30-83

Stockhammer K (1959) Die Orientierung nach der Schwingungsrichtung linear polarisierten Lichtes und ihre sinnesphysiologischen Grundlagen. Ergebn Biol 21:23-56

Stokes GG (1852) On the composition and resolution of streams of polarized light from different sources. Trans Cambr Phil Soc 9:233-258

Strutt JW (Lord Rayleigh) (1871) On the light from the sky, its polarisation and colour. Phil Magaz 41:107-120, 274-279

Timofeeva VA (1961) On the problem of polarization of light in turbid media. Izvestiya Akad Nauk SSSR, Geophysics 5:766-774

Timofeeva VA (1962) Spatial distribution of the degree of polarization of natural light in the sea. Izvestiya Akad Nauk SSSR, Geophysics 6:1843-1851

Timofeeva VA (1969) Plane of vibrations of polarized light in turbid media. Izvestiya Akad Nauk SSSR, Atmospheric and Oceanic Physics 5:603-607

Timofeeva VA (1974) Optics of turbid waters - results of laboratory studies. In: Jerlov N, Steeman-Nielsen E (eds) Optical aspects of oceanography. Academic Press, New York, pp 177-218

Tinbergen J, Abeln RG (1983) Spectral sensitivity of the landing blowfly. J Comp Physiol A 150:319-328

Tovée MJ (1995) Ultra-violet photoreceptors in the animal kingdom: their distribution and function. Trends Ecol Evol 10:455-460

Tricker RAR (1970) Introduction to meteorological optics. Elsevier Publ Co, New York

Tyler JE (1963) Estimation of per cent polarization in deep oceanic water. J Mar Res 21:102-109

Ugolini A, Melis C, Innocenti R (1999a) Moon orientation in adult and young sandhoppers. J Comp Physiol A 184:9-12

Ugolini A, Melis C, Innocenti R, Tiribilli B, Castellini C (1999b) Moon and sun compasses in sandhoppers rely on two separate chronometric mechanisms. Proc Roy Soc Lond B 266:749-752

Vanderbilt VC, Grant L (1985a) Polarization photometer to measure bidirection reflectance factor R(55^o, 0^o, 55^o, 180^o) of leaves. Opt Engin 25:566-571

Vanderbilt VC, Grant L (1985b) Plant canopy specular reflectance model. IEEE Trans Geosci Rem Sens 23:722-730

Vanderbilt VC, Grant L, Daughtry CST (1985a) Polarization of light scattered by vegetation. Proc IEEE 73:1012-1024

Vanderbilt VC, Grant L, Biehl LL, Robinson BF (1985b) Specular, diffuse and polarized light scattered by wheat canopies. Appl Opt 24:2408-2418

Varjú D (1959) Optomotorische Reaktionen auf die Bewegung periodischer Helligkeitsmuster: anwendung der Systemtheorie auf Experimente am Rüsselkäfer Chlorophanus viridis. Z Naturforsch 14b:724-735

Varjú D, Horváth G (1989) Looking into the water with a facet eye. Biol Cybern 62:157-165

Vebaek CL, Thirslund S (1992) The Viking compass. Humlebaek, Denmark

Verbelen JP, Kerstens S (2000) Polarization confocal microscopy and Congo Red fluorescence: a simple and rapid method to determine the mean cellulose fibril orientation in plants. J Microscopy 198:101-107

Vos HJJ, Coemans MAJM, Nuboer JFW (1995) No evidence for polarization sensitivity in the pigeon electroretinogram. J Exp Biol 198:325-335

Voss KJ, Liu Y (1997) Polarized radiance distribution measurements of skylight. I. System description and characterization. Appl Opt 36:6083-6094

Vries HL de, Kuiper JW (1958) Optics of the insect eye. Ann NY Acad Sci 74:196-303

Waack FG (1985) Stereo photography. Germany

Walcott C, Michener M (1971) Sun navigation in homing pigeons: attempts to shift sun coordinates. J Exp Biol 54:291-316

Waldvogel JA (1990) The bird's eye view. Am Scient 78:342-353

Walraven R (1977) Polarization imagery. In: Azzam RMA, Coffeen DL (eds) Optical polarimetry: instrumentation and applications. Proc Soc Photo-Opt Instrum Eng 112:164-167

Walraven RL (1981) Polarization imagery. Opt Engin 20:14-18

Wang M, Gordon HR (1993) Retrieval of the columnar aerosol phase function and single-scattering albedo from sky radiance over the ocean: simulations. Appl Opt 32:4598-4609

Wang RT, Hulst HC van de (1991) Rainbows: Mie computations and the Airy approximation. Appl Opt 30:106-117

Waterman TH (1954a) Polarization patterns in submarine illumination. Science 120:927-932

Waterman TH (1955) Polarization of scattered sunlight in deep water. Deep Sea Res 3: 426-434

Waterman TH (1981) Polarization sensitivity. In: Autrum H (ed) Handbook of sensory physiology. VII/6B Vision in invertebrates. Comparative physiology and evolution of vision in invertebrates B: invertebrate visual centers and behavior I, Springer, Berlin Heidelberg New York, pp 281-469

Waterman TH, Westell WE (1956) Quantitative effect of the sun's position on submarine light polarization. J Mar Res 15:149-169

Watson JAL (1992) Oviposition by exophytic dragonflies on vehicles. Notul Odonatol 3:137

Wehner R (1976) Polarized-light navigation by insects. Sci Am 235(7):106-115

Wehner R (1981) Spatial Vision in Arthropods. In: Autrum H (ed) Handbook of sensory physiology VII/6C Comparative physiology and evolution of vision in invertebrates C: Invertebrate visual centers and behavior II, Springer, Berlin Heidelberg New York, pp 287-616

Wehner R (1982) Himmelsnavigation bei Insekten. Neurophysiologie und Verhalten. Neujahrsbl Naturforsch Ges Zürich 184:1-132

Wehner R (1983) The perception of polarised light. In: Cosens DJ, Vince-Price D (eds) The biology of photoreception. Soc Exp Biol Symp 36, Cambridge Univ Press, Cambridge, London, pp 331-369

Wehner R (1984) Astronavigation in insects. Ann Rev Entomol 29:277-298

Wehner R (1989a) Neurobiology of polarization vision. Trends Neurosci 12:353-359

Wehner R (1989b) The hymenopteran skylight compass: matched filtering and parallel coding. J Exp Biol 146:63-85

Wehner R (1991) Visuelle Navigation: Kleinstgehirn-Strategien. Verhandlungen Deutschen Zool Gesellschaft 84:89-104

Wehner R (1992) Arthropods. In: Papi F (ed) Animal homing. Chapman and Hall, London, pp 45-144

Wehner R (1994a) The polarization-vision project: championing organismic biology. In: Schildberger K, Elsner N (eds) Neural basis of behavioural adaptations. Gustav Fischer Verlag, Stuttgart Jena New York, Fortschr Zool 39:103-143

Wehner R (1994b) Himmelsbild und Kompaßauge - Neurobiologie eines Navigationssystems. Verhandlungen der Deutschen Zoologischen Gesellschaft 87(2):9-37

Wehner R (1997) The ant's celestial compass system: spectral and polarization channels. In: Lehrer M (ed) Orientation and communication in arthropods. Birkhäuser, Basel, pp 145-185

Wehner R (1998) Der Himmelskompaß der Wüstenameisen. Spektrum Wissensch 1998 November:56-67

Wehner R (1999) Large-scale navigation: the insect case. In: Freksa C, Mark DM (eds) Spatial information theory: cognitive and computational foundations of geographic information science. Springer, Berlin Heidelberg, Lect Notes Computer Sci 1661:1-20

Wehner R (2001) Polarization vision - a uniform sensory capacity? J Exp Biol 204:2589-2596

Wehner R, Bernard GD (1993) Photoreceptor twist: a solution to the false-color problem. Proc Natl Acad Sci USA 90:4132-4135

Wehner R, Bernard GD, Geiger E (1975) Twisted and non-twisted rhabdoms and their significance for polarization detection in the bee. J Comp Physiol 104:225-245

Wehner R, Rossel S (1985) The bee's celestial compass - a case study in behavioural neurobiology. In: Hölldobler B, Lindauer M (eds) Experimental behavioral ecology and sociobiology. Gustav Fischer Verlag, Stuttgart, New York, Fortschr Zool 31:11-53

Wehner R, Strasser S (1985) The POL area of the honey bee's eye: behavioural evidence. Physiol Entomol 10:337-349

Wetzel RG (1975) Limnology. WB Saunders and Co, Philadelphia, USA

Whitehouse FC (1941) A guide to the study of dragonflies of Jamaica. Bull Inst Jamaica Sci Ser No 3, pp 1-69

Wildermuth H (1980) Die Libellen der Drumlinlandschaft im Zürcher Oberland. Vierteljahrsschr Naturf Ges Zürich 125:201-237

Wildermuth H (1992a) Habitate und Habitatwahl der Grossen Moosjungfer (Leucorrhinia pectorialis) Chap. 1825 (Odonata, Libellulidae). Z Ökol Natursch 1:3-22

Wildermuth H (1992b) Visual and tactile stimuli in choice of the oviposition substrates by the dragonfly Perithemis mooma Kirby, 1899 (Anisoptera: Libellulidae). Odonatologica 21:309-321

Wildermuth H (1993) Habitat selection and oviposition site recognition by the dragonfly Aeshna juncea (L.): an experimental approach in natural habitats (Anisoptera: Aeshnidae). Odonatologica 22:27-44

Wildermuth H (1994) Habitatselektion bei Libellen. Adv Odonatol 6:223-257

Wildermuth H (1998) Dragonflies recognize the water of rendezvous and oviposition sites by horizontally polarized light: a behavioural field test. Naturwissenschaften 85:297-302

Wildermuth H, Krebs A (1983) Sekundäre Kleingewässer als Libellenbiotope. Vierteljhrschr Naturforsch Ges Zürich 128:21-42

Wildermuth H, Krebs A (1987) Die Libellen der Region Winterthur. Mitteil Naturwiss Ges Winterthur 38:89-107

Wildermuth H, Spinner W (1991) Visual cues in oviposition site selection by Somatochlora arctica Zetterstedt (Anisoptera: Corduliidae). Odonatologica 20:357-367

Wilson EO (1971) Insect Societies. Harvard Univ Press, Cambridge, Massachusetts, USA

Wolf R, Gebhardt B, Gademann R, Heisenberg M (1980) Polarization sensitivity of course control in Drosophila melanogaster. J Comp Physiol A 139:177-191

Wolff LB (1990) Polarization-based material classification from specular reflection. IEEE Trans Pattern Anal Machine Intell 12:1059-1071

Wolff LB (1993) Polarization camera technology. Proc DARPA Image Understanding Works, April 1993, Washington DC, USA, pp 1031-1036

Wolff LB (1994) Polarization camera for computer vision with a beam splitter. J Opt Soc Am A 11:2935-2945

Wolff LB, Andreou AG (1995) Polarization camera sensors. Image Vision Comp 13:497-510

Wolff LB, Boult TE (1991) Constraining object features using a polarization reflectance model. IEEE Trans Pattern Analys Machine Intellig 13:635-657

Wolken JJ (1995) Light detectors, photoreceptors, and imaging systems in nature. Chap 13, Polarized light in nature: detection by animals. Oxford Univ Press, Oxford, New York

Wolstencroft RD, Brandt JC (1974) Multicolor polarimetry of the night sky. In: Gehrels T (ed) Planets, stars and nebulae studied with photopolarimetry. Univ Arizona Press, Tucson, Arizona, pp 768-780

Wyniger R (1955) Beobachtungen über die Eiablage von Libellula depressa (L.) (Odonata, Libellulidae). Mitt entomol Ges Basel NF5:62

YES (2001) Description of the TSI-990 Total Sky Imager, Yankee Environmental Systems, Inc., Airport Industrial Park, 101 Industrial Blvd., Turners Falls, MA 01376, USA, http://www.yesinc.com, e-mail: info@yesinc.com

Young AT (1982) Rayleigh scattering. Phys Today 35(1):42-48

Zalom FG, Grigarick AA, Way MO (1979) Seasonal and diel flight periodicities of rice field Hydrophilidae. Environm Entomol 8:938-943

Zalom FG, Grigarick AA, Way MO (1980) Diel flight periodicities of some Dytiscidae (Coleoptera) associated with California rice paddies. Ecol Entomol 5:183-187

Zufall F, Schmitt M, Menzel R (1989) Spectral and polarized light sensitivity of photoreceptors in the compound eye of the cricket (Gryllus bimaculatus). J Comp Physiol A 164:597-608

Zwick P (1990) Emergence, maturation and upstream oviposition flights of Plecoptera from Breitenbach, with notes on the adult phase as a possible control of stream insect populations. Hydrobiol 194:207-223